ISSN en trámite

volumen 55, número 2, octubre 2019

instituto de astronomía

unam

revista mexicana de astronomía y astrofísica

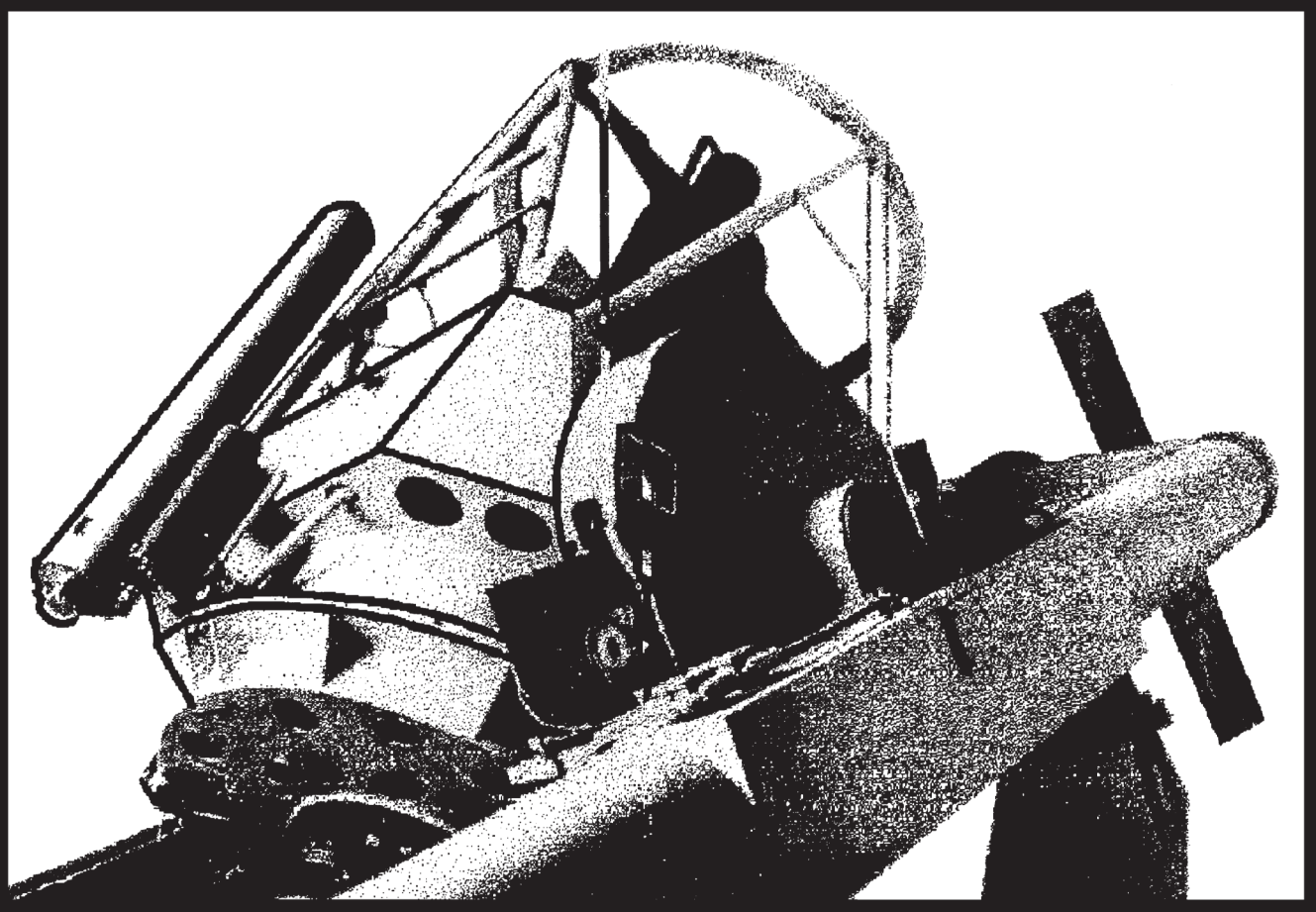

volumen 56
número 2
octubre 2020

revista mexicana de astronomía y astrofísica

Instituto de Astronomía
Universidad Nacional Autónoma de México

revista mexicana de astronomía y astrofísica

ISSN en trámite

URL de DOI: https://doi.org/10.22201/ia.01851101p.2019.55.02

rmaa@astro.unam.mx

http://www.astroscu.unam.mx/RMxAA/

La *RMxAA* aparece indexada en Current Contents, Science Citation Index, Astronomy and Astrophysics Abstracts, Physics Briefs, Publicaciones Científicas en América Latina, Astronomy and Astrophysics Monthly Index, PERIODICA, RedALyC, Latindex y SciELO.

Revista Mexicana de Astronomía y Astrofísica, volumen 55, número 2, octubre 2019, es una publicación semestral, editada y distribuida por el Instituto de Astronomía, UNAM, Circuito Exterior, Ciudad Universitaria, 04510, Alcaldía Coyoacán, Ciudad de México, Teléfono: 5556223906, Correo Electrónico: rmaa@astro.unam.mx, ISSN en trámite. Editora responsable: Christine Patricia Allen Armiño. Distribución: Bienes y Servicios del Instituto de Astronomía, UNAM. Impresa por Grupo Edición, S.A. de C.V., Xochicalco 619, Colonia Letrán Valle, 03650, Alcaldía Benito Juárez, Ciudad de México. Fecha de impresión: 27 de septiembre de 2019. Número de ejemplares impresos: 500 en papel Couché de 100 gramos los interiores y en cartulina Couché de 250 gramos los forros. Precio de la publicación: gratuito.

THREE SPECTROSCOPIC BINARIES IN THE BRIGHT STAR CATALOG SUPPLEMENT *C. D. Scarfe* 131

INTERSTELLAR ABSORPTION TOWARDS THE NOVAE V339 DEL AND V5668 SGR *D. Jack & K.-P. Schröder* 141

RELATIVISTIC BEAMING EFFECTS AND STRUCTURAL ASYMMETRIES IN HIGHLY ASYMMETRIC DOUBLE RADIO SOURCES *J. A. Alhassan, A. A. Ubachukwu, F. C. Odo, & C. C. Onuchukwu* 151

ENHANCED MASS LOSS RATES IN RED SUPERGIANTS AND THEIR IMPACT ON THE CIRCUMSTELLAR MEDIUM *L. Hernández-Cervantes, B. Pérez-Rendón, A. Santillán, G. García-Segura, & C. Rodríguez-Ibarra* 161

MINIMIZING FUEL CONSUMPTION IN ORBIT TRANSFERS USING UNIVERSAL VARIABLE AND PARTICLE SWARM OPTIMIZATION *L. M. Echeverry & Y. Villanueva* 177

THE ENVIRONMENTAL DEPENDENCE OF GALAXY AGE AND STELLAR MASS IN THE REDSHIFT REGION $0.6 \leq z \leq 0.75$ *Xin-Fa Deng* 185

ON THE NATURE OF THE HADS STAR V2455 CYG *J. H. Peña, A. Rentería, C. Villarreal, & D. S. Piña* 193

STUDY OF THE OPEN CLUSTER NGC 1528 THROUGH $uvby-\beta$ PHOTOELECTRIC PHOTOMETRY *J. H. Peña, J. Calderón, & D. S. Piña* 203

3D HYDRODYNAMIC NUMERICAL MODELS FOR NEBULAE AROUND RUNAWAY WOLF-RAYET STARS *J. Reyes-Iturbide, Pablo F. Velázquez, M. Rosado, E. Matías Schneiter, & I. Ramírez-Ballinas* 211

SOME REMARKS ON THE OPEN CLUSTER UPGREN 1 USING $uvby-\beta$ PHOTOELECTRIC PHOTOMETRY *J. H. Peña, A. Rentería, H. Huepa, & A. Pani* 221

GRAVITATIONAL WAVE ENHANCEMENT AS A TOOL TO DISTINGUISH DARK MATTER HALO PROFILES *S. Grijalva Castillo & C. Calcáneo-Roldán* 231

DYNAMICS OF CLUSTERS OF GALAXIES WITH EXTENDED $F(\chi)$ GRAVITY *T. Bernal, O. López-Corona, & S. Mendoza* 237

CONTENTS

METALLICITY GRADIENTS IN M 31, M 33, NGC 300 AND THE MILKY WAY USING ABUNDANCES OF DIFFERENT ELEMENTS
M. Peña & S. N. Flores-Durán 255

SUBSTRUCTURE FORMATION IN TIDAL STREAMS OF GALACTIC MINOR MERGERS
D. A. Noreña, J. C. Muñoz-Cuartas, L. F. Quiroga, & N. Libeskind 273

MILLIMETER AND FAR-IR STUDY OF THE IRDC SDC 341.232-0.268
M. M. Vazzano, C. E. Cappa, M. Rubio, V. Firpo, C. H. López-Caraballo, & N. U. Duronea 289

SEARCHING FOR MID-RANGE PLANAR ORBITS TO OBSERVE DEIMOS
M. P. O. Cavalca, A. F. B. A. Prado, V. M. Gomes, & D. M. Sanchez 305

CHAOS IN GROWING BAR MODELS
L. A. Caritá, I. Rodrigues, I. Puerari, & L. E. C. A. Schiavo 321

NGC 1261: A TIME-SERIES *VI* STUDY OF ITS VARIABLE STARS
A. Arellano Ferro, I. H. Bustos Fierro, J. H. Calderón, & J. A. Ahumada 337

A NEW METHOD FOR ACTIVELY TUNING FBG'S TO PARTICULAR INFRARED WAVELENGTHS FOR OH EMISSION LINES SUPPRESSION
R. Benítez-Álvarez, F. Martínez-Piñón, & V. G. Orlov 351

OPTICAM: A TRIPLE-CAMERA OPTICAL SYSTEM DESIGNED TO EXPLORE THE FASTEST TIMESCALES IN ASTRONOMY
A. Castro, D. Altamirano, R. Michel, P. Gandhi, J. V. Hernández Santisteban, J. Echevarría, C. Tejada, C. Knigge, G. Sierra, E. Colorado, J. Hernández-Landa, D. Whiter, M. Middleton, B. García, G. Guisa, & N. Castro Segura 363

EXTENSIVE ONLINE SHOCK MODEL DATABASE
A. Alarie & C. Morisset 377

AUTHOR INDEX 393

Revista Mexicana de Astronomía y Astrofísica, **55**, 131–139 (2019)

DOI: https://doi.org/10.22201/ia.01851101p.2019.55.02.01

THREE SPECTROSCOPIC BINARIES IN THE BRIGHT STAR CATALOG SUPPLEMENT

C. D. Scarfe[1,2]

Received November 28 2018; accepted February 28 2019

ABSTRACT

This paper presents spectroscopic orbits of three binaries, HD 121212, HD 148434 and HD 148912, with evolved primaries and periods of order a year, found in a survey of late-type stars listed in the Supplement to the Yale Bright Star Catalog. All the orbits were determined from observations made with the DAO 1.2-m telescope and coudé spectrograph. Observations were obtained using the radial velocity spectrometer until it was decommissioned in 2004, and since then using a CCD detector and cross-correlating the spectra with those of standard stars.

RESUMEN

Se presentan las órbitas espectroscópicas de tres binarias (HD 121212, HD 148434 y HD 148912) con primarias evolucionadas y períodos de cerca de un año, encontradas en el relevamiento de estrellas tardías listado en el suplemento al Yale Bright Star Catalog. Las órbitas se determinaron a partir de observaciones hechas en el telescopio de 1.2 m del DAO con el espectrógrafo coudé. Las observaciones se obtuvieron con el espectrómetro para velocidades radiales antes de su cancelación en 2004, y a partir de entonces con un detector CCD y mediante la correlación cruzada de los espectros con estrellas estándar.

Key Words: binaries:spectroscopic

1. INTRODUCTION

About thirty years ago the author began a program of observations of the radial velocities of late-type stars in the Supplement to the Yale Bright Star Catalog (Hoffleit et al. 1983), for which no radial velocity was listed in that publication. That program makes use of the coudé spectrograph of the Dominion Astrophysical Observatory's 1.22-m telescope, at a dispersion of 0.24 nm mm^{-1}. The three binaries whose orbits are presented here are among the first to be discovered in this program, in part due to their relatively short periods and consequent rapid changes in radial velocity.

2. BACKGROUND INFORMATION

2.1. *HD 121212*

HD 121212 (HIP 67803, CW CVn, $\alpha = 13^h52^m13^s$, $\delta = 33°47'12''$ [2000]) is to be found in the eastern part of Canes Venatici, following α CVn by almost exactly an hour at a closely similar declination. Its BV magnitude and colour were determined by *Hipparcos* and are listed in the Tycho-2 catalogue (Hog et al. 2000) as $V = 6.97$, $B-V = 1.49$, consistent with its MK type, K5 III.

The *Gaia* (2018) parallax of HD 121212 is $\pi = 2.31 \pm 0.05$ mas, which yields $M_v = -1.21 \pm 0.28$, in good agreement with its classification as a late K giant. *Gaia* also measured its proper motion components, which are -41.79 mas yr^{-1} in right ascension and -3.17 mas yr^{-1} in declination. Together with the parallax these yield the velocity of 71.5 km s^{-1} perpendicular to the line of sight.

HD 121212 was found by *Hipparcos* (ESA 1997) to be a semiregular variable star of type SRD. However, its amplitude is $0^m.25$, much larger than that of most variables of that type (Adelman 2000). Over the years it did seem to the author to vary in brightness to a modest extent, but this seemed to be uncorrelated with the variation in radial velocity.

[1]University of Victoria, BC, Canada.
[2]Guest worker, Dominion Astrophysical Observatory, Herzberg Institute of Astrophysics, National Research Council of Canada.

TABLE 1

STANDARD STARS USED FOR CROSS-CORRELATION

Standard Star	Spectral Type	*R.V.* km s^{-1}	Binaries HD 121212	HD 148434	HD 148912
α Ari	K2 III	14.49 ± 0.03		x	x
α Boo	K2 III	-5.30 ± 0.03		x	x
α Cas	K0 II-III	-4.25 ± 0.03		x	x
α Hya	K3 III	-4.40 ± 0.06	x		x
α Tau	K5 III	54.26 ± 0.04	x		x
β Gem	K0 III	3.28 ± 0.02		x	x
β Oph	K2 III	-12.20 ± 0.02		x	x
δ Oph	M1 III	-19.40 ± 0.07	x		x
μ Psc	K4 III	34.45 ± 0.05	x		x
16 Vir	K0 III	36.52 ± 0.04		x	x
35 Peg	K0 III	54.36 ± 0.03		x	x
HR 3145	K2 III	71.71 ± 0.08		x	x

2.2. *HD 148434*

HD 148434 (HIP 80528, $\alpha = 16^h26^m22^s$, $\delta = 40°48'34''$ [2000]) is located in the northern part of the constellation of Hercules, a little to the south of σ Her. Its BV magnitude and colour were found by *Hipparcos* (Hog et al. 2000) to be $V = 6.91$, $B-V = 1.11$, in agreement with its spectral type of K0 III.

The *Gaia* (2018) parallax of HD 148434 is $\pi = 7.31 \pm 0.03$ mas, which yields $M_v = 1.23 \pm 0.01$, supporting its classification as a giant. *Gaia* also measured the proper motion of HD 148434, obtaining $\mu_\alpha = 21.368 \pm 0.033$ mas yr^{-1}, $\mu_\delta = -53.462 \pm 0.035$ mas yr^{-1}. With the parallax these yield a tangential velocity of 36.2 km s^{-1}.

2.3. *HD 148912*

HD 148912 (HIP 80907, $\alpha = 16^h31^m21^s$, $\delta = 1°18'32''$ [2000]) lies in the constellation of Ophiuchus, but close to its boundaries with both Hercules and Serpens, and near the bright star λ Oph. Its BV magnitude and colour are $V = 6.78$, $B-V = 1.39$ and its MK type is K2-3 III.

The *Gaia* (2018) parallax of HD 148912 is $\pi = 2.51 \pm 0.11$ mas, which yields $M_v = -1.22 \pm 0.10$, consistent with its status as a late-K giant. The proper motion components, also measured by *Gaia*, are $\mu_\alpha = -17.119 \pm 0.202$ mas yr^{-1}, $\mu_\delta = 22.117 \pm 0.138$ mas yr^{-1}. The tangential velocity determined from these and the parallax is 52.8 km s^{-1}.

3. OBSERVATIONS

Initially the radial velocities were determined at the telescope with the radial-velocity spectrometer (RVS) (Fletcher et al. 1982). Numerous observations of IAU standard stars have been used to adjust the zero-point of the RVS system to the scale defined by Scarfe (2010). Since 2004, when the spectrometer was decommissioned, observations have been made through the same spectrograph optics, but using a CCD as detector, and reduced with a 'pipeline' program developed by D. Bohlender. Radial velocities were determined by averaging the results from cross-correlation with standard stars. The choice of standard stars for each binary is based on the precision of the cross-correlation, which in turn depends on the match in spectral type between the binary and the standards. The standards for each binary discussed here are listed in Table 1, where the velocities are on the scale and zero-point of Scarfe (2010), although the velocities differ very slightly from those in that paper, owing to the inclusion of slightly more data since its publication. The uncertainties are those of the mean value, and the binaries for which each standard was used are indicated.

For HD 121212, 95 observations were obtained with the RVS between JD 2447216 and 2452880, and 68 with the CCD between JD 2453117 and JD 2457497. The total span of 10281 days is just over 87 orbital cycles, so that the period is determined quite precisely, with a formal uncertainty of less than three minutes. The RVS velocities are presented in Table 2, and those obtained with the CCD in Table 3.

For HD 148434, 42 observations were obtained with the RVS between JDs 2447303 and 2452886, followed by 76 with the CCD between JDs 2453117 and 2457941. The span of 10638 days is just over 50 orbital cycles, and as a result the period of this binary is also determined fairly precisely, with a for-

TABLE 2

RVS RADIAL VELOCITIES OF HD 121212

Julian Date −2,400,000	Cycle No. & Phase	*R.V.* km s^{-1}	$O-C$ km s^{-1}	Julian Date −2,400,000	Cycle No. & Phase	*R.V.* km s^{-1}	$O-C$ km s^{-1}
47216.01	0.0553	−22.7	−0.6	50973.80	31.8653	5.1	−3.0[a]
47259.88	.4267	−18.5	1.0	50976.74	.8903	5.0	0.0
47263.87	.4605	−13.7	0.7	51166.13	33.4935	−9.3	−0.1
47291.79	.6968	12.7	−1.8	51224.04	.9836	−10.9	−0.8
47303.77	.7982	14.0	−0.1	51279.88	34.4564	−15.4	−0.4
47324.72	.9755	−8.8	−0.1	51284.86	.4985	−8.8	−0.4
47346.77	1.1622	−33.9	0.5	51309.86	.7101	15.0	−0.0
47676.76	3.9556	−4.7	0.6	51317.80	.7773	13.4	−1.6
47694.74	4.1078	−30.0	−0.6	51325.79	.8450	10.2	−0.2
47725.76	.3704	−26.6	0.6	51333.74	.9123	1.4	−0.4
47940.02	6.1841	−36.4	−0.6	51344.74	35.0054	−15.0	−1.1
47962.96	.3783	−26.7	−0.5	51365.73	.1831	−34.9	0.8
47996.87	.6654	13.6	1.0	51370.73	.2254	−37.0	−0.3
48037.76	7.0115	−15.0	−0.2	51623.93	37.3688	−27.2	0.1
48059.76	.1978	−36.1	0.2	51634.88	.4614	−15.2	−1.0
48075.72	.3328	−30.6	0.7	51662.86	.6984	14.6	0.0
48080.72	.3752	−26.2	0.3	51689.79	.9263	−0.2	0.3
48388.80	9.9831	−10.8	−0.8	51697.72	.9934	−11.4	0.3
48418.73	10.2365	−36.5	0.2	51711.76	38.1123	−30.2	−0.4
48605.06	11.8138	13.6	0.5	51718.74	.1714	−35.2	−0.1
48681.97	12.4648	−14.4	−0.7	51730.77	.2732	−33.8	1.8
48730.81	.8782	7.5	0.9	51737.72	.3320	−31.1	0.3
48735.84	.9208	0.5	0.0	51785.67	.7379	15.3	−0.3
48780.75	13.3010	−34.3	−0.3	52009.89	40.6360	9.8	−0.2
48960.05	14.8188	13.0	0.3	52026.84	.7794	14.6	−0.4
48998.08	15.1407	−32.0	0.7	52033.79	.8383	11.3	0.3
49041.96	.5122	−6.1	0.2	52044.80	.9315	−0.2	1.1
49061.07	.6739	13.2	0.0	52052.76	.9988	−11.9	0.8
49084.90	.8756	6.6	−0.2	52073.74	41.1765	−34.7	0.6
49121.84	16.1883	−36.2	−0.3	52086.74	.2865	−34.5	0.5
49370.08	18.2897	−34.2	0.5	52096.73	.3711	−27.7	−0.6
49417.97	.6951	14.8	0.3	52150.67	.8277	11.0	−1.0
49442.93	.9064	3.8	1.2	52387.85	43.8355	11.2	−0.1
49459.84	19.0496	−22.0	−0.8	52417.79	44.0889	−26.5	0.4
49507.75	.4551	−15.7	−0.5	52438.74	.2662	−35.5	0.5
49557.71	.8780	7.2	0.7	52460.72	.4523	−15.2	0.4
49803.91	21.9621	−6.2	0.2	52465.73	.4947	−8.8	0.3
49849.80	22.3506	−28.8	0.6	52481.71	.6300	10.0	0.5
50125.04	24.6805	13.3	−0.4	52648.11	46.0385	−18.2	1.2
50160.95	.9845	−10.0	0.2	52702.98	.5031	−8.0	−0.2
50181.89	25.1618	−33.2	1.2	52761.84	47.0013	−14.1	−1.0
50232.76	.5924	4.4	−0.8	52768.83	.0604	−23.9	−1.1
50279.71	.9898	−13.3	−2.2[a]	52774.78	.1108	−30.2	−0.5
50504.00	27.8884	7.6	2.4[a]	52796.78	.2971	−36.1	−1.9
50577.79	28.5131	−5.9	0.3	52809.73	.4067	−22.8	−0.5
50917.93	31.3925	−26.0	−0.7	52817.72	.4744	−12.5	−0.3
50925.88	.4597	−14.4	0.1	52880.66	48.0071	−13.4	0.8
50931.83	.5100	−7.3	−0.7				

[a]Rejected observation.

mal uncertainty of a little more than an hour. The RVS data are presented in Table 4 and those from the CCD in Table 5.

For HD 148912, 68 observations were obtained with the RVS between JDs 2447263 and 2452886, followed by 82 with the CCD between JDs 2453117

TABLE 3

CCD RADIAL VELOCITIES OF HD 121212

Julian Date −2,400,000	Cycle No. & Phase	*R.V.* km s^{-1}	$O-C$ km s^{-1}	Julian Date −2,400,000	Cycle No. & Phase	*R.V.* km s^{-1}	$O-C$ km s^{-1}
53117.84	50.0149	−15.93	−0.47	54531.97	61.9857	−10.26	0.17
53132.81	.1416	−33.12	−0.27	54561.91	62.2391	−36.57	0.07
53144.79	.2430	−36.43	0.16	54585.86	.4418	−17.31	−0.10
53165.72	.4202	−20.72	−0.29	54593.81	.5091	−6.64	0.14
53180.73	.5473	−0.96	0.06	54594.81	.5176	−5.07	0.40
53187.73	.6065	6.99	0.12	54602.77	.5850	4.53	0.33
53204.74	.7505	15.54	−0.05	54614.76	.6864	13.57	−0.40
53213.76	.8264	11.82	−0.28	54625.75	.7795	14.92	−0.03
53418.04	52.5561	0.40	0.15	54853.10	64.7040	14.72	−0.10
53425.01	.6151	8.24	0.38	54926.90	65.3287	−31.84	−0.14
53452.94	.8515	9.29	−0.40	54929.90	.3541	−29.60	−0.53
53468.96	.9871	−10.40	0.28	54966.81	.6666	13.01	0.32
53495.74	53.2138	−36.21	0.40	54987.74	.8438	10.80	0.30
53507.78	.3158	−33.37	−0.51	55013.73	66.0638	−23.37	−0.01
53515.78	.3835	−25.85	−0.35	55302.90	68.5116	−6.61	−0.22
53525.74	.4678	−13.37	−0.16	55310.87	.5791	3.88	0.46
53542.74	.6117	7.32	−0.15	55321.82	.6718	13.03	−0.03
53594.69	54.0515	−21.75	−0.28	55671.89	71.6351	10.38	0.41
53782.97	55.6453	11.07	0.14	56038.87	74.7416	15.72	0.11
53785.03	.6627	12.63	0.23	56391.90	77.7301	15.06	−0.46
53788.96	.6961	14.32	−0.15	56405.87	.8483	10.20	0.17
53823.94	.9921	−11.67	−0.13	56419.81	.9663	−6.53	0.57
53836.87	56.1015	−28.69	−0.13	56661.09	80.0089	−14.95	−0.52
53850.86	.2199	−36.56	0.12	56661.95	.0161	−16.39	−0.73
53860.80	.3041	−33.89	−0.11	56663.95	.0330	−18.56	−0.06
53871.81	.3973	−23.77	−0.11	56678.90	.1596	−34.28	0.00
53906.78	.6933	14.27	−0.07	56779.87	81.0143	−14.45	0.91
53916.75	.7777	14.52	−0.50	57089.96	83.6393	10.62	0.24
53927.74	.8707	7.90	0.43	57098.97	.7155	15.04	−0.17
54180.96	59.0143	−15.74	−0.38	57119.91	.8928	5.01	0.44
54238.78	.5037	−7.62	−0.01	57151.80	84.1627	−34.51	−0.01
54245.79	.5631	1.29	0.05	57167.79	.2981	−33.30	0.91
54253.75	.6305	9.34	−0.17	57465.01	86.8141	12.71	−0.35
54285.73	.9011	3.95	0.57	57496.84	87.0835	−26.30	−0.10

and 2457941. The span of 10678 days is over 22 orbital cycles, and as a result of this and the relatively high eccentricity, the period of this binary is also determined fairly precisely, with a formal uncertainty of a little less than an hour. The RVS data are presented in Table 6 and those from the CCD in Table 7.

4. ORBITS

For all three binaries, solutions were obtained from the RVS and CCD data separately, and weights based upon the standard deviations from those solutions were assigned for a solution from the combined data. The weight for the CCD data was always set to 1.0. In all cases the weight for the RVS data was lower than for the CCD data, being 0.25, 0.18 and 0.10 respectively for HD 121212, HD 148434 and HD 148912. The orbital elements are presented in Table 8 for all three binaries, and their velocity curves are given in Figures 1, 2 and 3.

5. DISCUSSION

All three binaries discussed in this paper show no trace of faint companions in our data, and it must be concluded that the companions must be at least 2.5 magnitudes fainter than the primaries, especially if their spectral types are similar, since then they are likely to cause some slight distortion of the cross correlation function. Moreover, if the secondaries are main sequence stars a difference of only 2.5 magnitudes would indicate that the secondaries are of type

TABLE 4

RVS RADIAL VELOCITIES OF HD 148434

Julian Date −2,400,000	Cycle No. & Phase	*R.V.* km s^{-1}	$O-C$ km s^{-1}	Julian Date −2,400,000	Cycle No. & Phase	*R.V.* km s^{-1}	$O-C$ km s^{-1}
47303.87	0.5629	−4.4	−0.2	52184.63	.4274	−5.8	1.1
47324.83	0.6610	−2.6	−0.3	52387.93	24.3797	−8.1	−0.5
47328.81	0.6797	−2.0	−0.1	52417.89	.5201	−5.1	0.0
49508.84	10.8923	−1.2	0.1	52438.84	.6182	−2.8	0.3
50973.86	17.7553	−1.3	−0.3	52460.77	.7210	−1.0	0.3
51689.86	21.1096	−6.5	0.1	52465.80	.7445	−1.1	−0.1
51697.78	.1467	−6.5	0.8	52481.76	.8193	−1.0	−0.3
51718.80	.2451	−8.4	0.1	52488.72	.8519	−0.7	0.2
51730.77	.3012	−8.3	0.0	52516.69	.9830	−3.9	−0.7
51785.69	.5585	−5.0	−0.7	52537.66	25.0812	−4.7	1.2
51796.69	.6100	−3.4	−0.2	52544.64	.1139	−7.1	−0.4
51824.63	.7409	−0.9	0.2	52564.63	.2075	−8.0	0.2
51952.06	22.3379	−7.6	0.6	52579.60	.2776	−8.9	−0.4
52010.96	.6138	−2.7	0.4	52648.12	.5986	−2.6	0.9
52026.93	.6886	−1.6	0.2	52761.95	26.1319	−8.2	−1.2
52051.88	.8055	−0.8	−0.2	52774.85	.1923	−8.1	−0.1
52073.83	.9083	−1.7	−0.1	52796.84	.2953	−9.7	−1.4
52086.81	.9691	−2.6	0.2	52809.82	.3562	−6.0	1.9
52096.78	23.0158	−4.0	0.1	52817.80	.3935	−7.2	0.2
52150.66	.2682	−8.8	−0.3	52873.74	.6556	−2.5	−0.2
52163.68	.3292	−8.7	−0.5	52885.72	.7117	−0.9	0.5

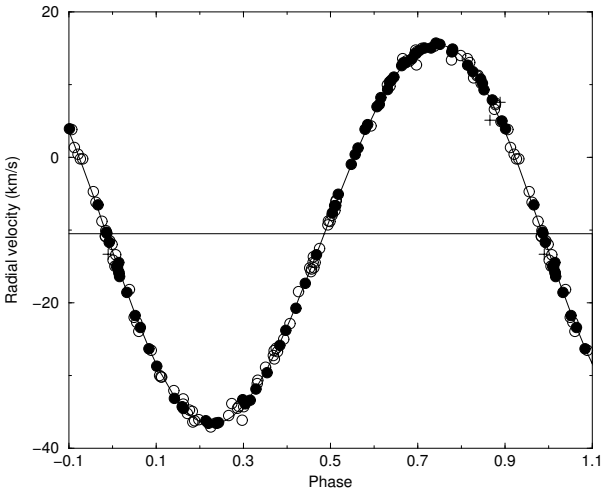

Fig. 1. The observed radial velocities of HD 121212, with the curve derived from the adopted elements drawn through them. The DAO CCD data are shown as filled circles and the spectrometer data as open circles. Rejected RVS velocities are shown as plus signs.

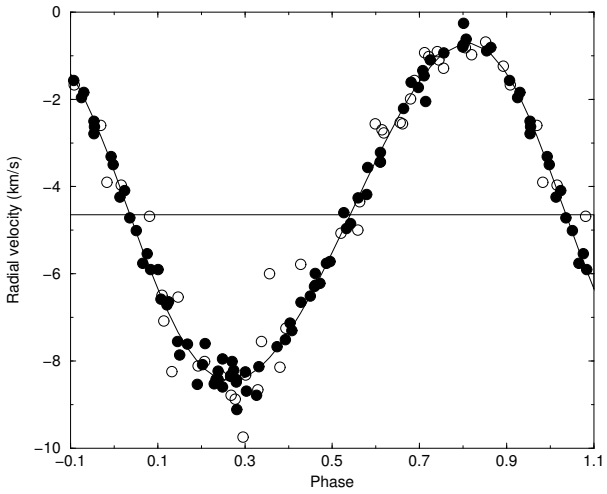

Fig. 2. The observed radial velocities of HD 148434, with the curve derived from the adopted elements drawn through them. The symbols have the same meaning as in Figure 1, except that there are no rejected data.

about A0 for HD 121212 and HD 148912, and about F5 for HD 148434. The former would have mass near 3 $M_{\odot}$, and the latter, 1.3 $M_{\odot}$. Either should be detectable in the system's colour indices, and indeed in the spectra of HD 121212 and 148912. Thus we conclude that the secondaries are either main-sequence stars that are fainter than the primaries by more than 2,5 magnitudes, or slightly evolved subgiants, in which case their masses are only a little less than those of the primaries, given the evolutionary timescales of stars once they leave the main se-

TABLE 5

CCD RADIAL VELOCITIES OF HD 148434

Julian Date −2,400,000	Cycle No. & Phase	*R.V.* km s^{-1}	$O-C$ km s^{-1}	Julian Date −2,400,000	Cycle No. & Phase	*R.V.* km s^{-1}	$O-C$ km s^{-1}
53117.97	27.7997	−0.76	−0.04	54695.71	.1908	−8.53	−0.52
53145.86	.9304	−1.84	0.12	54714.69	.2797	−8.42	0.01
53165.86	28.0240	−4.09	0.22	54724.68	.3265	−8.78	−0.58
53213.77	.2485	−7.95	0.47	54926.98	36.2742	−8.21	0.23
53258.71	.4590	−6.29	0.03	54966.94	.4614	−6.26	0.02
53425.09	29.2384	−8.23	0.15	54987.87	.5595	−4.26	−0.00
53515.86	.6637	−2.21	−0.03	54998.80	.6107	−3.44	−0.25
53525.82	.7103	−1.46	−0.02	55013.77	.6808	−1.61	0.28
53544.78	.7991	−0.80	−0.08	55050.72	.8539	−0.89	−0.01
53601.68	30.0657	−5.76	−0.30	55302.95	38.0355	−4.72	−0.09
53618.71	.1455	−7.55	−0.23	55321.94	.1245	−6.64	0.26
53619.69	.1501	−7.86	−0.46	55386.73	.4280	−6.65	0.23
53640.65	.2482	−8.59	−0.17	55393.78	.4610	−5.99	0.29
53647.63	.2810	−9.11	−0.68	55407.76	.5265	−4.60	0.36
53785.06	.9248	−1.96	−0.11	55425.71	.6106	−3.22	−0.03
53823.99	31.1071	−6.58	−0.07	55720.80	39.9929	−3.31	0.15
53836.96	.1679	−7.61	0.09	55766.76	40.2083	−7.60	0.59
53850.98	.2336	−8.42	−0.06	56106.75	41.8010	−0.26	0.46
53860.92	.2801	−8.48	−0.05	56148.74	.9977	−3.50	0.08
53871.90	.3316	−8.13	0.03	56170.71	42.1006	−5.90	0.46
53906.83	.4952	−5.72	−0.11	56405.93	43.2025	−8.08	0.05
53914.79	.5325	−4.96	−0.13	56419.92	.2681	−8.32	0.12
53916.83	.5420	−4.85	−0.22	56486.77	.5813	−3.56	0.24
53994.69	.9068	−1.57	−0.05	56513.73	.7075	−1.34	0.14
54004.67	.9536	−2.79	−0.33	56779.99	44.9549	−2.63	−0.14
54238.84	33.0506	−5.01	0.04	56853.76	45.3005	−8.25	0.11
54245.84	.0834	−5.90	0.03	56875.73	.4034	−7.13	0.16
54253.85	.1209	−6.71	0.11	57090.04	46.4073	−7.30	−0.08
54285.75	.2703	−8.01	0.43	57099.01	.4494	−6.51	−0.01
54292.75	.3031	−8.69	−0.34	57151.92	.6972	−1.73	−0.10
54307.72	.3732	−7.67	0.04	57232.74	47.0758	−5.54	0.19
54328.71	.4716	−6.22	−0.14	57478.99	48.2294	−8.52	−0.18
54351.67	.5791	−4.18	−0.34	57486.99	.2669	−8.35	0.09
54593.91	34.7139	−2.05	−0.65	57533.87	.4865	−5.76	0.02
54602.91	.7561	−0.94	0.00	57584.75	.7249	−1.10	0.16
54613.84	.8073	−0.62	0.10	57847.00	49.9534	−2.50	−0.04
54625.85	.8635	−0.81	0.15	57907.82	50.2384	−8.42	−0.04
54657.79	35.0132	−4.24	−0.23	57940.75	.3926	−7.51	−0.06

quence. One final possible alternative is that the secondaries are white dwarfs, which would again be very much fainter than the primaries, offering little hope of detection.

Despite these considerations, it might be possible to detect the companions interferometrically. The best chance of doing so, as suggested in the preceding paragraph, is in the case that they are evolved objects only slightly less massive than the primaries. We estimate below values of the angular size of the major semiaxes of the systems' orbits. As an example, we make the plausible assumption that the primary star's mass is twice that of the sun for all three systems. We make use of the following two equations. The first is the equation of the mass function, in which M_1 is the primary's mass, M_2 is that of the secondary, and $q = M_2/M_1$.

$$\frac{f(M)}{M_1 \sin^3 i} = \frac{q^3}{(1+q)^2} \tag{1}$$

The second equation is for the projected angular size a of the major semiaxis, in terms of the parallax π, the mass ratio q, the inclination i, and the product

TABLE 6

RVS RADIAL VELOCITIES OF HD 148912

Julian Date −2,400,000	Cycle No. & Phase	*R.V.* km s^{-1}	$O-C$ km s^{-1}	Julian Date −2,400,000	Cycle No. & Phase	*R.V.* km s^{-1}	$O-C$ km s^{-1}
47263.97	0.6578	−68.2	0.7	51796.68	.0677	−70.7	0.0
48418.82	3.0553	−69.2	−0.3	51824.61	.1257	−75.1	0.4
50232.83	6.8211	−61.9	−0.0	51952.07	.3903	−75.4	−0.3
50246.83	.8502	−60.9	−0.9	52010.97	.5125	−72.6	0.1
50518.05	7.4132	−74.7	0.0	52026.94	.5457	−72.2	−0.2
50577.89	.5375	−72.7	−0.5	52051.89	.5975	−70.5	0.2
50609.85	.6038	−71.2	−0.7	52073.84	.6430	−68.9	0.5
50917.98	8.2435	−77.1	−0.2	52086.82	.6700	−68.9	−0.4
50925.96	.2601	−76.4	0.4	52096.78	.6907	−67.9	−0.0
50973.86	.3595	−76.2	−0.6	52150.65	.8025	−63.5	−0.6
51070.64	.5604	−72.0	−0.4	52163.69	.8296	−61.8	−0.4
51279.96	.9950	−56.5	−0.3	52184.64	.8731	−58.4	0.0
51289.93	9.0157	−60.8	−0.3	52387.94	11.2951	−78.1	−1.7
51309.92	.0572	−68.8	0.4	52417.91	.3573	−75.0	0.6
51317.93	.0738	−72.8	−1.2	52438.85	.4008	−74.8	0.2
51325.94	.0904	−74.4	−1.1	52460.77	.4463	−73.8	0.3
51333.85	.1068	−75.6	−1.1	52465.81	.4568	−74.0	−0.1
51344.80	.1296	−76.5	−0.7	52481.77	.4899	−73.2	0.1
51365.76	.1731	−76.5	0.2	52488.73	.5043	−72.2	0.8
51414.68	.2746	−77.4	−0.7	52516.68	.5624	−72.1	−0.5
51438.64	.3244	−76.8	−0.7	52527.67	.5852	−71.4	−0.4
51444.65	.3369	−76.9	−0.9	52544.63	.6204	−71.3	−1.3
51452.63	.3534	−76.1	−0.4	52564.62	.6619	−68.5	0.3
51624.00	.7092	−67.2	−0.0	52579.59	.6930	−67.7	−0.0
51632.01	.7258	−66.0	0.5	52648.13	.8353	−60.4	0.6
51662.98	.7901	−63.7	−0.1	52703.06	.9493	−52.8	0.6
51689.86	.8459	−60.4	−0.1	52761.94	12.0715	−71.5	−0.3
51697.82	.8624	−59.4	−0.3	52768.93	.0860	−73.2	−0.3
51710.80	.8894	−57.4	−0.2	52774.86	.0984	−73.5	0.5
51718.81	.9060	−55.9	0.1	52796.86	.1440	−77.6	−1.4
51730.78	.9309	−53.5	0.7	52808.80	.1688	−75.2	1.5
51737.75	.9453	−53.6	−0.2	52817.80	.1875	−77.2	−0.3
51785.70	10.0449	−66.5	0.4	52873.73	.3036	−75.5	0.9
51787.70	.0490	−67.5	0.2	52885.72	.3285	−75.6	0.4

$a_1 \sin i$, determined from the orbit.

$$a = \pi\,(a_1\ \sin\ i)\,(1 + q^{-1})\ \csc\ i\,. \qquad (2)$$

As indicated above we assume that despite the luminosity differences between the stars, they are similar in mass and surface temperature, as was found for the components of HR 6046 by Scarfe et al. (2007), where the companion was detected with difficulty, despite being almost equal in mass to the primary. Here, let us assume that $q = 0.9$ for all three binaries. Then we solve equation 1 for the inclination of each orbit, and insert its cosecant into equation 2 along with the values of $a_1 \sin i$ from the orbit solutions, the parallaxes and the assumed values of q to find the projected major semiaxes.

An alternative, more direct, approach is to estimate the angular sizes of the systems' major semiaxes, using Kepler's Third Law and their parallaxes, by means of equation (3), in which a is the angular major semiaxis, π is the parallax, P is the period in years and M is the total mass of the system in solar units.

$$a = \pi\, P^{2/3}\, M^{1/3} \qquad (3)$$

A note of caution - choice of too small a value for M, coupled with too low a value of the mass ratio q, may lead to values of $\sin i$ that exceed unity when the mass function is large, as it is for HD 121212. For example our choice of 3.8 solar masses for the total mass of that system does not permit the mass

TABLE 7

CCD RADIAL VELOCITIES OF HD 148912

Julian Date −2,400,000	Cycle No. & Phase	*R.V.* km s^{-1}	$O-C$ km s^{-1}	Julian Date −2,400,000	Cycle No. & Phase	*R.V.* km s^{-1}	$O-C$ km s^{-1}
53117.99	12.8107	−62.48	−0.02	54602.89	.8933	−56.99	−0.11
53144.92	.8666	−58.92	−0.05	54625.82	.9409	−53.66	−0.02
53165.84	.9100	−55.39	0.22	54657.76	16.0072	−58.77	−0.11
53180.82	.9411	−53.60	0.03	54695.70	.0860	−73.44	−0.55
53187.79	.9556	−53.23	0.00	54714.67	.1254	−75.37	0.17
53204.78	.9909	−55.92	−0.31	54724.66	.1461	−76.78	−0.53
53213.76	13.0095	−58.87	0.28	54927.00	.5662	−71.35	0.15
53251.68	.0882	−73.20	−0.10	54943.99	.6014	−70.47	0.11
53258.69	.1028	−73.84	0.44	54966.92	.6490	−68.98	0.21
53272.65	.1318	−75.80	−0.01	54987.83	.6925	−67.67	0.08
53283.61	.1545	−76.14	0.31	54998.80	.7152	−67.19	−0.28
53418.10	.4337	−74.52	−0.16	55013.76	.7463	−65.44	0.20
53453.05	.5063	−73.16	−0.26	55055.70	.8333	−61.03	0.08
53515.86	.6366	−69.80	−0.23	55302.99	17.3467	−75.93	−0.12
53525.85	.6574	−68.82	0.11	55321.96	.3861	−75.08	0.12
53542.79	.6926	−67.99	−0.25	55386.75	.5206	−72.13	0.45
53545.81	.6988	−67.77	−0.25	55393.74	.5351	−72.15	0.10
53594.72	.8004	−63.02	0.01	55407.73	.5641	−71.46	0.09
53601.69	.8148	−62.17	0.05	55720.84	18.2142	−76.78	0.21
53618.67	.8501	−60.15	−0.13	55766.73	.3094	−75.73	0.58
53619.68	.8522	−60.02	−0.14	56106.79	19.0154	−60.22	0.24
53640.62	.8957	−56.55	0.15	56148.72	.1024	−74.00	0.26
53647.61	.9102	−55.81	−0.21	56170.69	.1480	−76.05	0.25
53785.09	14.1956	−77.05	−0.10	56405.95	.6364	−69.71	−0.13
53824.02	.2764	−76.78	−0.11	56419.95	.6655	−68.51	0.16
53836.98	.3033	−76.56	−0.18	56486.75	.8042	−62.52	0.30
53850.96	.3323	−76.12	−0.11	56549.67	.9348	−53.78	0.17
53860.94	.3530	−75.74	−0.02	56799.87	20.4542	−73.90	0.07
53871.92	.3758	−75.37	−0.01	56853.75	.5661	−71.56	−0.06
53906.86	.4484	−74.13	−0.05	56875.71	.6117	−70.09	0.20
53916.81	.4690	−73.77	−0.09	57090.05	21.0566	−69.01	0.06
53994.65	.6306	−69.75	−0.00	57120.02	.1188	−75.17	0.06
54004.64	.6513	−69.13	−0.01	57160.92	.2038	−77.12	−0.14
54238.86	15.1376	−75.84	0.16	57232.73	.3528	−75.70	0.02
54245.86	.1521	−76.47	−0.07	57479.01	.8641	−59.13	−0.08
54263.87	.1895	−76.83	0.09	57487.01	.8807	−57.73	0.11
54285.77	.2350	−76.88	0.07	57533.89	.9780	−54.18	−0.11
54292.77	.2495	−77.05	−0.18	57584.76	22.0836	−72.72	−0.07
54307.75	.2806	−76.77	−0.14	57847.02	.6281	−69.59	0.23
54328.74	.3242	−76.09	0.03	57907.85	.7544	−65.57	−0.28
54351.66	.3718	−76.30	−0.87[a]	57940.76	.8227	−61.73	0.03

[a]Rejected observation.

ratio to be as small as 0.6. One can avoid this pitfall by checking with equation 1.

Since our choice of primary mass and system mass ratio are the same for both the method using the mass function and that using Kepler's Third Law, it is not surprising that both methods yield the same results for the angular major semiaxes, 1.7 mas for HD 121212, 9.1 mas for HD 148434, and 5.4 mas for HD 148912. The angular separations at any orbital phase should be of this order of magnitude for our representative choice of masses, and any plausible masses and mass ratios are unlikely to yield very different results, as indicated by the weak dependence of equation 3 on the total mass. High inclinations like that of HD 121212 will make the separation significantly smaller at times, and large eccentricities like that of HD 148912 will give occasionally larger separations. The major axes estimated here

TABLE 8

TABLE 8 ORBITAL ELEMENTS

Object	HD 121212	HD 148434	HD 148912
P (days)	118.132 ± 0.002	213.464 ± 0.046	481.699 ± 0.040
T (J.D − 2,450,000)	3470.5 ± 1.4	4868.4 ± 4.8	3690.9 ± 3.1
K (km s^{-1})	26.16 ± 0.05	3.86 ± 0.04	11.88 ± 0.04
e	0.026 ± 0.002	0.070 ± 0.011	0.497 ± 0.002
ω (degrees)	94.2 ± 4.3	76.1 ± 8.1	48.2 ± 0.3
γ (km s^{-1})	−10.49 ± 0.04	−4.64 ± 0.03	−69.05 ± 0.02
S.E. (wt. 1) (km s^{-1})	0.341	0.253	0.197
$a_1 \sin i$ (Gm)	42.48 ± 0.09	11.31 ± 0.12	68.28 ± 0.25
$f(M)$ ($M_\odot$)	0.2194 ± 0.0013	0.00127 ± 0.00004	0.0548 ± 0.0006

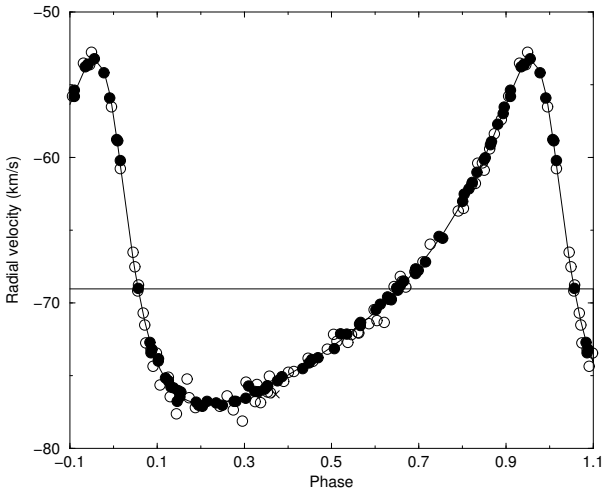

Fig. 3. The observed radial velocities of HR 148912, with the curve derived from the adopted elements drawn through them. The symbols have the same meaning as for Figure 1, except that a rejected CCD velocity is shown as a cross.

would make resolution of the pairs challenging for *Gaia* and very difficult, if not impossible, for earlier instruments. Nor do any of the inclinations estimated here offer much hope of detecting eclipses, despite the likely angular sizes of the giant primaries. Determination of the actual masses thus remains a challenge.

The author would like to acknowledge the National Research Council of Canada for the provision of observing time at the Dominion Astrophysical Observatory for a period now exceeding half of the century of that observatory's existence, and especially to thank members of the DAO staff, in particular D. Bohlender, D. Monin and the late L. Saddlemyer for their greatly appreciated support and assistance. He would also like to thank a kindly referee for some helpful advice.

REFERENCES

Adelman, S. J. 2000, IBVS, 4959, 1
ESA 1997, The Hipparcos and Tycho Catalogs, SP 1200
Fletcher, J. M., Harris, H. C., McClure, R. D., & Scarfe, C. D. 1982, PASP, 94, 1017
Gaia Collaboration 2018, A&A, arXiv1804.09365
Hoffleit, D., Saladyga, M. & Wlasuk, P. 1983, A Supplement to the Bright Star Catalogue (New Haven, CT: Yale Univ. Obs.)
Hog, E., Fabricius, C., Makarov, V. V., et al. 2000, A&A, 355, L27
Scarfe, C. D. 2010, Obs, 130, 214
Scarfe, C. D., Griffin, R. F., & Griffin, R. E. M. 2007, MNRAS, 376, 1671

C. D. Scarfe: Department of Physics and Astronomy, University of Victoria, Victoria, BC V8W 3P6, Canada (scarfe@uvic.ca).

Revista Mexicana de Astronomía y Astrofísica, **55**, 141–149 (2019)

DOI: https://doi.org/10.22201/ia.01851101p.2019.55.02.02

INTERSTELLAR ABSORPTION TOWARDS THE NOVAE V339 DEL AND V5668 SGR

D. Jack[1,2] and K.-P. Schröder[1]

Received December 27 2018; accepted March 27 2019

ABSTRACT

We present a search and study of interstellar (IS) absorption features in the observed spectra of two Novae V339 Del and V5668 Sgr. We obtained high resolution spectra ($R \approx 20,000$) in the wavelength range between 3800 and 8800 Å of both novae with the TIGRE telescope. Common IS features of Na I and Ca II were identified in both novae, and the Ca II H and K features of Nova V339 Del show substructures, while a blueshifted absorption feature was found in the spectra of Nova V5668 Sgr. Absorption of K I was identified only in the spectra of Nova V5668 Sgr. The DIBs 6196, 6203, 6379, 6614 and 7562 were found in both novae, and in the spectra of Nova V5668 Sgr we could also identify the DIBs 5780, 5797 and 6660. We present the equivalent widths of all features and determined the column densities of Ca II, K I and hydrogen in the direction of Nova V5668 Sgr ($\log N_{\mathrm{Ca\,II}} = 12.50$, $\log N_{\mathrm{K\,I}} = 11.55$, $\log N_{\mathrm{H}} = 18.5$).

RESUMEN

Presentamos una búsqueda y un estudio de características de absorción interestelar (IS) en los espectros de las novas V339 Del y V5668 Sgr. Obtuvimos espectros de alta resolución ($R \approx 20,000$) en el intervalo de longitud de onda de 3800 a 8800 Å con el telescopio TIGRE. Identificamos las características IS comunes de Na I y Ca II; las características de Ca II H y K muestran subestructuras en la Nova V339 Del, mientras que encontramos una segunda característica de absorción en los espectros de la Nova V5668 Sgr. Se identificó absorción de K I sólo en los espectros de la Nova V5668 Sgr. Las DIBs 6196, 6203, 6379, 6614 y 7562 se encontraron en ambas novas, y en los espectros de la Nova V5668 Sgr pudimos también identificar las DIBs 5780, 5797 y 6660. Presentamos los anchos equivalentes de todas las características y determinamos las densidades de columna de Ca II, K I e hidrógeno en la dirección de la nova V5668 Sgr ($\log N_{\mathrm{Ca\,II}} = 12.50$, $\log N_{\mathrm{K\,I}} = 11.55$, $\log N_{\mathrm{H}} = 18.5$).

Key Words: ISM: lines and bands — novae, cataclysmic variables — techniques: spectroscopic

1. INTRODUCTION

Most of the interstellar and intergalactic gas present in our Universe is not directly visible. However, a suitable way of studying the interstellar medium (ISM) is to analyze the absorption features found in the spectra of bright astrophysical objects in the background. Spectra of bright stars like O-type stars or evolved red giant stars may contain interstellar absorption lines. Typically, absorption features of the lines of atomic species like Na I, Ca II, K I and Mg II are found in observed spectra. To study these features in detail, e.g. resolving possible substructures, mid to high resolution spectroscopy of the background object is necessary.

With recent modern spectroscopy several unidentified features of interstellar absorption lines in the spectra of luminous objects have been found. These so called diffuse interstellar bands (DIBs) have been detected in high resolution spectra of massive stars (Herbig 1995; Sonnentrucker et al. 2018) and can be found in the spectra of more distant objects like

[1]Departamento de Astronomía, Universidad de Guanajuato, Guanajuato, México.
[2]Hamburger Sternwarte, Universität Hamburg, Hamburg, Germany.

those in the Small and Large Magellanic Clouds (Vladilo et al. 1987; Ehrenfreund et al. 2002; Cox et al. 2006, 2007; Welty et al. 2006). In a recent study of DIBs a galactic nucleus has been used as the background light source (Ritchey & Wallerstein 2015). Further very useful and distant background light sources are extragalactic supernovae (SN) (D'Odorico et al. 1989; Sollerman et al. 2005; Cox & Patat 2008, 2014), which offer the opportunity to study also the ISM of the respective SN host galaxy. The first study of the ISM with SN spectra was performed with the bright type II SN 1987A (de Boer et al. 1987), which exploded in the Large Magellanic Cloud. The latest very bright supernova SN 2014J offered also an excellent opportunity to study the interstellar absorption in our Galaxy and in the host galaxy M82 with high resolution spectra (Welty et al. 2014; Graham et al. 2015; Ritchey et al. 2015; Jack et al. 2015).

In our Galaxy, the outbreaks of cataclysmic variables are suitable objects for studying the interstellar material (Mauche et al. 1988; Ritchey et al. 2013). In general, events of classical novae present the opportunity to study the ISM using the absorption features in the respective nova spectra, since they are bright sources, and IS absorption features should also be visible in high resolution nova spectra. Recently, the IS absorption features in several nova spectra have been studied in the X-ray spectral range (Gatuzz et al. 2018). However, we are not aware of any publication that reports a study of the ISM using high resolution optical spectra of classical novae, motivating us to investigate our high resolution spectra of two recently observed classical novae.

In this work, we present a search and study of the absorption features of the ISM in the high resolution spectra of the two classical novae V339 Del and V5668 Sgr obtained with the TIGRE telescope. In § 2, we present details about the observations that we obtained from both novae. In the following § 3, we present the identification and analysis of the ISM features found in the spectra of both novae including atomic lines and DIBs. We are closing with a summary and our conclusions in the final § 4.

2. OBSERVATIONS

2.1. *The TIGRE Telescope*

All the nova spectra used in this work have been obtained with the 1.2 m robotic telescope el TIGRE (Telescopio Internacional de Guanajuato Robótico Espectroscópico) situated at the La Luz Observatory in the state of Guanajuato, Central Mexico. The design of the telescope with its automatic observation program and reduction software is ideal for obtaining time series of spectra, especially of novae and supernovae. The telescope is equipped with the HEROS (Heidelberg Extended Range Optical Spectrograph) échelle spectrograph which has a resolution of $R \approx 20,000$ and covers the optical wavelength range from about 3800 to 8800 Å divided into two channels. The blue channel covers the range in wavelength from about 3800 to 5700 Å, while the range of the red channel goes from about 5800 to 8800 Å, thus leaving a small gap of roughly 100 Å between the two channels. For a more detailed technical description of the hardware and software of the telescope please consult Schmitt et al. (2014). The automated wavelength calibration with a ThAr hollow cathode lamp used for our observations has a standard deviation of about 130 m s^{-1}.

2.2. *Nova V339 Del*

Nova V339 Del (Nova Delphini 2013, PNV J20233073+2046041) was discovered on August 14 in 2013 (Nakano et al. 2013) and reached its maximum on August 16 with an apparent brightness of $V = 4.46$ mag (Munari et al. 2013). The TIGRE telescope had been just recently installed at its new site, and we were able to obtain a time series of 18 spectra during the different spectral phases of that nova. Please consult De Gennaro Aquino et al. (2015) for all the details about the observations and an analysis of the spectra of Nova V339 Del obtained with the TIGRE telescope.

For our study of the ISM absorption features in this work, we added the first two spectra observed on August 17 and 19 in 2013 in order to obtain one spectrum with a higher signal-to-noise ratio. We selected only the first two spectra since the following spectra already showed stronger changes in the nova features and the continuum started to fade as well. The two added spectra were taken around maximum light during the absorption phase of Nova V339 Del.

2.3. *Nova V5668 Sgr*

On March 15 in 2015 a nova explosion was discovered in the constellation of Sagittarius (Williams et al. 2015). The Nova V5668 Sgr (Nova Sagittarii 2015 No. 2, PNV J18365700-2855420) was also a very bright event and has been studied intensively covering all parts of the electromagnetic spectrum. Using the TIGRE telescope, we obtained a long time series of optical high resolution spectra of this nova during our observation campaign of about two years

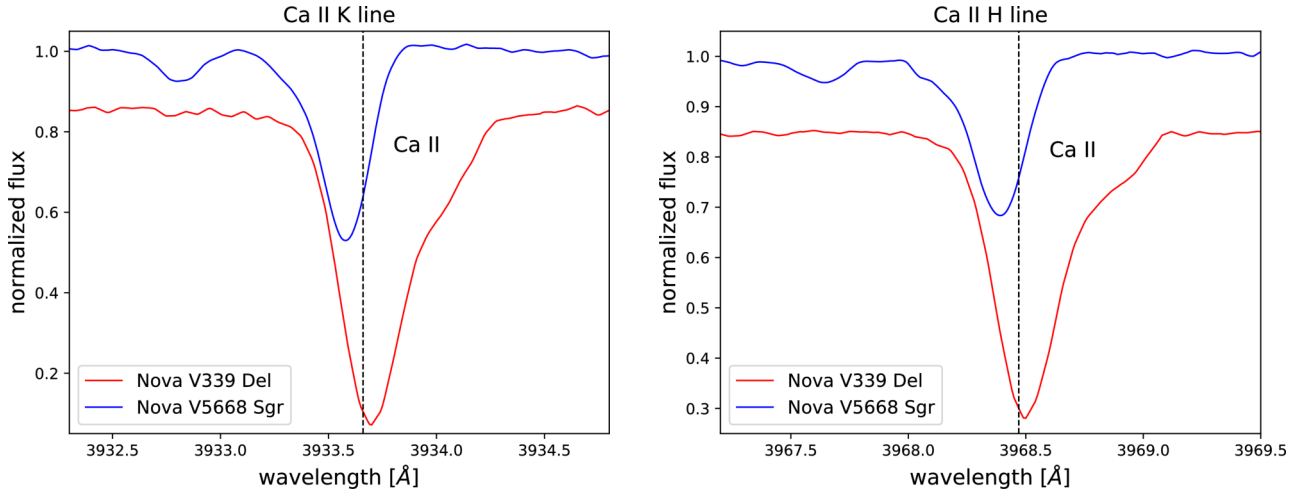

Fig. 1. Features of interstellar absorption of the Ca II H and K lines in the spectra of Novae V339 Del and V5668 Sgr. The spectra in Nova V339 Del seem to have a substructure in the red part of the main feature. The spectra of Nova V5668 Sgr show second weaker blueshifted absorption features in both lines. The vertical lines mark the rest wavelengths of the H and K lines. The color figure can be viewed online.

since this nova was of type DQ Her having a long lasting variation phase. Details about the observations and a presentation of the spectra can be found in Jack et al. (2017). The spectra of Nova V5668 Sgr are calibrated for relative fluxes.

To study the ISM absorption in the direction of Nova V5668 Sgr we added the first three spectra observed on March 19, 20 and 21 in 2015 to obtain one spectrum with a higher signal-to-noise ratio. These three spectra, observed during the absorption phase, were still similar and still showed a strong continuum flux. Adding more spectra would surely increase the signal-to-noise ratio. However, since the spectrum of a nova changes within days (or even hours), adding too many spectra may cause the appearance of false features, and complicates the continuum determination.

3. ABSORPTION FEATURES OF THE ISM IN THE SPECTRA OF THE NOVAE V339 DEL AND V5668 SGR

Having high resolution spectra of both novae, the goal is to identify in these spectra all absorption features of the interstellar medium. As commented in the previous section, we added several spectra to obtain one spectrum with a higher signal-to-noise ratio. All used spectra were obtained during the absorption phase so that enough continuum flux in the nova spectrum is present to be able to identify the absorption features of the interstellar gas, which can be due to absorption either by atomic lines or by diffuse interstellar bands. Nova features are very broad, having widths of up to a few 10 Å, which makes it easy to distinguish them from the narrow features of IS absorption that have widths of the order of only a few 0.1 Å.

3.1. *Interstellar Absorption of Atomic Lines*

In the first part of our analysis, we searched for the most common features of interstellar absorption by atomic lines in the spectra of both Novae V339 Del and V5668 Sgr. While the absorption features of the Ca II H and K lines as well as the two Na I D lines are clearly present in both novae, we could identify features of two K I lines only in Nova V5668 Sgr. However, in the spectra of Nova V339 Del they might be blended with telluric absorption lines.

Figure 1 presents a graph of the features of both the Ca II H and K lines in the observed normalized spectra of both novae. The main feature in Nova V339 Del is slightly redshifted, while the main feature in Nova V5668 Sgr is found to be slightly blueshifted. The features in the spectra of Nova V339 Del seem to have a substructure meaning that they are blended with a second feature that is shifted slightly to the right of the main feature, thus, causing a slight bump around 3934.1 and 3969.0 Å respectively. Both the Ca II H and K lines in Nova V5668 Sgr have a second smaller blueshifted feature at around 3932.8 and 3967.7 Å.

Another usually strong ISM absorption feature originates from the Na I D lines. Figure 2 shows a graph of the spectra of Novae V339 Del and

TABLE 1

EQUIVALENT WIDTHS AND VELOCITIES OF THE ISM*

		Velocity [km/s]		Equivalent width [mÅ]	
Feature	Wavelength [Å]	V339 Del	V5668 Sgr	V339 Del	V5668 Sgr
Ca II	3933.66	3.0 ± 0.4	-6.1 ± 0.4	345.3 ± 3.4	141.9 ± 1.3
			-65.5 ± 1.5		22.1 ± 2.6
Ca II	3968.47	2.3 ± 0.4	-6.0 ± 0.4	221.0 ± 1.8	93.2 ± 1.1
			-62.7 ± 1.5		9.5 ± 1.9
Na I	5889.95	2.5 ± 0.4	-5.1 ± 0.4	394.9 ± 5.3	289.1 ± 3.3
Na I	5895.92	3.1 ± 0.4	-5.1 ± 0.4	306.4 ± 8.4	247.8 ± 1.3
K I	7664.91		-5.5 ± 0.4		46.9 ± 1.2
K I	7698.97		-5.6 ± 0.4		80.1 ± 0.5

*Features Found in the Spectra of Novae V339 Del and V5668 Sgr.

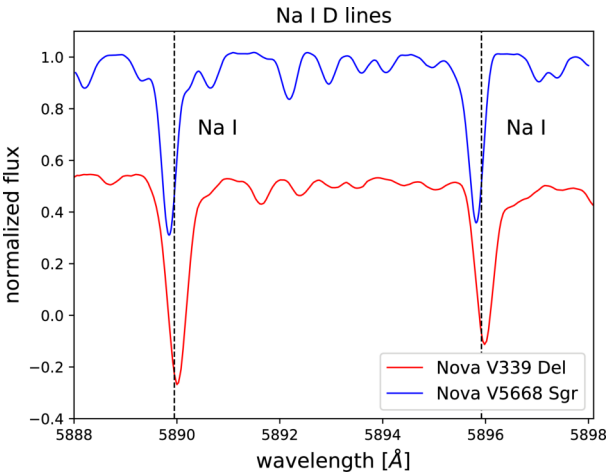

Fig. 2. Features of interstellar absorption of the Na I D lines in the spectra of Novae V339 Del and V5668 Sgr. The features are present in both novae and have about the same position when compared to the rest wavelengths (marked by vertical lines) as in the Ca I H and K lines. The color figure can be viewed online.

V5668 Sgr around the Na I D lines. Like for the Ca I H and K lines, the features of Nova V339 Del are slightly redshifted. However, there is no clear indication of a substructure in this feature. The features of Nova V5668 Sgr are slightly blueshifted, but we could not identify a second feature, because the region around the Na I D lines is contaminated with several telluric lines.

Figure 3 shows the spectrum of Nova V5668 Sgr where two features of interstellar absorption of K I lines could be identified. The features closer to the rest wavelengths are the absorption features of the ISM, which like the other IS absorption features in Nova V5668 Sgr are slightly blueshifted. The other two features in each plot are telluric lines which belong to the A band of O_2 in the Earth's atmosphere. In the spectra of Nova V339 Del the positions of both K I lines unfortunately coincide with the telluric lines, and we could therefore not confirm the presence of interstellar K I absorption in that nova.

We measured the equivalent widths of all the identified features in the spectra of Novae V339 Del and V5668 Sgr. By measuring the position of the minimum of the features, we could determine the relative velocities of the ISM features in both novae. The position of the minimum was determined by fitting a Gauss profile to the features. Table 1 presents the results of these measurements. All the features of ISM absorption in Nova V339 Del have a similar velocity between 2 and 3 km s^{-1} meaning that the features of all lines correspond to the same ISM cloud. All the main features of the ISM in Nova V5668 Sgr also show similar velocities between -6 and -5 km s^{-1} corresponding to the same IS gas cloud. Both the Ca II H and K lines have a second absorption feature with velocities of -65.5 and -62.7 km s^{-1} respectively, so that a second IS gas cloud could lie in the direction towards Nova V5668 Sgr. However, we could not observe this feature in the Na I D lines, maybe also because there are several telluric absorption features in this wavelength range.

The IS absorption features in Nova V339 Del show in general greater equivalent widths than the ones in Nova V5668 Sgr. As is usually found for interstellar absorption, the features of Na I are the strongest in the spectra of both Novae. As can also

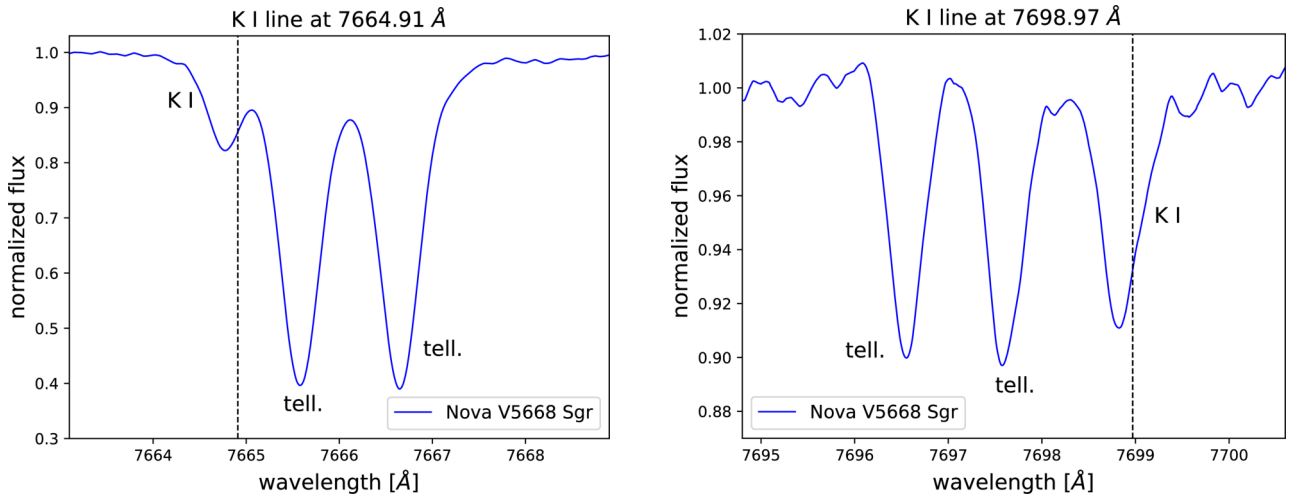

Fig. 3. Features of interstellar absorption of two K I lines in the spectra of Nova V5668 Sgr. The rest wavelengths are marked by vertical lines. The two stronger features in each plot come from telluric line absorption. The color figure can be viewed online.

be seen in Figures 1 and 2 the IS absorption features of Ca II and Na I are saturated in the spectra of Nova V339 Del.

Using the analysis of pure absorption lines, formerly applied by us to special problems in the field of stellar atmospheres (Schroeder et al. 1994), we fitted the IS absorption features of Ca II and K I of Nova V5668 Sgr assuming optically thin lines. The Ca II H and K lines of Nova V5668 Sgr are ideal to determine both the column density $N_{\mathrm{Ca\,II}}$ and the turbulence velocity v_{tur} as they are intermediate-optically thick. By contrast, in Nova V339 Del this doublet is already very saturated and unfavorable to derive either parameter. The same is true, in both Novae, for the very strong Na I D doublet. In our analysis, we determined a turbulence velocity for the ISM of $v_{\mathrm{tur}} = 4.5$ km s^{-1}. For the $\log(fg)$-values of the Ca II K and H lines we used 0.69 and 0.34 respectively (Wiese et al. 1969). The $\log(fg)$-values for both K I lines are 0.59 and 0.29 respectively (Nandy et al. 2012).

With the analysis of the depth and profile of the Ca II features assuming small saturation and solving for the best fit of the two parameters we obtained a column density for the ground level of Ca II of $\log N_{\mathrm{Ca\,II}} = 12.50 \pm 0.05$ and a turbulence velocity of the ISM of $v_{turb} = 4.5$ km s^{-1} reproducing well the line profiles and equivalent widths. The obtained ISM turbulence velocity matches well the values obtained by Wilson et al. (2011). Analyzing the K I features with the same method we found a column density of $\log N_{\mathrm{K\,I}} = 11.55 \pm 0.05$ with the same determined turbulence velocity. Assuming that all the potassium is found in the K I state (low ionization), we obtained for the column density of calcium a value of $\log N_{\mathrm{Ca}} = 12.8$ assuming solar abundances (Reddy et al. 2003). Comparing this value with the measured value for the column density of Ca II of $\log N_{\mathrm{Ca\,II}} = 12.5$, we can estimate that the ionization ratio of Ca II to Ca I is about 1:1. Assuming again solar abundances, the value of the column density of Ca of $\log N_{\mathrm{Ca}} = 12.8$ corresponds to a column density of hydrogen of about $\log N_{\mathrm{H}} = 18.5$ which results in a very small extinction of about $O(0.01)$.

3.2. *Diffuse Interstellar Bands*

Apart from the common absorption features of atomic lines, spectra may contain much weaker absorption features of still unknown origin, of so called diffuse interstellar bands (DIBs). Since the spectra of Novae V339 Del and V5668 Sgr have a good signal-to-noise ratio and a high resolution we searched in the spectra of both novae for features of the commonly known DIBs. For this analysis we made use of published catalogs (Jenniskens & Desert 1994; Galazutdinov et al. 2000; Hobbs et al. 2008, 2009) for the identification of the DIBs in our spectra.

Figure 4 shows the normalized spectrum of Nova V5668 Sgr in the wavelength range of the DIBs 5780 and 5797, which are strong DIBs and are commonly observed in the spectra of luminous objects. DIB 5780 is also the strongest DIB feature in the spectra of Nova V5668 Sgr. However, concerning the spectra of Nova V339 Del this wavelength region was unfor-

TABLE 2

EQUIVALENT WIDTHS (EW) AND VELOCITIES (VEL) OF THE DIB*

Feature	Nova V339 Del		Nova V5668 Sgr	
	Vel. [km/s]	EW [mÅ]	Vel. [km/s]	EW [mÅ]
DIB 5780			1.6 ± 2.6	180.9 ± 2.1
DIB 5797			-1.6 ± 3.1	42.95 ± 1.2
DIB 6196	2.0 ± 1.0	12.0 ± 2.8	-5.8 ± 1.5	17.8 ± 0.6
DIB 6203	0.2 ± 1.9	33.8 ± 4.7	-6.8 ± 2.2	25.6 ± 1.3
DIB 6379	-0.8 ± 1.0	8.2 ± 2.5	-4.7 ± 1.4	31.0 ± 2.6
DIB 6614	2.9 ± 2.2	30.6 ± 4.3	-10.9 ± 5.4	70.2 ± 4.6
DIB 6660			-2.3 ± 3.6	12.9 ± 1.4
DIB 7562	-19.4 ± 5.4	21.1 ± 4.1	-9.5 ± 4.3	30.3 ± 2.3

*Features found in Novae V339 Del and V5668 Sgr.

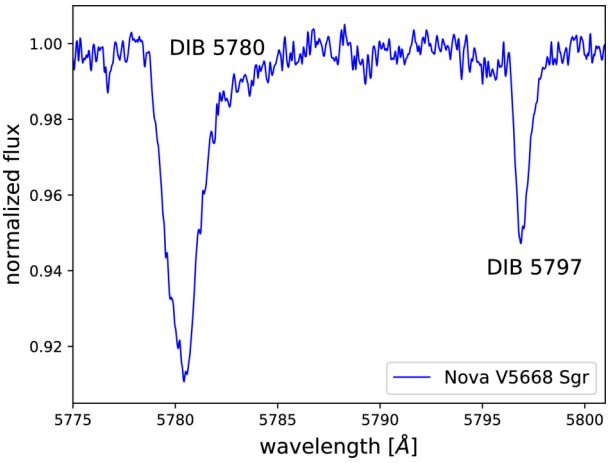

Fig. 4. Normalized spectrum of Nova V5668 Sgr showing the absorption features of the two strong DIBs 5780 and 5797. The color figure can be viewed online.

tunately in the gap between the two channels of the HEROS spectrograph. Thus, we could not look for features of the DIBs 5780 and 5797 in the spectra of Nova V339 Del.

We found features of the DIBs 6196, 6203, 6379 and 7562 in the spectra of both Novae. In Figure 5, we show in subplot (a) the normalized spectra in the wavelength region around the DIBs 6196 and 6203. The DIBs of Nova V5668 Sgr are slightly shifted to the blue when compared to the features of Nova V339 Del. This is in good agreement with the observation of the atomic IS absorption lines where the features of V5668 Sgr are also slight shifted to the blue when compared to Nova V339 Del. The subplots (b) and (c) of Figure 5 show the DIBs 6379 and 6614 respectively. Both DIBs in the spectra of Nova V5668 Sgr are also slightly blueshifted compared to the features of Nova V339 Del. The DIB 6660 is a relatively weak DIB, and we could clearly identify it only in the spectra of Nova V5668 Sgr, as can be seen in subplot (d) of Figure 5. The weakest feature was detected for DIB 7562 and is shown in subplot (e).

We normalized all spectra of the Novae V339 Del and V5668 Sgr using a spline fit to the continuum around the DIB features. The velocities of the features were determined using the rest wavelengths published in the catalog of Galazutdinov et al. (2000), and we measured the respective equivalent widths. We present in Table 2 the results and give the values of the velocity (in km/s) and equivalent width (in mÅ) of all identified DIB features. The strongest feature in Nova V5668 Sgr is the DIB 5780, while in Nova V339 Del the DIB 6203 is the strongest. The weakest feature in terms of the equivalent width in Nova V5668 Sgr is the DIB 6660. The velocities for Nova V5668 Sgr are widely spread from -10.9 to 1.6 km s^{-1}, which is probably due to the unknown origin and rest wavelengths of the DIBs and the difficulty of determining the exact position of the minimum due to the low signal-to-noise ratio of the observed features. However, the velocities of the DIB features roughly coincide with the blueshifted atomic ISM absorption features. For Nova V339 Del the velocities range from -0.8 to 2.9 km s^{-1} with the exception of DIB 7562 where the determination of the velocity is difficult and the measurements gave a velocity of -19.4 km s^{-1}. These velocities also coincide roughly with the values measured for the atomic ISM features, which are also slightly redshifted.

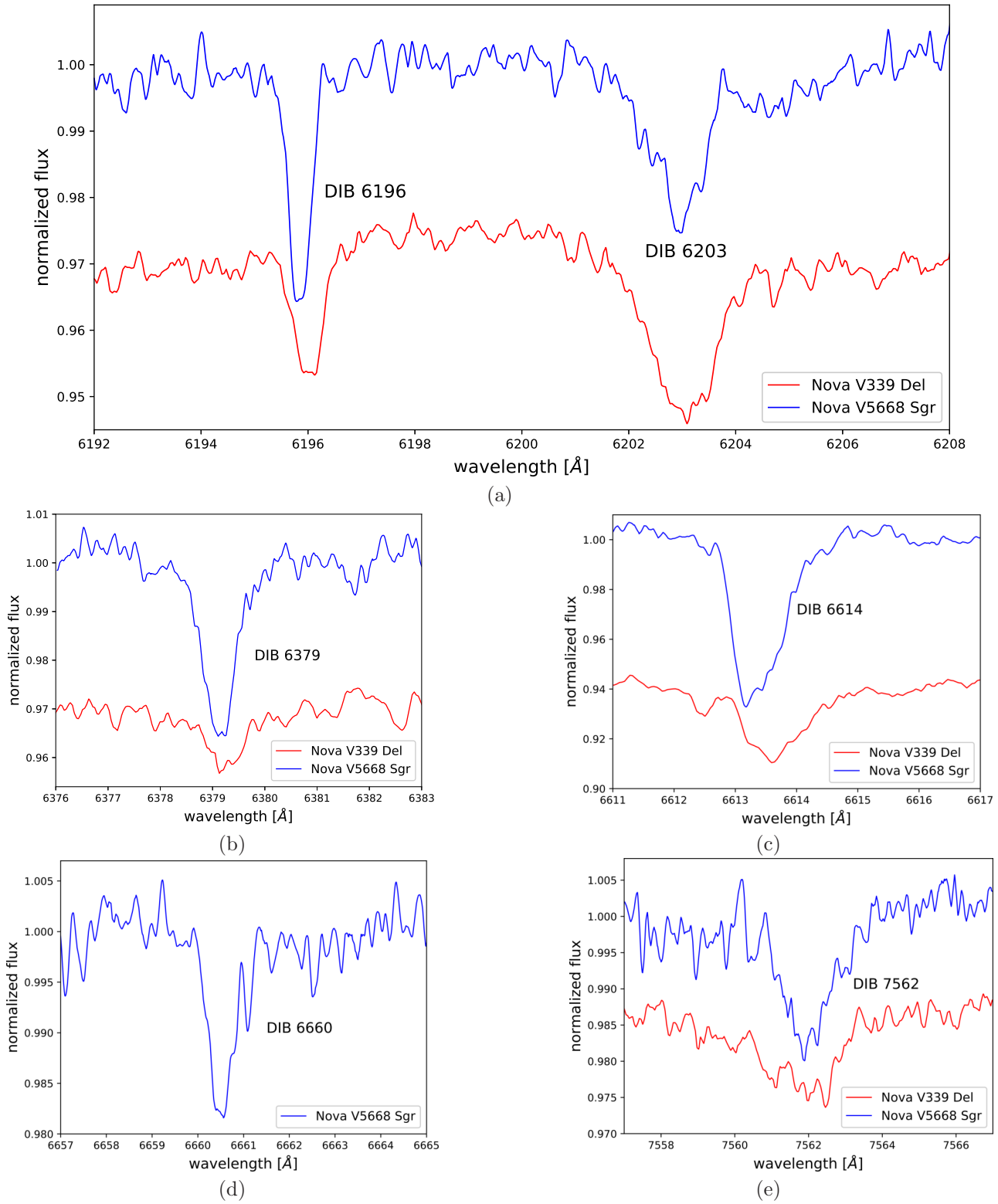

Fig. 5. Normalized spectra of Novae V339 Del and V5668 Sgr in the wavelength range of the DIBs 6196, 6203, 6379, 6614, 6660 and 7562. The spectra of Nova V339 Del are shifted for a better illustration. The color figure can be viewed online.

4. SUMMARY AND CONCLUSIONS

We used high resolution spectra ($R \approx 20,000$) of the two bright novae, V339 Del and V5668 Sgr, observed with the TIGRE telescope to search for signs of interstellar absorption by both atomic lines and diffuse interstellar bands. We were able to identify several features of interstellar absorption by atomic lines as well as DIBs and we measured the velocities and equivalent widths of these features.

We found in the spectra of both novae interstellar absorption features of the Ca II H and K lines. The detected features in the spectra of Nova V339 Del seem to show substructures having a second, blended, weaker and slightly redshifted feature. Apart from the main slightly blueshifted features, we found in the spectra of Nova V5668 Sgr additional weaker and blueshifted features with velocities of -65.5 and -62.7 km s^{-1} respectively. Absorption features observed in the atomic lines of Na I D show velocities similar to Ca II in both novae, meaning that they originate from the same IS gas cloud. However, we could not identify substructures or secondary features. Evidence for absorption of K I lines could only be found in the spectra of Nova V5668 Sgr. Two features of the lines with rest wavelengths of 7664.91 and 7698.97 Å are present. However, in Nova V339 Del these features might be hidden in the telluric lines. The main features of Nova V339 Del have velocities between 2 and 3 km s^{-1}, while the main features of Nova V5668 Sgr are blueshifted showing velocities between -6 and -5 km s^{-1}. Consulting the literature we found that the ISM absorption in the emission-line star 9 Sgr has components at velocities of ≈ -62 and ≈ -10 km s^{-1} (Pwa & Pottasch 1986). The ISM absorption towards the Galactic Center in Sgr shows, among others, foreground arms with velocities of ≈ -55 and ≈ -5 km s^{-1} (Oka et al. 1998). This all agrees well with our velocity determination of both observed ISM components in our spectra of Nova V5668 Sgr.

The ISM absorption features in Nova V339 Del are in general stronger with greater equivalent widths when compared to the ones in Nova V5668 Sgr. In both novae, the IS absorption of Na I is strongest. The atomic IS features in Nova V339 Del are all saturated. However, for Nova V5668 Sgr using the IS absorption of Ca II and K I we could reproduce the equivalent widths and profiles of the features with a turbulence velocity for the ISM of $v_{\rm tur} = 4.5$ km s^{-1} and column densities for Ca II of $\log N_{\rm Ca\,II} = 12.50 \pm 0.05$ and for K I of $\log N_{\rm K\,I} = 11.55 \pm 0.05$. Assuming solar abundances we determined the column density of hydrogen to be about $\log N_{\rm H} = 18.5$, which corresponds to low extinction.

We also performed an identification of diffuse interstellar bands in the spectra of both novae. The DIBs 6196, 6203, 6379, 6614 and 7562 could be detected in both novae. The DIB 6660 shows a weak feature only in the spectra of Nova V5668 Sgr. The DIBs 5780 and 5797 could only be identified in the Nova V5668 Sgr, because in the spectra of Nova V339 Del these DIBs fall into the gap between the two channels of the HEROS spectrograph. By determining the velocities we found that the DIBs of Nova V5668 Sgr are slightly blueshifted, which is in good agreement with the measured velocities of the ISM absorption features in the atomic lines, meaning that the DIBs have probably the same origin as the atomic lines. The equivalent widths of the DIB features in the spectra of Novae V339 Del and V5668 Sgr were presented.

In this work, we demonstrated that high resolution spectroscopy of classical novae offers a further opportunity to study the interstellar medium since the absorption features of both atomic lines and diffuse interstellar bands can be found and studied in detail.

This research has been made possible in part by grants of the Universidad de Guanajuato (UG) through the DAIP project CIIC 021/2018 and also by CONACYT in several bilateral grants. D. Jack would like to thank the staff of the Hamburger Sternwarte for the hospitality during his sabbatical stay.

REFERENCES

Cox, N. L. J., Cordiner, M. A., Cami, J., et al. 2006, A&A, 447, 991
Cox, N. L. J., Cordiner, M. A., Ehrenfreund, P., et al. 2007, A&A, 470, 941
Cox, N. L. J. & Patat, F. 2008, A&A, 485, L9
_____. 2014, A&A, 565, A61
de Boer, K. S., Richtler, T., & Savage, B. D. 1987, ESO Workshop on the SN 1987A, (Germany: ESO) 26, 549
De Gennaro Aquino, I., Schröder, K.-P., Mittag, M., et al. 2015, A&A, 581, A134
D'Odorico, S., di Serego Alighieri, S., Pettini, M., et al. 1989, A&A, 215, 21
Ehrenfreund, P., Cami, J., Jiménez-Vicente, J., et al. 2002, ApJ, 576, L117
Galazutdinov, G. A., Musaev, F. A., Krełowski, J., & Walker, G. A. H. 2000, PASP, 112, 648
Gatuzz, E., Ness, J.-U., Gorczyca, T. W., et al. 2018, MNRAS, 479, 2457

Graham, M. L., Valenti, S., Fulton, B. J., et al. 2015, ApJ, 801, 136
Herbig, G. H. 1995, ARA&A, 33, 19
Hobbs, L. M., York, D. G., Snow, T. P., et al. 2008, ApJ, 680, 1256
Hobbs, L. M., York, D. G., Thorburn, J. A., et al. 2009, ApJ, 705, 32
Jack, D., Mittag, M., Schröder, K.-P., et al. 2015, MNRAS, 451, 4104
Jack, D., Robles Pérez, J. d. J., De Gennaro Aquino, I., et al. 2017, AN, 338, 91
Jenniskens, P. & Desert, F.-X. 1994, A&AS, 106, 39
Mauche, C. W., Raymond, J. C., & Cordova, F. A. 1988, ApJ, 335, 829
Munari, U., Henden, A., Dallaporta, S., & Cherini, G. 2013, IBVS, 6080
Nakano, S., Itagaki, K., Denisenko, D., et al. 2013, CBET, 3628
Nandy, D. K., Singh, Y., Shah, B. P., & Sahoo, B. K. 2012, PhRvA, 86, 2517
Oka, T., Hasegawa, T., Sato, F., Tsuboi, M., & Miyazaki, A. 1998, ApJS, 118, 455
Pwa, T. H. & Pottasch, S. R. 1986, A&A, 164, 116
Reddy, B. E., Tomkin, J., Lambert, D. L., & Allende Prieto, C. 2003, MNRAS, 340, 304
Ritchey, A. M. & Wallerstein, G. 2015, PASP, 127, 223
Ritchey, A. M., Wallerstein, G., & McKeever, J. 2013, PASP, 125, 1429
Ritchey, A. M., Welty, D. E., Dahlstrom, J. A., & York, D. G. 2015, ApJ, 799, 197
Schmitt, J. H. M. M., Schröder, K.-P., Rauw, G., et al. 2014, AN, 335, 787
Schroeder, K.-P., Griffin, R. E. M., & Hunsch, M. 1994, A&A, 288, 273
Sollerman, J., Cox, N., Mattila, S., et al. 2005, A&A, 429, 559
Sonnentrucker, P., York, B., Hobbs, L. M., et al. 2018, ApJS, 237, 40
Vladilo, G., Crivellari, L., Molaro, P., & Beckman, J. E. 1987, A&A, 182, L59
Welty, D. E., Federman, S. R., Gredel, R., Thorburn, J. A., & Lambert, D. L. 2006, ApJS, 165, 138
Welty, D. E., Ritchey, A. M., Dahlstrom, J. A., & York, D. G. 2014, ApJ, 792, 106
Wiese, W. L., Smith, M. W., & Miles, B. M. 1969, NSRDS-NBS, 22, 268
Williams, S. C., Darnley, M. J., & Bode, M. F. 2015, ATel, 7230, 1
Wilson, C. D., Warren, B. E., Irwin, J., et al. 2011, MNRAS, 410, 1409

D. Jack and K.-P. Schröder: Departamento de Astronomía, Universidad de Guanajuato, A.P. 144, 36000 Guanajuato, Gto., México (dennis, kps@astro.ugto.mx).
D. Jack: Hamburger Sternwarte, Universität Hamburg, Hamburg, Germany.

Revista Mexicana de Astronomía y Astrofísica, **55**, 151–159 (2019)

DOI: https://doi.org/10.22201/ia.01851101p.2019.55.02.03

RELATIVISTIC BEAMING EFFECTS AND STRUCTURAL ASYMMETRIES IN HIGHLY ASYMMETRIC DOUBLE RADIO SOURCES

Jibrin A. Alhassan[1,2], Augustine A. Ubachukwu[1,2], Finbar C. Odo[1,2], and Chika C. Onuchukwu[3]

Received February 4 2019; accepted May 6 2019

ABSTRACT

We have studied the comparative importance of the relativistic beaming model (RBM) and the density variation model (DVM) in our understanding of asymmetries in double radio sources, using their lobe separation ratio (Q) and flux density ratio (F). Our result shows an $F - Q$ correlation in the sense expected for the RBM but contrary to the DVM. We attributed the result for the DVM to varying beam power, as its efficiency is density profile-dependent. From the core-dominant parameter-linear size $R - D$ relation for the RBM subsample, we found that sources in this subsample are beamed within an optimum cone angle $\phi_c \approx 8°$. We posit that relativistic beaming is largely accountable for the observed structural asymmetries in radio sources, though other effects cannot be ruled out.

RESUMEN

Hemos estudiado la importancia comparativa del modelo relativista de colimación del haz (RBM) y el modelo de densidad variable (DVM) para explicar las asimetrías de las fuentes de radio dobles, usando el cociente de la separación de los lóbulos (Q) y el de las densidades de flujo (F). Nuestros resultados muestran una correlación $F - Q$ en el sentido esperado para el modelo RBM, pero contrario al esperado para el modelo DVM. Atribuímos el resultado para el DVM a una potencia variable en el haz, puesto que la eficiencia depende del perfil de densidad. A partir de la relación $R - D$ (parámetro central dominante vs. tamaño lineal) para las fuentes de la sub-muestra RBM encontramos que sus haces están colimados dentro de un cono óptimo con un ángulo $\phi_c \approx 8°$. Proponemos que la colimación relativista es la principal responsable de las asimetrías estructurales observadas, si bien no pueden descartarse otros efectos.

Key Words: galaxies: active — galaxies: jets — methods: data analysis

1. INTRODUCTION

High luminosity extragalactic radio sources (HLEGRSs) are known to show double structure, with the extended lobes straddling the compact optical component, which is often coincident with the nucleus of the parent galaxy or quasar. One of the most striking features of these double sources is that their jets are observed only on one side of the lobes (e.g. Bridle & Perley 1984; Onuchukwu & Ubachukwu 2013). Asymmetries have also been found in the angular size separation, flux densities and depolarization of the two components/lobes, which could be correlated with jet-sidedness (e.g. Garrington 1988; Garrington et al. 1988). Whether the one sidedness of jets in powerful radio sources is intrinsic or due to Doppler and projection effects has been a subject of continued controversy (e.g Saikia 1984; Onah et al. 2014). Moreover, because the jets have to interact with the intergalactic medium (IGM), the overall structure of these sources could depend on the nature of the ambient medium.

In classical double radio sources, the twin radio lobes are believed to move out symmetrically from the core at relativistic speeds. Thus, in powerful Fanaroff and Riley (1974) class II (FR II) radio galaxies, which supposedly form the less beamed coun-

[1]Department of Physics and Astronomy, Faculty of Physical Sciences, University of Nigeria, Carver Building, 1 University Road, Nsukka, Nigeria.

[2]Astronomy and Astrophysics Research Lab, University of Nigeria, Nsukka, Nigeria.

[3]Department of Industrial Physics, Chukwuemeka Odumegwu Ojukwu University, Anambra State, Nigeria.

terparts of quasars and which are believed to be observed more or less in the plane of the sky, the twin radio lobes are expected to be highly symmetric both in terms of size and emitted power (e.g. Gopal-Krishna et al. 1996). However, observational evidence (e.g. Barthel 1989; Scheuer 1995) suggests that this symmetric scenario is not exactly the case, as varying degrees of structural asymmetries and misalignments of the radio lobes are present in many samples of FR II radio sources. These asymmetries can be attributed to factors that could be intrinsic, environmental and/or arising from relativistic beaming and orientation effects. Thus, the ratios of angular separation (Q) and that of flux densities (F) of the two components are crucial symmetry parameters, which could be used to study the dynamical evolution of double radio sources (e.g. Longair and Ryle 1979; Banhatti 1980; Kapahi & Saikia 1982). Although Swarup & Banhatti (1981) have proposed a possible connection between Q and F in asymmetric sources with constant beam power, the effects of relativistic beaming appear to have significantly contaminated the $F - Q$ data, so that this connection between the two asymmetry parameters is yet to be satisfactorily understood (Conway & Strom 1985; Onuchukwu and Ubachukwu 2013).

In the present paper, we wish to re-examine the distribution of the angular separation ratio of the highly asymmetric double radio sources in connection with approaching and receding lobes. This will be based on the two popular models of asymmetries in Active Galactic Nuclei (AGNs), namely: relativistic beaming model (RBM) and density variation model (DVM), which among other effects have been held largely responsible for explaining the structural asymmetries of double radio sources (e.g Kharb et al. 2008; Onah et al. 2014). We seek also to quantitatively examine the statistical consequences of relativistic beaming on the structural asymmetries of the highly asymmetric sources.

2. RELATIVISTIC BEAMING AND ORIENTATION MODEL FOR ASYMMETRIC SOURCES

If the ambient medium and jets emanating from the opposite directions of the active galactic nuclei are both symmetrical, then the approaching component would always appear further from the core than the receding component. In the relativistic beaming model (Scheuer and Readhead, 1979), the ratio Q of the angular separation of the approaching ($\theta_{\rm app}$) and receding ($\theta_{\rm rec}$) components of a double radio source is given in terms of the viewing angle (ϕ) by (e.g Gopal-Krishna & Wiita 2004; Onuchukwu and Ubachukwu, 2013)

$$Q = \frac{\theta{\rm app}}{\theta{\rm rec}} = \frac{1 + \beta\cos\phi}{1 - \beta\cos\phi}, \tag{1}$$

where β is the separation velocity of the two components from the parent object in units of the speed of light. The study of the distribution of Q for a complete sample of sources is crucial to understand the physics of radio source evolution as well as the nature of the environment in which these sources are located (Onuchukwu, 2017).

If the approaching and receding lobes are intrinsically symmetric and the observed flux asymmetries are predominantly a result of Doppler beaming, it has been shown (Ryle & Longair, 1967; Longair & Riley, 1979) that the flux density ratio can be expressed as (e.g. Arshakian & Longair, 2004)

$$F = \left(\frac{1 + \beta\cos\phi}{1 - \beta\cos\phi}\right)^{n+\alpha}, \tag{2}$$

where α is the spectral index ($S_\nu \approx \nu^{-\alpha}$), while n is a factor that defines the assumed flow model: $n = 2$ for a continuous beam model, while $n = 3$ if the radiating plasma consists of blobs. Radio emission from the core is characterized by flat spectra ($0 \leq \alpha < 0.5$), while radio lobe emission has steep spectra ($\alpha \geq 0.5$).

Equation (2) corresponds to the ratio (τ) between the ages of the receding-and-approaching lobes given (e.g. Gopal-Krishna and Wiita, 2004; Onuchukwu et al. 2014) by:

$$\tau = \frac{\tau_{\rm rec}}{\tau_{\rm app}} = \frac{1 - \beta\cos\phi}{1 + \beta\cos\phi}. \tag{3}$$

However, relativistic beaming is fundamentally characterized by a Doppler enhancement factor: $\delta = [\gamma\,(1 - \beta\cos\phi)]^{-1}$, where $\gamma = \left(1 - \beta^2\right)^{-1/2}$. Hence, the observed radio flux (S_0) depends strongly on the viewing angle (ϕ) and can be expressed in terms of the intrinsic value (S_i) as $S_0 = S_i\delta^{n+\alpha}$. Thus, in general it can be deduced from equations (1) and (2) that F and Q have some form of jet model-dependent relationship, which can be expressed in logarithmic scales as

$$\log F \approx (n + \alpha)\log Q. \tag{4}$$

It is obvious from equation (4) that for any assumed jet model the slope of $\log F - \log Q$ data takes on a range of positive values ($n + \alpha > 0$) depending on the assumed value of α. Thus, a positive correlation between F and Q is envisaged in asymmetric

radio source samples, if the observed asymmetries arise due to relativistic beaming effect at small orientation angles. Apparently, the measurement of both Q and F is expected to be world model-dependent due to the tight dependence of radio size (D) and luminosity (P) on the assumed world model. In the Friedmann-Robertson-Walker universe, D and P respectively depend on luminosity distance (d_L) as (Ubachukwu 1998b)

$$D = \theta d_L \left(1+z\right)^{-1}, \tag{5}$$

and

$$P = 4\pi\theta {d_L}^2 S \left(1+z\right)^{\alpha+1}. \tag{6}$$

In the current inflationary cosmology

$$d_L = H_0^{-1} \int_0^z \left[\left(1+z\right)^2 \left(1+\Omega_m\right) - z\left(2+z\right)\Omega_\Lambda\right]^{-1/2} dz, \tag{7}$$

where Ω_m and Ω_Λ are, respectively, the contributions of baryonic matter and cosmological constant to the energy content of the expanding universe.

Similarly, the orientation effect in AGNs posits that the projected linear size (D) depends on the viewing angle as

$$D = D_0 \sin\phi, \tag{8}$$

where D_0 is the intrinsic linear size.

Consequently, in a continuous jet model, the ratio R of the beamed flux of the core to the unbeamed flux of the lobe can be expressed in terms of its value at transverse alignment (R_T) in a general form (e.g. Hough & Readhead, 1987; Fan & Zhang, 2003)

$$R = \frac{R_T}{2}\left[\left(1-\beta\cos\phi\right)^{-n+\alpha} + \left(1+\beta\cos\phi\right)^{-n+\alpha}\right]. \tag{9}$$

Analysis of equations (1) and (9) shows that if the relativistic beaming effect accounts for the observed asymmetries in EGRSs, a clear correlation is also expected between R and Q in asymmetric sources, whose radio axes are supposedly aligned close to the line of sight. In particular, the most asymmetric sources are expected to be the most beamed sources.

Thus, the relativistic beaming model for asymmetries postulates that radio sources inclined at small angles to the line of sight should have brighter radio cores and foreshortened projected linear sizes (Orr & Browne 1982; Ubachukwu 2002), which should result in a strong $R-D$ anti-correlation, with a consequent $R-Q$ correlation. The anti-correlation is expected to yield an upper envelope function, where the relativistic beaming effect is expected to dominate, and which should provide the best fit to the observed $R-D$ data of source samples (e.g. Ubachukwu and Chukwude, 2002). In fact, Odo et al. (2015) have shown that for this optimum beaming, equation (9) can simplify to

$$R_{\max} = \frac{R_T \gamma^{2(n+\alpha)}}{2}, \tag{10}$$

where, $R_{\max}$ corresponds to the upper envelope $R-D$ function, which is expected to occur within a critical cone angle ϕ_c. Within the critical cone angle, the Doppler factor δ is fairly constant which yields (e.g. Ubachukwu and Chukwude, 2002):

$$\phi_c = \sin^{-1}\gamma^{-1}. \tag{11}$$

3. DENSITY VARIATION MODEL FOR ASYMMETRIC SOURCES

According to the beam model of Scheuer (1974), energy is continuously supplied to the lobes through beams of relativistic plasma. The beams plough their way through first the ambient interstellar medium (ISM) of the parent object, and then through the much hotter intergalactic medium (IGM) until the ram pressure of the IGM finally stops them. Studies of the environments of active galaxies and quasars have revealed that these sources are located in relatively dense environments and often show signs of interaction (e.g. Yee and Green 1987, Yates et al. 1989, Hutchings and Neff 1990, Ramos Almeida et al. 2013, Orsiet al. 2016).

Swarup and Banhatti (1981) proposed a model to account for the observed distributions of the flux density and separation ratios of the two components in the Ooty occultation and 3CR samples, based on the density variation of the IGM into which the beams propagate. This implies that there is an active beam in the receding lobe but due to less interaction with the IGM, its intrinsic emissivity is much lower than that of the approaching lobe. The observed asymmetry in Q would result if the two components were located in dense matter of different density profiles.

According to Swarup and Banhatti (1981), the ratio of the two components of a radio source can be given in terms of the beam power L and ambient density ρ, and can be equivalently written in terms of approaching (app) and receding (rec) lobes as

$$Q = \left(\frac{L_{\rm app}\rho_{\rm rec}}{L_{\rm rec}\rho_{\rm app}}\right)^{1/4}, \tag{12}$$

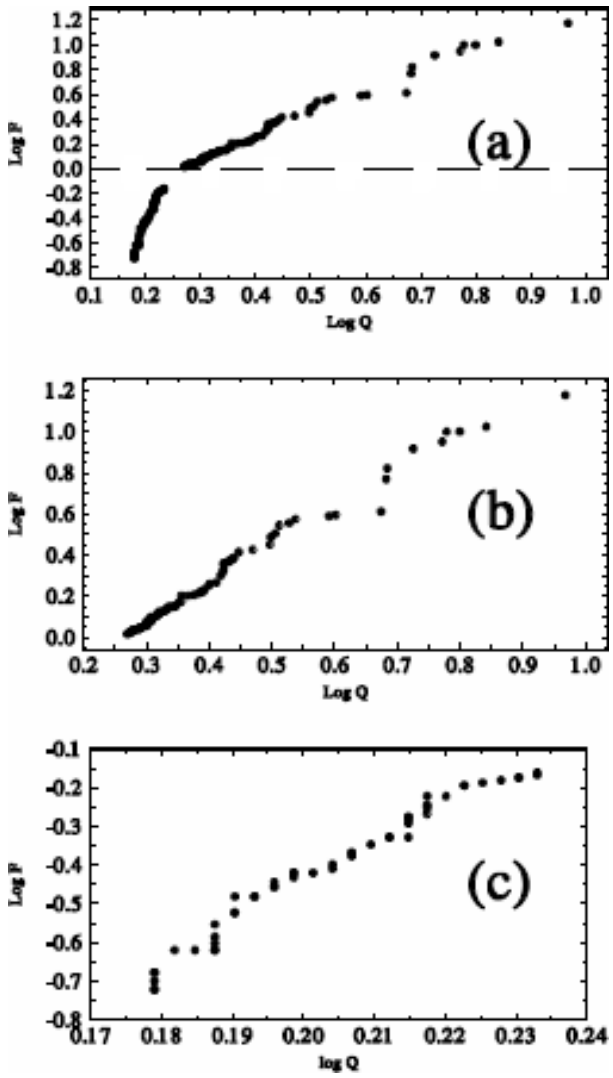

Fig. 1. Scatter plot of $\log F$ against $\log Q$ for 128 highly asymmetric objects (a); 79 RBM objects (b); 49 DVM objects (c).

and

$$F = \left(\frac{L_{\rm app}}{L_{\rm rec}}\right)^{13/8} \left(\frac{\rho_{\rm app}}{\rho_{\rm rec}}\right)^{1/8}. \qquad (13)$$

Equations (12) and (13) above suggest that in the density variation model there should be some form of $F-Q$ relation. In fact, for constant beam power, we can deduce a functional $F-Q$ relation of asymmetric radio sources in the form

$$\log F \approx -0.5 \log Q. \qquad (14)$$

4. DESCRIPTION OF SOURCE SAMPLE

The present analysis is based on the sample of 1045 edge brightened double radio sources drawn from a large database contained in Tables 1 and 2 of Nilsson (1998). Sources with information on separation ratio (Q), flux density ratio (F), linear size (D), core-dominance parameter (R) and redshift (z) were selected and updated with the recently updated 3CRR sample (Singal 2014). 555 objects in the sample have information on Q, out of which 468 objects show asymmetric structure with $Q > 1$. Analysis of Q-values of the 468 asymmetric objects yields a mean value $Q_m \approx 1.59 \pm 0.05$. Since the present investigation is concerned with highly asymmetric objects with $Q >> 1$, we adopt the lower limit of the mean Q-value ($Q_m \approx 1.5$) as the dividing line between highly asymmetric ($Q > Q_m$) and less asymmetric ($Q \leq Q_m$) sources. There are 153 highly asymmetric objects ($Q > 1.5$). It is found that 25 objects in the sample have signatures of compact steep spectrum (CSS) sources with $D \leq 15$ kpc (Peacock and Wall 1982; Ezeugo and Ubachukwu 2010). Since the CSS sources are believed to form a distinct class of EGRSs, we excluded these CSS sources from the current analysis, leaving only 128 objects. These 128 objects, representing $\approx 27\%$ of the asymmetric objects form our sample for current investigation.

Throughout the paper, we have adopted the modern concordance (ΛCDM) cosmology with $H_0 = 70\ {\rm km\,s^{-1}Mpc^{-1}}$ and $\Omega_0 = \Omega_m + \Omega_\Lambda = 1; (\Omega_m = 0.3; \Omega_\Lambda = 0.7)$. All relevant data are adjusted in line with this concordance cosmology. For the analyses in this paper the degree of relationship between source parameters is deduced by the Pearson Product Moment correlation coefficient (r) using the AXUM analytical software.

5. ANALYSES AND RESULTS

In § 2, we presented the implications of two models that appear to explain the observed asymmetries in EGRSs. Each of these models makes specific predictions, which can be tested using well-defined samples of radio sources.

5.1. $F-Q$ *Correlations*

In Figure 1 we show the scatter plots of flux density ratio (F) as a function of separation ratio (Q), on logarithmic scales, for the whole sample and two subsamples of highly asymmetric objects. Since we are considering the lobe emission, which is characterized by steep spectra, we have assumed $n = 3$ and $\alpha = 0.8$ for the F-data (e.g. Nilsson 1998). From the plot in Figure 1(a) of the 128 highly asymmetric objects, it is observed that F increases with Q over all values of Q. However, there is a steep

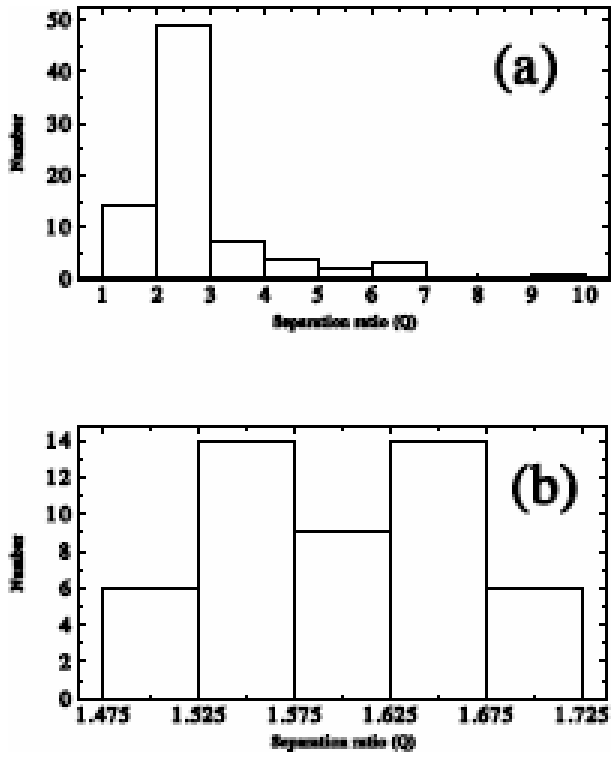

Fig. 2. Distribution of the 128 highly asymmetric sources in Q, with RBM sources (a) and DVM objects (b).

change in slope of the $F - Q$ at $F \approx 1$ (shown with a broken line) which corresponds to $Q \approx 1.7$. Linear regression analysis of the $F - Q$ data yields $\log F = -(0.81 \pm 0.03) + (2.50 \pm 0.08) \log Q$, with a tight positive correlation $r \approx 0.9$. The change in slope of the $F - Q$ data around $F = 1$, shown with a dotted line in Figure 1(a), suggests that the underlying physics in the two panels may not be the same for the highly asymmetric sources. Perhaps, the truncation in Figure 1(a) at $F = 1$ can be used as the dividing line between the RBM ($F > 1$) and DVM ($F < 1$) models outlined in § 2. Thus, in subsequent analyses, for purposes of comparison of effects of the two asymmetry models, the RBM and DVM, we have divided the sample into two subsamples in line with the two slopes indicating that the physics in the two planes is not the same: one with $Q > 1.5$ and $F > 1$, which we call the RBM subsample because their properties fit into the relativistic beaming model. On the other hand, because the sample used defines $Q > 1$, we assume that all sources with $Q > 1.5$ and $F < 1$ should correspond to the DVM. There are 79 objects in the RBM sub-sample and 49 objects in the DVM sub-sample.

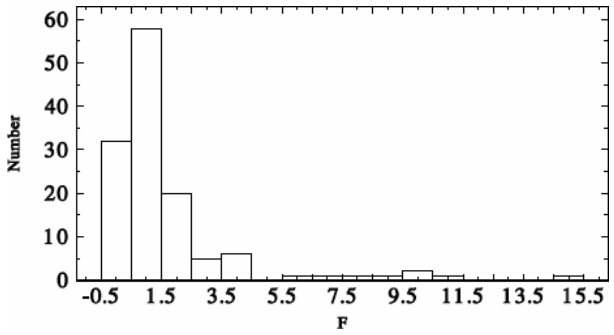

Fig. 3. Distribution of flux density ratio (F) for the 128 highly asymmetric sources.

The plot in Figure 1(b) for the RBM subsample shows a tight correlation between F and Q in which more highly asymmetric sources tend to have higher flux ratio as expected in the relativistic beaming model of asymmetries (c.f. equation 3). Linear regression analysis of the $F - Q$ data yields $\log F = -(0.47 \pm 0.01) + (1.82 \pm 0.03) \log Q$ with a near perfect correlation coefficient, $r \approx 0.99$, at 95% confidence. Similarly, the $F - Q$ plot in Figure 3(c) for the DVM subsample yields $\log F = -(2.48 \pm 0.06) + (10.19 \pm 0.28) \log Q$, with a tight positive correlation $r \approx 0.98$ at 95% confidence, which is hard to understand in terms of the density variation of ambient medium that predicts an inverse $F - Q$ relation (c.f. equation 11).

5.2. *F and Q Distributions*

The distribution of the separation ratios (Q) of the 128 highly asymmetric objects is shown in Figure 2. The distribution gives mean values of 2.76 ± 0.15 and 1.60 ± 0.01 respectively for the RBM and DVM subsamples. An obvious feature of the plot is the wide difference in range of Q-data for the RBM and DVM sub-samples, with that of RBM being much wider than DVM, perhaps due to the beaming effect. Furthermore, while the distribution in (a) is somewhat unitary, with a long asymmetric tail, that in (b) appears to be bimodal. This again seems to suggest that the mechanisms that produce the observed structural symmetries in the two subsamples are different. However, a two sample K-S test on the Q-data of the samples yields a chance probability $p = 0.37$. Thus, there is no statistically significant difference between the underlying distributions of RBM and DVM objects in Q. We interpret this to mean that relativistic beaming and density variation effects play comparable roles in determining the structural asymmetries of the whole

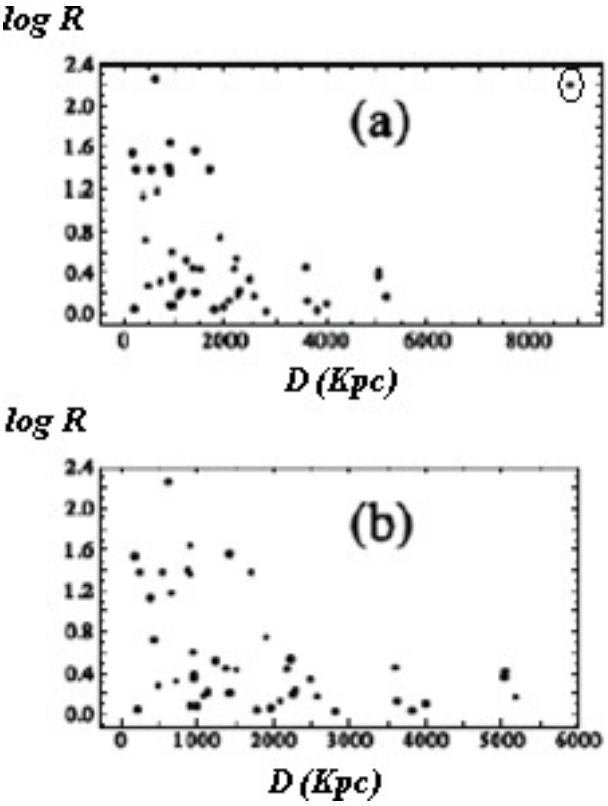

Fig. 4. Scatter plot of R against D for the RBM sample. (a) with outlier; (b) without outlier

sample. The asymmetric tail in Figure 2(a) is a signature of two sources, namely, (2359 - 690) and (2359 - 691), which are actually among the unidentified objects in the sample. Nevertheless, their exclusion in the analysis does not change our results significantly.

The histogram distribution of the sample in flux density ratio (F) is shown in Figure 3. The distribution is apparently unitary, with a mean value of 1.72 ± 0.20. We observe that 49 objects representing 38% of the asymmetric sources are consistent with the density variation model, while the other 79 objects $\approx 62\%$ are consistent with relativistic beaming model and are difficult to understand in terms of the density variation of the ambient medium.

Thus, in general, it could be argued from the distributions of Q and F that relativistic beaming and density variation in ambient medium have comparable effects in determining the structural asymmetries of the sample. A unified model would therefore be required to account for all the observed features of the Q and F distributions of the asymmetric sources. This is taken up in a follow-up paper (Alhassan et al. in preparation).

5.3. $R - D$ Relation

To investigate the effects of relativistic beaming in the current sample, the core-to-lobe luminosity ratio (R) is plotted as a function of projected linear size (D) for the RBM sub sample of highly asymmetric sources in Figure 4. There appears to be a general $R - D$ trend suggestive that larger sources are less beamed. However, the presence of an outlier (2347+30) among the RBM objects (enclosed in a circle in Figure 4(a)) is significant and seems to distort the general trend. The observed radio properties of this object (e.g. Nilsson et al. 1993) suggest that it is a weak FR II radio galaxy, for which relativistic beaming can be considered less important. Thus, we exclude the object from further analyses of the RBM sample. One-dimensional regression analysis of the data (without the outlier) yields $\log R = (0.910 \pm 0.130) - (0.0002 \pm 0.0001)D$, with a correlation coefficient $r \approx -0.4$. This result suggests that for the RBM objects there is a tendency for smaller sources to be beamed, compared to larger sources, as expected in the relativistic beaming scenario.

It is interesting to observe that removal of the outlier from the analysis reveals a well-defined upper envelope, which corresponds to the extremely beamed sources in our sample, as shown in Figure 4(b). Optimum beaming is expected to occur in the upper envelope function. We therefore carried out an analysis of the upper envelope function in four uniform bins of D, namely, $D \leq 1000$; $1000 < D \leq 2000$; $2000 < D \leq 3000$ and $D > 3000$ kpc. The linear fit to the upper envelope data yields: $\log R = (2.441 \pm 0.471) - (0.0007 \pm 0.0002)$ with $r \approx -0.9$, which is consistent with $R_{\max} \approx 275$. Thus, using $R_T = 0.0008$, which appears to be consistent with low frequency (178 MHz) surveys such as considered here (e.g. Ubachukwu 1998; Alhassan et al. 2011), we obtain a bulk Lorentz factor $\gamma = 7$ with the radiation beamed into a cone angle of $\phi_c = 8^\circ$ via equations (10) and (11) respectively, with $n = 3$ and average spectral index, $\alpha = 0.75$.

5.4. $R - Q$ Relation

To check the consistency of our results on the effects of relativistic beaming and orientation in the current sample, the core-to-lobe luminosity ratio (R) is plotted as a function of angular separation ratio (Q) for the two sub samples of highly asymmetric sources in Figure 5. Linear regression of the data yields $\log R = (1.38 \pm 0.30) - (0.81 \pm 0.85) \log Q$, with a correlation coefficient $r \approx -0.4$, for the RBM subsample and $\log R = (1.35 \pm 2.83) - (2.85 \pm 14.16) \log Q$

TABLE 1

MEDIAN VALUES OF ASYMMETRIC PARAMETERS FOR LOW AND HIGH REDSHIFT

z	$F_{\rm med}$	$Q_{\rm med}$	$D_{\rm med}$	$R_{\rm med}$
$z > 1$	2.36 ± 0.92	2.71 ± 2.32	89.70 ± 30.04	0.21 ± 0.12
$z \leq 1$	0.79 ± 0.03	1.72 ± 0.02	101.90 ± 32.99	0.38 ± 0.09

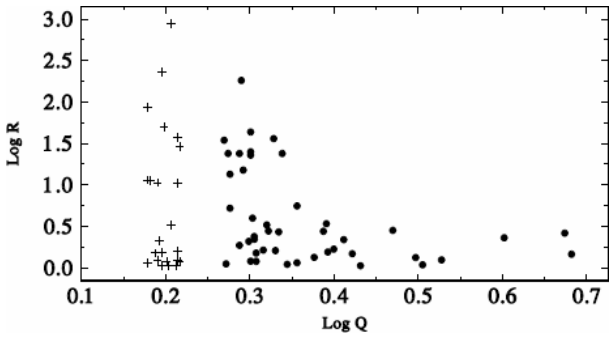

Fig. 5. Scatter plot of core-dominance parameter as a function of separation ratio for the RBM objects (filled circle) and DVM objects (plus +).

with $r \approx -0.04$, for the DVM subsample. The DVM subsample shows no $R-Q$ correlation as expected in the DVM model while the RBM subsample suggests a marginally significant $R-Q$ correlation, but in the sense opposite to that expected of the RBM model.

5.5. *Effects of Redshift* (z)

A redshift-dependent density variation of asymmetric sources of the form $\rho \approx (1+z)^3$ has been predicted to explain the variation of intergalactic medium (IGM) of extragalactic radio sources. This is expected to yield more asymmetric sources at an earlier epoch, implying that smaller sources should be more asymmetric than larger sources (Gaibler and Krause, 2011).

We tested the consistency of this effect on the present sample of highly asymmetric sources. Thus, we divided the sample into low and high z ($z \leq 1$ and $z > 1$) respectively and compared the median value data of flux density ratio, separation ratio, linear size and core-dominance parameter at the two-redshift regimes for consistency. The results are consistent with the prediction that smaller sources are located at higher redshifts and tend to be more asymmetric, with higher values of the asymmetry parameters F and Q than larger sources. A summary of the results is presented in Table 1.

6. DISCUSSION AND CONCLUSION

We have investigated the effects of relativistic beaming and density variations to account for the observed structural asymmetries of highly asymmetric radio sources. Our results suggest that neither the relativistic beaming nor the density variation model alone is adequate to account for all the observed features in terms of the distributions of the angular separation ratio Q and flux density ratio F of the present sample. The results, however, show that the relativistic beaming model and the density variation model have somewhat comparable effects on the evolution of double radio sources.

A major result of the current investigation is the similarity in trends and strength of correlation between the flux ratio and separation ratio of the sample. While the RBM sample in this sense can be explained fully in terms of relativistic beaming effect, the DVM sample is yet to be understood in terms of an underlying density variation hypothesis (Onuchukwu and Ubachukwu, 2015). Although the $F-Q$ trend in the DVM sample is consistent with the opinion that the radio source flux density ratio is sensitive to structural asymmetry (Gaibler and Krause, 2011), it appears not to be consistent with the $F-Q$ anti-correlation expected in the density variation model (Swarup and Banhatti 1981). Figure 3 thus appears to be more consistent with the RBM hypothesis, which predicts a positive correlation between F and Q. The density variation model predicts an inverse correlation between F and Q which is not observed here. If we assume that there is no intrinsic variation in L, then a density variation of about six orders of magnitude would be required to explain the largest F values in the present sample.

Gopal-Krishna and Wiita (1991) have shown that the beam efficiency depends on the density through which the relativistic beams propagate. In other words, L is not expected to be constant but to decrease with an increase in density. It should therefore be expected that $\rho_{\rm app} > \rho_{\rm rec}; L_{\rm app} < L_{\rm rec}$ so that small Q values do not necessarily imply large F values. This could explain the observed $F-Q$ correlation for the DVM contrary to expectation.

The results obtained from the RBM are consistent with Onuchukwu et al. (2014), which argued that the observed asymmetries in radio sources are a result of Doppler boosting or orientation effects. The apparent lack of correlation between R (the beaming indicator) and Q (the asymmetry parameter) in the DVM subsample does not seem to suggest that relativistic beaming accounts for all observed structural asymmetries of the sample. The result appears to be in agreement with some previous results (e.g. Onah et al. 2014; Onuchukwu et al 2014) that argued for both intrinsic and environmental effects (in addition to relativistic beaming) to account for the observed asymmetries in powerful radio sources. In fact, Kharb et al. (2008) suggested that Q appears to be more sensitive to intrinsic and environmental asymmetries than to the relativistic beaming effect for a sample of FR II radio galaxies. Perhaps the strong dependence of Q on intrinsic/environmental effects has given rise to the apparent lack of $R-Q$ correlation in the DVM subsample analysis.

We have also shown that smaller sources located at higher redshifts are associated with asymmetries higher than those of larger sources located at lower redshifts. Perhaps it could be argued that the strong positive correlation between F and Q obtained for both RBM and DVM samples is a result of the redshift effect on the samples. Thus, we tested the dependence of the source asymmetry parameters on redshift by looking for any correlation between the parameters and redshift for both the high redshift ($z > 1$) and low redshift ($z \leq 1$) sources. The result yields $r > 0.8$ as the correlation coefficient for the $Q - z$ and $F - z$ relations at all redshifts. This actually shows that the redshift effect is significant in these parameters. However, we eliminated the redshift effect by subtracting out the common dependence of Q and F on redshift from the $F - Q$ correlation using the Spearman partial correlation statistic, which is a non-parametric statistic involving cross-correlation of the parameters, and is given in general by (e.g. Ubachukwu et al. 2002)

$$r_{12,3} = \frac{r_{12} - r_{12}r_{23}}{\left[\left(1 - r_{13}^2\right)\left(1 - r_{23}^2\right)\right]^{1/2}}. \qquad (15)$$

This tests whether there is a significant correlation between two quantities 1, 2 (F, Q) that does not result from both being separately correlated with a third quantity 3 (z). This implies that a correlation between the first two parameters is kept constant. This statistic varies from -1 (for a perfect inverse correlation) to $+1$ (for a perfect positive correlation) with 0 representing null correlation. The results of the non-parametric analysis at 95% confidence give $r_{QF,z} > 0.9$ at all redshift regimes. Thus, we argue in this paper that the $F-Q$ correlations observed in the two model subsamples are independent of cosmological effects. The tight correlations may therefore be intrinsic, rather than an artifact of redshift in the present sample of highly asymmetric radio sources.

REFERENCES

Alhassan, J. A., Ubachukwu, A. A., & Chukwude, A. E. 2011, AfrSk, 15, 11
Arshakian, T. G. & Longair, M. S. 2004, MNRAS, 351, 727
Banhatti, D. G. 1980, A&A, 84, 112
Barthel, P. D. 1989, ApJ, 336, 606
Bridle, A. H. & Perley, R. A. 1984, ARA&A, 22, 319
Conway, R. G. & Strom, R. G. 1985, A&A, 146, 392
Ezeugo, J. C. & Ubachukwu, A. A. 2010, MNRAS, 408, 2256
Fan, J. H. & Zhang, J. S. 2003, A&A, 407, 899
Fanaroff, B. L. & Riley, J. M. 1974, MNRAS, 167, 31
Gaibler, V. & Krause, S. K. 2011, MNRAS, 411, 155
Garrington, S. T. 1988, Unpublished Ph.D Thesis, University of Manchester
Garrington, S. T., Leahy, J. P., Conway, R. G. & Laing, R. A. 1988, Natur, 331, 147
Gopal-Krishna & Wiita, P. J. 1991, ApJ, 373, 325
_____. 2004, arXiv:Astroph/0409761v2
Gopal-Krishna, Kulkarni, V. K., & Wiita, P. J. 1996, ApJ, 463, L1
Hough, D. H. & Readhead, A. C. S. 1987, ApJ, 321, L11
Hutchings, J. P. & Neff, S. G. 1990, AJ, 99, 1715
Kapahi, V. K. & Saikia, D. J. 1982, JApA, 3, 465
Kharb, P., ODea, C. P., Baum, S. A., et al. 2008, ApJ, 174, 74
Longair, M. S. & Ryle, J. M. 1979, MNRAS,188, 625
Nilsson, K., Valtonen, M. J., Katilainen, J., & Jaakkola, T. 1998, ApJ, 413, 453
Onah, C. I., Ubachukwu, A. A., & Odo, F. C. 2014, JApA, 35, 619
Onuchukwu, C. C. 2017, Ap&SS, 362, 100
Onuchukwu, C. C. & Ubachukwu, A. A. 2013, Ap&SS, 344, 211
_____. 2015, Ap&SS, 357, 145
Onuchukwu, C. C., Ubachukwu, A. A., & Odo, F. C. 2014, RMxAA, 50, 93
Orr, M. J. L. & Browne, I. W. A. 1982, MNRAS, 200, 1067
Orsi, A. A., Fanidakis, N., Lacy, C. G., & Baugh, C. M. 2016, MNRAS, 456, 3827
Peacock, J. A. & Wall, J. V. 1981, MNRAS, 194, 331
Ramos Almeida, C., Bessiere, P. S., Tadhunter, C. N., et al. 2013, MNRAS, 436, 997
Ryle, M. & Longair, M. S. 1967, MNRAS, 136, 123
Saikia, D. J. 1984, MNRAS, 208, 231

Scheuer, P. A. G. 1974, MNRAS, 166, 513
_____. 1995, MNRAS, 277, 331
Scheuer, P. A. G. & Readhead, A. C. S. 1979, Natur, 277, 182
Singal, A. K. 2014, AJ, 148, 16
Swarup, G. & Banhatti, D. G. 1981, MNRAS, 194, 1025
Ubachukwu, A. A. 1998a, Ap&SS, 257, 23
_____. 1998b, AuJPh, 51, 585
_____. 2002, Ap&SS, 279, 251
Ubachukwu, A. A., Chukwude, A. E., & Alhassan, J. A. 2002, Ap&SS, 281, 601
Yates, M. G., Miller, L., & Peacock, J. A. 1989, MNRAS, 240, 129
Yee, H. K. C. & Green, R. 1987, ApJ, 319, 28

Jibrin A. Alhassan, Finbar C. Odo, and Augustine A. Ubachukwu: Department of Physics and Astronomy, Faculty of Physical Sciences, University of Nigeria, Carver Building, 1 University Road, Nsukka, Nigeria (jibrin.alhassan, finbarr.odo, augustine.ubachukwu@unn.edu.ng).
Jibrin A. Alhassan, Finbar C. Odo, and Augustine A. Ubachukwu: Astronomy and Astrophysics Research Lab, University of Nigeria, Nsukka, Nigeria (jibrin.alhassan, finbarr.odo, augustine.ubachukwu@unn.edu.ng).
Chika C. Onuchukwu: Department Of Industrial Physics, Chukwuemeka Odumegwu Ojukwu University, Anambra State, Nigeria (cc.onuchukwu@coou.edu.ng).

Revista Mexicana de Astronomía y Astrofísica, **55**, 161–175 (2019)

DOI: https://doi.org/10.22201/ia.01851101p.2019.55.02.04

ENHANCED MASS LOSS RATES IN RED SUPERGIANTS AND THEIR IMPACT ON THE CIRCUMSTELLAR MEDIUM

L. Hernández-Cervantes[1,2], B. Pérez-Rendón[3], A. Santillán[4], G. García-Segura[5], and C. Rodríguez-Ibarra[6]

Received September 25 2018; accepted May 8 2019

ABSTRACT

In this work, we present models of massive stars between 15 and 23 $M_\odot$, with enhanced mass loss rates during the red supergiant phase. Our aim is to explore the impact of extreme red supergiant mass-loss on stellar evolution and on their circumstellar medium. We computed a set of numerical experiments, on the evolution of single stars with initial masses of 15, 18, 20 and, 23 $M_\odot$, and solar composition ($Z = 0.014$), using the numerical stellar code BEC. From these evolutionary models, we obtained time-dependent stellar wind parameters, that were used explicitly as inner boundary conditions in the hydrodynamical code ZEUS-3D, which simulates the gas dynamics in the circumstellar medium (CSM), thus coupling the stellar evolution to the dynamics of the CSM. We found that stars with extreme mass loss in the RSG phase behave as a larger mass stars.

RESUMEN

En este trabajo presentamos modelos evolutivos de estrellas en el intervalo de 15 a 23 $M_\odot$, usando un incremento en la tasa de pérdida de masa durante su fase de supergigante roja para explorar el impacto de una fuerte pérdida de masa en la evolución de la estrella y en la dinámica de su medio circunestelar. Calculamos un conjunto de experimentos numéricos simulando la evolución de estrellas aisladas con masas iniciales de 15, 18, 20 y 23 $M_\odot$ y metalicidad solar ($Z = 0.014$) usando el código estelar BEC. De los modelos evolutivos obtuvimos parámetros característicos del viento estelar dependientes del tiempo para usarlos como condiciones de contorno en el código hidrodinámico explícito ZEUS-3D para simular la evolución del medio circunestelar. Encontramos que las estrellas con altas tasas de pérdida de masa durante la etapa de supergigante roja se comportan como estrellas de mayor masa.

Key Words: ISM: bubbles — stars: early-type — stars: evolution — stars: mass-loss — stars: winds, outflows

1. INTRODUCTION

The evolution and fate of massive stars ($M > 8\ M_\odot$) is strongly influenced by their mass loss history(Chiosi & Maeder 1986), whereas their photon and mechanical luminosities affects the dynamics and energetics of the circumstellar medium (CSM). Massive stars ($8 - 40\ M_\odot$) experience large mass loss during the red supergiant (RSG) phase. Those stars generate low temperature winds during this phase, reaching mass loss rates from 10^{-4} to $10^{-6}\ M_\odot\ \mathrm{yr}^{-1}$ (Salasnich et al. 1999; Moriya et al. 2011)and ejecting an important fraction of their initial mass. The amount of mass loss during the RSG

[1]Instituto de Astronomía, Universidad Nacional Autónoma de México, México.
[2]Programa de Doctorado Ciencias (Física), Universidad de Sonora, Hermosillo, Sonora, México.
[3]Departamento de Investigación en Física, Universidad de Sonora, Hermosillo, Sonora, México.
[4]Dirección General de Cómputo y de Tecnologías de Información y Comunicación, Universidad Nacional Autónoma de México, México.
[5]Instituto de Astronomía, Universidad Nacional Autónoma de México, Ensenada, Baja California, México.
[6]Departamento de Física, Universidad de Sonora, Hermosillo, Sonora, México.

phase is critical to determine the fate of those massive stars. They can either explode as supernova in the RSG stage or they can evolve bluewards in the Hertzsprung-Rusell (HR) diagram, giving a completely different appearance to the core-collapse progenitor. The amount, velocity and chemical composition of the subsequent wind stages during the post-RSG stages influence the structure and energetics of the circumstellar gas, prior to the supernova (SN) explosion. Therefore, it is important to understand the main features of mass loss rate during and after the RSG phase.

The measurements of mass loss rates for RSG stars using multiwavelength observations are still very uncertain (Smith 2014). Thus, our knowledge of the stellar wind parameters and evolution for late type supergiants remains poor. Numerical evolution models use empirical "recipes" to set the RSG mass loss rates. Some of them are based on observational prescriptions for hot stars (de Jager et al. 1988; Nieuwenhuijzen & de Jager 1990), but slightly enhanced to ensure post-RSG evolution of stars with initial masses greater than 25 - 30 $M_{\odot}$, according to observations (Humphreys et al. 1985). Other approaches use empirical mass loss recipes specific for RSG (Reimers 1975; Salasnich et al. 1999; Van Loon et al. 2005), that only describe time-averaged and smoothed mass-loss rates derived from observational diagnostics. Using those mass loss rates as input in numerical models predicts that massive stars between 8 and 25 $M_{\odot}$ will end their life as a RSG with a massive hydrogen envelope, leading to a type II-P or II-L SN. However, Smartt et al. (2009) found that none of the observed progenitors of confirmed SN-IIP are more massive than 15 - 17 $M_{\odot}$ and it is unclear why no RSG with an initial mass range of 15 - 25 $M_{\odot}$ has been observed to explode as a SN-IIP, as expected from numerical simulations. This is known as the "RSG problem".

A possible solution for the RSG problem would be to invoke higher mass loss rates than those currently used in canonical stellar models (Vanbeveren 1998; Yoon & Cantiello 2010; Georgy 2012A; Georgy et al. 2013A; Meynet et al. 2015), leading to a smaller hydrogen content in the SN progenitor envelope, and resulting in a H-poor SN type II, or even a SN-Ib/c. There is some evidence in favor of higher RSG mass loss rates than those currently in use; Schröder & Cuntz (2005) derived a semiempirical relation for the mass loss by cool winds and found that the RSG mass loss rates must be higher relative to Reimer's classical parametrization. Pérez-Rendón et al. (2009) also found that some observational features of Cass A could be better explained with higher RSG mass loss rates. Additionally, there are observations of low luminosity WC stars that cannot be explained with current stellar models (Maeder & Meynet 1994; Georgy et al. 2012B), but these could be explained if WNE and WC were (probably) less massive, due to an enhanced mass loss in previous evolutionary stages, i.e. in the RSG phase. However, these stars could also be the result of binary evolution. Van Loon et al. (2005) observed that dust-enshrouded RSG present mass loss rates are a factor 3 - 50 times higher than those obtained by de Jager et al. (1988) for galactic RSG, but Mauron & Josselin (2011) found that RSG mass-loss rates based on infrared excesses agree within a factor of 4 with de Jager et al. (1988) rates. Alternatively, Beasor & Davies (2016) have proposed that dust extinction could affect the determination of the SN-IIP progenitor masses, lowering their estimated initial mass. Thus, if this effect is taken into account, the inferred SN-IIP progenitor masses often increase, making the required larger RSG mass loss rate unnecessary.

In this work we explore the consequences of higher mass loss rates for RSG stars with initial masses in the range of 15 to 23 $M_{\odot}$, regardless of the underlying physical mechanisms that could cause such an increase. We examine its impact on the structure of the circumstellar gas and uncover some clues to better understand the "RSG problem". We also study the influence of this extreme mass loss on the evolution and on the pre-supernova structure. Depending on stellar parameters (L, M, Z, etc.), stellar winds are closely linked to stellar evolution, coupling the evolution of the CSM to the star itself.

The evolution of a set of stellar models with inital masses in the range 15 - 23 $M_{\odot}$ and different mass loss rates during the RSG phase (taking care to keep them within the observational uncertainties) was calculated with the code BEC (Binary Evolutionary Code). Then the magnetohydrodynamical ZEUS-3D code was used to follow the evolution of the CSM. The effect of RSG extreme mass loss has been explored recently by Georgy et al. (2012B); Meynet et al. (2015); Renzo et al. (2017). They found that the evolution of the models strongly depends on the chosen RSG mass-loss prescription. This behavior has important implications regarding the connection between stellar evolution and their CSM, which will be explored in this work.

We propose to study the impact of enhanced RSG mass loss on the stellar evolution, and thereafter on their circumstellar medium. In § 2 we briefly summarize the physics, and numerical setup used to explore

the stellar evolution with the BEC code. In § 3 we explore the dynamics of the CSM with ZEUS-3D. In § 4 we show our results and describe the impact of the higher RSG mass loss rates on the stellar evolution and the circumstellar medium. In § 5 we discuss the results.

2. INPUT PHYSICS OF STELLAR MODELS

We built a set of single star models using the stellar code BEC (Binary Evolutionary Code), extensively described by Petrovic et al. (2005); Yoon et al. (2006). The models consider ZAMS masses of 15, 18, 20 and 23 $M_\odot$ and a fixed chemical composition of $Z = 0.014$ (Asplund et al. 2009). The simulations are performed with OPAL opacities (Iglesias & Rogers, 1996), and a nuclear network including the major H, He, C, Ne and O burning reactions. The models were built either without rotation (Case A models), or with initial rotational velocities of $V_{\rm rot} = 100$ km s^{-1} at the ZAMS (Case B). We used the Ledoux criterion to define the zones of stellar convection, and the processes of convective transport. Rotation triggers some additional transport mechanisms of chemical species inside the star and, following (Heger et al. 2000), the effects of rotational mixing were considered as diffusive processes. Convective overshooting was taken into account using a moderate overshoot parameter of 0.2 times the local pressure scale height. We set the α parameter $\alpha = {\rm L/H_P} = 1.6$ on the main sequence. This α parameter in the RSG phase was set to 2.5, in order to fit the observational position of galactic RSG in the H-R diagram(Levesque et al. 2005). Mass loss rates used in each evolutionary stage are described in § 3.

The stellar models were computed from the ZAMS up to carbon core exhaustion. After this point, the stellar core evolution is faster than in previous stages, and the external layers are not affected. Thus, our final models correspond to the structure of the supernova progenitor star. Due to numerical difficulties, the 23 $M_\odot$ rotating models were evolved up to core He exahustion, but their final features are uncertain and must be taken with caution.

3. WIND PARAMETERS AND CIRCUMSTELLAR MEDIUM MODELS

To build the stellar models we adopted empirical mass-loss rate formulations ("recipes") that depend on stellar parameters such as mass, radius, luminosity, metallicity, etc. These parameters, in turn, are dependent on stellar evolution: one parameter affects the behavior of the others.

3.1. *Mass Loss Prescriptions*

Mass loss rates are a key ingredient in this work. In this section, we describe the specific parametrization used at each stellar evolutionary stage in order to obtain mass-loss rates and wind velocities as a function of time. These can be regarded as an output from the stellar models. Wind mass loss rates for hot stars were calculated according to the prescription given in equation (24) of Vink et al. (2001), for OB stars in the temperature range of $27500 < T_{\rm eff} \leq 50000$ K (see their equation (24)), and for $12500 < T_{\rm eff} \leq 22500$ K we used their equation (25). Outside this temperature range, we applied the Nieuwenhuijzen & de Jager (1990) mass loss rate (hereafter NdJ90):

$$\log \dot{M} = 1.24 \log(L/L_\odot) + 0.16 \log(M/M_\odot) + 0.81 \log(R/R_\odot) - 14.016, \quad (1)$$

including a metallicity dependence of $\dot{M} \propto Z^{0.86}$ (Vink & de Koter 2005).

For the RSG phase (defined when $\log T_{\rm eff} < 3.65$), we explored the influence of increasing the mass loss rates to values higher than commonly used in the evolution of the star and their circumstellar medium. For this purpose, we simply increased those of equation (1) in NdJ90 by a factor of 2 (hereafter, "canonical" mass loss), 6 and 10. The evidence that RSG mass-loss rates are higher than those by de Jager et al. (1988) can be found elsewhere (Salasnich et al. 1999; Yoon & Cantiello 2010). Here, we have chosen our factors to maintain the rates within the observational limits (Mauron & Josselin 2011; Van Loon et al. 2005). Non-rotating models are labeled with an "`A`" tag whereas models with an initial rotation of ($v_{\rm rot} = 100$ km s^{-1}) are tagged with a "`B`". The number next to this rotational label indicates the initial mass of the star and the mass loss rate enhancement factors during the RSG phase are labeled by "`×2`" , "`×6`" and "`×10`", for models with increased loss rates by a factor of 2, 6, and 10, respectively. Note that all RSG mass loss rates thus obtained lie within observational values for Galactic stars (Figure 1). It is likely that the numerical mass loss rates could be increased by an even higher factor.

The mass loss rates for the post-RSG evolution when the surface hydrogen mass fraction falls below $X_{\rm s} < 0.45$ and $T_{\rm eff} > 10000$ K are set according to Hamann et al. (1995):

$$\log \dot{M} = 1.50 \log(L/L_\odot) + 0.86 \log (Z/Z_\odot) - 11.95 \quad (2)$$

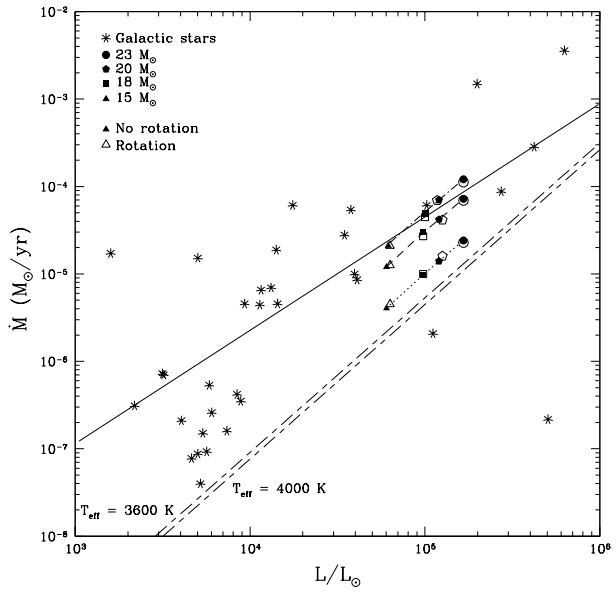

Fig. 1. RSG mass loss averages obtained from our numerical models in comparison with observational mass loss rates for oxygen-rich AGB, and RSG Galactic stars. The solid line shows the mass-loss versus luminosity relation fitted to a Galactic sample (Matsuura et al. 2016). The short-dash line connects our "×2" models, long-dash and dot-dash lines our "×6" and "×10" models, respectively. We note that our numerical mass-loss rates lie within the observational ones. For a comparison to canonical numerical models, the long-dash/short-dash line shows the linear approximation of the empirical mass-loss formula of de Jager et al. (1988) for typical temperatures of RSG ($T_{\rm eff}$ = 3600 K, upper line; $T_{\rm eff}$ = 4000 K lower line).

and we have further adopted the Nugis & Lamers (2000) mass-loss rate when the surface H fraction drops below $X_{\rm s} < 0.3$ (WNE star):

$$\log \dot{M} = \quad 1.29 \log(L/L_{\odot}) + 1.73 \log Y + 0.50 \log Z - 11.00. \quad (3)$$

For rotating stars there is an increase in the mass-loss rates due to the effect of the centrifugal forces at the outermost stellar layers. The rotational mass loss rate is enhanced (Friend & Abbott 1986) by a factor of:

$$\dot{M}(\omega) = \dot{M}(\omega = 0) \times (1 - \Omega)^{\xi}, \quad (4)$$

where $\xi = -0.43$, $(\omega = 0)$ is the mass-loss rate of the non-rotating star and $\Omega \equiv v/v_{\rm critic}$ is the ratio of the the surface equatorial velocity to the critical rotation velocity (break-up speed) defined as $v^2_{\rm critic} = 1/2\ v^2_{\rm escape}$ [equation 5].

The escape velocity is calculated as a function of the stellar parameters, changing over time:

$$v_{\rm escape} = \left[\frac{2GM_{\star}}{R_{\star}}(1 - \Gamma)\right]^{1/2}, \quad (5)$$

and the corresponding stellar wind velocity was set to:

$$v^2_{wind} = \beta v^2_{escape}\ . \quad (6)$$

β is a free parameter which accounts for the relation between wind velocity and the escape velocity and Γ is the Eddington's factor. To set the value of β, we used the criterion from Eldridge et al. (2006) and made a linear interpolation for uncovered ranges. The wind velocity of WR stars was derived according to Nugis & Lamers (2000):

$$\log\left(\frac{v_{\rm wind}}{v_{\rm escape}}\right) = 0.61 - 0.13\ \log L_{\star} + 0.30\ \log Y\ . \quad (7)$$

Using these equations, we obtained the mass-loss rates and wind velocities as a function of time during the entire evolution, from the ZAMS until the end of core C-burning, for stars with initial masses of 15,18, 20 and 23 $M_{\odot}$. At this point the outer layers of the star have their final configuration (pre-SN stage). These results are then used to perform numerical models of the CSM structure and dynamics that are closely linked to the details of stellar evolution.

3.2. *Hydrodynamical Models*

To simulate the circumstellar gas around our stars, we used the hydrodynamical code ZEUS-3D, which is a three-dimensional, finite-difference Eulerian explicit code that integrates the hydrodynamical ideal gas equations in the absence of viscosity (Stone & Norman, 1992; Clarke, 1996). The stellar evolution outputs (mass loss rate, velocity, effective temperature and stellar radius) are used as the time-dependent, inner boundary conditions in the hydrodynamical simulations. This is done in a similar way as in Pérez-Rendón et al. (2009), but in this paper we follow the gas dynamical evolution in a 2D grid over the entire stellar lifetime, from ZAMS to supernova explosion. The average wind velocities, total mass lost and lifetimes at each stage are given in Tables 3 to 7 for some typical models. Post-main sequence stages are defined as a function of the stellar effective temperature as follows: we considered a RSG star when $\log(T_{\rm eff}/{\rm K}) < 3.65$; a yellow supergiant (YSG) when $3.75 < \log(T_{\rm eff}/{\rm K}) < 3.9$; and a luminous blue supergiant star (LBSG) when $\log(T_{\rm eff}/{\rm K}) > 4.0$ (but the star is not a Wolf-Rayet

star). The "YSG/LBSG" label refers only to post-RSG phases. In the WR stage we distinguished two subtypes: the star is a WNL when it is a Wolf-Rayet star with some presence of hydrogen ($X_s < 0.45$ and $\log(T_{\rm eff}/{\rm K}) > 4.0$); whereas it is a WNL star when $X_s < 0.30$.

For the physical grid, we used spherical coordinates with periodic boundary conditions in the alt-azimuthal direction. The simulations were done on a two-dimensional $r-\theta$ grid of 200 cells in radial direction and 90 cells in the angular coordinates. For the 15 $M_\odot$ models, the physical radial extension is 12 pc (giving a spatial resolution of 0.06 pc/cell) whereas the rest of the models have a radial length of 15 pc (0.075 pc/cell). In colatitude, we considered a range of $(0, 90\,^\circ)$, giving an angular resolution of $1\,^\circ$/cell.

Here we do not consider the effects of photoionization from the stellar UV flux, nor the effects of magnetic fields or heat conduction. To simulate the ionization, we set the lower cutoff temperature to 10^4 K. The hydrodynamical calculations start at the ZAMS, with the stellar wind flowing into an almost uniform and homogeneous interstellar medium (ISM), of $n_o = 100$ cm^{-3} (typical of molecular clouds), with small random perturbations of 1.0 % in density, and an initial thermal energy density corresponding to a background temperature of $T_b = 10$ K.

4. RESULTS

4.1. *Stellar Models*

Figures 2 and 3 show the evolutionary tracks in the Hertzsprung-Russell diagram (HRD) for non-rotating (Case `A`) and rotating stellar models (Case `B`). For models having the same initial mass, rotational velocity and metallicity, the differences in evolution are a consequence of the adopted value for the RSG mass-loss rate.

Figure 2 shows evolutionary tracks for non-rotating models. In Figure 2-*left*, we show the "canonical" models, whose RSG mass loss rate is that of NdJ90, but increased by a factor of 2 ("×2" tag). All these models evolve redwards after the main sequence, crossing only once the HR diagram towards the cool side to end their life as a red supergiants.The RSG mass loss is not large enough to produce a bluewards track. Massive stars produce core-collapse supernovae, so we assume that all our models will end up as a SN. As expected, all our canonical models end their lives as RSG stars keeping a massive H-envelope, and will lead to a II-L or II-P supernovae, according to Heger et al. (2003).

The evolutionary paths change for models with a higher RSG mass loss rate. For "×6" models, only the 15 $M_\odot$ star ends up as a red supergiant. In the rest of the models, the increase of the RSG mass loss peels off a significant mass from the H-envelope and triggers post-RSG evolution in stars of 18 $M_\odot$ and larger, which evolve bluewards through a short yellow and blue supergiant phase, diminishing or losing their H-rich envelope, to become Wolf-Rayet stars (WR). When their He-core fraction drops below 0.10 ($Y_c < 0.10$), the stars stop their path towards the blue and evolve to slightly cooler temperatures, describing a blue loop beyond the main sequence band. The Wolf-Rayet stars will remain the rest of their life on the blue side of the HRD, to finally explode as stars with an H-poor envelope (WNL), or as an hydrogen lacking one (WNE). Table 1 shows the supernova progenitor for all our models: `A18×6` model will explode as a WNL star, whereas the `A20×6` and `A23×6` models end their lives as lack-of-H WNE stars. The final supernova type will be II-L/b for the WNL star and a SN-Ib for WNE progenitors (Heger et al. 2003) .

All the models with extreme RSG mass loss ("×10") undergo post-RSG evolution to end their lives as Wolf-Rayet stars. Only the `A15×10` model keeps a small H-envelope, ending as WNL, whereas more massive stars end their life as more evolved WNE stars. The mass loss was insufficient to produce a WC star (a bare core of CO).

The time that the stars spend in each post-MS stage changes depending on the RSG mass-loss rate: Tables 3 to 7 show the stellar lifetimes in each evolutionary phase for some interesting models. We note that the lifetime as a red supergiant decreases as the mass-loss rate grows. This occurs because the post-RSG evolution to bluewards is triggered when the ratio of the mass of the envelope to that of the stellar core drops to a value of 0.4-0.6 (Giannone 1967; Meynet et al. 2015) . In our simulations, this ratio is reached when the models lose the same amount of their envelope mass (the mass loss rate does not affect the size of the He core). For larger mass loss rates, the critical ratio is attained at shorter times. Our `A18×2` model lost 5.16 $M_\odot$ during the RSG stage, whereas the models `A18×6` and `A18×10` lost 10.48 $M_\odot$ and 10.60 $M_\odot$, respectively, before evolving bluewards to become WRS. The same occurs for the 20 $M_\odot$ models: the `A20×2` model lost 7.23 $M_\odot$, whereas the `A20×6` and `A20×10` models lost 11.35 $M_\odot$ and 11.39 $M_\odot$ as RSGs to end their lives as blue WR stars. The mass lost by quiescent winds during Wolf-Rayet phases is only a small amount of the total mass (less than 5 % of the initial mass).

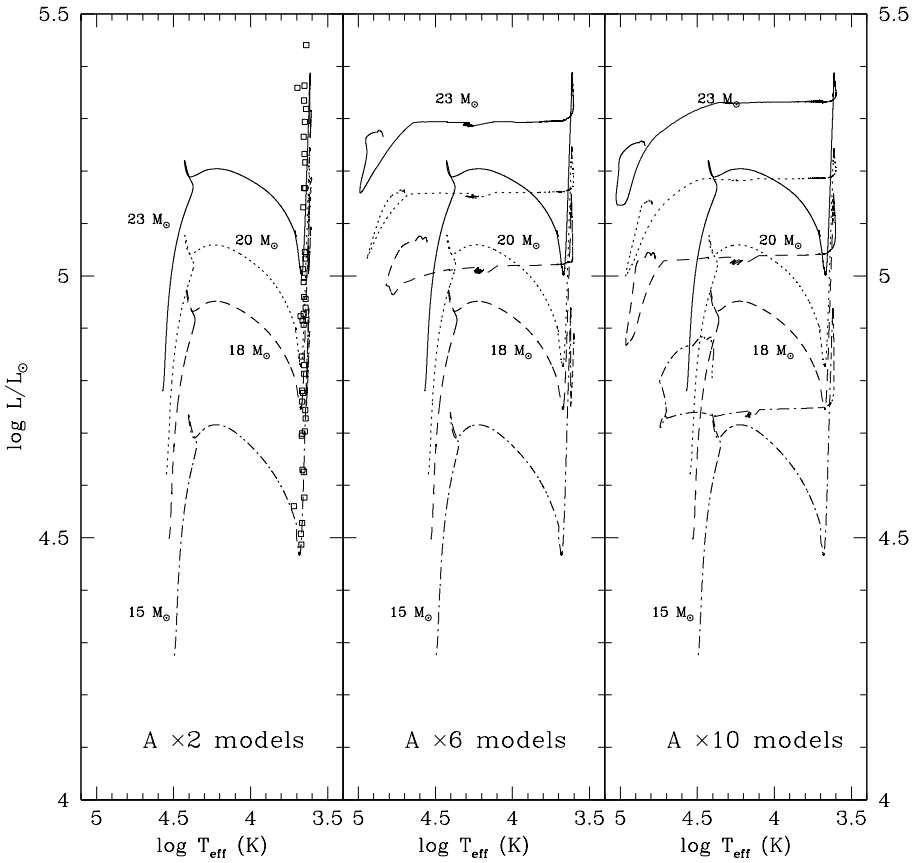

Fig. 2. Case `A` ($v_{\rm rot} = 0$ km s^{-1}): Set of evolutionary tracks for stars in the range 15-23 $M_{\odot}$, from the ZAMS up to the exhaustion of carbon in the stellar core. The left panel shows the evolution using a mass-loss rate of Nieuwenhuijzen & de Jager (1990) increased by a factor of 2 during the red supergiant phase ("×2" models). The squares indicate the position of galactic RSG observed by Levesque et al. (2005). Models displayed in the central panel are calculated with RSG mass-loss rate enhanced by a factor of 6 ("×6") and in the right panel they are enhanced by a factor of 10 ("×10"). Note that the differences in the evolutionary tracks come only from the enhancement of the RSG mass loss rates.

We must remember that the wind blown mass, the duration of each evolutionary phase and the final stage of the stellar evolution have a strong influence not only on the final core-collapse supernova explosion, but also on the evolution and morphology of the circumstellar medium.

Table 1 shows the pre-supernova properties of non-rotating models. The symbols have the usual meaning: "$M_{\rm fin}$" and "$R_{\rm fin}$" refer to final mass and radius, "$Y_{\rm s}$" is the He fraction on the surface, "$T_{\rm c}$" is the stellar core temperature and the "pre-SN" column refers to the supernova progenitor type. Note that a 15 $M_{\odot}$ single non-rotating star could become a WR star if it has an extreme RSG mass loss rate (increased by a factor of 10 or more), so we have found that the minimum initial mass necessary to form a Wolf-Rayet star decreases as the RSG mass-loss rates increase, as expected. For the rest of models we found a similar behavior.

Figure 3 shows evolutionary tracks for rotating stars (`Case B`). As expected, stellar rotation increases the MS lifetimes with respect to non-rotating models, due to the increase of the core size, and its enrichment with fresh fuel coming from the outer layers. Stellar rotation also modifies the later evolutionary paths, in comparison to the `Case A` models: for example, for a low RSG mass loss rate ("×2" tag) the rotating 23 $M_{\odot}$ model (`B23×2`) evolves post-RSG, unlike the non-rotating case.

Rotational mixing also modifies the chemical composition of the stellar surface, more efficiently bringing nucleosynthesis products from the core to the surface. The outer envelopes of rotating models are slightly He-enriched, even during the MS, favoring the formation of WR stars and causing rotat-

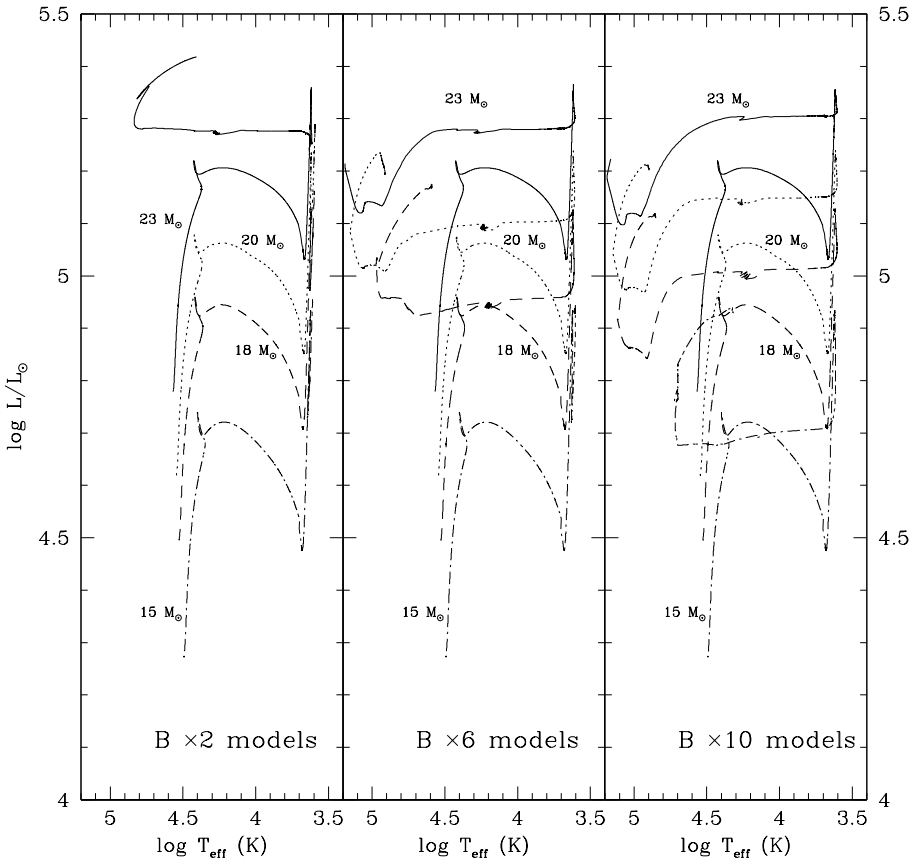

Fig. 3. Case B ($v_{\rm rot}$ = 100 km s^{-1}): Set of evolutionary tracks from the ZAMS up to the exhaustion of carbon in the core, for rotating stars with masses in the range 15-23 $M_\odot$. The left panel shows the evolution using the mass-loss rate of Nieuwenhuijzen & de Jager (1990) increased by a factor of 2 during the red supergiant phase ("×2" models). The central panel models are calculated with RSG mass-loss rates enhanced by a factor of 6 and the right panel is calculated with mass-loss rates enhanced by a factor of 10 in RSG. Due to numerical difficulties the 23 $M_\odot$ models were only evolved until He core exhaustion.

ing stars to end their lives with a higher surface He abundance, or even as WC/WO stars. This enriched material is wind-blown away from the star, impacting the chemical evolution of the surrounding stellar gas.

All our models will end up as supernova progenitors, but rotation often changes their mass, radius and/or color, in comparison to Case A models, as shown in Table 2. We observe that the pre-SN luminosity increases compared to non-rotating models, yielding more evolved progenitors, as a consequence of the higher rotational mass loss and mixing.

4.2. *Circumstellar Medium*

The evolution of the circumstellar gas strongly depends on the stellar evolution, through stellar wind properties such as the mass loss rate, velocity, and temperature. These properties change dramatically depending on the evolutionary phase, causing the dynamical behaviour of circumstellar gas to be quite distinctive in each stage. In this section we will describe the formation of shells and bubbles around the star as a consequence of the variation of the mass loss rate and wind velocity in the course of stellar evolution.

Main Sequence Stage: The evolution of circumstellar gas in all our models is qualitatively the same during the main sequence; only in the physical dimensions of the sculpted structures and the values of physical parameters vary. During the main sequence, a massive star blows a hypersonic wind ($\approx 2-3\times10^3$ km s^{-1}) that collides with the cold ISM leading to the formation of a double shock structure: an outer shock traveling outwards (in the star's reference frame) colliding with the ISM and a reverse shock that separates the free blowing wind from the

TABLE 1

PRE-SUPERNOVA PROPERTIES OF NON-ROTATING STELLAR MODELS (CASE A)

Model	$t_{\rm life}$(yrs)	$M_{\rm fin}/M_\odot$	$R_{\rm fin}/R_\odot$	$T_{\rm eff}$ (K)	$\log L/L_\odot$	$Y_{\rm s}$	$T_{\rm c}(10^8$ K)	pre-SN star
A15×2	12 717 026	12.0	538.0	4 143	4.89	0.295	13.0	RSG
A15×6	12 716 338	6.2	574.0	4 000	4.88	0.295	13.0	RSG
A15×10	12 724 001	5.2	13.2	25 275	4.80	0.677	12.5	WNL
A18×2	10 232 270	12.5	708.0	4 061	5.09	0.310	15.1	RSG
A18×6	10 219 431	6.8	8.8	36 040	5.07	0.707	12.0	WNL
A18×10	10 225 965	6.4	3.1	59 364	5.04	0.976	17.8	WNE
A20×2	8 910 644	12.4	807.5	4 019	5.19	0.300	15.0	RSG
A20×6	8 909 797	7.6	5.0	50 129	5.16	0.782	15.1	WNE
A20×10	8 913 075	7.4	3.2	62 010	5.14	0.936	12.0	WNE
A23×2	7 684 136	12.6	933.5	4 026	5.32	0.314	15.1	RSG
A23×6	7 684 127	8.9	3.0	68 942	5.27	0.987	12.5	WNE
A23×10	7 689 342	8.6	2.9	69 027	5.25	0.987	13.0	WNE

TABLE 2

PRE-SUPERNOVA FEATURES OF ROTATING STELLAR MODELS (CASE B). $V_{\rm rot} = 100$ km s^{-1}

Model	$t_{\rm life}$(yrs)	$M_{\rm fin}/M_\odot$	$R_{\rm fin}/R_\odot$	$T_{\rm eff}$ (K)	$\log L/L_\odot$	$Y_{\rm s}$	$T_{\rm c}(10^8$ K)	p-SN
B15×2	12 972 695	11.7	599.2	4 070	4.95	0.301	15.0	RSG
B15×6	12 951 069	5.7	598.2	4 030	4.93	0.305	11.6	RSG
B15×10	12 957 966	5.1	22.6	20 753	4.93	0.663	12.2	WNL
B18×2	10 299 185	11.6	811.1	3 950	5.16	0.316	10.7	RSG
B18×6	10 347 978	6.6	8.3	39 283	5.17	0.770	19.1	WNE
B18×10	10 386 567	5.9	2.4	71 123	5.11	0.986	15.3	WNE
B20×2	9 186 509	10.4	1009.0	3 900	5.29*	0.318	11.6	RSG
B20×6	9 255 333	6.8	2.0	81 313	5.19	0.985	17.0	WNE
B20×10	9 253 252	6.5	2.1	80 222	5.21	0.985	16.5	WNE
B23×2	7 965 195	9.4	26.3	25 429	5.42*	0.708	6.6	WNL
B23×6	8 010 574	7.6	0.6	152 871	5.21	0.980	4.9	WNE
B23×10	8 019 565	7.4	0.7	144 412	5.22	0.978	5.4	WNE

shocked one. This reverse shock advances inwards leaving a hot and initially isobaric region of shocked stellar wind (called *stellar bubble)* surrounding the free wind zone. The bubble region is pressure dominated, and has high temperatures and low densities ($T \approx 10^7$ K, $\rho \approx 10^{-28}$ g cm^{-3}).

In the main sequence, the mass loss rate is approximately $10^{-7} - 10^{-8}$ $M_\odot$ yr^{-1} , and increases slightly with time, as a function of the effective stellar radius and luminosity. The wind velocity drops in an opposite way, as shown in Figure 4 for the A18×6 model. The kinetic energy of the free blowing wind is converted into thermal energy inside the stellar bubble, which progressively grows in size. The external shock pushes an overdense shell of swept interstellar material (called MS shell), which surrounds the bubble (Weaver et al. 1977).

As the bubble grows, we observe the appearance of turbulence as a consequence of pressure and density fluctuations (Dwarkadas, 2007). The dense MS shell shows shear instabilities due to variations in the shock front position, maybe as a result of the initial perturbations in our simulations, or due to Vishniac instabilities in radiative shells (Ryu & Vishniac,

TABLE 3

WIND PROPERTIES OF THE A15×2 MODEL

Stage	Δt (Myr)	$\log \dot{M}$ ($M_\odot\,\mathrm{yr}^{-1}$)	ΔM ($M_\odot$)	v_∞ ($\mathrm{km\,s}^{-1}$)
MS	11.997	−7.93	0.14	2200
RSG	0.699	−5.38	2.89	35

Note: Δt refers to the duration of the stage, $\log\ \dot{M}$ is the logarithm of the mass loss rate, ΔM is the mass lost during each phase and v_∞ is the average velocity of stellar wind. Same notation for Tables 4, 5, 6 and 7.

TABLE 4

WIND PROPERTIES OF THE A15×10 MODEL

Stage	Δt (Myr)	$\log \dot{M}$ ($M_\odot\,\mathrm{yr}^{-1}$)	ΔM ($M_\odot$)	v_∞ ($\mathrm{km\,s}^{-1}$)
MS	12.017	−7.93	0.14	2200
RSG	0.428	−4.66	9.28	35
YSG/LBSG	0.217	−5.83	0.32	800
WNL	0.061	−5.74	0.11	2000

TABLE 5

WIND PROPERTIES OF THE A18×6 MODEL

Stage	Δt (Myr)	$\log \dot{M}$ ($M_\odot\,\mathrm{yr}^{-1}$)	ΔM ($M_\odot$)	v_∞ ($\mathrm{km\,s}^{-1}$)
MS	9.723	−7.53	0.29	2265
RSG	0.318	−4.48	10.48	30
YSG/LBSG	0.082	−5.59	0.21	800
WNL	0.080	−5.51	0.25	2100

TABLE 6

WIND PROPERTIES OF THE A20×6 MODEL

Stage	Δt (Myr)	$\log \dot{M}$ ($M_\odot\,\mathrm{yr}^{-1}$)	ΔM ($M_\odot$)	v_∞ ($\mathrm{km\,s}^{-1}$)
MS	8.483	−7.41	0.33	2300
RSG	0.209	−4.27	11.35	25
YSG/LBSG	0.004	−4.76	0.07	900
WNL	0.127	−5.47	0.43	2800
WNE	0.073	−5.56	0.20	2000

1987). However, these instabilities grow slowly as the MS shell expands, and they do not fragment the shell, or affect its sphericity; this is the CSM structure where the RSG will expand afterwards. Table 8 shows the final position of MS shells at pre-SN time for RSG supernova progenitors.

TABLE 7

WIND PROPERTIES OF THE B20×2 MODEL

Stage	Δt (Myr)	$\log \dot{M}$ ($M_\odot\,\mathrm{yr}^{-1}$)	ΔM ($M_\odot$)	v_∞ ($\mathrm{km\,s}^{-1}$)
MS	8.531	−7.41	0.33	2300
RSG	0.642	−4.84	9.27	20

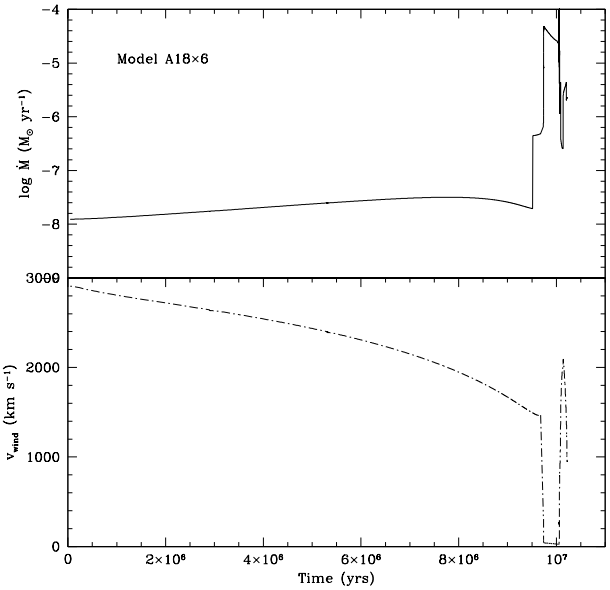

Fig. 4. Plots of typical stellar mass loss rate (top) and wind velocity (bottom) as a function of time for the A18×6 model. The main sequence, red supergiant and Wolf-Rayet phases are clearly distinguishable. These data were used as input for the circumstellar hydrodynamic simulations.

Red Supergiant Stage: After the main sequence, all our models evolve toward the cool side of the HRD to become a red supergiant. The mass loss rate increases and the RSG wind becomes denser and slower, with velocities fluctuating between ≈ 10-160 km s^{-1} . Ram pressure of the dense RSG wind eventually balances the thermal pressure of the hot main sequence bubble, and a termination shock is formed. The RSG wind is decelerated and piles up into the shock to build a second shell (RSG shell) which expands at low velocity (≈ 5 km s^{-1}). The outer edge of the RSG shell presents Rayleigh-Taylor instabilities (Dwarkadas 2007), and we could observe the growth of RT "fingers" that, in some cases, extend far: up to 1-2 pc beyond the shell. Fig-

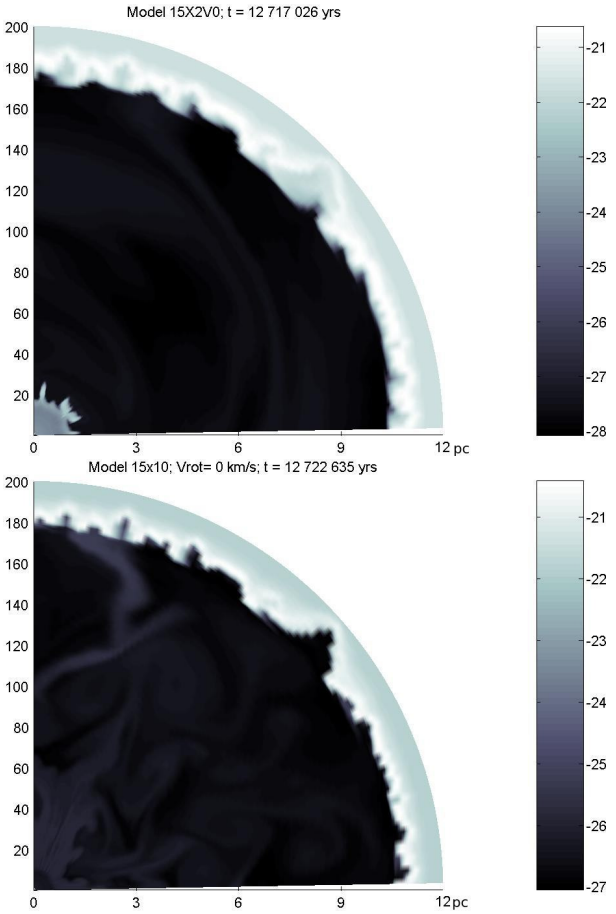

Fig. 5. *Top:* Logarithm of the circumstellar gas density (g cm^{-3}) of the `A15×2` model at the presupernova stage ($t = 12,717,026$ yrs). The initial density of the ISM is $n = 100$ cm^{-3} and the grid has dimensions of 200×90 cells in $r \times \theta$ direction, corresponding to a physical distance of 12 pc in radial extension (0.075 pc/cell) and 90 degrees in latitude (1 deg/cell). Stellar equator is on the x-axis. The main sequence shell has a radius of ≈ 10.8 pc. An unstable RSG shell appears at a distance of $r \approx 1.2$ pc from the star. Note the presence of "Rayleigh-Taylor" fingers. The RSG wind and shell have a combined mass of 2.9 $M_\odot$. Labels on y-axis indicate the r-cell number in our simulation. *Bottom:* Same representation for the `A15×10` model at pre-SN ($t = 12,724,001$ yrs). The MS shell encloses the hot bubble with a turbulent structure. The RSG shell and the WR shells previously built have already merged with the outer MS shell before the SN explosion. The color figure can be viewed online.

ure 5 (top), shows the pre-supernova circumstellar medium around a typical RSG star (model `A15×2`); we note the MS shell with a radius of 10.8 pc enclosing the hot and rarefied stellar bubble. Inside the bubble, near to the star, we observe an unstable RSG shell with a radius of $r \approx 1.2$ pc. This CSM configuration is the same for all models that end their lives as red supergiants, only the position of the MS and the RSG shells vary, due to the difference of the stellar phase's lifetimes, and of the injected mechanical luminosity. Table 8 shows the position of the MS and the RSG shell at the pre-supernova stage for our RSG supernova progenitor models. The pre-SN circumstellar medium consists of a dense and free streaming RSG wind with a profile $\rho \propto r^{-2}$, inside an unstable and massive RSG shell. The hot MS bubble remains beyond the RSG shell bordered by the shocked MS shell. This will be the circumstellar medium, where the supernova blast wave will expand, producing a SNII-L or SNII-P lightcurve. The circumstellar medium pre-supernova for some typical RSG progenitors is shown in Figure 5 (*top*) and Figure 9.

TABLE 8

FINAL POSITION OF STELLAR SHELLS FOR RSG SUPERNOVA PROGENITORS

Model	RSG shell radius (pc)	MS shell radius (pc)
`A15×2`	1.2	9.8
`A15×6`	2.3	9.8
`A18×2`	1.7	13.1
`A20×2`	3.2	13.9
`A23×2`	3.6	15.0
`B15×2`	2.0	11.0
`B15×6`	3.0	11.0
`B18×2`	2.3	13.5
`B20×2`	3.0	13.8

Wolf-Rayet Stage: Some of our models include post-RSG evolution[7]. These stars shed the H-envelope to become Wolf-Rayet stars that blow a less dense and faster wind (of order $2500 - 3000$ km s^{-1}), whereas the star evolves back to the blue side of the HRD, to finally explode as supernova.

At the onset of the Wolf-Rayet phase, the fast wind sweeps the previous slow RSG wind forming a miniature version of the MS bubble: differences

[7]We should point out that after the RSG stage we keep the multiplied mass loss rate, maybe this carries the star to the HRD blue side. In their evolution between RSG to WR, the stars loose less than 1% of their initial mass (except for 15 $M_\odot$ models, that loses up to 3 %), the transitional stage being shorter as the initial mass and mass loss rate grows.

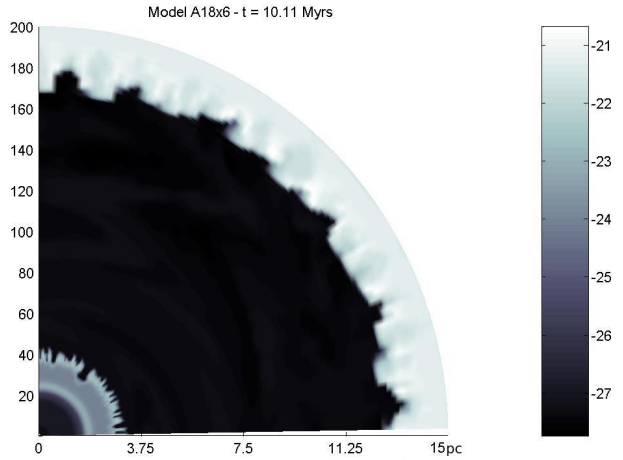

Fig. 6. Logarithm of gas density (g cm^{-3}) surrounding a star of 18 $M_\odot$ (model `A18×6`) at a time of 10,110,512 yrs. The grid (200 × 90 cells) has a radial length of 15 pc (0.075 pc/cell) and 90 degrees in latitude (1 °/cell). Three shells are formed during the entire evolution of the star: near to the star is the fast WR shell at $r \approx 1.9$ pc bordered by the dense RSG wind and the RSG shell at a position of ≈ 3 pc. Between this and the outer MS shell ($r_{\rm MS} \approx 12.8$ pc) a hot pressure dominated bubble with a slightly turbulent structure is formed. The color figure can be viewed online.

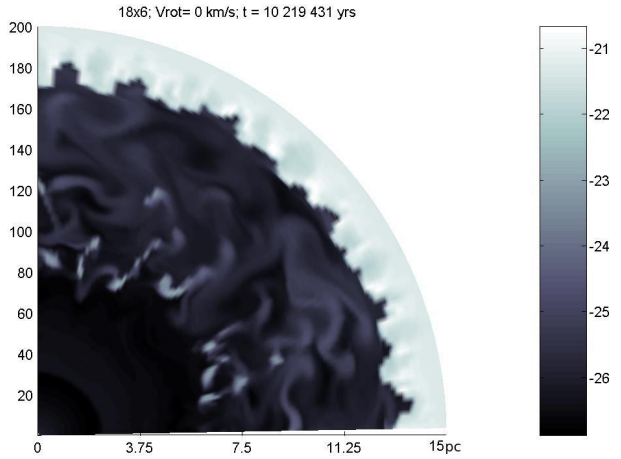

Fig. 7. Logarithm of gas density (g cm^{-3}) surrounding a star of 18 $M_\odot$ (model `A18×6`) at pre-SN stage ($t = 10,219,431$ yrs). The physical dimensions are the same than Figure 6. The MS shell has a radius of ≈ 12.8 pc surrounding a turbulent hot bubble with some knots of dense debris from the former RSG + WR shell (broken by their collision). The debris spreads from 6 to 8 pc. Note the high turbulence inside the hot bubble. The color figure can be viewed online.

in velocity in the transition zone result in a rarefaction wave, possibly accompanied by a shock (Georgy, Walder et al. 2013), and build-up in the interface a new WR shell expanding with high velocity (≈ 100 km s^{-1}). This fast WR shell is Rayleigh-Taylor unstable, and presents a filamentary structure.

In Figure 6, we show the shell formed near the star in the WR phase for the `A18×6` model ($r \approx 1.7$ pc) bordered by the dense RSG wind zone and the previous RSG shell ($r \approx 3.0$ pc). Eventually, the fast WR shell will strongly collide with the slower RSG shell, and both shells will merge and break up in some zones, forming clumps and tails of dragged material, which travel outwards into the interior of the MS bubble, spreading the WR+RSG shell debris in an asymmetrical manner. The stellar bubble has a turbulent structure with dense knots and irregular tails expanding into it. Depending on the time remaining until the final core collapse, the fingers and knot debris could reach the outer MS shell to stop and/or merge into it. This is important for the morphology of the circumstellar medium at the pre-supernova stage.

The circumstellar medium for WR progenitors is shown in Figures 5 (bottom), 7, and 8, for three different cases of interest. Figure 5 (bottom) corresponds to the `A15×10` model which ends life as a WNL star, after following the next evolutionary path:

$$\text{MS} \rightarrow \text{RSG} \rightarrow \text{LBSG} \rightarrow \text{WNL} \rightarrow \text{SN IIL/b} .$$

During the evolution of this star, we observe the formation of the MS, RSG, and WR shells. As presupernova, the outer MS shell has a radius of $r \approx 10.8$ pc. The fast WR shell has already collided with the previous RSG shell, breaking both and traveling outwards; the debris are spread into the hot stellar bubble. This fragmented material reaches the MS shell, merges with it and in some cases bounces back.

The presupernova medium for this first case consists of a zone of a fast WR wind, that blows into an anisotropic and slightly turbulent hot bubble, where the pressure and density vary from point to point. The interaction of the SN blast wave with this turbulent medium will be highly wrinkled, with the transmitted and reflected wave shocks traveling outward at slightly different velocities (Dwarkadas 2007).

As second case of interest, Figure 7 shows the presupernova medium of the `A18×6` model. This star follows a similar evolutionary path, ending its life as a SN IIL/b. During the evolution, the star develops its MS, RSG and WR shells. The last two also collide

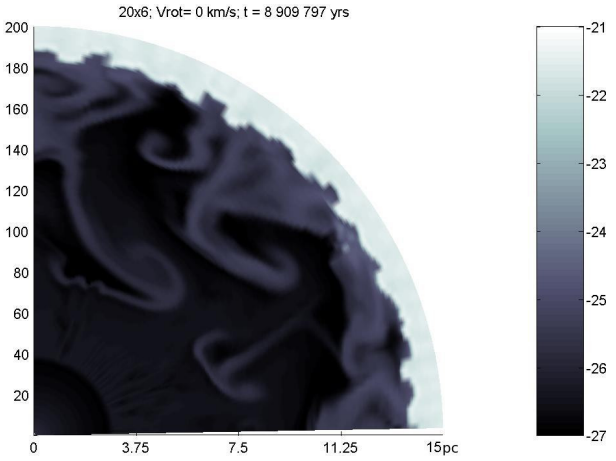

Fig. 8. Logarithm of gas density (g cm^{-3}) of the CSM for the A20×6 model at pre-supernova stage ($t = 10,272,006$ yrs). The dimensions are the same as in Figure 6. The WR shell has collided and merged with the former RSG shell, both dissipating into the hot wind shocked bubble. Most of the mass of these shells has merged with the outer MS shell. The color figure can be viewed online.

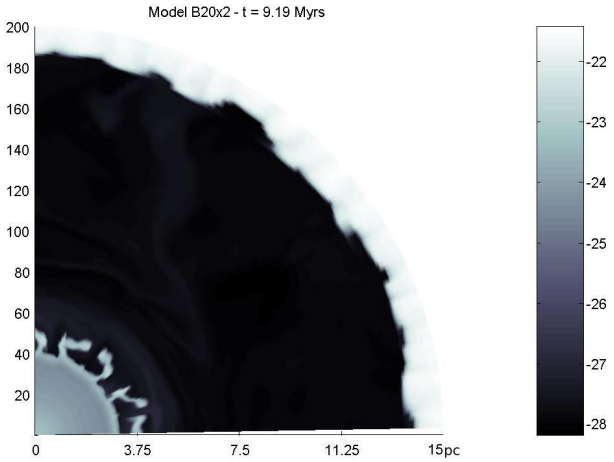

Fig. 9. Logarithm of gas density (g cm^{-3}) of the CSM at pre-SN of the B20×2 model at pre-supernova ($t = 9,186,509$ yrs). The RSG shell has a radius of 3 pc. Note the presence of large "Rayleigh-Taylor" fingers formed in the outer edge of the decelerated RSG wind. The color figure can be viewed online.

and break up just as before. However, in this case the time between the onset of the WR shell and the supernova explosion is too short and the collisional debris traveling outwards (WR + RSG shell) do not have enough time to reach the outer MS shell. As a result, the CSM presupernova for this case consists of the free WR wind still carrying the shell debris dense knots ($\rho \approx 10^{-22}$ g cm^{-3}) traveling outwards with low velocities. We can see the complex velocity field in the regions of free WR wind, the dense WR+RSG shell debris and an aspherical termination shock. The interaction of the supernova shock wave with the densest zones will result in an increased temperature of the X-rays, and in optical emission of the knots (Dwarkadas 2005) at different times, due to their uneven positions.

Figure 8 shows the presupernova CSM of the model A20×6. The evolutionary path is similar to the previous cases, except for the supernova progenitor stage:

$$\text{MS} \rightarrow \text{RSG} \rightarrow \text{LBSG} \rightarrow \text{WNL} \rightarrow \text{WNE} \rightarrow \text{SN Ib} .$$

The interaction of the supernova blast wave with the CSM will be similar to the first case (A15×10 model), but with a more turbulent medium. However, the SN ejecta will be hydrogen lacking, leading to a very different chemical return into the circumstellar gas.

5. DISCUSSION AND CONCLUSIONS

In this work, we have built numerical models of stellar evolution and circumstellar gas dynamics for single stars with initial masses of 15, 18, 20 and 23 $M_\odot$ (rotating and non-rotating) to explore the impact of increased mass loss rates in the RSG phase. We found that the stellar evolution post-RSG (if any) is fully determined by the RSG mass-loss rate, also having a strong impact on the gas distribution around the star at pre-supernova time.

We found that an extreme RSG mass-loss has a strong impact mainly on:

•*Post-RSG stellar evolution.* Canonical models of stellar evolution predict that all massive stars with masses smaller than $\approx 25\ M_\odot$ will end their lives as RSG stars, producing a supernova explosion of type SNII-P, or even a SNII-L. In agreement with this, our "canonical" simulations ("×2" models) end their lives as RSG stars, except for the rotational model of a 23 $M_\odot$ star (B23×2) where the rotational internal mixing favors post-RSG evolution bluewards. When we increased the RSG mass-loss rate by a factor of 6, the stellar evolutionary tracks were different, presenting post-RSG evolution to blueward for stars with lower masses, which is in agreement with other authors (Salasnich et al. 1999; Ekström et al. 2012). Our 18, 20 and 23 $M_\odot$ stars evolve bluewards after the RSG stage to become Wolf-Rayet stars. We noted that a consequence of increasing

the RSG mass-loss rate is a lower minimum mass limit for the formation of a Wolf-Rayet star (for single stars).

The models with an RSG mass-loss rate increased by a factor of 10 ("×10" models) further decrease the lower mass limit to develop post-RSG evolution. In this case, even a 15 $M_\odot$ star becomes a WR star. Extreme RSG mass-loss is also a possible channel for the formation of low luminosity WR stars from stars evolving away from their RSG phase, at lower masses than predicted by models with a standard mass loss rate.

• *The lifetime that the star spends in each evolutionary stage and the chemical yields.* The time spent by the star in each evolutionary stage is strongly influenced by the RSG mass-loss rate, but the total stellar lifetime seems not to depend on it. Larger RSG mass-loss rates modify the time that the star spends in the red and blue zones of the HRD during the He-main sequence, shortening the RSG and the YSG-LBSG stages, and lengthening in some cases the duration of the Wolf-Rayet phase. This behavior has a strong impact on the blue to red supergiant (B/R) ratio: a shorter RSG phase combined with an increase in the WR lifetime leads to a B/R ratio that grows with higher RSG mass loss rates.

Larger RSG mass-loss rates also contribute to the metal enrichment of the circumstellar medium by favoring the subsequent evolution to WR stars. Surface abundances of (post-RSG) WR stars are enriched with He-burning products and their stellar winds change the metals proportion of the chemical composition of the CSM gas bubble and shells. Lowering the mass limit to form WR stars causes a more efficient return of enriched material into the ISM affecting the chemical evolution of the galaxies in a new way.

• *Supernova progenitor and SN type.* Increasing RSG mass-loss plays a dominant role in determining the outcome stellar evolution, and even modifies the type of SN progenitor. Our simulations with a standard mass loss end their lives as red supergiants (SNIIP), but the largest RSG mass-loss rates cause the red supergiant phase to become only a transition phase, and triggers extended blue loops to form Wolf-Rayet stars that will end their lives as supernovae of type IIL/b or Ib. An increase in the RSG mass-loss rate causes stars to be supernova progenitors for masses as low as 15 $M_\odot$ (with extreme RSG mass-loss rate and rotation), lowering the mass that we expect for a star to explode in the blue side of the HRD. This could explain the lack of observed supernova progenitors of Type II-P with masses $M \geq 15 - 17\ M_\odot$ due to the strip-off of their H-rich envelope before the explosion. This is a crucial point to understand the "RSG problem".

Note that even though all our models end their lives as red (RSG) or blue (WR) supernova progenitors, none of them explodes as a YSG or LBSG stars. This behavior contradicts other authors (Meynet et al. 2015) who also study the increase of the RSG mass-loss for massive stars. They find that none of their models become WR stars despite their higher RSG mass-loss rates; their RSG stars usually lose less mass during their red stage but the final models are less massive than ours (for non-rotating simulations).

• *The circumstellar medium.* Stellar evolution has a strong impact on the interstellar gas dynamics through the amount of lost mass and the wind velocity. Both quantities are set in the evolutive stage. The blown wind sculpts the surrounding gas, leading to the formation of distinctive bubbles and shells. Canonical models predict that $15 - 23\ M_\odot$ stars will end their lives as red supergiants surrounded by a dense and slow wind, and enclosed by a massive RSG shell lying at different distances from the star (depending on the mechanical luminosity during the RSG phase). However, in our models we found that this canonical behavior deviates when the stellar evolutionary path changes. By increasing the RSG mas-loss rate we found that 18 $M_\odot$ stars (or even 15 $M_\odot$ with extreme mass loss) are able to become WRs and explode as supernova in this phase. Unlike the RSG case, the Wolf-Rayet star develops a fast third shell that collides and breaks the former RSG shell, spreading their coupled debris into the wind-blown bubble. The turbulence inside the bubble leads to an inhomogeneous distribution of the stellar material and of the chemical species. This turbulence is the former circumstellar medium around the Wolf-Rayet progenitors, except for one case, where the time between the WR onset and the supernova event is too short, and the RSG+WR clumps are still near the star at the moment of the supernova explosion. This will change the supernova blast wave dynamics and may show strong lines of He and N from the knots being photoionized or shocked by the supernova front.

RSGs are pulsationally unstable during a part of their lifetimes (Yoon & Cantiello 2010), perhaps playing a key role in driving strong mass loss in an episodic way. We have explored this scenario and found that massive ejections in the RSG phase are swept away by the intense WR wind. This behavior will be investigated in a forthcoming paper.

We have shown that larger mass-loss rates during the RSG stage modify the stellar evolution for stars with the same initial mass, rotational velocity and metallicity. We found that the evolution of massive stars (15 to 23 $M_{\odot}$) depends on the initial mass, metallicity, rotational velocity and RSG mass-loss rate. The gas dynamics of their circumstellar medium also changes, because it is tightly bound to the stellar evolution, so that the distribution of density, temperature, velocity field and chemical composition at the pre-supernova stage vary with the RSG mass-loss rates, even for the same initial stellar mass. We note that the global appearance of CSM for a specific type of SN progenitor star is not unique, because the gas dynamics is also strongly affected by the duration of each evolutionary stage in the star's life.

The authors thank N. Langer and S.-Ch. Yoon for the use of BEC. We also thank José Franco, Javier Sánchez and Omar López-Cruz for their advice and suggestions. B.P-R. acknowledges project USO315002206 of Universidad de Sonora and L.H-C. and A.S. acknowledge support from Universidad Nacional Autónoma de México. The authors would like to thank the referee for valuable comments which improved this manuscript.

REFERENCES

Asplund, M., Grevesse, N., Sauval, A. J., & Scott, P. 2009, ARA&A, 47, 481
Beasor, E. R. & Davies, B. 2016, MNRAS, 463, 1269
Chiosi, C. & Maeder, A. 1986, ARA&A, 24, 329
Clarke, D. A. 1996, ApJ, 457, 291
de Jager, C., Nieuwenhuijzen, H., & van der Hucht, K. A. 1988, A&AS, 72, 259
Dwarkadas, V. 2005, ApJ, 630, 892
_____. 2007, ApJ, 667, 226
Ekström, S., Georgy, C., Eggenberger, P., et al. 2012, A&A, 537, A146
Eldridge, J. J., Genet, F., Daigne, F., & Mochkovitch, R. 2006, MNRAS, 367, 186
Friend, D. B. & Abbott, D. C. 1986, ApJ, 311, 701
Georgy, C. 2012, A&A, 538, L8
Georgy, C., Ekström, S., Meynet, G., et al. 2012, A&A, 542, A29
Georgy, C., Ekström, S., Saio, H., et al. 2013, EAS Publication Series, 60, 43
Georgy, C., Walder, R., Folini, D., et al. 2013, A&A, 559, A69
Giannone, P. 1967, ZA, 65, 226
Hamann, W.-R., Koesterke, L., & Wessolowski, U. 1995, A&A, 299, 151
Heger, A., Langer, N., & Woosley, S. E. 2000, ApJ, 528, 368
Heger, A., Fryer, C. L., Woosley, S. E., Langer, N., & Hartmann, D. H. 2003, ApJ, 591, 288
Humphreys, R. M., Nichols, M., & Massey, P. 1985, AJ, 90, 101
Levesque, E. M., Massey, P., Olsen, K. A. G., et al. 2005, ApJ, 628, 973
Maeder, A. & Meynet, G. 1994, A&A, 287, 803
Matsuura, M., Sargent, B., Swinyard, B., et al. 2016, MNRAS, 462, 2995
Mauron, N. & Josselin, E. 2011, A&A, 526, A156
Meynet, G., Chomienne, S., Ekström, S., et al. 2015, A&A, 575, A60
Moriya, T., Tominaga, N., Blinnikov, S. I., Baklanov, P. V., & Sorkina, E. I. 2011, MNRAS, 415, 199
Nieuwenhuijzen, H. & de Jager, C. 1990, A&A, 231, 134
Nugis, T. & Lamers, H. J. G. L. M. 2000, A&A, 360, 227
Pérez-Rendón, B., Garcia-Segura, G., & Langer, N. 2009, A&A, 506, 1249
Petrovic, J., Langer, N., Yoon, S., & Heger, A. 2005, A&A, 435, 247
Reimers, D. 1975, MSRSL, 8, 369
Renzo, M., Ott, C. D., Shore, S. N., & de Mink, S. E. 2017, A& A, 603, A118
Ryu, D. & Vishniac, E. T. 1987, ApJ, 313, 820
Salasnich, B., Bressan, A., & Chiosi, C. 1999, A& A, 342, 131
Schröder, K. P. & Cuntz, M. 2005, ApJ, 630, L73
Smartt, S. J., Eldridge, J. J., Crockett, R. M., & Maund, J. R. 2009, MNRAS, 395, 1409
Smith, N. 2014, ARA&A, 52, 487
Stone, J. M. & Norman, M. L. 1992, ApJS, 80, 753
Vanbeveren, D., De Donder, E., Van Bever, J., Van Rensbergen, W., & De Loore, C. 1998, NewA, 3, 443
Van Loon, J. T., Cioni, M.-R. L., Zijlstra, A. A., & Loup, C. 2005, A&A, 438, 273
Vink, J. S., de Koter, A., & Lamers, H. J. G. L. M. 2001, A&A, 369, 574
Vink, J. S. & de Koter, A. 2005, A&A, 442, 587
Weaver, R., McCray, R., Castor, J., Shapiro, P., & Moore, R. 1977, ApJ, 218, 377
Yoon, S.-C., Langer, N., & Norman, C. 2006, A&A, 460, 199
Yoon, S.-C. & Cantiello, M. 2010, ApJL, 717, L62

G. García-Segura: Instituto de Astronomía, Universidad Nacional Autónoma de México, Apartado Postal 877, Ensenada C. P. 22800, Baja California, México.
L. Hernández-Cervantes: Instituto de Astronomía, Universidad Nacional Autónoma de México, Apartado Postal 70-264, CDMX, C.P. 04510, México (liliana@astro.unam.mx).
L. Hernández-Cervantes: Programa de Doctorado Ciencias (Física), Universidad de Sonora, Hermosillo, Sonora, México (liliana@astro.unam.mx).
B. Pérez-Rendón: Departamento de Investigación en Física, Universidad de Sonora. Apdo. Postal 5-088. Hermosillo, Sonora, México.
C. Rodríguez-Ibarra: Departamento de Física, Universidad de Sonora. Apdo. Postal 5-088. Hermosillo, Sonora, México.
A. Santillán: Dirección General de Cómputo y de Tecnologías de Información y Comunicación, Universidad Nacional Autónoma de México, México.

Revista Mexicana de Astronomía y Astrofísica, **55**, 177–184 (2019)

DOI: https://doi.org/10.22201/ia.01851101p.2019.55.02.05

MINIMIZING FUEL CONSUMPTION IN ORBIT TRANSFERS USING UNIVERSAL VARIABLE AND PARTICLE SWARM OPTIMIZATION

L. M. Echeverry[1,2] and Y. Villanueva[1,3]

Received April 24 2019; accepted May 9 2019

ABSTRACT

Minimizing fuel consumption in space travels is becoming increasingly important for spatial development. In the present paper, the fuel consumption in orbit transfers (without gravitational assistance) is minimized, where a spacecraft performs a change from an orbit around the Earth to another one around a different celestial body. Two methods are presented: one of immediate transfer and another with wait time. Minimizing is done by solving a nonlinear system, obtained by applying Lagrange multipliers to the equation modelling the keplerian system, and using the seeds coming from the particle swarm algorithm to execute the Newton's method. Numerical simulations with real values were made to compare these methods with the Hohmann transfer and data from the specialized literature.

RESUMEN

La minimización del gasto de combustible en los viajes espaciales es cada día más importante para el desarrollo espacial. En el presente trabajo se minimiza el gasto de combustible en transferencias de órbita (sin asistencia gravitacional), donde se ejecuta un cambio de órbita de una nave alrededor de la Tierra a una órbita alrededor de otro cuerpo celeste. Se presentan dos métodos, uno de transferencia inmediata y otro con tiempo de espera. La minimización se hace resolviendo un sistema no lineal que aparece después de aplicar multiplicadores de Lagrange a las ecuaciones que modelan el sistema kepleriano, usando las semillas que vienen del algoritmo de enjambres de partículas para ejecutar el método de Newton. Se hicieron simulaciones numéricas con valores reales para comparar estos métodos con la transferencia de Hohmann y los datos que aparecen en la literatura especializada.

Key Words: celestial mechanics — methods: numerical — planets and satellites: fundamental parameters — space vehicles

1. INTRODUCTION

Recently, authors such as (Gang et al. 2014; Shan et al. 2014; Zotes et al. 2012) have given important contributions to the study of spatial trajectory optimization. The latter have considered a geometric method with results far from those presented in this article, by having a large flight time with a Δv similar to ours.

Thus, to minimize fuel consumption in the acceleration Δv [as in (Sharaf & Saad 2016)], the present article considers the methods proposed in Leeghim (2013), which are variations of the Lambert problem, with neither direction of motion in a plane nor the time t of the transfer at the beginning given; both are calculated. Another difference of our approach is the obtainment of the wait time t_1 (Vallado 1997), where the interceptor does not leave its initial orbit until the relative positions of the bodies are convenient. This is presented in § 2.

The problem becomes a constrained optimization system. Its direct solution leads to several systems of nonlinear equations (9 equations as in § 3, 11 equations as in § 4). The solution method, presented in § 5 (Newton's method) needs an appropriate starting point (seed). This seed is usually found from an exhaustive model that takes a long time to locate a suitable value (grids). Therefore, an heuristic tech-

[1]School of Exact Sciences and Engineering, Sergio Arboleda University, Bogotá, Colombia.
[2]Department of Mathematics, University of the Andes, Bogotá, Colombia.
[3]Institute of Mathematics and Statistics, Federal University of Goiás, Goiania, Brazil.

nique, the particle swarm optimization presented in § 5.1, is used to approximate the seed in a reasonable time. Such methods were applied to trips with real data in the solar system and are presented in § 6. The results of the first case (immediate transfer) were compared with information released from missions of several space agencies in Villanueva (2013) and here the two problems are compared with the data shown in Kemble (2006), who deals with the Lambert problem directly from a geometric point of view.

2. PRELIMINARIES

The two-body problem (Keplerian) described in Bate (1971) was considered. The equation

$$\ddot{\vec{r}}(t) = -\frac{\mu}{|\vec{r}(t)|^3}\vec{r}(t) \tag{1}$$

models the dynamic of the system, with $\mu = GM$. The position of the particle on an ellipse is $\vec{r}(t) = [x_1(t), x_2(t)]$, such that

$$x_1(t) = a(\cos E(t) - \epsilon), \qquad x_2(t) = a\sqrt{1-\epsilon^2}\sin E(t),$$

where a is the semi-major axis, ϵ the eccentricity, E the eccentric anomaly. Using the fact that the norm of the angular momentum of the particle is constant we get

$$\dot{E} = \frac{\sqrt{\mu}}{a^{3/2}(1-\epsilon\cos E)},$$

and therefore Kepler's equation is obtained:

$$E(t) - \epsilon\sin E(t) = \frac{\sqrt{\mu}}{a^{3/2}}(t-t_0) = M, \tag{2}$$

where M is the mean anomaly (Bate 1971). To find a solution E for Kepler's equation (2) at any time normally Newton's method is used, but it does not converge or converges too slowly when $\epsilon \approx 1$ (Elipe et al. 2017). From Danby (1962, p. 168) we use Taylor's expansion in (2) to derive the equations of the dynamics related to the problem for any type of trajectory (classical curves). Then

$$\begin{aligned}\sqrt{\mu}(t-t_0) = &\ a^{3/2}\left[E - \epsilon\left(E - \tfrac{E^3}{3!} + \tfrac{E^5}{5!} - \tfrac{E^7}{7!} + \cdots\right)\right] \\ = &\ (a^{3/2}(1-\epsilon)E) + \epsilon\left(\tfrac{(\sqrt{a}E)^3}{3!} - \tfrac{1}{a}\tfrac{(\sqrt{a}E)^5}{5!}\right. \\ &\left. + \tfrac{1}{a^2}\tfrac{(\sqrt{a}E)^7}{7!} - \cdots\right).\end{aligned}$$

With $x = \sqrt{a}E$, we obtain

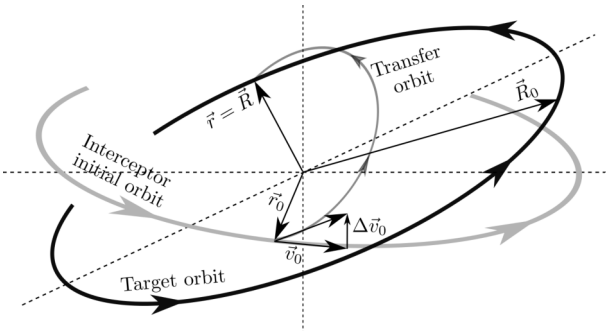

Fig. 1. Description of the first problem.

$$\sqrt{\mu}(t-t_0) = (a(1-\epsilon)x) + \epsilon\left(\frac{x^3}{3!} - \frac{1}{a}\frac{x^5}{5!} + \frac{1}{a^2}\frac{x^7}{7!} - \cdots\right).$$

This equation accepts any value of ϵ and $a \neq 0$. Therefore, using the fact $r = a(1-\epsilon\cos E)$, (Bate 1971, p. 187), and with the expression of $\dot{E}$, an universal variable, $x \in \mathbb{R}$ is defined as $\dot{x} := \frac{\sqrt{\mu}}{r}$.

So, the following expressions are obtained for t and r (Bate 1971) using equation (1), integrating the universal variable as $\sqrt{\mu}dt = rdx$:

$$\begin{aligned}\sqrt{\mu}t = &\ a\left(x - \sqrt{a}\sin\left(\tfrac{x}{\sqrt{a}}\right)\right) + \tfrac{\langle\vec{r}_0,\vec{v}_0\rangle}{\sqrt{\mu}}a\left(1-\cos\left(\tfrac{x}{\sqrt{a}}\right)\right) \\ &+ r_0\sqrt{a}\sin\left(\tfrac{x}{\sqrt{a}}\right),\end{aligned} \tag{3}$$

$$r = a + a\left[\frac{\langle\vec{r}_0,\vec{v}_0\rangle}{\sqrt{\mu a}}\sin\left(\frac{x}{\sqrt{a}}\right) + \left(\frac{r_0}{a} - 1\right)\cos\left(\frac{x}{\sqrt{a}}\right)\right].$$

Since the initial position and velocity vectors $\vec{r}_0$ and $\vec{v}_0$ are linearly independent, and having $\vec{r}$, and $\dot{\vec{r}} = \vec{v}$ in the same plane, the vectors of position and velocity are expressed in terms of the initial vectors and the universal variable (Bate 1971):

$$\vec{r}(t) = f\vec{r}_0 + g\vec{v}_0, \qquad \vec{v}(t) = \dot{f}\vec{r}_0 + \dot{g}\vec{v}_0. \tag{4}$$

3. PROBLEM STATEMENT

The target travels in its own orbit, and the interceptor orbits around the Earth. To calculate the orbit to be taken by the interceptor to fly by the target the initial position and initial velocity of the interceptor $\vec{r}_0$, $\vec{v}_0$ and the target $\vec{R}_0$, $\vec{V}_0$ are required. We look for the minimum change of velocity $\Delta\vec{v}_0$, $\vec{v}_{transfer} = \vec{v}_0 + \Delta\vec{v}_0$, allowing overflight to be achieved. See Figure 1.

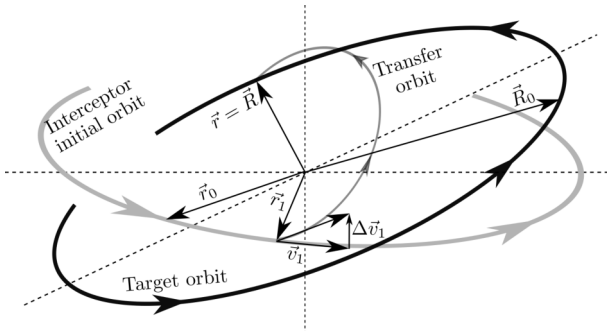

Fig. 2. Description of the second problem.

Using equation (3), let A and X be the semi-major axis and the universal variable, respectively, associated with $\vec{R}$, and a and x the semi-major axis and the universal variable, respectively, associated with $\vec{r}$ (in the orbit transfer). The following functions modelling the movement of the two bodies in the solar system are defined:

$$\eta_1 = A\Big(X - \sqrt{A}\sin\Big(\frac{X}{\sqrt{A}}\Big)\Big) + \frac{\langle \vec{R}_0, \vec{V}_0\rangle}{\sqrt{\mu}} A\Big(1 - \cos\Big(\frac{X}{\sqrt{A}}\Big)\Big) + R_0\sqrt{A}\sin\Big(\frac{X}{\sqrt{A}}\Big) - \sqrt{\mu}t,$$

$$\eta_2 = a\Big(x - \sqrt{a}\sin\Big(\frac{x}{\sqrt{a}}\Big)\Big) + \frac{\langle \vec{r}_0, \vec{v}_0 + \Delta\vec{v}_0\rangle}{\sqrt{\mu}} a\Big(1 - \cos\Big(\frac{x}{\sqrt{a}}\Big)\Big) + r_0\sqrt{a}\sin\Big(\frac{x}{\sqrt{a}}\Big) - \sqrt{\mu}t.$$

We call $\vec{\eta}_s := (\eta_1, \eta_2)$. Let $\vec{R}$ and $\vec{r}$ be the positions of the target and the interceptor, respectively, shown in equation (4) and let the functional $J = \frac{1}{2}\Delta\vec{v}_0^T\Delta\vec{v}_0$. Then we have the following optimization problem:

- Minimize $J(\Delta\vec{v}_0)$.
- Restricted to $\vec{\eta}_s(X, x, t, \Delta\vec{v}_0) = 0$ and $(\vec{R} - \vec{r})(X, x, t, \Delta\vec{v}_0) = 0$.

To solve the problem, Lagrange multipliers are used in the following functional:

$$H_s = J(\Delta\vec{v}_0) + \vec{\lambda}^T\vec{\eta}_s + \vec{\phi}^T(\vec{R} - \vec{r}),$$

where $\vec{\lambda} \in \mathbb{R}^2$ and $\vec{\phi} \in \mathbb{R}^3$.

After setting $\nabla H_s = 0$ as Leeghim (2013), we obtain the following system of nonlinear equations:

$$\vec{f}_s = \begin{cases} \vec{\eta}_s = (\eta_1, \eta_2) = 0, \\ \vec{R} - \vec{r} = 0, \\ \vec{\phi}^T\Big[\Big(\frac{\partial\vec{R}}{\partial X} - \frac{\partial\vec{r}}{\partial x}\Big) + \frac{r}{\sqrt{\mu}}\Big(\frac{\partial\vec{R}}{\partial t} - \frac{\partial\vec{r}}{\partial t}\Big)\Big] = 0, \\ \frac{\partial J}{\partial\Delta\vec{v}_0} + \frac{1}{r}\vec{\phi}^T\frac{\partial\vec{r}}{\partial x}\frac{\partial\eta_2}{\partial\Delta\vec{v}_0} - \vec{\phi}^T\frac{\partial\vec{r}}{\partial\Delta\vec{v}_0} = 0. \end{cases} \quad (5)$$

4. WAIT TIME

From Vallado (1997, p. 318) the wait time for planar and circular orbits is given by

$$t_1 = \frac{\theta - \theta_i + 2k\pi}{W - w},$$

where θ_i and θ are the initial and final angles (after t_1) between $\vec{R}$ and $\vec{r}$, and w and W are the angular speeds of the interceptor and the target, respectively. In this paper we calculate t_1 (the wait time), which is one of the results of the problem to be minimized for any kind of transfer orbit (in space) and maintains the same functional to be minimized. See Figure 2.

Let $\vec{\eta}_c = (\eta_1, \eta_2, \eta_3)$ such that:

$$\eta_1 = A\Big(X - \sqrt{A}\sin\Big(\frac{X}{\sqrt{A}}\Big)\Big) + \frac{\langle \vec{R}_0, \vec{V}_0\rangle}{\sqrt{\mu}} A\Big(1 - \cos\Big(\frac{X}{\sqrt{A}}\Big)\Big) + R_0\sqrt{A}\sin\Big(\frac{X}{\sqrt{A}}\Big) - \sqrt{\mu}t,$$

$$\eta_2 = a_0\Big(x_1 - \sqrt{a_0}\sin\Big(\frac{x_1}{\sqrt{a_0}}\Big)\Big) + \frac{\langle \vec{r}_0, \vec{v}_0\rangle}{\sqrt{\mu}} a_0\Big(1 - \cos\Big(\frac{x_1}{\sqrt{a_0}}\Big)\Big) + r_0\sqrt{a_0}\sin\Big(\frac{x_1}{\sqrt{a_0}}\Big) - \sqrt{\mu}t_1,$$

$$\eta_3 = a\Big(x - \sqrt{a}\sin\Big(\frac{x}{\sqrt{a}}\Big)\Big) + \frac{\langle \vec{r}_1, \vec{v}_1 + \Delta\vec{v}_1\rangle}{\sqrt{\mu}} a\Big(1 - \cos\Big(\frac{x}{\sqrt{a}}\Big)\Big) + r_1\sqrt{a}\sin\Big(\frac{x}{\sqrt{a}}\Big) - \sqrt{\mu}(t - t_1),$$

where η_1 is the equation of motion of the target, η_2 the equation of motion for the interceptor in its initial orbit during the wait time, and η_3 is the equation of motion of the interceptor after the wait time. Then we have a problem similar to the previous one:

- Minimize $J(\Delta\vec{v}_1)$.
- Restricted to $\vec{\eta}_c(X, x_1, x, t, t_1, \Delta\vec{v}_1) = 0$ and $(\vec{R} - \vec{r})(X, x_1, x, t, t_1, \Delta\vec{v}_1) = 0$.

Where $J = \frac{1}{2}\Delta\vec{v}_1^T\Delta\vec{v}_1$. Therefore, the new functional is:

$$H_c = J(\Delta\vec{v}_1) + \vec{\lambda}^T\vec{\eta}_c + \vec{\phi}^T(\vec{R}-\vec{r}),$$

where $\vec{\lambda}, \vec{\phi} \in \mathbb{R}^3$.

The system we obtain after setting $\nabla H_c = 0$ as Leeghim (2013) is:

$$\vec{f}_c = \begin{cases} \vec{\eta}_c = 0, \\ \vec{R}-\vec{r} = 0, \\ \vec{\phi}^T\left[\left(\frac{\partial\vec{R}}{\partial X} - \frac{\partial\vec{r}}{\partial x}\right) + \frac{r}{\sqrt{\mu}}\left(\frac{\partial\vec{R}}{\partial t} - \frac{\partial\vec{r}}{\partial t}\right)\right] = 0, \\ \frac{\partial J}{\partial\Delta\vec{v}_1} + \frac{1}{r}\vec{\phi}^T\frac{\partial\vec{r}}{\partial x}\frac{\partial\eta_3}{\partial\Delta\vec{v}_1} - \vec{\phi}^T\frac{\partial\vec{r}}{\partial\Delta\vec{v}_1} = 0, \\ \vec{\phi}^T\left[\frac{1}{r}\left(\frac{\sqrt{mu}}{r_1}\frac{\partial\eta_3}{\partial x_1} + \frac{\partial\eta_3}{\partial t_1}\right)\frac{\partial\vec{r}}{\partial x} - \left(\frac{\sqrt{mu}}{r_1}\frac{\partial\vec{r}}{\partial x_1} + \frac{\partial\vec{r}}{\partial t_1}\right)\right] = 0. \end{cases} \quad (6)$$

5. SOLUTION METHOD

To find the roots of the systems (5) and (6) we use Newton's multivariate method (Bate 1971; Leeghim 2013). That is, we want to calculate $\vec{f}(x) = 0$ using

$$\vec{y}_n = \vec{y}_{n-1} - (J_{\vec{f}}(y_{n-1}))^{-1}\vec{f}(y_{n-1}),$$

where $J_{\vec{f}}$ is the Jacobian matrix of $\vec{f}$. The variables of the first problem are $\vec{y}_s = (X, x, t, \Delta\vec{v}_0, \vec{\phi}) \in \mathbb{R}^9$ and the second one has $\vec{y}_c = (X, x_1, x, t_1, t, \Delta\vec{v}_1, \vec{\phi}) \in \mathbb{R}^{11}$.

For each case presented in § 6, it was necessary to find a seed (an initial value for Newton's method). However, this seed must be very close to the solution for the method to converge (Local Convergence Theorem). Given the importance of calculating the seed, we used the following heuristic method to approximate the solutions, which gave us very good results.

5.1. *Particle Swarm Optimization*

Particle Swarm Optimization (PSO) can be found in Kennedy et al. (1995); Clerc (2002); Parsopoulos & Vrahatis (2002); Conway (2010); Hvass (2010); Geetha et al. (2013). Let $J : D \subseteq \mathbb{R}^m \to \mathbb{R}$ be the function to be optimized, then:

- N particles are randomly selected $\vec{x}_i = (x_{i_1}, \ldots, x_{i_m}) \in D$ and also their initial velocities $\vec{v}_i = (v_{i_1}, \ldots, v_{i_m}) \in [0,1]^m$, $i = 1, \ldots, N$.

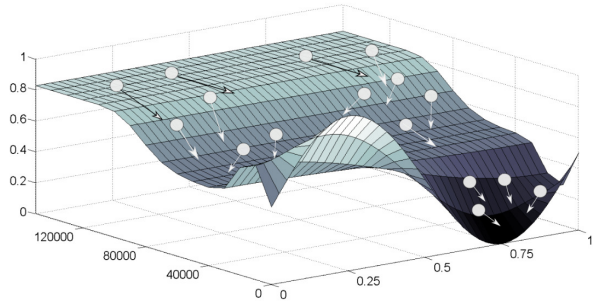

Fig. 3. Particle Swarm Optimization.

Then, for each iteration k:

1. We find the minimum of $\{J(\vec{x}_i^j)\}_{j\le k}$ (the minimum in the history of the specific particle) and it is set as $\vec{p}_i^k = \vec{x}_{i_{min}}^k$ for each $i = 1, \ldots, N$. Then we look for the minimum of $\{J(\vec{x}_i^m)\}_{m\le k}$, $i = 1, \ldots, N$ (the minimum in the history of the entire set of particles) and after $\vec{g}^k = \vec{x}_{i_{min}}^m$.

2. The velocity vector is updated:

   $$\vec{v}_i^{k+1} = c_1r_1\vec{v}_i^k + c_2r_2[\vec{p}_i^k - \vec{x}_i^k] + c_3r_3[\vec{g}^k - \vec{x}_i^k],$$

   where $c_1, c_2, c_3 \in (0, 2]$ are adjustment parameters and $r_1, r_2, r_3 \in [0, 1]$ are random numbers.

3. The particles are moved to their new position:

   $$\vec{x}_i^{k+1} = \vec{x}_i^k + \vec{v}_i^{k+1}.$$

To solve (3) or (4) we minimized $J_e = ||\vec{f}||$ with the PSO, looking for different points $\vec{x}_{pso}$ in $\mathbb{R}^9$ or $\mathbb{R}^{11}$. If $J_e \approx 0$, then we have a small region where the solution of $\vec{f}(\vec{x}) = 0$ is expected to be found. The region is defined by constructing an hyper-cube around the point found by the PSO, and then a grid of the region is made until Newton's method converges to $\vec{x}_{nw}$ for any of those seeds. Thus the desired solution is obtained.

Table 1 shows the efficiency of the PSO in the search for critical points in large regions (such as $\mathbb{R}^{11}$). Simulations were made using C and figures were obtained using Inkscape and MatLab, with a computer Lenovo ThinkCentre E73z i5-4430s, 2.7 GHz, with Windows 7.

6. RESULTS

The methods were applied to the following problem, proposed in Vallado (1997, p. 352), which deals with orbit transfers near Earth (Low Earth Orbit, LEO).

TABLE 1

RESULTS OF PSO

		Processing Methods				
Case	Computing Time (s)	$J_e(\vec{x}_{pso})$	# Iter (pso)	$J_e(\vec{x}_{nw})$	# Iter (nw)	$\|\|\vec{x}_{pso} - \vec{x}_{nw}\|\|$
LEO	25,94	10^{-4}	5538	10^{-12}	3641	$1.61e^{-5}$
Mercury	2,62	0,3	241	10^{-12}	60	2,28
Venus	1,05	0,1	313	10^{-12}	95	0,38
Mars	0,67	0,5	72	10^{-12}	61	0,47
Jupiter	2,63	0,5	321	10^{-12}	36	0,71
Saturn	12,92	0,5	1804	10^{-12}	26	0,27

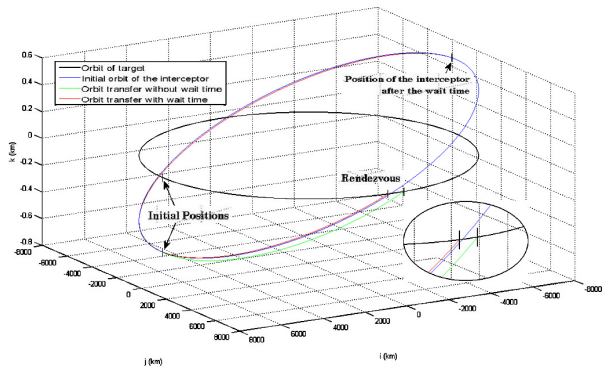

Fig. 4. Transfers between Hubble (blue) - Shuttle (black). The color figure can be viewed online.

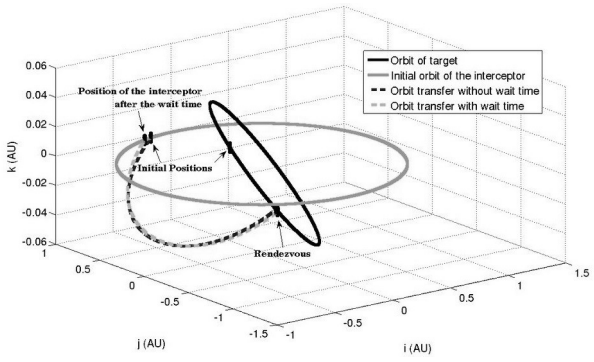

Fig. 5. Transfers between Earth (blue) - Mercury (black). The color figure can be viewed online.

The Hubble telescope will be released from the space shuttle, which is in a circular orbit at 590 km from the Earth's surface. The relative ejection speed (viewed from the shuttle) is $[-0,1\ -0,4\ -0,2]^T$ m/s. After 4 minutes, the Hubble needs to meet the shuttle. The change of RSW to IJK coordinates is shown in Vallado (1997, p. 367).

After applying the algorithm, the optimal orbit transfer without wait time has the parameters of the first row of Table 2 (for LEO), and has universal variables $X = 136.206$ and $x = 136.207$. With a wait time (shown by an asterisk in Table 2), $X = 651.694$, $x_1 = 265.476$ and $x = 386.215$ are obtained. The orbits are shown in Figure 4.

The Hohmann transfer gives the optimal change of velocity in planar and circular orbits. Leeghim's method deals with more general orbits: elliptic and hyperbolic; this method gives a smaller flight time.

It is also seen in Table 2 that for LEO orbits the time of flight of the transfer with wait time decreases 32.1% with respect to the one of Hohmann. In addition, Hohmann's change in velocity is 33.3% higher than that with wait time, the latter evidencing significant fuel savings.

The following examples are the orbit transfers from Earth to the other planets of the solar system with a launch date on January 1^{st}, 2014.

Figure 5 shows the current positions of Earth and Mercury for the assumed launch date, and the subsequent flight times. The resulting wait time is 3 days; with this, the change of velocity is reduced by one third and the flight time is reduced by 3 days with respect to the calculation without wait time.

These results are better than the values obtained in Kemble (2006, p. 50), where different launch dates for the optimization were assumed.

Computations were done without taking into account technical constraints. For example, the fastest space probe that NASA has launched is *New Horizons* with a $|\Delta\vec{v}|$ of 16.26 km/s relative to Earth, so the first $|\Delta\vec{v}|$ obtained without wait time is not feasible for such a mission, even though the flight time is the shortest.

TABLE 2

APPLICATIONS

		Change of Velocity				
LEO	t (min)	$\lvert\Delta\vec{v}\rvert$ (m/s)	$\Delta\vec{v}_{\hat{i}}$	$\Delta\vec{v}_{\hat{j}}$	$\Delta\vec{v}_{\hat{k}}$	Ignition
Leeghim	25.06	0.34	0.2	−0.27	−0.05	0
Leeghim*	71.04	0.15	0.0023	0.15	−0.01	48 min
Hohmann	48.24	0.2	···	···	···	48 min
Mercury	t (d)	$\lvert\Delta\vec{v}\rvert$ (km/s)	$\Delta\vec{v}_{\hat{i}}$	$\Delta\vec{v}_{\hat{j}}$	$\Delta\vec{v}_{\hat{k}}$	Ignition
Leeghim	102	6.99	6.49	2.06	−1.61	01-01-2014
Leeghim*	99	6.96	6.53	1.8	−1.61	04-01-2014
Kemble	158	9.37	···	···	···	11-05-2012
Venus	t (d)	$\lvert\Delta\vec{v}\rvert$ (km/s)	$\Delta\vec{v}_{\hat{i}}$	$\Delta\vec{v}_{\hat{j}}$	$\Delta\vec{v}_{\hat{k}}$	Ignition
Leeghim	85	20.33	20.24	−1.87	−0.05	01-01-2014
Leeghim*	142	2,42	−2.41	0.1	0.05	08-06-2014
Kemble	158	2.77	···	···	···	02-11-2013
Mars	t (d)	$\lvert\Delta\vec{v}\rvert$ (km/s)	$\Delta\vec{v}_{\hat{i}}$	$\Delta\vec{v}_{\hat{j}}$	$\Delta\vec{v}_{\hat{k}}$	Ignition
Leeghim	200	3.15	−2.63	−1.13	1.25	01-01-2014
Leeghim*	207	2.99	−2.68	−0.63	−1.15	10-01-2014
Kemble	207	3.82	···	···	···	18-01-2014
Jupiter	t (y)	$\lvert\Delta\vec{v}\rvert$ (km/s)	$\Delta\vec{v}_{\hat{i}}$	$\Delta\vec{v}_{\hat{j}}$	$\Delta\vec{v}_{\hat{k}}$	Ignition
Leeghim	7.19	9.69	−9.46	−1.28	0.99	01-01-2014
Leeghim*	2.22	9.39	−6.67	6.05	2.68	15-11-2016
Kemble	2.13	9.23	···	···	···	30-04-2009
Saturn	t (y)	$\lvert\Delta\vec{v}\rvert$ (km/s)	$\Delta\vec{v}_{\hat{i}}$	$\Delta\vec{v}_{\hat{j}}$	$\Delta\vec{v}_{\hat{k}}$	Ignition
Leeghim	2.73	70.4	70.07	−6.34	−2.13	01-01-2014
Leeghim*	6.21	10.25	−9.33	−4.23	−0.02	13-01-2014
Kemble	9.2	10.49	···	···	···	22-12-2009

Sometimes the direction of the Earth's velocity ($[-29.61\ -6.41\ 0]^T$ for January 1^{st}, 2014) and the initial positions of the planets are not suitable for orbit transfers. This means that, in some cases, a very large change of velocity (which translates to a large fuel consumption) is required, as presented in the first row of Table 2 (for Venus). See Figure 6.

Adding the wait time (167 days) results in a much lower change of velocity (12% of the first one, which requires less fuel), and the flight time increases by 57%, improving the results presented in Kemble (2006, p. 51) for comparable parameters.

The transfer of Earth-Mars orbit was calculated with wait time and without wait time. The difference lies in the fact that, with a wait time, the change of velocity was better and the flight time increased by a week. The results obtained are better than those of Kemble (2006, p. 53). See Figure 7.

The system proposed in § 5.1 can have different solutions (local maximums of the index of performance J). The algorithm used to solve it finds many of them; here the optimal are shown.

For the example Earth-Jupiter, Figure 8, the three changes in velocity without a wait time, with wait time and as found in Kemble (2006, p. 55) are very similar, but the time of flight with wait time is smaller than the one without, and it is very close to the values obtained in Kemble (2006, p. 55). In this

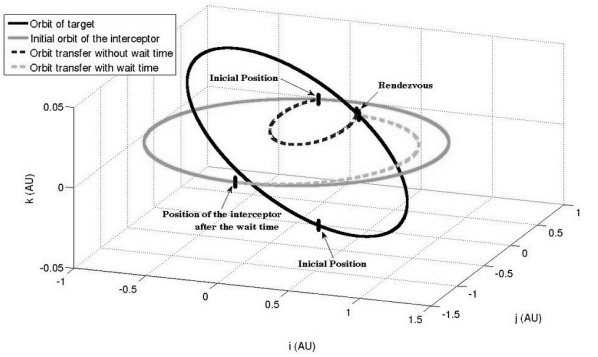

Fig. 6. Transfers between Earth (blue) - Venus (black). The color figure can be viewed online.

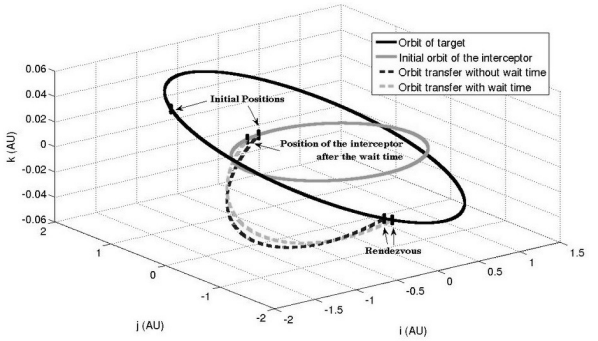

Fig. 7. Transfers between Earth (blue) - Mars (black). The color figure can be viewed online.

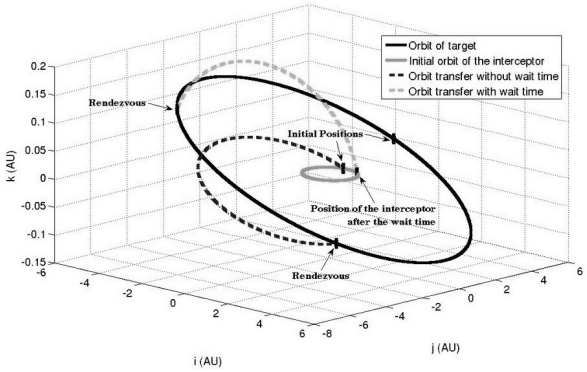

Fig. 8. Transfers between Earth (blue) - Jupiter (black). The color figure can be viewed online.

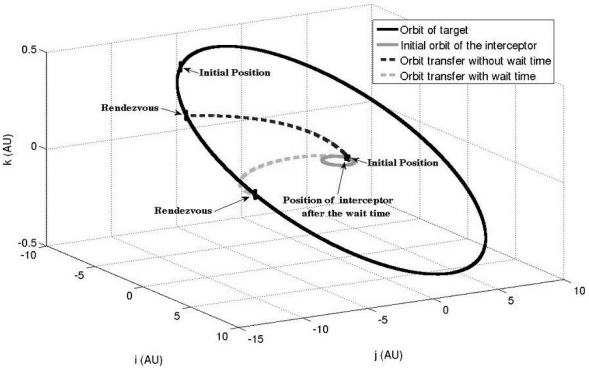

Fig. 9. Transfers between Earth (blue) - Saturn (black). The color figure can be viewed online.

case, the eccentricity of the orbit transfers found is greater than the one of the previous cases ($e = 0.75$).

The solution without a wait time for the system Earth-Saturn, Figure 9, is on a parabola (with eccentricity equal to 1, an uncommon result) and $|\Delta\vec{v}|$ is extremely large. The transfer with wait time has an eccentricity of 0.82, giving a better change of velocity than the one presented in Kemble (2006, p. 56) and the flight time is 3 years shorter.

7. CONCLUSIONS

The two techniques presented here make it possible to optimize the fuel consumption. However, its use is purely theoretical, leaving aside the technical constraints, but considering only constraints of the trajectory to make a more general model. For Newton's multivariate method, the search of the starting point was performed with the help of the PSO with excellent results. It perfectly bounds the search region of the starting point. The PSO is an heuristic method that needs no derivatives and has a rapid convergence. As future work we propose to use this method it in other situations and to perform the convergence analysis (local and semi-local) of the methods.

The authors are grateful with the young researcher fellowship of the Sergio Arboleda University from which this paper is one of its results.

REFERENCES

Bate, R. R., Mueller, D. D., & White, J. E. 1971, Fundamentals of Astrodynamics (New York: Dover Publications)

Clerc, M. & Kennedy, J. 2002, ITEVC, 6(1), 58

Conway, B. 2010, Spacecraft Trajectory Optimization (Cambridge, MA: CUP)

Danby, J. M. A. 1992, Fundamentals of Celestial Mechanics, (New York, NY: Macmillan)

Elipe, A., Montijano, J. I., Rández, L., & Calvo, M. 2017, CeMDA, 129, 415

Gang, Z., Xiangyu, Z., & Xibin, C. 2014, ChJA, 27(3), 577

Geetha, T., Sowmiya, B., JayaKumar, L., & Sarang Sukumar, A. 2013, IJETAE, 3(4), 672

Hvass, M. 2010, Tuning And Simplifying Heuristical Optimization [Thesis], (Southampton: University of Southampton)
Kemble, S. 2006, Interplanetary Missions Analysis and Design, (Berlin: Springer-Verlag Berlin Heidelberg)
Kennedy, J. & Eberhart, R. 1995, Particle Swarm Optimization, (Perth, WA: IEEEP)
Leeghim, H. 2013, CeMDA, 115, 1
Parsopoulos, K. & Vrahatis, M. 2002, In Frontiers in Artificial Intelligence and Applications, ed. P. Sinkad et al. (Amsterdam: IOS Press), 76, 214
Sharaf, M. A. & Saad, A. S. 2016, RMxAA, 52, 283
Shan, J. & Ren, Y. 2014, Aerospace Science and Technology, 36, 114
Vallado, D. A. 1997, Fundamentals of Astrodynamics and Applications (New York, NY: McGraw-Hill)
Villanueva. Y. 2013, Lagrangian Optimization in Interplanetary Trajectories [Thesis], (Bogotá: Universidad Sergio Arboleda)
Zotes, F. & Santos, M. 2012, Engineering Applications of Artificial Intelligence, 25(1), 189

L. M. Echeverry and Y. Villanueva: School of Exact Sciences and Engineering, Sergio Arboleda University, Bogotá, Colombia (lechever@uniandes.edu.co, yovaniing@gmail.com).
L. M. Echeverry: Department of Mathematics, University of the Andes, Bogotá, Colombia (lechever@uniandes.edu.co).
Y. Villanueva: Institute of Mathematics and Statistics, Federal University of Goiás, Goiania, Brazil (yovaniing@gmail.com).

Revista Mexicana de Astronomía y Astrofísica, **55**, 185–191 (2019)

DOI: https://doi.org/10.22201/ia.01851101p.2019.55.02.06

THE ENVIRONMENTAL DEPENDENCE OF GALAXY AGE AND STELLAR MASS IN THE REDSHIFT REGION $0.6 \leq z \leq 0.75$

Xin-Fa Deng

School of Science, Nanchang University, Jiangxi, China.

Received February 11 2019; accepted May 13 2019

ABSTRACT

In this work, I construct a LRG (Luminous Red Galaxy) sample with redshifts $0.6 \leq z \leq 0.75$ from the Sloan Digital Sky Survey Data Release 15 (SDSS DR15), which contains 184172 CMASS LRGs and 27158 eBOSS LRGs, and examine the environmental dependence of galaxy age and stellar mass in this galaxy sample. I divide this LRG sample into subsamples with a redshift binning size of $\Delta z = 0.01$, and analyze the environmental dependence of galaxy age and stellar mass for these subsamples in each redshift bin. Overall, galaxy age and stellar mass in the LRG sample with redshift $0.6 \leq z \leq 0.75$ are very weakly correlated with the local environment, which shows that minimal environmental dependence of galaxy parameters can continue to larger redshifts.

RESUMEN

En este trabajo se compila una muestra de galaxias luminosas rojas (LRG) con corrimientos al rojo $0.6 \leq z \leq 0.75$ extraída del Sloan Digital Sky Survey Data Release 15 (SDSS DR15), que contiene 184172 CMASS LRGs y 27158 eBOSS LRGs. Se estudia la dependencia ambiental de las edades de las galaxias de esta muestra y de las masas estelares. Se divide la muestra de LGRs en submuestras usando una $\Delta z = 0.01$ y se analiza la dependencia ambiental de las edades de las galaxias y las masas estelares en cada intervalo de z. En general, la correlación de las edades galacticas y las masas estelares en la muestra LRG con $0.6 \leq z \leq 0.75$ con el medio ambiente local es leve, lo que muestra que la mínima dependencia ambiental de los parámetros galácticos puede extenderse a corrimientos al rojo mayores.

Key Words: galaxies: fundamental parameters — galaxies: statistics

1. INTRODUCTION

In the past, many works have shed light on the environmental dependence of galaxy parameters. The extended Baryon Oscillation Spectroscopic Survey (eBOSS) of the Sloan Digital Sky Survey IV (SDSS-IV) aims to map the galaxy, quasar, and neutral gas distributions between $z \simeq 0.6$ and 3.5 (Dawson et al. 2016). The LRG component of SDSS-IV /eBOSS will obtain spectroscopy of a sample of luminous early-type galaxies in the redshift range $0.6 < z < 1.0$ (median redshift 0.71) (Prakash et al. 2016). The SDSS-IV /eBOSS LRGs will cover a volume either not probed, or not probed at high density, by SDSS-III /BOSS, and will provide a powerful extension of SDSS-III /BOSS for many studies of galaxies at high redshifts. The primary goal of this study is to explore the environmental dependence of galaxy age and stellar mass in the redshift range $0.6 \leq z \leq 0.75$.

In the local Universe, galaxy age and stellar mass strongly depend on the environment: galaxies in high density regions are generally older and more-massive than galaxies in low density regions (e.g., Bernardi et al. 1998; Trager et al. 2000; Kuntschner et al. 2002; Terlevich & Forbes 2002; Kauffmann et al. 2004; Proctor et al. 2004; Mendes de Oliveira et al. 2005; Thomas et al. 2005; Gallazzi et al. 2006; Li et al. 2006; Sánchez-Blázquez et al. 2006; Sil'chenko 2006; Reed et al. 2007; Rakos et al. 2007; Wegner & Grogin 2008; Deng et al. 2011, 2012a; Smith et al. 2012). Proctor et al. (2004) and Mendes de Oliveira et al. (2005) noted that field galaxies are generally younger than member galaxies of compact groups. Rakos et al. (2007) showed the

correlation between galaxy mean age and distance from the cluster center: older galaxies inhabit the core. Kauffmann et al. (2004) reported that galaxies in high-density environments have larger masses than galaxies in low-density environments. Li et al. (2006) found that more-massive galaxies cluster more strongly than less-massive galaxies. But some studies demonstrated the environmental dependence of galaxy age and stellar mass becomes weak with increasing redshift. Deng et al. (2012b) argued that the stellar mass of SDSS LRGs with redshifts $0.16 \leq z \leq 0.3$ is nearly independent of local environments. Grützbauch et al. (2011a) claimed that galaxies at intermediate redshifts also have only a weak dependence of stellar mass on environment. Deng & Zou (2014) and Deng (2015, 2019) found that galaxy age and stellar mass in the CMASS sample of SDSS-III/BOSS (Eisenstein et al. 2011) are very weakly correlated with environment. To demonstrate the variation of the environmental dependence of galaxy age and stellar mass with redshift, it is important to examine the environmental dependence of these two galaxy parameters in the higher redshift region.

The outline of this paper is as follows. In § 2, I describe the galaxy sample. I present statistical result in § 3 and a discussion in § 4. I summarize my main results and conclusions in § 5.

In calculating the distance, I used a cosmological model with a matter density of $\Omega_0 = 0.3$, a cosmological constant of $\Omega_\Lambda = 0.7$, and a Hubble constant of H_0=70km·s^{-1}· Mpc^{-1}.

2. SAMPLE

The Constant Mass (CMASS) sample SDSS-III/BOSS (Eisenstein et al. 2011) is a high redshift sample with a redshift of $0.43 < z < 0.7$. Anderson et al. (2012) and Dawson et al. (2013) claimed that the BOSS galaxies are selected to have approximately uniform comoving number density only out to a redshift $z = 0.6$. Maraston et al. (2013) also showed that BOSS is a mass-uniform sample over the redshift range 0.2 to 0.6. Thus, in my previous works, the CMASS sample was limited to the redshift region of $0.44 \leq z \leq 0.59$ (Deng 2015, 2019). I hope to extend studies for the environmental dependence of galaxy age and stellar mass to a higher redshift region. In this work, the data of the galaxy sample was downloaded from the Catalog Archive Server of SDSS Data Release 15 (Aguado et al. 2019) by the SDSS SQL Search (`https://www.sdss.org/dr15/`). I extracted 194380 CMASS LRGs (with SDSS flag: BOSS_TARGET1&128>0) and 48131 eBOSS LRGs (with SDSS flag: eBOS _TARGET1 & $(2 \mid 4 \mid 8) > 0$) in the redshift region of $0.6 < z < 1.0$. Because the number of galaxies at redshifts $z > 0.75$ is too small to ensure an ideal statistical analysis, I constructed a LRG sample with redshift of $0.6 \leq z \leq 0.75$, which contains 184172 CMASS LRGs and 27158 eBOSS LRGs.

3. STATISTICAL RESULTS

Like Deng (2012) did, I measure the projected local density $\Sigma_5 = N/\pi d_5^2$ (Galaxies Mpc^{-2}) where d_5 is the distance to the 5th nearest neighbor within $\pm$1000 km s^{-1} in redshift (e.g., Goto et al. 2003; Balogh et al. 2004a, 2004b), and divide the LRG sample with redshifts of $0.6 \leq z \leq 0.75$ into subsamples with a redshift binning size of $\Delta z = 0.01$. Table 1 lists the density ranges in each redshift bin. As shown by Table 1, the projected local density in this sample is much smaller than the one in the CMASS sample of SDSS-III/BOSS (Eisenstein et al. 2011) with redshifts of $0.44 \leq z \leq 0.59$ (see Table 1 of Deng 2014), which is consistent with the results of Dawson et al. (2013) and Anderson et al. (2012). Dawson et al. (2013) and Anderson et al. (2012) showed that the number-density of CMASS galaxies dramatically drops with increasing redshifts at $z > 0.6$.

In each subsample, I arrange galaxies in density order from the smallest to the largest, select approximately 5% of the galaxies, construct two samples at both extremes of density according to the density, and compare the distribution of galaxy age and stellar mass in the lowest density regime with those in the densest regime.

Following Deng (2012), Deng (2015, 2019) divided a CMASS sample of SDSS-III/BOSS (Eisenstein et al. 2011) with redshifts $0.44 \leq z \leq 0.59$ into subsamples with a redshift binning size of $\Delta z = 0.01$, and then analyzed the environmental dependence of age and stellar mass of subsamples in each redshift bin. The result of Deng (2015, 2019) demonstrated that age and stellar mass of CMASS galaxies are very weakly correlated with the local environment in all redshift bins. Figures 1-2 show the age and stellar mass distributions at both extremes of density in different redshift bins for the CMASS + eBOSS LRG sample with redshifts $0.6 \leq z \leq 0.75$. As shown by these two figures, age and stellar mass of LRGs with redshifts $0.6 \leq z \leq 0.75$ are nearly independent of the local environment in all redshift bins.

TABLE 1

K-S PROBABILITIES OF GALAXY AGE AND STELLAR MASS*

Redshift bins	Number of Galaxies	Projected local density range (Galaxies $\mathrm{M\,pc^{-2}}$)	P(age)	P(stellar mass)
0.60-0.61	27622	$2.55 \times 10^{-5} \longrightarrow 94.78$	0.110	0.0130
0.61-0.62	25835	$1.67 \times 10^{-5} \longrightarrow 22.47$	0.329	0.261
0.62-0.63	23002	$1.57 \times 10^{-5} \longrightarrow 19.64$	0.0612	0.140
0.63-0.64	20378	$2.42 \times 10^{-5} \longrightarrow 73.91$	0.375	0.763
0.64-0.65	18037	$4.55 \times 10^{-5} \longrightarrow 5.39$	0.843	0.251
0.65-0.66	16001	$1.40 \times 10^{-5} \longrightarrow 5.19$	0.859	0.0435
0.66-0.67	14474	$2.08 \times 10^{-5} \longrightarrow 50.81$	0.887	0.0248
0.67-0.68	12443	$1.45 \times 10^{-5} \longrightarrow 5.85$	0.499	0.129
0.68-0.69	11062	$1.47 \times 10^{-5} \longrightarrow 5.37$	0.141	0.00270
0.69-0.70	9623	$1.97 \times 10^{-5} \longrightarrow 2.54$	0.174	0.000348
0.70-0.71	8532	$1.45 \times 10^{-5} \longrightarrow 9.49$	0.174	0.350
0.71-0.72	7440	$1.14 \times 10^{-5} \longrightarrow 2.70$	0.313	0.00996
0.72-0.73	6362	$1.23 \times 10^{-5} \longrightarrow 3.16$	0.863	0.00123
0.73-0.74	5514	$1.24 \times 10^{-5} \longrightarrow 2.00$	0.799	0.0713
0.74-0.75	5005	$7.92 \times 10^{-6} \longrightarrow 3.73$	0.817	4.754e-05

*The two samples at both density extremes are drawn from the same distribution.

The step figures can directly present some properties of the statistical result. But this procedure is not ideal because the error bars in the step figures may change with binning sizes. The Kolmogorov-Smirnov (KS) test is well-suited for a quantitative comparison, which demonstrates the degree of similarity or difference between two independent distributions by calculating a probability value. Table 1 lists the K-S probabilities of each panel in Figures 1-2. As shown by Table 1, the K-S probabilities of the CMASS + eBOSS LRG sample with redshifts $0.6 \leq z \leq 0.75$ are much larger than those obtained by Deng (2012) and Deng et al. (2012a) (see Table 1 of Deng 2012 and Deng et al. 2012a) and even in many redshift bins much larger than 0.05 (5% is the standard in a statistical analysis). This is in good agreement with the conclusion obtained by the step figures.

The weak environmental dependence of some galaxy parameters in intermediate and high redshift regions is likely due to the color-density relation and the tight correlations between colors and other galaxy parameters. In the local Universe, Deng et al. (2013) concluded that color is fundamental in correlations between galaxy properties and the environment and that a large part of the other galaxy properties-density relation is likely due to the relation between color and density. Grützbauch et al. (2011a) observed a weak environmental dependence of galaxy color at $0.4 < z < 0.7$. Deng (2014) also reported that all five colors in the CMASS sample with redshifts $0.44 \leq z \leq 0.59$ are very weakly correlated with the local environment. A possible interpretation for this is that the environmental processes that exert the essential influence on galaxy properties proceed slowly over cosmic time. Some of the most influential high-density environments may still be in the process of being built up and cannot yet affect galaxy colors (Grützbauch et al. 2011b). The weak environmental dependence of age and stellar mass in intermediate and high redshift regions is likely due to weak color-density relation and tight correlations between colors and these two parameters. For example, Grützbauch et al. (2011a,b) remarked that there is a strong correlation between galaxy color and stellar mass in these redshift regions.

4. DISCUSSION

These results demonstrate that the strong environmental dependence of galaxy age and stellar mass in the local Universe cannot be extended to intermediate- and high-redshift regions. Cucciati et al. (2006) also reported that the color-density relation at $0.25 < z < 0.60$ progressively disappears at

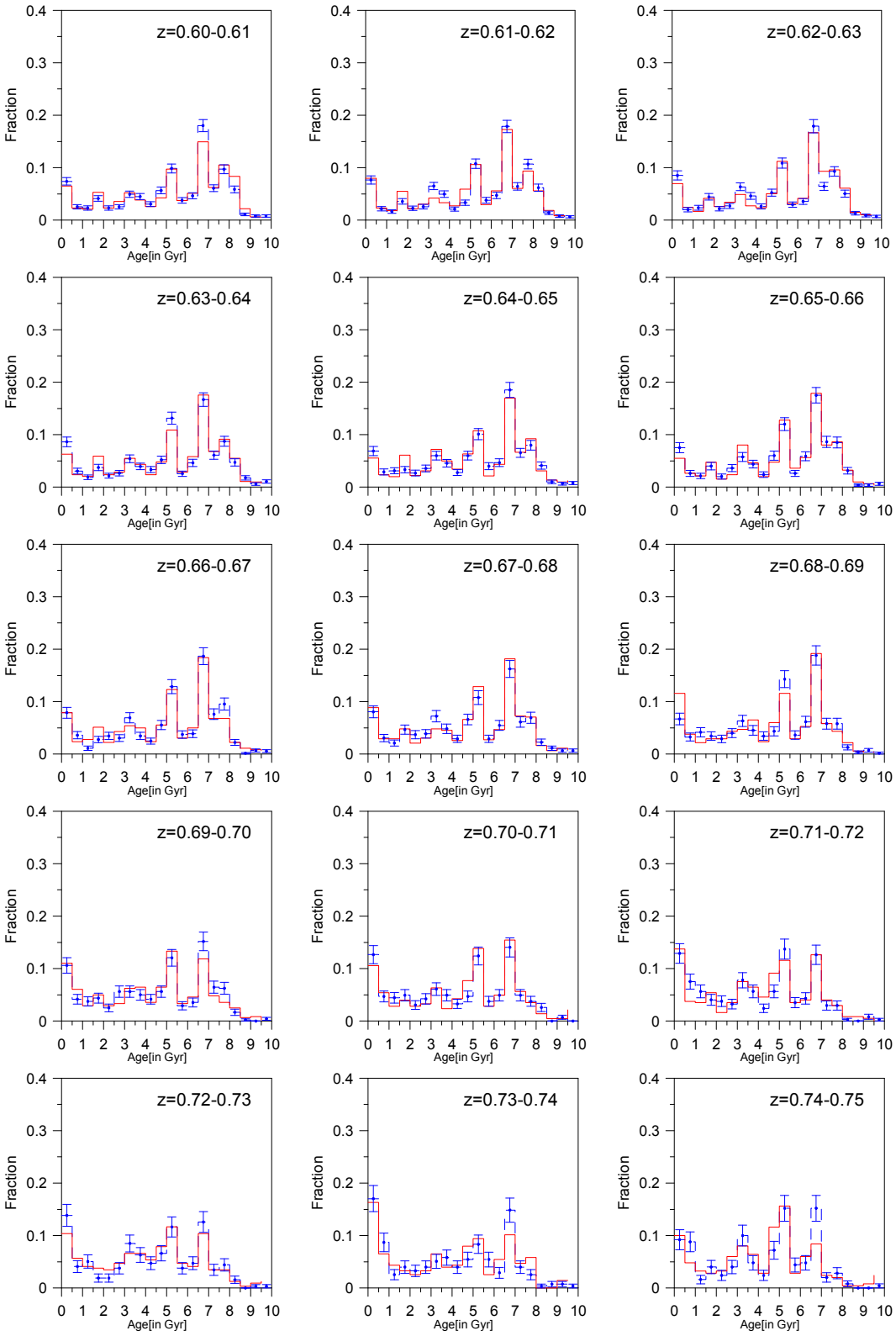

Fig. 1. Age distribution at both extremes of density in different redshift bins: the red solid line represents the sample at high density, the blue dashed line represents the sample at low density. The error bars of the blue lines are 1 σ Poissonian errors. The error-bars of the red lines are omitted for clarity. The color figure can be viewed online.

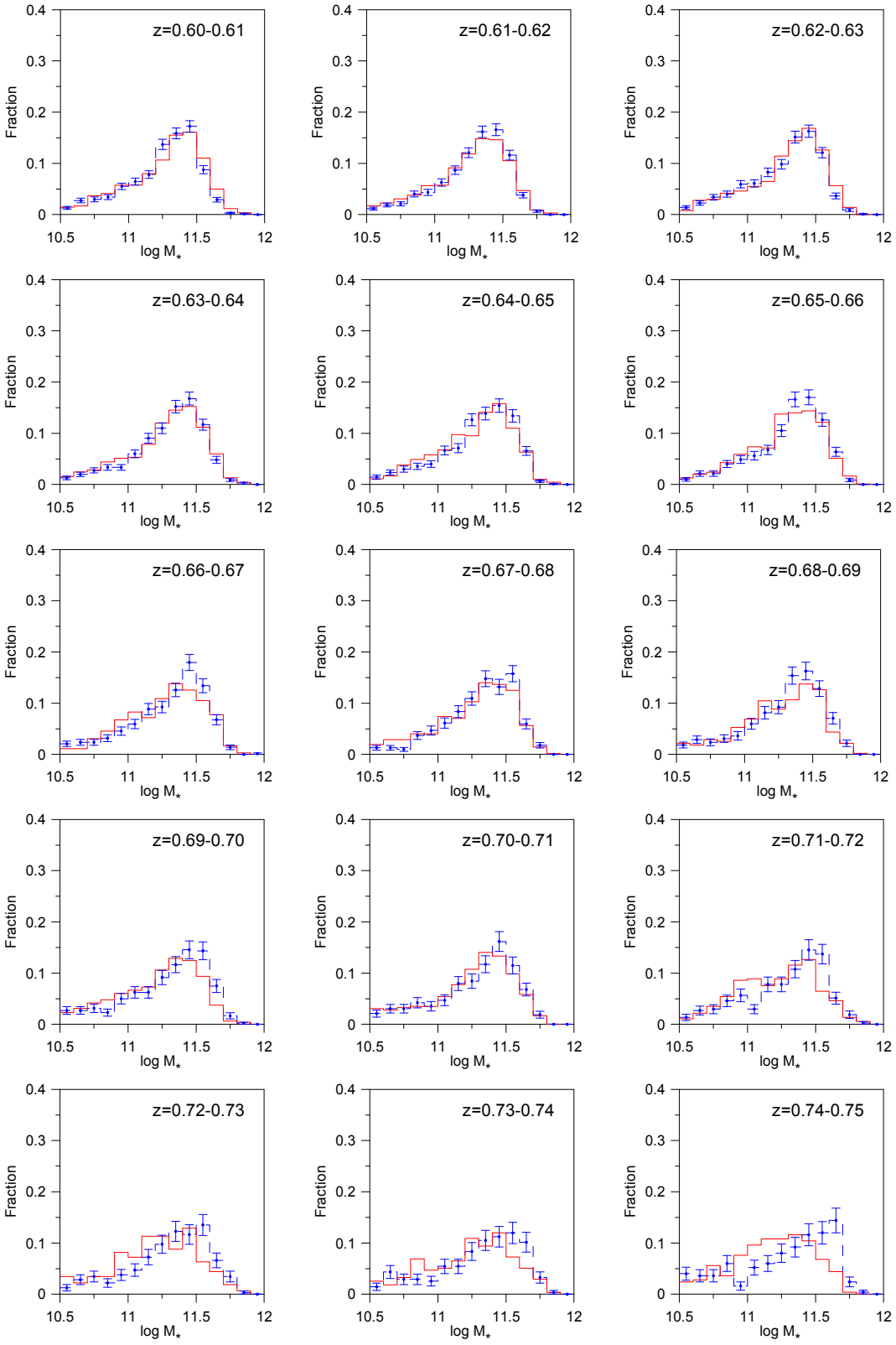

Fig. 2. Same as Figure 1, but for the stellar mass distribution at both density extremes in different redshift bins. The color figure can be viewed online.

higher redshift until it is undetectable at $z \simeq 0.9$. The method of Deng (2012) is well-suited for exploring the variation of the environmental dependence of galaxy properties with redshift. Using this method, Deng et al. (2012a) noted that the environmental dependence of galaxy properties becomes weak with increasing redshifts in the apparent magnitude-limited Main Galaxy Sample (Strauss et al. 2002) and argued that this is likely due to a selection effect, i.e., galaxies at the higher end of a redshift region are restricted to a fairly narrow high-luminosity region due to the Malmquist bias (Malmquist 1920; Teerikorpi 1997), which consequently leads to the limitation of other galaxy properties to within a narrow region. However, such a phenomenon is also likely due to a real physical effect, which subsequently leads to the variation of the environmental dependence of galaxy properties with redshift. The Main(Strauss et al. 2002), LOWZ and CMASS galaxy samples of SDSS can be used to demonstrate the variation of the environmental dependence of galaxy properties with redshift in a fairly wide redshift region. For example, Deng et al. (2017) explored the environmental dependence of K-band luminosity in the Main, LOWZ and CMASS Galaxy Samples of the SDSS. The environmental dependence of K-band luminosity in the LOWZ Galaxy Sample becomes weak with increasing redshift, like the one in the apparent magnitude-limited Main Galaxy Sample does. In the LOWZ Galaxy Sample, the K-band luminosity of galaxies shows substantial correlation with the local environment only in the redshift region $0.16 \leq z \leq 0.21$, which seemingly is a continuation of that in the apparent magnitude-limited Main Galaxy Sample, while minimal environmental dependence of the K-band luminosity in the high redshift region in the LOWZ galaxy sample continues as far as the CMASS sample can reach. The result of this work shows that minimal environmental dependence of galaxy parameters can continue to higher redshifts.

5. SUMMARY

To demonstrate the variation of the environmental dependence of galaxy age and stellar mass with redshift, I construct a LRG sample with redshifts of $0.6 \leq z \leq 0.75$, which contains 184172 CMASS LRGs and 27158 eBOSS LRGs, and examine the environmental dependence of these two galaxy parameters in this sample. Following Deng (2012), I divide this LRG sample into subsamples with a redshift binning size of $\Delta z = 0.01$, and analyze the environmental dependence of galaxy age and stellar mass for these subsamples in each redshift bin. As shown by Table 1 and Figures 1-2, overall, galaxy age and stellar mass in LRG sample with the redshifts $0.6 \leq z \leq 0.75$ are very weakly correlated with the local environment, which shows that minimal environmental dependence of galaxy parameters can continue to higher redshifts.

I thank the anonymous referee for many useful comments and suggestions. This study was supported by the National Natural Science Foundation of China (NSFC, Grant 11533004, 11563005).

Funding for the Sloan Digital Sky Survey IV has been provided by the Alfred P. Sloan Foundation, the U.S. Department of Energy Office of Science, and the Participating Institutions. SDSS acknowledges support and resources from the Center for High-Performance Computing at the University of Utah. The SDSS web site is `www.sdss.org`.

SDSS is managed by the Astrophysical Research Consortium for the Participating Institutions of the SDSS Collaboration including the Brazilian Participation Group, the Carnegie Institution for Science, Carnegie Mellon University, the Chilean Participation Group, the French Participation Group, Harvard-Smithsonian Center for Astrophysics, Instituto de Astrofisica de Canarias, The Johns Hopkins University, Kavli Institute for the Physics and Mathematics of the Universe (IPMU) / University of Tokyo, the Korean Participation Group, Lawrence Berkeley National Laboratory, Leibniz Institut für Astrophysik Potsdam (AIP), Max-Planck-Institut für Astronomie (MPIA Heidelberg), Max-Planck-Institut für Astrophysik (MPA Garching), Max-Planck-Institut für Extraterrestrische Physik (MPE), National Astronomical Observatories of China, New Mexico State University, New York University, University of Notre Dame, Observatório Nacional / MCTI, The Ohio State University, Pennsylvania State University, Shanghai Astronomical Observatory, United Kingdom Participation Group, Universidad Nacional Autónoma de México, University of Arizona, University of Colorado Boulder, University of Oxford, University of Portsmouth, University of Utah, University of Virginia, University of Washington, University of Wisconsin, Vanderbilt University, and Yale University.

REFERENCES

Aguado, D. S., Ahumada, R., Almeida, A., et al. 2019, ApJS, 240, 23

Anderson, L., Aubourg, E., Bailey, S., et al. 2012, MNRAS, 427, 3435

Balogh, M. L., Baldry, I. K., Nichol, R., et al. 2004a, ApJ, 615, L101
Balogh, M. L., Eke, V., Miller, C., et al. 2004b, MNRAS, 348, 1355
Bernardi, M., Renzini, A., & da Costa, L. 1998, ApJ, 508, L143
Cucciati, O., Iovino, A., Marinoni, C., et al. 2006, A&A, 458, 39
Dawson, K. S., Schlegel, D. J., Ahn, C. P., et al. 2013, AJ, 145, 10
Dawson, K. S., Kneib, J. P., Percival, W. J., et al. 2016, AJ, 151, 44
Deng, X. F. 2012, AJ, 143, 15
_____. 2014, RAA, 14, 553
_____. 2015, AN, 336, 1017
_____. 2019, AN, submitted
Deng, X. F., Chen, Y. Q., & Jiang, P. 2011, ChJPh, 49, 1137
Deng, X. F., Jiang, P., Ding, Y. P., et al. 2017, AN, 338, 720
Deng, X. F., Luo, C. H., Xin, Y., et al. 2013, RMxAA, 49, 181
Deng, X. F., Wu, P., Qian, X. X., et al. 2012a, PASJ, 64, 93
Deng, X. F., Yang, B., Ding, Y. P., et al. 2012b, AN, 333, 644
Deng, X. F. & Zou, S. Y. 2014, CaJPh, 92, 36
Eisenstein, D. J., Weinberg, D. H., Agol, E., et al. 2011, AJ, 142, 72
Gallazzi, A., Charlot, S., Brinchmann, J., et al. 2006, MNRAS, 370, 1106
Goto, T., Yamauchi, C., Fujita, Y., et al. 2003, MNRAS, 346, 601
Grützbauch, R., Conselice, C. J., Varela, J., et al. 2011a, MNRAS, 411, 929
Grützbauch, R., Chuter, R. W., Conselice, C. J., et al. 2011b, MNRAS, 412, 2361
Kauffmann, G., White, S. D. M., Heckman, T. M., et al. 2004, MNRAS, 353, 713
Kuntschner, H., Smith, R. J., Colless, M., et al. 2002, MNRAS, 337, 172
Li, C., Kauffmann, G., Jing, Y. P., et al. 2006, MNRAS, 368, 21
Malmquist, K. G. 1920, MeLus II, 22, 1
Maraston, C., Pforr, J., Henriques, B. M., et al. 2013, MNRAS, 435, 2764
Mendes de Oliveira, C., Coelho, P., González, J. J., et al. 2005, ApJ, 130, 55
Prakash, A., Licquia, T. C., Newman, J. A., et al. 2016, ApJS, 224, 34
Proctor, R., Forbes, D., Hau, G., et al. 2004, MNRAS, 349, 1381
Rakos, K., Schombert, J., & Odell, A. 2007, ApJ, 658, 929
Reed, D. S., Governato, F., Quinn, T., et al. 2007, MNRAS, 378, 777
Sánchez-Blázquez, P., Gorgas, J., Cardiel, N., et al. 2006, A&A, 457, 809
Sil'chenko, O. K. 2006, ApJ, 641, 229
Smith, R. J., Lucey, J. R., Price, J., et al. 2012, MNRAS, 419, 3167
Strauss, M. A., Weinberg, D. H., Lupton, R. H., et al. 2002, AJ, 124, 1810
Teerikorpi, P. 1997, ARA&A, 35, 101
Terlevich, A. & Forbes, D. 2002, MNRAS, 330, 547
Thomas, D., Maraston, C., Bender, R., & Mendes de Oliveira, C. 2005, ApJ, 621, 673
Trager, S. C., Faber, S. M., Worthey, G., et al. 2000, AJ, 120, 165
Wegner, G., Grogin, N. A. 2008, AJ, 136, 1

Xin-Fa Deng: School of Science, Nanchang University, Jiangxi, China, 330031 (xinfadeng@163.com).

Revista Mexicana de Astronomía y Astrofísica, **55**, 193–202 (2019)

DOI: https://doi.org/10.22201/ia.01851101p.2019.55.02.07

ON THE NATURE OF THE HADS STAR V2455 CYG[1]

J. H. Peña[2,3,4], A. Rentería[2,4], C. Villarreal[2,4], and D. S. Piña[2,4]

Received November 21 2018; accepted May 22 2019

ABSTRACT

Using $uvby-\beta$ photoelectric photometry obtained with the 0.84 m telescope of the Observatorio Astrónomico Nacional de San Pedro Mártir, México, we determined some of the physical characteristics, such as effective temperature and surface gravity of the high amplitude Delta Scuti star V2455 Cyg (=HD 204615). Newly determined times of maximum light gathered at the Observatorio Astrónomico Nacional de Tonantzintla, México with small 10 inch telescopes equipped with CCD cameras were combined with times of maxima in the literature, and used to study the secular variation of the pulsational period of the star.

RESUMEN

A partir de fotometría fotoeléctrica $uvby-\beta$ adquirida con el telescopio de 0.84 m del Observatorio Astrónomico Nacional de San Pedro Mártir, México de la estrella Delta Scuti de gran amplitud V2455 Cyg (=HD 204615) hemos determinado sus parámetros físicos tales como temperatura efectiva y gravedad superficial. Con nuevos tiempos de máximo recopilados con telescopios pequeños de 10 pulgadas provistos de cámaras CCD en el Observatorio Astrónomico Nacional de Tonantzintla, México, junto con tiempos de máximo de la literatura, hemos estudiado el período secular de la estrella.

Key Words: stars: variables: delta Scuti — techniques: photometric

1. INTRODUCTION

This high amplitude Delta Scuti (HADS) star, V2455 Cyg, was first described recently by Wils et al. (2003), who found it to be a new variable star. They reported that its variability was suspected by Yoss et al. (1991) who derived the following characteristics: a distance of 215 pc, an absolute magnitude of 2.2 and a total space velocity S of 32 km/s. They also determined $V = 8.86$, and $(B\text{-}V)$=+0.27 which classifies this star as spectral type F2. A period of 0.094206 d was proposed by Piquard (2001) from available Tycho data.

2. OBSERVATIONS

This article is a product of a long campaign devoted to several objects, one of which was NGC 6633 (Peña et al. 2017, Paper I) already published. Another article in progress is devoted to the open clusters IC 4665, NGC 6871 and Dzim 5 (Paper II). In these works we have explained in detail the procedures followed in the acquisition and reduction of the data. Here we present the data of the pulsating variable V2455, a HADS star. The observations were done at the Observatorio Astronómico Nacional of San Pedro Mártir (SPM) in México. Table 1 presents the log of observations, as well as the new times of maximum light.

2.1. *Data Acquisition and Reduction*

The observations were done in the summer of 2016, along with those of other variable stars and clusters. The procedure to determine the physical parameters has been reported elsewhere (Peña et al., 2016). The photometric system, if well-defined and calibrated, provides an efficient method to investigate physical conditions, such as effective temperature and surface gravity, using a direct comparison of the unreddened indexes with those obtained

[1]Based on observations collected at the Observatorio Astrónomico Nacional de San Pedro Mártir, México.

[2]Instituto de Astronomía, Universidad Nacional Autónoma de México, México.

[3]Observatorio Astronómico Nacional de Tonantzintla, México.

[4]Facultad de Ciencias, Universidad Nacional Autónoma de México, México.

TABLE 1

LOG OF OBSERVING SEASONS OF V 2455 CYG

Date year/month/day	Observer	Number of points	Observed time (day)	Nmax	HJD (day)
2016/06/26	ARL	85	0.08	1	2457565
2016/06/27	ARL	32	0.06	0	2457566
2016/06/28	ARL	62	0.07	0	2457567
2016/07/05	CVR	41	0.09	1	2457574
2016/07/06	CVR	48	0.11	1	2457575

TABLE 2

TRANSFORMATION COEFFICIENTS OBTAINED FOR THE OBSERVING SEASON

Season	B	D	F	J	H	I	L
Summer 2016	0.006	0.971	1.049	0.033	1.016	0.103	−1.356
σ	0.033	0.005	0.051	0.016	0.034	0.052	0.044

from theoretical models. These calibrations have been described and used in previous analyses (Peña & Peniche; 1994; Peña & Sareyan, 2006).

The observations consisted of one long season with two different observers (ARL and CVR), one in June (22 to 30 by ARL) and the other in July, 2016 (1 to 8 by CVR) with different target objects in each one, although two were obtained in both seasons (NGC 6633 (Paper I) and V2455 Cyg).

The reduction was done considering both seasons together to make a longer season in order to increase the accuracy provided by the standard stars. Over the five nights of observation of V 2455 Cyg, the following procedure was used: for each measurement we took at least five ten-second integrations of each star and one ten-second integration of the sky for the *uvby* filters and the narrow and wide filters that define Hβ.

We also observed a series of standard stars nightly to transform the data into the standard system. The chosen system was that defined by the reported values of Olsen (1983) although some standard bright stars were chosen from the Astronomical Almanac (2006). The transformation equations are those defined by Crawford & Barnes (1970) and by Crawford & Mander (1966).

The coefficients defined by the following equations and which adjusted the data to the standard system were:

$$\begin{aligned} V_{\rm std} &= A + B(b-y)_{\rm inst} + y_{\rm inst}, \\ (b-y)_{\rm std} &= C + D(b-y)_{\rm inst}, \\ m_{1_{\rm std}} &= E + F(m_1)_{\rm inst} + J(b-y)_{\rm inst}, \\ c_{1_{\rm std}} &= G + H(c_1)_{\rm inst} + I(b-y)_{\rm inst}, \\ H\beta_{\rm std} &= K + L(H\beta)_{\rm inst}. \end{aligned}$$

In these equations the coefficients D, F, H and L are the slope coefficients for $(b-y)$, m_1, c_1 and β, respectively. The coefficients B, J and I are the color terms of V, m_1, and c_1. The averaged transformation coefficients of the season are listed in Table 2 along with their standard deviations. Season errors were evaluated with the eighteen standard stars observed for a total of 272 observed points. These uncertainties were calculated through the differences in magnitude and colors for all nights, for (V, $b-y$, m_1, c_1 and β) as (0.024, 0.010, 0.011, 0.015, 0.015) respectively, which provide a numerical evaluation of our uncertainties for the season. Emphasis is made on the large range of standard stars in the magnitude and color ranges: V:(5.0, 8.8); $(b-y)$:(-0.06, 0.80); m_1:(0.10, 0.68); c_1:(0.11, 1.18) and β:(2.60, 2.82).

Table 3 lists a sample of the photometric values of the observed star. The complete data set will be published elsewhere. In this table Columns 1 to 4 list the Strömgren values V, $(b-y)$, m_1 and c_1, respectively; Column 5, Hβ, whereas Column 6 reports the time of the observation in HJD. The photometry is presented in Figure 1.

TABLE 3

$uvby-\beta$ PHOTOELECTRIC PHOTOMETRY OF V2455 CYG

V	$(b-y)$	m_1	c_1	β	HJD
9.011	0.195	0.169	0.759		2457565.8898
9.022	0.195	0.167	0.761	2.732	2457565.8902
9.007	0.200	0.167	0.763		2457565.8913
9.010	0.206	0.161	0.768		2457565.8937
9.009	0.210	0.154	0.775	2.749	2457565.8941

3. PERIOD DETERMINATION

To determine the period behavior of V 2455 Cyg the following methods were employed: (1) differences of consecutive times of maximum light were evaluated to determine a coarse period; (2) a time series analysis of the data set was utilized; (3) $O-C$ differences were calculated using a compiled collection of times of maximum light (MSDR); (4) Period determination through $O-C$ differences minimization (PDDM).

The previously determined ephemerides equations as well as the newly determined ones are listed in Table 4. In this table Column 1 indicates the method followed; Columns 2 and 3 the elements of the proposed ephemerides. The goodness of the elements can be discriminated by the mean and standard deviation values listed in Columns 4 and 5.

3.1. *Differences of Consecutive Times of Maximum Light, DCTM*

To determine the period from scratch, as a first guess we considered the period calculated through the differences of two or three times of maxima that were observed on the same night. Since they are separated by only one cycle they are, by definition, one period apart. The sample of periods determined in this fashion is constituted of 44 times of maxima difference and was compiled from both those listed in the literature and the few that we measured two years later (Table 5). There were fourteen consecutive times of maxima; the mean value was 0.0944 ± 0.0006 (d). The uncertainty is merely the standard deviation of the mean.

This period served as seed and was utilized with T_0, the first time of maximum of Wils et al. (2003), and the epochs in the list of times of maximum light, Table 5, to calculate new ephemerides through a linear regression of epoch vs. HJD, thus determining

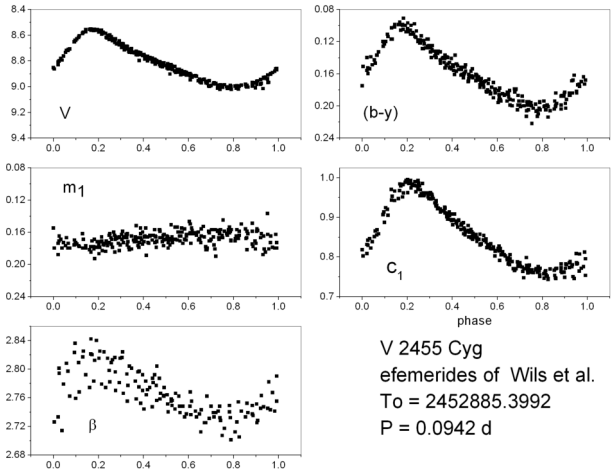

Fig. 1. Phase light curves of V 2455 Cyg obtained in $uvby-\beta$ absolute photometry in 2016. The magnitude and the color indexes are shown in each frame.

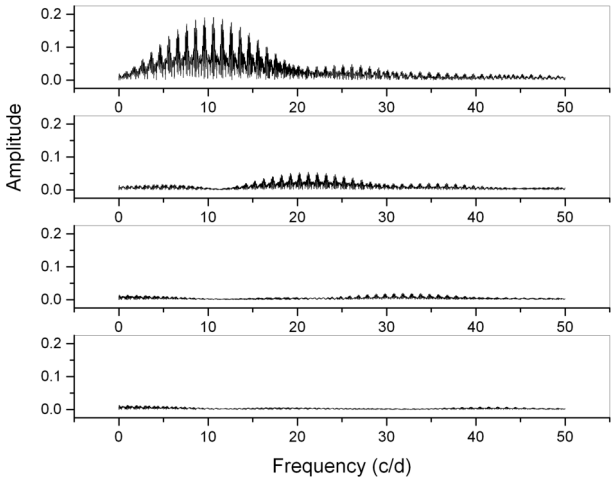

Fig. 2. Power spectra of V 2455 Cyg with the SPM data. Top to bottom: first is the power spectra of the original data; then, the sets of residuals. The scale of the Y axis is the same to show the relative importance of each frequency.

refined values of T_0 and P. The period we established in this fashion (0.0944 d) is in agreement with the assumed period reported in the literature. The results of this method are presented in the second row of Table 4.

3.2. *Time Series*

As a second method to determine the period we used a time series method favored by the δ Scuti star community: Period04 (Lenz & Breger, 2005). The V magnitude of the $uvby-\beta$ set was analyzed with this code.

TABLE 4

V 2455 CYG EPHEMERIDES EQUATIONS

Method	T_0	P	Mean	Std Dev
Wils et al. (2003)	2452885.3992 ± 0.0001	$0.0942075 \pm 3 \times 10^{-7}$	−0.0031	0.0213
DCTM (consecutive Tmax)		0.0944	−0.0041	0.0189
Period04 ($uvby - \beta$ data)		0.0942080868	−0.0136	0.0195
MSDR ($O - C$)	2452885.3996 ± 0.0002	$0.094205989 \pm 1.2 \times 10^{-8}$	0.0009	0.0066
PDDM (Chord lenght)	2457575.9157	0.094205855		
PDDM (Sinusoidal fit)	2457575.9157	0.094205903		

The analysis of these data gave the results listed in Table 6 with a zero point of 8.8184 mag, residuals of 0.0178 mag and 5 iterations. The analysis of Period04 is presented in Figure 2. Beginning at the top is the power spectra of the original data; followed by the consecutive set of residuals. The scale of the Y axis is the same to show the relative importance of the residuals. The frequencies obtained from this analysis are presented in Table 6. Three different frequency values are reported, but one must realize that $F2 = 2\ F1$ and $F3 = 3\ F1$, that the second and third frequencies are multiples of the first.

3.3. *$O - C$ differences*

Before calculating the coefficients of the ephemeris equation, we searched the literature for previous papers related to V 2455 Cyg. Only one source conducted studies of the $O - C$ behavior of this particular object (Wils et al., 2003). The reported ephemerides are listed in Table 4; the newly observed ephemerides are also presented.

3.4. *Period Determination Through Minimization of the Standard Deviation of the $O - C$ Residuals* (MSDR)

The well-known $O - C$ diagram method is a tool utilized to compare and analyze the difference between the observations and the calculated value obtained with the model; in this case, the ephemerides equation. A good reference for this method can be found in Sterken (2005).

To find the ephemerides equation of the variability of V2455 Cyg we implemented a method based on the minimization of the standard deviation of multiple $O - C$ diagrams for V2455 Cyg (see Peña et al., 2016 for details). This method is based on the minimization of the standard deviation of the $O-C$ residuals by considering that the model must be fairly close to the data. Therefore, its differences tend to zero and the standard deviation has to be close to zero. The first step was to calculate the mean of the differences of all the consecutive times of maxima available in the literature (first method) and its standard deviation. All these differences of consecutive times of maxima have the approximate length of the period of the star. Then, with each of the periods given in the range provided by the mean of the consecutive, plus and minus its standard deviation, the number of cycles E was calculated for these multiple $O - C$ diagrams. In all cases, the T_0 utilized was the oldest time of maxima in the literature. The step precision in this range was of 1×10^{-9}. After obtaining the number of cycles for each period, a linear fit was performed to every set of times of maximum with the cycle number E (HJD vs. E). With the new fitted parameters, the diagrams were calculated as well as their standard deviation. Finally, the diagram with the smallest standard deviation of the residuals was selected and the parameters with which it was calculated are taken to be the parameters of the ephemerides equation.

Sweeping around the average of the differences of consecutive times of maxima within a short period range, taking as limits the standard deviation of the differences around 0.0943052 d, and utilizing the minimization of the standard deviation of the $O - C$ values as criterion of goodness, the best period is 0.094205989 d (Figure 3). The resulting ephemerides equation is

$$\begin{aligned} T_{max} &= 2452885.3996 \pm 0.0002 + \\ &\quad (0.094205989 \pm 1.2 \times 10^{-8}) \times E \end{aligned}$$

Even with the maximum resolution (1×10^{-9}) in the MSDR method, there was some scatter around the minimum in the Standard Deviation vs. Period plot (Figure 3). To clarify this, a binning procedure

TABLE 5

COMPILED TIMES OF MAXIMA OF THE HADS STAR V 2455 CYG

Time of Maximum	Reference
2452885.3991	Wils03
2452885.3993	Wils03
2452887.3777	Wils03
2452887.3778	Wils03
2452887.4720	Wils03
2452887.4720	Wils03
2452887.5656	Wils03
2452887.5658	Wils03
2452887.6599	Wils03
2452928.2634	Wils03
2452928.3582	Wils03
2452928.4520	Wils03
2452928.5465	Wils03
2452929.2996	Wils03
2452929.3940	Wils03
2452929.4885	Wils03
2452929.5823	Wils03
2452931.4667	Wils03
2454357.5561	wils09
2454642.4354	wils09
2454642.5296	wils09
2454646.4860	wils09
2454652.5157	wils09
2454694.4383	wils09
2454694.5327	wils09
2454730.3298	wils09
2454730.4239	wils09
2454730.5182	wils09
2454730.6126	wils09
2454758.4973	wils09
2454759.3447	wils09
2454759.4389	wils09
2454759.5332	wils09
2456862.3963	Hubsecher15
2456862.4903	Hubsecher15
2456862.5842	Hubsecher15
2456867.4869	Hubsecher15b
2456867.5832	Hubsecher15b
2456914.5926	Hubsecher15b
2456914.5930	Hubsecher15b
2457565.9307	pp
2457574.8801	pp
2457575.9157	pp

TABLE 6

OUTPUT OF PERIOD04 WITH THE V MAGNITUDE OF THE PRESENT PAPER $uvby-\beta$ DATA

Nr.	Frequency	Amplitude	Phase
$F1$	10.6148	0.2977	0.8419
$F2$	21.2300	0.0566	0.0782
$F3$	31.8389	0.0205	0.6833

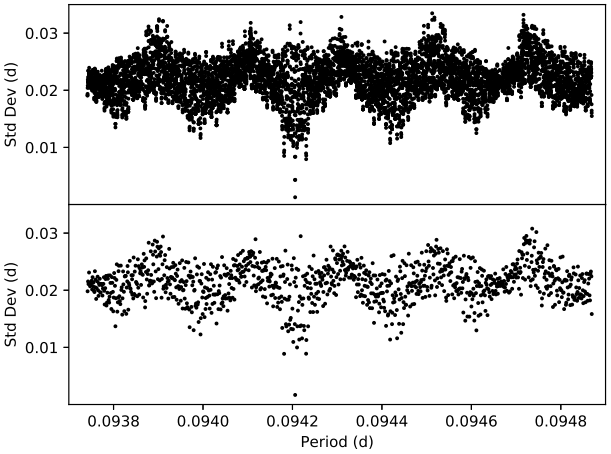

Fig. 3. Standard deviation vs. period. This diagram served to determine the best period. In the upper panel the original data that served to determine the best period are shown. In the lower panel the data have been binned with a window of 1×10^{-6}.

was implemented. For this binning the size of the intervals was 1×10^{-8}. After this operation the minimum value of the standard deviation was checked. This was 0.094205989, which is the same as the original before the binning procedure. Continuing with the analysis, two new binning procedures were implemented, but this time with intervals of 1×10^{-7} and 1×10^{-6}. In the first new case, the period for the minimum standard deviation remained the same, but in the final case the period with the minimum standard deviation was 0.094206015. The value of the period changes only after the size of the intervals for the binning is three orders of magnitude larger than the original precision.

With these elements we calculated the $O-C$ residuals which are shown schematically in Figure 4. They are clearly fitted by straight line, which implies a constant period (at least at this stage) with a time basis of 12.8 yrs.

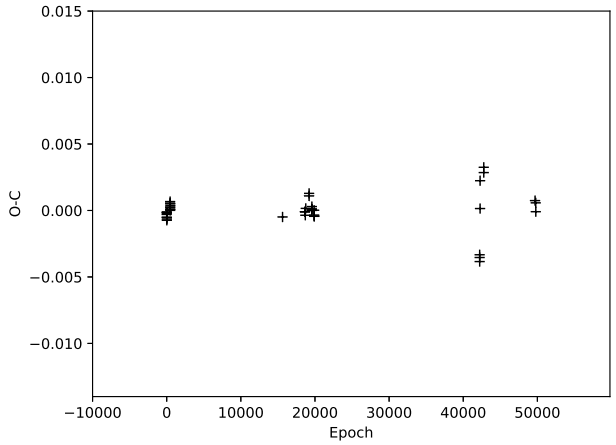

Fig. 4. Behavior of the $O-C$ values with the proposed ephemerides determined utilizing the method of Minimization of the Standard Deviation of the $O-C$ Residuals (MSDR)

3.5. *Period Determination Through an $O-C$ Differences Minimization* (PDDM)

We implemented a method based on the idea of searching for the period which minimizes the chord length which links all the points in the $O-C$ diagram for different values of the periods. Being a classical $O-C$ diagram, we plotted the time in the x-axis and the $O-C$ values in the y-axis. Since in the x-axis distances remain constant, we just concentrated on the change in the distance in the y-axis generated by each period. Once the difference was calculated for each period, the minimum one indicated, at this stage, the best period (period determination through an $O-C$ differences minimization PDDM).

We considered the set of T_{max} listed in Table 5. Given the mean period determined from the consecutive times of maxima and the associated standard deviation, (0.0938 days and 0.0944 days), we calculated values of epoch and $O-C$ by sweeping the period in the range provided by the standard deviation limits, calculating 595,956 steps, a number fixed by the the difference of the deviation limits and the desired precision of one billionth. This provided the new period for the minimum difference (Figure 5). The T_0 time used for the present analysis was the one of the last observation run, 2457575.9157, because we are certain of its precision. As a result we determined the linear ephemerides equation as:

$$T_{max} = (2457575.9157) + (0.094205855 \times E) \quad (1)$$

Figure 6 shows the $O-C$ diagram for the ephemerides equation found by the above method (PDDM).

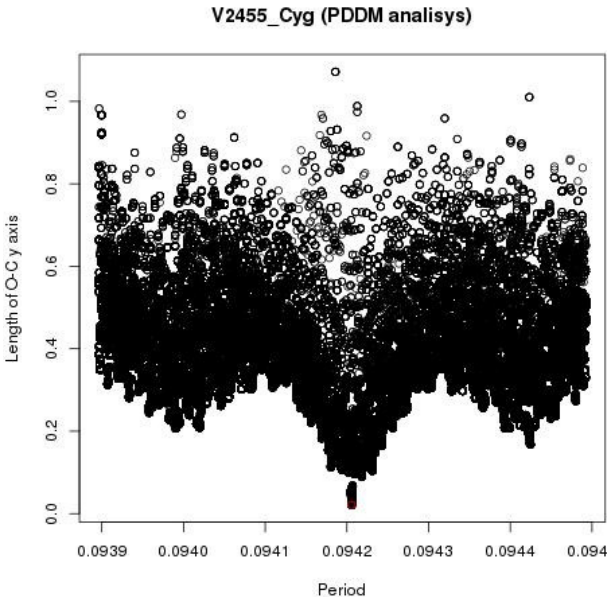

Fig. 5. Period Determination Through an $O-C$ Differences Minimization (PDDM).

Assuming the wave behavior is caused by a light travel time effect (LTT) as a part of the mechanics of the system, we adjusted a sinusoidal function to the $O-C$, performing a fit with the Levenberg-Marquardt algorithm for the best 1,000 $O-C$ lengths. This would be, in this particular case, another way of finding the best period (if the LTT effect is present) and, at the same time, the sinusoidal function that gave us a first approach to the orbital period of a two body system. The parameters which best represent the system are listed in Table 7. The parameter used to test the goodness of the fit is the residual sum of squares RSS. Then, we plotted the periods of the best $O-C$ lengths vs the RSS value of every fit (Figure 7).

After this, the ephemeris equation was set as:

$$T_{max} = (2457575.9157) + (0.094205903 \times E) \quad (2)$$

As can be seen, we do not have enough data to say more about the $O-C$ diagram. The parameters presented in Table 7 are shown schematically in Figure 8.

3.6. *Period Determination Conclusions*

V 2455 Cyg has been little observed. Since the first report more information has been gathered, but no period analysis has been done. In the present paper, different approaches were utilized to determine the stability of the pulsation. First, differences of

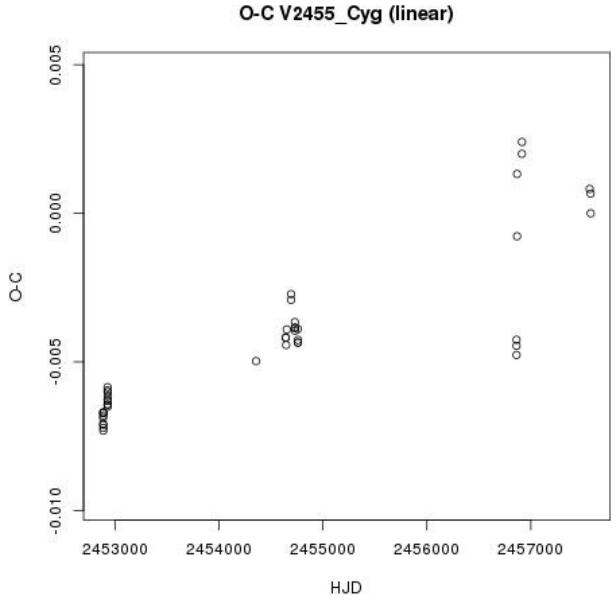

Fig. 6. $(O-C)$ diagram obtained with the period of the PDDM method.

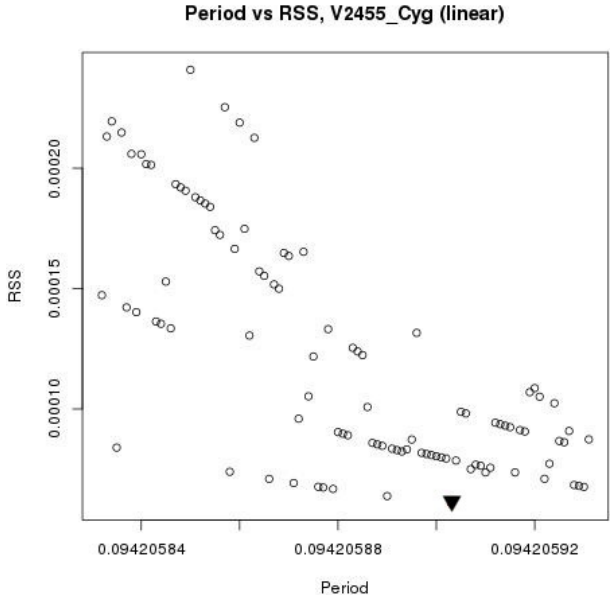

Fig. 7. Period vs RSS. The best value is indicated by a triangle.

TABLE 7

EQUATION PARAMETERS FOR THE SINUSOIDAL FIT OF THE LINEAR $O-C$

Value	PDDM
Z	-13.62×10^{-4}
Ω	3.14×10^{-4}
A	-27.93×10^{-4}
Φ	-27.14
RSS	6.1×10^{-5}

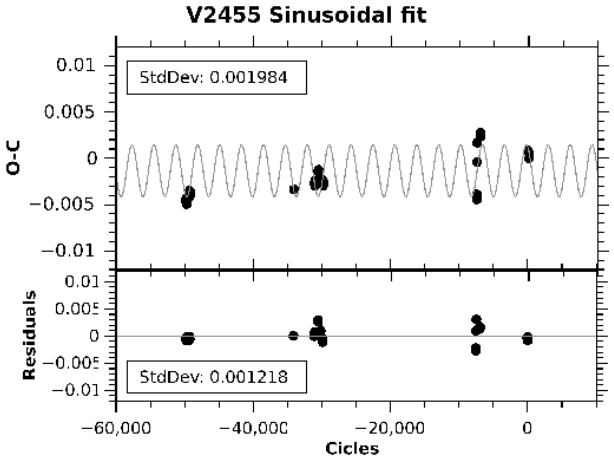

Fig. 8. Diagram of the $O-C$ adjusted to a sinusoidal function. The time span of the observations is of 4691 d or 12.8 years which is 49795 cycles.

consecutive times of maximum light were evaluated to determine a coarse period. The second method utilized time series analyses. The set employed was that of the V magnitude of the $uvby-\beta$ photometry of the present paper. However, we had a very limited time coverage, only 10 d, merely 107 cycles. The third and fourth methods utilized the entire coverage of this star since its discovery, with the times of maximum light, which in this case are 4691 d or 12.8 years (49795 cycles). The four methods used the available data up to now. The goodness of each method and that proposed previously were determined using the mean and the standard deviation of the residuals of the $O-C$ values, the minimum chord length, and RSS (residual sum of squares) for the sinusoidal fitting of the $O-C$ diagrams. They were obtained for each ephemeris listed in Table 4 and numerically they are listed in Columns 4, 5 and 6 of this table. It is quite evident that the MSDR method yields the smallest standard deviations for the $O-C$ residuals, but if we consider the sinusoidal behavior as part of the mechanics of the system, the PDDM gives us the best ephemerides equation.

However, this star was discovered to be a variable very recently and has been observed too little to be able to make a solid conclusion since a large spread can be seen in a section of the $O-C$ diagram (Figures 4 and 6). Those points belong to the ob-

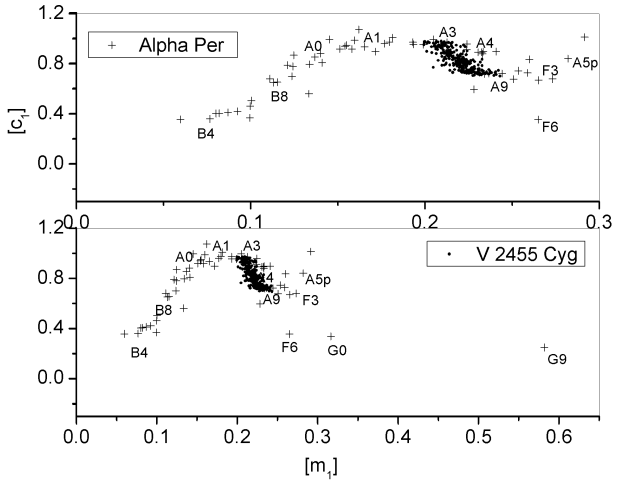

Fig. 9. Location of V 2455 Cyg in the $[m_1]$ vs. $[c_1]$ diagram of Alpha Per.

servational group of Hubscher (2015, 2015b). There are two possible explanations for the large spreads: an inaccurate determination of the times of maxima for those seasons or the possibility that this group is a set of observations acquired during one of the changes in the period inflicted by the presence of a second body which corresponds to the LTT effect mentioned in the PDDM method. We feel that more time must pass, with a more frequent sampling, before we can definitively arrive at conclusions about the pulsational nature of V 2455 Cyg, the LTT effect, and a possible secular variation.

4. PHYSICAL PARAMETERS

The physical parameters can be determined utilizing the $uvby-\beta$ photoelectric photometry and the adequate empirical calibrations. These calibrations were proposed by Nissen (1988) for A and F type stars. Therefore, it is necessary to first determine if this star varies in this range of spectral class. It was reported by Yoss et al. (1991) that V2455 Cyg is spectral type F2, but it has a reported MK spectral type A9. The spectral type can be determined very accurately with the $uvby-\beta$ photometric data. We determined its unreddened photometric indexes $[m_1]$ and $[c_1]$ and positioned it in the plot determined for Alpha Per (Paper I), whose stars have well-determined spectral types. This is presented in Figure 9, where we can see that the spectral type is earlier, since it ranges between A2 and F0.

Application of the numerical unreddening package (see Peña & Martinez, 2014 for a detailed description) gives the results listed in Table 7 for V 2455 Cyg.

TABLE 8

REDDENING AND UNREDDENED PARAMETERS OF V 2455 CYG

Phase	$E(b-y)$	$(b-y)_0$	m_0	c_0	Hβ	M_V
0.05	0.006	0.157	0.177	0.851	2.778	1.737
0.15	0.002	0.122	0.179	0.953	2.809	1.313
0.25	0.001	0.127	0.175	0.968	2.801	1.075
0.35	0.005	0.145	0.171	0.920	2.784	1.251
0.45	0.007	0.159	0.169	0.871	2.772	1.511
0.55	0.002	0.180	0.166	0.833	2.751	1.548
0.65	0.002	0.197	0.167	0.788	2.734	1.634
0.75	0.005	0.201	0.165	0.768	2.732	1.758
0.85	0.006	0.199	0.163	0.763	2.735	1.859
0.95	0.004	0.184	0.170	0.776	2.752	2.066

Since there were so many $uvby-\beta$ photoelectric data points, we calculated the mean values in phase bins of 0.05 step. These mean values are listed in Table 7. This table lists (ordered by increasing phase) in the first column, the phase; subsequent columns present the reddening, the unreddened indexes, and the absolute magnitude. Mean values were calculated for $E(b-y)$ for two cases: (i) the whole data sample and (ii) in phase limits between 0.3 and 0.8, which is customary for pulsating stars to avoid the maximum. It gave, for the whole cycle, values of 0.004 ± 0.007; 7.2 ± 0.4 and 284 ± 47 for $E(b-y)$, DM and distance (in pc), respectively whereas for the mentioned phase limits, we obtained, 0.004 ± 0.007; 7.3 ± 0.3 and 292 ± 37 respectively. For the metal content [Fe/H] it gives 0.04 ± 0.11 and 0.01 ± 0.11, respectively. The uncertainty is merely the standard deviation. In the case of the reddening, most of the values of the spectral type in the F stage of V 2455 Cyg produced negative values which are non-physical. In those cases we forced the reddening to be zero. If the negative values are included, the mean $E(b-y)$ is 0.009 ± 0.038.

To determine the range of effective temperature and surface gravity over which V2455 Cyg varies we must locate the unreddened points on some theoretical grids, such as those of LGK86 calculated from $uvby-\beta$ photometric data for several metallicities. Hence, in order to locate our unreddened points on the theoretical grids, a metallicity has to be assumed. The metallicity of V 2455 Cyg can be determined from the $uvby-\beta$ photometry when the star passes through the F type stage (Nissen, 1988). We deter-

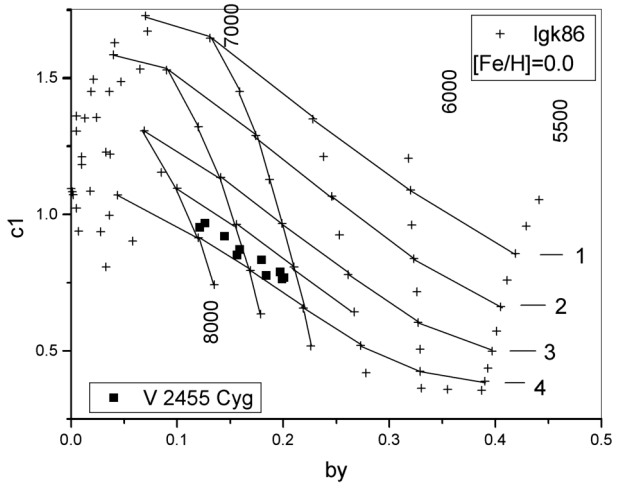

Fig. 10. Location of the unreddened points of V 2455 Cyg (dots) in the LGK86 grids.

TABLE 9

EFFECTIVE TEMPERATURE AND SURFACE GRAVITY OF V 2455 CYG AS A FUNCTION OF PHASE

phase	$T_e(0.0)$	T_e(P&J72)	T_e(Mean)	$\log g(0.0)$
0.05	7600	7663	7232	3.9
0.15	7900	7931	7916	3.8
0.25	7800	7864	7832	3.5
0.35	7700	7717	7708	3.5
0.45	7600	7615	7607	3.5
0.55	7300	7431	7366	3.5
0.65	7200	7282	7241	3.5
0.75	7200	7266	7233	3.5
0.85	7300	7291	7296	3.5
0.95	7300	7444	7372	3.9

Note: Values in parenthesis specify the [Fe/H] values.

mined a mean metallicity of [Fe/H]= 0.042 ± 0.106 for the whole data sample, and of 0.011 ± 0.113 for the values within the specified 0.3 to 0.8 phase limits. The model which is applicable is, therefore, that of solar composition [Fe/H]= 0.0.

To decrease the noise and to see the variation of the star in phase, mean values of the unreddened colors were calculated in phase bins of 0.1 starting at phase 0.05. As can be seen in Figure 10, the case of [Fe/H] = 0.0 the star varies between effective temperature 7200 K and 7900 K; the surface gravity $\log g$ varies between 3.6 and 3.9. Table 9 lists these values. Column 1 shows the phase, Column 2 lists the temperature obtained from the plot for each [Fe/H] value; Column 3, the effective temperature obtained from the theoretical relation reported by Rodriguez (1989) based on a relation of Petersen & Jorgensen (1972, hereinafter P&J72) $T_e = 6850 + 1250 \times (\beta - 2.684)/0.144$ for each value, averaged in the corresponding phase bin, and Column 4, the mean value. Column 5 shows the surface gravity $\log g$ taken from the plot.

4.1. *Physical Parameters: Conclusions*

New $uvby-\beta$ photoelectric photometry observations were carried out for the HADS star V 2455 Cyg. From these observations we first determined its spectral type, which varies between A3V and F0V, different from that previously found. From Nissen's (1988) calibrations the reddening was determined, as well as the unreddened indexes. This served to obtain the physical characteristics of the star: effective temperature in a range from 7200 K to 7900 K and log g from 3.6 to 3.9 with two methods: (1) from the location of the unreddened indexes in the LGK86 grids and (2) through the theoretical relation (P&J72).

5. CONCLUSIONS

We studied V2455 Cyg, which was recently described by Wils et al.(2003). In the present study we demonstrated that V 2455 Cyg is pulsating with one stable period. We carried out three different procedures in the analysis of the periodic content of the star: difference calculation of consecutive times of maximum, the canonical Fourier transform using Period04, and using the compilation of all the times of maximum light since its discovery by minimization of the standard deviation of the $O-C$ Residuals (MSDR). All converge to the ephemerides equation of

$$T_{max} = 2452885.3996 \pm 0.0002 + (0.094205989 \pm 1.2 \times 10^{-8}) \times E\,.$$

By means of $uvby-\beta$ photoelectric photometry we were able to determine its spectral type. We have classified this star spectroscopically between types A2 and F0. With the $uvby-\beta$ data and the empirical calibrations of Nissen (1988) we were able to determine the reddening of each point. With this information we obtained the unreddened color indexes. Evaluating between phases in the range 0.3 to 0.8 we obtained: 0.004 ± 0.007; 7.3 ± 0.3 and 292 ± 37

for $E(b-y)$, DM and distance (in pc), respectively. The unreddened color indexes were compared with the output $uvby-\beta$ grids of the models of LGK86. With this we were able to determine an effective temperature between 7200 K and 7900 K and a surface gravity log g from 3.6 to 3.9. To do this we had to assume a metal content [Fe/H] from the measurements when the star passes through the F spectral type stage. We determined a mean metallicity of [Fe/H]= 0.042±0.106 for the whole data sample, and of 0.011±0.113 for the values within the specified 0.3 to 0.8 phase limits. The model which is applicable is, therefore, that of solar composition [Fe/H]= 0.0.

We would like to thank the staff of the OAN at SPM for their assistance in securing the observations. This work was partially supported by PAPIIT IN104917 and PAPIME PE113016. Proofreading and typing were done by J. Miller and J. Orta, respectively. Fruitful discussions and help of J. Guillen is acknowledged. C. Guzmán, F. Ruiz, A. Díaz B. Juárez and G. Pérez assisted us at different stages. ARL and CVR thank the IA for allotting the telescope time. We acknowledge an anonymous referee whose comments and suggestions certainly improved this work. We have made use of the SIMBAD databases operated at CDS, Strasbourg, France and NASA ADS Astronomy Query Form.

REFERENCES

Astronomical Almanac. 2006, Dept. of the Navy
Crawford, D. L. & Mander, J. 1966, AJ, 71, 114
Hubscher, J. & Lehmann, P. B. 2015, IBVS, 6149, 1
Hubscher, J. 2015b, IBVS, 6152, 1
Lenz, P. & Breger, M. 2005, CoAst, 146, 53
Lester, J. B., Gray, R. O., & Kurucz, R. I. 1986, ApJS, 61, 509
Nissen, P. 1988, A&A, 199, 146
Olsen, E. H. 1983, A&AS, 54, 55
Peña, J. H. & Peniche, R. 1994, RMxAA, 28, 139
Peña, J. H. & Sareyan, J. P. 2006, RMxAA, 42, 179
Peña, J. H., Sareyan, P., Cervantes-Sodi, B., et al. 2007, RMxAA, 43, 217
Peña, J. H., Villarreal, C., Piña, D. S., et al. 2016, RMxAA, 52, 385
Peña, J. H. & Martinez, A. 2014, RMxAA, 50, 119
Peña, J. H., Robleto-Orús, A., Piña, et al. 2017, RMxAA, 53, 309
Peña, J. H., Rentería, Huepa, H., & Pani, A. 2019, RMxAA, 55, 219
Peña, J. H., Rentería, A., Villarreal, C., et al. 2015, IBVS, 6154
Petersen, J. O. & Jorgensen, H. E. 1972, A&A, 17, 367
Piquard, S., Halbwachs, J.-L., et al. 2001, A&A, 373, 576
Rodríguez, E. 1989, Tesis Doctoral, Univ. Granada, CSIC
Sterken, C. 2005, ASPC, 335, 3
Wils, P., Van Cauteren, P., & Lampens, P. 2003, IBVS, 5475
Wils, P., Kleidis, S., et al. 2009, IBVS, 5878
Yoss, K. M., Bell, D. J., & Detweiler, H. L. 1991, AJ, 102, 975

J. H. Peña: Observatorio Astronómico Nacional de Tonantzintla, México, México.
J. H. Peña, D. S. Piña, A. Rentería, and C. Villarreal: Facultad de Ciencias, Universidad Nacional Autónoma de México, Cd. de México, México.
J. H. Peña, D. S. Piña, A. Rentería, and C. Villarreal: Instituto de Astronomía, Universidad Nacional Autónoma de México, Apdo. Postal 70-264, Cd. de México, México (jhpena@astro.unam.mx).

Revista Mexicana de Astronomía y Astrofísica, **55**, 203–209 (2019)

DOI: https://doi.org/10.22201/ia.01851101p.2019.55.02.08

STUDY OF THE OPEN CLUSTER NGC 1528 THROUGH $uvby - \beta$ PHOTOELECTRIC PHOTOMETRY[1]

J. H. Peña[2,3,4], J. Calderón[2,4], and D. S. Piña[2,4]

Received November 21 2018; accepted May 22 2019

ABSTRACT

$uvby - \beta$ photoelectric photometry of sixty-five stars in the direction of the open cluster NGC 1528 is presented. From the $uvby - \beta$ photometry of the cluster we classified the spectral types of the stars which allowed us to determine the reddening (E(b-y) of 0.196 ± 0.054) and hence, their distance, in parsecs, of (954 ± 154). We determined membership of the stars to the cluster and the age (Log age equal 8.04) of the cluster. A metallicity [Fe/H] of -0.31 ± 0.08 was calculated.

RESUMEN

Se presenta fotometría fotoeléctrica $uvby - \beta$ de 65 estrellas en la dirección del cúmulo abierto NGC 1528. Ésta nos permite la determinación de los tipos espectrales de cada estrella y su enrojecimiento (E(b-y) de 0.196 ± 0.054), el cálculo de la distancia a cada una y, por ende, la pertenencia de las estrellas al cúmulo (954 ± 154) pc. Se establece la membresía de cada estrella al cúmulo y la edad de éste (Log age de 8.04). Se determinó una metalicidad [Fe/H] de -0.31 ± 0.08.

Key Words: open clusters and associations: individual (NGC 1528) — techniques: photometric

1. MOTIVATION

The study of open clusters provides many possibilities for the investigation of different astronomical topics. For example, establishing membership of the stars to the cluster throws light on the initial mass function; determining their ages gives clues on stellar evolution; and fixing their distances and chemical compositions helps to accurately establish the chemical enrichment of the galaxy as a function of the galactocentric distance. This line of research began long ago with the work of Villa Vargas (1999) and the purpose of the present study is to complement the previous one with higher precision data, since Strömgren photometry provides both an accurate determination of the distance to the cluster and, through the observation of stars of spectral type F, of their metallicity.

The open cluster NGC 1528 has been a subject of much research since its discovery in 1907 by Holetschek.

According to the compilation of data of open clusters in Paunzen and Mermilliod (2007), WEBDA, NGC 1528 has a distance [pc] of 776; a reddening [mag] of 0.258; a distance modulus [mag] of 10.25; a log age of 8.568 and no reported value for the metallicity.

In this paper, the distances to each one of the stars are determined using $uvby - \beta$ photoelectric photometry with an already tested method, (See for example Peña & Sareyan, 2006).

2. OBSERVATIONS

The observations were carried out at the Observatorio Astronómico Nacional de San Pedro Mártir, México. The 0.84 m telescope, to which a spectrophotometer was attached, was used. The observing season lasted for six nights in December, 2017. NGC 1528 was observed only on one night, that of December 8, 2017. The cluster was also observed in December, 2016 by one of us (DSP). The ID charts used were those of WEBDA, selected for

[1]Based on observations collected at the San Pedro Mártir Observatory, México.

[2]Instituto de Astronomía, Universidad Nacional Autónoma de México, México.

[3]Observatorio Astrónomico Nacional de Tonantzintla, Universidad Nacional Autónoma de México, México.

[4]Facultad de Ciencias, Universidad Nacional Autónoma de México, México.

TABLE 1

TRANSFORMATION COEFFICIENTS FOR THE OBSERVING SEASON

season	B	D	F	J	H	I	L
2017	0.084	1.013	1.002	0.023	1.020	0.131	−1.309
σ	0.084	0.047	0.040	0.035	0.015	0.029	0.082

a limiting magnitude around 12 mag, which is the reasonably reachable limit given by the telescope-spectrophotometer system used during both seasons. A sample of sixty-five stars is presented.

2.1. *Data Acquisition and Reduction*

The procedure followed has been extensively used and a description can be found in Peña et al. (2008), Peña & Martinez (2014) or, more recently, in Peña et al. (2017). What matters in the present paper are the coefficients of the transformation equations to the standard system and the numerical errors which provide the goodness and confidence of our numerical results.

In the transformation equations the coefficients D, F, H and L are the slope coefficients for $(b-y)$, m_1, c_1 and Hβ, respectively. The coefficients B, J and I are the color terms of V, m_1, and c_1. The averaged transformation coefficients for each night are listed with their standard deviations in Table 1. Season errors were evaluated using the twenty-one standard stars observed for a total of 37 observed points. These uncertainties were calculated through the differences in magnitude and colors for all nights, for (V, $b-y$, m_1, c_1 and Hβ) as (0.010, 0.011, 0.015, 0.013, 0.001) respectively, providing a numerical evaluation of our uncertainties for the season. Emphasis is made on the large range of the magnitude and color values of the standard stars: V:(5.2, 8.8); $(b-y)$:(0.00, 0.80); m_1:(0.09, 0.68); c_1:(0.08, 1.05) and Hβ:(2.50, 2.90). The numerical results obtained are presented in Table 2. Column 1 lists the V value; Columns two to five the standard deviations of the color indexes $(b-y)$, m_1, c_1 and Hβ. The standard deviations values are a few hundredths or thousandths of magnitude for each color index, and provide an estimate of the accuracy of our photometry.

Table 3 lists the photometric values of the observed cluster stars. In this table, Columns one and two list the ID of the stars in WEBDA (Paunzen and Mermilliod, 2006) and in the TYC2 catalogue. Columns 3 to 6 show the Strömgren values V, $(b-y)$, m_1 and c_1, respectively; Column 7 lists the Hβ. The unreddened indexes $[m_1]$ & $[c_1]$ are also presented. The last column lists the spectral types derived from Strömgren photometry.

TABLE 2

SEASONAL STANDARD DEVIATIONS

σV	$\sigma(b-y)$	σm_1	σc_1	$\sigma\beta$
0.0125	0.007	0.009	0.010	0.002

3. COMPARISON WITH OTHER PHOTOMETRIES

Since the cluster was observed in 2016 and 2017, the first and obvious step was to compare both seasons. This was done and the results were awkward. Hence, our first problem was to elucidate which season was correct, if any.

Since no $uvby-\beta$ data had been obtained previously for this cluster, a comparison of our values was done with the available UBV photometry reported in WEBDA. However, the intersection of both sets $uvby-\beta$ vs. UBV was very limited (eighteen entries) despite the fact that our sample was significant (sixty-five observed stars). In view of this we compared our photometry from 2016 and 2017 with the much larger sample of WEBDA CCD data. The intersection of both sets was forty-one entries.

The comparison with the 2016 season showed that the data of this season were inaccurate due to bad weather conditions, whereas the 2017 season gave more accurate results. A linear fit between both sets, 2017 $uvby-\beta$ vs. UBV(CCD) yielded the equation $V_{WEBDA} = 0.056 + 0.9994\ V_{pp}$ with a correlation coefficient of 0.9974 and a standard deviation of 0.050. The color relationship yielded $(B-V) = 0.027 + 0.6176\ (b-y)$ with a correlation coefficient R of 0.9954 and a standard deviation of 0.024.

4. METHODOLOGY

Once we were sure of the quality of our $uvby-\beta$ data set, further analysis was necessary in order to determine the physical characteristics of the stars in the cluster.

The main problem was, of course, to determine which stars belong to the cluster. To do this, the distance to each star had to be fixed. To evaluate the reddening we first established to which spectral class the stars belonged: early (B and early A) or late (late A and F stars) types; the later class stars (G or later)

TABLE 3

$uvby-\beta$ PHOTOELECTRIC PHOTOMETRY OF THE OPEN CLUSTER NGC 1528

WEBDA	TYC2	V	$b-y$	m_1	c_1	Hβ	$[m_1]$	$[c_1]$	SpTyp (photometry)
1	3340-0786-1	8.760	0.190	0.052	0.710	2.697	0.111	0.672	B7V
2	3340-0288-1	9.637	0.183	0.088	1.147	2.833	0.145	1.110	A3
4	3340-1195-1	10.045	0.621	0.168	0.633	2.596	0.361	0.509	LATE
5	3340-1015-1	10.132	0.760	0.343	0.425	2.548	0.579	0.273	LATE
6	3340-0790-1	10.096	0.426	0.131	0.550	2.620	0.263	0.465	F5
7	3340-0782-1	10.094	0.220	0.191	1.086	2.871	0.259	1.042	A4p
8	3340-0290-1	10.430	0.227	0.097	1.222	2.839	0.167	1.177	A0V
9	3340-0429-1	10.390	0.267	0.120	0.918	2.789	0.203	0.865	A4V
10	3340-0905-1	10.803	0.195	0.082	1.162	2.846	0.142	1.123	B9
11	3340-0922-1	11.220	0.194	0.092	1.032	2.839	0.152	0.993	B8V
12	3340-0659-1	11.300	0.189	0.102	1.085	2.790	0.161	1.047	A9V
13	3340-0831-1	11.316	0.225	0.107	0.987	2.787	0.177	0.942	A2
14	3340-0914-1	12.010	0.206	0.201	0.935	2.862	0.265	0.894	A6p
31	3340-0803-1	9.400	0.343	0.139	0.575	2.676	0.245	0.506	F2
32	3340-0819-1	10.112	0.924	0.546	0.278	2.528	0.832	0.093	LATE
33	3340-0311-1	10.185	0.252	0.072	1.283	2.816	0.150	1.233	B9V
34	3340-1090-1	10.505	0.236	0.061	1.129	2.816	0.134	1.082	B9
35		10.477	0.395	0.201	0.315	2.568	0.323	0.236	G2V
36	3340-0812-1	10.746	0.185	0.074	1.049	2.806	0.131	1.012	B8V
37	3340-0890-1	11.008	0.163	0.140	1.001	2.819	0.191	0.968	A3
38	3340-1018-1	11.059	0.200	0.103	0.982	2.779	0.165	0.942	A4
39	3340-1001-1	11.026	0.209	0.091	1.057	2.833	0.156	1.015	B9V
40	3340-0521-1	11.199	0.228	0.062	1.171	2.827	0.133	1.125	A3
41	3340-1192-1	11.254	0.217	0.074	1.157	2.797	0.141	1.114	B9
42	3340-0774-1	11.335	0.271	0.138	1.032	2.799	0.222	0.978	A4V
43	3340-1021-1	11.493	0.198	0.082	1.097	2.815	0.143	1.057	B9V
44	3340-0858-1	11.337	0.152	0.143	0.966	2.815	0.190	0.936	A5
45	3340-1208-1	11.410	0.256	0.158	0.988	2.815	0.237	0.937	A5V
46	3340-0638-1	11.335	0.242	0.119	1.069	2.820	0.194	1.021	A4V
47	3340-0801-1	11.460	0.230	0.088	1.144	2.818	0.159	1.098	F5V
48	3340-0181-1	11.582	0.206	0.084	1.127	2.850	0.148	1.086	B9
49	3340-0685-1	14.427	1.824	−2.017	1.875	2.848	−1.452	1.510	
50	3340-0800-1	11.928	0.342	0.131	0.848	2.689	0.237	0.780	A8V
51	3340-1250-1	11.973	0.190	0.134	1.088	2.956	0.193	1.050	A4V
63		9.949	0.202	0.064	1.202	2.791	0.127	1.162	B9
172	3340-0813-1	11.842	0.219	0.110	1.152	2.790	0.178	1.108	A2V
182	3340-0983-1	11.089	0.202	0.135	0.964	2.820	0.198	0.924	A5
185	3340-1041-1	11.762	0.154	0.098	0.645	2.695	0.146	0.614	B6V
193	3340-1381-1	11.877	0.286	0.128	1.070	2.854	0.217	1.013	A4V
194	3340-1527-1	11.621	0.256	0.160	1.078	2.886	0.239	1.027	A4
195		10.965	1.336	0.803	0.344	2.581	1.217	0.077	LATE
196	3340-1157-1	11.524	0.233	0.071	1.070	2.887	0.143	1.023	A1
197	3340-0784-1	10.769	0.204	0.045	0.609	2.739	0.108	0.568	B6V
204	3340-0136-1	11.597	0.249	0.130	1.146		0.207	1.096	A4V
205	3340-0403-1	11.851	0.209	0.056	1.143	2.849	0.121	1.101	B8V
206	3340-1154-1	11.901	0.390	0.143	0.469	2.619	0.264	0.391	F9
207		11.620	0.652	0.626	0.093	2.467	0.828	−0.037	LATE
209	3340-1222-1	9.068	0.153	0.032	0.565	2.673	0.079	0.534	B5V
210	3340-0846-1	11.962	0.239	0.097	0.997	2.866	0.171	0.949	B8
211	3340-0575-1	9.613	0.151	0.024	0.480	2.682	0.071	0.450	B5V
218	3340-0546-1	11.223	0.498	0.108	0.542	2.663	0.262	0.442	F9

TABLE 3 (CONTINUED)

WEBDA	TYC2	V	$b-y$	m_1	c_1	Hβ	$[m_1]$	$[c_1]$	SpTyp (photometry)
219		12.240	0.242	0.108	1.082	2.858	0.183	1.034	A2V
220		10.318	0.253	0.069	1.121	2.812	0.147	1.070	B9V
1017		10.466	0.432	0.155	0.371	2.584	0.289	0.285	G0V
1038		11.487	0.353	0.154	0.578	2.689	0.263	0.507	F2
1044	3340-1259-1	11.240	0.837	0.318	0.235	2.511	0.577	0.068	LATE
1551		11.432	0.300	0.151	1.097	2.822	0.244	1.037	A4p
1566		10.592	0.689	0.333	0.362	2.577	0.547	0.224	LATE
1580		11.609	0.820	0.346	0.382	2.530	0.600	0.218	LATE
1582		11.804	0.443	0.111	0.407		0.248	0.318	F8V
1584		11.295	0.437	0.132	0.432	2.611	0.267	0.345	F9
1590		11.299	0.254	0.127	1.015	2.878	0.206	0.964	A5
1613		12.117	0.428	0.105	0.517	2.635	0.238	0.431	F9
1618		10.467	0.333	0.009	1.168	2.749	0.112	1.101	A8I
6465		9.703	1.067	0.724	0.331	2.531	1.055	0.118	LATE

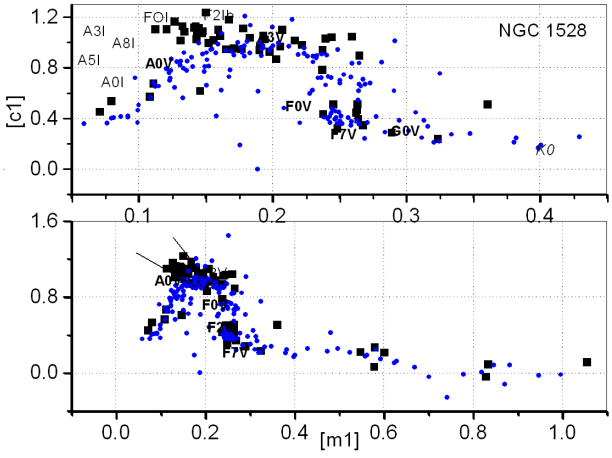

Fig. 1. Position of the stars in the $[m_1]-[c_1]$ diagram of Alpha Per (Peña & Sareyan, 2006)) for NGC 1528. Small crosses are points for Alpha Per; black squares are points for NGC 1528. The color figure can be viewed online.

were not considered in the analysis since there is no reddening calibration for these stars. We determined each star's spectral type through its location in the $[m_1]-[c_1]$ diagram (Figure 1).

The application of the calibrations for each spectral type (Balona & Shobbrook 1984; Shobbrook 1984) for O and early A type and Nissen (1988) for late A and F stars, respectively allowed us to determine their reddening, and hence their unreddened color indexes. The procedure has been extensively described in Peña & Martínez (2014).

5. RESULTS

Figure 1 shows the position in the $[m_1]-[c_1]$ diagram for stars in the direction of NGC 1528, along with that of the stars with well-determined spectral types in the open cluster Alpha Per (Peña & Sareyan 2006). In Table 3 the photometrically determined spectral class is shown. Only a few stars have photometrically determined spectral types in WEBDA and the agreement between both classifications is adequate.

The physical parameters can be determined using the $uvby-\beta$ photometry data and adequate empirical calibrations. These calibrations were proposed by Nissen (1988) for A and F type stars and Balona & Shobbrook (1984) and Shobbrook (1984) for the O and early A types.

The application of these numerical packages gave the results shown in Table 4, where the ID, reddening, unreddened indexes, absolute magnitude, DM and distance (in parsecs), are listed. The last two columns present the membership probabilities described below.

To establish membership of the stars to the cluster the distance modulus or distance histograms (in pc) are built. The goodness of the method has been tested in the past by comparing results to the proper motion studies for a well-studied cluster like α Per (Peña & Sareyan 2006).

When the histogram of distance modulii for NGC 1528 was built (Figure 2), the distances of the stars showed a clear accumulation at a distance modulus of 9.8 ± 0.6, a peak determined by a Gaussian fit to the distribution.

TABLE 4

REDDENING AND UNREDDENED PARAMETERS OF THE OPEN CLUSTER NGC 6633

WEBDA	$E(b-y)$	$(b-y)_0$	m_0	c_0	Hβ	V_0	M_V	DM	Distance	[Fe/H]	Membership (Present Paper)	Probab. WEBDA (382)
31	0.079	0.264	0.163	0.559	2.68	9.06	2.18	6.9	237	0.02	N	0.00
218	0.214	0.284	0.172	0.499	2.66	10.30	2.28	8.0	402	0.11	N	0.00
1584	0.093	0.344	0.160	0.413	2.61	10.89	2.77	8.1	422	−0.30	N	0.00
6	0.097	0.329	0.160	0.531	2.62	9.68	1.28	8.4	478	−0.25	N	0.00
2	0.152	0.031	0.134	1.118	2.83	8.98	0.41	8.6	518		N	0.99
7	0.162	0.058	0.240	1.054	2.87	9.40	0.82	8.6	518		N	0.00
9	0.300	−0.033	0.210	0.861	2.79	9.10	0.10	9.0	629		M:	0.00
1	0.236	−0.046	0.123	0.665	2.70	7.75	−1.28	9.0	640		M:	0.00
1590	0.275	−0.021	0.209	0.963	2.88	10.12	1.07	9.1	644		M:	0.00
220	0.242	0.011	0.142	1.075	2.81	9.28	0.18	9.1	661		M:	0.99
206	0.056	0.334	0.160	0.458	2.62	11.66	2.39	9.3	712	−0.25	M	0.00
34	0.220	0.016	0.127	1.087	2.82	9.56	0.22	9.3	739		M	0.99
14	0.126	0.080	0.239	0.910	2.86	11.47	2.11	9.4	744		M	0.99
196	0.239	−0.006	0.143	1.025	2.89	10.49	1.13	9.4	748		M	0.56
8	0.144	0.083	0.140	1.195	2.84	9.81	0.39	9.4	765		M	0.98
51	0.188	0.002	0.190	1.052	2.96	11.17	1.71	9.5	778		M	0.99
1613	0.122	0.306	0.142	0.493	2.64	11.59	2.04	9.6	814	−0.37	M	0.00
39	0.218	−0.009	0.156	1.016	2.83	10.09	0.53	9.6	816		M	0.99
10	0.156	0.039	0.129	1.132	2.85	10.13	0.57	9.6	819		M	0.99
182	0.229	−0.027	0.204	0.920	2.82	10.10	0.46	9.6	848		M	0.00
45	0.143	0.113	0.201	0.959	2.82	10.80	1.11	9.7	864		M	0.99
11	0.209	−0.015	0.155	0.992	2.84	10.32	0.63	9.7	869		M	0.99
63	0.133	0.069	0.104	1.177	2.79	9.38	−0.32	9.7	870		M	0.99
36	0.195	−0.010	0.132	1.012	2.81	9.91	0.17	9.7	885		M	0.72
209	0.210	−0.057	0.095	0.525	2.67	8.17	−1.63	9.8	911		M	0.00
37	0.183	−0.020	0.195	0.966	2.82	10.22	0.40	9.8	919		M	0.99
33	0.097	0.155	0.101	1.265	2.82	9.77	−0.06	9.8	922		M	0.99
193	0.295	−0.009	0.217	1.014	2.85	10.61	0.78	9.8	922		M	0.86
210	0.262	−0.023	0.176	0.947	2.87	10.83	0.96	9.9	943		M	0.98
46	0.249	−0.007	0.194	1.022	2.82	10.26	0.36	9.9	958		M	0.99
211	0.217	−0.066	0.089	0.439	2.68	8.68	−1.33	10.0	1006		M	0.70
197	0.257	−0.053	0.122	0.560	2.74	9.66	−0.40	10.1	1029		M	0.00
40	0.187	0.041	0.118	1.135	2.83	10.39	0.31	10.1	1041		M	0.99
48	0.188	0.018	0.140	1.091	2.85	10.77	0.66	10.1	1052		M	0.99
1618	0.306	0.027	0.101	1.110	2.75	9.15	−1.01	10.2	1075		M	0.00
44	0.177	−0.025	0.196	0.932	2.82	10.57	0.39	10.2	1090		M	0.85
42	0.149	0.122	0.183	1.002	2.80	10.69	0.48	10.2	1104		M	0.00
38	0.224	−0.024	0.170	0.939	2.78	10.09	−0.14	10.2	1114		M	0.99
13	0.249	−0.024	0.182	0.940	2.79	10.24	−0.02	10.3	1127		M	0.99
1551	0.203	0.097	0.212	1.056	2.82	10.56	0.23	10.3	1164		M	0.00

To determine membership to the cluster we assumed that to be a member, the distance to the star should be within one sigma of the mean average distance. The mean distance modulus value of these stars is 9.87 ± 0.35. For the accumulation of stars, membership is indicated by an M in the twelfth column of Table 4. There are some stars close to these limits and they are indicated by M. Those beyond the membership limits are denoted by N, non-members.

We compared our membership assignation with that reported in WEBDA for NGC1528. The membership probabilities reported are listed in the last column of Table 4. It is remarkable that out of the thirty-four stars we found to be members, twenty-seven have a high membership probability and only nine have low membership probabilities in WEBDA. However, some stars that we classified as non-members have high membership probabilities in WEBDA.

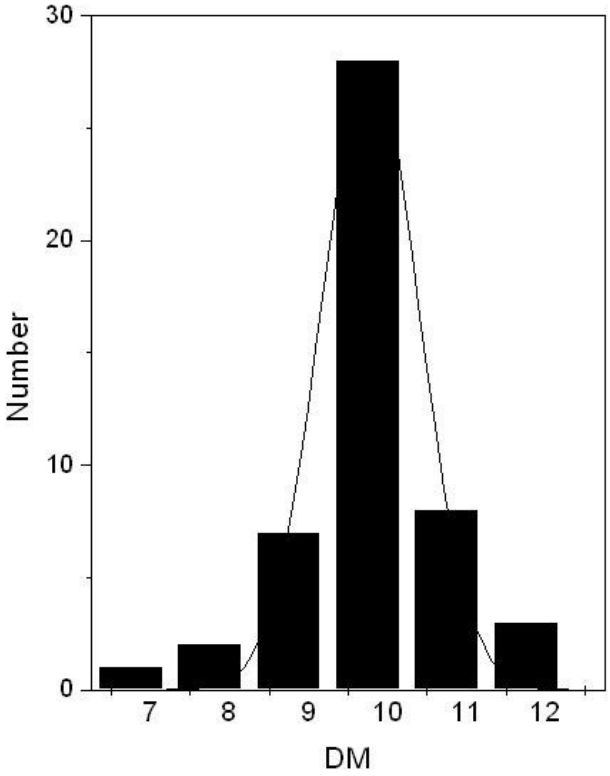

Fig. 2. Histogram of the DM of the stars in the direction of NGC 1528. The peak is at 9.8 ± 0.6.

The effective temperature of the hottest stars was fixed by plotting the location of all stars on the theoretical grids of Lester, Gray & Kurucz (hereinafter LGK86), after calculating the unreddened colors (Figure 3) for the correct chemical composition of the model considered. The metallicity of NGC 1528 was not reported by WEBDA but it is reported by Linga (1987) as -0.10. We found two F type stars to be cluster members for which metallicity can be evaluated. The metallicities of these stars, W206 and W1613 are -0.25 and -0.37, respectively. However, the membership probability assigned in WEBDA is, in both cases, 0.0. In view of this, we will consider models of solar metallicity.

We used the $(b-y)$ vs. Hβ diagram of LGK86 which allows the determination of the temperatures of the hottest stars with an accuracy of a few hundredths of degrees. The temperature for the hottest star, W211, is around 16200 K. W211 has a membership probability of 0.70 according to WEBDA and is a member of the cluster according to our results. The second hottest star is W209 with a Te of 15500 K; according to WEBDA it is a non-member star although it belongs to the cluster in our findings. However, both W211 and W209 have $\log g$ values of 3.0 and

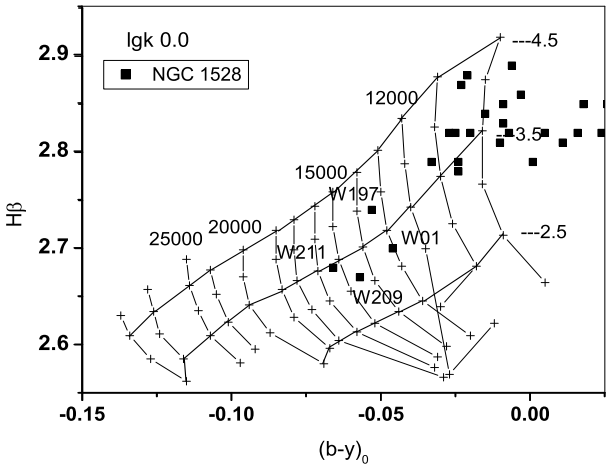

Fig. 3. Location of the unreddened points (filled squares) in the LGK86 grids. Values of the effective temperature and surface gravity are indicated.

3.5 respectively. Furthermore, W197 has log g of 4 and an effective temperature of 13500 K ($\log T$e of 4.13). Once the membership and effective temperature of the hottest star are established, an age for NGC 1528 can be determined through the calibrations of Meynet, Mermilliod & Maeder (1993) from the relation $\log(age) = -3.611 \times (\log T\mathrm{e}) + 22.956$ valid in the range $\log T$e within the limits [3.98, 4.25]. The results is $\log(age) = 8.04$. All these quantities are summarized in Table 5.

6. DISCUSSION

With the procedures we have described we obtained distances for stars of spectral types B, A and F. Membership was assigned in the histogram for those stars within one sigma of the distance mean value. Out of our sample of sixty-five stars, thirty-four were considered to be members in this fashion, six to be marginally members and nine non-members. Eleven were late type stars and no distance was determined for them. A mean reddening value was calculated for the member stars. The age was fixed from the temperature of the hottest star which, by the way, is considered to be a member of the cluster both in the literature and in our findings. This age is in agreement with its spectral type, B5V.

7. CONCLUSIONS

The physical characteristics we determined in the present study coarsely agree with the previously determined ones. As was mentioned at the beginning, the distance was fixed at 776 pc. Our value

TABLE 5

CHARACTERISTICS OF THE OPEN CLUSTER NGC 1528

	WEBDA	Lynga (1987)	Present Paper
Distance [pc]	776	776	954 ± 154
Reddening [mag]$E(B-V)$	0.258	0.258	0.251 ± 0.069
Reddening [mag]$E(b-y)$		0.145	0.196 ± 0.054
Distance modulus [mag]	10.25		9.87 ± 0.35
Log age	8.568	8.57	8.04
[Fe/H]		-0.10	-0.31 ± 0.08

is 954 ± 154 pc. Of the 65 stars studied 14 are early type stars, 16 A type stars, and only two are of spectral type F with a mean [Fe/H] of -0.310 ± 0.079; the reddening $E(B-V)$ was 0.258 mag, whereas our value for $E(b-y)$ of 0.196 ± 0.054 gives an $E(B-V)$ of 0.251 ± 0.069 if the well-known relation of $E(b-y) = 0.78E(B-V)$ is applied. The reported age is $\log(age) = 8.568$, whereas our determined value is 8.04. However, the values from the $uvby-\beta$ photoelectric photometry were determined on a star-by-star basis whereas the literature values were determined by the main sequence fitting method, which does not consider the membership probability of each star, but rather the overall behavior of the all stars in a coarse statistical manner.

We would like to thank the staff of the OAN for their assistance in securing the observations. This work was partially supported by Papiit IN104917 and PAPIME PE113016. DSP & JCC thank the IA-UNAM for the opportunity to carry out the observations. Typing and proofreading were done by J. Orta and J. Miller, respectively. C. Guzmán, F. Salas and A. Diaz assisted us in the computing. This research has made use of the Simbad databases operated at CDS, Strasbourg, France and NASA ADS Astronomy Query Form.

REFERENCES

Balona, L. & Shobbrook, R. R. 1984, MNRAS, 211, 375
Holetschek, J. 1907, AnWie, 20, 39
Lester, J. B., Gray, R. O., & Kurucz, R. I. 1986, ApJ, 61, 509
Lynga, G. 1987, Catalogue of Open Cluster Data (5th ed.) Lund Observatory
Meynet, G., Mermilliod, J. C., & Maeder, A. 1993, A&AS, 98, 477
Nissen, P. 1988, A&A, 199, 146
Paunzen, E. & Mermilliod, J. C. 2007, Webda, A Site Devoted to Stellar Open Clusters
Peña, J. H., Peniche, R., Garrido, R., Paparo, M., & Garcia-Cole, A. 2008, RMxAA, 44, 111
Peña, J. H. & Sareyan, J. P. 2006, RMxAA, 42, 179
Peña, J. H. & Martínez, A. 2014, RMxAA, 50, 119
Peña, J. H., Robleto-Orús, A., Piña, D. S., et al. 2017, RMxAA, 53, 309
Shobbrook, R. R. 1984, MNRAS, 211, 659
Villa Vargas, J. 1999, Gradiente de abundancia en el disco galactico a partir de cúmulos abiertos. Tesis. Facultad de Ciencias, UNAM

J. Calderón, J. H. Peña, and D. S. Piña: Facultad de Ciencias, Universidad Nacional Autónoma de México, México.
J. Calderón, J. H. Peña, and D. S. Piña: Instituto de Astronomía, UNAM, Apdo. Postal 70-264, Ciudad de México, México (jhpena@astroscu.unam.mx).
J. H. Peña: Observatorio Astrónomico Nacional de Tonantzintla, Universidad Nacional Autónoma de México, México.

Revista Mexicana de Astronomía y Astrofísica, **55**, 211–219 (2019)

DOI: https://doi.org/10.22201/ia.01851101p.2019.55.02.09

3D HYDRODYNAMIC NUMERICAL MODELS FOR NEBULAE AROUND RUNAWAY WOLF-RAYET STARS

J. Reyes-Iturbide[1,2], Pablo F. Velázquez[2], M. Rosado[3], E. Matías Schneiter[4,5], and I. Ramírez-Ballinas[3]

Received January 14 2019; accepted May 29 2019

ABSTRACT

We present 3D hydrodynamical simulations of the circumstellar bubble from a Wolf-Rayet runaway star. In the models two properties were taken into account: (a) the proper motion of the central star through the interstellar medium (ISM) and (b) the evolution of the stellar wind from the red supergiant (RSG) stage to the Wolf-Rayet (WR) stage. From the hydrodynamic results synthetic X-ray maps in the $[0.3 - 1.2]$ keV energy range were computed. These maps show that the bubble morphology is affected by the stellar motion, producing a bow shock in the RSG stage that can explain the limb-brightened morphology observed. Additionally, these synthetic maps show filamentary and clumpy appearance produced by instabilities triggered from the interaction between the WR wind and the RSG shell. It was found that these types of collisions can explain the origin of the X-ray emission observed in the nebulae of Wolf- Rayet stars.

RESUMEN

Presentamos simulaciones hidrodinámicas 3D para nebulosas producidas por estrellas Wolf-Rayet con movimiento propio. En los modelos tomamos en consideración el movimiento de la estrella a través del medio interestelar (ISM), la tasa de pérdida de masa y la velocidad del viento estelar correspondientes a las fases de súper-gigante roja (RSG) y Wolf-Rayet (WR). A partir de los resultados numéricos, generamos mapas sintéticos de emisión en rayos X en el intervalo de energía $[0.3 - 1.2]$ keV. Los mapas muestran una asimetría debida al choque de proa que se produce en la fase de RSG. Adicionalmente, los mapas presentan estructuras filamentarias originadas en la colisión de las burbujas producidas por la RSG y WR. Esta colisión explica también el origen de la emisión de rayos X que se observa en las nebulosas producidas por estrellas Wolf-Rayet.

Key Words: ISM: bubbles — methods: numerical — stars: evolution — stars: winds, outflows — stars: Wolf-Rayet

1. INTRODUCTION

Hot massive stars exhibit fast stellar winds that sweep up the surrounding interstellar medium (ISM) creating structures known as interstellar bubbles. Weaver et al. (1977) described an analytical model used to predict the X-ray emission of such objects, considering an inner zone of shock-heated gas with temperatures of order 10^6 K enclosed within a dense spherical shell with temperatures of order 10^4 K. This analytical model considered an isotropic stellar wind with constant mechanical luminosity interacting with a homogeneous ISM, and predicted a center-filled X-ray sphere surrounded by optical emission.

Wolf-Rayet stars offer an ideal laboratory for the study of such bubbles because they are massive stars (progenitor stellar masses greater than 30 $M_\odot$) with mass loss rates of $\dot{M} \approx 10^{-5} - 10^{-6} M_\odot \mathrm{yr}^{-1}$ and stellar wind velocities that go from 1000 to 2000 $\mathrm{km\,s^{-1}}$. However, observations show bubbles with asymmetric structures meaning that the predictions of the

[1]Tecnológico de Estudios Superiores de Tianguistenco, Santiago Tianguistenco, Estado de México, México.
[2]Instituto de Ciencias Nucleares, Universidad Nacional Autónoma de México, Ciudad de México, México.
[3]Instituto de Astronomía, Universidad Nacional Autonóma de México, Ciudad de México, México.
[4]Instituto de Astronomía Teórica y Experimental, Córdoba, Argentina.
[5]Departamento de Materiales y Tecnología, Universidad Nacional de Córdoba, Córdoba, Argentina.

analytical models are not valid in general (Chu et al. 1983; Heckathorn et al. 1982; Miller & Chu 1993; Marston et al. 1994a,b). This observed asymmetry can be caused either by inhomogeneities in the ISM (Toalá et al. 2017) or by anisotropic mass loss rates (Chita et al. 2007, 2008). An alternative mechanism considers the stellar motion that provides a pressure asymmetry, producing asymmetric stellar wind bubbles. The stellar proper motion is supersonic for many massive stars and produces bow shocks when interacting with the ISM (van Buren & McCray 1988; Cox et al. 2012; Peri et al. 2012, 2015). Both analytical models (van Buren et al. 1990; Mac Low et al. 1991; van Buren & Mac Low 1992) and numerical models (Brighenti & D'Ercole 1995a,b; Mackey et al. 2015; Meyer et al. 2015) have been presented to describe stellar wind bow shocks.

Additionally, filamentary structures and clumps have been observed in these WR nebulae in optical bands (Chu 1981; Chu et al. 1983; Moore et al. 2000; Gruendl et al. 2000; Stock & Barlow 2010) and X-ray emission (Wrigge et al. 1994, 2005; Chu et al. 2003; Zhekov & Park 2011; Toalá et al. 2012, 2014). These features can be obtained with numerical models that take into account the evolution of the star (mainly the change in mechanical luminosity over time) and its interaction with the circumstellar gas. The evolution history that precedes the WR phase starts from the main-sequence (MS) phase to either the red supergiant (RSG) or luminous blue variable (LBV) phases. Each stage of the stellar evolution is characterized by its own mechanical luminosity and by the formation of a new shell. The interaction between these shells develops instabilities that give rise to the formation of clumps and filamentary structures that have been reproduced by hydrodynamic simulations (Garcia-Segura et al. 1996a,b; Brighenti & D'Ercole 1997) and radiation-hydrodynamic simulations (Toalá & Arthur 2011; Dwarkadas & Rosenberg 2013; Freyer et al. 2006). An important result obtained from these works is the conclusion that the X-ray luminosity is dominated by the emission from the WR shell rather than the shocked WR wind which is the source of the X-ray in the analytical models (Freyer et al. 2006). The numerical models show that soft X-ray emission can be enhanced by thermal conduction, in agreement with the observations (Toalá & Arthur 2011).

In this work we tested, by means of three-dimensional hydrodynamic numerical simulations, the joint effects of the evolutionary phases of a Wolf-Rayet star that moves through the ISM during its lifetime. The hydrodynamic simulations were carried out with the adaptive grid code YGUAZÚ-A with the aim of reproducing the morphology observed in the X-ray emission. We used the numerical results to obtain synthetic thermal X-ray emission maps. This manuscript is organized in the following way: in § 2 the models of the WR nebulae are presented. In § 3 the initial conditions of the numerical simulations are listed as well as an explanation on how the simulation of the thermal X-ray emission was carried out. The results are given in § 4 and a comparison with observations is given in § 5. Finally in § 6 a summary of the conclusions is presented.

2. MODELLING WR NEBULA

The runaway WR nebula was modelled considering the evolution of the central star from RSG to WR. The first step was to simulate the RSG phase which will produce a bow shock as a result of the motion of the runaway star. This was done in the frame of reference of the runaway star, i.e., the star was kept at the center of the computational domain with the ISM moving at the velocity at which the star travels ($-V_\star$). The momentum balance between the stellar wind ram pressure and the ISM, known as stand-off distance (R_0) (see Wilkin 1996), is:

$$R_0 = \left(\frac{\dot{M}_{\rm w} V_{\rm w}}{4\pi n_0 \mu m_H V_\star^2} \right)^{1/2}, \qquad (1)$$

where $\dot{M}_{\rm w}$ and $V_{\rm w}$ are the stellar mass-loss rate and the wind velocity respectively, $V_\star$ is the velocity of the star, n_0 is the numerical density of the uniform ISM, μ is the mean atomic mass and m_H is the mass of the hydrogen atom. For the RSG stage we chose the values for the mass loss rate and the stellar wind velocity as $\dot{M}_{\rm w} = \dot{M}_{\rm RSG}$ and $V_{\rm w} = V_{\rm RSG}$ respectively. The cells where the wind is injected were imposed within a sphere of radius 5×10^{17}cm for both the RSG and the WR stages. At a certain integration time, when the shell reaches R_0, the RSG stage enters a quasi-stationary state. At this time the second step of the simulation is imposed by replacing the RSG wind with a WR stellar wind.

The parameters for the different winds used in these simulations are summarized in Table 1 and correspond to the values obtained by Garcia-Segura et al. (1996b) for $35 M_\odot$ stars. The RSG wind velocities range from 30 $\mathrm{km\,s^{-1}}$ to 75 $\mathrm{km\,s^{-1}}$, with the velocity of the star assumed to be within typical values of $V_\star < 100$ $\mathrm{km\,s^{-1}}$. The table also shows the numerical density values of the ISM.

TABLE 1

SIMULATED MODELS

Models	$\dot{M}_{SRG}$ $M_\odot$ yr^{-1}	V_{SRG} km s^{-1}	$V_\star$ km s^{-1}	$\dot{M}_{WR}$ $M_\odot$ yr^{-1}	V_{WR} km s^{-1}	n_0 cm^{-3}	R_0 pc
M1	8×10^{-5}	75	75	3×10^{-5}	2000	0.4	2.4
M2	3×10^{-5}	50	75	3×10^{-5}	1600	0.1	2.5
M3	8×10^{-5}	50	50	3×10^{-5}	1600	1.0	1.9
M4	3×10^{-5}	30	75	3×10^{-5}	1600	1.0	0.6

The second step in the simulation is carried out until a bubble is formed by the interaction between the WR wind and the shell produced by the RSG stellar wind. We used a constant mechanical luminosity for each stage similar to Garcia-Segura et al. (1996a) and did not include the stellar ionization photon flux. The notation for the models is: model 1 (M1), model 2 (M2), model 3 (M3) and model 4 (M4).

3. THE NUMERICAL MODEL

The 3D numerical simulations where carried out with the Yguazú-a hydrodynamical code (Raga et al. 2000, 2002). The code integrates the gas dynamic equations with a second-order accurate implementation of the flux vector splitting method (see van Leer 1982) on a binary adaptive grid, along with a system of rate equation for the atomic/ionic species: [H I], [H II], [He III], [He II], [He III], [C II], [C III], [C IV], [N I], [N II], [N III], [O I], [O II], [O III], [O IV], [S II] and [S III]. A computational domain with a physical size of (16pc$\times$8pc$\times$16pc) along the $x-$, $y-$, and $z-$ directions, respectively, with a maximum spatial resolution of 9.7×10^{16}cm, was employed. The xz-plane was chosen as the plane of the sky.

The numerical simulation provided us with density and temperature distributions which were combined with synthetic X-ray spectra to simulate the X-ray emission of the WR nebulae. The X-ray emissivity coefficient (j_ν(n, Z, T)) was calculated in the limit of low-density regime, which is $j_\nu(\mathrm{n,Z,T}) = \mathrm{n}^2\chi(\mathrm{Z,T})$, where $\chi(Z,T)$ is a function of the metallicity and the temperature. Both the gas electron density (n) and temperature (T) were obtained from the numerical results. The synthetic spectra were obtained with the CHIANTI data base (Dere et al. 1997; Landi et al. 2006), where a thermal optically-thin plasma in ionization equilibrium (IEQ) was considered. To compare with observations the X-ray emission coefficient ($j_\nu(n,T)$) was calculated in the energy range $[0.3-1.2]$ keV assuming an ISM absorption due to a hydrogen column density of $N_H = 3.13\times10^{21}\mathrm{cm}^{-2}$. Abundances in the WR stage were selected from Mesa-Delgado et al. (2014) for the WR nebulae NGC 6888 since this is a WR nebula in which a diffuse X-ray emission was detected (Toalá et al. 2016, 2014; Zhekov & Park 2011; Wrigge & Wendker 2002).

4. RESULTS

4.1. *RSG Stage*

As mentioned in § 2, the RSG phase was simulated until an integration time corresponding to when the stand-off distance R_0 was reached in each model. The top row panels of Figures 1, 2, 3, and 4 (left panel) display the temporal evolution of the density distribution on the $xz-$ plane. These show a characteristic bow shock bubble produced by the interaction of the isotropic RSG wind and the plane-parallel wind (modelled as the ISM moving towards the star due to our reference system moving with the star).

The axisymmetry of the bow shock bubble is broken by the development of Vishniac instabilities (Vishniac 1983). At this stage of the evolution the RSG wind is dense enough to produce a radiative terminal shock forming a thin, dense shell which is observed in the [H II] density distribution for M1 (see Figure 5 top row panel). We show that this region has temperatures, at 80 kyr, of $\approx 10^4$ K as shown in Figure 6. The models are hydrodynamic and do not take into account the stellar radiation, so they are expected to produce a thin shell in the H II density distribution, produced by the shock wave. In works where stellar radiation is included the ionization regions are extended and fully ionized (Dwarkadas & Rosenberg 2013; Meyer et al. 2015).

At 80 kyr and 100 kyr for models M1 and M2, respectively, and at 120 kyr for both models M3 and M4 the balance between the ram pressure of the stellar wind and the ISM are achieved. Stellar evolution

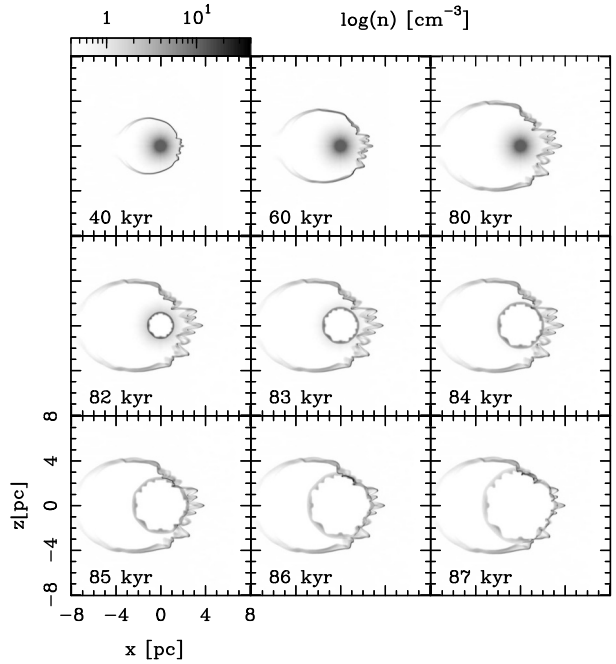

Fig. 1. For the M1 run temporal evolution of the density distribution is shown, on the $xz-$plane, for several integration times. The three top panels display the interaction between the RSG stellar wind and the plane-parallel ISM wind, which produces a characteristic bow shaped morphology. The evolution of the WR stellar wind into the asymmetric RSG shell is shown in the middle three panels, while the three bottom panels display the interaction between the RSG and WR shells. Both axes are given in units of pc, while the logarithmic grey scale gives the density in units of cm^{-3}.

models for $35M_{\odot}$ predict that the duration of this stage is ≈ 200 kyr (Garcia-Segura et al. 1996b), approximately twice to what was obtained.

4.2. *WR Stage*

As mentioned above the WR stage starts at times $t = 80$, $t = 100$ kyr for M1 and M2, respectively, and at $t = 120$ kyr for both M3 and M4, i.e. when the WR stellar wind is turned on. The middle row panels in Figures 1, 2, 3, and 4 (middle panel) show how the WR stellar wind evolves through the RSG wind material. A spherical shell is formed due to the fast-slow wind interaction which takes place inside the smooth RSG medium, showing the development of Rayleigh-Taylor instabilities. A similar behavior is observed for the ionized hydrogen, H II density distribution in Figure 5 (middle panel) for M1. At integration times of $t = 84$, 103, 124 and 122 kyr for M1, M2, M3, and M4, respectively, the collisions between RSG and WR shells have just started.

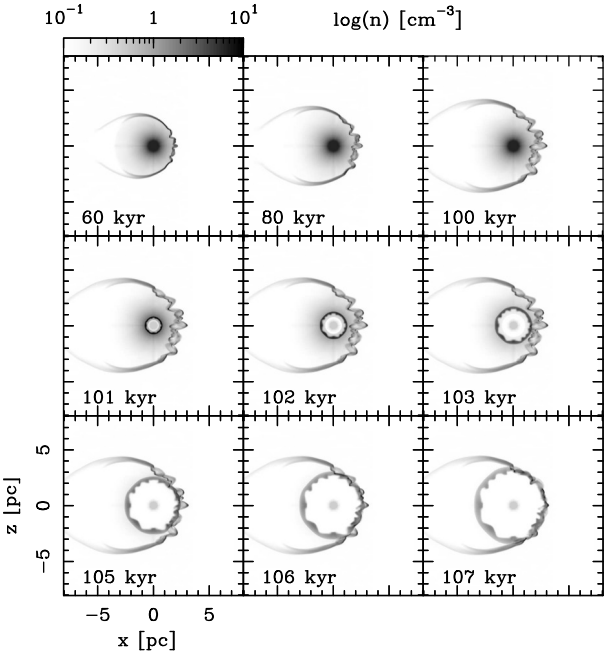

Fig. 2. The same as in Figure 1 but for M2.

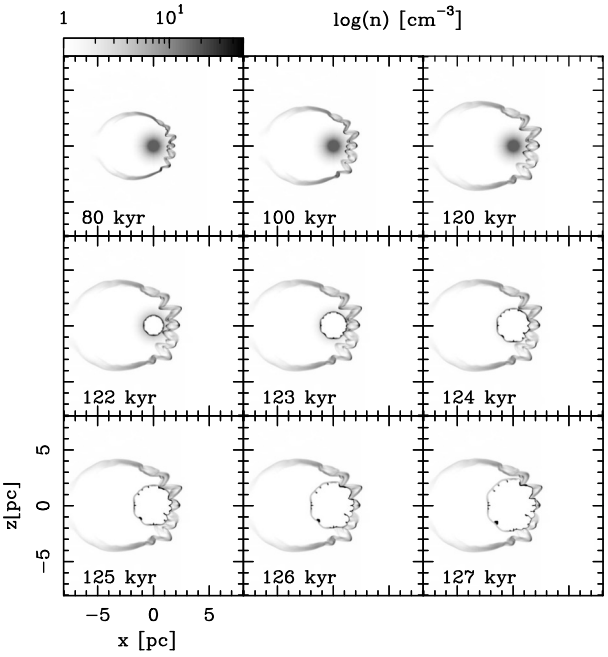

Fig. 3. The same as in Figure 1 but for M3.

4.3. *Shell Collision*

The hypothesis is that Wolf-Rayet nebulae are originated in the collision between the shells formed during the WR and RSG stages. In order to check this, the evolution of the collision of the wind shells was followed. The panels in the bottom row of Figures 1, 2, 3, and 4 (middle and right panel) display

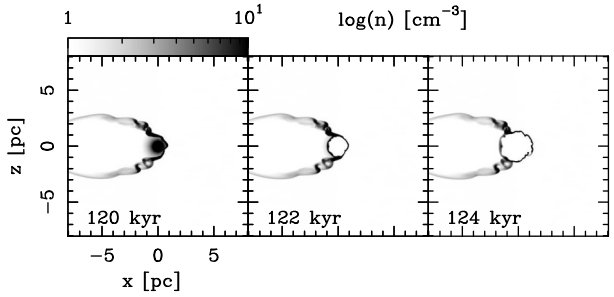

Fig. 4. The same as in Figure 1 but for M4.

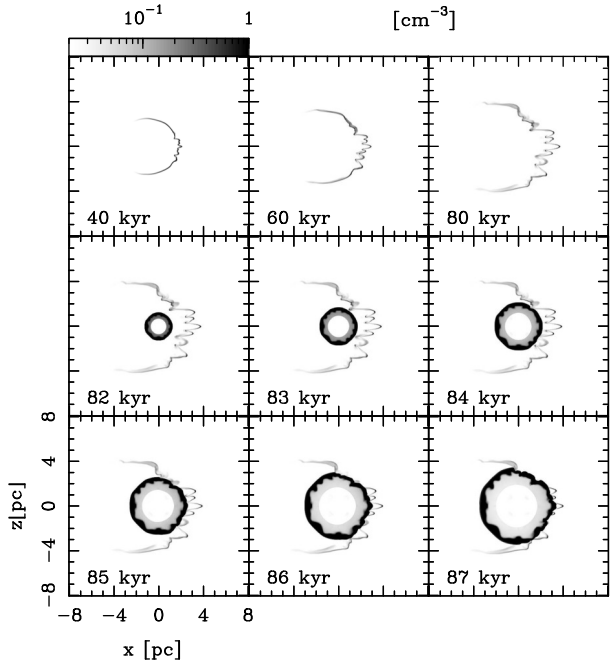

Fig. 5. For the M1 run, the temporal evolution of the number density distribution of the ionized hydrogen, [H II], is shown. These synthetic maps were computed considering that the line of the sight is along the $y-$ axis (i.e. $xz-$ plane is the plane of the sky). Both axes are in units of pc. The logarithmic gray scale is given in units of cm^{-3}

this evolution. They show that for M1 the start of the interaction occurs at an integration time between 84 and 85 kyr. The end of this interaction occurs at a time of 87 kyr, when the WR wind has passed completely through the bow shock structure generated by the RSG wind. Similarly, for M2 the shell collision takes place at an integration time [105−107] kyr, for M3 [124 − 127] kyr, and 122 kyr for M4.

4.4. *X-ray Emisson From Shell Collision*

Synthetic maps were created for each model for X-ray emission in the [0.3 − 0.7], [0.7 − 1.2], and

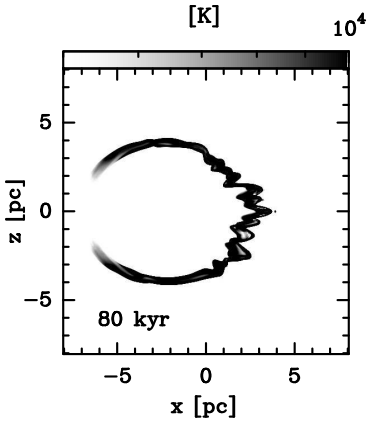

Fig. 6. For M1 the synthetic temperature map at pre-collision time $t = 80$ kyr is shown. This synthetic map was computed considering that the line of the sight is along the $y-$ axis (i.e. $xz-$ plane is the plane of the sky). Both axes are in units of pc. The logarithmic gray scale gives the temperature in units of degrees K.

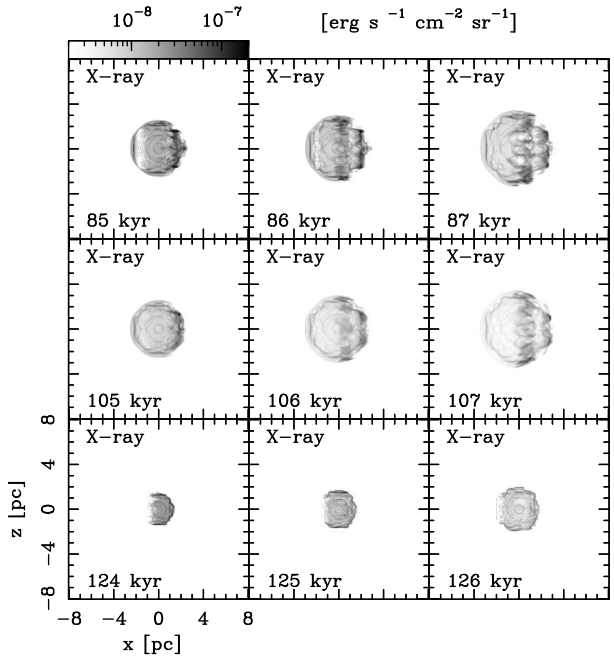

Fig. 7. X-ray emission in the [0.3 − 1.2] keV band. Top row panel, middle row panel, and bottom row panel for M1, M2, and M3, respectively. Both axes are in units of pc. The logarithmic gray scale gives the flux in units of erg s^{-1} cm^{-2} sr^{-1}

[1.2 − 3] keV bands. We found only soft emission, so there is no considerable emission in the interval [1.2 − 3.0] keV. The emission is significant for the ([0.3−1.2]) keV energy band which is displayed in the top, middle, and bottom row panels of Figure 7, for

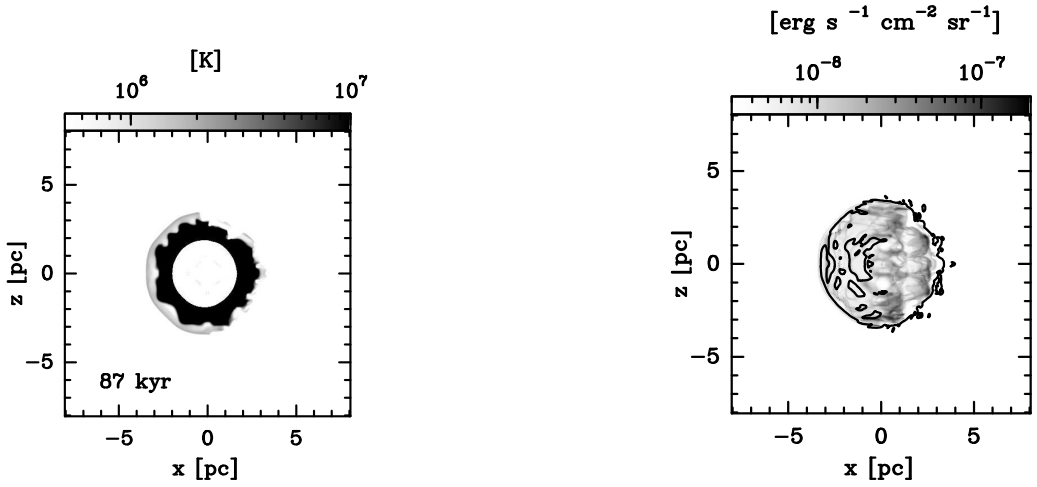

Fig. 8. Left panel. For M1 the synthetic temperature map at collision time $t = 87$ kyr is shown. This synthetic map was calculated considering that the line of the sight is along the $y-$ axis (i.e. $xz-$ plane is the plane of the sky). Both axes are in units of pc. The logarithmic gray scale gives the temperature in units of degrees K. Right panel. For Mod1 a comparison between the X-ray (in gray scale) and the [H α] emissions is shown (black contours at level 4×10^{-9}) for an integration time of 87 kyr. Both axes are in pc. The logarithmic gray scale is in units of erg s^{-1} cm^{-2}sr^{-1}

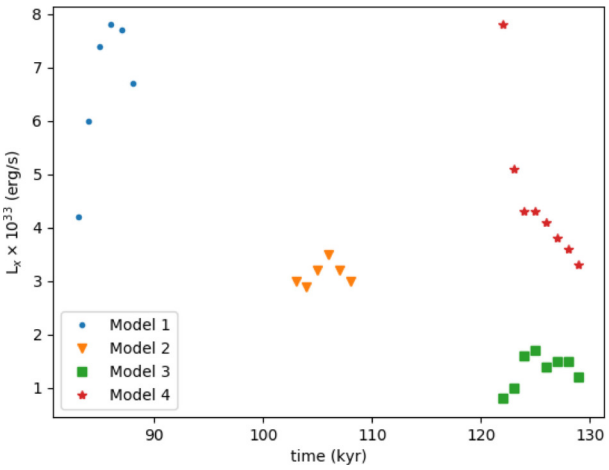

Fig. 9. X-ray luminosity in the $[0.3 - 1.2]$ Kev band as a function of time for M1, M2, M3, and M4. The color figure can be viewed online.

models M1, M2, and M3, respectively (these maps correspond to the collision times). These maps show a clumpy and filamentary morphology. The size of the emitting region increases as the collision evolves in time, to a lesser extent for M3. This suggests that this nebula could be the product of the collision between the WR and the RSG winds. Figure 8 (left panel) shows the spatial distribution of the temperature at a time $t = 87$ kyr for M1. A shell with temperatures $10^6 - 10^7$ K, surrounded by an outer shell with temperatures of $10^5 - 10^4$ K is observed.

In order to analyze the spatial distribution of the H α and X-ray emission, the right panel of Figure 8 compares both emissions. In gray scale the thermal X-ray emission is displayed while the H α emission is shown as black contours. From this figure we can see that the optical emission appears to wrap around the thermal X-ray emission. An important result is that the maximum in X-ray emission occurs in the collision, as shown in Figure 9. The maximum emission for M1 takes place at a time of 86 kyr with a value of 7.8×10^{33} erg s^{-1}. For M2 it occurs at 107 kyr with a value of 3.5×10^{33} erg s^{-1}, M3 reaches maximum at 125 kyr with value 1.7×10^{33} erg s^{-1}, and for M4 the maximum occurs at 122 kyr, with a value of 7.8×10^{33} erg s^{-1}.

5. DISCUSSION

The standard model from Weaver et al. (1977) proposes thermal conduction at the interface between hot gas (or shocked wind) and cold and dense gas (or shocked interstellar medium) with temperatures of 10^6 K and 10^4 K, respectively, as the mechanism for explaining the X-ray emission in stellar wind bubbles. The density of the hot gas increases due to the photoevaporation caused by the thermal conduction in the interface, producing an increase on the X-ray emission. However, their predictions are not compatible with the low luminosities observed.

Soft X-ray emission has been detected in Wolf-Rayet nebulae with luminosities in the range $L_x = 10^{33} - 10^{34}$ ergs^{-1} (Chu et al. 2003; Toalá et

TABLE 2

LUMINOSITIES OF THE MODELS

Model	L_x[erg/s]				Time [kyr]
	$[0.3-0.7]^a$ keV	$[0.3-1.2]^a$ keV	$[0.3-0.7]^b$keV	$[0.3-1.2]^b$ keV	
M1	6.9×10^{33}	7.8×10^{33}	1.6×10^{31}	6.5×10^{31}	86
M2	3.0×10^{33}	3.5×10^{33}	0.8×10^{31}	3.5×10^{31}	107
M3	1.5×10^{33}	1.7×10^{33}	0.2×10^{31}	2.2×10^{31}	125
M4	6.8×10^{33}	7.8×10^{33}	1.5×10^{31}	9.9×10^{31}	122

[a]Corrected for absorption.

[b]With absorption.

al. 2012, 2015, 2016). Our models show that the total X-ray luminosity L_x (corrected by absorption) at the time of collision is close to these values, summarized in Table 2. A large part of the emission in the $[0.3-1.2]$ keV band comes from the subinterval $[0.3-0.7]$ keV; for our models it represents ≈ 90 %. The soft X-ray emission is associated to a short period of time of the order of ≈ 1 to 2 kyr (see Figure 9). Hydrodynamic models with thermal conduction show a similar behavior, although soft X-ray emission lasts for periods of time < 50 kyr (Toalá & Arthur 2011). If we consider the ISM absorption in our calculation of the X-ray luminosities they turn out to be lower by two orders of magnitude (see Table 2).

The synthetic maps show a clumpy structure formed by instabilities due to the wind interaction. We also note that the brightness distribution of these emissions exhibits limb-brightening (at most one order of magnitude higher to the right of our synthetic nebulae). The limb-brightening is observed to a lesser degree for M3 (see Figure 7).

The synthetic X-ray emission maps (see Figure 7) show that most of the emission is coming from several filaments produced by the wind collisions between the shells from the RSG and WR stages, while according to the theory the X-ray profile should be centrally filled. Previous works have shown that soft X-ray emissions in models of WR nebulae come from clumps and can be enhanced by thermal conduction (Freyer et al. 2006; Toalá & Arthur 2011). In spite of our models being hydrodynamic, which do not consider the effect of thermal conduction, we measure luminosities similar to the ones obtained by Freyer et al. (2006) and Toalá & Arthur (2011).

Only 12 runaway WR stars in our Galaxy have been reported. For WR 3, WR 148, and WR 124 corrected absorbed luminosities of $\approx L_x = 10^{32}$ erg s^{-1} (Rosslowe & Crowther 2015) were obtained, one order of magnitude lower than the ones obtained in these models, see Table 2. The asymmetric nebula observed in NGC 6888 can be due to the motion of the star through the ISM. The star WR 136 is classified as a runaway star with a velocity (from the proper motion) ≈ 100 km/sec. However, the orientation between the bow shock symmetry axis and the velocity is 90 degrees (van Buren et al. 1995).

6. CONCLUSIONS

We have carried out 3D hydrodynamical simulations in order to model the evolution and emission of WR nebulae. As in previous works (Garcia-Segura et al. 1996a) we have followed the evolution of the stellar wind of the central star from the RSG to WR phase. We considered the velocity of the central star in the nebula as moving in an ISM with a constant density. This produces a RSG shell with bow shock morphology. From the density and temperature distributions obtained from our numerical results several synthetic X-ray emission maps (in the $[0.3-1.2]$ keV energy range) were generated. These synthetic X-ray emission maps show a non-uniform brightness distribution. Limb-brightened, clumpy, and filamentary emissions are displayed in Figure 7, in good agreement with observational results (Gruendl et al. 2000; Moore et al. 2000). This spatial distribution of the emission is generated by the joint action of the stellar motion and the stellar evolution from the RSG to WR phases. The limb-brightened structure is produced by the collision of the SRG shell with the WR stellar wind. This collision produces an enhancement of the density and the temperature, giving as a result an increase in the X-ray emission, with a difference between the low and high emission regions of one order of magnitude at most. The total X-ray luminosity computed from the sim-

ulations displays an increase after the shell collision (see Figure 9). The emission in hard X-rays is weak, only the soft X-ray emission is considerable.

In summary, our model, which includes the stellar wind evolution from the RSG to the WR stage and the motion of the central star of the WR nebulae, can reproduce an asymmetric morphology in X-ray emission.

We thank the anonymous referee for her/his very useful comments and suggestions, which helped us to improve the previous version of this manuscript. We also thank Artemi Camps-Fariña for reading this manuscript. Finally, we Acknowledge finantial support from TNM-SEP, PAPIIT IG100218, CONACYT CY-253085 and UNAM DGAPA-PAPIIT IN 109919.

REFERENCES

Brighenti, F. & D'Ercole, A. 1995, MNRAS, 273, 443
_____. 1995, MNRAS, 277, 53
_____. 1997, MNRAS, 285, 387
Chita, S. M., van Marle, A. J., Langer, N., & García-Segura, G. 2007, RMxAC, 30, 80
Chita, S. M., Langer, N., van Marle, A. J., García-Segura, G., & Heger, A. 2008, A&A, 488, L37
Chu, Y.-H. 1981, ApJ, 249, 195
Chu, Y.-H., Treffers, R. R., & Kwitter, K. B. 1983, ApJS, 53, 937
Chu, Y.-H., Guerrero, M. A., Gruendl, R. A., García-Segura, G., & Wendker, H. J. 2003, ApJ, 599, 1189
Cox, N. L. J., Kerschbaum, F., van Marle, A.-J., et al. 2012, A&A, 537, A35
Dere, K. P., Landi, E., Mason, H. E., Monsignori Fossi, B. C., & Young, P. R. 1997, A&AS, 125, 149
Dwarkadas, V. V. & Rosenberg, D. L. 2013, HEDP, 9, 226
Freyer, T., Hensler, G., & Yorke, H. W. 2006, ApJ, 638, 262
Garcia-Segura, G., Langer, N., & Mac Low, M.-M. 1996, A&A, 316, 133
Garcia-Segura, G., Mac Low, M.-M., & Langer, N. 1996, A&A, 305, 229
Gruendl, R. A., Chu, Y.-H., Dunne, B. C., & Points, S. D. 2000, AJ, 120, 2670
Heckathorn, J. N., Bruhweiler, F. C., & Gull, T. R. 1982, ApJ, 252, 230
Landi, E., Del Zanna, G., Young, P. R., et al. 2006, ApJS, 162, 261
Mackey, J., Gvaramadze, V. V., Mohamed, S., & Langer, N. 2015, A&A, 573, A10
Mac Low, M.-M., van Buren, D., Wood, D. O. S., & Churchwell, E. 1991, ApJ, 369, 395
Marston, A. P., Chu, Y.-H., & Garcia-Segura, G. 1994, ApJS, 93, 229
Marston, A. P., Yocum, D. R., Garcia-Segura, G., & Chu, Y.-H. 1994, ApJS, 95, 151
Mesa-Delgado, A., Esteban, C., García-Rojas, J., et al. 2014, ApJ, 785, 100
Meyer, D. M.-A., Langer, N., Mackey, J., Velázquez, P. F., & Gusdorf, A. 2015, MNRAS, 450, 3080
Miller, G. J. & Chu, Y.-H. 1993, ApJS, 85, 137
Moore, B. D., Hester, J. J., & Scowen, P. A. 2000, AJ, 119, 2991
Peri, C. S., Benaglia, P., Brookes, D. P., Stevens, I. R., & Isequilla, N. L. 2012, A&A, 538, A108
Peri, C. S., Benaglia, P., & Isequilla, N. L. 2015, A&A, 578, A45
Raga, A. C., Navarro-González, R. & Villagrán-Muniz, M. 2000, RMxAA, 36, 67
Raga, A. C., de Gouveia Dal Pino, E. M., Noriega-Crespo, A., Mininni, P. D., & Velázquez, P. F. 2002, A&A, 392, 267
Rosslowe, C. K. & Crowther, P. A. 2015, MNRAS, 447, 2322
Stock, D. J. & Barlow, M. J.2010, MNRAS, 409, 1429
Toalá, J. A. & Arthur, S. J. 2011, ApJ, 737, 100
Toalá, J. A., Guerrero, M. A., Chu, Y.-H., et al. 2012, ApJ, 755, 77
Toalá, J. A., Guerrero, M. A., Gruendl, R. A., & Chu, Y.-H. 2014, AJ, 147, 30
Toalá, J. A., Guerrero, M. A., Chu, Y.-H., & Gruendl, R. A. 2015, MNRAS, 446, 1083
Toalá, J. A., Marston, A. P., Guerrero, M. A., Chu, Y.-H., & Gruendl, R. A. 2017, ApJ, 846, 76
Toalá, J. A., Guerrero, M. A., Chu, Y.-H., et al. 2016, MNRAS, 456, 4305
van Buren, D. & McCray, R. 1988, ApJ, 329, L93
van Buren, D., Mac Low, M.-M., Wood, D. O. S., & Churchwell, E. 1990, ApJ, 353, 570
van Buren, D. & Mac Low, M.-M. 1992, ApJ, 394, 534
van Buren, D., Noriega-Crespo, A., & Dgani, R. 1995, AJ, 110, 2914
van Leer, B. 1982, International Conference on Numerical Methods in Fluid Dynamics, 8th ed. (Berlin: Springer), 507
Vishniac, E. T. 1983, ApJ, 274, 152
Weaver, R., McCray, R., Castor, J., Shapiro, P., & Moore, R. 1977, ApJ, 218, 377
Wilkin, F. P. 1996, ApJ, 459, L31
Wrigge, M., Wendker, H. J., & Wisotzki, L. 1994, A&A, 286, 219
Wrigge, M. & Wendker, H. J. 2002, A&A, 391, 287
Wrigge, M., Chu, Y.-H., Magnier, E. A., & Wendker, H. J. 2005, ApJ, 633, 248
Zhekov, S. A. & Park, S. 2011, ApJ, 728, 135

E. Matías Schneiter: Instituto de Astronomía Teórica y Experimental CP: X5000BGR, Córdoba, Argentina.
E. Matías Schneiter: Departamento de Materiales y Tecnología, Universidad Nacional de Córdoba CP: X5016GCA, Córdoba, Argentina.
J. Reyes-Iturbide: Tecnológico de Estudios Superiores de Tianguistenco, Carretera Tenango-La Marquesa Km. 22, Santiago Tianguistenco, Estado de México, México (jr.iturbide@gmail.com).
J. Reyes-Iturbide and Pablo F. Velázquez: Instituto de Ciencias Nucleares, Universidad Nacional Autónoma de México, Apdo. Postal 70-543, CP: 04510, Ciudad de México, México (jr.iturbide@gmail.com).
I. Ramírez-Ballinas and M. Rosado: Instituto de Astronomía, Universidad Nacional Autonóma de México, Apdo. Postal 70-264, C.P. 04510, Ciudad de México, México.

Revista Mexicana de Astronomía y Astrofísica, **55**, 221–229 (2019)

DOI: https://doi.org/10.22201/ia.01851101p.2019.55.02.10

SOME REMARKS ON THE OPEN CLUSTER UPGREN 1 USING $uvby-\beta$ PHOTOELECTRIC PHOTOMETRY[1]

J. H. Peña[2,3,4], A. Rentería[4], H. Huepa[3], and A. Pani[3]

Received September 4 2018; accepted June 5 2019

ABSTRACT

The open cluster Upgren 1 presents peculiar features that in the past led to divergent opinions about its existence. In previous studies of other clusters, $uvby-\beta$ photoelectric photometry has shown results in agreement with other techniques; therefore, the photometry obtained in the present work has been combined with data from previous studies to examine the brightest stars in the direction of the cluster. Analyzing the unreddened indexes, we found that all the stars are of late spectral types. Applying the empirical relations of Nissen (1987) to determine the reddening and, consequently, the unreddened indexes, we found that all but three are located at a distance of 123 ± 17 pc. The assigned membership in this study is in concordance with that of Upgren, Philip and Beaver (1982) obtained through radial velocities.

RESUMEN

El cúmulo abierto Upgren 1 presenta características muy particulares que hacen que las investigaciones lleguen a conclusiones divergentes sobre su existencia. Debido a que en el pasado la fotometría fotoeléctrica $uvby-\beta$ ha probado ofrecer resultados acordes con otras técnicas, la hemos conjuntado con estudios previos con la misma fotometría para estudiar las estrellas más brillantes en la dirección del cúmulo. Mediante el analisis de los índices desenrojecidos hemos encontrado que todas las estrellas son del tipo tardío. Aplicando las calibraciones empíricas de Nissen (1988) para determinar el enrojecimiento y, por ende, los índices desenrojecidos, encontramos que todas, salvo tres, son estrellas agrupadas a una distancia de 123 ± 17 pc. La membresía asignada a este estudio está en concordancia con el trabajo de Upgren, Philip and Beaver (1982) obtenido por una técnica totalmente diferente, mediante velocidades radiales.

Key Words: open clusters and associations: individual (Upgren 1) — techniques: photometric

1. BACKGROUND

In 1965 Upgren and Rubin (1965) in an objective-prism study of the distribution in a North Galactic Pole region noted a compact grouping of F-type stars at coordinates RA 12 35 01 and Dec. +36 22 18 (2000). They studied these stars with a one-slit spectrogram on the Cassegrain spectrograph (125Å/mm) of the 36-inch reflector of the Kitt Peak National Observatory. In addition, photoelectric magnitudes and colors in the U, B, V system were determined for five stars with the 28-inch reflector of the Flower and Cook Observatory of the University of Pennsylvania. The separation of the F stars in the sky is about 15 minutes of arc. At a mean distance of 140 parsecs, this separation corresponds to a linear separation of about one parsec. Finally they concluded that the narrow range in the radial velocities and distance modulii for these seven stars suggested that they formed a cluster. If it is assumed that the five dwarf stars define a main sequence, then the turnoff was at about spectral class F2, the same point found

[1]Based on observations collected at the San Pedro Mártir Observatory, México.

[2]Instituto de Astronomía, Universidad Nacional Autónoma de México, México.

[3]Observatorio Astrónomico Nacional de Tonantzintla, Universidad Nacional Autónoma de México, México.

[4]Facultad de Ciencias, Universidad Nacional Autónoma de México, México.

for the old galactic cluster M 67. They later stated that the apparent great age of the group indicated that a number of fainter stars of low mass, which once belonged to the cluster, may have escaped.

In 1982 Upgren, Philip, & Beavers (1982) in a study through narrow-band photometry with the four-color system and radial velocities stated that these data indicate that five of the seven stars were physically associated and formed a small cluster. The other two stars could also be members. The cluster distance is about 117 pc and its turnoff point is near $(B-V)=0.5$, which again suggests an age similar to that of the old open cluster M67. They also concluded that it forms the residual core of a much larger cluster, whose fainter members are no longer associated, and is probably in its final stage of dissolution.

In their discussion they stated that Anderson (1966) and Osborn (1967) published proper motions for the stars in an attempt to determine the existence of a mutual association among them. Both concluded that the seven stars do not form a single physical group, although they found that some of them do share a common proper motion.

Upgren et al. (1982) emphasized that if the group were real, it would be a very unusual open cluster. The member stars are very unlikely to be in bound motion around each other. Thus, it is most probable that the group is a residual core of a small open cluster whose fainter and less massive members have had time to dissociate from the loosely bound group.

Later, in 1997, Stefanik et al. (1997) monitored the radial velocities of the seven stars reported by Upgren and Rubin (1965) and determined that two of the stars have velocities which are clearly inconsistent with a physical association with the other five stars.

In 1998 Baumgardt (1998) carried out a study entitled "The nature of some doubtful open clusters as revealed by Hipparcos", in which the cluster Upgren 1 is included. Based on the parallaxes and proper motions obtained by Gatewood et al. (1988) who concluded that Upgren 1 consists of two dynamically different groups, they collected the parallaxes and proper motions of the 7 stars that could be found in the Hipparcos catalogue. They determined that, with the exception of stars 3 and 5, the proposed members share no common motion and conclude that Upgren 1 is not a cluster.

This result was reinforced later when Baumgardt, Dettbarn & Wielen (2000), in a paper on membership probabilities through proper motions, found that none of the six studied stars belong to a cluster.

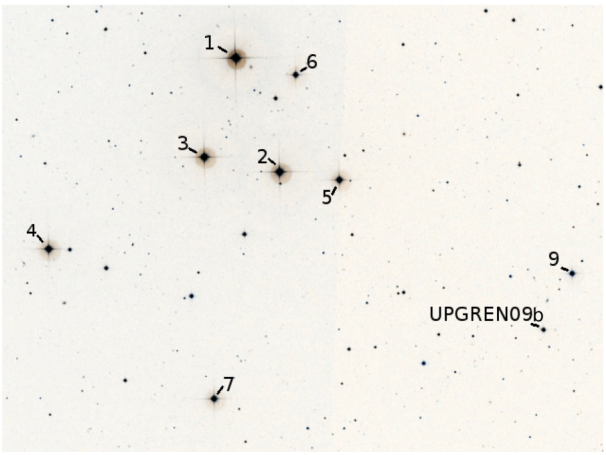

Fig. 1. ID chart of the observed stars as in Webda. The studied stars are indicated.

There are several reports on $uvby-\beta$ photoelectric photometry (see Table 1) of the stars originally supposed to belong to Upgren 1; hence, we decided to study this cluster once more using $uvby-\beta$ photometry, because the question of membership has not been settled. We obtained new $uvby-\beta$ photoelectric photometry since this system provides a different approach for determining correct distances to each one of the stars (see, for example Peña & Sareyan, 2006). Therefore, the present study could throw fresh light on this matter.

In the compilation of data of open clusters of Paunzen and Mermilliod (2007, WEBDA), no characteristics of Upgren 1 have been reported and no membership of the stars to the cluster is provided.

2. OBSERVATIONS

The observations were carried out at the Observatorio Astronómico Nacional (OAN) at San Pedro Mártir, Mexico using a 0.84m telescope with an attached sepctrophotometer during six nights in the summer of 2018. On June 1 and June 2 the open cluster was observed. The nomenclature of Rufener (1971) was used to assign IDs to every star, except for a faint star near Star 9 at 2" in the SE direction. We identified this star as Upgren 09b. All are indicated in Figure 1.

2.1. *Data Acquisition*

The procedure used to acquire the data has been amply utilized in Mexico since the arrival of the "Danish" spectrophotometer in 1986. A description of the typical procedure can be found in Guerrero

TABLE 1

OBSERVATION OF UPGREN 1 WITH $uvby-\beta$ PHOTOELECTRIC PHOTOMETRY

Author	Reference	Number
Perry (1969)	AJ 74, 705	1 star
Hilditch, Hill & Barnes (1976)	MRAS 82.95	4 stars
Upgren, Philip & Beavers (1982)	PASP 94,229	7 stars
Hill & Barnes (1982)	PDAO XVI 297	1 star
Olsen (1983)	AAS54,55	3 stars
Castelaz, Persinger, Stein et al. (1991)	AJ 102, 2103	3 stars
Olsen(1993)	AAS 102,890	1 star
Present Paper		9 stars

TABLE 2

TRANSFORMATION COEFFICIENTS OBTAINED FOR THE OBSERVED SEASON

Season	B	D	F	J	H	I	L
2018	0.031	0.976	1.020	0.015	0.096	0.080	−1.369
σ	0.038	0.011	0.027	0.015	0.046	0.081	0.124

et al. (2011). What is emphasized here are the numerical values that throw light on the accuracy of the data. The averaged transformation coefficients for each night are listed in Table 2 along with their standard deviations. Season errors were evaluated with the eighteen standard stars observed for a total of 316 observed points. These uncertainties were calculated through the differences in magnitude and colors for all nights, for (V, $b-y$, m_1, c_1 and β) as (0.028, 0.006, 0.006, 0.014, 0.006) respectively, which provide a numerical evaluation of our uncertainties for the season. Emphasis is made on the large range of the standard stars in magnitude and color values: V:(5.2, 8.8); $(b-y)$:(−0.07, 0.79); m_1:(0.10, 0.68); c_1:(0.07, 1.12) and β:(2.53, 2.92).

A verification of the goodness of our data was done with the standard stars observed during the season. Transformation coefficients were obtained for each night. With these coefficients, magnitude and colors were obtained for the standard stars. The differences of the obtained values with those of the literature were evaluated for the magnitude and the colors V, $(b-y)$, m_1, c_1 and β.

Once this was done for each night, a compilation of the transformation coefficients was carried out, and mean values and standard deviations were calculated. These are presented in Table 3. In this table Column 1 lists the V value; Columns two to six present the color indexes $(b-y)$, m_1, c_1 and β and the standard deviations. These values are a few hundredths or thousandths of magnitude for each color index providing the accuracy of our photometry. Emphasis must be made on the fact that in total thirty-three *uvby* measurements (twenty-eight for Hβ) of the standard stars were calculated.

Furthermore, to verify the consistency of our derived standard stars values, mean values for each star were calculated, as well as their standard deviations. These are presented in Table 4 in increasing brightness. The last Column of this table is, N, the number of entries. In all but HD190849 the standard deviations are on the order of hundredths of magnitude. The large dispersion of this star could be due to variability, as in the case of HD 115520 (Peña et al., 2007).

With the average coefficients we transformed our instrumental magnitudes and colors to the standard system. In particular, since there were two measurements for each star of the cluster Upgren 1, mean values were obtained and the standard deviations calculated. All are below the standard deviation limits.

3. COMPILATION OF $uvby-\beta$ PHOTOELECTRIC PHOTOMETRY

Since Upgren 1 has several measurements in $uvby-\beta$ photoelectric photometry reported in the literature and listed in Table 4, we decided to combine all measurements into only one averaged, more significant, value. As we can see in Table 4 the *uvby*

TABLE 3

SEASONAL MAGNITUDE AND COLOR INDEXES DEVIATIONS

σV	$\sigma(b-y)$	σm_1	σc_1	$\sigma\beta$
0.0125	0.007	0.009	0.010	0.002

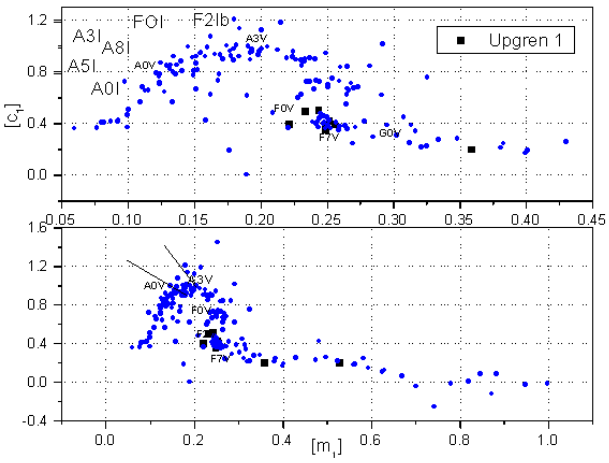

Fig. 2. Position of the stars in the $[m_1]-[c_1]$ diagram of Alpha Per (Peña & Sareyan, 2006) for Upgren 1. The color figure can be viewed online.

coverage is adequate, but the situation is worse for Hβ, with only four sources: Hilditch, Hill, Barnes (1976), 4 stars; Perry, Johnston, Crawford (1982), 1 star; Hill G., Barnes (1982) (1 star and Castelaz, Persinger, Stein et al. (1991), (4 stars). We measured the nine reported stars.

Table 5 compiles all the photometric values of the observed stars for the cluster. In this table, Column 1 reports the ID of the stars as listed by WEBDA (Paunzen & Mermilliod, 2006.), Columns 2 to 5 the Strömgren values V, $(b-y)$, m_1 and c_1, respectively; next, Column N specifies the number of entries on average presented for each point; next column, the β value, and last Nβ, the number of entries for the average of β. Finally, for each star we present the mean value and in the following row, the standard deviation. As we can see, the standard deviation is on the order of a few hundredths of magnitude and the number of entries is always larger than four, except for β which has a smaller number in a few cases.

4. METHODOLOGY

Once we were sure of the quality of the $uvby-\beta$ data set, further analysis was carried out in order to determine the physical characteristics of the stars in the cluster.

The main problem to tackle was, of course, the determination of membership to the cluster. To do this, the distance to each star had to be calculated. To evaluate the reddening we first established to which spectral class the stars belonged, although it was reported that all were late types (late A and F stars) for which there are calibrations (Nissen, 1988). The procedure has been extensively described in Peña & Martínez (2014). In that article, in § 4 the procedure employed utilizing the prescription of Nissen (1988) is amply described. Photoelectrically we corroborated each star's spectral type through its location in the $[m_1]-[c_1]$ diagram (Figure 2).

5. RESULTS

Figure 2 shows the position of the stars in the $[m_1]-[c_1]$ diagram for those located in the direction of Upgren 1 on the same diagram of the stars with well-determined spectral types in the open cluster Alpha Per (Peña & Sareyan (2006)).

The application of the above mentioned numerical packages gave the results listed in Table 6 in which the ID, reddening, unreddened indexes, absolute magnitude, DM and distance (in parsecs), are listed. The last two columns present the membership probabilities described below.

To establish membership of the stars to the cluster the distance modulus or distance histogram (in pc) were built. The goodness of the method has been tested in the past by comparing our results to the proper motion studies for a well-studied cluster, α Per (Peña & Sareyan, 2006). In this paper the intersection of our data set with the Strömgren photometry of Crawford & Barnes (1974) plus the V photometry from Mitchell (1960) constituted 45 entries. The results were compared with the work of Heckmann et al. (1956) and the agreement was remarkable: Sixty stars coincide in membership. In that paper we wrote that given the previous numbers, we can draw the following conclusions: out of 75 stars in the membership interval, 53 are assumed to be members by HDK and there is disagreement on three. Considering the results of Prosser (19932) the matching is more than adequate. Out of 75 stars which we have defined as member stars, only three are non-members according to Prosser (1992), although two were established as members by Heckmann et al. (1956). A final comparison of membership was done with the data of the Hipparcos and Tycho catalogues proper motions. Among the sample of stars we observed, 58 had measurements in these

TABLE 4

STANDARD STARS MEAN PHOTOMETRIC VALUES AND STANDARD DEVIATIONS

ID	V	$(b-y)$	m_1	c_1	β	σV	$\sigma(b-y)$	σm_1	σc_1	$\sigma\beta$	N
BS8085	5.171	0.653	0.665	0.140	2.495	0.011	0.002	0.004	0.015	0.024	5
BS6332	5.249	−0.003	0.180	1.113	2.863	0.013	0.002	0.006	0.012	0.022	5
BS7858	5.355	0.017	0.215	1.002	2.895	0.010	0.002	0.003	0.006	0.013	4
BS7253	5.496	0.168	0.192	0.766	2.749	0.011	0.003	0.005	0.007	0.012	5
BS7503	5.948	0.397	0.207	0.396	2.590	0.010	0.005	0.003	0.005	0.004	3
BS5633	6.021	0.031	0.187	1.061	2.900	0.018	0.004	0.001	0.008	0.023	5
BS8086	6.031	0.799	0.648	0.075	2.477	0.044	0.005	0.003	0.018	0.023	5
BS5270	6.186	0.627	0.093	0.483	2.537	0.026	0.003	0.005	0.009	0.014	4
BS7504	6.206	0.403	0.211	0.384	2.595	0.013	0.005	0.002	0.005	0.012	4
HD156026	6.389	0.692	0.695	0.282	2.532	0.023	0.010	0.005	0.015	0.023	4
HD183085	6.709	0.241	0.129	0.898	2.706	0.031	0.005	0.009	0.013	0.012	4
HD190849	7.368	0.057	0.152	1.000	2.884	0.560	0.022	0.019	0.012	0.019	4
HD201193	7.884	0.335	0.147	0.436	2.622	0.041	0.002	0.009	0.012	0.000	2
HD207608	8.029	0.313	0.143	0.544	2.627	0.008	0.006	0.011	0.015	0.006	2
HD182941	8.069	0.277	0.123	1.032	2.802	0.017	0.005	0.005	0.012	0.019	4
HD190296	8.090	0.069	0.152	1.152	2.879	0.143	0.020	0.003	0.029	0.011	4
HD125607	8.092	0.548	0.384	0.336	2.583	0.018	0.005	0.005	0.007	0.028	5
HD125375	8.121	0.197	0.134	0.859	2.731	0.015	0.001	0.004	0.010	0.008	3
HD106509	8.144	0.327	0.134	0.474	2.648	0.013	0.004	0.005	0.020	0.014	4
HD188755	8.262	0.098	0.204	1.015	2.844	0.025	0.005	0.008	0.011	0.014	3
HD162503	8.286	0.454	0.183	0.443	2.591	0.019	0.006	0.004	0.012	0.012	6
HD107550	8.343	0.489	0.143	0.413	2.566	0.021	0.004	0.008	0.006	0.009	5
HD156392	8.409	0.341	0.151	0.647	2.710	0.039	0.006	0.007	0.026	0.019	5
HD176014	8.673	0.341	0.109	0.575	2.642	0.012	0.004	0.003	0.015	0.029	4
HD108641	8.821	0.515	0.274	0.331	2.575	0.006	0.004	0.006	0.014	0.014	5
HD186025	8.847	0.385	0.125	0.540	2.670	0.059	0.020	0.007	0.020	0.011	4

catalogues. Only a few stars in the catalogues did not belong to the *uvby* data sample. Assuming membership for those stars within the one sigma criterion, the coincidences were remarkable: only three of the stars that we supposed to be non-members could be members according to the Hipparcos results. For the stars that we considered to be members, only seven were not assigned cluster membership according to the Hipparcos measurements. On the other hand, 33 stars that Hipparcos measurements consider members were also clearly members according to our analysis. In view of the previously reported results on Alpha Per compared with the cannonical membership methods, we conclude that determining membership by the $uvby-\beta$ calibration technique provides reliable results.

When the histogram of distance for Upgren 1 was built (Figure 3), the distances of the stars showed a clear accumulation at a distance of (123 ± 17) pc; the peak was determined by a Gaussian fit to the distribution.

To determine membership to the cluster we established a numerical criterion that to be a member of the cluster, the distance to the star should be within one sigma of the mean average distance. For the accumulation of stars, membership of each one is indicated by M in the twelfth Column of Table 6. Those outside of the membership limits are denoted by N, non-member. We have compared our memberships with those reported in WEBDA for Upgren 1. The membership probabilities reported are listed in

TABLE 5

$uvby-\beta$ PHOTOELECTRIC PHOTOMETRY OF THE OPEN CLUSTER UPGREN 1

ID	Ref	V	$(b-y)$	m_1	c_1	N	β	Nβ
1	19	7.26	0.295	0.158	0.542	2		
1	166	7.28	0.296	0.161	0.541	3	2.648	3
1	297						2.661	7
1	305	7.27	0.295	0.194	0.567	2		
1	345	7.284	0.298	0.161	0.54	1		
1	pp	7.286	0.296	0.152	0.566	2	2.668	2
1	mean	7.276	0.296	0.165	0.551		2.659	
1	std dev	0.011	0.001	0.017	0.014		0.010	
2	166		0.312	0.17	0.44	3	2.634	3
2	305	8.13	0.316	0.2	0.443	2		
2	345	8.114	0.325	0.154	0.455	1		
2	468	8.16	0.3	0.17	0.47	1	2.64	1
2	pp	8.118	0.314	0.156	0.493	2	2.658	2
2	mean	8.131	0.313	0.170	0.460		2.644	
2	std dev	0.021	0.009	0.018	0.022		0.012	
3	166	8.23	0.262	0.165	0.512	3	2.679	3
3	305	8.2	0.267	0.185	0.531	2		
3	345	8.215	0.271	0.155	0.514	1		
3	pp	8.223	0.270	0.147	0.554	2	2.699	2
3	mean	8.217	0.268	0.163	0.528		2.689	
3	std dev	0.013	0.004	0.016	0.019		0.014	
4	166	8.75	0.309	0.181	0.407	3	2.639	3
4	305	8.76	0.313	0.204	0.408	2		
4	468						2.65	1
4	pp	8.736	0.320	0.149	0.449	2	2.653	2
4	mean	8.749	0.314	0.178	0.421		2.647	
4	std dev	0.012	0.005	0.028	0.024		0.007	
5	305	9.09	0.291	0.172	0.427	2		
5	468	9.12	0.28	0.14	0.46	1	2.64	1
5	504	9.102	0.291	0.141	0.408	1		
5	pp	9.086	0.293	0.129	0.462	2	2.654	2
5	mean	9.099	0.289	0.146	0.439		2.647	
5	std dev	0.015	0.006	0.018	0.026		0.010	
6	305	9.86	0.332	0.12	0.38	1		
6	318	9.87	0.337	0.163	0.385	3		
6	pp	9.863	0.331	0.156	0.42	2	2.656	2
6	mean	9.864	0.333	0.146	0.395		2.656	
6	std dev	0.005	0.003	0.023	0.022			
7	305	9.35	0.364	0.187	0.443	2		
7	468	9.36	0.32	0.19	0.43	1	2.61	1
7	pp	9.323	0.344	0.148	0.475	2	2.641	
7	mean	9.344	0.343	0.175	0.449		2.626	
7	std dev	0.019	0.022	0.023	0.023		0.022	
9	pp	10.284	0.566	0.350	0.311	2	2.592	2
UPGREN 09b	pp	11.568	0.391	0.235	0.275		2.640	2

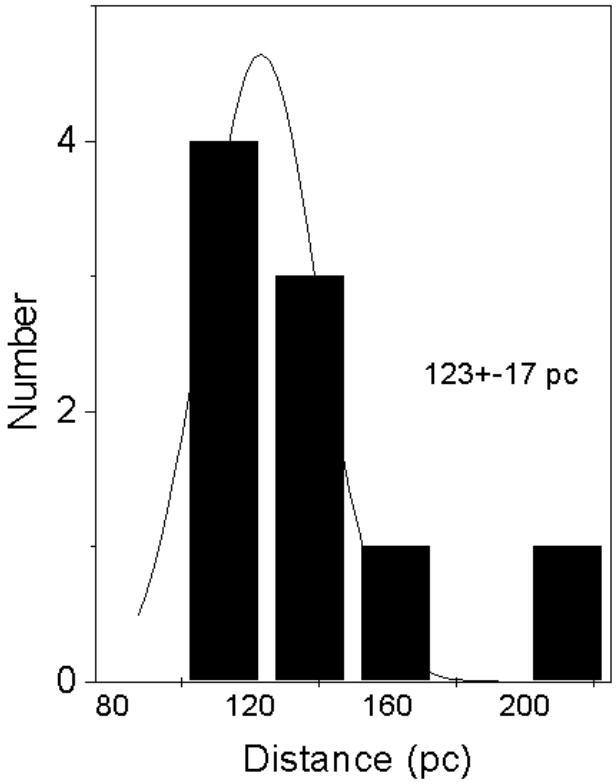

Fig. 3. Histogram of the distance of the stars in the direction of Upgren 1.

the last Column of Table 6. In the previous column the photometric membership is also presented.

The effective temperature of the hottest stars was fixed by plotting the location of all stars on the theoretical grids of Lester, Gray & Kurucz (hereinafter LGK86), after calculating the unreddened colors (Figure 4) for the correct chemical composition of the considered model. The metallicity of Upgren 1 was not reported by WEBDA, but it is calculated in this work. Discarding the high value of Star 9, a [Fe/H] value of 0.039 ± 0.08 is obtained.

Once the membership and effective temperature are established for the hottest star, its age is determined through the calibrations of Meynet, Mermilliod & Maeder (1993). For the cool stars of this cluster the valid relation is given by a log age of $15.142(\log Te)2 - 122.810(\log Te) + 257.518$ valid in the range of $\log Te[3.79; 3.98)$. For the hottest star, Star 6, it gives a log age of 8.85.

The obtained results are compared to those previously known in Table 7.

6. DISCUSSION

Membership was assigned for those stars within one sigma of the mean value. Five stars were considered to be members in this fashion and three to be non-members.

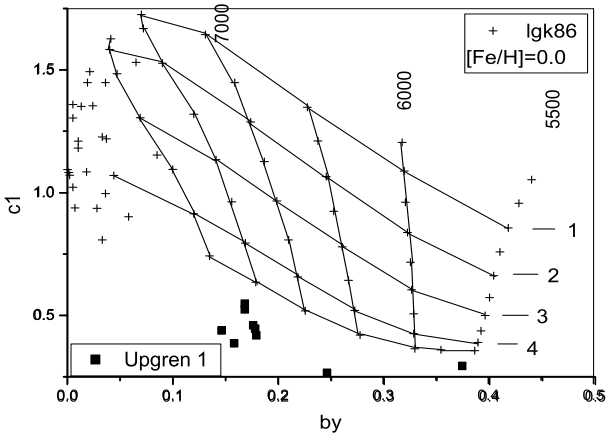

Fig. 4. Location of the unreddened points (filled squares) in the LGK86 grids. Values of effective temperature and surface gravity are indicated. X axis presents $(b-y)_0$, Y axis is c_0

Upgren et al (1982) concluded that Stars 3, 4, 5, 6, and 7 are associated, since the radial velocities, photometry, and spectral classifications are all concordant and the proper motions for 4 and 6 are not grossly different from those of the other three stars. Star no. 1 is not likely to be a member based on its radial velocity and its proper motion. Star no. 2 is a possible but unlikely member, since it too has a radial velocity in disagreement with the other stars. The distance modulus of the group determined from the five most probable stars alone is close to that given above based on all seven stars; it is 5.34 ± 0.25 which leads to a distance of 117 ± 13 pc.

Our findings are somewhat discordant with those of Stefanik et al. (1997) who determined that the radial velocity data indicated that five Stars (3, 4, 5, 6, and 7) had very similar radial velocities and could be kinematically associated, whereas the radial velocities of Stars 1 and 2 indicated no association with the other five. They stated that the proper motions and trigonometric parallaxes of Stars 3 and 6 may not be reliable, because of the multiple nature of these systems.

In their concluding remarks Upgren et al (1982) stated that: "Unlike any other star-poor cluster, Upgren 1 is old, and is perhaps unique among all known clusters for this reason. Its probable uniqueness suggests that it is being observed just prior to its final dissolution and that this stage is a relatively short one". However, in another cluster under investigation (Dzim 5) we have found (Peña et al. 2018) that it has analogous characteristics, and we concluded

TABLE 6

REDDENING AND UNREDDENED PARAMETERS OF THE OPEN CLUSTER UPGREN 1

Webda	$E(b-y)$	$(b-y)_0$	m_0	c_0	Hβ	V_0	M_V	DM	Distance	Membership		
										pp	Upgren (1982)	Stefanik (1997)
3	.015	.253	.168	.525	2.689	8.15	3.01	5.14	107	M	M	M
1	.009	.287	.168	.549	2.659	7.24	2.09	5.15	107	M	N	N
6	.038	.295	.158	.387	2.656	9.70	3.92	5.78	143	M	M	M
4	.003	.311	.179	.420	2.647	8.74	3.46	5.28	114	M	M	M
5	.000	.299	.146	.439	2.647	9.10	3.23	5.87	149	N	M	M
2	.001	.312	.176	.460	2.644	8.13	2.93	5.20	110	M	N	N
UPG09b	.038	.353	.246	.267	2.640	11.41	5.27	6.13	168	N		
7	.008	.335	.178	.447	2.626	9.31	2.80	6.51	200	N	M	M
9	.079	.487	.374	.295	2.592	9.94	4.29	5.65	135	M		

TABLE 7

NEWLY DETERMINED CHARACTERISTICS OF THE OPEN CLUSTER UPGREN 1

ID	Upgren (1982)	PP
Distance [pc]	120 ± 10 pc	119 ± 16 pc
Reddening [mag]E(b-y)	0.0	0.024 ± 0.030
Distance modulus [mag]	5.39 ± 0.18	5.3 ± 0.3
Log age	9.5	8.85
[Fe/H]	–	0.04 ± 0.08

that Dzim 5, according to us and to WEBDA, might or not be a cluster. Our findings are puzzling. There is a small group of five or six stars, basically at the same distance, but all of late spectral type. There is no indication of early type stars present or past. Nevertheless, our results are uncontroversial.

7. CONCLUSIONS

The main problem we tackled remains. From $uvby-\beta$ photoelectric photometry determined from the average of all existing measurements, we derived reddening and distances to each star. We assigned membership from the coarse average of all of them. Our memberships agree with those determined by Upgren, Philip and Beaver (1982) from radial velocities, photometry, and spectral classifications for three of the stars and disagree for another three. There is agreement with some Stars (3, 4 6) that seem to conform a physical group; three more (1, 2, 5) have contradictory results. The WEBDA membership, on the other hand, assigns zero probability of membership to the cluster for all the stars.

The location of the stars in the theoretical grids of Lester, Gray and Kurucz (1986) shows values of log g higher than 4.5, implying compact objects. The temperatures lie around 7500 K to 8000 K, concordant with their spectral types.

At any rate, different studies with radically different techniques find that there is a physical attached group of stars.

We would like to thank the staff of the OAN for their assistance in securing the observations. This work was partially supported by Papiit IN104917 and PAPIME PE113016. ARL & HH thank the IA-UNAM for the opportunity to carry out the observations. Typing and proofreading were done by J. Orta and J. Miller, respectively. D. S. Pina helped us with the editorial work. C. Guzmán, F. Salas and A. Diaz assisted us in the computing and B. Juarez and G. Perez provided bibliographic support. We thank an anonymous referee whose comments improved this work. This research has made use of the Simbad databases operated at CDS, Strasbourg, France and NASA ADS Astronomy Query Form.

REFERENCES

Anderson, J. H. 1966, PASP, 78, 256
Arellano-Ferro, A. & Parrao, L. 1988, Reporte Técnico 57, IA-UNAM
Baumgardt, H., Dettbarn, C., & Wielen, R. 2000, ASS, 146, 251
Castelaz, M. W., Persinger, T., Stein, J. W., et al. 1991, AJ, 102, 2103
Crawford, D. L. & Barnes, J. V. 1970, AJ, 75, 978
_____. 1974, AJ, 79, 687
Crawford, D. L. & Mander, J. 1966, AJ, 71, 114
Gatewood, G., de Jonge, J. K., Castelaz, M., et al. 1988, ApJ, 332, 917
Guerrero, C. A., Peña, J. H., & Sareyan, J. P. 2011, RMxAA, 47, 185
Heckmann, O., Dieckvoss, W., & Kox, H. 1956, AN, 283, 109
Hilditch, R. W., Hill, G., & Barnes, J. V. 1976, MmRAS, 82, 95
Hill, G. & Barnes, J. V. 1982, PDAO, 16, 297
Lester, J. B., Gray, R. O., & Kurucz, R. I. 1986, ApJ, 61, 509
Lynga, G. & Palous, J. 1987, A&A, 188, 35
Meynet, G., Mermilliod, J. C., & Maeder, A. 1993, AAS, 98, 477
Mitchell, R. I. 1960, AJ, 132, 68
Nissen, P. 1988, A&A, 199, 146
Olsen, E. H. 1983, AAS, 54, 55
Osborn, W. 1967, AJ, 72, 93
Paunzen, E. & Mermilliod, J. C. 2007, Webda, A Site Devoted to Stellar Open Clusters
Peña, J. H. & Sareyan, J.-P. 2006, RMxAA, 42, 179
Peña, J. H., Sareyan, J. P., Cervantes-Sodi, B., et al. 2007, RMxAA, 43, 217
Peña, J. H. & Martínez, A. 2014, RMxAA, 50, 119
Peña, J. H., Piña, D. S., Rentería, A., et al. 2018, RMxAA, 54, 85
Perry, C. L. 1969, AJ, 74, 705
Perry, C. L., Johnston, L., & Crawford, D. L. 1982, AJ, 87, 1751
Prosser, C. H. 1992, AJ, 103, 488
Rufener, F. G. 1971, A&AS, 3, 181
Stefanik, R. P., Caruso, J. R., Torres, G., Jha, S., & Latham, D. W. 1997, BaltA, 6, 137
The Astronomical Almanac. 2006, Dept. of the Navy
Upgren, A. R. & Rubin, V. C. 1965, PASP, 77, 355
Upgren, A. R., Philip, A. G. D., & Beavers, W. I. 1982, PASP, 94, 229

H. Huepa, A. Pani, and J. H. Peña: Observatorio Astrónomico Nacional de Tonantzintla, Universidad Nacional Autónoma de México, México.
J. H. Peña: Instituto de Astronomía, UNAM, Apdo. Postal 70-264, Ciudad de México, México (jhpena@astroscu.unam.mx).
A. Rentería and J. H. Peña: Facultad de Ciencias, Universidad Nacional Autónoma de México, México.

Revista Mexicana de Astronomía y Astrofísica, **55**, 231–235 (2019)

DOI: https://doi.org/10.22201/ia.01851101p.2019.55.02.11

GRAVITATIONAL WAVE ENHANCEMENT AS A TOOL TO DISTINGUISH DARK MATTER HALO PROFILES

Sergio Grijalva Castillo[1,2] and Carlos Calcáneo-Roldán[2]

Received November 29 2018; accepted June 5 2019

ABSTRACT

The recent success of the dark matter model has proven to be an invaluable tool for describing the formation, evolution and stability of galaxies. In this work we study the enhancement function, F, of the gravitational lensing of gravitational waves by galactic dark matter halos and show how this function may be used to distinguish between halo models. In particular we compare an isothermal sphere with an NFW type density distribution, both of which are assumed to be spherically symmetric, and find that our technique clearly distinguishes between the models.

RESUMEN

El éxito reciente del modelo de materia oscura ha probado ser una herramienta invaluable para describir la formación, evolución y estabilidad de galaxias. En este trabajo estudiamos la función de amplificación, F, del lente gravitacional de las ondas gravitacionales por halos galácticos de materia oscura y mostramos como esta función puede usarse para distinguir entre modelos de halos. En particular, comparamos una esfera isotérmica con una distribución de densidad tipo NFW, ambas asumidas esféricamente simétricas, y encontramos que esta técnica distingue claramente entre los modelos.

Key Words: dark matter — galaxies: halos — gravitational lensing — gravitational waves

1. GENERAL

Recent successes in gravitational wave detection, (Abbott et al. 2016), together with the well documented effect of gravitational lensing (GL) (Bate et al. 2018), have given strength to the idea of using general relativity to describe the gravitational field. One of the first complete treatments of the combination of these effects, i.e. the gravitational lensing of gravitational waves has been discussed by Schneider et al. (1992), it is from this source that we take most of our notation and the geometrical interpretation.

For this work we compare the amplitude ϕ of a gravitational wave when it propagates through a weak gravitational field $|U| << 1$ in a flat spacetime metric, see *e.g.* Schutz (2009):

$$ds^2 = -(1+2U)dt^2+(1-2U)(dx^2+dy^2+dz^2), \quad (1)$$

that is, a Minkowski spacetime plus a slight disturbance. The amplitude ϕ itself satisfies the wave equation (Peters 1974),

$$(\nabla^2 + \omega^2)\phi = 4\omega^2 U\phi; \quad (2)$$

while the deflection potential under the thin lens approximation is totally defined by its 2-dimensional lensing potential (Moylan et al. 2008),

$$\psi(\vec{x}) = 2\int U(\vec{x}, z)dz, \quad (3)$$

that lies between the source and the observer. This integral is carried out over the optical axis.

Due to the fact that we limit our analysis to the case in which the wave length, λ, of the gravitational wave is larger than the Schwarzschild radius of the thin lens, we must use wave optics instead of geometric optics, as in Takahashi (2004). In this framework, the change in the amplitude is quantified via the enhancement factor or complex amplification factor (Nakamura & Deguchi 1999):

$$F = \frac{\phi^L}{\phi}, \quad (4)$$

[1]Departamento de Investigación en Física, Universidad de Sonora, México.
[2]Departamento de Física, Universidad de Sonora, México.

where ϕ^L is the lensed wave amplitude and ϕ is the wave amplitude before lensing. We consider the magnitude of this function as a function of frequency ω and show that we can use it to distinguish between dark matter halo models.

In order to adjust our results to the frequency sensitivity of LIGO, we will limit our study to gravitational waves emitted by the source at around 200 Hz, or $\omega = 400\pi \frac{rad}{s}$ (Moylan et al. 2008).

If we wish to consider the cosmological effect on our results a further correction implies replacing ω with $\omega(1+z)$, as discussed by Yoo et al. (2007) and Takahashi & Nakamura (2003), which is beyond the scope of this particular study.

The paper is organized as follows, after this brief introduction, in § 2 we summarize the basic theory of lensing, such as the geometry involved and the related distances in this phenomenon, the wave optics related to the problem (such as the enhancement factor and the time delay). § 2.1 is a very short review on constructing the thin lens potential for a spherical isothermal matter distribution, while § 2.2 reviews the same for a Navarro, Frenk and White type halo, including a simple but very effective method to fix the gauge for time delay. We close with a discussion on the effectiveness of the method to distinguish between dark matter halo models.

2. THE ENHANCEMENT FACTOR AND HALO MODELS

We now turn our attention to the particular problem of quantifying the amount of enhancement due to our specific halo models. In each case the geometrical situation is that of a source of gravitational radiation far behind a galactic halo distribution (where the space-time is deformed) and an observer on the earth, which is itself at a great distance from the halo. Since the astronomical distances are so huge we use the thin lens approximation for the halo. The approximate lens geometry is illustrated in Figure 1.

The enhancement factor F discussed above is defined via Kirchhoff's diffraction integral, which is obtained in Schneider et al. (1992):

$$F(w,\eta) = \frac{D_s}{D_d D_{ds}} \int_{R^2} e^{iwt_d(\xi,\eta)} d^2\xi. \qquad (5)$$

Here, the function F is integrated in the lens plane, ξ is the impact parameter on the lens plane and η, the source displacement on the source plane. As defined in Schneider et al. (1992), t_d is known as the *Fermat potential* or more commonly the *time delay*, and carries the information of the lens potential:

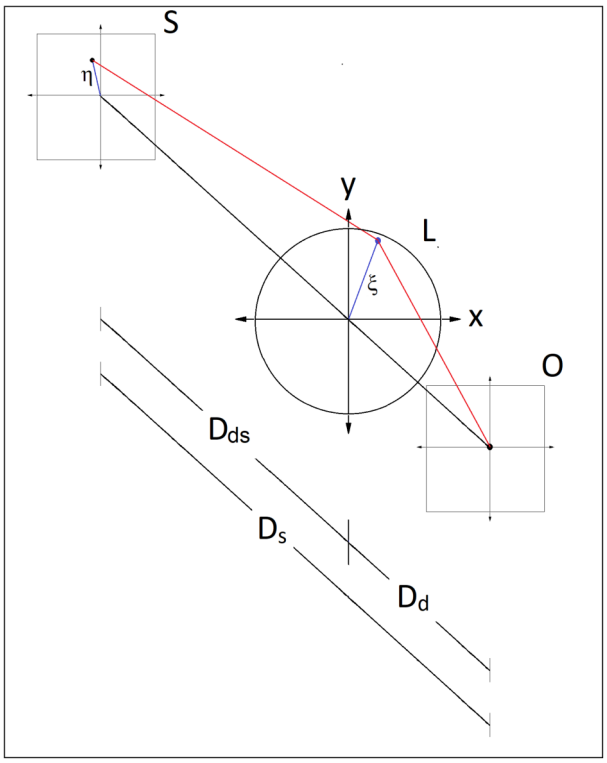

Fig. 1. The standard geometry for GL. A mass distribution located at D_d, a gravitational wave source located at D_s and the distance D_{ds} between lens and source; all measured from the observer. The color figure can be viewed online.

$$t_d(\xi,\eta) = \frac{D_d D_s}{2D_{ds}} \left(\frac{\xi}{D_d} - \frac{\eta}{D_s} \right)^2 - \hat{\psi}(\xi) + \hat{\phi}_m(y), \quad (6)$$

where $\hat{\psi}(\xi)$ is the deflection potential due to the dark matter halo (the thin lens potential) and $\hat{\phi}_m(\eta)$ is a gauge that must be chosen such that the minimal value of time delay is zero (Takahashi 2004). From this point on, it is more convenient to work with dimensionless quantities, so we introduce the following variable changes:

$$\boldsymbol{x} = \frac{\xi}{\xi_0},\ \boldsymbol{y} = \frac{D_d}{\xi_0 D_s}\eta,\ \boldsymbol{\omega} = \frac{D_s}{D_{ds} D_d}\xi_0^2 w,\ \mathbf{T} = \frac{D_d D_{ds}}{D_s \xi_0^2} t_d, \qquad (7)$$

as discussed in Takahashi (2004) and Nambu (2013); ξ_0 is a length scale that reduces to the Einstein radius on the lens plane). With these changes, the enhancement function becomes

$$F(\omega, y) = \frac{\omega}{2\pi i} \int_{x^2} e^{i\omega T(x,y)} dx^2, \qquad (8)$$

with the time delay

$$T(x,y) = \frac{1}{2}(x-y)^2 - \psi(x) + \phi_m(y), \qquad (9)$$

where

$$(\psi(x), \phi_m(y)) = \frac{D_L D_{LS}}{(D_S \xi_0^2)} (\hat{\psi}(\xi), \hat{\phi}_m(\eta)).$$

We can now explore different forms for the gravitational potential of the dark matter halo. The only assumption we make is that it has complete spherical symmetry. When this is the case, equation (8) becomes

$$F(w,y) = -iwe^{\frac{1}{2}iwy^2} \int_0^\infty x J_0(wxy) e^{iw[\frac{1}{2}x^2 - \psi(x) + \phi_m(y)]} dx, \qquad (10)$$

where J_0 is the Bessel Function of zeroth order.

To test weather our method can distinguish between halo models we will develop the enhancement function for two different mass distributions: a singular isothermal sphere (hereafter SIS) and one which reproduces the density distribution found in N-body dark matter simulations as discussed by Navarro et al. (1997, hereafter NFW).

2.1. *SIS Case*

The singular isothermal sphere is a very useful mass distribution model used for both stellar and galactic clusters as gravitational lenses. SISes are characterised by their surface mass density

$$\sum(\xi) = \frac{\sigma_v^2}{2\xi}, \qquad (11)$$

where ξ is a radial coordinate in the lens plane and σ_v is the velocity dispersion of the constituents of the halo. As Schneider et al. (1992) point out, this model was motivated to match the flat rotation curves of spiral galaxies for $\xi >> 1$, but breaks down for low values of ξ due to the divergence at $\xi = 0$. Using this density distribution we obtain the deflection potential, which can be found in Takahashi & Nakamura (2003):

$$\nabla_x^2 \psi(x) = \frac{2\Sigma(\xi)}{\Sigma_{cr}}, \qquad (12)$$

where Σ_{cr} is the critical surface mass density, as described by Bartelmann (1996).

This procedure leads to a thin lens potential, $\psi(x) = x$ and requires the additional phase, $\phi_m(y) = \frac{1}{2} + y$, such that the minimum of the time delay is zero. In Figure 2 we reproduce the results found by

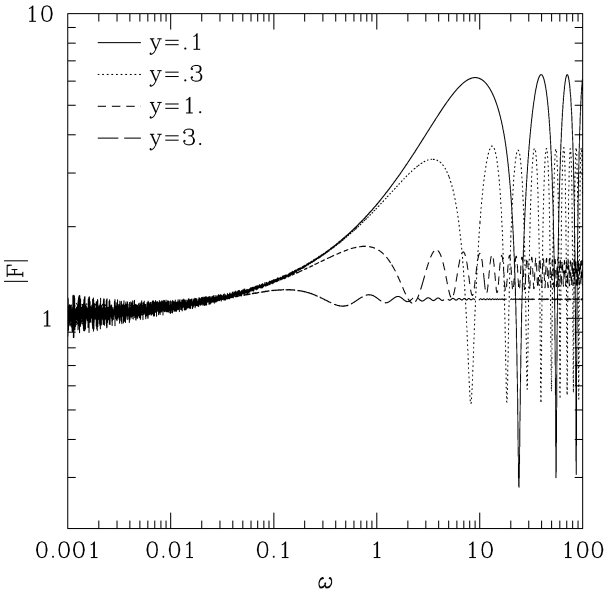

Fig. 2. Behavior of the enhancement factor $|F|$ vs frequency ω, the dimensionless frequency, given by $\boldsymbol{\omega} = \frac{D_s}{D_{ds} D_d} \xi_0^2 w$, where w its the original frequency of the source for the SIS thin lens.

Takahashi & Nakamura (2003) for the SIS matter distribution. There we have plotted the norm of the enhancement function, or *amplification factor*, $|F|$ as a function of frequency scaled to the Eisenstein radius, $\xi_0 \left(\boldsymbol{\omega} = \frac{D_s}{D_{ds} D_d} \xi_0^2 w\right)$.

As we can see, the closer the source is from the optic axis, the enhancement effect on the amplitude of the gravitational wave is more effective. For direct comparison, we take the same values chosen by Takahashi & Nakamura (2003) for the distance between source and lens, namely: $y = 0.1$, $y = 0.3$, $y = 1.0$ and $y = 3.0$. For low frequencies this enhancement factor is very low due to the diffraction effect (and we can also notice some noise due to our numerical method).

As the frequency increases, and for $y > 0.3$, we notice a considerable amount of dampening, in spite of the fact that no multiple images should form. These results allow us to calibrate our numerical procedure and motivate us to continue the study for other halo models.

2.2. *NFW Case*

One of the most successful density distributions found in high resolution N-body simulations is the NFW model (Navarro et al. 1997), which corresponds to a two-power density model:

$$\rho(r) = \frac{\rho_0}{(\frac{r}{a})(1+\frac{r}{a})^2}\,. \qquad (13)$$

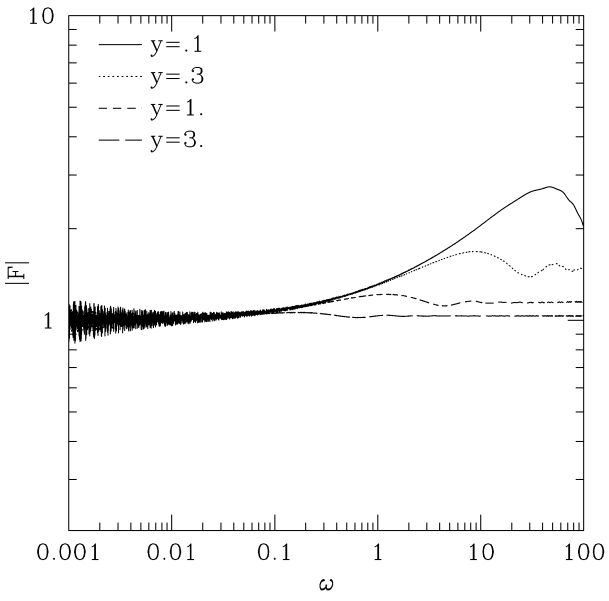

Fig. 3. Behavior of the enhancement factor $|F|$ vs frequency ω, the dimensionless frequency, given by $\boldsymbol{\omega} = \frac{D_s}{D_{ds}D_d}\xi_0^2 w$, where w is the original frequency of the source for the NFW thin lens.

Here a and ρ_0 are the pair of parameters that completely define the halo structure (and, as it turns out, ρ_0 is defined by the cosmology). Since we are interested in proving that our method may clearly distinguish between the models, we consider for this purpose the scaled radius $x = \frac{r}{a}$. Although the specific form of the density distribution for realistic dark matter halos is yet to be confirmed, this can be regarded as a good initial test for the purpose of our studies.

We will again use (12) to obtain the deflection potential, assuming that the lens surface mass density is completely defined by (13). In this way, we find the NFW potential, in accordance with Bartelmann (1996):

$$\psi(x) = \begin{cases} \frac{1}{2}\left[\left(\ln\frac{x}{2}\right)^2 - \left(\operatorname{arctanh}\sqrt{1-x^2}\right)^2\right], & x \leq 1. \\ \\ \frac{1}{2}\left[\left(\ln\frac{x}{2}\right)^2 + \left(\arctan\sqrt{x^2-1}\right)^2\right], & x \geq 1. \end{cases} \tag{14}$$

In order to obtain the time delay $T(x, y)$, we must first fix the phase, $\phi(y)$, such that the minimum of the time delay is zero. In contrast with the SIS case there is no simple algebraic means of doing the full calculation for arbitrary values of y; thus, we proceed to set the particular values that are of interest for this experiment ($y = 0.1$, $y = 0.3$, $y = 1.0$ and $y = 3.0$), and find the numerical value that makes zero the minimum of the time delay $T(x, y)$. Table 1 shows the particular values obtained for our selection of y.

TABLE 1

THE PARAMETER y^*

y	$\phi_m(y)$
0.1	0.0243401
0.3	0.0764808
1.0	0.288078
3.0	0.878223

*Which relates the axial distance from the source of gravitational waves and the corresponding values of $\phi_m(y)$ needed for the minimum of the time delay $T(x, y)$ to be zero.

Using these values for $\phi_m(y)$, we may now evaluate the diffraction integral (10) for the NFW model in the same way as before. Our results are shown in Figure 3, where we maintain the same frequency and enhancement range for a direct comparison.

For the NFW model we can appreciate, as in the SIS case, that the amplification in the wave amplitude starts at around $\boldsymbol{\omega} = 0.1$. We notice that there is a clear difference between the models. For NFW type halos, the enhancement is less noticeable and there are fewer oscillations. We also notice considerable more dampening in this case. To confirm this behavior we plot, in Figure 4 the enhancement in a frequency range $0.01 < \boldsymbol{\omega} < 1000$. Here we can clearly see a more dramatic dampening behavior for the NFW model. We also notice that the amplification factor is always $|F| > 1$, which only happens in this model. This implies that the interference between lensed gravitational waves is always constructive.

3. CONCLUSIONS

In this paper we have shown that a detailed study using more realistic dark matter halos could provide a distinct signal for gravitational wave enhancement.

This result shows that we may use gravitational lensing of gravitational waves as a further probe for the dark matter structure in observed galaxies (or clusters of galaxies). When we compare the enhancement factor for this type of radiation, the more concentrated NFW profile can lead to a factor of up to 50%, when compared with lensing by a SIS type halo.

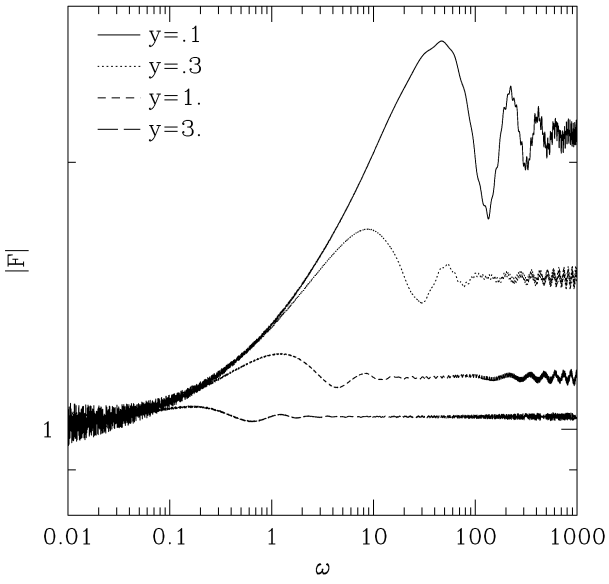

Fig. 4. As in Figure 3, with modified ranges in frequency, $\boldsymbol{\omega}$, and amplification factor, $|F|$, to show the distinct behavior of the NFW model.

For this reason we propose the following observation: if we find suitable gravitational wave sources (GWS) far from any galactic field we could compare the amplitude of this radiation with the amplitude of similar sources found behind galaxy clusters. If we were able to find a sufficiently numerous population of GWS, we could compare these populations and find an empirical enhancement factor. This in turn would allow us to fine tune dark matter halo parameters.

As it is early days for GWS detection, we will continue to study the behavior of this radiation in the hope of finding further signals that may be measured as more and more data become available.

Sergio Grijalva Castillo acknowledges the generous support of CONACyT through a grant for postgraduate training. Numerical work for this project was carried out using facilities of the Fundamental Physics group at the Universidad de Sonora which are partially supported by a grant from the División de Ciencias Exactas y Naturales of the Universidad de Sonora, Grant no: USO315001752.

REFERENCES

Abbott, B. P., Abbott, R., Abbott, T. D., et al. 2016, PhRvL, 116, 061102
Bartelmann, M. 1996, A&A, 313, 697
Bate, N. F., Vernardos, G., O'Dowd, M. J., et al. 2018, MNRAS, 479, 4796
Moylan, A. J., McClelland, D. E., Scott, S. M., Searle, A. C., & Bicknell, G. V. 2008, The Eleventh Marcel Grossmann Meeting On Recent Developments in Theoretical and Experimental General Relativity, Gravitation and Relativistic Field Theories, ed. H. Kleinert, R. T. Jantzen, & R. Ruffini (World Scientific Publishing), 807
Nakamura, T. T. & Deguchi, S. 1999, PThPS, 133, 137
Nambu, Y. 2013, IJAA, 3, 1
Navarro, J. F., Frenk, C. S., & White, S. D. M. 1997, ApJ, 490, 493
Peters, P. C. 1974, PhRvD, 9, 2207
Schneider, P., Ehlers, J., & Falco, E. E. 1992, Gravitational Lenses (Berlin, Heidelberg, New York, NY: Springer-Verlag)
Schutz, B. 2009, A First Course in General Relativity, (Cambridge, MA: CUP)
Takahashi, R. 2004, A&A, 423, 787
Takahashi, R. & Nakamura, T. 2003, ApJ, 595, 1039
Yoo, C.-M., Nakao, K.-i., Kozaki, H., & Takahashi, R. 2007, ApJ, 655, 691

Sergio Grijalva Castillo: Departamento de Investigación en Física, Universidad de Sonora, Rosales y Boulevard Luis Encinas S/N, Hermosillo, Sonora, 83000 México (sergio.grijalva@fisica.uson.mx).
Sergio Grijalva Castillo and Carlos Calcáneo-Roldán: Departamento de Física, Universidad de Sonora, Rosales y Boulevard Luis Encinas S/N, Hermosillo, Sonora, 83000 México (carlos.calcaneo@fisica.uson.mx).

Revista Mexicana de Astronomía y Astrofísica, **55**, 237–254 (2019)

DOI: https://doi.org/10.22201/ia.01851101p.2019.55.02.12

DYNAMICS OF CLUSTERS OF GALAXIES WITH EXTENDED $F(\chi)$ GRAVITY

Tula Bernal[1], Oliver López-Corona[2,3], and Sergio Mendoza[2]

Received October 2 2017; accepted June 14 2019

ABSTRACT

In this article, we present the results of a fourth order perturbation analysis of the metric theory of gravity $f(\chi) = \chi^{3/2}$, with χ a suitable dimensionless Ricci scalar. Such a model corresponds to a specific $f(R)$ metric theory of gravity, where the mass of the system is included in the gravitational field's action. In previous works we have shown that, up to the second order in perturbations, this theory reproduces the flat rotation curves of galaxies and the details of the gravitational lensing in individual, groups, and clusters of galaxies. Here, leaving fixed the results from our previous works, we show that the theory reproduces the dynamical masses of 12 *Chandra* X-ray galaxy clusters, without the need of dark matter, through the metric coefficients up to the fourth order of approximation. In this sense, we calculate the first relativistic correction of the $f(\chi)$ metric theory and apply it to fit the dynamical masses of clusters of galaxies.

RESUMEN

En este artículo presentamos los resultados del análisis de perturbaciones al cuarto orden de la teoría métrica de gravedad $f(\chi) = \chi^{3/2}$, donde χ es un escalar de Ricci adimensional. Dicho modelo corresponde a una teoría métrica $f(R)$ en la que la masa del sistema está incluida en la acción del campo gravitacional. En trabajos previos hemos mostrado que, hasta el segundo orden de perturbaciones, la teoría reproduce las curvas de rotación planas de galaxias y los detalles de lentes gravitacionales en galaxias, grupos y cúmulos de galaxias. Aquí, dejando fijos los resultados de nuestros trabajos anteriores, mostramos que la teoría reproduce las masas dinámicas de 12 cúmulos de galaxias del Observatorio *Chandra* de rayos X, sin materia oscura, a partir de los coeficientes métricos al cuarto orden de aproximación. En este sentido, calculamos la primera corrección relativista de la teoría métrica $f(\chi)$ y la aplicamos para ajustar las masas dinámicas de los cúmulos de galaxias.

Key Words: dark matter — gravitation — galaxies: clusters: general — X-rays: galaxies: clusters

1. INTRODUCTION

From recent observations of the European space mission *Planck*, the contribution of the baryonic matter to the total matter–energy density of the Universe was inferred to be only $\approx 5\%$, while the dark sector constitutes $\approx 95\%$, of which $\approx 26\%$ is dark matter (DM) and $\approx 69\%$ is dark energy (DE), or a positive cosmological constant Λ (Planck Collaboration et al. 2016). The observations of type Ia supernovae, the anisotropies observed in the cosmic microwave background, the acoustic oscillations in the baryonic matter, the power–law spectrum of galaxies, among others, represent strong evidences for the standard cosmological model, the so–called ΛCDM *concordance model*.

The DM component was postulated in order to explain the observed rotation curves of spiral galaxies, as well as the mass-to-light ratios in giant galaxies and clusters of galaxies (Zwicky 1933, 1937; Smith 1936; Rubin 1983), the observed gravitational lenses and the structure formation in the early Universe, among other astrophysical and cosmological phe-

[1]Universidad Autónoma Chapingo.
[2]Instituto de Astronomía, Universidad Nacional Autónoma de México.
[3]Centro de Ciencias de la Complejidad, Universidad Nacional Autónoma de México.

nomena (see e.g. Bertone et al. 2005; Bennett et al. 2013). On the other hand, the DE or Λ has been postulated in order to explain the accelerated expansion of the Universe (Perlmutter et al. 1999). The ΛCDM model fits quite well most of these observations. However, direct or indirect searches of candidates to DM have yielded null results. In addition, the lack of any further evidence for DE opens up the possibility to postulate that there are no dark entities in the Universe, but instead, the theory associated to these astrophysical and cosmological phenomena needs to be modified.

Current models of DM and DE are based on the assumption that Newtonian gravity and Einstein's general relativity (GR) are valid at all scales. However, their validity has only been verified with high-precision for systems with mass to size ratios of the order or greater that those of the Solar System. In that sense, it is conceivable that both the accelerated expansion of the Universe and the stronger gravitational force required in different systems represent a change in our understanding of gravitational interactions.

Moreover, from the geometrical point of view, theories of modified gravity are viable alternatives to solve the astrophysical and cosmological problems that DM and DE are trying to solve (see e.g. Schimming & Schmidt 2004; Nojiri & Odintsov 2011a; Capozziello & Faraoni 2011; Nojiri et al. 2017). In this sense, any theory of modified gravity that attempts to supplant the DM of the Universe, must account for two crucial observations: the dynamics observed for massive particles and the observations of the deflection of light for massless particles.

The first non-relativistic modification, proposed to fit the rotation curves and the Tully-Fisher relation observed in galaxies, was the Modified Newtonian Dynamics (MOND) (Milgrom 1983b,a). Due to its phenomenological nature and its success in reproducing the rotation curves of disc galaxies (see Famaey & McGaugh 2012, for a review), it is understood that any fundamental theory of modified gravity should adapt to it on galactic scales in the low accelerations regime. However, from the study of groups and clusters of galaxies it has been shown that, even in the deep MOND regime, a dominant DM component is still required in these systems (60 to 80% of the dynamical or virial mass). The central region of galaxy clusters could be explained with a halo of neutrinos with 2 eV mass (which is about the upper experimental limit), but on the scale of groups of galaxies, the central contribution cannot be explained by a contribution of neutrinos with the same mass (Angus et al. 2008). Moreover, the Lagrangian formulation of MOND/AQUAL (Bekenstein & Milgrom 1984), is not able to reproduce the observed gravitational lensing for different systems (see e.g. Takahashi & Chiba 2007; Natarajan & Zhao 2008), mainly because it is not a relativistic theory and, as such, it cannot explain gravitational lensing and cosmological phenomena, which require a relativistic theory of gravity.

Through the years, there have been some attempts to find a correct relativistic extension of MOND. The first one was proposed by Bekenstein (2004), with a Tensor-Vector-Scalar (TeVeS) theory. This approach presents some cumbersome mathematical complications and it cannot reproduce crucial astrophysical phenomena (see e.g. Ferreras et al. 2009). Later, Bertolami et al. (2007) showed that for a particular generalization of the $f(R)$ metric theories, with R the Ricci scalar, by coupling the $f(R)$ function with the Lagrangian density of matter $\mathcal{L}_m$, an extra force arises, which in the weak field limit can be connected with MOND's acceleration and can explain the Pioneer anomaly. Also, Bernal et al. (2011b) showed that from the weak field limit of a particular $f(\chi)$ metric theory, with χ a dimensionless Ricci scalar, it is possible to recover the MONDian behavior in the metric formalism, as explained below. Another relativistic version of MOND recovers, in an empirical way, the MONDian limit through modifications to the energy-momentum tensor (Demir & Karahan 2014). Barrientos & Mendoza (2016) obtained the MONDian acceleration from an $f(\chi)$ theory in the Palatini formalism. In Barrientos & Mendoza (2017), MOND's acceleration was obtained from an $f(R)$ metric theory of gravity with torsion. And more recently, Barrientos & Mendoza (2018) showed that MOND's acceleration can be obtained in the weak field limit of a metric $F(R, \mathcal{L}_m)$ theory with a curvature-matter coupling.

In this article we focus on the $f(\chi)$ theories in the metric formalism, proposed in Bernal et al. (2011b), where the dimensionless Ricci scalar χ is constructed by introducing a fundamental constant of nature with dimensions of acceleration of order $\approx 10^{-10}\,\mathrm{m/s^2}$. Through the inclusion of the mass of the system into the gravitational field's action, the authors showed that the $f(\chi) = \chi^{3/2}$ metric theory is equivalent to the MONDian description in the non-relativistic limit for some systems, e.g. for those with spherical symmetry, but with remarkable advantages. From the second order perturbation analysis, this metric theory accounts in detail for two observational facts. First, it is possible to recover the

phenomenology of flat rotation curves and the baryonic Tully-Fisher relation of galaxies, i.e. a MOND-like weak field limit. Second, this construction also reproduces the details of observations of gravitational lensing in individual, groups, and clusters of galaxies, without the need of any DM component (Mendoza et al. 2013). At the same second order also, the theory is coherent with a parametrized post-Newtonian description (PPN) where the parameter $\gamma = 1$ (Mendoza & Olmo 2015).

The $f(\chi)$ metric theories are an extension of the $f(R)$ metric gravity, which has been extensively studied as an alternative to DM and DE (see e.g. Sotiriou & Faraoni 2010; De Felice & Tsujikawa 2010; Capozziello & Faraoni 2011; Nojiri & Odintsov 2011a). In cosmology, it has been shown that $f(R)$ metric theories can account for the accelerated expansion of the Universe, as well as for an inflationary era, e.g. for $f(R) = R+\alpha R^2$ (Starobinsky 1980), where α is a coupling constant. Moreover, there are models for unification of DE and inflation, or DE and DM (see e.g. Nojiri & Odintsov 2011; Nojiri et al. 2017).

As shown in Carranza et al. (2013), an $f(\chi)$ description of gravity can be understood as a particular $F(R,T)$ theory (Harko et al. 2011), where the gravitational action is an arbitrary function of the Ricci scalar and the trace of the energy-momentum tensor T. Within the $F(R,T)$ description, Harko et al. (2011) have shown that, through the choice of suitable $F(T)$ functions, it is possible to obtain arbitrary FLRW universes, and that the model is equivalent to having an effective cosmological constant. For the particular $f(\chi) = \chi^{3/2}$ metric theory used here, Carranza et al. (2013) have shown that the model can fit data of type Ia supernovae with a dust FLRW Universe, showing that the accelerated expansion of the Universe at late times ($\chi \approx 1$) could be explained by an extended theory of gravity deviating from GR at cosmological scales.

In general, both descriptions result in field equations that depend on the mass of the source, except for the particular case $f(\chi) = \chi$, where GR is recovered. This scenario presents even more richness than standard $f(R)$ theories, because of the matter-geometry coupling, since it is possible to reconstruct diverse cosmological evolution by choosing different functions for the trace of the stress-energy tensor. Further research on the cosmological implications of $f(\chi)$ theories must be done in order to accept or discard models trying to replace the DM, or the DM and the DE of the Universe.

In the present work, we extend the perturbation analysis developed in Mendoza et al. (2013) for $f(\chi) = \chi^{3/2}$ in the metric formalism in powers of v/c (where v is the velocity of the components of the system and c is the speed of light), up to the fourth order of the theory, and focus on applications to clusters of galaxies. As shown in Sadeh et al. (2015) and first hypothesized in Wojtak et al. (2011), there exist observational relativistic effects of the velocity of galaxies at the edge of galaxy clusters, showing a difference of the inferred background potential with the galaxy's inferred potential. With this motivation in mind, we have calculated the fourth order relativistic corrections and shown that they can fit the observations of the dynamical masses of 12 *Chandra* X-ray clusters of galaxies from Vikhlinin et al. (2006).

The article is organized as follows: In § 2, the weak field limit for a static spherically symmetric metric of any theory of gravity is established and we define the orders of perturbation to be used throughout the article. In § 3, we show the particular metric theory to be tested with astronomical observations. The results from the perturbation theory for the vacuum field equations, up to the fourth order in perturbations, are presented. With these results, we obtain the gravitational acceleration generated by a point-mass source and its generalization to extended systems, particularly for applications to clusters of galaxies. In § 6, we establish the calibration method to fit the free parameters for the metric coefficients, from the observations of the dynamical masses of 12 *Chandra* X-ray clusters of galaxies. Finally, in § 7, we show the results and the discussion.

2. PERTURBATIONS IN SPHERICAL SYMMETRY

In this section, we define the relevant properties of the perturbation analysis for applications to any relativistic theory of gravity. Einstein's summation convention over repeated indices is used. Greek indices take values $0, 1, 2, 3$ and Latin ones $1, 2, 3$. In spherical coordinates $(x^0, x^1, x^2, x^3) = (ct, r, \theta, \varphi)$, with t the time coordinate and r the radial one, θ and φ the polar and azimuthal angles respectively; the angular displacement is $\mathrm{d}\Omega^2 := \mathrm{d}\theta^2 + \sin^2\theta\,\mathrm{d}\varphi^2$. We use a $(+,-,-,-)$ signature for the metric of the space-time.

Let us consider a fixed point-mass M at the center of coordinates; in this case, the static, spherically symmetric metric $g_{\mu\nu}$ is generated by the interval

$$\mathrm{d}s^2 = g_{\mu\nu}\mathrm{d}x^\mu \mathrm{d}x^\nu = g_{00}\,c^2\mathrm{d}t^2 + g_{11}\mathrm{d}r^2 - r^2\mathrm{d}\Omega^2, \quad (1)$$

where, due to the symmetry of the problem, the unknown functions g_{00} and g_{11} are functions of the radial coordinate r only.

The geodesic equations are given by

$$\frac{\mathrm{d}^2x^\alpha}{\mathrm{d}s^2} + \Gamma^\alpha_{\mu\nu}\frac{\mathrm{d}x^\mu}{\mathrm{d}s}\frac{\mathrm{d}x^\nu}{\mathrm{d}s} = 0\,, \tag{2}$$

where $\Gamma^\alpha_{\mu\nu}$ are the Christoffel symbols. In the weak field limit, when the speed of light $c \to \infty$, $\mathrm{d}s = c\ \mathrm{d}t$, and since the velocity $v \ll c$, then each component $v^i \ll \mathrm{d}x^0/\mathrm{d}t$, with $v^i := (\mathrm{d}r/\mathrm{d}t,\ r\,\mathrm{d}\theta/\mathrm{d}t,\ r\sin\theta\,\mathrm{d}\varphi/\mathrm{d}t)$. In this case, the radial component of the geodesic equations (2), for the interval (1), is given by

$$\frac{1}{c^2}\frac{\mathrm{d}^2r}{\mathrm{d}t^2} = -\frac{1}{2}g^{11}g_{00,r}\,, \tag{3}$$

where the subscript $(\ )_{,r} := \mathrm{d}/\mathrm{d}r$ denotes the derivative with respect to the radial coordinate r. In this limit, a particle bounded to a circular orbit around the mass M experiences the radial acceleration given by equation (3), such that

$$|\boldsymbol{a}_c| = \frac{v^2}{r} = \frac{c^2}{2}g^{11}g_{00,r} \tag{4}$$

for a circular or tangential velocity v. At this point, it is important to note that the last equation is a general kinematic relation, and does not introduce any particular assumption about the specific gravitational theory. In other words, it is completely independent of the field equations associated to the structure of space-time produced by the energy-momentum tensor.

In the weak field limit of the theory, the metric coefficients take the following form (see e.g. Landau & Lifshitz 1975):

$$g_{00} \;=\; 1 + \frac{2\phi}{c^2}, \qquad g_{11} = -1 + \frac{2\psi}{c^2}, \tag{5}$$

for the Newtonian gravitational potential ϕ and an extra gravitational potential ψ. As extensively described in Will (1993, 2006), when working in the weak field limit of a relativistic theory of gravity, the dynamics of massive particles determines the functional form of the time-time component g_{00} of the metric, while the deflection of light determines the form of the radial g_{11}. At the weakest order of the theory, the motion of material particles is described by the potential ϕ, taking $\psi = 0$ (Landau & Lifshitz 1975). The motion of relativistic massless particles is described by taking into consideration not only the second order corrections to the potential ϕ, but also the same order in perturbations of the potential ψ (Will 1993).

For circular motion about a mass M in the weak field limit of the theory, the equations of motion are obtained when the left-hand side of equation (3) is of order v^2/c^2 and when the right-hand side is of order ϕ/c^2. Both are orders $\mathcal{O}(c^{-2})$ of the theory, or simply $\mathcal{O}(2)$. When lower or higher order corrections of the theory are introduced, we use the notation $\mathcal{O}(n)$ for $n = 0, 1, 2, \ldots$ meaning $\mathcal{O}(c^0)$, $\mathcal{O}(c^{-1})$, $\mathcal{O}(c^{-2}), \ldots$, respectively.

Now, the extended regions of clusters of galaxies need a huge amount of DM to explain the observed velocity dispersions of stars and gas in those systems. In the outer regions, the velocity dispersions are typically of order $10^{-4} - 10^{-3}$ times the speed of light. Hence, the Newtonian physics given by an $\mathcal{O}(2)$ approximation might be extended to post-Newtonian $\mathcal{O}(4)$ corrections or, equivalently in our model, "post-MONDian" physics.

In order to test a gravitational theory through different astrophysical observations (e.g. the motion of material particles, the bending of light-massless particles, etc.), the metric tensor $g_{\mu\nu}$ is expanded about the flat Minkowski metric $\eta_{\mu\nu}$, for corrections $h_{\mu\nu} \ll \eta_{\mu\nu}$, in the following way:

$$g_{\mu\nu} = \eta_{\mu\nu} + h_{\mu\nu}. \tag{6}$$

The metric $g_{\mu\nu}$ is approximated up to second perturbation order $\mathcal{O}(2)$ for the time and radial components and up to zeroth order for the angular components, in accordance with the spherical symmetry of the problem. At this lowest perturbation order, Mendoza et al. (2013) found the time $g^{(2)}_{00}$ and radial $g^{(2)}_{11}$ metric components, for the $f(\chi) = \chi^{3/2}$ metric theory of gravity. These metric values are necessary to compare with the astrophysical observations of motion of material particles and of photons through gravitational lensing (Will 1993, 2006). In fact, through the observations of the rotation curves of galaxies and the Tully-Fisher relation and the details of the gravitational lensing in individual, groups and clusters of galaxies, Mendoza et al. (2013) fixed the unknown potentials ϕ and ψ of the theory.

In this paper, we develop perturbations of the relativistic extended model $f(\chi) = \chi^{3/2}$ up to the fourth order in the time-time metric component, $g^{(4)}_{00}$, corresponding to the next order of approximation, to describe the motion of massive particles (Will 1993). In this case, the metric components can

be written as

$$g_{00} = 1 + g_{00}^{(2)} + g_{00}^{(4)} + \mathcal{O}(6), \quad (7)$$

$$g_{11} = -1 + g_{11}^{(2)} + \mathcal{O}(4). \quad (8)$$

In other words, the metric is written up to the fourth order in the time component and up to the second order in the radial one. The contravariant metric components of the previous set of equations are given by

$$g^{00} = 1 - g_{00}^{(2)} - g_{00}^{(4)} + \mathcal{O}(6), \quad (9)$$

$$g^{11} = -1 - g_{11}^{(2)} + \mathcal{O}(4). \quad (10)$$

3. EXTENDED $F(\chi)$ METRIC THEORIES

3.1. *Field Equations*

The $f(\chi)$ metric theories, proposed in Bernal et al. (2011b), are constructed through the inclusion of MOND's acceleration scale a_0 (Milgrom 1983 a,b) as a fundamental physical constant that has been shown to be of astrophysical and cosmological relevance (see e.g. Bernal et al. 2011a; Carranza et al. 2013; Mendoza et al. 2011; Mendoza 2012; Hernandez et al. 2010, 2012; Hernandez & Jiménez 2012; Mendoza et al. 2013; Mendoza & Olmo 2015; Mendoza 2015).

The action $S_{\rm f}$ for metric theories of gravity, rewritten with correct dimensional quantities for a mass M generating the gravitational field, is given by (Bernal et al. 2011b)

$$S_{\rm f} = -\frac{c^3}{16\pi G}\int \frac{f(\chi)}{L_M^2}\sqrt{-g}\,{\rm d}^4x\,, \quad (11)$$

where G represents Newton's gravitational constant, for any arbitrary function $f(\chi)$ of the dimensionless Ricci scalar χ:

$$\chi := L_M^2 R; \quad (12)$$

$$L_M := \zeta\left(r_{\rm g} l_M\right)^{1/2}, \quad (13)$$

where L_M is a length-scale depending on the gravitational radius $r_{\rm g}$ and the mass-length scale l_M of the system, given by (Mendoza et al. 2011)

$$r_{\rm g} := \frac{GM}{c^2}, \qquad l_M := \left(\frac{GM}{a_0}\right)^{1/2}, \quad (14)$$

with $a_0 = 1.2\times10^{-10}\,{\rm m/s^2}$ the MOND's acceleration constant (see e.g. Famaey & McGaugh 2012, and references therein) and ζ is a coupling constant of order one calibrated through astrophysical observations.

The matter action takes its ordinary form

$$S_{\rm m} = -\frac{1}{2c}\int \mathcal{L}_{\rm m}\sqrt{-g}\,{\rm d}^4x\,, \quad (15)$$

with $\mathcal{L}_{\rm m}$ the Lagrangian matter density of the system.

Equation (11) is a particular case of a full gravity-field action formulation in which the details of the mass distribution appear inside the gravitational action through L_M, except for $f(\chi) = \chi$, where the Hilbert-Einstein action is recovered. For the particular case of spherical symmetry, the mass inside action (11) becomes the mass of the central object generating the gravitational field. It is also expected that for systems with a high degree of symmetry, the mass M is related to the trace of the energy-momentum tensor T through the standard definition

$$M := (4\pi/c^2)\int Tr^2{\rm d}r. \quad (16)$$

In what follows, we work with $f(\chi)$ theories in the metric formalism. Note that a metric-affine formalism can also be taken into account (see e.g. Barrientos & Mendoza 2016).

Now, the null variation of the complete action, i.e. $\delta\left(S_{\rm f} + S_{\rm m}\right) = 0$, with respect to the metric tensor $g_{\mu\nu}$, yields the following field equations:

$$f'(\chi)\chi_{\mu\nu} - \frac{1}{2}f(\chi)g_{\mu\nu} - L_M^2\left(\nabla_\mu\nabla_\nu - g_{\mu\nu}\Delta\right)f'(\chi) = \frac{8\pi G L_M^2}{c^4}T_{\mu\nu}, \quad (17)$$

where the prime denotes the derivative with respect to the argument, the Laplace-Beltrami operator is $\Delta := \nabla^\mu\nabla_\mu$ and the energy-momentum tensor $T_{\mu\nu}$ is defined through the standard relation $\delta\mathcal{L}_{\rm m} = -(1/2c)T_{\alpha\beta}\delta g^{\alpha\beta}$. Also, in equation (17), the dimensionless Ricci tensor is defined as

$$\chi_{\mu\nu} := L_M^2 R_{\mu\nu}\,, \quad (18)$$

where $R_{\mu\nu}$ is the standard Ricci tensor. The trace of equations (17) is given by

$$f'(\chi)\,\chi - 2f(\chi) + 3L_M^2\,\Delta f'(\chi) = \frac{8\pi G L_M^2}{c^4}T\,, \quad (19)$$

where $T := T^\alpha{}_\alpha$.

Bernal et al. (2011b) and Mendoza et al. (2013) have shown that the function $f(\chi)$ must satisfy the following limits:

$$f(\chi) = \begin{cases}\chi, & \text{when } \chi \gg 1 \text{ (General relativity)},\\ \chi^{3/2}, & \text{when } \chi \ll 1 \text{ (Relativistic MOND)},\end{cases} \quad (20)$$

in order to recover Einstein's GR in the limit $\chi \gg 1$ and a relativistic version of MOND in the regime $\chi \ll 1$.

Now, a complete extended cosmological model without the introduction of any DM and/or DE components should explain several cosmological observations, e.g. the cosmic microwave background, large scale structure formation, baryonic acoustic oscillations, etc. However, when mass-energy to scale ratios reach sufficiently large numbers, of the order or greater than the ones associated to the Solar System, then GR must be the correct theory to describe them. In this direction, Mendoza (2012) has proposed a "transition function" between both regimes, GR and "relativistic MOND", to describe the complete cosmological evolution:

$$f(\chi) = \chi^{3/2}\frac{1 \pm \chi^{1+p}}{1 \pm \chi^{3/2+p}} \to \begin{cases} \chi^{3/2}, & \text{for} \quad \chi \ll 1, \\ \chi, & \text{for} \quad \chi \gg 1. \end{cases} \tag{21}$$

For this function, GR is recovered when $\chi \gg 1$ in the strong field regime and the relativistic version of MOND is recovered when $\chi \ll 1$ in the weak field limit. Some observations suggest an abrupt transition between both limits of function (20) (see Mendoza et al. 2013; Hernandez et al. 2013; Mendoza 2015), meaning that it might be possible to choose the following step function to describe the evolution of the Universe:

$$f(\chi) = \begin{cases} \chi^{3/2}, & \text{for} \quad \chi \leq 1, \\ \chi, & \text{for} \quad \chi \geq 1. \end{cases} \tag{22}$$

However, in this work we are interested in the regime where GR should be modified, which in our case corresponds to the relativistic regime of MOND, assuming that where GR works well there should not be a modification. Thus, in the following, we work in the limit $\chi \ll 1$ only.

Note that the "transition functions" (21) and (22) converge to GR at very early cosmic times, when inflation should dominate the behavior of the Universe. This can be thought of as a correct limit by including an inflaton field for the exponential expansion of the Universe, or one can think that at the very early epochs the $f(\chi)$ function should be proportional to the square of the Ricci scalar in such a way that a Starobinsky (1980) exponential expansion is reached (see also Nojiri et al. 2017).

3.2. *Relativistic MOND ($\chi \ll 1$)*

For the case $\chi \ll 1$, the first two terms on the left-hand side of equation (19) are much smaller than the third one, i.e. $f'(\chi)\,\chi - 2f(\chi) \ll 3L_M^2\,\Delta f'(\chi)$, at all orders of approximation (Bernal et al. 2011b). This fact means that the trace (19) can be written as

$$3L_M^2 \Delta f'(\chi) = \frac{8\pi G L_M^2}{c^4} T. \tag{23}$$

For the field produced by a point mass M, the right-hand side of last equation (23) is null far from the source, and so the last relation in vacuum at all perturbation orders can be rewritten as

$$\Delta f'(\chi) = 0. \tag{24}$$

Now, as a simple case of study, we assume a power-law form for the function $f(\chi)$:

$$f(\chi) = \chi^b, \tag{25}$$

for a real power b. In this case, relation (24) is equivalent to

$$\Delta f'(R) = 0, \tag{26}$$

at all orders of approximation for a power-law function of the Ricci scalar

$$f(R) = R^b. \tag{27}$$

Substitution of function (25) into the null variations of the gravitational field's action (11) in vacuum leads to

$$\delta S_{\rm f} = -\frac{c^3}{16\pi G} L_M^{2(b-1)} \delta \int R^b \sqrt{-g}\, {\rm d}^4x = 0\,, \tag{28}$$

and so

$$\delta \int R^b \sqrt{-g}\, {\rm d}^4x = 0\,. \tag{29}$$

From the last relation, we can see that the same field equations in vacuum are obtained for a power-law function (25) in the $f(\chi)$ theory, as well as for a standard power-law $f(R)$ metric theory (27), but with the important restriction (26) needed to yield the correct relativistic extension of MOND ($\chi \ll 1$ limit). Mendoza et al. (2013) showed that this condition is crucial to describe the details observed for gravitational lensing for individuals, groups and clusters of galaxies, and differs from the results obtained in Capozziello et al. (2007), for a standard $f(R)$ power-law description in vacuum. As discussed in Mendoza et al. (2013), such a discrepancy occurs from the sign convention used in the definition of the Riemann tensor, giving two different choices of signature that effectively bifurcate on the solution space, a property which does not appear in Einstein's general relativity. This is due to higher order

derivatives with respect to the metric tensor that appear in metric theories of gravity (cf. equations (17) and (19)). Following the results in Mendoza et al. (2013), we use the same definition of Riemann's tensor sign and the branch of solutions that recover the correct weak field limit of the theory, in order to explain the rotation curves of spiral galaxies based on the Tully-Fisher relation, and the gravitational lensing observed at the outer regions of groups and clusters of galaxies, within the point-mass description.

Given the equivalence of the power-law $f(\chi)$ models with the standard $f(R)$ metric theories, the standard perturbation analysis for $f(R)$ theories constrained by equation (26) is developed for the power-law description of gravity (25) in the weak field limit, and for the first-order MOND-like relativistic correction in Mendoza et al. (2013). In this case, the standard field equations (17) reduce to (see e.g. Capozziello & Faraoni 2011)

$$f'(R)R_{\mu\nu} - \frac{1}{2}f(R)g_{\mu\nu} + \mathcal{H}_{\mu\nu} = 0\,, \qquad (30)$$

where the fourth-order terms are grouped into $\mathcal{H}_{\mu\nu} := -\left(\nabla_\mu\nabla_\nu - g_{\mu\nu}\Delta\right) f'(R)$. The trace of equation (30) is given by

$$f'(R)R - 2f(R) + \mathcal{H} = 0\,, \qquad (31)$$

with $\mathcal{H} := \mathcal{H}_{\mu\nu}g^{\mu\nu} = 3\Delta f'(R)$.

For the case of the static spherically symmetric space-time (1), it follows that

$$\begin{aligned}\mathcal{H}_{\mu\nu} =& -f''\Big\{R_{,\mu\nu} - \Gamma^1_{\mu\nu}R_{,r} \\ & -g_{\mu\nu}\left[\left(g^{11}_{,r} + g^{11}\left(\ln\sqrt{-g}\right)_{,r}\right)R_{,r} + g^{11}R_{,rr}\right]\Big\} \\ & -f'''\left(R_{,\mu}R_{,\nu} - g_{\mu\nu}g^{11}R_{,r}{}^2\right); \end{aligned} \qquad (32)$$

and the trace

$$\begin{aligned}\mathcal{H} \;=\; & 3f''\left[\left(g^{11}_{,r} + g^{11}\left(\ln\sqrt{-g}\right)_{,r}\right)R_{,r} + g^{11}R_{,rr}\right] \\ & +3f'''g^{11}R_{,r}{}^2\,. \end{aligned} \qquad (33)$$

4. PERTURBATION THEORY

In this subsection, we present the perturbation analysis for $f(\chi)$ metric theories. Perturbations applied to metric theories of gravity, including GR, are extensively detailed in the monograph by Will (1993). In particular, for $f(R)$ metric theories, Capozziello & Stabile (2009) have developed a second order perturbation analysis and applied it to lenses and clusters of galaxies (Capozziello et al. 2009).

The general field equations (30)-(31) are of fourth order in the derivatives of the metric tensor $g_{\mu\nu}$. In dealing with the algebraic manipulations of the perturbations of an $f(R)$ metric theory of gravity, T. Bernal, S. Mendoza and L.A. Torres developed a code in the Computer Algebra System (CAS) Maxima, the MEXICAS (Metric Extended-gravity Incorporated through a Computer Algebraic System) code (licensed with a GNU Public License Version 3). The code is described in Mendoza et al. (2013) and can be downloaded from: *http://www.mendozza.org/sergio/mexicas*. We use it to obtain the field equations up to the fourth order in perturbations as described in the next subsections.

4.1. *Weakest Field Limit* $\mathcal{O}(2)$ *Correction*

Ricci's scalar can be written as follows:

$$R = R^{(2)} + R^{(4)} + \mathcal{O}(6)\,, \qquad (34)$$

which has non-null second and fourth perturbation orders in v/c powers. The fact that $R^{(0)} = 0$ is consistent with the flatness of space-time assumption at the lowest zeroth perturbation order. The $\mathcal{O}(2)$ term of Ricci's scalar, $R^{(2)}$, from the metric components (7)-(8), is given by

$$R^{(2)} = -\frac{2}{r}\left[g^{(2)}_{11,r} + \frac{g^{(2)}_{11}}{r}\right] - g^{(2)}_{00,rr} - \frac{2}{r}g^{(2)}_{00,r}\,. \qquad (35)$$

At the lowest perturbation order, $\mathcal{O}(2b-2)$, the trace (31) for a power-law theory (27) can be written as (Mendoza et al. 2013)

$$\mathcal{H}^{(2b-2)} = 3\Delta f'^{(2b-2)}(R) = 0. \qquad (36)$$

Note that this is the only independent equation at this perturbation order. Substitution of (9), (10), (27) and (34) into the previous relation leads to a differential equation for Ricci's scalar at order $\mathcal{O}(2)$, which has the solution (Mendoza et al. 2013)

$$R^{(2)}(r) = \left[(b-1)\left(\frac{\mathcal{A}}{r} + \mathcal{B}\right)\right]^{1/(b-1)}\,, \qquad (37)$$

where $\mathcal{A}$ and $\mathcal{B}$ are constants of integration. Far away from the central mass, space-time is flat and so, Ricci's scalar must vanish at large distances from the origin, i.e. the constant $\mathcal{B} = 0$.

Now, the case $b = 3/2$ has been shown to yield a MOND-like behavior in the limit $r \gg l_M \gg r_{\rm g}$ (Bernal et al. 2011b; Mendoza et al. 2013) and so,

after substituting $b = 3/2$ and $\mathcal{B} = 0$, solution (37) becomes

$$R^{(2)}(r) = \frac{\hat{R}}{r^2}, \tag{38}$$

where the constant $\hat{R} := \mathcal{A}^2/4$.

At the next perturbation order, $\mathcal{O}(2b)$, the metric components $g^{(2)}_{00}$, $g^{(2)}_{11}$, $g^{(4)}_{00}$ and Ricci's scalar $R^{(4)}$ can be obtained. In this case, the field equations (30) are given by (Mendoza et al. 2013)

$$bR^{(2)b-1}R^{(2)}_{\mu\nu} - \frac{1}{2}R^{(2)b}g^{(0)}_{\mu\nu} + \mathcal{H}^{(2b)}_{\mu\nu} = 0\,, \tag{39}$$

where $\mathcal{H}^{(2b)}_{\mu\nu} = -\left(\nabla_\mu\nabla_\nu - g_{\mu\nu}\Delta\right) f'^{(2b)}(R)$. From constraint (26) it follows that $\Delta f'^{(2b)} = 0$, and the last equation simplifies greatly. Using relations (7)-(10) into the 00−component of equation (39) leads to (Mendoza et al. 2013)

$$bR^{(2)b-1}R^{(2)}_{00} - \frac{1}{2}R^{(2)b} + \frac{1}{2}b(b-1)g^{(2)}_{00,r}R^{(2)b-2}R^{(2)}_{,r} = 0\,. \tag{40}$$

The 00−component of Ricci's tensor at $\mathcal{O}(2)$ is given by

$$R^{(2)}_{00} = -\frac{rg^{(2)}_{00,rr} + 2g^{(2)}_{00,r}}{2r}\,; \tag{41}$$

by substituting this last expression, $b = 3/2$, and result (38) into equation (40), the following differential equation for $g^{(2)}_{00}$ is obtained:

$$r^2 g^{(2)}_{00,rr} + 3rg^{(2)}_{00,r} + \frac{2\hat{R}}{3} = 0, \tag{42}$$

which has the solution (Mendoza et al. 2013)

$$g^{(2)}_{00}(r) = -\frac{\hat{R}}{3}\ln\left(\frac{r}{r_s}\right) + \frac{k_1}{r^2}, \tag{43}$$

where k_1 and r_s are constants of integration. By substitution of this last result and relation (38) into equation (35), the following differential equation for $g^{(2)}_{11}$ is obtained:

$$rg^{(2)}_{11,r} + g^{(2)}_{11} + \frac{k_1}{r^2} + \frac{\hat{R}}{3} = 0, \tag{44}$$

with the following analytic solution (Mendoza et al. 2013):

$$g^{(2)}_{11}(r) = \frac{k_1}{r^2} + \frac{k_2}{r} - \frac{\hat{R}}{3}, \tag{45}$$

where k_2 is another constant of integration.

To fix the free parameters $\hat{R}$, k_1, k_2 in relations (43) and (45), Mendoza et al. (2013) compared the metric coefficients with observations of rotation curves of spiral galaxies and the Tully-Fisher relation, and with gravitational lensing results of individual, groups, and clusters of galaxies. They obtained:

$$g^{(2)}_{00}(r) = -\frac{2\left(GMa_0\right)^{1/2}}{c^2}\ln\left(\frac{r}{r_s}\right), \tag{46}$$

$$g^{(2)}_{11}(r) = -\frac{2\left(GMa_0\right)^{1/2}}{c^2}, \tag{47}$$

for $\hat{R} = 6(GMa_0)^{1/2}/c^2$ and $k_1 = 0 = k_2$. Their results are summarized in Table 1. Notice that the metric component $g^{(2)}_{00} = 2\phi/c^2$ reduces to the MONDian gravitational potential, $\phi_{\rm MOND} = -(GMa_0)^{1/2}\ln(r/r_s)$, and to obtain the acceleration the length r_s is left indeterminate at $\mathcal{O}(2)$. However, as explained in § 6, its value is necessary to describe the dynamics up to $\mathcal{O}(4)$ of the theory, and it will be fixed with observational data.

Now, it is worth to notice the minus sign in $g^{(2)}_{00}$ (equation (46)). To obtain the corresponding "deep-MOND" acceleration, $a_{\rm MOND}(r) = -(GMa_0)^{1/2}/r$, from such potential, we cannot use the standard definition $\boldsymbol{a}(r) = -\nabla\phi(r)$, as in Newtonian mechanics, since a positive gravitational potential cannot produce bounded orbits in this theory (cf. Landau & Lifshitz 1982). That is, we cannot choose $\phi_{\rm MOND}(r) = +(GMa_0)^{1/2}\ln(r/r_s)$, unlike the treatment followed in Campigotto et al. (2017). This fact explains their disagreement with the correct $(-)$ sign found in Bernal et al. (2011b); Mendoza et al. (2013), and in this article.

4.2. *"Post-MONDian" $\mathcal{O}(4)$ Correction*

In this subsection, we derive the first relativistic correction of the metric theory $f(\chi) = \chi^{3/2}$, i.e. we obtain $g^{(4)}_{00}$ and $R^{(4)}$ having in mind further applications for material particles moving at high velocities compared to the speed of light. Here, we assume the solutions for the $\mathcal{O}(2)$ metric coefficients as shown before, and fit the $\mathcal{O}(4)$ ones as explained below.

The $\mathcal{O}(4)$ component of Ricci's scalar is given by

$$\begin{aligned} R^{(4)} = & -\frac{2}{r}\left\{g^{(2)}_{11}\left[2g^{(2)}_{11,r} + g^{(2)}_{00,r} + \frac{g^{(2)}_{11}}{r}\right]\right. \\ & \left. + g^{(2)}_{00,r}\left[\frac{r}{4}\left(g^{(2)}_{11,r} - g^{(2)}_{00,r}\right) - g^{(2)}_{00}\right] + g^{(4)}_{00,r}\right\} \\ & + g^{(2)}_{00,rr}\left[g^{(2)}_{00} - g^{(2)}_{11}\right] - g^{(4)}_{00,rr}\,. \end{aligned} \tag{48}$$

To obtain the $\mathcal{O}(4)$ metric coefficients, we use another independent field equation. Substitution of

TABLE 1

EMPIRICAL $\mathcal{O}(2)$ METRIC COEFFICIENTS

Metric coefficient	$g_{00}^{(2)}$	$g_{11}^{(2)}$
Observations	$-\frac{2(GMa_0)^{1/2}}{c^2}\ln\left(\frac{r}{r_s}\right)$ (Tully-Fisher)	$-\frac{2(GMa_0)^{1/2}}{c^2}$ (Lensing)
Theory $f(\chi)=\chi^{3/2}$	$-\frac{\hat{R}}{3}\ln\left(\frac{r}{r_s}\right)+\frac{k_1}{r^2}$, $\hat{R}=\frac{6(GMa_0)^{1/2}}{c^2}$, $k_1=0$	$\frac{k_1}{r^2}+\frac{k_2}{r}-\frac{\hat{R}}{3}$, $\hat{R}=\frac{6(GMa_0)^{1/2}}{c^2}$, $k_1=0=k_2$

The table shows the results obtained for the metric components $g_{00}^{(2)}$ and $g_{11}^{(2)}$ for a static spherically symmetric space-time. The metric coefficients are empirically obtained from astronomical observations in the scales of galaxies (Tully-Fisher relation) and lensing at the outer regions of individual, groups and clusters of galaxies, and compared to the ones predicted by the $f(\chi)=\chi^{3/2}$ metric theory of gravity. Any proposed metric of a theory of modified gravity must converge to the observational values presented in this table. As shown in Mendoza et al. (2013), the theory $f(\chi)=\chi^{3/2}$ is in perfect agreement with the metric components derived from observations.

relations (7)-(10) into the 22−component of equation (39) yields

$$b(b\text{–}1)rR^{(2)b-2}\Big[R^{(4)}_{,r}+g^{(2)}_{11}R^{(2)}_{,r}+(b-2)R^{(2)-1}R^{(2)}_{,r}R^{(4)}\Big]$$

$$-bR^{(2)b-1}R^{(2)}_{22}-\frac{r^2}{2}R^{(2)b}=0, \tag{49}$$

where the 22−component of the Ricci tensor at order $\mathcal{O}(2)$ is given by

$$R^{(2)}_{22}=g^{(2)}_{11}+\frac{r}{2}\left[g^{(2)}_{00,r}+g^{(2)}_{11,r}\right]. \tag{50}$$

By substitution of the last equation together with solutions (38), (43) and (45) for $R^{(2)}$, $g^{(2)}_{00}$ and $g^{(2)}_{11}$, respectively, into equation (49) for $b=3/2$, we obtain the following differential equation for Ricci's scalar at $\mathcal{O}(4)$:

$$r^4R^{(4)}_{,r}+r^3R^{(4)}+\hat{R}^2r-3k_2\hat{R}=0, \tag{51}$$

which has the following exact solution:

$$R^{(4)}(r)=\frac{\hat{R}^2}{r^2}-\frac{3k_2\hat{R}}{2r^3}-\frac{4k_3}{c^4r}, \tag{52}$$

where k_3 is a constant of integration.

Now, from the definition (48) of Ricci's scalar $R^{(4)}$ and from equation (52), together with (38), (43) and (45), we obtain the following differential equation for $g^{(4)}_{00}$:

$$-9g^{(4)}_{00,rr}-\frac{18}{r}\left(g^{(4)}_{00,r}-\frac{2k_3}{c^4}\right)+\frac{\hat{R}^2}{r^2}\left[\ln\left(\frac{r}{r_s}\right)-\frac{23}{2}\right]$$
$$+\frac{3k_2}{r^3}\left(5\hat{R}+\frac{6k_2}{r}\right)-\frac{3k_1\hat{R}}{r^4}\left[2\ln\left(\frac{r}{r_s}\right)+1\right]$$
$$+\frac{45k_1k_2}{r^5}+\frac{54k_1^2}{r^6}=0\,, \tag{53}$$

with the exact solution for $g^{(4)}_{00}$:

$$g^{(4)}_{00}(r) = \frac{\hat{R}^2}{18}\ln^2\left(\frac{r}{r_s}\right)-\frac{25\hat{R}^2}{18}\ln\left(\frac{r}{r_s}\right)+\frac{2k_3}{c^4}r$$
$$+\frac{2k_4}{c^4r}+\frac{k_5}{c^4}-\frac{k_1\,\hat{R}}{3\,r^2}\left[\ln\left(\frac{r}{r_s}\right)+2\right]+\frac{{k_2}^2}{r^2}$$
$$-\frac{5\,k_2\,\hat{R}}{3\,r}\left[\ln\left(\frac{r}{r_s}\right)+1\right]+\frac{5\,k_1\,k_2}{6\,r^3}+\frac{{k_1}^2}{2\,r^4}\,, \tag{54}$$

where k_4 and k_5 are constants of integration.

Now, by using the same results for the parameters $\hat{R}=6(GMa_0)^{1/2}/c^2$, $k_1=0=k_2$, from Mendoza et al. (2013) (see Table 1), the metric coefficient $g^{(4)}_{00}$ and Ricci's scalar $R^{(4)}$ reduce to

$$g^{(4)}_{00} = \frac{2GMa_0}{c^4}\ln\left(\frac{r}{r_s}\right)\left[\ln\left(\frac{r}{r_s}\right)-25\right]$$
$$+\frac{2k_3}{c^4}r+\frac{2k_4}{c^4r}+\frac{k_5}{c^4}\,; \tag{55}$$

$$R^{(4)} = \frac{36GMa_0}{c^4}\frac{1}{r^2}-\frac{4k_3}{c^4r}\,. \tag{56}$$

To fix the constants k_3 and k_4 (k_5 vanishes upon derivation of $g^{(4)}_{00}$ with respect to r (cf. equation (57)), we fit the observational data of 12 clusters of galaxies, as described in § 6.

5. GENERALIZATION TO EXTENDED SYSTEMS

In Mendoza et al. (2013), the details of gravitational lensing for individual, groups and clusters of galaxies at the outer regions of those systems were obtained considering a point-mass lens. Campigotto et al. (2017) compared those results with specific observations of gravitational lensing and found a large discrepancy between the $\mathcal{O}(2)$ terms in the metric coefficients of the $f(\chi) = \chi^{3/2}$ gravity and the observations. However, to obtain the correct gravitational lensing it is necessary to take into account the mass-density distribution, using a suitable gravitational potential.

In this section, we assume the solution for the MONDian point-mass gravitational potential for the $f(\chi) = \chi^{3/2}$ model, and generalize it to spherically symmetric mass distributions through potential theory. To this aim, we take into account the potential due to differentials of mass and integrate for the interior and exterior shells for a given radius r.

Let us take the radial component (3) of the geodesic equations (2) in the weak field limit of the theory. In this limit, the rotation curve for test particles bounded in a circular orbit about a mass M with circular velocity $v(r)$ is given by equation (4). Such equation, up to $\mathcal{O}(4)$ of approximation, is given by

$$\frac{a_c}{c^2} = \frac{1}{c^2}\frac{\mathrm{d}^2 r}{\mathrm{d}t^2} = \frac{1}{2}\left[g^{(2)}_{00,r} + g^{(2)}_{11}g^{(2)}_{00,r} + g^{(4)}_{00,r}\right]. \quad (57)$$

Substitution of the $\mathcal{O}(2)$ results for the metric coefficients, $g^{(2)}_{00}$ and $g^{(2)}_{11}$ (see Table 1), and solution (54) for $g^{(4)}_{00}$ in equation (57), results in the following expression for the acceleration of a test-mass particle in the gravitational field generated by the point-mass M:

$$a_c(r) = -\frac{(GMa_0)^{1/2}}{r} - \frac{1}{c^2}\left[\frac{23GMa_0}{r} - \frac{2GMa_0}{r}\ln\left(\frac{r}{r_s}\right) - k_3 + \frac{k_4}{r^2}\right]. \quad (58)$$

The first term on the right-hand side of last equation corresponds to the "deep-MOND" acceleration. The remaining $\mathcal{O}(2)$ terms are the first relativistic correction to the gravitational acceleration.

In order to apply these results to extended systems, it is necessary to generalize the gravitational acceleration (58) to a spherical mass distribution $M(r)$. To do this, notice that the first term of such equation can be easily generalized: In this case, the deep-MONDian acceleration can be written as $f(x) = a/a_0 = x$, for $x := l_M/r$. As discussed in Mendoza et al. (2011), this function, and in general any analytic function which depends only on the parameter x, guarantees Newton's theorems. In other words, the gravitational acceleration exerted by the outer shells at position r cancels out and depends only on the mass $M(r)$ interior to r. Thus, the first MONDian term of the gravitational acceleration (58) due to a mass distribution can be written as

$$a_c(r) = -\frac{[GM(r)a_0]^{1/2}}{r}. \quad (59)$$

For the $\mathcal{O}(2)$ terms on the right-hand side of acceleration (58), let us take the corresponding gravitational potential generated by the point-mass M. After integrating the $\mathcal{O}(2)$ terms with respect to the radius r, according to the spherical symmetry assumption, we obtain

$$\phi^{(2)}(r) = -\frac{GMa_0}{c^2}\left\{-\frac{A}{r} - Br + \ln\left(\frac{r}{r_s}\right)\left[23 - \ln\left(\frac{r}{r_s}\right)\right]\right\}, \quad (60)$$

where we have assumed k_3 and k_4 are proportional to GMa_0 and we have defined, for convenience, the constants $A := k_4/GMa_0$ and $B := k_3/GMa_0$. This point-mass gravitational potential can be generalized considering that the extended system is composed of many infinitesimal mass elements $\mathrm{d}M$, each one contributing with a point-like gravitational potential (60), such that

$$M(r) = \int_V \mathrm{d}M = \int_V \rho(r')\,\mathrm{d}V', \quad (61)$$

where ρ is the mass-density of the system and the volume element is $\mathrm{d}V' = r'^2\sin\theta'\,\mathrm{d}\varphi'\,\mathrm{d}\theta'\,\mathrm{d}r'$, integrated over the volume V.

From equation (60), the generalized gravitational potential in spherical symmetry is the convolution

$$\int f(\mathbf{r}-\mathbf{r}')\rho(r')r'^2\sin\theta'\mathrm{d}\varphi'\mathrm{d}\theta'\mathrm{d}r', \quad (62)$$

of the function

$$f(\mathbf{r}-\mathbf{r}') = -\frac{Ga_0}{c^2}\left\{-\frac{A}{|\mathbf{r}-\mathbf{r}'|} - B|\mathbf{r}-\mathbf{r}'| + \ln\left(\frac{|\mathbf{r}-\mathbf{r}'|}{r_s}\right)\left[23 - \ln\left(\frac{|\mathbf{r}-\mathbf{r}'|}{r_s}\right)\right]\right\}, \quad (63)$$

with the differential $\mathrm{d}M$ defined in (61), for f and ρ locally integrable functions for $r > 0$ (see e.g. Vladimirov 2002). Due to the spherical symmetry

of the problem, the integration can be done in one direction, for example the z axis, where the polar angle $\theta = 0$ and $|\mathbf{r} - \mathbf{r}'| = \sqrt{r^2 + r'^2 - 2rr'\cos\theta'}$. Thus, the $\mathcal{O}(2)$ generalized gravitational potential for a mass distribution can be written as

$$\Phi^{(2)}(r) = -\frac{Ga_0}{c^2}\int_0^{\mathcal{R}}\int_0^{\pi}\int_0^{2\pi}\left\{-\frac{A}{|\mathbf{r}-\mathbf{r}'|} + \ln\frac{|\mathbf{r}-\mathbf{r}'|}{r_s}\left[23 - \ln\frac{|\mathbf{r}-\mathbf{r}'|}{r_s}\right] - B|\mathbf{r}-\mathbf{r}'|\right\}\rho(r')\,r'^2\,\sin\theta'\,\mathrm{d}\varphi'\,\mathrm{d}\theta'\,\mathrm{d}r', \quad (64)$$

integrated over the whole volume V. If the density distribution is known, the generalized potential (65) can be numerically integrated to obtain the gravitational acceleration, from $0 < r < r'$ and $r' < r < \mathcal{R}$, where $\mathcal{R}$ is the radius of the spherical configuration.

Notice that the term with constant A on the last integral is a Newtonian-like potential, and it is a well-known result that the matter outside the spherical shell of radius r does not contribute to the corresponding gravitational acceleration; thus we have

$$a_c^{(2)}(r) = -\frac{GM(r)a_0A}{c^2r^2}. \quad (65)$$

For the other terms, the integration is done for the interior and exterior shells of mass $\mathrm{d}M$ with respect to the radius r, giving as result the following expression:

$$\Phi_c^{(2)}(r) = -\tfrac{2\pi Ga_0}{c^2r}\int_0^{\mathcal{R}}\left\{-\tfrac{B}{3}\left[(r+r')^3 - |r-r'|^3\right] + (r-r')^2\ln\left(\tfrac{|r-r'|}{r_s}\right)\left[\tfrac{1}{2}\ln\left(\tfrac{|r-r'|}{r_s}\right) - 24\right] - (r+r')^2\ln\left(\tfrac{r+r'}{r_s}\right)\left[\tfrac{1}{2}\ln\left(\tfrac{r+r'}{r_s}\right) - 24\right]\right\}\rho(r')r'\,\mathrm{d}r'$$

$$+\frac{12Ga_0}{c^2}\int_0^{\mathcal{R}}4\pi\rho(r')r'^2\,\mathrm{d}r', \quad (66)$$

where the last term is constant. Now, after performing the derivation of the potential (65) with respect to r and simplifying some terms, the generalized gravitational acceleration for a spherical mass distribution $M(r)$ can be written as

$$a_c(r) = -\frac{[GM(r)a_0]^{1/2}}{r} + \frac{\mathrm{d}\Phi^{(2)}(r)}{\mathrm{d}r}, \quad (67)$$
$$= -\frac{[GM(r)a_0]^{1/2}}{r} - \frac{GM(r)a_0A}{c^2r^2} + \frac{\mathrm{d}\Phi_c^{(2)}(r)}{\mathrm{d}r},$$

which can be obtained for an arbitrary density profile $\rho(r)$. Notice that the parameters B and r_s appear only on the last term of last equation through (66).

6. FIT WITH OBSERVATIONS OF CLUSTERS OF GALAXIES

To compare the correction $g_{00}^{(4)}$ with the observations of clusters of galaxies, we suppose the $\mathcal{O}(4)$ terms might be important in order to describe these systems, since their observed typical velocity dispersions are of the order $10^{-4} - 10^{-3}$ times the speed of light. Also, as shown in Sadeh et al. (2015); Wojtak et al. (2011), there exist observational relativistic effects of the velocity of the galaxies at the edge of the clusters, showing a difference of the inferred background potential with the galaxy inferred potential. Here we test if the dynamical masses of the clusters can be explained with the extra $\mathcal{O}(4)$ terms from the metric coefficients of the $f(\chi) = \chi^{3/2}$ theory, without the need of DM.

6.1. *Galaxy Clusters Mass Determination*

To apply the results of the last subsection to the spherically symmetric X-ray clusters of galaxies reported in Vikhlinin et al. (2006), notice that there are two observables: the ionized gas profile $\rho_{\mathrm{g}}(r)$ and the temperature profile $T(r)$. Under the hypothesis of hydrostatic equilibrium, the hydrodynamic equation can be derived from the collisionless isotropic Boltzmann equation for spherically symmetric systems in the weak field limit (Binney & Tremaine 2008):

$$\frac{\mathrm{d}\left[\sigma_r^2\rho_{\mathrm{g}}(r)\right]}{\mathrm{d}r} + \frac{\rho_{\mathrm{g}}(r)}{r}\left[2\sigma_r^2 - \left(\sigma_\theta^2 + \sigma_\varphi^2\right)\right] = -\rho_{\mathrm{g}}(r)\frac{\mathrm{d}\Phi(r)}{\mathrm{d}r}, \quad (68)$$

where Φ is the gravitational potential and σ_r, σ_θ and σ_φ are the mass-weighted velocity dispersions in the radial and tangential directions, respectively. For an isotropic system with rotational symmetry there is no preferred transverse direction, and so $\sigma_\theta = \sigma_\varphi$. For an isotropic distribution of the velocities, we also have $\sigma_r = \sigma_\theta$.

The radial velocity dispersion can be related to the pressure profile $P(r)$, the gas mass density $\rho_{\mathrm{g}}(r)$ and the temperature profile $T(r)$ by means of the ideal gas law to obtain:

$$\sigma_r^2 = \frac{P(r)}{\rho_{\mathrm{g}}(r)} = \frac{k_{\mathrm{B}}T(r)}{\mu m_p}, \quad (69)$$

where k_{B} is the Boltzmann constant, $\mu = 0.5954$ is the mean molecular mass per particle for primordial He abundance and m_p is the proton mass. Direct substitution of equation (69) into (68) yields the

gravitational equilibrium relation:

$$|\boldsymbol{a}(r)| = \left|\frac{\mathrm{d}\Phi(r)}{\mathrm{d}r}\right| = \frac{k_{\mathrm{B}}T(r)}{\mu m_p r}\left[\frac{\mathrm{d}\ln\rho_{\mathrm{g}}(r)}{\mathrm{d}\ln r} + \frac{\mathrm{d}\ln T(r)}{\mathrm{d}\ln r}\right]. \quad (70)$$

The right-hand side of the previous equation is determined by observational data, while the left-hand side should be consistent through a given gravitational acceleration and distribution of matter.

In standard Newtonian gravity, the total mass of a galaxy cluster is given by the mass of the gas, M_{gas}, and the stellar mass of the galaxies, M_{stars}, inside it, with the necessary addition of an unknown DM component to avoid a discrepancy of one order of magnitude on both sides of last equation. In this case, the "dynamical" mass of the system, M_{dyn}, is determined by Newton's acceleration, a_{N}, as follows:

$$\begin{aligned} M_{\mathrm{dyn}}(r) &:= -\frac{r^2 a_{\mathrm{N}}(r)}{G} \quad (71)\\ &= -\frac{k_{\mathrm{B}}T(r)}{\mu m_p G} r\left[\frac{\mathrm{d}\ln\rho_{\mathrm{g}}(r)}{\mathrm{d}\ln r} + \frac{\mathrm{d}\ln T(r)}{\mathrm{d}\ln r}\right]. \end{aligned}$$

In the $f(\chi) = \chi^{3/2}$ model, the acceleration will be given by equation (67). In this case, we define the "theoretical" mass, M_{th}, as

$$\begin{aligned} M_{\mathrm{th}}(r) &:= -\frac{r^2 a_c(r)}{G}\\ &= \left[\frac{M_{\mathrm{b}}(r)a_0}{G}\right]^{1/2} r + \frac{M_{\mathrm{b}}(r)a_0 A}{c^2}\\ &\quad -\frac{r^2}{G}\frac{\mathrm{d}\Phi_c^{(2)}(r)}{\mathrm{d}r}, \quad (72) \end{aligned}$$

where the baryonic mass of the system, $M_{\mathrm{b}}(r)$, is given by

$$M_{\mathrm{b}}(r) = M_{\mathrm{gas}}(r) + M_{\mathrm{stars}}(r). \quad (73)$$

In order to reproduce the observations, the theoretical mass obtained from our modification to the gravitational acceleration must be equal to the dynamical mass coming from observations, i.e. $M_{\mathrm{th}} = M_{\mathrm{dyn}}$, without the inclusion of DM. This provides an observational procedure to fit the three free parameters of our model (r_s, A and B).

6.2. *Chandra Clusters Sample*

For this work, we used 12 X-ray galaxy clusters from the *Chandra* Observatory, analyzed in Vikhlinin et al. (2005, 2006). It is a representative sample of low-redshift ($z \approx 0.01 - 0.2$, with median $z = 0.06$), relaxed clusters, with very regular X-ray morphology and weak signs of dynamical activity. The effect of evolution is small within such redshift interval (Vikhlinin et al. 2006), thus we did not include the effects of the expansion of the Universe in our analysis. The observations extend to a large fraction of the virial radii, with total masses M_{500}[4] $\approx (0.5-10)\times 10^{14} M_\odot$; thus, the obtained values of the clusters properties (gas density, temperature and total mass profiles) are reliable (Vikhlinin et al. 2006).

The keV temperatures observed in clusters of galaxies imply that the gas is fully ionized and the hot plasma is mainly emitted by free-free radiation processes. There is also line emission by the ionized heavy elements. The radiation process generated by these mechanisms is proportional to the emission measure profile $n_p n_e(r)$. Vikhlinin et al. (2006) introduced a modification to the standard β-model (Cavaliere & Fusco-Femiano 1978), in order to reproduce the observed features from the surface brightness profiles, the gas density at the centers of relaxed clusters and the observed X-ray brightness profiles at large radii. A second β-model component (with small core radius) is added to increase the accuracy near the clusters' centers. With these modifications, the complete expression for the emission measure profile has 9 free parameters. The 12 clusters can be adequately fitted by this model. The best fit values to the emission measure for the 12 clusters of galaxies can be found in Table 2 of Vikhlinin et al. (2006).

To obtain the baryonic density of the gas, the primordial abundance of He and the relative metallicity $Z = 0.2\, Z_\odot$ are taken into account, and so

$$\rho_{\mathrm{g}}(r) = 1.624 m_p \sqrt{n_p n_e(r)}. \quad (74)$$

In order to have an estimation of the stellar component of the clusters, we used the empirical relation between the stellar and the total mass (baryonic + DM) in the Newtonian approximation (Lin et al. 2012):

$$\frac{M_{\mathrm{stars}}}{10^{12} M_\odot} = (1.8 \pm 0.1)\left(\frac{M_{500}}{10^{14} M_\odot}\right)^{0.71\pm0.04}. \quad (75)$$

However, the total stellar mass is $\approx 1\%$ of the total mass of the clusters, so we simply estimate the baryonic mass with the gas mass.

For the temperature profile $T(r)$, Vikhlinin et al. (2006) used a different approach from the polytropic

[4] M_{500} is the mass at the radius r_{500}, where the density is $500\rho_{\mathrm{crit}}$, with ρ_{crit} the critical density of the Universe.

law to model non-constant cluster temperature profiles at large radii. All the projected temperature profiles show a broad peak near the centers and decrease at larger radii, with a temperature decline toward the cluster center, probably because of the presence of radiative cooling (Vikhlinin et al. 2006). To model the temperature profile in three dimensions, they constructed an analytic function such that outside the central cooling region the temperature profile can be represented as a broken power law with a transition region:

$$T(r) = T_0 \frac{x + T_{\rm min}/T_0}{1+x} \frac{(r/r_t)^{-a}}{[1+(r/r_t)^b]^{c/b}}, \qquad (76)$$

where $x := (r/r_{\rm cool})^{a_{\rm cool}}$. The 8 best-fit parameters (a, b, c, r_t, T_0, $T_{\rm min}$, $r_{\rm cool}$, $a_{\rm cool}$) for the 12 clusters of galaxies can be found in Table 3 of Vikhlinin et al. (2006).

The total dynamical masses, obtained with equation (71) from the derived gas densities (74) and temperature profiles (76) for the 12 galaxy clusters, were kindly provided by Alexey Vikhlinin, along with the 1σ confidence levels from their Markov Chain Monte Carlo simulations. We used such data to fit our model as described in the next subsection.

6.3. *Parameters Estimation Method*

We conceptualized the free parameters calibration, A, B and r_s, as an optimization problem and proposed to solve it using Genetic Algorithms (GAs), which are evolutionary based stochastic search algorithms that, in some sense, mimic natural evolution. In this heuristic technique, points in the search space are considered as individuals (solution candidates), which as a whole form a population. The particular fitness of an individual is a number indicating their quality for the problem at hand. As in nature, GAs include a set of fundamental genetic operations that work on the genotype (solution candidate codification): mutation, recombination and selection operators (Mitchell 1998).

These algorithms operate with a population of individuals $P(t) = x_1^t, ..., x_N^t$, for the t-th iteration, where the fitness of each x_i individual is evaluated according to a set of objective functions $f_j(x_i)$. These objective functions allow to order individuals of the population in a continuum of degrees of adaptation. Then, individuals with higher fitness recombine their genotypes to form the gene pool of the next generation, in which random mutations are also introduced to produce new variability.

A fundamental advantage of GAs versus traditional methods is that GAs solve discrete, non-convex, discontinuous, and non-smooth problems successfully, and thus they have been widely used in many fields, including astrophysics and cosmology (see e.g. Charbonneau 1995; Cantó et al. 2009; Nesseris 2011; Curiel et al. 2011; Rajpaul 2012; López-Corona 2015).

It is important to note that, as it is well known from Taylor series, any (normal) function may be well approximated by a polynomial, up to certain correct order of approximation. Of course, although this is correct from a mathematical point of view, it is possible to consider that a polynomial approximation is not universal for any physical phenomenon. In this line of thought, one may fit any data using a model with many free parameters, and even if in this approximation we may have a great performance in a statistical sense, it could be incorrect from the physical perspective.

In this sense, an important question to ask is: How much better is a complex model in a fitting process, justifying the incorporation of extra parameters? In a more straightforward sense, how do we carry out a fit with simplicity? Such question has been the motivation in the recent years for new model selection criteria development in statistics, all of them defining simplicity in terms of the number of parameters or the dimension of a model (see e.g. Forster & Sober 1994, for a non-technical introduction). These criteria include Akaike's Information Criterion (AIC) (Akaike 1974, 1985), the Bayesian Information Criterion (BIC) (Schwarz 1978) and the Minimum Description Length (MDL) (Rissanen 1989). They fit the parameters of a model differently, but all of them address the same problem as a significance test: Which of the estimated "curves" from competing models best represents reality? (Forster & Sober 1994).

Akaike (1974, 1985) has shown that choosing the model with the lowest expected information loss (i.e., the model that minimizes the expected Kullback-Leibler discrepancy) is asymptotically equivalent to choosing a model M_j, from a set of models $j = 1, 2, ..., k$, that has the lowest AIC value, defined by

$$\mathrm{AIC} = -2\ln(\mathcal{L}_j) + 2V_j, \qquad (77)$$

where $\mathcal{L}_j$ is the maximum likelihood for the candidate model and is determined by adjusting the V_j free parameters in such a way that they maximize the probability that the candidate model has generated the observed data. This equation shows that AIC rewards descriptive accuracy via the maximum

TABLE 2

PARAMETER ESTIMATION FOR THE GALAXY CLUSTERS

Cluster	$r_{\rm min}$ (kpc)	$r_{\rm max}$ (kpc)	$M_{\rm gas}$ ($10^{13}M_\odot$)	$M_{\rm th}$ ($10^{14}M_\odot$)	$M_{\rm dyn}$ ($10^{14}M_\odot$)	A (10^8kpc)	B (kpc^{-1})	r_s (10^{-8}kpc)
A133	92.10	1005.81	3.193	3.269	3.359	2.0727	96.563	3.42
A262	62.33	648.36	1.141	0.825	0.8645	1.7825	358.82	2.40
A383	51.28	957.92	4.406	2.966	3.17	1.9714	151.99	2.96
A478	62.33	1347.89	10.501	7.665	8.18	1.9271	61.436	3.91
A907	62.33	1108.91	6.530	4.499	4.872	1.9024	101.05	3.56
A1413	40.18	1347.89	9.606	7.915	8.155	1.9423	51.150	71293
A1795	92.10	1222.57	6.980	6.071	6.159	1.9255	61.757	3.79
A1991	40.18	750.55	1.582	1.198	1.324	2.3703	340.56	2.49
A2029	31.48	1347.89	10.985	7.872	8.384	2.1837	75.339	440.9
A2390	92.10	1415.28	16.621	11.151	11.21	1.1517	16.935	4.55
MKW4	72.16	648.36	0.676	0.805	0.8338	2.4413	367.55	2.28
RXJ1159 +5531	72.16	680.77	0.753	1.105	1.119	2.3460	171.94	2.39
					Mean value	2.0014	154.59	5980
					$<$ SD $>$	0.00868	1.6462	937.0

From left to right, the columns list the name of the cluster, the minimal $r_{\rm min}$ and maximal $r_{\rm max}$ radii for the integration, the mass of the gas $M_{\rm gas}$, the total theoretical mass $M_{\rm th}$ derived from our model, the total dynamical mass $M_{\rm dyn}$ from Vikhlinin et al. (2006), the best-fit parameters A, B and r_s, respectively. Also, at the bottom of the Table, we show the best-fit parameters obtained from the 12 clusters of galaxies data taken as a set of independent objective functions together, with their corresponding mean standard deviations $<$ SD $>$.

likelihood, and penalizes lack of parsimony according to the number of free parameters (note that models with smaller AIC values are to be preferred). In that sense, Akaike (1974, 1985) extended this paradigm by considering a framework in which the model dimension is also unknown, and must therefore be determined from the data. Thus, Akaike proposed a framework where both model estimation and selection could be simultaneously accomplished. For those reasons, AIC is generally regarded as the first, most widely known and used model selection tool.

Taking as objective function the AIC information index, we performed a GAs analysis using a modified version of the Sastry (2007) code in C++. The GA we used evaluates numerically equation (72) in order to compare the numerical results from the theoretical model with the cluster observational data, as explained in § 6.2. All parameters were searched for a broad range, from -1×10^4 to 1×10^{10}, generating populations of 1,000 possible solutions over a maximum of 500,000 generation search processes. We selected standard GAs: tournament selection with replacement (Goldberg et al. 1989; Sastry & Goldberg 2001), simulated binary crossover (Deb & Agrawal 1995; Deb & Kumar 1995) and polynomial mutation (Deb & Agrawal 1995; Deb & Kumar 1995; Deb 2001). The parameters were estimated taking the average from the first best population decile, checking the consistency of the $\mathcal{O}(2)$ corrections with respect to the zeroth order term in the gravitational acceleration (67). Finally, when we obtained

$$\Delta_{\rm AIC} := {\rm AIC}_i - \min\{{\rm AIC}_i\} < 2, \qquad (78)$$

for the parameters estimation, then the model was accepted as a good one (Burnham & Anderson 2002).

7. RESULTS AND DISCUSSION

The results for the best fits as explained in § 6 are summarized in Table 2. Figures 1 and 2 show the best fits of the theoretical masses compared to the total dynamical ones obtained in Vikhlinin et al. (2006). In all cases, the parameter $\Delta_{\rm AIC} < 2$ and so, in general, the $f(\chi) = \chi^{3/2}$ model fits well the observational data.

From the best-fit analysis, we see that our model is capable to account for the total dynamical masses of the 12 clusters of galaxies, except at the very inner regions for some of them, a persistent behavior more accentuated for A907 and A1991. Notice that the parameter A quantifies the extra Newtonian-like contribution to the dynamical mass [cf. equation (67)],

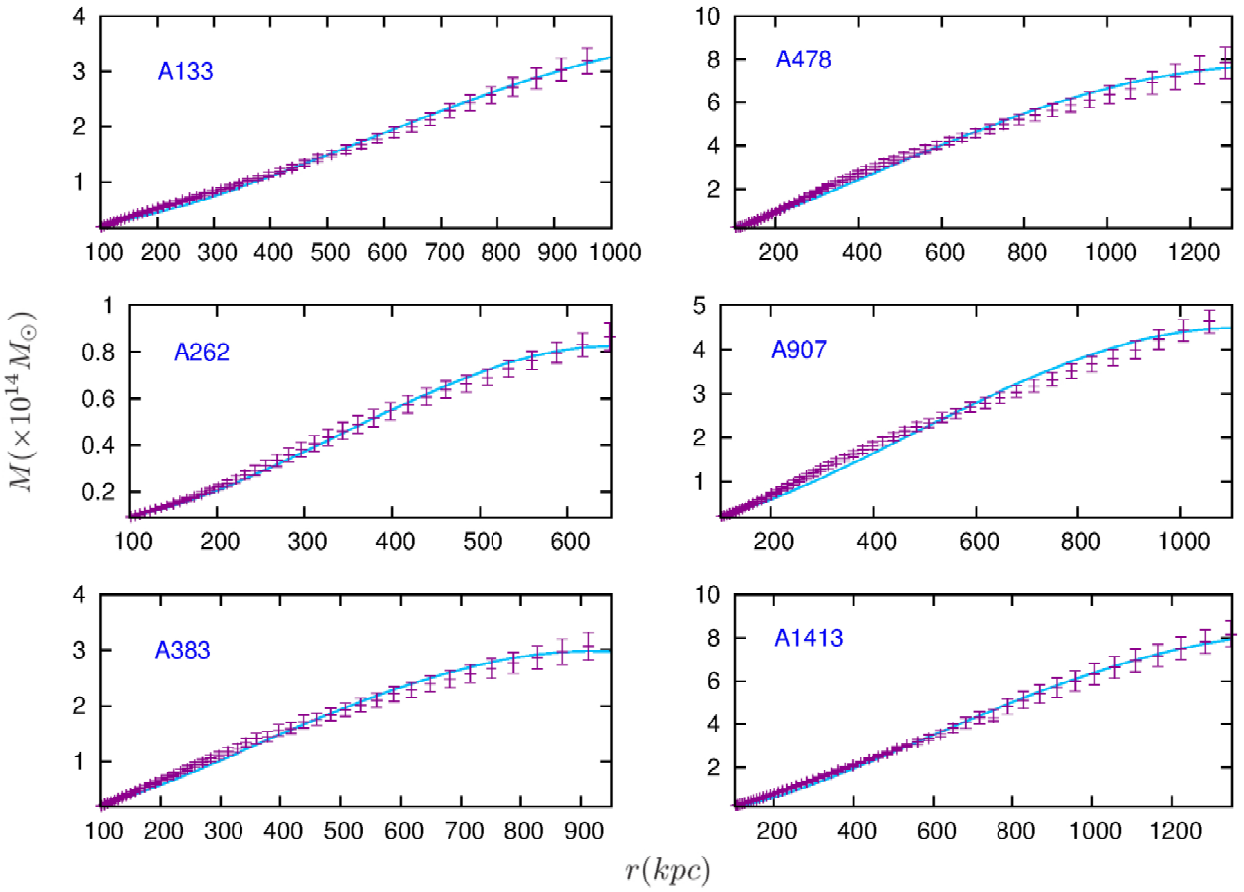

Fig. 1. **Dynamical mass vs. radius for the galaxy clusters.** Dynamical mass vs. radius for the first 6 clusters of galaxies, with the best-fit parameters as summarized in Table 1. The points with uncertainty bars are the 1σ dynamical masses obtained in Vikhlinin et al. (2006). The solid line is the best fit obtained with our model. The color figure can be viewed online.

and the parameters B and r_s are present in the $\Phi_c^{(2)}$ term only [equation (66)]. As can be seen in Table 2, there are two systems, A1413 and A2029, for which the estimated parameter r_s is very far from the mean value for the other clusters. Comparing its contribution to the acceleration with respect to the other two terms in equation (67), we found that the dominant second order term is the one with the parameter A, and the contribution of the derivative of the integral (66) is very small (since r_s appears inside a logarithm and because of the particular combination of the functions in such equation).

From the figures, we see that the "MOND-like" relativistic correction of our model is better in the outer regions of the galaxy clusters than standard MOND, which needs extra matter to fit the observations in these systems. Also, the second order perturbation analysis of the metric theory $f(\chi) = \chi^{3/2}$ is capable to account for the observations of the rotation curves of spiral galaxies and the Tully-Fisher relation, and the gravitational lensing in individual, groups and clusters of galaxies (Mendoza et al. 2013). In this work, we keep fixed those parameters at $\mathcal{O}(2)$ of perturbations to obtain the $\mathcal{O}(4)$ of the model, with the additional result that it is possible to fit the dynamical masses of clusters of galaxies without the need of extra DM.

Up to now it has generally been thought that a MOND-like extended theory of gravity was not able to explain the dynamics of clusters of galaxies without the necessary introduction of some sort of unknown DM component. Our aim has been to show that in order to account for this dynamical description without the inclusion of DM, it is necessary to introduce relativistic corrections in the proposed extended theory. To do so, we have chosen the particular $f(\chi) = \chi^{3/2}$ MOND-like metric extension (Bernal et al. 2011b), which has also proved to be

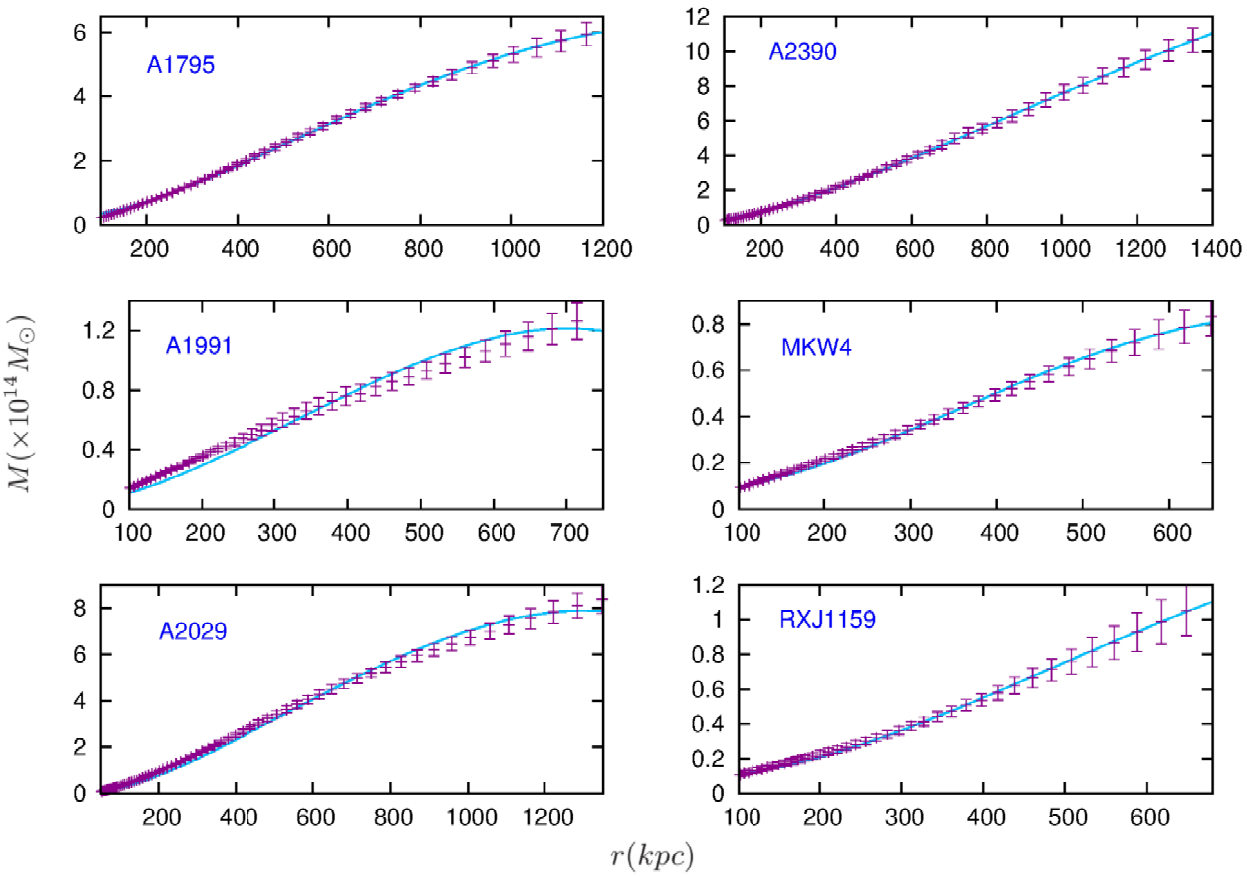

Fig. 2. **Dynamical mass vs. radius for the galaxy clusters.** The same as Figure 1 for the remaining 6 clusters of galaxies. The color figure can be viewed online.

in good agreement with gravitational lensing of individual, groups and clusters of galaxies, and with the dynamics of the Universe, providing an accelerated expansion without the introduction of any dark matter and/or energy entities (see Mendoza 2015, for a review).

A similar analogy occurred when studying the orbit of Mercury about a century ago. Its motions were mostly understood with Newton's theory of gravity. However it was necessary to add relativistic corrections to the underlying gravitational theory to account for the precession of its orbit. Mercury orbits at a velocity $v \approx 50\,\mathrm{km/s}$, implying $v/c \approx 10^{-4}$ and already relativistic corrections are required. Typical velocities of clusters of galaxies are $v \approx 10^3\,\mathrm{km/s}$, with $v/c \approx 10^{-3}$. This means that the dynamics of clusters of galaxies are about one order of magnitude more relativistic than the orbital velocity of Mercury and so, if the latter required relativistic corrections, then the corrections needed to describe the dynamics of clusters of galaxies are even more important.

We gratefully acknowledge Alexey Vikhlinin for kindly providing the data of the galaxy clusters used in this article. We thank J. C. Hidalgo for his valuable comments during the first discussions on this work, K. MacLeod for useful corrections on a previous version of this article and the anonymous referee who helped us with valuable comments to improve this article. This work was supported by Dirección General de Asuntos del Personal Académico (DGAPA)-UNAM(IN111513 and IN112019) and Consejo Nacional de Ciencia y Tecnología (CONACyT) México (CB-2014-01 No. 240512) grants. TB, OLC and SM acknowledge economic support from CONACyT (64634, 62929 and 26344).

REFERENCES

Akaike, H. 1974, ITAC, 19, 716
_____. 1985, in A Celebration of Statistics, ed. A. C. Atkinson & S. E. Fienberg (New York, NY: Springer), 1

Angus, G. W., Famaey, B., & Buote, D. A. 2008, MNRAS, 387, 1470
Barrientos, E. & Mendoza, S. 2016, EPJP, 131, 367
_____. 2017, EPJP, 132, 361
_____. 2018, PhRvD, 98, 4033
Bekenstein, J. & Milgrom, M. 1984, ApJ, 286, 7
Bekenstein, J. D. 2004, PhRvD, 70, 083509
Bennett, C. L., Larson, D., Weiland, J. L., et al. 2013, ApJS, 208, 20
Bernal, T., Capozziello, S., Cristofano, G., & de Laurentis, M. 2011a, MPLA, 26, 2677
Bernal, T., Capozziello, S., Hidalgo, J. C., & Mendoza, S. 2011b, EPJC, 71, 1794
Bertolami, O., Böhmer, C. G., Harko, T., & Lobo, F. S. N. 2007, PhRvD, 75, 4016
Bertone, G., Hooper, D., & Silk, J. 2005, PhR, 405, 279
Binney, J. & Tremaine, S. 2008, Galactic Dynamics, (2nd ed; Princeton NJ: PUP)
Burnham, K. P. & Anderson, D. R. 2002, Model selection and multimodel inference: a practical information-theoretic approach (New York, NY: Springer-Verlag)
Campigotto, M. C., Diaferio, A., Hernandez, X., & Fatibene, L. 2017, JCAP, 6, 057
Cantó, J., Curiel, S., & Martínez-Gómez, E. 2009, A&A, 501, 1259
Capozziello, S., de Filippis, E., & Salzano, V. 2009, MNRAS, 394, 947
Capozziello, S. & Faraoni, V. 2011, Beyond Einstein Gravity, (Netherlands: Springer)
Capozziello, S. & Stabile, A. 2009, CQGra, 26, 5019
Capozziello, S., Stabile, A., & Troisi, A. 2007, PhRvD, 76, 4019
Carranza, D. A., Mendoza, S., & Torres, L. A. 2013, EPJC, 73, 2282
Cavaliere, A. & Fusco-Femiano, R. 1978, AA, 70, 677
Charbonneau, P. 1995, ApJS, 101, 309
Curiel, S., Cantó, J., Georgiev, L., Chávez, C. E., & Poveda, A. 2011, A&A, 525, A78
De Felice, A. & Tsujikawa, S. 2010, LRR, 13, 3
Deb, K. 2001, Multi-objective optimization using evolutionary algorithms, (New York, NY: John Wiley & Sons)
Deb, K. & Agrawal, R. B. 1995, Complex systems, 9, 115
Deb, K. & Kumar, A. 1995, Complex systems, 9, 431
Demir, D. A. & Karahan, C. N. 2014, EPJC, 74, 3204
Famaey, B. & McGaugh, S. S. 2012, LRR, 15, 10
Ferreras, I., Mavromatos, N. E., Sakellariadou, M., & Yusaf, M. F. 2009, PhRvD, 80, 3506
Forster, M. & Sober, E. 1994, The British Journal Philosophy of Science, 45, 1
Goldberg, D. E., Korb, B., & Deb, K. 1989, Complex systems, 3, 493
Harko, T., Lobo, F. S. N., Nojiri, S., & Odintsov, S. D. 2011, PhRvD, 84, 4020
Hernandez, X. & Jiménez, M. A. 2012, ApJ, 750, 9
Hernandez, X., Jiménez, M. A., & Allen, C. 2012, EPJC, 72, 1884
_____. 2013, MNRAS, 428, 3196
Hernandez, X., Mendoza, S., Suarez, T., & Bernal, T. 2010, A&A, 514, A101
Landau, L. & Lifshitz, E. 1975, The classical theory of fields, Course of theoretical physics (Oxford: Pergamon Press)
_____. 1982, Mechanics, Course of theoretical physics No. 1 (Elsevier Science)
Lin, Y.-T., Stanford, S. A., Eisenhardt, P. R. M., et al. 2012, ApJL, 745, L3
López-Corona, O. 2015, JPhCS, 600, 2046
Mendoza, S. 2012, in Open Questions in Cosmology, ed. D. G. J. Olmo (InTech), available from: http://www.intechopen.com/books/open-questions-in-cosmology/extending-cosmology-the-metric-approach
Mendoza, S. 2015, CaJPh, 93, 217
Mendoza, S., Bernal, T., Hernandez, X., Hidalgo, J. C., & Torres, L. A. 2013, MNRAS, 433, 1802
Mendoza, S., Hernandez, X., Hidalgo, J. C., & Bernal, T. 2011, MNRAS, 411, 226
Mendoza, S. & Olmo, G. J. 2015, Astrophysics and Space Science 357, 133
Milgrom, M. 1983a, ApJ, 270, 371
_____. 1983b, ApJ, 270, 365
Mitchell, M. 1998, An Introduction to Genetic Algorithms, (Cambridge, MA: MIT Press)
Natarajan, P. & Zhao, H. 2008, MNRAS, 389, 250
Nesseris, S. 2011, JPhCS, 283, 012025
Nojiri, S. & Odintsov, S. D. 2011, TSPU Bulletin, N8(110), 7
Nojiri, S. & Odintsov, S. D. 2011a, PhR, 505, 59
Nojiri, S., Odintsov, S. D., & Oikonomou, V. K. 2017, PhR, 692, 1
Perlmutter, S., Aldering, G., Goldhaber, G., & Supernova Cosmology Project. 1999, ApJ, 517, 565
Planck Collaboration, Ade, P. A. R., Aghanim, N., et al. 2016, A&A, 594, A13
Rajpaul, V. 2012, ArXiv e-prints
Rissanen, J. 1989, Stochastic Complexity in Statistical Inquiry Theory (River Edge, NJ, USA: World Scientific Publishing Co., Inc.)
Rubin, V. C. 1983, Sci, 220, 1339
Sadeh, I., Feng, L. L., & Lahav, O. 2015, PhRvL, 114, 1103
Sastry, K. 2007, IlliGAL Report No. 2007016, 1
Sastry, K. & Goldberg, D. E. 2001, Intelligent Engineering Systems Through Artificial Neural Networks, 129
Schimming, R. & Schmidt, H. 2004, ArXiv General Relativity and Quantum Cosmology e-prints
Schwarz, G. 1978, AnSta, 6, 461
Smith, S. 1936, ApJ, 83, 23
Sotiriou, T. P. & Faraoni, V. 2010, RvMP, 42, 451
Starobinsky, A. A. 1980, PhLB, 91, 99

Takahashi, R. & Chiba, T. 2007, ApJ, 671, 45
Vikhlinin, A., Kravtsov, A., Forman, W., et al. 2006, ApJ, 640, 691
Vikhlinin, A., Markevitch, M., Murray, S. S., et al. 2005, ApJ, 628, 655
Vladimirov, V. 2002, Methods of the Theory of Generalized Functions, Analytical Methods and Special Functions (London, UK: CRC Press)
Will, C. M. 1993, Theory and Experiment in Gravitational Physics (Cambridge, MA: CUP)
_____. 2006, LRR, 9, 3
Wojtak, R., Hansen, S. H., & Hjorth, J. 2011, Natur, 477, 567
Zwicky, F. 1933, AcHPh, 6, 110
_____. 1937, ApJ, 86, 217

Tula Bernal: Área de Física, Departamento de Preparatoria Agrícola, Universidad Autónoma Chapingo, km. 38.5 Carretera México-Texcoco, 56230, Texcoco, Estado de México, México (ac13341@chapingo.mx).
Oliver López-Corona: Instituto de Astronomía, Universidad Nacional Autónoma de México, A.P. 70-264, Ciudad de México 04510, México. Current address: Cátedras CONACyT Comisión Nacional para el Conocimiento y Uso de la Biodiversidad (CONABIO), Liga Periférico-Insurgentes Sur No. 4903, Parques del Pedregal, 14010 Tlalpan, CDMX, México. Red Ambiente y Sustentabilidad, Instituto de Ecología A. C. de México (INECOL). Centro de Ciencias de la Complejidad (C3), UNAM (olopez@conacyt.mx).
Sergio Mendoza: Instituto de Astronomía, Universidad Nacional Autónoma de México, A. P. 70-264, Ciudad de México 04510, México (sergio@astro.unam.mx).

Revista Mexicana de Astronomía y Astrofísica, **55**, 255–271 (2019)

DOI: https://doi.org/10.22201/ia.01851101p.2019.55.02.13

METALLICITY GRADIENTS IN M31, M 33, NGC 300 AND THE MILKY WAY USING ABUNDANCES OF DIFFERENT ELEMENTS

Miriam Peña and Sheila N. Flores-Durán

Instituto de Astronomía, Universidad Nacional Autónoma de México, México.

Received April 23 2019; accepted July 3 2019

ABSTRACT

Metallicity gradients derived from planetary nebulae (PNe) using O, Ne, and Ar abundances are studied and compared to those from H II regions in the galaxies M 31, M 33, NGC 300 and the Milky Way. Galactocentric radii and chemical abundances were collected from the literature, carefully selecting a homogeneous sample for each galaxy. Metallicity gradients shown by PNe are flatter than those of H II regions in all cases. The extreme case is M 31 where PN abundances are not related to galactocentric distances and the gradients are consistent with zero. To analyze the evolution of gradients with time we build gradients for Peimbert Type I and non-Type I PNe finding that Type I PNe show steeper gradients than non-Type I PNe and more similar to the ones of H II regions indicating that the chemical gradients might steepen with time. Alternatively, the flat gradients for old PNe show that radial migration could have an important role in the evolution of galaxies.

RESUMEN

Estudiamos los gradientes de metalicidad de O, Ne y Ar, derivados de nebulosas planetarias (PNe), en comparación con los de regiones H II en las galaxias M 31, M 33, NGC 300 y la Vía Láctea. Radios galactocéntricos y abundancias fueron recopilados de la literatura, seleccionando con cuidado una muestra homogénea de objetos en cada galaxia. Los gradientes de las PNe son más planos que los de las regiones H II en todos los casos. El caso más extremo es el de M 31, donde las abundancias de las PNe no están relacionadas con la distancia galactocéntrica y los gradientes son consistentes con cero. Calculamos gradientes para PNe del Tipo I y no-Tipo I de Peimbert, encontrando que los gradientes del Tipo I son más empinados y más similares a los de las regiones H II, lo que indicaría que los gradientes de metalicidad se empinan con el tiempo. Alternativamente los gradientes planos de las PNe viejas indican que la migración radial juega un importante papel en las galaxias.

Key Words: galaxies: abundances — galaxies: individual: M 31, M 33, NGC 300 — galaxies: spiral — Galaxy: abundances — planetary nebulae: general

1. INTRODUCTION

Metallicity gradients in disk galaxies, provided by the analysis of the chemistry of H II regions at different galactocentric distances, have been long studied (Aller 1942; Searle 1971, and many others), as such an analysis gives information on the chemical history of the host galaxy. The history of star formation and the processes of accretion and mass loss in a galaxy can be determined by using chemical evolution models that reproduce the present chemical abundances of the interstellar medium (ISM) using the abundances of H II regions as constraint. See e.g., Carigi & Peimbert (2011).

It has been found that the metallicity gradients obtained from H II regions and other indicators are always negative, that is, chemical abundances are lower at larger galactocentric distances. Many galaxies have been analyzed showing the same result. Re-

cently Sánchez et al. (2014) analyzed the O abundance in a large number of H II regions in more than 300 galaxies observed by the CALIFA survey, reporting that in many galaxies with H II regions detected beyond two disk effective radii the slope presents a flattening at large distances and, in some cases, a drop or truncation of the O abundance occurs in the inner regions.

Since some time ago the abundances determined for PNe are also being used to analyze the chemical gradients in galaxies. Among the oldest studies of PNe in the Milky Way are those of D'Odorico, Peimbert, & Sabbadin (1976) and Kaler (1980). As PNe are objects with ages between 1 and 10 Gyr, they provide information of the past ISM abundances, helping then in the determination of the evolution of the chemical abundances in a galaxy, and providing additional constraints for chemical evolution models (Hernández-Martínez et al. 2011).

Oxygen is the most used element to determine the chemistry of H II regions because its abundance is well determined by just adding the ionic abundances of O^+ and O^{++}, whose lines are observed in the visual range of wavelengths. The determination of ionic abundances requires the determination of physical conditions in the plasma, in particular the electron temperature, which can be derived also in the visual range by detecting the faint auroral lines [OIII] λ4363 and [NII] λ5755, in order to use the so called *direct-method* to determine abundances.

Gradients based on oxygen abundances have been also calculated from PN data, although for the case of highly ionized objects a correction due to the presence of O^{+3} is required. However, it has been shown that O in PNe may be enriched (or depleted) due to stellar nucleosynthesis, particularly in low-metallicity environments (Peña, Stasińska, & Richer 2007; Flores-Durán, Peña, & Ruiz 2017) and also in Galactic PNe with carbon-rich dust (Delgado-Inglada et al. 2015). Therefore, metallicity gradients derived from O abundances in PNe could be perturbed by stellar nucleosynthesis and thus this element would be not adequate to analyze the chemical gradients and the evolution of galaxies. Apparently Ne abundances are also modified by stellar nucleosynthesis in low-metallicity environments (Karakas 2010; Milingo et al. 2010; Flores-Durán, Peña, & Ruiz 2017). On the other hand, Ar and S abundances in PNe are not expected to be modified in such processes during the PN progenitor lifetime, although their abundance determinations have large uncertainties due to large uncertainties in the ionization correction factors when only one ion (Ar^{++} or S^+) is observed (Delgado-Inglada, Morisset, & Stasińska 2014). Especially, the S abundance presents several problems, like 'the Sulphur anomaly'. See e.g., Henry et al. (2010).

In this work we propose to use Ar/H, together with O/H and Ne/H abundance ratios, to trace the PN metallicity gradients in the galaxies of the local universe: M 31, M 33, NGC 300, and the Milky Way (MW). Gradients of PNe will be discussed in comparison with those of H II regions. In §2 we present the data used for the different galaxies. In §3 the abundance gradients are calculated for each galaxy. In §4 our results are presented and discussed, and our conclusions are indicated in §5.

2. DATA ACQUISITION

Data used in this work consist of abundances and galactocentric distances of PNe and H II regions of the spiral galaxies M 31, M 33, NGC 300, and the Milky Way. Most data were obtained from the literature trying to include only abundances calculated with the *direct-method* (determined electron temperature), in a homogeneous way by one group of authors. However, in some cases data from different sources have been included in order to obtain a larger sample of objects for statistical studies, covering as large a galactic radius as possible. This introduced some degree of inhomogeneity that has been minimized by adopting only objects with determined electron temperature and by using recent ionization correction factors. We selected samples where O, Ne, and Ar abundances were available.

We intend to build gradients based only on data from genuine PNe and H II regions. Therefore, for all the galaxies, we carefully selected as genuine PNe those objects where the [OIII] λ5007 intensity relative to Hβ is larger than 3, because a lower value could correspond to a compact H II region and not to a bona-fide PN. This criterion has been used, for instance, by Ciardullo et al. (2002) to select PNe to build the PNLF in external galaxies. On the other hand, H II regions showing an [OIII] λ5007 intensity larger than 3 times Hβ were eliminated from the sample because these objects could correspond to nebulae around WR stars or SN remnants, whose abundances can be contaminated by the processes in the central stars and would not correspond to abundances of authentic pre-star nebulae.

In Table 1 we present several characteristics of the galaxies, such as their Hubble type, mass, distance to the Milky Way and the optical radius R_{25} (the 25 mag arcsec^{-2} isophotal radius).

TABLE 1

CHARACTERISTICS OF GALAXIES

Name	Hubble Type	Mass $M_\odot$	Dist. (kpc)	O/H[(a)]	R_{25} (kpc)	Refs. R_{25}[(b)]
M 31	SA(s)b	1.5E12	785	8.8	20.6	D14
MW	SBbc	8.0E11	—	8.8	11.5	S-M18
M 33	SA(s)cd	5.0E10	849	8.5	9.0	M07
NGC 300	SA(s)d	3.5E10	1880	8.6	5.3	B09

[(a)] O/H is the abundance at $R = 0$, 12+log O/H, for H II regions.

[(b)] D14: Draine et al. (2014), M07: Magrini, Corbelli, & Galli (2007), B09: Bresolin et al. (2009), S-M18: Sánchez-Menguiano et al. (2018).

2.1. M 31

The well known M 31 is the most massive spiral galaxy in the Local Group. It is at a distance of 785 kpc from the Milky Way (McConnachie et al. 2005).

Chemical gradients calculated from the abundances of H II regions have been studied by several authors, mostly based on abundances derived by using *strong-line* methods because due to the high metallicity in this galaxy, the auroral lines indicative of electron temperature, such as [OIII]λ4363 and [NII]λ5755, are faint and difficult to detect. The largest sample analyzed in this way is the one by Sanders et al. (2012), which included 192 H II regions. They reported an O abundance gradient of about -0.0195 ± 0.0055 dex kpc^{-1}, but found that the slope depended on the choice of the *strong-line* method used.

Zurita & Bresolin (2012) obtained abundances based on the *direct-method* for 31 H II regions concentrated at two galactocentric distances of 3.9 and 16.1 kpc. These authors discussed the O/H abundance gradient finding a robust negative slope of ΔO/H / ΔR $= -0.023$ dex kpc^{-1}, based on both the *direct-method* and the *strong-line* method. This value is similar to the values reported by other authors, based on *strong-line* methods (Zaritsky, Kennicutt, & Huchra 1994; Sanders et al. 2012).

Interestingly, Zurita & Bresolin (2012) found that O abundances determined with the *direct-method* for their H II regions are lower, by about 0.3 dex, than the values determined with the *strong-line* methods and the values derived for supergiant stars, at any galactocentric distance. The authors attribute this discrepancy to a bias in their sample, which would not be representative of the mean H II region population (because only high-temperature, and thus low-metallicity regions could be detected in their search), and to the probable depletion of O in dust grains. The abundance data for H II regions used in this work, are taken from Zurita & Bresolin (2012).

Data for PNe were collected from the articles by Kwitter et al. (2012); Sanders et al. (2012); Balick et al. (2013); and Fang et al. (2013, 2015). The use of data from different authors can introduce undesirable inhomogeneities. Therefore, in order to analyze chemical abundances on a more homogeneous system, physical conditions and ionic abundances of PNe were recalculated by us from the extinction-corrected line intensities published by the cited authors. The IRAF 2.16 five level nebular modelling package "stsdas.analysis.nebular", with the tasks *temden* and *ionic*, was employed to determine the physical conditions and ionic abundances. For the full sample the [O III] temperature was derived and occasionally the [N II] temperature was available, but all the ionic abundances were calculated with the [O III] temperature (one-temperature zone model). Total abundances were derived from the ionic abundances by using the ionization correction factors (ICFs) by Delgado-Inglada, Morisset, & Stasińska (2014) which correct for the ions not seen. The results, although not too different from the ones published by the cited authors, are now in a homogeneous system.

The PN distribution in this galaxy extends up to $R/R_{25} \approx 5$ ($R \geq 100$ kpc) while data for the H II regions cover only up to $R/R_{25} \approx 1$ ($R \approx 20$ kpc).

The galactocentric distances used in the diagrams for the gradients were collected from the same references used for the abundance ratios.

2.2. M 33

M 33 is the third most-massive spiral galaxy in the Local Group. Its Hubble type is very late, SA(s)cd, and its mass is much lower than the masses

TABLE 2

LINEAR FITS FOR METALLICITY GRADIENTS IN M 31, THE MILKY WAY, M 33, AND NGC 300

	Oxygen				Neon				Argon			
	X_0	err	$\Delta X/\Delta R$ dex/kpc	err	X_0	err	$\Delta X/\Delta R$ dex/kpc	err	X_0	err	$\Delta X/\Delta R$ dex/kpc	err
M 31												
All PNe	8.46	0.03	-0.001	0.001	8.01	0.04	-0.002	0.001	6.22	0.05	-0.002	0.001
Type I	8.43	0.03	-0.002	0.001	8.03	0.05	-0.004	0.002	6.31	0.09	-0.005	0.002
non-Type I	8.57	0.03	-0.003	0.001	8.01	0.06	0.000	0.001	6.17	0.07	-0.000	0.001
H II reg.	8.76	0.10	-0.030	0.007	7.99	0.23	-0.036	0.016	6.38	0.18	-0.021	0.013
MW												
All PNe	8.85	0.05	-0.024	0.003	8.20	0.03	-0.021	0.005	6.58	0.03	-0.018	0.015
Type I	8.75	0.05	-0.019	0.002	8.24	0.06	-0.026	0.014	6.60	0.02	-0.010	0.006
non-Type I	8.84	0.05	-0.022	0.003	8.20	0.05	-0.027	0.009	6.45	0.03	-0.018	0.006
H II reg.	8.79	0.05	-0.040	0.005	8.21	0.04	-0.027	0.012	7.18	0.14	-0.071	0.029
M 33												
All PNe	8.34	0.07	-0.038	0.016	7.70	0.06	-0.036	0.030	6.17	0.06	-0.031	0.014
Type I	8.52	0.34	-0.032	0.020	7.83	0.40	-0.039	0.050	6.31	0.25	-0.058	0.030
non Type I	8.34	0.15	-0.010	0.020	7.59	0.15	-0.024	0.015	6.01	0.11	-0.010	0.020
H II reg.	8.48	0.03	-0.047	0.008	7.76	0.04	-0.043	0.010	6.34	0.04	-0.064	0.016
NGC 300												
PNe	8.37	0.03	-0.030	0.011	7.65	0.03	-0.029	0.013	6.31	0.02	-0.051	0.014
H II reg.	8.57	0.03	-0.077	0.008	7.71	0.05	-0.065	0.016	6.33	0.04	-0.104	0.017

of the Milky Way and M 31, by factors of 16 and 30 respectively. It is located at 849 kpc from the Milky Way and appears almost face-on. The central metallicity in M 33 as given by H II regions, $12 + \log \mathrm{O/H} = 8.5$, is lower than that of the bigger spirals, and it is even lower than that of NGC 300 (see Table 2).

Gradients from PN abundances were given by Magrini, Stanghellini, & Villaver (2009) and Bresolin et al. (2010) who found that the slopes were equal to the ones of H II regions, or flatter.

For this galaxy, PN data were collected from Bresolin et al. (2010) and Magrini et al. (2010), and H II region data from Magrini et al. (2010). The distributions of H II regions and PNe extend up to $R/R_{25} \simeq 1$ ($R \approx 9$ kpc). As said in the Introduction, in the sample of PNe we excluded those objects showing [O III]λ5007/Hβ intensity ratios smaller than 3 and, consistently, for the H II regions we excluded the objects showing ratios larger than 3. This is to avoid contamination by compact H II regions in the PN sample, and to avoid contamination by supernova remnants, W-R nebulae and other highly excited objects in the H II region sample. Our diagrams then contain only genuine PNe and H II regions.

The galactocentric distances employed to build the gradient diagrams were calculated by us, according to the procedure described by Cioni (2009).

2.3. NGC 300

The almost face-on spiral NGC 300 is the least massive galaxy of the sample studied here and the only one outside the Local Group. Also, it has the latest Hubble type, SA(s)d. It is similar to M 33 in several aspects. Several authors have studied the H II regions. Bresolin et al. (2009) were the first to determine the oxygen abundance gradient based on *direct-method* abundance determinations. They found $\Delta \mathrm{O}/\Delta \mathrm{R} = -0.077$ dex kpc^{-1} with a central abundance of 12+log O/H $\simeq$ 8.57.

Stasińska et al. (2013) analyzed the chemical gradients provided by H II region and PN abundances finding that gradients of PNe appear flatter than those of H II regions.

In this work we have re-analyzed the PN data presented by Stasińska et al. (2013), to compare the case of NGC 300 with the other galaxies of the sample. The abundances presented by Stasińska et al. (2013) were derived by adopting the ICFs proposed by Kingsburgh & Barlow (1994), and in this work we have used the more recent ICFs presented by Delgado-Inglada, Morisset, & Stasińska (2014). With these new ICFs we found that our O/H values were equal to the Stasińska et al. (2013) ones, with differences of less than 0.03 dex, our Ne/H values show differences, on average, of less than 0.05 dex, while our Ar/H values show differences of 0.07 dex on average. Data for H II regions are from Bresolin et al. (2009).

In this galaxy PNe and H II regions have been found up to $R/R_{25} \simeq 1$ ($R \approx 5$ kpc). Galactocentric distances were collected from the same authors as the abundances.

2.4. *Milky Way*

Metallicity gradients have been widely studied in the MW by means of H II regions, PNe, Cepheid stars, stellar clusters and other objects; see e.g., Deharveng et al. (2000); Maciel, Costa, & Ushida (2003); Henry et al. (2010); Stanghellini & Haywood (2018, 2010); Esteban et al. (2017); the compilation by Mollá et al. (2019), etc. The reported results for PNe have been contradictory. It has been claimed that the PN gradients coincide with those of H II regions or that the PN gradients are shallower, that gradients have flattened (or steepened) with time, or that the gradient changes slope at certain distance from the galactic center. One of the main problem in these determinations is the large uncertainties in the distances to PNe.

Determining the distance to galactic PNe is a difficult task. The trigonometric parallax method is available only for a handful of nearby objects. Even the parallaxes measured by GAIA are limited to distances of a few kpc around the Solar System, and in GAIA Data Release 2 less than a hundred PNe have confidently measured parallaxes (Kimeswenger & Barría 2018). Therefore, the distances for a large sample of PNe are based on model-dependent statistical methods which, on occasion, lead to different results. At present, the most used distance scales are those proposed by Stanghellini & Haywood (2010), hereafter S10, and by Frew, Parker, & Bojičić (2016), hereafter F16. The latter authors established a robust optical statistical distance indicator, the Hα surface brightness vs. radius ($S_{H\alpha}$-r) indicator, where the intrinsic radius is calculated by using the angular size, the integrated Hα flux, and the reddening to the PNe. This radius, combined with the angular size, yields directly the distance. On the other hand, S10 determine statistical distances based on apparent diameters and 5 Ghz fluxes of PNe. A comparison of both distance scales are presented below.

In this work we used the PN chemical abundances reported by Henry, Kwitter, & Balick (2004), Milingo et al. (2010), and Henry et al. (2010). These authors belong to the same group; therefore, all physical conditions were calculated with the same method, and total chemical abundances were obtained using the ICFs described in Kwitter & Henry (2001). The Galactic sample consists of 156 PNe covering galactocentric distances in the range $0.21\,\mathrm{kpc} \leq R \leq 22.73\,\mathrm{kpc}$ ($0.02 \leq R/R_{25} \leq 1.97$). More than 40 of these PNe lie at distances larger than the solar galactocentric distance and are crucial for the gradient determination.

Oxygen abundances for H II regions were taken from Esteban et al. (2017), while neon and argon abundances were collected from García-Rojas et al. (2004), García-Rojas et al. (2005), García-Rojas et al. (2006), García-Rojas et al. (2007), Esteban et al. (2004), Esteban et al. (2013), and Fernández-Martín et al. (2017). As said above, the use of data processed by different authors can introduce some inhomonogeneities and uncertainties in the Ne and Ar gradients of H II regions, that should be considered carefully.

In Figure 6 we present the comparison of the metallicity gradients of oxygen, argon and neon for the Galactic H II regions and the PN sample. This figure will be discussed in detail in § 3.4, Here we want to show that for the case of PNe we are using the distances by F16 and S10 for a comparison. As seen in this figure the oxygen, neon, and argon abundances show a very large dispersion at all galactocentric distances, but the linear regressions for PNe are similar for both distance indicators. Therefore in the following F16 distances will be used as an independent way to compare with other works.

3. ABUNDANCE GRADIENTS

Abundance gradients for the different elements and the different galaxies were calculated by fitting a straight line to the abundances versus the fractional galactocentric distance R/R_{25} and also versus the distance R (kpc). For each elemental abundance we computed one fit for PNe and one for H II regions. Gradients are shown in the respective figures. In

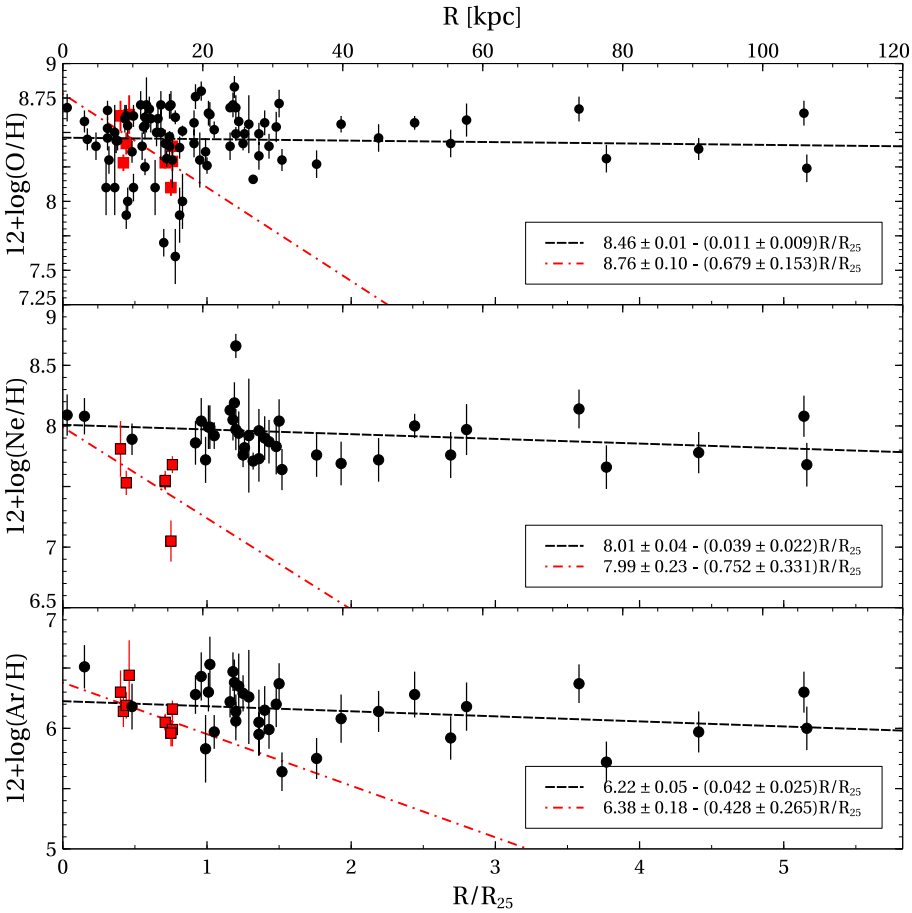

Fig. 1. Radial metallicity gradients of O (top), Ne (center) and Ar (bottom) for M 31, are presented. Black circles represent PNe and red squares, H II regions. Black dashed lines correspond to the linear fit for PN data and dashed-dotted red lines correspond to the linear fits for H II regions. The color figure can be viewed online.

Table 2 a compendium of the abundance gradients versus galactocentric distance R (kpc) is listed. For each fit the table gives the values of the intercept, X_0, and the slope, calculated by the equation:

$$Y = \mathrm{X}_0 + \Delta\mathrm{X}/\Delta R \times R\ (\mathrm{kpc}).$$

Errors have been calculated at 1 sigma. The errors in the gradients of Ne and Ar are much larger than in O, due to the large dispersion of the abundances at any galactocentric distance, and to the uncertainties in the abundance determination, because large ICFs are used for these elements.

3.1. M 31

In Figure 1 the radial gradients for O/H, Ne/H and Ar/H, for PN and H II region abundances are plotted vs. R/R_{25}. The gradients vs. R (kpc) are presented in Table 2.

A linear fit to the gradients is included in each case. The abundances of elements in PNe present a large dispersion at any given galactocentric distance, but in particular in the central zone. It is worth to notice that there are some PNe in the central region with very low O/H abundance, which do not have Ne/H or Ar/H abundance determinations. H II regions also show a large dispersion in the elemental abundances at any galactocentric distance (Zurita & Bresolin 2012; Sanders et al. 2012).

For the case of O in H II regions, we obtain:

$$12 + \log(\mathrm{O/H}) = (8.76 \pm 0.10) - (0.679 \pm 0.153) R/R_{25}$$

or equivalently

$$12 + \log(\mathrm{O/H}) = (8.76 \pm 0.10) - (0.030 \pm 0.007) R\ (\mathrm{kpc}).$$

The O gradient found is equal, within the uncertainties, to the one derived by Zurita & Bresolin (2012). For Ne, we find

$$12 + \log(\mathrm{Ne/H}) = (7.99 \pm 0.23) - (0.036 \pm 0.016)\ R\ (\mathrm{kpc}),$$

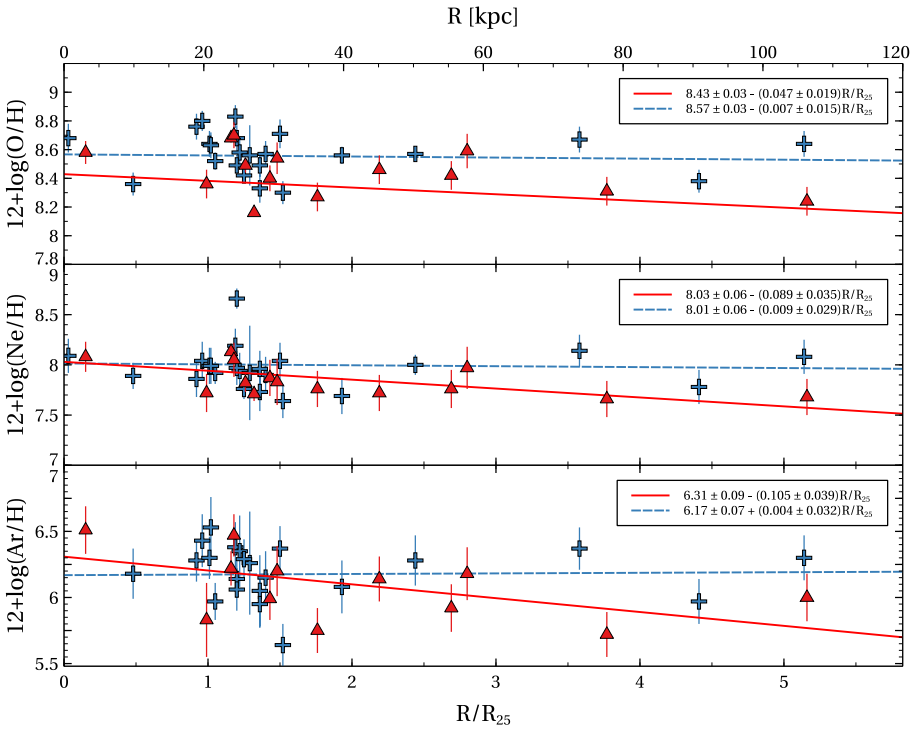

Fig. 2. Radial metallicity gradients for different Peimbert Type PNe in M 31. The data for Type I PNe are shown as red triangles, the data for non-Type I PNe as blue crosses. The color figure can be viewed online.

and for Ar, we find

$$12+\log(\mathrm{Ar/H})=(6.38\pm0.018)-(0.021\pm0.013)\,R\,(\mathrm{kpc}).$$

In all the cases, the errors correspond to 1 sigma.

PN abundances seem unrelated to the galactocentric distance; the PN gradients are really flat, showing slopes of -0.001 ± 0.001 dex kpc^{-1} for O, -0.002 ± 0.001 dex kpc^{-1} for Ne, and -0.002 ± 0.001 dex kpc^{-1} for Ar, which considering the errors are consistent with 0. This indicates that at large galactocentric distances PNe present on average the same O/H abundances as the central zones; the same is true for Ar and Ne.

The O/H value at the intercept for H II regions, 12+log O/H = 8.76±0.10, seems slightly larger than the value for PNe, 12+log O/H = 8.46±0.03, while the Ne/H and Ar/H central values are similar for H II regions and PNe, within uncertainties. However, due to the negative gradients for H II regions, at large distances ($R \leq R_{25}$,) the O/H, Ne/H and Ar/H abundances in PNe are always larger than the abundances in H II regions.

The larger value of O at the intercept for H II regions seems to be an artifact due to the limited sample of Zurita & Bresolin (2012), which moreover presents large uncertainties. In addition, there are a large number of PNe with low O abundances in the central zone, with no Ne and Ar measurements, that could be contributing to the low O/H central value for PNe. In this zone a very large dispersion is observed.

In the central zone the value at $R = 0$ of $\log \mathrm{Ne/O}=-0.77$ for H II regions is about solar and excludes the possibility indicated by Zurita & Bresolin (2012) of a large O depletion in dust grains. On the other hand, Ne in H II regions is similar to Ne in PNe in the central zone. Relative to Ar, $\log \mathrm{Ar/O\,(H\,II)} = -2.38$ and $\log \mathrm{Ar/O\,(PNe)} = -2.24$ which correspond well with the solar or Orion values.

In Figure 2 we show the abundance gradients for PNe separated by Peimbert types. Peimbert (1978) called Type I those PNe with a N/O abundance ratio larger than 0.5 and a He/H abundance ratio larger than 0.14. This group includes the PNe with central stars with initial masses larger than about 3.0 $M_\odot$ and therefore they are the youngest objects among PNe. They have enriched their nitrogen abundances by nucleosynthesis processes, such as CNO and hot-bottom-burning (HBB) and the newly formed N has been transported to the surface in different dredge-up events. In the Galaxy, Type I PNe belong to the

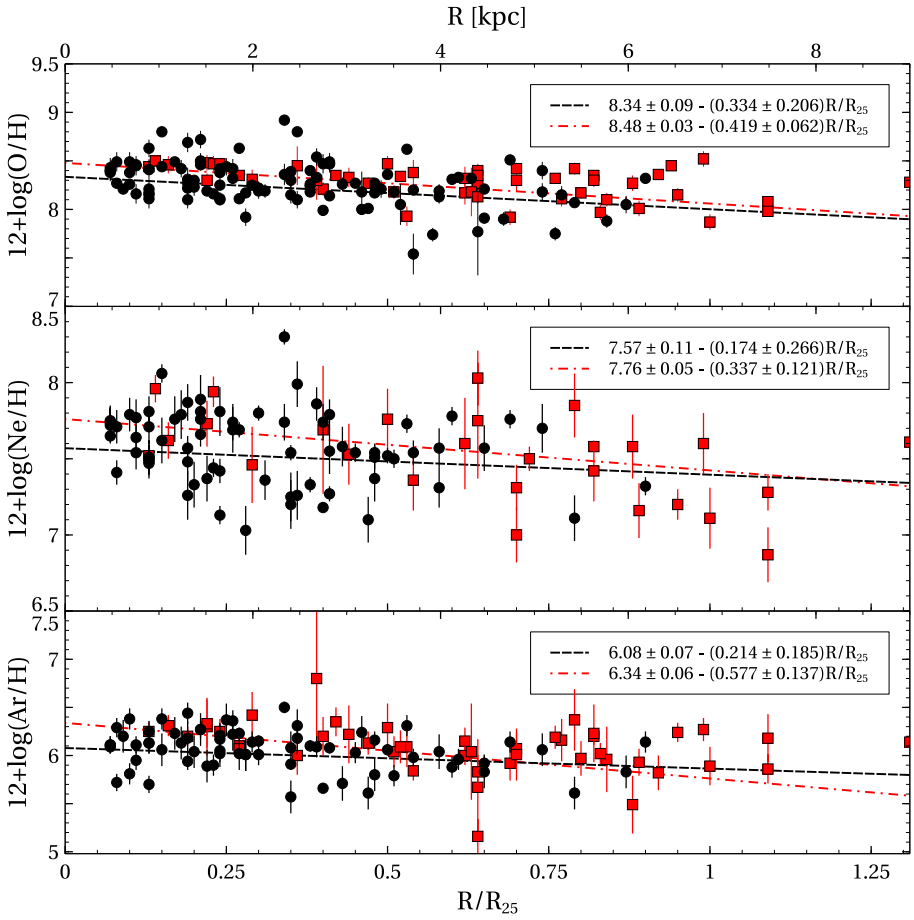

Fig. 3. Radial metallicity gradients in M 33. Symbols are as in Figure 1. The color figure can be viewed online.

thin disk and their ages are about 1 Gyr. Non-Type I PNe include the Peimbert Types II and III, which are classified based on their radial velocity, being smaller or larger than 60 km s^{-1}, and are located in the thick disk. They correspond to older objects with initial masses smaller than 2 $M_{\odot}$, where no large N-enrichment is present. Their ages are between 2 to 8 Gyr.

Thus our Figure 2 represents an effort to determine the behavior of the abundance gradient over time. It is evident that although the gradients are very flat and the uncertainties are large, Type I PNe show slightly steeper gradients for the three elements: O, Ne and Ar. Additionally, Type I PNe seem to be O-poorer than non-Type I, possibly showing the effect of CNO and HBB processes which operates in these massive stars. This phenomenon will be discussed in more detail in § 4.1.

It should be mentioned here that the value of the N/O abundance ratio, used to define a Peimbert Type I PN is slightly dependent on the metallicity. The N/O ratio defined by Peimbert (1978) applies to the metallicities of the Milky Way and M 31, and should be slightly lower for M 33 and NGC 300, but the difference is not important for this work and the results are not much affected.

We will discuss the results for M 31 in sections ahead, together with the results for the other galaxies.

3.2. M 33

Metallicity gradients for H II regions and PNe in M 33 are presented in Figures 3 and 4. In the latter one, PNe are separated into Peimbert Type I and non-Type I objects. Differently to what happens in M 31, in this galaxy O, Ne and Ar abundances of PNe and H II regions are similar, within uncertainties, at any galactocentric distance.

For PNe the straight-line fit of the gradients gives 12+log O/H = (8.34±0.07) −(0.038±0.016) R (kpc) and for H II regions, 12+log O/H=(8.48±0.03) − (0.047 ± 0.008) R (kpc). That is, the slope for PNe seems shallower than the slope for H II regions, by

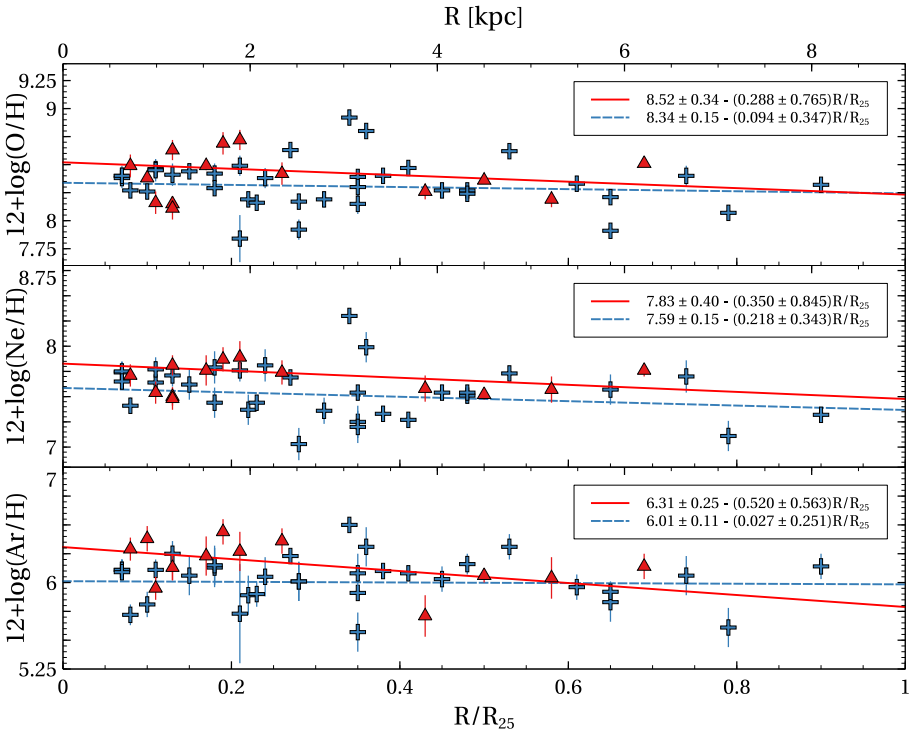

Fig. 4. Radial metallicity gradients for PNe of different Peimbert Type in M 33. In red the data for Type I PNe are shown and in blue, the data for non-Type I PNe. The color figure can be viewed online.

about 30% for O and by larger factors for Ne and Ar, but the uncertainties are large making these results inconclusive. However, we consider them indicative of shallower PN gradients.

In Figure 4, the gradients of PNe with different Peimbert Types are shown. There are only a few Type I PNe in the sample (about 20%) and the uncertainties are very large. However, the central values can be considered to be equal, within errors, for both PN types. Despite the uncertainties, slightly steeper gradients are apparent for Type I PNe, while the gradients for non-Type I PNe are flatter. The slopes shown by Type I PNe are more similar to those of H II regions. The huge uncertainties in these results make them inconclusive, but only indicative. We consider them reliable because M 33 shows results similar to M 31 and NGC 300.

3.3. NGC 300

PN data in this galaxy were analyzed by Stasińska et al. (2013), where O, Ne, S and Ar abundance gradients were presented. These authors found that the formal O/H, NeH and Ar/H abundance slopes for PNe are shallower than those of H II regions and attributed this to a steepening of the metallicity gradients during the last Gyr. The O/H central value of PNe is smaller by 0.15 dex than the central value of H II regions. Ne/H and Ar/H, on the other hand, present the same central abundances for PNe and H II regions, and almost flat gradients, although affected by large dispersion at any galactocentric distance. According to Stasińska et al. (2013), due to the difference in the O/H value at $R = 0$, O abundances in PNe could be affected by nucleosynthesis of their central stars.

Our analysis of these data, calculated with the ICFs by Delgado-Inglada, Morisset, & Stasińska (2014), shows similar results, presented in Figure 5. O, Ne and Ar metallicity gradients for PNe in NGC 300 are flatter than the values for H II regions. Their $\Delta X/\Delta R$ values are about half the values found for H II regions, in very good agreement with the results of Stasińska et al. (2013). In the central zone, H II regions show 12+log O/H = 8.57±0.03, log Ne/O = −0.86±0.008 and log Ar/O= −2.20±0.07. These abundance ratios are similar to the solar or Orion values, while PNe show values 12+log O/H= 8.37±0.03, log Ne/O =−0.73±0.06, and log Ar/O = −2.06±0.05, also similar to the solar and Orion values but with an apparent O decrease by 0.2 dex, relative to the O of H II regions, as already indicated

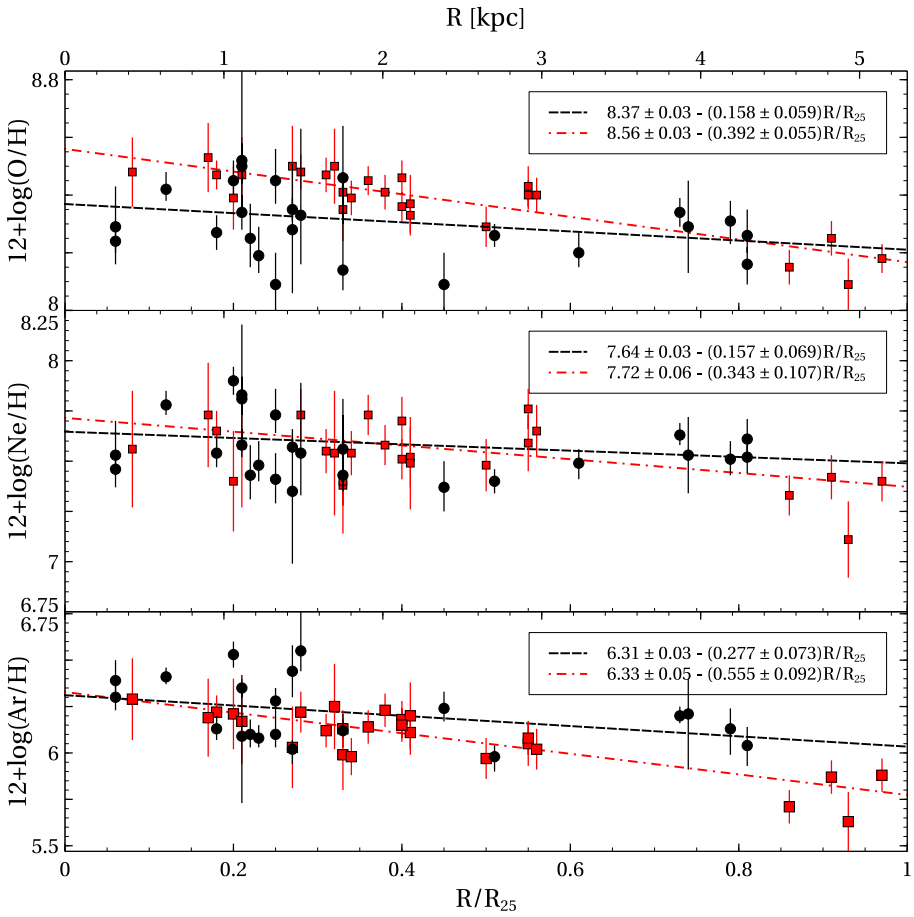

Fig. 5. Radial metallicity gradients in NGC 300. Symbols are as in Figure 1. The color figure can be viewed online.

by Stasińska et al. (2013). This will be discussed in §4. The central values of Ne/H and Ar/H are similar for PNe and H II regions.

In this case, an analysis discriminating between the Peimbert Type PNe is not possible, because there are very few Type I PNe in the sample.

3.4. *The Milky Way*

Metallicity gradients have been widely studied in the MW by means of many kind of objects. See references in §2.4.

Henry et al. (2010), using distances by Cahn, Kaler, & Stanghellini (1992) derived an O gradient for PNe of -0.058 ± 0.006 dex kpc^{-1}, which changes to -0.042 ± 0.004 dex kpc^{-1} if the distances by Stanghellini, Shaw, & Villaver (2015) are used. Henry et al. (2010) suggested that the gradient steepens beyond a galactocentric distance of 10 kpc. In a recent work, Stanghellini & Haywood (2018), using distances given by S10, reported that out to $R/R_{25} \simeq 2.4$ ($R \approx 28$ kpc) the radial gradient of oxygen for PNe is shallow, with a slope of ≈ -0.02 dex kpc^{-1} and a central abundance of 12+log(O/H)$\simeq$ 8.68. These authors suggest that the gradient changes with R in the sense that the significant slope is limited to R between 10 and 13.5 kpc, and outside this range the gradient is almost flat.

We analyzed the gradients derived from the data for PNe and H II regions mentioned in §2.4. PN abundances were calculated by us in a homogeneous way. The results are presented in Figures 6 and 7. In the latter figure the data have been binned in distance taking bins of 1 kpc, for clarity. The distances by F16 are used for PNe.

Clearly, PN gradients are flatter that those of H II regions. $\Delta X/\Delta R$ is about twice larger for H II regions (see Figure 7 and Table 2). The binning of data with distances introduced an artifact in Figure 7 in the sense that the O and Ne abundances for PNe seem larger than the values for H II regions at $R = 0$. But this does not occur in Figure 6, where the original data, not binned, were used. In these graphs

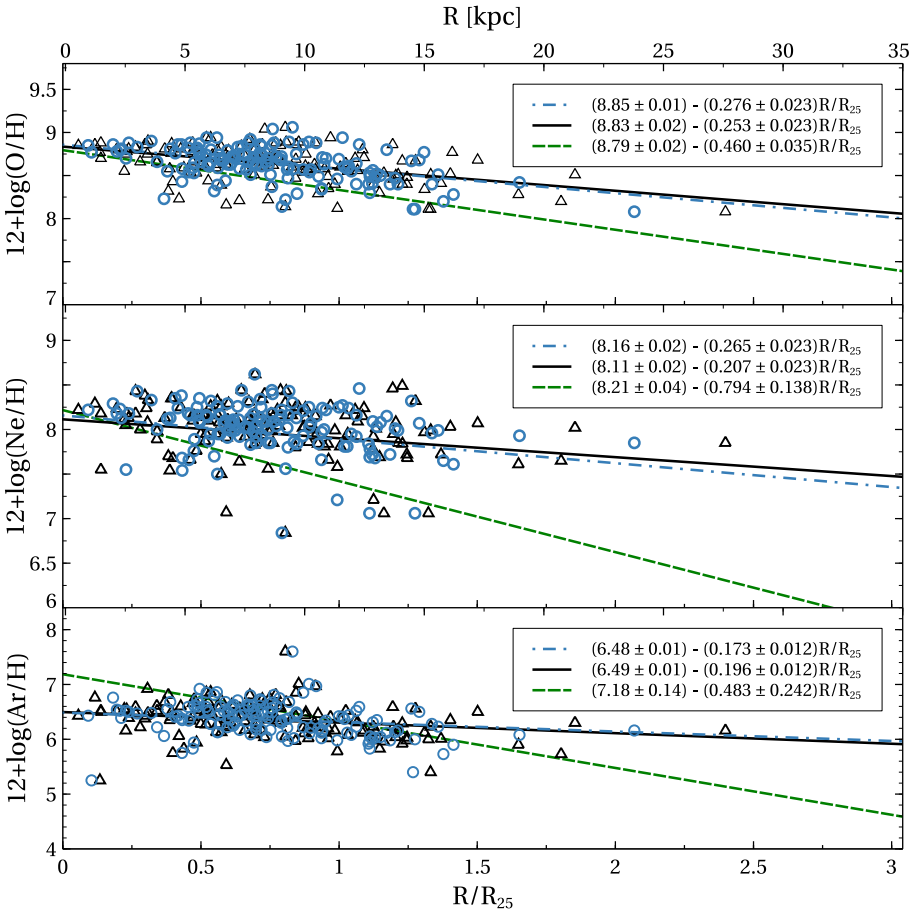

Fig. 6. Radial metallicity gradients of O, Ne and Ar, in the Milky Way. Open blue circles and black triangles are PNe with distances from Frew et al. (2016) and Stanghellini & Haywood (2010) respectively. The dotted-dashed line is the linear fit for F16 distances and the solid line that for Stanghellini & Haywood distances. The green dashed line is the linear fit for H II regions by Esteban et al. (2016). The color figure can be viewed online.

it is observed that the O and Ne values at the central zones coincide for PNe and H II regions, within uncertainties, while the Ar/H abundance is lower in PNe by 0.7 dex. However, due to the shallower gradients for PNe, at galactocentric distances larger than a few kpc the average abundances of PNe are larger than those of H II regions, similarly to what happens in M 31 and NGC 300. This can explain in part the results by Rodríguez & Delgado-Inglada (2011), who found that in the solar vicinity, PNe appear richer than H II regions.

The gradients derived for PNe of different Peimbert types are shown in Figure 8. In this case, gradients of Type I and non-Type I PNe are equal within uncertainties. A possible change in the slope, at R≈ 14 kpc, is appreciated, which will be discussed in the next section.

We used the known GAIA distances of PNe to analyze the gradient for PNe. Using the same set of abundances as for the MW, we searched for those PNe that have calculated parallaxes in GAIA Data Release 2 (GAIA DR2). We did not take into account those objects with negative parallax and those with errors in parallax (dp/p) larger than 0.4. We found 22 PNe meeting these requirements. No gradient was found in this interval for the three analyzed elements, because GAIA galactocentric distances are limited from 6 to 10 kpc, and this interval is too short to show any gradient, due to the large dispersion in abundances.

4. RESULTS AND DISCUSSION

The radial gradients of the elements O, Ne and Ar are analyzed for homogeneous samples of PNe and H II regions in four disk galaxies of different Hubble type, different masses and different metallicities, M 31, M 33, NGC 300 and the Milky Way. A com-

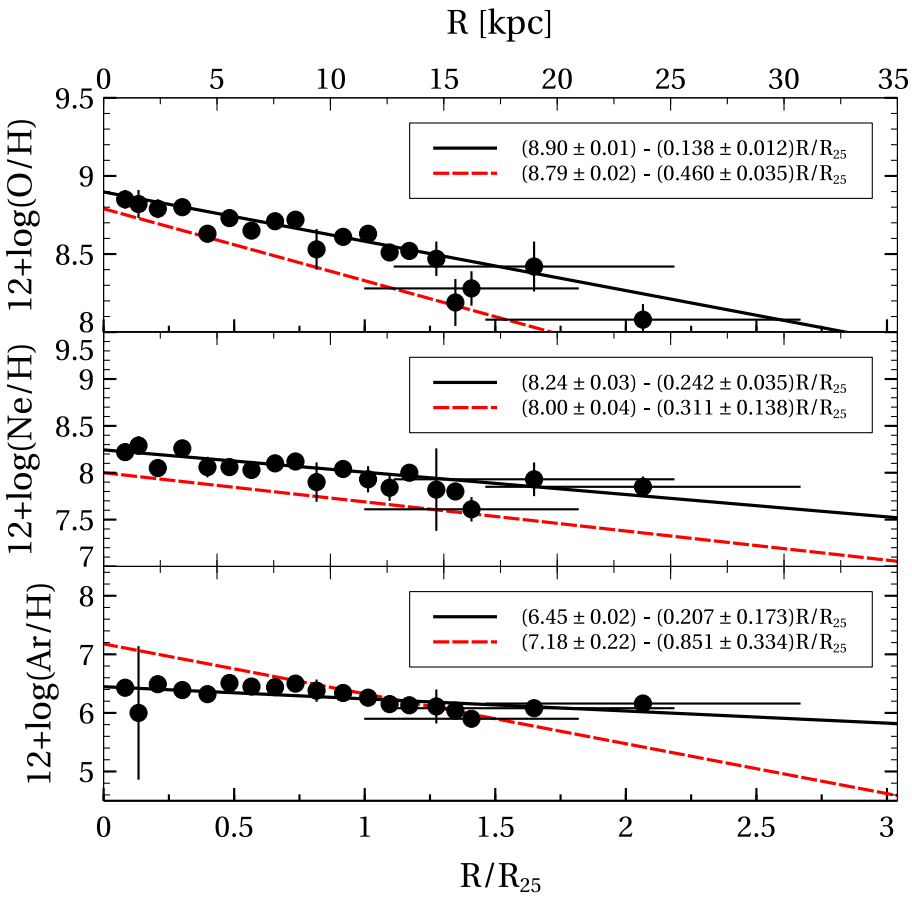

Fig. 7. Radial metallicity gradients. The black circles correspond to PNe with F16 distances in bins of 1 kpc. Solid lines are the fits for PNe and dashed lines those for H II regions. The top panel shows the radial gradient for O, the center panel the gradient for Ne, and the bottom the gradient for Ar. The color figure can be viewed online.

pendium of our results, with all the linear fits and slopes $\Delta X/\Delta R$ in dex kpc^{-1}, is presented in Table 2. In the following we discuss the results.

4.1. M 31

Our work extends the PN sample, including objects from 2 kpc up to a distance larger than 100 kpc (0.2 – 5 R_{25}). In this interval the abundance gradients for PNe are flat, consistent with a slope of zero. The average abundances of PNe are the same at all galactocentric distances, showing a very large dispersion.

On the other hand the gradients for H II regions are always negative, with values -0.030 ± 0.010 dex kpc^{-1} for O, -0.036 ± 0.016 dex kpc^{-1} for Ne and -0.021 ± 0.013 dex kpc^{-1} for Ar. These slopes are much shallower than the slopes in the other three galaxies. The very flat gradients found in M 31 could indicate, according to Sánchez et al. (2014), that M 31 has been perturbed by interactions or merging. It is clear that these phenomena have had an important role in the formation and growth of M 31, a galaxy that shows numerous stellar substructures in its outskirts (McConnachie et al. 2009, and references therein).

At the central position PNe appear to have an average O/H abundance slightly lower than the average of H II regions, but similar Ne/H and Ar/H abundances. This could be due to the presence of several PNe with very low O abundance (and not known Ne and Ar) in the central region, as it was explained in § 3.1

Similarly to our work, Sanders et al. (2012) and Magrini et al. (2016) reported that the O/H gradient from PN abundances is flat in M 31. Sanders et al. (2012) in particular, from the analysis of O abundances of 52 PNe derived with the *direct-method* and located at galactocentric distances from 5 to 25 kpc (0.2 to 1.2 R_{25}), found no relation between PN abundances and their galactocentric distances. The same

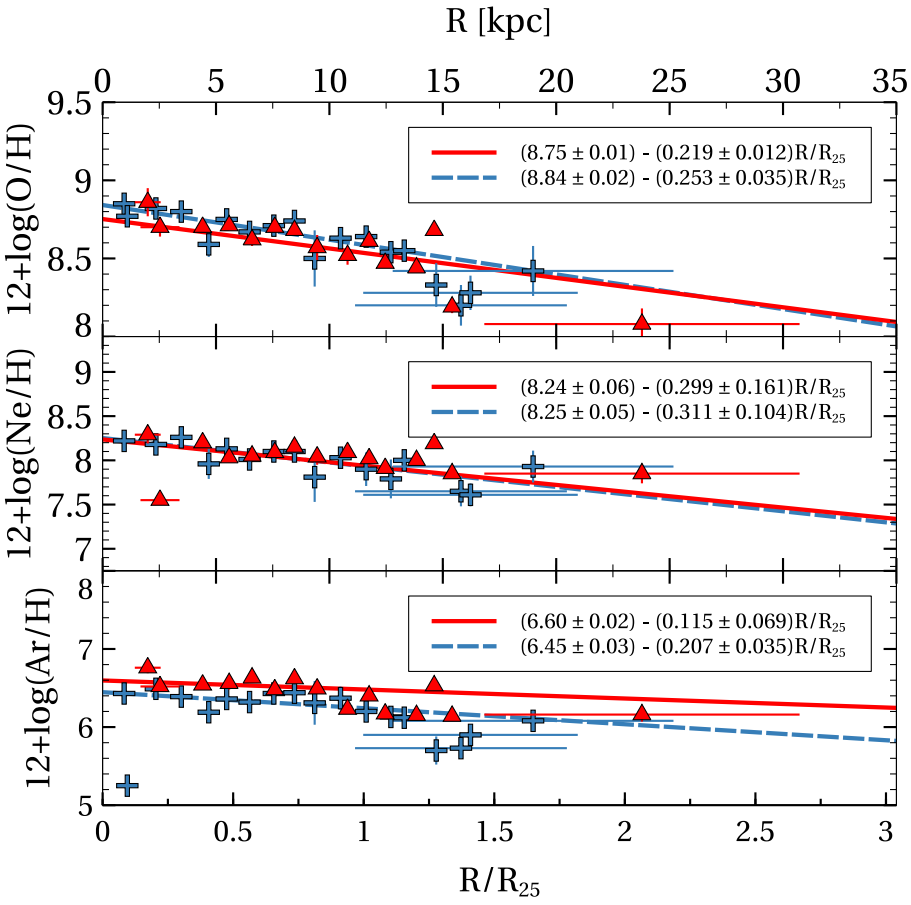

Fig. 8. The PNe of the MW with distances binned as in Figure 7. Red diamonds represent Type I PNe and blue stars non-Type I PNe. Solid lines show the linear fits for Type I SNe, the dotted lines those for non-Type I SNe. The color figure can be viewed online.

PN sample was re-analyzed by Magrini et al. (2016), who reported that radial migration plays an important role in PNe of M 31, which possibly explains the extreme flatness of PNe gradients, since PNe may have migrated far from their place of origin.

When the sample is divided into Peimbert Type I PNe (young objects) and non-Type I PNe (older objects), we found that the young objects show a steeper gradient, although still very flat (Figure 2). Due to their youth (ages lower than about 1 Gyr), Type I PNe have had less time to migrate from their birth places. Thus they might be showing the gradient at about 1 Gyr ago, but considering that these gradients are very flat (compared to those of H II regions) migration could have been an important role for these young PNe too.

It is important to mention that the results found for M 31 corroborate models of galactic chemical evolution, which besides including the star formation rate, gas infall rate accross the disk, inflows and outflows of gas, stellar evolution and yields, among other processes, also include radial redistribution of stars (stellar migration). Models by Ruiz-Lara et al. (2017) predict that radial redistribution and accretion increase the metallicity dispersion, and flatten the age and metallicity profiles of galaxies; the greater the efficiency of the redistribution, the larger the flattening effect and, as a consequence, a steeper metallicity gradient should be expected at the birth of the objects. Type I PNe being closer to their birth places, they show steeper gradients.

Peimbert Type I PNe present slightly lower O abundances than non-Type I's, while the Ne and Ar abundances are similar. This can be due to nucleosynthesis, because CNO and HBB processes are expected to occur in these more massive central stars, modifying their initial O abundance. Such an O decrease is predicted by recent sophisticated evolutionary stellar models for low-intermediate mass stars of the MW, computed at different metallicities, by

Ventura et al. (2017). Using the sequence of models with $z \approx 0.014$ (solar metallicity) it is found that stars with masses larger than 3 $M_{\odot}$ decrease their O/H abundance by up to 0.2 dex at the end of their evolution, while stars of lower masses do not modify their original O/H. This is the effect we are finding in the comparison of Type I and non-Type I PNe in M 31.

4.2. M 33

For M 33, a late Hubble-type galaxy, the results are presented in Figures 3 and 4. In this case O, Ne and Ar in PNe show central values similar to those of H II regions. Therefore there was no important enrichment of the ISM since the time of formation of these PNe. Similarly, the O abundance gradients of PNe and H II regions are equal, within uncertainties, but the Ne and Ar abundance slopes in PNe seem significantly flatter, although the large dispersion and large uncertainties make these results doubtful.

Due to the similarity of metallicity gradients and the large dispersion, Magrini, Stanghellini, & Villaver (2009) claimed that gradients are equal for PNe and H II regions. In a recent paper, Magrini et al. (2016) analyzed the possible effects of radial migration in M 33 and concluded that it is not important. Also Bresolin et al. (2010) declared that PNe and H II regions have gradients equal within uncertainties, but an analysis of their Table 8 shows that the slopes of PNe are systematically flatter than those of H II regions, even when the uncertainties are large.

It is interesting to notice that PNe in M 33 do not show O reduction compared to H II regions, as occurs in NGC 300 (see next section), despite the similar low metallicity of both galaxies. It seems that the initial masses of the central stars in this galaxy are not as large as in NGC 300. Thus, they are not affected by nucleosynthesis in the same way as seen in NGC 300. According to Ventura et al. (2016) models, the initial masses should have been not much larger than 2 $M_{\odot}$.

Although the uncertainties are huge due to the small number of objects, Type I PNe in M 33 seem to present slopes steeper than non-Type I PNe, and more similar to the ones of H II regions. Again these results are very uncertain, but we consider them indicative of a behavior similar to that of M 31.

4.3. NGC 300

For NGC 300, the latest Hubble-type galaxy, with a metallicity similar to M 33, the abundance gradients of PNe are about twice smaller than the gradients of H II regions (see Figure 5). The gradients presented by H II regions are the largest (ΔO / $\Delta R = -0.077 \pm 0.008$ dex kpc^{-1}) of the whole galaxy sample.

The average O/H central abundance of PNe is lower than the value of H II regions by 0.2 dex, while Ne and Ar have the same central values. Such an O decrease, which does not occur for Ne and Ar, could be the result of stellar nucleosynthesis and dregde-up events. Stellar evolution models performed by Ventura et al. (2016) for PNe in the SMC (which has a metallicity similar to that of NGC 300) predict a decrease of the initial O occurring in stars with masses larger than 3 $M_{\odot}$, due to HBB; simultaneously, a large N-enrichment occurs. Such an N-enrichment is observed for the PNe of NGC 300 (Stasińska et al. 2013). Therefore, we conclude that the central stars of PNe analyzed in this galaxy had, in general, large initial masses; they are younger than 1–2 Gyr. This is certainly due to a bias in the sample because only the brightest objects were observed at the distance of NGC 300 (Peña et al. 2012).

The central values of Ne/H and Ar/H are similar for PNe and H II regions. Once again, this indicates that PNe are young objects, which had initial abundances similar to the present ISM.

An interesting fact is that at R/R_{25} larger than 0.6, the Ar/H abundances of PNe are definitely larger than those of H II regions, independently of the large dispersion. This is also found for Ne, but it is less marked. Since Ar it is not expected to have been modified by stellar nucleosynthesis of the central stars, this is indicating that radial migration should have been important for PNe (despite their youth), and that PNe have changed their initial galactocentric distances, being churned in the galaxy, although not at the level of migration found in M 31.

4.4. *The Milky Way*

The results for the MW are presented in Figures 6 and 7. The latter figure shows PNe data in distance bins of 1 kpc. The PN sample covers a galactocentric distance interval 0.21 kpc $\leq R \leq$ 22.73 kpc ($0.02 \leq R/R_{25} \leq 1.97$). The gradient obtained for O in PNe is -0.024 dex kpc^{-1}, similar to the ones derived for Ne and Ar. As occurs in M 31, and NGC 300, PN gradients are flatter, by about a factor of 2, than the gradients of H II regions.

The gradients for Type I and non-Type I PNe are shown in Figure 8. In this figure the slopes of both kinds of nebulae seem indistinguishable. Our result is different from that reported by Stanghellini & Haywood (2010) and Stanghellini & Haywood (2018)

for their young and old PN samples, using the distances by S10. They claim that young PNe definitely present a steeper gradient of -0.027 dex kpc^{-1} versus -0.015 dex kpc^{-1} for old PNe. We are not sure if our different result is due to the different PN samples (a much larger sample from the literature, not homogenized, was used by Stanghellini & Haywood) or to the different distance scale used. In any case we concur with them in that PN gradients are flatter than those of H II regions. Therefore, it appears than PNe have moved from their birth places due to radial migration and are showing flatter gradients. Alternatively, it is possible that the abundance gradients were flatter several Gyr ago.

Although a linear fit to these gradients produces acceptable results, it should be noticed that at distances larger than about 14 kpc, the observed abundances (in particular O/H and Ar/H) decrease to a value below the linear fit and continue flat outwards, showing a break. Unfortunately, in our sample there are few PNe there and this result is not conclusive. A break at a distance $R \approx$13.5 kpc was reported by Stanghellini & Haywood (2018) for the same sample of outer PNe. Following Halle et al. (2015) they attributed this behavior to the effect of the galactic bar, whose outer Lindblad resonance would be located at about this distance according to N-body simulations. It is crucial to observe a larger number of PNe in the outskirts of the Galaxy to verify this behavior.

It is interesting to compare the gradients of H II regions (-0.040 dex kpc^{-1}) and PNe (-0.024 dex kpc^{-1}) with other gradients provided by well measured indicators of different ages. Mollá et al. (2019) prepared a compilation of gradients for objects of different ages, computed by various authors, in order to compare them with results from their chemical evolution models. From this compilation we selected the gradients calculated by Mollá et al. for Cepheid stars, (which are young objects with ages of about 0.1 Gyr and show an O/H gradient of -0.049 dex kpc^{-1}) and open clusters (OC) which span ages from 2 to more than 8 Gyr. The O/H gradient for OC younger than 2 Gyr is -0.030 dex kpc^{-1}, and for ages between 2 and more than 8 Gyr, it is -0.027 dex kpc^{-1}. It is clear that the gradients of H II regions and Cepheid stars are equal within uncertainties, indicating that in the Galaxy the chemical gradients have not changed significantly at least in the last 0.1 Gyr, while gradients of PNe (Type I's and non-Type I's) are equal to those of OC older than 2 Gyr. Therefore for objects of 2–8 Gyr the gradient is flatter (-0.027 dex kpc^{-1}) than those for Cepheids and H II regions (-0.049 and -0.040 dex kpc^{-1}). PNe and OC certainly could have been affected by migration, but not in as an extreme way as in M 31. Alternatively, PN and OC gradients could correspond to the true gradients present several Gyr ago.

Mollá et al. (2019) discussed the possible effects of migration in the MW. By analyzing models by different authors, their conclusion was that radial migration seems not to be important for stars younger than 4 Gyr. Only for objects older than 8 Gyr, radial migration may be important. Models by Mollá et al. of the time evolution of chemical gradients in the Milky Way (without considering migration, bar or spiral arms) predict a very smooth evolution of the radial gradient within the optical disk. Some models show a steepening of the gradient, from -0.02 to -0.04 dex kpc^{-1} over a time of 10 Gyr. Therefore the gradients shown by PNe and OC could be the gradients at the time of formation of these objects, not affected by migration.

5. CONCLUSIONS

From the analysis of abundance gradients of O, Ne, and Ar in PNe and H II regions in four galaxies, it is found that in NGC 300 (a late Hubble-type spiral of low metallicity) and the Milky Way, the abundance gradients for PNe are flatter than those of H II regions, by factors of 2. This result is less conclusive in the case of M 33, but there also slightly flatter gradients for PNe than for H II regions are found.

M 31 represents an extreme case, where the PN abundances are not related to the galactocentric distances and show the same values at any distance from the center, up to more than a 100 kpc. Merging, interactions with other galaxies and important radial migration of PNe are the cause of this behavior. It is worth to notice that considering H II regions, M 31 presents the shallowest gradients, which again is a possible consequence of merging and interactions.

In the four galaxies analyzed here, there is a large dispersion of the abundances at any galactocentric distance, larger for PNe than for H II regions. This is possibly caused by migration. PNe could have been churned in the galactic disk far from their birth places; thus, their abundances do not correspond to the place where they presently are. To understand this it is important to analyze the abundances of elements that have been not been modified by stellar nucleosynthesis, like Ar, since O and Ne can be modified depending on the metallicity and the stellar

mass. However, Ar abundance determinations have large uncertainties; therefore, the results based on Ar only should be viewed with care.

Considering the PNe separated by Peimbert types, M 31 is a clear case where the gradients seem to be steepening with time, since Type I PNe, which correspond to the youngest objects, with ages smaller than 1 Gyr, show steeper slopes than non-Type I PNe, with ages between 2 to 9 Gyr. Type I PN gradients are more similar to, but still much flatter than, H II region slopes. The gradients for non-Type I PN are most probably altered by radial migration which has moved the old PNe from their initial position in the galaxy. Type I PNe, due to their youth, have had less time to migrate from their place of birth, but the flatness of their gradients also indicates perturbations due to migration.

In the Milky Way, H II region and PNe gradients can be compared to the gradients of objects of similar ages, such as Cepheid stars (younger than 0.1 Gyr) and open clusters (ages between 2 and more than 8 Gyr). H II regions and Cepheid stars show the same O/H gradients, which indicates that the chemical enrichment in the Galaxy has not increased in the last few hundreds of Myr. On the other hand PNe and open clusters (OC) show similar gradients, flatter than those of Cepheids and H II regions. This could indicate that the gradients steepen slowly with time (from -0.02 to -0.04 dex kpc^{-1} over several Gyr). Alternatively, it could indicate that radial migration could have perturbed the slopes shown by these relatively old disk objects. Chemical evolution models for the Galaxy by Mollá et al. (2019) seem to favor the first option.

In the Milky Way a break in the PN gradient seems to exist, in the sense that inside $R \approx 14$ kpc there is a measurable gradient of about -0.024 dex kpc^{-1} for all the three elements. Outside this galactocentric distance, PNe show a flat slope. Stanghellini & Haywood (2018) reported the same phenomenon, based on the same data for PNe in the outskirts. However, there are only a handful of objects observed in this zone, and a larger sample should be analyzed to confirm this break in the abundance gradients.

In general, the central abundances of O, Ne and Ar of PNe are similar to the central abundances of H II regions (the differences could be of about 0.2 dex), indicating that the central enrichment has not been important since the time of birth of PNe, and dust depletion of O in H II regions is not large. However, due to the flat gradients of PNe, at galactocentric distance larger than about 0.5 R/R_{25}, the average abundances in PNe are larger than the average abundances in H II regions.

We found that in PNe formed in low metallicity environment ($Z \leq 0.004$, like in NGC 300), with initial masses of about 3 $M_{\odot}$ or larger, the oxygen abundance could have been modified by stellar nucleosynthesis and its value in the nebula does not represent the initial value at the time of stellar formation. This is not the case in higher metallicity environments, or for stars with smaller initial masses. In the former case we suggest to use Ar as an element that shows the initial abundance in the nebula, even though Ar abundance determinations have large uncertainties.

Our results are very useful for the computation of chemical evolution models in these galaxies, since the present ISM, represented by H II regions, and the older component, represented by PNe, can be used to constrain the models. Non-Type I PNe are very useful to study the effect of radial migration in disk galaxies.

This work received financial support from DGAPA-UNAM PAPIIT 103117 and CONACyT Project 241732. S.N.F.-D. acknowledges a postdoctoral scholarship from project CONACyT 241732. We acknowledge an anonymous referee for her/his careful revision and comments that helped to improve this manuscript.

REFERENCES

Aller, L. H. 1942, ApJ, 95, 52
Balick, B., Kwitter, K. B., Corradi, R. L. M., & Henry, R. B. C. 2013, ApJ, 774, 3
Bresolin, F., Gieren, W., Kudritzki, R-P., et al. 2009, ApJ, 700, 309
Bresolin, F., Stasińska, G., Vílchez, J. M., Simon, J. D., & Rosolowsky, E. 2010, MNRAS, 404, 1679
Cahn, J. H., Kaler, J. B., & Stanghellini, L. 1992, A&AS, 94, 399
Carigi, L. & Peimbert, M. 2011, RMxAA, 47, 139
Ciardullo, R., Feldmeier, J. J., Jacoby, G. H., et al. 2002, ApJ, 577, 31
Cioni, M.-R. L. 2009, A&A, 506, 1137
Deharveng, L., Peña, M., Caplan, J., & Costero, R. 2000, MNRA, 311, 329
Delgado-Inglada, G., Morisset, C., & Stasińska, G. 2014, MNRAS, 440, 536
Delgado-Inglada, G., Rodríguez, M., Peimbert, M., Stasińska, G., & Morisset, C. 2015, MNRAS, 449, 1797
D'Odorico, S., Peimbert, M., & Sabbadin, F. 1976, A&A, 47, 341
Draine, B. T., Aniano, G., Krause, O., et al. 2014, ApJ, 780, 172

Esteban, C., Peimbert, M., García-Rojas, J., et al. 2004, MNRAS, 355, 229
Esteban, C., Carigi, L., Copetti, M. V. F., et al. 2013, MNRAS, 433, 382
Esteban, C., Mesa-Delgado, A., Morisset, C., & García-Rojas, J. 2016, MNRAS, 460, 4038
Esteban, C., Fang, X., García-Rojas, J., & Toribio San Cipriano, L. 2017, MNRAS, 471, 987
Fang, X., Zhang, Y., García-Benito, R., Liu, X.-W., & Yuan, H.-B. 2013, ApJ, 774, 138
Fang, X., García-Benito, R., Guerrero, M. A., et al. 2015, ApJ, 815, 69
Fernández-Martín, A., Pérez-Montero, E., Vílchez, J. M., & Mampaso, A. 2017, A&A, 597, A84
Flores-Durán, S. N., Peña, M., & Ruiz, M. T. 2017, A&A, 601, A147
Frew, D. J., Parker, Q. A., & Bojičić, I. S. 2016, MNRAS, 455, 1459
García-Rojas, J., Esteban, C., Peimbert, M., et al. 2004, ApJS, 153, 501
García-Rojas, J., Esteban, C., Peimbert, A., et al. 2005, MNRAS, 362, 301
García-Rojas, J., Esteban, C., Peimbert, M., et al. 2006, MNRAS, 368, 253
García-Rojas, J., Esteban, C., Peimbert, A., et al. 2007, RMxAA, 43, 3
Halle, A., Di Matteo, P., Haywwod, M., & Combes, F. 2015, A&A, 578, A58
Henry, R. B. C., Kwitter, K. B., & Balick, B. 2004, AJ, 127, 2284
Henry, R. B. C., Kwitter, K. B., Jaskot, A. E., et al. 2010, ApJ, 724, 748
Hernández-Martínez, L., Carigi, L., Peña, M., & Peimbert, M. 2011, A&A, 535, 118
Kaler, J. B. 1980, ApJ, 239, 78
Karakas, A. I. 2010, MNRAS, 403, 1413
Kimeswenger, S. & Barría, D. 2018, A&A, 616, L2
Kingsburgh, R. L. & Barlow, M. J. 1994, MNRAS, 271, 257
Kwitter,K. B. & Henry, R. B. C. 2001, ApJ, 562, 804
Kwitter, K. B., Lehman, E. M. M., Balick, B., & Henry, R. B. C. 2012, ApJ, 753, 12
Maciel, W. J., Costa, R. D. D., & Ushida, M. M. M. 2003, A&A, 397, 667
Magrini, L., Stanghellini, L., & Villaver, E. 2009, ApJ, 696, 729
Magrini, L., Corbelli, E., & Galli, D. 2007, A&A, 470, 843
Magrini, L., Stanghellini, L., Corbelli, E., Galli, D., & Villaver, E. 2010, A&A, 512, A63
Magrini, L., Coccato, L., Stanghellini, L., Casasola, V., & Galli, D. 2016, A&A, 588, A91
McConnachie, A. W., Irwin, M. J., Ferguson, A. M. N., et al. 2005, MNRAS, 356, 979
McConnachie, A. W., Irwin, M. J., Ibata, R. A., et al. 2009, Natur, 461, 66
Milingo, J. B., Kwitter, K. B., Henry, R. B. C., & Souza, S. P. 2010, ApJ, 711, 619
Mollá, M., Díaz, Á. I., Cavichia, O., et al. 2019, MNRAS, 482, 3071
Peimbert, M. 1978, in Planetary Nebulae, IAUS, 76, 215
Peña, M., Reyes-Pérez, J., Hernández-Martínez, L., & Pérez-Guillén, M. 2012, A&A, 547, 78
Peña, M., Stasińska, G., & Richer, M. G. 2007, A&A, 476, 745
Rodríguez, M. & Delgado-Inglada, G. 2011, ApJL, 733, 50
Ruiz-Lara, T., Few, C. G., Florido, E., et al. 2017, A&A, 608, 126
Sánchez-Menguiano, L., Sánchez, S. F., Pérez, I., et al. 2018, A&A, 609, A119
Sánchez, S. F., Rosales-Ortega, F. F., Iglesias-Páramo, J., et al. 2014, A&A, 563, A49
Sanders, N. E., Caldwell, N., McDowell, J., & Harding, P. 2012, ApJ, 758, 133
Searle, L. 1971, ApJ, 168, 327
Stanghellini, L. & Haywood, M. 2010, ApJ, 714, 1096
_____. 2018, ApJ, 862, 45
Stanghellini, L., Shaw, R. A., & Villaver, E. 2008, ApJ, 689, 194
Stasińska, G., Peña, M., Bresolin, F., & Tsamis, Y. G. 2013, A&A, 552, 12
Ventura, P., Stanghellini, L., Di Criscienzo, M., García-Hernández, D. A., & Dell' Agli, F. 2016, MNRAS, 460, 3940
Zaritsky, D., Kennicutt, R. C., Jr., & Huchra J. P. 1994, ApJ, 420, 87
Zurita, A. & Bresolin, F. 2012, MNRAS, 427, 1463

S. N. Flores-Durán and M. Peña: Instituto de Astronomía, Universidad Nacional Autónoma de México, Apdo. Postal 70264, Ciudad de México, 04510, México (miriam@astro.unam.mx).

Revista Mexicana de Astronomía y Astrofísica, **55**, 273–288 (2019)

DOI: https://doi.org/10.22201/ia.01851101p.2019.55.02.14

SUBSTRUCTURE FORMATION IN TIDAL STREAMS OF GALACTIC MINOR MERGERS

D. A. Noreña[1], J. C. Muñoz-Cuartas[1], L. F. Quiroga[1], and N. Libeskind[2,3]

Received June 27 2018; accepted July 16 2019

ABSTRACT

In this work, we explore the idea that substructures like stellar clusters could be formed from the tidal stream produced in galactic minor mergers. We use N-body and SPH simulations of satellite galaxies interacting with a larger galaxy. We study the distribution of mass in streams to identify overdensity regions in which a substructure could be formed. We find that without gas, no substructure forms as none of the overdensities shows a definite morphology nor dynamical stability. Including gas we find that several clumps appear and prove to be real long standing physical structures ($t \geq 1$ Gyr). We analyze the orbits, ages and masses of these structures, finding their correspondence with the halo subsystems. We conclude that it is possible to form cluster-like structures from the material in tidal streams and find evidence in favour of the presence of dark matter in these systems.

RESUMEN

En este trabajo se explora si subestructuras como cúmulos estelares se pueden formar del puente de marea producido durante una fusión menor. Usamos simulaciones de N-cuerpos y SPH de una galaxia satélite interactuando con su galaxia anfitriona. Estudiamos la distribución de masa en los puentes para identificar sobredensidades en las que se podrían formar subestructuras. Encontramos que sin gas no se da formación de subestructuras pues ninguna sobredensidad muestra morfología definida ni estabilidad dinámica. Incluyendo gas encontramos la formación de muchos grumos, estructuras longevas físicamente ligadas ($t \geq 1$ Gyr). Analizamos las órbitas, edades y masas de estas estructuras, y encontramos una correspondencia con los subsistemas del halo. Concluimos que es posible formar estructuras como cúmulos estelares del material disponible en los puentes de marea y encontramos evidencia en favor de la presencia de materia oscura en esos sistemas.

Key Words: galaxies: evolution — galaxies: interactions — galaxies: star clusters: general — globular clusters: general — methods: numerical — open clusters and associations: general

1. INTRODUCTION

The galactic halo has plenty of astrophysical systems evolving under the interaction of the different galactic components. These substructures have diverse nature, dynamics and origins and together constitute the building blocks of the ongoing galaxy formation process. Among others, there are many stellar subsystems, such as the open and globular clusters (Binney & Tremaine 2008), pure gaseous ones, such as high velocity clouds (HVC) (Wakker & van Woerden 1997) and combined gaseous and stellar systems such as tidal streams and satellite galaxies (Ibata et al. 2001).

Open and globular clusters are segregated by several characteristics. Open clusters are considered to be younger and metal richer than their globular counterparts. In addition, open clusters are associated spatially with the galactic disc, while globulars are mostly distributed spherically in the halo. This segregation suggests that their formation processes are diverse. On one hand, the formation of open clusters is considered to be well understood as a result of

[1]FACom - Instituto de Física, FCEN, Universidad de Antioquia (UdeA), Medellín, Colombia.
[2]Leibniz-Institut für Astrophysik Potsdam (AIP), Germany.
[3]l'Institut de Physique Nucléaire de Lyon (IPNL), University of Lyon; Lyon, France.

the collapse and fragmentation of molecular clouds in the galactic disk (Elmegreen & Efremov 1997). The case of globular clusters exhibits a greater degree of complexity because, actually, there are two subpopulations of them. There is a metal poor globular cluster population (MPGC) extended across the halo, and a young, metal rich population (MRGC) (Carroll & Ostlie 2006). In addition, there are several cases that do not fit very well in the two previous subpopulations, as it is the case of the globular cluster ω Centauri (henceforth ω Cen) mainly due to its unusual size and metallicity dispersion (Harris 1999). This variety suggests that even considering only the globular clusters there are diverse formation mechanisms.

Different models have been proposed to explain the formation of the two subpopulations of globular clusters in the Galaxy. For the old MPGC subpopulation the widely accepted hypothesis is that they come from primordial density fluctuations in the density field at very high redshift, when the universe expanded and cooled to a temperature of about 4000 K and the baryonic density was approximately 10^4 atoms cm^{-3} (Reina-Campos et al. 2019). Under these conditions, the only density fluctuations that can grow with time have wavelength in excess of the critical Jeans length of about 5 pc (Peebles & Dicke 1968).

For the young MRGC subpopulation, it appears that there is not a single mechanism that can form all existing MRGC in a given galaxy (Ashman & Zepf 1992; Bekki & Freeman 2003; Shapiro, et al. 2010). One of the models suggests that a significant fraction of the metal-rich subpopulation may have originated in interacting galaxies, both minor and major mergers (Ashman & Zepf 1992). Major mergers cause several starburst episodes in the gaseous component of each galaxy, and globular clusters can be formed in regions with high gas density (Li et al. 2004). Minor mergers may also contribute to the young population with clusters formed within the small satellite galaxy from the interaction with the larger galaxy (Zepf & Ashman 1993). Also, the globular cluster system of the minor galaxy would eventually be accreted by the largest galaxy, also contributing to the MPGCs subpopulation (Forbes & Bridges 2010). The minor merger scenario can be seen in the Magellanic Clouds, where there is observational evidence of ongoing cluster formation and of an ancient cluster system bound to the clouds (Harris 1998; Georgiev et al. 2010). It was further suggested that the very central region of a satellite galaxy could form a globular cluster as the bound structure surviving the effects of the tidal stripping induced by its host galaxy (Bekki & Chiba 2002).

Moreover, recent observational evidence that suggests that several (if not all) GCs contain various stellar populations has come to light. For example, many GC stars have the same amount of Fe (and other heavy elements) inside a specific radius, but a wide variation in light elemental abundance (Li-Al) on a star-to-star basis (Conroy et al. 2011). Norris & Kannapan (2011) in a crucial study on this problem showed that some ultra-compact dwarf galaxies have color magnitude diagrams indistinguishable from those of GCs and the nuclei of dwarf galaxies. Bekki & Freeman (2003) found that the multiple stellar populations of ω Cen can be explained in terms of a nucleated dwarf galaxy scenario: the tidal field of the host galaxy induces gas inflow towards the center of the cluster progenitor, triggering multiple star bursts that lead to chemical enrichment. Other GC candidates that are thought to have formed in ostensibly dark matter potential wells deep enough to retain self-enriched Fe produced by supernovae Ia explosions include M22, NGC 1851 and Andromeda's G1. The evidence showing chemical complexity of the cluster stellar populations suggests that the classical picture of all GC's belonging to a single monolithic population should be reevaluated.

Similarly, HVCs appear to be the result of two possible mechanisms: One is the return to the disc of gas and dust expelled via supernovae events and the other is the infall of gas and dust from stripped subsystems, such as globular clusters or satellite galaxies (Wakker & van Woerden 1997).

A combination of both processes is necessary to explain the current distribution of high and intermediate velocity clouds. For example, from hydrodynamical simulations it is concluded that most massive HVC, such as the well known Complex C, were originated from ejection of material from the Milky Way's disc (Fraternali et al. 2015); but the velocity dispersion, the metallicity, sizes and masses of the smallest clouds are consistent with an extragalactic origin (Blitz et al. 1999; Binney et al. 2009).

As a result of the tidal disruption of the Galaxy subsystems, the so-called tidal streams are originated. They are composed in most cases by stars and gas (Belokurov et al. 2006), like the Magellanic Stream, where recent observations have confirmed the presence of a young open star cluster most likely formed in the stream (Price-Whelan et al. 2018). Remarkably, all the streams observed in the Milky Way galaxy are clearly inhomogeneous and exhibit overdensities (Küpper et al. 2012). These overdensi-

ties evolve in the galactic potential as well, undergoing different processes that could eventually transform them into self gravitating systems like clusters. The main purpose of this work is to determine through $N-$body simulations of galaxy minor mergers if the overdensities in the tidal streams could really meet the conditions to be considered self-gravitating substructures. In a future work, we will investigate under what conditions the evolution of such substructures could lead to the formation of real astrophysical systems, such as globular clusters and high velocity clouds.

This paper is organised as follows: In § 2 we describe the setup of the $N-$body simulations, from the determination of the satellite galaxy initial position to the structure of the host galaxy passing through the astrophysical characteristics of the satellite. In § 3 we describe the analysis performed to the simulation outputs in order to search and characterise the overdensities. In § 4 we present our results. We finally discuss them and present the conclusions in § 5.

2. NUMERICAL PROCEDURES

The numerical setup of the $N-$ body simulations used in this work comprises two stages. In the first stage the galaxies are generated in isolation. In this case, we generate a host disc galaxy and a spheroidal satellite galaxy, both with and without gas. We use these galaxy models to explore different merger configurations. In the following sections we describe in detail each part of the procedure.

We used the code Gadget2 to run all our simulations (details of the code can be found in Springel 2005). Gadget2 is a general purpose code to study the evolution of collisionless gravitational systems. Collisionless particles representing stars and dark matter evolve only under gravity using a tree method. To follow the evolution of gas an entropy based smoothed particle hydrodynamics (SPH) scheme (Springel & Hernquist 2002) is used with adaptive smoothing lengths, allowing conservation of energy and entropy in adiabatic regions. A synchronization scheme within the integration scheme is used; this is a quasi-symplectic KDK leap-frog with adaptive individual time-steps. The code uses a parallelization algorithm based on a space-filling curve to achieve high flexibility with high accuracy in tree force estimation.

2.1. *Initial Conditions*

2.1.1. *Isolated Galaxies*

The host galaxy in this work consists of a disk galaxy composed of a stellar disk and a dark matter halo. Neither gas in the disk nor a central spheroid are included in the model. The satellite galaxy is modelled as a spherical galaxy with a collisionless spheroid hosting a gaseous sphere in hidrostatic equilibrium. Initial conditions are computed using moments of the collisionless Boltzmann equation (Hernquist 1993; Springel et al. 2004). The dark matter halo of both galaxies follows a Hernquist density profile with scale length parameter adjusted to fit the shape of the NFW density profile, as done in Springel (2005).

Masses for the galaxies are taken from the CLUES simulations (Gottloeber et al. 2010; Forero-Romero et al. 2011). The mass of the dark matter halo hosting the disk galaxy is $7.9\times10^{11}h^{-1}M_{\odot}$ with a concentration parameter of $c = 4.15$. The satellite galaxy has a total mass of $3.2 \times 10^{10}h^{-1}M_{\odot}$, and $c = 4.26$. Since it is not reasonable to simulate the formation of globular clusters observed today using properties of current host galaxies, the masses and properties of these two progenitor galaxies are related to the properties of the Milky Way galaxy and one of its satellites at $z = 2$, as observed from the constrained simulations made by CLUES. Galaxy disk structure (disk scale length, etc.) is modelled using the prescription of Mo et al. (1998), from which the scale parameters of the disk are $r_d = 1.53$ kpc and $z_0 = 0.31$ kpc.

The host galaxy has a stellar disk with a mass of $3.3 \times 10^{9}h^{-1}M_{\odot}$, where we have used Moster et al. (2001) to estimate the total stellar mass for the given dark matter halo at $z = 2$ and assumed that all the stellar mass is deposited in the disk. Since we are not interested in the evolution of the gas in the disk of the host galaxy and we assume it does not have a dominant effect on the dynamics of the merger, we do not include a gaseous component in this galaxy.

The satellite galaxy is composed of collisionless particles representing dark matter or stars, and has also a gaseous component. Initially, the gas follows a density profile similar to the profile of the dark matter halo in hydrostatic equilibrium. Hydrostatic equilibrium is guaranteed through a gas temperature computed as Mastropietro et al. (2005)

$$T(r) = \frac{m_p}{k_B\rho_g(r)}\int_r^{\infty}\rho(r)\frac{GM(r)}{r^2}\mathrm{d}r, \qquad (1)$$

where m_p is the proton mass, k_B is the Boltzmann constant and $\rho_g(r)$ is the gas mass density. In order to provide a favorable scenario for the formation of clusters from the material deposited in the stream, the total gas mass of the satellite has been chosen to

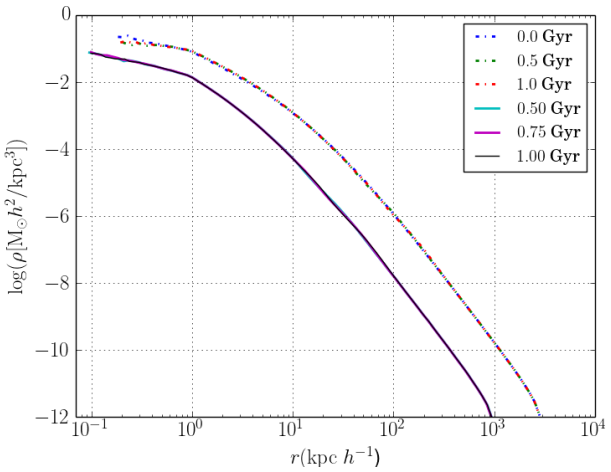

Fig. 1. Convergence of the density profiles of the host (top) and satellite (bottom) dark matter halos under numerical relaxation. The galaxies were evolved in isolation for 1 Gyr. The color figure can be viewed online.

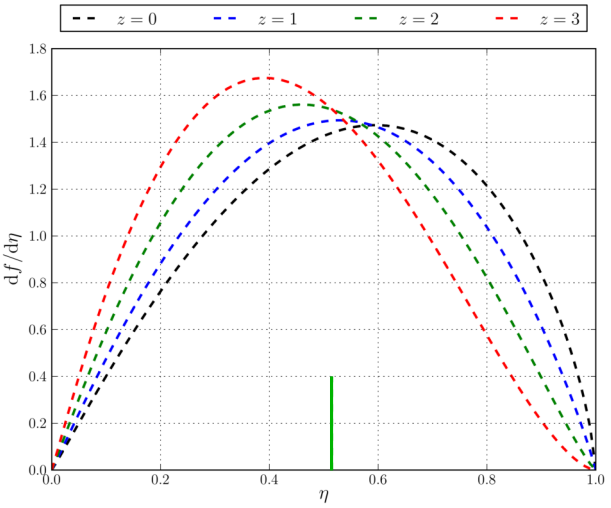

Fig. 2. Circularity distribution for the infalling satellites at different redshifts. The small vertical line indicates the average circularity at $z = 2$. The color figure can be viewed online.

be $\approx 16\%$ of its total mass, providing the scenario for a gas rich merger. Although arbitrary, the gas fraction is in no way larger than the cosmological baryon fraction in a dark matter halo (Lin, et al. 2008). We could have included a disk of cold gas in the satellite; however, this would have implied a new degree of freedom in our simulations (see next section). Since the direction of the disk may affect the formation of a stream and the formation of potential candidates to GCs in our simulations, we decided to adopt a simpler spherical distribution looking for a solution general enough to study the formation of potential GCs in our simulations. We claim that if any structures are formed with this setup, for sure they can be formed in more favorable conditions where a disk provides cold gas to the stream.

All galaxies are simulated in isolation after the generation of initial conditions in order to allow for numerical relaxation of the initial conditions. Figure 1 shows, for the dark matter halos, the convergence of the profiles from the initial conditions to the final relaxed density profiles. Note that the mass distribution only changes in the very inner region, and that after the first 1 Gyr the profile is relaxed. Also, the satellite galaxy reaches relaxation basically very close to the beginning. This check is relevant since it is important to make sure that there is no numerical artificial evolution on the density distribution of the galaxies, since in this way we can ensure that any change in the mass distribution of the system during the merger is due to the dynamics of the merger and is not spurious numerical noise or an instability originated from the initial conditions.

2.1.2. *Merger Configuration*

The mergers we plan to study in this work are somehow artificial in the sense that they do not correspond to any realistic system. However these simulations must reproduce the reality of our universe. In that sense, there is an infinite set of possible merger simulations we could run, each with a different orbit. To avoid running many orbits, and at the same time to try to reproduce the expected results from our understanding of the universe, we will use the results shown in Wetzel (2011) to choose the orbits to be studied in this work. In their work Wetzel (2011) study the probability distribution of orbital parameters of infalling satellite galaxies. From them, we use the mean orbital parameters as those of a representative merger that is in agreement with the current cosmological paradigm.

Then, to configure the merger we need to obtain realistic values of the initial position $\mathbf{r}_0$ and velocity $\mathbf{v}_0$ of the satellite galaxy. For that, from Wetzel (2011), we use the circularity η and the pericenter r_p distance, which depend on the host halo mass $M_{\rm host}$ and redshift z, and which for our host halo mass are distributed at the moment of their passage through the host's virial radius according to the distribution functions shown in Figures 2 and 3. In both figures, the mean values of the circularity and the pericentre at $z = 2$ are highlighted with a small vertical green line.

TABLE 1

SPECIFICATIONS OF THE SATELLITE'S INITIAL ORBITAL CONFIGURATIONS CHOSEN FOR EACH SIMULATION*

Name	Nomenclature	$\mathbf{r}_0$ (kpc)	$\mathbf{v}_0$(km/s)
Perpendicular	*p*	(0,0,198.34)	(0,34.9,0)
Planar Corotating	*pcr*	(0,198.34,0)	(-34.9,0,0)
Planar Contrarotating	*pct*	(0,198.34,0)	(34.9,0,0)
Inclined Corotating	*icr*	(99.6,99.6,140.25)	(-24.67,24.67,0)
Inclined Contrarotating	*ict*	(99.6,99.6,140.25)	(24.67,-24.67,0)

*For a schematic view of each configuration, see Figure 4.

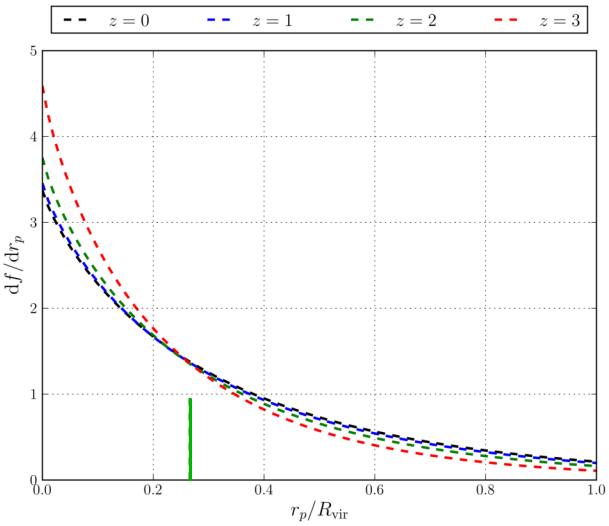

Fig. 3. Pericentre distribution for the infalling satellites; the redshift dependence is explicitly noted. The small vertical line indicates the average pericentric distance value at $z = 2$. The color figure can be viewed online.

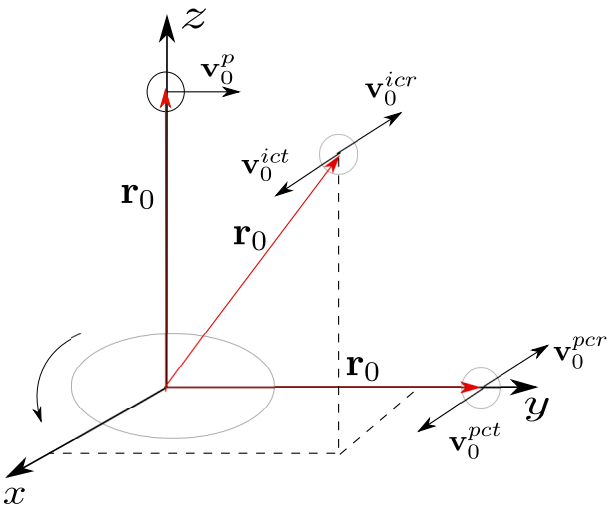

Fig. 4. Schematic representation of the initial orbital configurations for the original five simulations. The host disc is rotating counterclockwise in the $x - y$ plane. $\mathbf{r}_0$ and $\mathbf{v}_0$ are the initial position and velocity in each case. For the inclined configurations, the angle with the z axis is $\phi = 45°$. See Table 1 for details on the coordinate values. The color figure can be viewed online.

Orbit circularity has a nearly constant small rate of decrease with redshift, while pericenter distance exhibits a decrease in its average values with z. In particular, at $z = 2$ we obtain an average pericentric distance of $0.27R_{\rm vir}$, with $R_{\rm vir}$ the virial radius of the host halo. For this halo $R_{\rm vir} \approx r_{200} = 63.29$ kpc. The average circularity at $z = 2$ is 0.54. With this two values we calculate the eccentricity e and apocentric distance r_a using the two body approximation as

$$e = \sqrt{1 - \eta^2}, \tag{2}$$

$$r_a = \left(\frac{1+e}{1-e}\right) r_p. \tag{3}$$

For our system, the numerical values were found to be $e = 0.84$ and $r_a = 198.34$ kpc. Finally, making use of the *vis-viva* equation, the velocity at apogalacticon is simply

$$v_a = \sqrt{2\frac{GM}{r_a}(1-e)}, \tag{4}$$

which turns to be 34.9 km/s for our infalling satellite.

In all simulations the host galaxy disk was always in the $x-y$ plane with its angular momentum aligned with the z-axis. Based on the orbital parameters given in the previous paragraph, the merger was disposed in five different configurations. The only difference between each configuration is their location relative to the disc plane and its orbital motion direction relative to the disc rotation. The configuration parameters are shown in Table 1 and a schematic illustration of all of them is represented in Figure 4.

2.2. *Simulations*

Some of our simulations include star formation modeled as shown in Springel & Hernquist (2003). In this model a cold gas particle (cloud) is able to convert part of its mass into stars when several criteria are met. Its temperature should be lower than 10^4 K and its density should be larger than a predefined threshold density ($\rho_{\rm th}$). Additionally, the cooling time should be shorter than the collapse time of the cloud $t_{cooling} < \frac{1}{\sqrt{G\rho}}$ and the local gas flow must be negative ($\nabla \cdot \vec{v} < 0$). These conditions guarantee that gas-rich regions, where the star formation process must happen, are colder, denser and undergoing collapse. Once a gas particle meets criteria to form stars, they are formed stochastically with a sampling determined by the local star formation rate. We refer the reader to Springel & Hernquist (2003) for further details on the model and implementation of the star formation. Our goal is to study the posibility of formation of globular cluster-like structures in this kind of mergers. We are not interested to study the process of star formation in these candidate structures since it will be very much dependent on the model and implementation of the different feedback mechanisms. Our interest in introducing star formation and feedback in our simulations is to provide the gas with some sort of realistc conditions that can be meet for candidate structures to form.

As it is well known, SPH suffers from fragmentation instabilities that lead small gas clumps to cluster, forming a set of non-physical structures (Bate & Burkert 1997; Torrey et al. 2013). Since what we are looking for in our simulations is exactly fluctuations in the mass distribution we need to make sure that we find candidates that are not just spurious numerical fragments formed due to the SPH instability. In order to avoid this, we ran the same set of initial conditions for several different particle resolutions and we found that the substructures present in the lower resolution simulation were recognizable in the higher resolution simulations, maybe with a little spatial displacement due to changes in the global dynamics of the system, as it can be seen in Figure 13 (In § 3.2 we show how these substructures were identified). Increasing the resolution of the simulations allows us to verify that what we find as substructure candidates are true candidates and not numerical artifacts. § 3.3 describes in better detail the results of our convergence study.

We design two sets of experiments to explore the formation of substructures in the tidal streams of the satellite galaxy. The first consists in pure collisionless systems, or in other words, gas-free simulations. The main purpose of this first experiment is to verify if the collisionless matter alone could cluster and form bound systems without the influence of gas. This set of simulations was named DMO (Dark Matter Only), specifically DMO1 and DMO2 whose only difference is the number of particles in the satellite. In Table 2 we show the masses, number of particles and mass per particle of each galactic component in our models.

The second set of simulations includes gas in the satellite and are designated as GAS. The difference among them is the increased resolution, GAS3 being the one with the highest resolution. Table 2 summarizes the resolution specifications of the GAS experiment.

As can be seen in Table 2, the SPH particle mass is of the order of $5 \times 10^3\ h^{-1}M_\odot$ for GAS3. If we assume that typical masses for globular cluster candidates are of the order of 10^5 to $10^7\ h^{-1}M_\odot$ in this simulation we can resolve globular cluster like structures with 20 to 2000 gas particles. Again, we are not interested to study star formation in those objects (which will imply the necessity of larger resolution simulations in order to properly sample star formation inside the clusters) but only to study study the collapse of gas in the candidate structures. Therefore, these numbers are good enough for the purposes of our work. We ran our simulations for a time interval of the order of 7 Gyr, long enough to study the evolution of the satellite remnants as would be observed at present.

3. ANALYSIS

3.1. *Density Estimation*

Overdensities are, by definition, regions with a spatial mass density larger than that of its surroundings. Hence, the best way to identify them is by estimating the mass density in the body of the tidal streams. High density regions will be the best candidates to form autogravitating substructures. We use the EnBiD (Entropy Based Binary Decomposition) algorithm to calculate the density distribution in real and phase spaces (Sharma & Steinmetz 2006).

The EnBiD algorithm is sensitive to the spatial anisotropies of the mass distribution through the implementation of an anisotropic smoothing tensor. In this way, any density underestimation is prevented due to the ability of the method to use particles along a preferred direction, and not only spherically symmetric around the point of interest, as the isotropic kernels do. Figure 5 shows the estimated density for

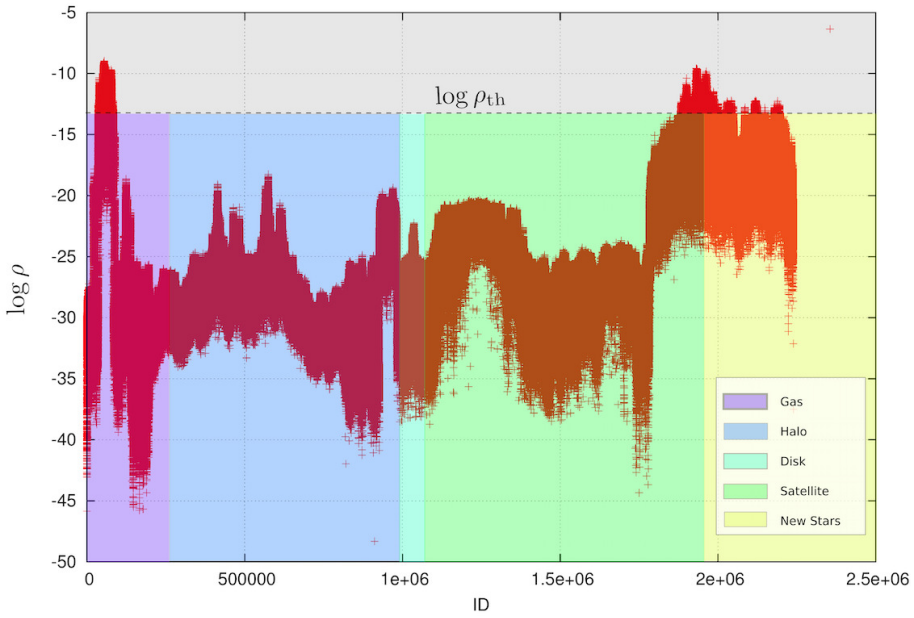

Fig. 5. Density values for the particles in GAS2 $p-$simulation against the identification particle number. This plot correspond to the snapshot at 3.75 Gyr after simulation starts. Density units are $10^{10} M_{\odot}/\mathrm{kpc}^3$. The color figure can be viewed online.

TABLE 2

COLLISIONLESS AND COLLISIONAL SIMULATIONS DATA*

Name	Component	Mass ($M_{\odot}$)	N_p	m_p ($M_{\odot}$)
COLLISIONLESS SIMULATIONS				
DMO1	Satellite	3.2×10^{10}	1.0×10^5	3.2×10^5
	Disk	3.3×10^9	5.6×10^4	6.4×10^4
	Halo	7.9×10^{11}	7.3×10^5	1.1×10^6
DMO2	Satellite	3.2×10^{10}	2.0×10^5	1.6×10^5
	Disk	3.3×10^9	5.6×10^4	6.4×10^4
	Halo	7.9×10^{11}	7.3×10^5	1.1×10^6
COLLISIONAL SIMULATIONS				
GAS1	Satellite	2.5×10^{10}	4.0×10^5	6.2×10^4
	Gas	5.0×10^9	2.0×10^5	2.5×10^4
	Disk	3.3×10^9	5.6×10^4	6.0×10^4
	Halo	7.9×10^{11}	7.3×10^5	1.1×10^6
GAS2	Satellite	2.5×10^{10}	8.0×10^5	3.1×10^4
	Gas	5.0×10^9	4.0×10^5	1.2×10^3
	Disk	3.3×10^9	5.6×10^4	6.4×10^4
	Halo	7.9×10^{11}	7.3×10^5	1.1×10^6
GAS3	Satellite	2.5×10^{10}	3.0×10^6	8.3×10^3
	Gas	5.0×10^9	1.0×10^6	5.0×10^3
	Disk	3.3×10^9	5.6×10^4	6.4×10^4
	Halo	7.9×10^{11}	1.0×10^7	7.9×10^4

*N_p and m_p are the number of particles and mass per particle, respectively.

the total number of particles in one of the GAS simulations at $t = 3.75$ Gyr. In the figure we show the density of gas, halo dark matter, disk and satellite particles. New stars formed from gas particles are also included. Note that this figure not only shows the densities of particles ranked by ID (and type) but allows to see the high density peaks. As we know, these density peaks are associated to gravitational instabilities and should be related to anisotropies in the density distribution of each galactic component. Therefore, an adequate density threshold can be selected to extract the prominent overdensities in the particle distribution.

As can be seen in the figure, the overal densities of the halo, disk and a fraction of particles of the satellite have a lower value than that for a fraction of particles of gas and stream material (which in this case corresponds to the last bump composed of satellite particles and new-born stars). The peaks in the values of the estimated density can be used to fix a density threshold ρ_{th} that can serve to identify global overdensities, as shown by the horizontal line in Figure 5. Notice that only a fraction of gas, satellite and new star particles are above this threshold, and one expects that since those overdensities are induced by the gravitational instability, they would be spatially correlated, as can be seen in Figure 13. This density threshold is an important part of the process of identification of high density peaks corresponding to the seed of the identification of potential cluster candidates.

3.2. *Identification of Substructure Candidates*

Once the densities of the particles have been calculated, we aim to identify the overdensities in the field of the stream in order to label them as possible candidates. We start by estimating density maps as described in the previous section. These maps highlight the overdensities above the underlying distribution of particles, as shown in Figures 10 and 11. Then, the identification is carried out by the following series of steps:

- First the candidates are identified by performing a selection of particles through a phase space density threshold $\rho_{\rm th}$. Particles with phase-space densities below the density threshold are ruled out as potential center of some candidate clump. The value of $\rho_{\rm th}$ was chosen examining the values of the density of the simulation using, for instance, a plot like the one shown in Figure 5, in which we clearly distinguish between particles of high and low density. The density threshold could be different from one simulation to another.

- Once the particles with $\rho < \rho_{\rm th}$ are ruled out, we construct a three dimensional spatial plot of the particles that are left. In this plot, we identify, *by eye* a centre of each overdensity. The coordinates of the centre at that particular snapshot are then estimated to be $\mathbf{r}_c = (x_c, y_c, z_c)$. For this we choose a random snapshot, but it is preferable for the system to be sufficiently evolved, maybe after the satellite has passed several times through the disk. The fact that at this point we choose by eye the position of the candidate has no effect on the results. Using for example a method like spherical overdensity would work equally well, since we are just guessing the position of the overdensity.

- Based on the three dimensional plot built before, the size of the overdensity can be roughly estimated. We assign a spherical radius R_0, measured from the centre $\mathbf{r}_c$, trying to encompass the largest number of overdensity particles. Then, particles with position $\mathbf{r}_p = (x_p, y_p, z_p)$, which meet the condition $|\mathbf{r}_p - \mathbf{r}_c| < R_0$ are said to be in the first guess of the candidate list. After inspection, we found that using a value of $R_0 \approx 2.0$ Kpc was enough to encompass all initial particles in each substructure that will be used later to track the actual set of bound particles.

- With the ID number of each particle in the candidate list, we track the position and velocities of such particles in all the snapshots of the simulations. At this point, we compute the center of mass of the particles in the candidate clump (for each snapshot) and look for particles of any kind that lie within a sphere of radius $R_{th} = 0.7\,$kpc, including dark matter particles from the host and the satellite halos, gas and disk particles, and new stars born during the interaction. Notice that across the snapshots particles can come in and out of the sphere of $R_{th} = 0.7\,$kpc, meaning that the list of particles that actually belong to the candidate has to be updated dynamically.

- Then, for every snapshot, we compute the properties of the clump in order to tie the evolution of the visually identified clouds to an astrophysical observed system. Such properties are center of mass, binding energy, total mass, mass by type of particle, central and mean densities, tidal and core radii, and the tidal heating.

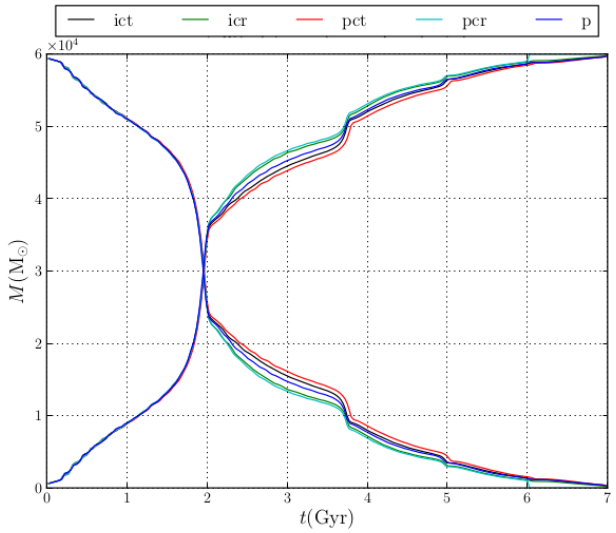

Fig. 6. Mass stripped from the satellite galaxy as a function of simulation time represented by the descending curves for each orbital configuration. The mass gained by the stream for each orbital configuration is shown by the ascending curves. The color figure can be viewed online.

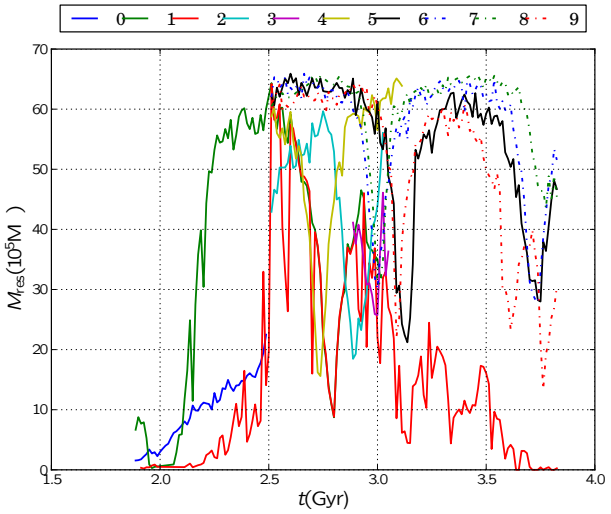

Fig. 7. Minimum resolvable masses for the nine candidates in GAS3 (equation 6). The minimum mass remain much smaller than the candidates total mass, see Figure 9. The color figure can be viewed online.

3.3. *Resolution Study Against Artificial Fragmentation*

The numerical scheme used to simulate the hydrodynamics of the gas could impact the formation of clumps within the molecular clouds in an artificial way. The resolution of a SPH simulation involving gravity is therefore a critical quantity in order to obtain realistic results from physical process rather than artificially ones induced by numerical fluctuations.

As it is widely known, in SPH the properties of gas particles are obtained by summing the properties of all the particles that lie within a sphere with a radius known as the smoothing length h. The smoothing lengths are constrained to contain approximately a number of particles, called number of neighbours $N_{\rm ngb}$, in the sphere of radius h. Since the gravitational softening is set equal to h, the mass contained in the sphere cannot be roughly equal to the local Jeans mass, otherwise the collapse would be inhibited by the softening of the gravitational forces.

Thus, the called *minimum resolvable mass*, $M_{\rm res}$ must always be less than the local Jeans mass M_J given by

$$M_J = \left(\frac{3}{4\pi\rho}\right)^{1/2}\left(\frac{5k_BT}{\mu m_H G}\right)^{3/2}, \qquad (5)$$

where ρ is the density of the gas at temperature T, k_B is the Boltzmann constant, m_H is the mass of the hydrogen atom and μ is the gas mean molecular weight (Draine 2011). Taking $M_{\rm res}$ as the mass of $2N_{\rm ngb}$ particles, it can be estimated as (Bate & Burkert 1997):

$$M_{\rm res} = M_{\rm gas}\left(\frac{2N_{\rm ngb}}{N_{\rm gas}}\right), \qquad (6)$$

where $M_{\rm gas}$ and $N_{\rm gas}$ are the total mass and particle number of the gas. The previous expression explicitly shows that for a larger number of particles, the minimum resolvable mass decreases and the collapse and fragmentation will be less affected for the numerical implementation.

The condition (6) with $N_{\rm ngb} = 128$ was tested for the clumps in the satellite galaxy gas that we selected as substructure candidates with the previous recipe. The strategy adopted for the identification of the progenitors and the results obtained of such strategy are depicted in the next sections.

Figure 7 shows the time evolution of the minimum resolvable mass for each cluster according to equation 6, which remains much smaller than the local Jeans mass.

4. RESULTS

In Figure 6 we show the mass stripped from the satellite galaxy as a function of simulation time. Each line in Figure 6 represents the evolution of the mass stripped from the satellite for each of the five orbital configurations presented in Table 1. As can

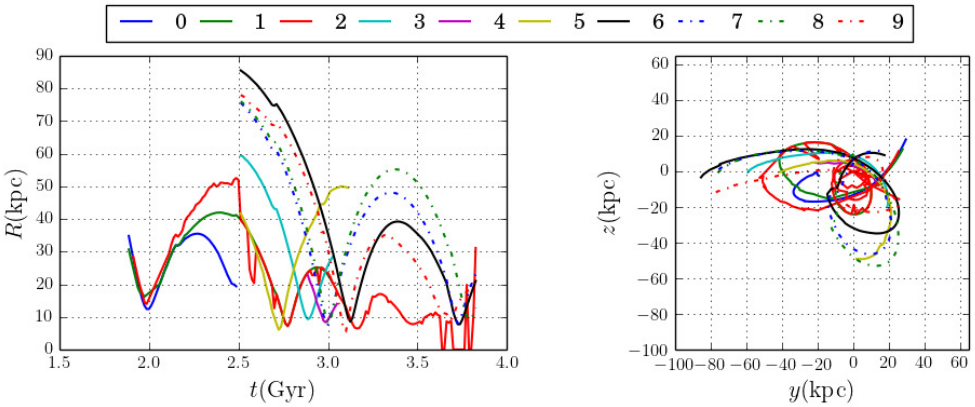

Fig. 8. Orbital structure of the nine candidates identified in GAS3. *Left panel*, Magnitude of the galactocentric vector position as a function of time. *Right panel*, Projection of the orbits in the $y - z$ plane. The color figure can be viewed online.

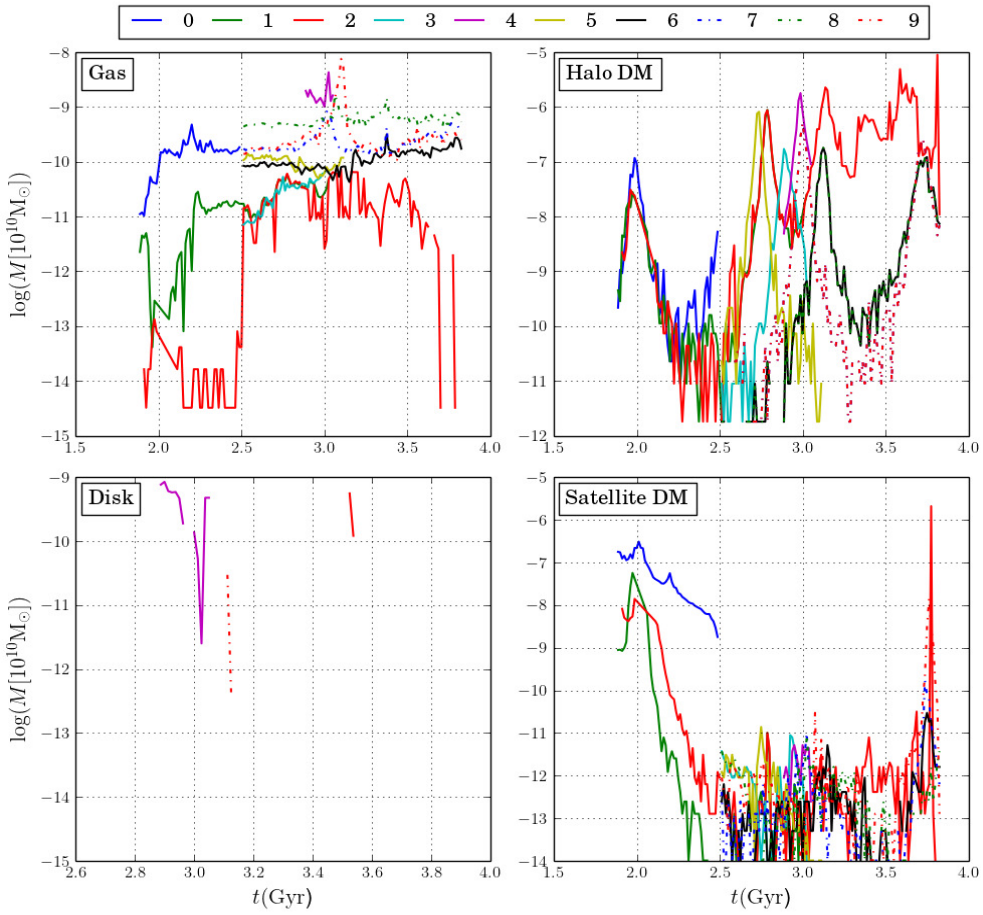

Fig. 9. Mass as a function of time for each candidate, segregated by type. The color figure can be viewed online.

be seen in the figure, the rate of mass loss is quite similar for every orbital configuration of the merger. For this reason, since in our experiments we found no reason to prefer any orbit over another on the basis of the amount of mass stripped of the satellite, we decided, without loss of generality, to run our high resolution simulations only for the orbit perpendicular to the plane of the galaxy.

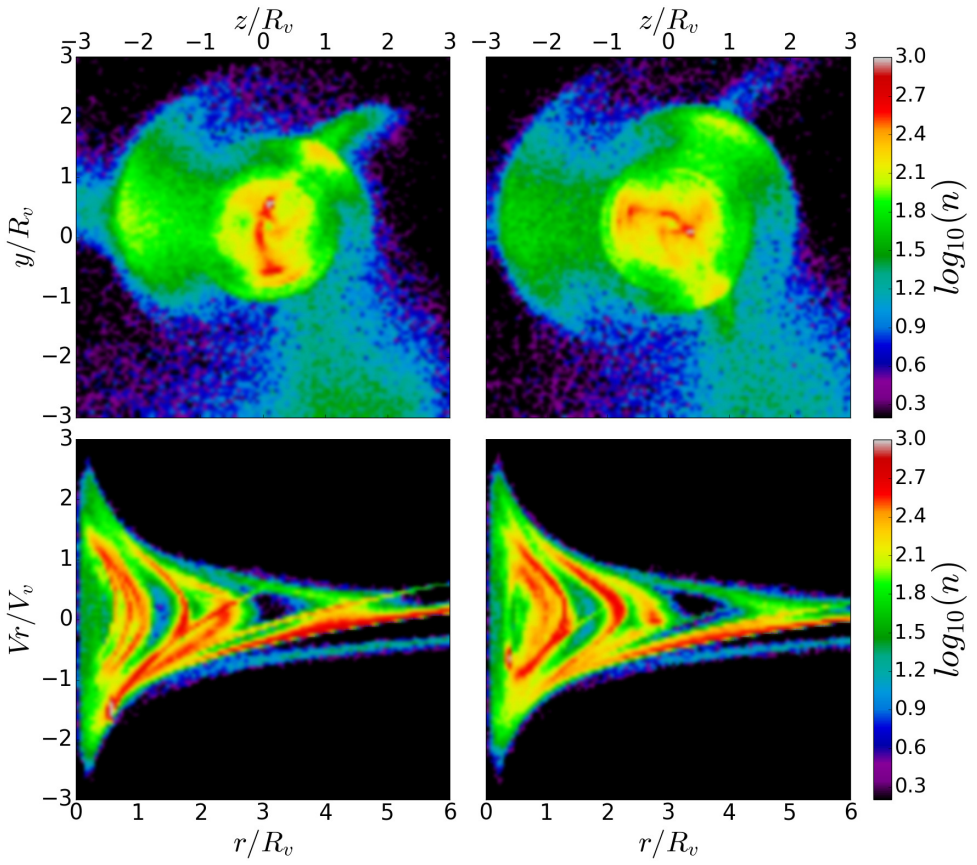

Fig. 10. *Top Panels:* Real space projection on the $z-y$ plane density-coded for the DMO2 simulation. *Bottom Panels:* Phase space projection on the $r-v_r$ plane with same density code. The density contrast is high in the elongated radial structures found in the tidal tails, but still does not exhibit the morphology of globular clusters. Panels on the left correspond to a time of 6.0 Gyr, right panels to 7.0 Gyr. Color values correspond to number density of points in log scale. The color figure can be viewed online.

As can be seen in the figure, there are breaks in the mass curve located at about 2, 3.8 and 5 Gyr. These breaks are associated with the periastron passages during the merger. Clearly, the first passage strips the largest amount of mass from the satellite. Most of the mass ejected during the first passage is gas that is heated up during the collision and should remain bounded to the host galaxy, potentially forming the overdensities that are interesting for our study.

Figure 10 shows the projected particle distribution of the DMO2 simulation at two different time snapshots, $t = 6$ Gyr and $t = 7$ Gyr. The figure shows (at the top, in color code) the density of the streams; the umbrella effects associated to the distribution of the merger remnant of a satellite interacting with a massive host galaxy can be seen. At the bottom, each figure shows the pseudo phase space diagrams; the disturbances in phase space associated to the structures of the streams and merger remnants can be seen. As shown at the two different time snaps, there is a diffuse structure that appears at time 6 Gyr (in real space and in phase-space) but after 1 Gyr it is already washed out. This happens to all structures observed in the simulations with only collisionless matter.

Figure 11 shows the same projected particle distribution coded in Figure 10 but for the GAS2 simulation. Unlike the previous case, it is clear from the projected density and phase-space density that there are more overdensities, and that they survived for several orbital periods keeping their structure for a significant fraction of their lifetime. Figure 12 shows a zoom of the inner region of Figure 11 near the galactic disc. From this result, constrained by the resolution of our DMO simulations, we conclude that to form long lasting structures we need cold gas which helps to keep the particles gravitationally bound.

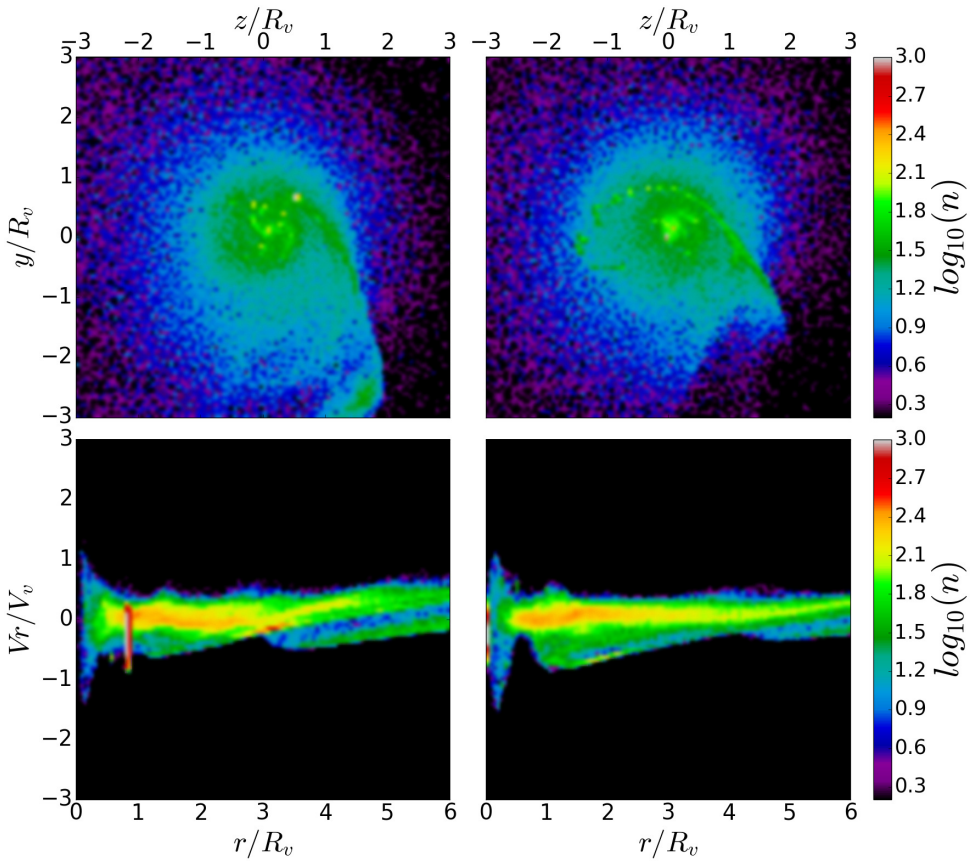

Fig. 11. *Top Panels:* Real space projection on the $z-y$ plane coded with density. *Bottom Panels:* Phase space projection on the $r-v_r$ plane with same density code. R and V are the virial radius and velocity, respectively. A couple of snapshots of GAS2 are shown. The left panels correspond to a time of 5.00 Gyr, the right panels to 6.25 Gyr. Color values correspond to number density of points in log scale. The color figure can be viewed online.

GAS simulations are thus the ones with better results for the formation of stream substructures. Consequently, we targeted them to apply the algorithm for identification of substructure candidates; results are shown in Figure 13, where the galactic disc of the host galaxy is also shown as a reference. The plots show the candidates identified in the simulations GAS1, GAS2 and GAS3, all for a simulation time of 3 Gyr. for comparison purposes. It is clear that among all the simulations of this work the higher resolution simulation has the greater number of substructures, which in turn, have the highest number of particles. For this reason we only study the properties of the substructures of GAS3.

For each substructure identified in the simulation we investigated several properties. In GAS3 we identified 10 overdensities associated to the 10 densest peaks, labeled with numbers 0 to 9; for each one we start by determining their orbital evolution. Figure 8 (b) shows the $y-z$ projection of the orbit of the center of mass followed by each candidate. Figure 8 (a) shows the distance of each candidate to the center of the disk of the host galaxy as a function of time. The notable aspect of this plot is the fact that the candidates persist during a significant amount of time, with lifetimes of the order of 1 Gyr or longer.

Figure 9 shows the evolution of the mass content of each candidate in GAS3. For all the candidates, the principal constituent is gas. The high peaks of host dark matter content present in the candidates are circumstantial particles that are counted by the algorithm when the candidate traverses the central region of the dark halo where the density is sufficiently high to cause miscounting of host dark particles as candidate particles. The masses found for each candidate correspond to the masses measured for globular clusters and high-velocity clouds, both ranging from $10^3 M_\odot$ to a maximum of $10^6 M_\odot$ on

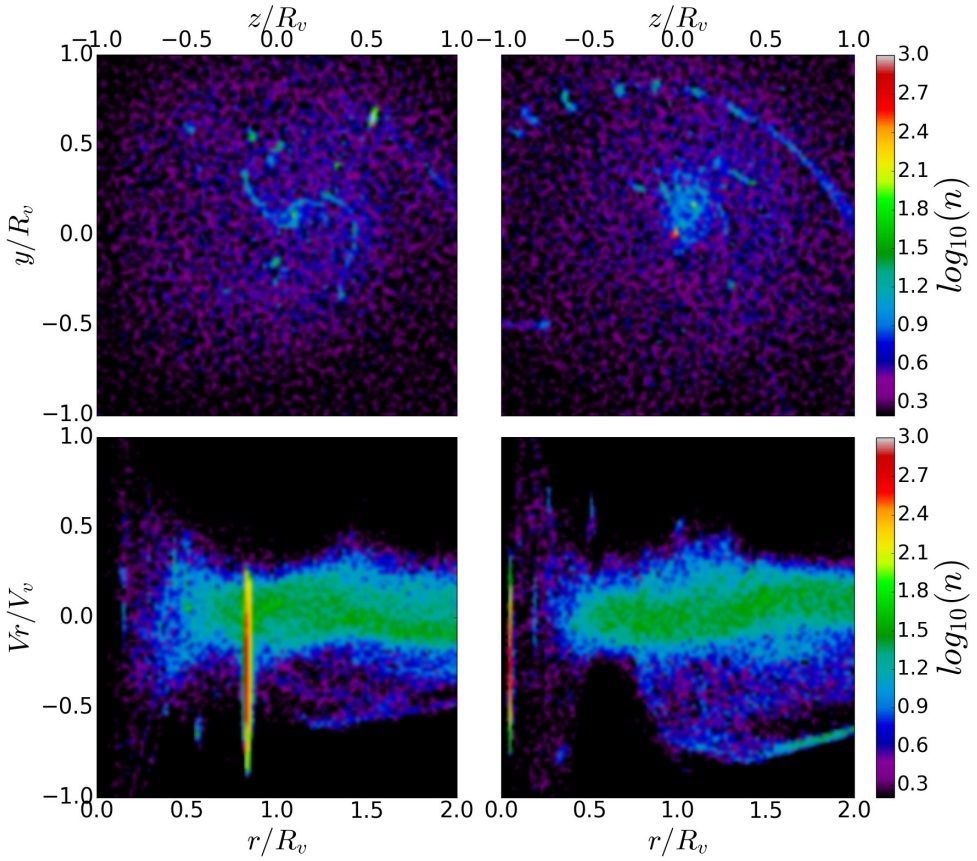

Fig. 12. *Top Panels:* Real space projection on the $z-y$ mapped with density. *Bottom Panels:* Phase space projection on the $r-v_r$ plane with same density color code. This plot is exactly Figure 10 but zooming to the internal region near the galactic disc for GAS2. Panels at the left correspond to a time of 5.00 Gyr while panels at the right are at 6.25 Gyr. Color values correspond to number density of points in log scale. The color figure can be viewed online.

average. However, there are several cases of clusters with masses over $10^6 M_\odot$ (Harris 1999; Wakker & van Woerden 1997).

4.1. *Dark Matter in Cluster Candidates*

The candidate labeled as Candidate 0 was the only one formed by gas and particles of another species. Figure 9 (a) clearly shows that the predominant mass component is the dark matter of the satellite from where it comes. This dark matter component is not circumstantial, and is an important part of this candidate during its lifetime. The rest of the candidates are basically cores of gas, without dark matter or disc stars. This suggests that through this formation mechanism one could expect to find dark matter in globular cluster.

5. SUMMARY AND DISCUSSION

In this work we use N-body simulations of satellite galaxies undergoing minor merger with a larger host galaxy. Our goal is to find if there is formation of globular cluster-like systems in the tidal stream formed by the material stripped from the satellite. The work is divided in two main parts: The first part is performed to explore the possibility of formation of structures from pure collisionless simulations, the second part is dedicated to simulate the formation of cluster-like structures from mergers that included gas.

We performed several estimations in the simulations to identify the stream and the possible autogravitating substructures inside it. The approach adopted to identify substructures was the estimation of the phase-space density which reveals the presence of substructures as density peaks.

The density estimation clearly identifies overdensity regions in which a cluster-like structure could be formed. As a first conclusion we argue that without gas, the substructures that could be formed (if at all) have a short life time, as none of the overden-

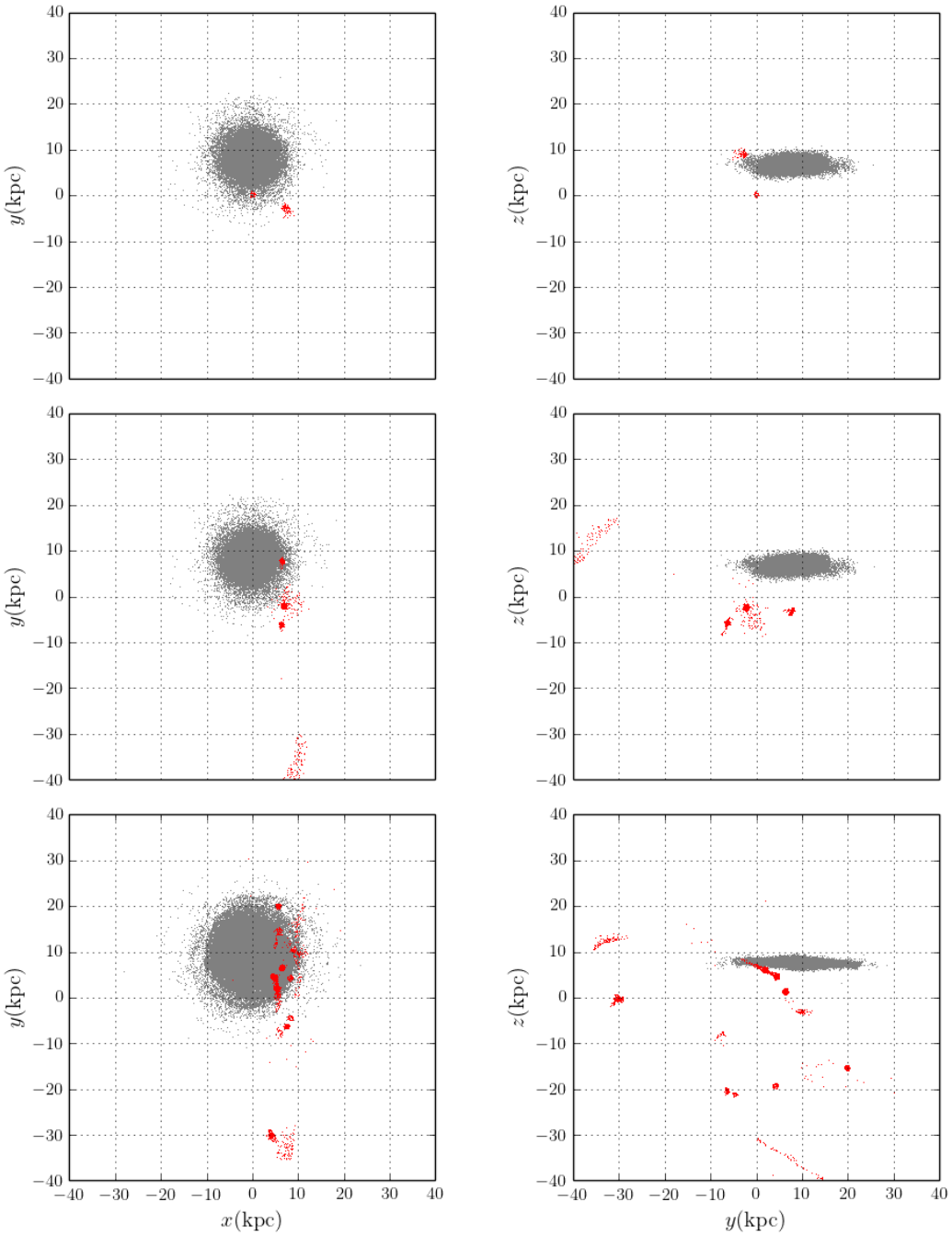

Fig. 13. Candidates identified with the algorithm described in § 3.2. The number of clumps increases with increasing resolution. All plots correspond to a 3 Gyr simulation time. *Top row*, shows the candidates in GAS1. *Middle row*, candidates in GAS2. *Bottom row*, candidates in GAS3. In each row, at the *left*, the disc is seen face on, and at the *right*, the disc is seen edge on. The color figure can be viewed online.

sities show a definite morphology or stability over time. When gas is included, several clumps appear.

The results including gas physics are remarkably different. The candidates identified in the simulation proved to be real physical structures that live for a considerable amount of time and whose orbital evolution shows them to be objects in the surroundings of the galactic disk. The total absence of stars formed within the clumps is mainly due to the thermodynamic setup of the gas as an initially isothermal sphere; the temperature of the gas is high enough to inhibit instantaneous star formation in the can-

didates. Another factor at play is that the implementation/parameters of the feedback we used in the simulations, make the feedback too strong in the satellite galaxy. Oppenheimer & Davé (2006) discuss that the original implementation of Springel & Hernquist (2003) does not work equally well for all halo masses, and that the model and the parameters should be somehow mass dependent. As it was already mentioned, due to the physics involved in the problem of star formation in complex scenarios, it is beyond the scope of this work to study star formation in these candidate structures.

The main conclusion of this work is that substructures (globular clusters and high velocity clouds) could be formed in the tidal streams of gas rich satellites. The validity and scope of this main conclusion should be tested by running simulations with higher resolutions and taking in to account different feedback and star formation models. This is the road map for future work that will contribute to improve and supplement the results presented here.

Certainly our experiments are limited. First of all, we could study all other orbital configurations to complement the study. However, having found that one of the merger configurations already produced candidate clusters, the goals of our work were already meet. Studying under which conditions (merger orbits) it is easier to form this kind of structures is an interesting idea, but indeed it would require a larger amount of computing time in order to run a suite of simulations.

We could have included gas in the disk of the host galaxy; we could also have included a hot gas halo in the main galaxy; we did not do it because it made the simulations much more expensive. Indeed both aspects are important because these gaseous components could affect the dynamics of the merger and the dynamics of the gas in the stream through ram pressure stripping and shock heating. Both processes could work stripping more gaseous material from the satellite, thus increasing the amount of gas in the stream. We expect that this will contribute to increase the fraction of gas that could end up falling into cluster candidates. However the limited design of our experiment suffices to answer the question of the formation of candidate globular cluster structures by this kind of processes, and we expect that including other gaseous components will not change the main conclusions of the work.

Research work was supported by COLCIENCIAS (Doctorados Nacionales, Convocatoria 617 de 2013) and Project 111571250082 (Convocatoria 715-2015). N.I.L acknowledges financial support of Project IDEXLYON at the University of Lyon under the Investments for the Future Program (ANR-16-IDEX-0005). Aditionally, simualtions performed in this work were run in the computer facilities of GFIF in the Instituto de Física, Universidad de Antioquia, Hipercubo in the Instituto de Pesquisa e Desenvolvimento (IP&D-Univap), Leibniz-Institut Für Astrophysik Potsdam. The authors gratefully acknowledge the computing time granted by the John von Neumann Institute for Computing (NIC) and provided on the supercomputer JURECA at Jülich Supercomputing Centre (JSC). Finally, L.F.Q. & D.A.N. thank Mario Sucerquia for his meaningful comments during the preparation of the paper.

REFERENCES

Ashman, K. & Zepf, S. 1992, ApJ, 384, 50
Bate, M. R. & Burkert, A. 1997, MNRAS, 288, 1060
Bekki, K. & Chiba, M. 2002, ApJ, 556, 245
Bekki, K. & Freeman, K. 2003, MNRAS, 346, L11
Belokurov, V., Zucker, D. B., Evans, N. W., et al. 2006, ApJ, 642, 137
Binney, J. & Tremaine, S. 2008, Galactic Dynamics: Second Edition, (Princeton, NJ: PUP)
Binney, J., Nipoti, C., & Fraternali F. 2009, MNRAS, 397, 1804
Blitz L., Spergel, D. N., Teuben, P. J., Hartmann, D., & Burton, W. B. 1999, ApJ, 514, 818
Carroll, B. W. & Ostlie, D. A. 2008, An Introduction to Modern Astrophysics, (Addison-Wesley)
Conroy C., Loeb, A., & Spergel, D. N. 2011, ApJ, 741, 72
Draine, B. T. 2011, Physics of the Interstellar and Intergalactic Medium, (Princeton, NJ: PUP)
Elmegreen, B. G. & Efremov, Y. N. 1997, ApJ, 480, 235
Forbes, D. & Bridges, T. 2010, MNRAS, 404, 1203
Forero-Romero, J. E., Hoffman, Y., Yepes, G., et al. 2011, MNRAS, 417, 1434
Fraternali F., Marasco, A., Armillotta, L., & Marinacci, F. 2015, MNRAS, 447, 70
Georgiev, I. Y., Puzia, T. H., Goudfrooij, P., & Hilker, M. 2010, MNRAS, 406, 1967
Gottloeber, S., Hoffman, Y., & Yepes, G. 2010, arXiv:1005.2687
Harris, W. E. 1998, Globular Clusters Systems (Springer)
_____. 1999, glcl.conf, 325
Hernquist, L. 1993, ApJS, 86, 389
Ibata, R., Lewis, G. F., Irwin, M., Totten, E., & Quinn, T. 2001, ApJ, 551, 294
Jülich Supercomputing Centre. 2018, Journal of large-scale research facilities, 4, A132, http://dx.doi.org/10.17815/jlsrf-4-121-1
Kúpper, A. H. W., Lane, R. R., & Heggie, D. C. 2012, MNRAS, 420, 2700
Li, Y., Law, M., & Klessen, R. 2004, ApJ, 614, L29

Lin, L., Patton, D. R., Koo, D. C., et al. 2008, ApJ, 681, 232
Mastropietro, C., Moore, B., Mayer, L., Wadsley, J., & Stadel, J. 2005, MNRAS, 363, 509
Mo, H. J., Mao, S., & White, S. D. M. 1998, MNRAS, 295, 319
Monaghan, J. 1992, ARA&A, 30, 543
Moster, B. P., Somerville, R. S., Maulbetsch, C., et al. 2001, ApJ, 710, 903
Norris, M. A. & Kannapan, S. J. 2011, MNRAS, 414, 739
Oppenheimer, B. D. & Davé, R. 2006, MNRAS, 373, 1265
Peebles, P. J. E. & Dicke, R. H. 1968, ApJ, 154, 891
Price-Whelan, A. M., Nidever, D. L., Choi, Y., et al. 2018, arXiv:1811.05991
Reina-Campos, M., Kruijssen, J. M. D., Pfeffer, J. L., Bastian, N., & Crain, R. A. 2019, MNRAS, 486, 5838
Shapiro, K. L., Genzel, R., & Förster Schreiber, N. M. 2010, MNRAS, 403, L36
Sharma, S. & Steinmetz, M. 2006, MNRAS, 373, 1293
Springel, V. 2005, MNRAS, 364, 1105
Springel V., White, S. D. M., & Hernquist L. 2004, IAUS, 220, 421
Springel, V. & Hernquist, L. 2002, MNRAS, 333, 649
_____. 2003, MNRAS, 339, 289
Torrey, P., Cox, T. J., Kewley, L., & Hernquist, L. 2013, ASPC, 477, 237
Wakker, B. P. & van Woerden, H. 1997, ARA&A, 35, 217
Wetzel, A. R. 2011, MNRAS, 412, 49
Zepf, S. & Ashman, K. 1993, MNRAS, 264, 611

N. Libeskind: Leibniz-Institut für Astrophysik Potsdam (AIP), An der Sternwarte 16, D-14482 Potsdam, Germany.
N. Libeskind: l'Institut de Physique Nucléaire de Lyon (IPNL), University of Lyon; UCB Lyon 1/CNRS/IN2P3; Lyon, France.
J. C. Muñoz-Cuartas, D. A. Noreña, and L. F. Quiroga: FACom - Instituto de Física, FCEN, Universidad de Antioquia (UdeA), Calle 70 No. 52-21, Medellín, Colombia (david.norena@udea.edu.co).

Revista Mexicana de Astronomía y Astrofísica, **55**, 289–303 (2019)

DOI: https://doi.org/10.22201/ia.01851101p.2019.55.02.15

MILLIMETER AND FAR-IR STUDY OF THE IRDC SDC 341.232-0.268

M. M. Vazzano[1], C. E. Cappa[2], V. Firpo[4,5], C. H. López-Caraballo[6], M. Rubio[3], and N. U. Duronea[1]

Received April 1 2019; accepted July 17 2019

ABSTRACT

We analyze the molecular gas and dust associated with the infrared dark cloud SDC 341.232-0.268 in order to investigate the characteristics and parameters of the gas, determine the evolutionary status of four embedded EGO candidates, and establish possible infall or outflow gas motions. We base our study on ^{12}CO(2-1), ^{13}CO(2-1), and C^{18}O(2-1) data obtained with the APEX telescope, molecular data of high density tracers from the MALT90 survey and IR images from *Spitzer*, *Herschel* and ATLASGAL. The study reveals two clumps at -44 km s^{-1} towards the IRDC, with densities of $> 10^4$cm^{-3}, typical of IRDCs, while high density tracers show H_2 densities $> 10^5$. FIR images reveals the presence of cold dust linked to the molecular clumps and EGOs. A comparison of the spectra of the optically thin and optically thick molecular lines towards the EGOs suggests the existence of infall and outflow motions.

RESUMEN

Analizamos el gas molecular y el polvo asociado a la nube oscura infrarroja SDC 341.232-0.268 con el fin de investigar las características y parámetros físicos del gas, determinar el estado evolutivo de los cuatro EGOs embebidos y establecer posibles movimientos de acreción o flujo molecular. Nos basamos en datos de ^{12}CO(2-1), ^{13}CO(2-1) y C^{18}O(2-1) obtenidos con el telescopio APEX, trazadores de alta densidad extraídos de MALT90, e imágenes infrarrojas de *Spitzer*, *Herschel* y ATLASGAL. El estudio revela dos grumos moleculares a -44 km s^{-1} coincidentes con la IRDC con una densidad $> 10^4$cm^{-3}, típica de IRDCs. Los trazadores de alta densidad arrojan densidades de $H_2 > 10^5$. Las imágenes en el lejano IR muestran polvo frío asociado a los grumos moleculares y a los EGOs. La comparación de espectros moleculares ópticamente gruesos y finos sugiere la existencia de acreción y flujos moleculares.

Key Words: dust, extinction — ISM: clouds — ISM: individual objects: IRDC SDC 341.232-0.268 — ISM: kinematics and dynamics — ISM: molecules — stars: formation

1. INTRODUCTION

Infrared dark clouds (IRDCs) are sites of recent star formation within molecular clouds. These are detected as dark silhouettes against a bright background in the mid-infrared. These regions, which are also detected in the FIR, are believed to be places that may contain compact cores which probably host the early stages of high-mass star formation (e.g., Rathborne et al. 2007; Chambers et al. 2009). In fact, their cold ($T < 25$ K) and dense (10^2-10^4 cm^{-3}) ambient conditions, and their sizes of ≈1-3 pc and masses of 10^2-10^4 $M_\odot$ (Rathborne et al. 2006, 2007) favor star formation mechanisms. Evidences of active high-mass star formation in IRDCs are inferred from the presence of ultracompact HII regions (Battersby et al. 2010), hot cores (Rathborne et al. 2008), embedded 24 μm sources (Chambers et al. 2009), maser emission (Wang et al. 2008; Chambers et al.

[1]Instituto Argentino de Radioastronomía, CONICET, CCT-La Plata, Villa Elisa, Argentina.
[2]Facultad de Ciencias Astronómicas y Geofísicas, Universidad Nacional de La Plata, La Plata, Argentina.
[3]Departamento de Astronomía, Universidad de Chile, Chile.
[4]Gemini Observatory, Southern Operations Center, La Serena, Chile.
[5]Departamento de Astronomía y Física, Universidad de la Serena, La Serena, Chile.
[6]Departamento de Matemáticas, Universidad de La Serena, La Serena, Chile.

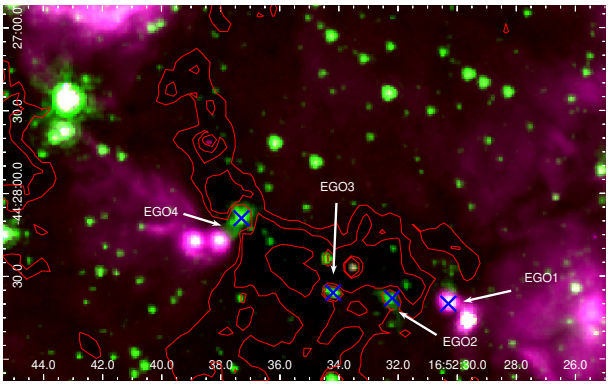

Fig. 1. Composite image showing the *Spitzer*-IRAC emission at 4.5 (green) and 8.0 μm (red), and *Spitzer*-MIPS emission at 24 μm (blue) of the region of SDC 341.232-0.268. Contours correspond to the emission at 8.0 μm at 80, 90, and 95 MJy/ster. The positions of the candidate EGOs are marked with blue crosses. The color figure can be viewed online.

2009), and/or outflow and infall processes (e.g. Sanhueza et al. 2010; Chen et al. 2011; Ren et al. 2011; Beuther et al. 2002; Zhang et al. 2007).

Many IRDCs are also associated with extended enhanced 4.5 μm emission (named extended green objects, EGOs, for the common coding of the [4.5] band in green in the 3-color composite IRAC images), the so-called "green fuzzies", indicating the presence of shocks. Following photometric criteria, Cyganowski et al. (2008) suggested that most of EGOs fall in the region of the color-color space occupied by the youngest MYSOs, and are surrounded by accreting envelopes (see Figure 13 in their work). This hypothesis is supported by Chen et al. (2010), whose observations are consistent with the speculation that EGOs trace a population with ongoing outflow activity and an active rapid accretion stage of massive protostellar evolution. The emission at 4.5 μm includes both H_2 (v = 0-0, S(9, 10, 11)) lines and CO (v = 1-0) band heads (Cyganowski et al. 2008), which are excited by shocks, such as those expected when protostellar outflows impinge on the ambient interstellar medium (ISM) (Cyganowski et al. 2008).

Using IRAC images, Peretto & Fuller (2009) catalogued and characterized many IRDCs using 8 and 24 μm *Spitzer* data. In this catalogue, the IRDCs were defined as connected structures with H_2 column density peaks $N_{H_2} > 2{\times}10^{22}$ cm^{-2} and boundaries defined by $N_{H_2} = 1{\times}10^{22}$ cm^{-2}. Single-peaked structures found in the H_2 column density maps were identified by the authors as fragments. These dark and dense patches are associated with molecular gas and dust emission (Sanhueza et al. 2012).

As a part of a project aimed at studying in detail the physical properties of the IR bubble complex S21-S24, we present here an analysis of the molecular gas and dust associated with SDC 341.232-0.268, a poorly studied IRDC of the southern hemisphere, which is member of this complex. Our aims are to determine the physical parameters and kinematics of the gas and to characterize the interstellar dust associated with the IRDC, to investigate the presence of embedded young stellar objects, and to establish possible infall or outflow gas motions. To accomplish this project, we analyze molecular data of the ^{12}CO(2-1), ^{13}CO(2-1), and C^{18}O(2-1) lines obtained with the APEX telescope, and HCO^+(1-0), HNC(1-0), and N_2H^+(1-0) lines from the MALT90 survey (Jackson et al. 2013; Foster et al. 2013, 2011)[7], mid- and far-IR continuum data from *Spitzer*-IRAC, *Herschel*-PACS and -SPIRE, and ATLASGAL (APEX) images (Schuller et al. 2009). We introduce the IRDC SDC 341.232-0.268 in § 2, the used database in § 3, the results of the molecular gas in § 4, and those of the infrared emission in § 5; signs of star formation are discussed in § 6, and a summary in § 7.

2. IRDC SDC 341.232-0.268

The IRDC SDC 341.232-0.268 (RA, Dec.(J2000)= 16:52:35.67, –44:28:21.8) has a mid-IR radiation field intensity $I_{MIR} \approx 88.3$ MJy ster^{-1} at 8.0 μm and a peak opacity of 1.09. From the Multiband Infrared Photometer for *Spitzer* (MIPS) images Peretto & Fuller (2009) detected a 24 μm point source in the field of the IRDC, and two clumps. The clumps were classified by Bergin & Tafalla (2007) as structures with sizes $\approx 10^{-1}$-100 pc, masses ≈ 10-$10^3 M_\odot$, and volume densities $\approx 10^3$-10^4 cm^{-3}.

Figure 1 shows the *Spitzer*-IRAC images at 4.5 (green) and 8.0 μm (red), and the *Spitzer*-MIPS image at 24 μm (blue) in the region of SDC 341.232-0.268. Green contours correspond to low emission levels at 8 μm, revealing a region of high extinction at 8.0 μm at the location of the IRDC, in contrast with the environment, a typical feature of these objects. The 90 MJy/ster contour delineates the IRDC. Four candidate EGOs catalogued by Cyganowski et al. (2008) appear projected toward this region: the "likely" MYSO outflow candidates G 341.22-0.26(b)(R.A., Decl.(J2000) = 16:52:30.3,

[7] http://malt90.bu.edu/data.html

–44:28:40.0), G 341.22-0.26(a) (16:52:32.2, –44:28:38.0), the "possible" MYSO outflow candidate G 341.23-0.27 (16:52:34.2, –44:28:36.0), and the "likely" MYSO outflow candidate G 341.24-0.27 (16:52:37.3, –44:28:09.0). These authors categorized the EGOs as a "likely" or "possible" MYSO outflow candidate based primarily on the angular extent of the extended excess 4.5 μm emission. Any source in which it was possible to confuse multiple nearby point sources and/or image artifacts from a bright IRAC with truly extended 4.5 μm emission was considered a "possible" candidate; these are likely still good YSO candidates, but not necessarily MYSOs with outflows, and so likely to be actively accreting.

From here on, they will be named EGO 1, EGO 2, EGO 3, and EGO 4, in increasing order of R.A. EGO 1 is associated with 8 and 24 μm emission and is located in the border of the IRDC, while EGOs 2, 3, and 4 are detected at 4.5 and 8 μm. EGO 1 and EGO 4 coincide with ATLASGAL Compact Sources AGAL 341.219-00.259 and AGAL 341.236-00.271. Their integrated flux densities are 12.85±2.20 Jy and 16.81±2.80 Jy, and their effective radii are $\approx 37''$ and $47''$, respectively (Contreras et al. 2013).

Methanol maser emission was detected towards EGO 2 and EGO 4 at 6 and 95 GHz, within the velocity range -43 to -52 km s^{-1}(Caswell et al. 2010; Chen et al. 2011; Hou & Han 2014; Yang et al. 2017). Methanol masers provide a signpost to the very earliest stages of the massive star formation process, prior to the onset of the UCHII region phase. They are associated with embedded sources whose bolometric luminosities suggest that they will soon become OB stars (Burton et al. 2002; Sobolev et al. 2005). The methanol masers are independent tracers and they give proven signatures of ongoing star formation (see Ellingsen 2006; Breen et al. 2013). Masers of water or hydroxyl have also been detected in in star-forming regions, as well as in evolved stars or supernova remnants. Therefore, the presence of these maser types in the vicinity of these EGOs could be a signspot of ongoing star formation.

3. DATABASE

3.1. *Molecular Line Observations*

The ^{12}CO(2-1), ^{13}CO(2-1), and C^{18}O(2-1) data were acquired with the APEX-1 receiver of the Swedish Heterodyne Facility Instrument (SHeFI; Vassilev et al. 2008) in the Atacama Pathfinder EXperiment (APEX) telescope, located in the Puna de Atacama (Chile). The backend for the observations was the eXtended bandwidth Fast Fourier Transform Spectrometer2 (XFFTS2) with a 2.5 GHz bandwidth divided into 32768 channels. The main parameters of the molecular transitions (rest frequency ν_0, half-power beam-width θ, velocity resolution Δv$_{\rm res}$, and *rms* noise of the individual spectra obtained using the OTF mode) are listed in Table 1. The selected off-source position free of molecular emission was RA, Dec.(J2000)= (16:36:40.56, −42:03:40.6).

TABLE 1

OBSERVATIONAL PARAMETERS OF THE MOLECULAR TRANSITIONS

Transition	ν_0	θ	Δv_{res}	rms
	GHz	$''$	km s^{-1}	K
^{12}CO(2-1)	230.538	30	0.1	0.35
^{13}CO(2-1)	220.398	28.5	0.1	0.35
C^{18}O(2-1)	219.560	28.3	0.1	0.35
HNC(1-0)	90.664	38.0	0.11	0.35
HCO$^+$(1-0)	89.189	38.0	0.11	0.35
N_2H^+(1–0)	93.173	38.0	0.11	0.35

Calibration was done using the chopper-wheel technique. The antenna temperature scale was converted to the main-beam brightness-temperature scale by $T_{\rm mb} = T_{\rm A}/\eta_{\rm mb}$, where $\eta_{\rm mb}$ is the main beam efficiency. For the SHeFI/APEX-1 receiver we adopted $\eta_{\rm mb} = 0.75$. Ambient conditions were good, with a precipitable water vapor (PWV) between 1.5 - 2.0 mm.

The molecular spectra were reduced using the CLASS90 software of the IRAM's GILDAS software package.

In addition, we used molecular data from the Millimetre Astronomy Legacy Team 90 GHz Survey (MALT90) taken with the Mopra spectrometer (MOPS). We used beam efficiencies between 0.49 at 86 GHz and 0.42 at 230 GHz (Ladd et al. 2005). The data analysis was conducted with CLASS90 software. Emission was detected in the HCO$^+$(1-0), HNC(1-0), and N_2H^+(1-0) lines, which were used to detect high density regions within SDC 341.232-0.268. Their main parameters are included in Table 1.

3.2. *Images in the Infrared*

We used near- and mid-infrared (NIR, MIR) images from the *Spitzer*-IRAC archive at 4.5 and 8.0 μm of the Galactic Legacy Infrared Mid-Plane Survey

Extraordinaire (GLIMPSE)[8] (Benjamin et al. 2003), and the Multiband Imaging Photometer for *Spitzer* (MIPS) image at 24 μm from the MIPS Inner Galactic Plane Survey (MIPSGAL)[9] (Carey et al. 2005) to delineate the IRDC and investigate their correlation with the EGO candidates.

To trace the cold dust emission we utilized far-infrared (FIR) images from the *Herschel Space Observatory* belonging to the Infrared GALactic (Hi-GAL) plane survey key program (Molinari et al. 2010). The data were obtained out in parallel mode with the instruments PACS (Poglitsch et al. 2010) at 70 and 160 μm, and SPIRE (Griffin et al. 2010) at 250, 350, and 500 μm. The angular resolutions for the five photometric bands spans from 8″ to 35.″2 for 70 μm to 500 μm. *Herschel* Interactive Processing Environment (HIPE v12[10], Ott 2010) was used to reduce the data, with reduction scripts from standard processing. The data reduction and calibration (including zero-level and color correction) is described in detail in § 2.2 of Cappa et al. (2016).

We also used images at 870 μm from the APEX Telescope Large Area Survey of the Galaxy (ATLASGAL) (Schuller et al. 2009) with a beam size of 19.″2. This survey covers the inner Galactic plane, with an *rms* noise in the range 0.05-0.07 Jy beam^{-1}. The calibration uncertainty in the final maps is about 15%.

4. MOLECULAR CHARACTERIZATION OF THE IRDC

4.1. *CO data: Morphological and Kinematical Description*

To visualize the spatial distribution of the molecular emission the upper panel of Figure 2 exhibits the ^{13}CO(2-1) brightness temperature distribution from ≈ -47.0 to -42.5 km s^{-1} in steps of 0.3 km s^{-1}. The most intense ^{13}CO(2-1) emission appears in the range -45.2 to -44 km s^{-1}. The bottom central panel of Figure 2 shows the average ^{13}CO(2-1) emission in the range -47.0 to -42.8 km s^{-1}, revealing two molecular clumps centered at RA, Dec.(J2000)= (16:52:37.06, −44:28:13.9) *(Clump A)* and RA, Dec.(J2000)= (16:52:29.72, −44:28:40.1) *(Clump B)*. The coincidence of the clumps with EGO 1, 2, and 4 (indicated with crosses in this figure) is clear. The effective radii of the clumps are 37.″6 and 45.″6 for *Clump A* and *Clump B*, respectively, as obtained taking into account the average ^{13}CO(2-1) emission higher that 6.2 K. Finally, the bottom left and right panels of the same figure display the C^{18}O(2-1) and ^{12}CO(2-1) average emission in velocity intervals similar to that in the image of ^{13}CO(2-1). Both clumps A and B are detected at C^{18}O(2-1) revealing the existence of dense molecular gas in the clumps. The ^{12}CO(2-1) emission delineates the IRDC but the clumps are not well defined.

Figure 3 shows the averaged ^{12}CO(2-1), ^{13}CO(2-1), and C^{18}O(2-1) spectra within the area corresponding to *Clump A* and *Clump B*. The *rms* noise of the averaged spectra is 0.019 K for *Clump A*, and 0.017 for *Clump B*. For *Clump A*, the ^{12}CO(2-1) line exhibits a multi-peak structure with components in the interval from -70 to -20 km s^{-1}, with the most intense features between -48 and -35 km s^{-1}. Three velocity componentes are detected within the latter velocity interval, peaking at -46.6 km s^{-1}, -42.2 km s^{-1}, and -36.8 km s^{-1}. The ^{13}CO(2-1) and C^{18}O(2-1) spectra peak at around -44.0 km s^{-1}, coincident with a minimum in the ^{12}CO(2-1) spectrum. Components outside this range will be analyzed in § 6.2. For *Clump B*, the ^{12}CO(2-1) line also shows a multi-peak structure between –55 and –25 km s^{-1}, with the maximum at –45.4 km s^{-1}. The ^{13}CO(2-1) and C^{18}O(2-1) profiles peak at –44.0 km s^{-1}.

Taking into account that the C^{18}O(2-1) emission is generally optically thin, we adopted systemic velocities ($v_{\rm sys}$) of –44.0 km s^{-1} for *Clump A* and *Clump B*. The adopted systemic velocity coincides with the velocity for EGO 2 and 4 reported by Yang et al. (2017) (−44.6 and −44.9, respectively) from methanol maser emision, and from masers by Chen et al. (2011). It is also compatible with the velocity of NH_3 clouds identified by Purcell et al. (2012) at -43.7 km s^{-1} at a position distant 15″ from EGO 3, and from the CS(2-1) line emission obtained by Bronfman et al. (1996), who observed toward [RA, Dec.(J2000)= (16:52:34.2, –44:28:36.0)], revealing the presence of high density regions (n_{crit} = 3.0×10^5 cm^{-3}). Circular galactic rotation models predict that gas with velocities of -44 km s^{-1} lies at the near kinematical distance of 3.6 kpc (see, for example, Brand & Blitz 1993). Adopting a velocity dispersion of 6 km s^{-1}, the uncertainty in distance is 0.5 kpc (15%). The distance coincides also with that of S 24 (Cappa et al. 2016) indicating that the IRDC belongs to the same complex.

[8] http://irsa.ipac.caltech.edu/data/SPITZER/GLIMPSE/

[9] http://irsa.ipac.caltech.edu/data/SPITZER/MIPSGAL/

[10] *HIPE* is a joint development by the Herschel Science Ground Segment Consortium, consisting of ESA, the NASA Herschel Science Center, and the HIFI, PACS and SPIRE consortia members, see http://herschel.esac.esa.int/HerschelPeople.shtml.

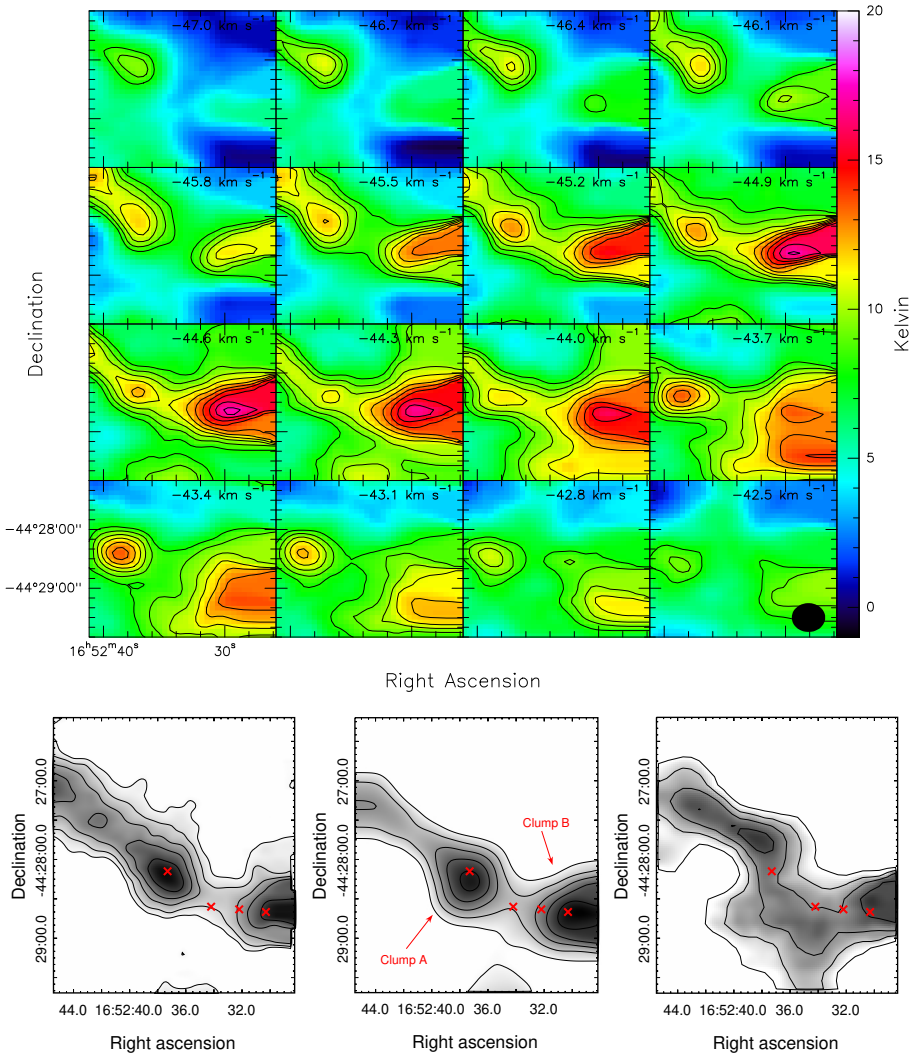

Fig. 2. *Upper panel:* $T_{\rm mb}$-maps of the ^{13}CO(2-1) emission within the velocity interval from –47.0 to –42.5 km s^{-1} in steps of 0.3 km s^{-1}. Contours range from 8 to 17 K in steps of 1 K in $T_{\rm mb}$. *Lower left panel:* Average C^{18}O(2-1) emission in the range –47.2 to –43.8 km s^{-1}. Contours are 0.8, 1.0, 1.3, 1.6, and 2.0 K. The red crosses mark the position of the EGOs. *Lower central panel:* Average ^{13}CO(2-1) emission in the range −47.0 to −42.8 km s^{-1}. Contours range from 6.2 to 9.4 K in steps of 0.8 K. *Lower right panel:* Average ^{12}CO(2-1) emission in the range −48.2 to −42.5 km s^{-1}. Contours range from 10 to 13 K in steps of 1 K. The color figure can be viewed online.

TABLE 2

PARAMETERS OF THE GAUSSIAN FITS FOR *Clump A* AND *Clump B*

	Line	v km s^{-1}	Δv km s^{-1}	$T_{\rm peak}$ K	Area K km s^{-1}
Clump A	^{13}CO(2-1)	–44.56(0.03)	5.56(0.07)	6.82	40.33(0.41)
	C^{18}O(2-1)	–44.23(0.02)	4.46(0.05)	1.37	6.49(0.06)
Clump B	^{13}CO(2-1)	–43.85(0.01)	2.56(0.08)	9.52	25.96(0.18)
	C^{18}O(2-1)	–43.70(0.01)	2.61(0.03)	2.46	6.84(0.07)

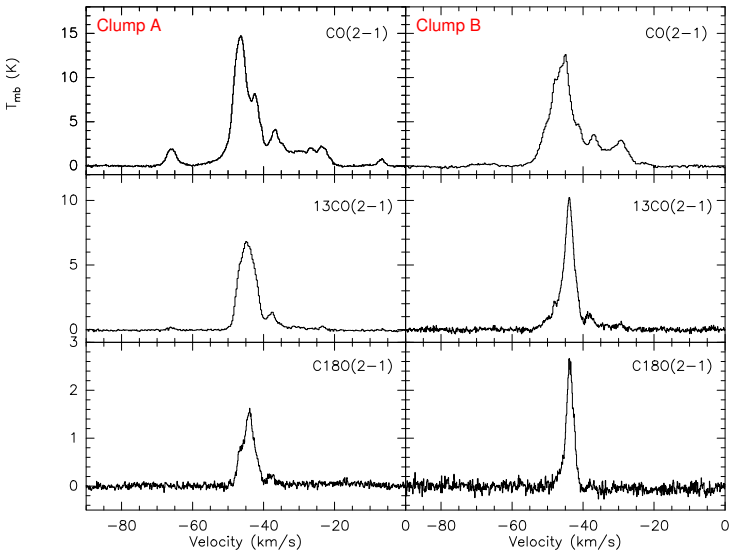

Fig. 3. Averaged ^{12}CO(2-1), ^{13}CO(2-1) and C^{18}O(2-1) spectra towards *Clump A* (left) and *Clump B*(right).

TABLE 3

DERIVED PARAMETERS OF THE MOLECULAR COMPONENTS

	τ_{13}	τ_{18}	$T_{\rm exc}$ K	$N(^{13}{\rm CO})$ 10^{16} cm^{-2}	$N({\rm H_2})$ 10^{22} cm^{-2}	r pc	$M({\rm H_2})$ $M_\odot$	$n_{\rm H2}$ 10^4cm^{-3}	$M_{\rm vir}$ $M_\odot$	$\frac{M_{\rm vir}}{M({\rm H_2})}$
Clump A	3.4	0.6	11.5	14.20	7.1	0.7	2400±960	2.6±1.3	1000-1670	0.41-0.69
Clump B	1.1	0.1	14.4	4.12	2.06	0.9	1200±480	0.5±0.2	750-1240	0.62-1.0

4.2. *Parameters Derived From CO Data*

Bearing in mind that the spatial distribution of the ^{13}CO(2-1) and C^{18}O(2-1) emission coincides with the IRDC, we used these lines to estimate the main parameters of the molecular gas assuming local thermodynamic equilibrium (LTE). All the calculations were carried out from the Gaussian fits to the lines averaged in the area of *Clump A* and *Clump B* shown in Table 2. The columns list the central velocity of each component v, the full-width at half-maximum, the peak temperature, and the integrated emission. We applied the following expression to estimate optical depths (e.g. Scoville et al. 1986):

$$\frac{T^{13}_{\rm mb}}{T^{18}_{\rm mb}} = \frac{1-e^{-\tau^{13}}}{1-e^{-\tau^{13}/7.6}}, \qquad (1)$$

where τ^{13} is the optical depth of the ^{13}CO(2-1) gas and 7.6 = [^{13}CO(2-1)]/[C^{18}O(2-1)] (Sanhueza et al. 2010) is the isotope abundance ratio. The ^{13}CO(2-1) optical depths are indicated in Column 2 of Table 3. To estimate the C^{18}O(2-1) optical depth we used

$$\tau_{18} = \frac{1}{7.6}\,\tau_{13}\left(\frac{\Delta {\rm v}_{13}}{\Delta {\rm v}_{18}}\right)\left(\frac{\nu^{13}}{\nu^{18}}\right)^2, \qquad (2)$$

where Δv is the full-width at half-maximum of the C^{18}O(2-1) and ^{13}CO(2-1) profiles. The results are listed in Column 3 of Table 3. Bearing in mind that ^{13}CO(2-1) is moderately optically thick we calculated the excitation temperature from the ^{13}CO(2-1) line using

$$T_{\rm exc} = \frac{T^*}{\ln\left[\left(\frac{T^{13}_{\rm mb}}{T^*}+\frac{1}{\exp(T^*/T_{\rm bg})-1}\right)^{-1}+1\right]}, \qquad (3)$$

where $T^* = \frac{h\nu}{k}$, ν is the frequency of the ^{13}CO(2-1) line and $T_{\rm bg}$ = 2.7 K. Values estimated for $T_{\rm exc}$ are listed in Table 3.

The column density for ^{13}CO(2-1) was derived using Rohlfs & Wilson (2004)

$$N(^{13}{\rm CO}) = 2.4\times10^{14}\exp\left(\frac{T^*}{T_{\rm exc}}\right) \times\frac{T_{exc}}{1-e^{-T^*/T_{\rm exc}}}\int\tau_{13}d{\rm v}. \qquad (4)$$

In this case we used the approximation for $\tau_{13} > 1$,

$$T_{exc}\int\tau_{13}d{\rm v} \simeq \times\frac{\tau^{13}}{1-exp(-\tau^{13})}\int T^{13}_{\rm mb}d{\rm v}. \qquad (5)$$

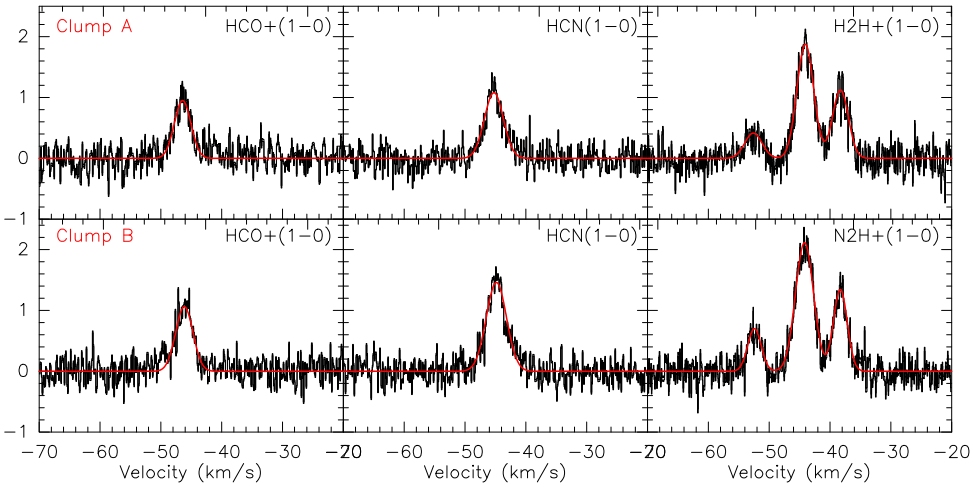

Fig. 4. HCO^+(1–0), HNC(1–0) and N_2H^+(1–0) profiles towards *Clump A* (top) and *Clump B* (bottom). The color figure can be viewed online.

This approximation helps to eliminate to some extent optical depth effects. The integral was evaluated as $T_{mean-mb} \times \Delta$v, where $T_{mean-mb}$ is equal to the average T_{mb} within the area of each clump.

To estimate $N(H_2)$ (Column 6 in Table 3) we adopted an abundance $[H_2][^{13}CO] = 5\times10^5$ (Dickman 1978). Then, the molecular mass (Column 9 in Table 3) was calculated from the equation

$$M(H_2) = (m_{sun})^{-1} \mu\ m_{\rm H}\ A\ N(H_2)\ d^2\,, \qquad (6)$$

where $m_{sun} = 2\times10^{33}$ g is the solar mass, the mean molecular weight $\mu = 2.76$ (which includes a relative helium abundance of 25% by mass, Allen 1973), and $m_{\rm H}$ is the hydrogen atomic mass. In this expression d is the distance, $N(H_2)$ is the H_2 column density, and A is the area of the source in cm^{-2}. The effective radius of each clump, as seen in the ^{13}CO(2-1) line, and the volume densities are listed in Colums 7 and 9 in Table 3.

The ambient volume densities, $n_{\rm H_2}$, was calculated assuming a spherical geometry for the clumps, using the formula

$$n_{\rm H_2} = \frac{M(H_2)}{\frac{4}{3}\pi\ r^3 \mu\, m_H}\,. \qquad (7)$$

Ambient densities are listed in Column 9 of Table 3. The parameters calculated in this work agree with Bergin & Tafalla (2007).

The virial mass can be determined following MacLaren et al. (1988):

$$\frac{M_{\rm vir}}{M_\odot} = k_2 \left[\frac{r}{\rm pc}\right] \left[\frac{\Delta {\rm v}^2}{\rm kms^{-1}}\right]\,, \qquad (8)$$

where r and Δv are the radius of the region and the velocity width measured from the Gaussian fit of the $C^{18}O$(2-1) emission, and k_2 depends on the geometry of the ambient gas in the region, being 190 or 126 according to $\rho \propto r^{-1}$ or $\rho \propto r^{-2}$, respectively. $M_{\rm vir}$ values are listed in Column 10 in Table 3. The ratios $M_{vir}/M(H_2)$ suggest that both clumps may collapse to form new stars; since the virial mass value is smaller than the LTE mass value this clump does not have enough kinetic energy to stop the gravitational collapse.

Uncertainties in both the molecular mass derived using LTE conditions, $M(H_2)$, and the virial mass $M_{\rm vir}$ are affected by the distance indetermination (15%) yielding a 30% error in $M(H_2)$ and 15% in $M_{\rm vir}$. Inaccuracies in the borders of the clumps originate errors in their sizes and thus additional uncertainties in the masses, suggesting errors of 40% in $M(H_2)$. Virial masses are not free of uncertainties, because of the existence of magnetic field support that may lead to an overestimate of the derived values (see MacLaren et al. 1988), and because of the unknown density profile of the clump.

4.2.1. *Analysis of the MALT90 Data*

The MALT90 data cubes of this region show emission of HCO^+(1–0), HNC(1–0), and N_2H^+(1–0) molecules, which are the most often detected molecules towards IRDCs (Sanhueza et al. 2012; Rathborne et al. 2016). These molecules have critical densities of 2×10^5, 3×10^5 and 3×10^5 cm^{-3}, respectively (Sanhueza et al. 2012), allowing us to infer a lower limit for the density of the clumps. These val-

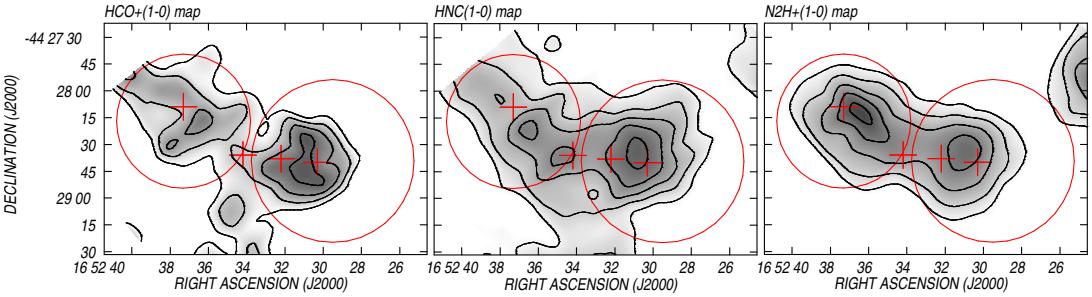

Fig. 5. HCO^+(1–0) (levs: 0.65, 0.7, 0.8 and 0.9 K), HNC(1–0) (levs: 0.7, 0.85, 1.0 and 1.15 K) and N_2H^+(1–0) (levs: 0.8, 1.0, 1.2 and 1.4 K) maps. Red circles have radii equal to the effective radii of the clumps as seen in ^{13}CO(2-1), and are located at their position. Crosses mark the location of the EGO candidates. The color figure can be viewed online.

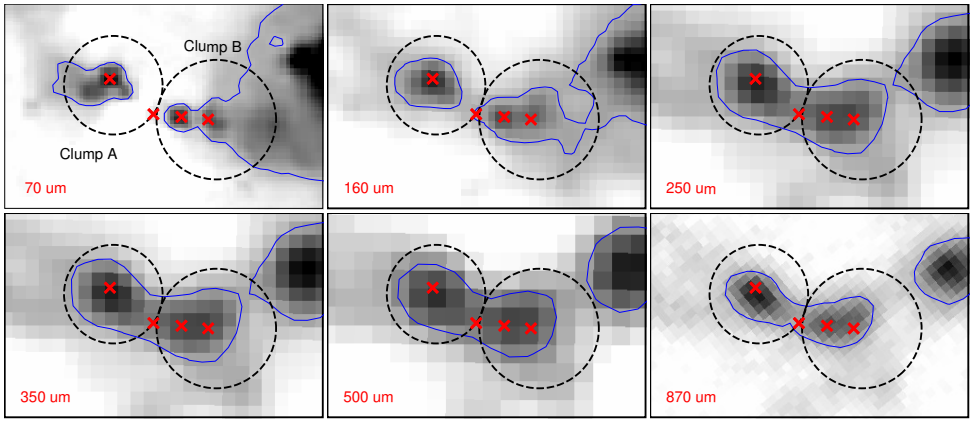

Fig. 6. FIR view of SDC 341.232-0.268 from Herschel (70-500 μm) and ATLASGAL data. The blue circles have the same meaning as in Figure 5 and show the areas where the flux densities were integrated. The crosses mark the position of the EGOs. Contours correspond to 20 *rms*. The color figure can be viewed online.

ues are higher than the H_2 ambient densities derived from CO lines (see Table 3).

Spectra of these lines, averaged over the area of the clumps, are shown in Figure 5. By applying a Gaussian fitting to the HCO^+ and HNC lines, a mean velocity of -46 km s^{-1} was derived. For the case of the N_2H^+ line, a multi Gaussian function was applied to take into account hyperfine structure. This molecule has seven hyperfine components in two blended groups of three lines (groups 2 and 3) and one isolated component (group 1). The rest frequencies of groups 1, 2 and 3 are 93.176, 93.173, and 93.171 GHz, respectively. The mean velocity is -44 km s^{-1}. The velocities of these lines coincide with the systemic velocities derived from CO data.

These tracers of dense gas provide slightly different information: HCO^+ often shows infall signatures and outflow wings (e.g. Rawlings et al. 2004; Fuller et al. 2005). However, in our case no signs of infall can be identified. HNC is specially preponderant in cold gas and is a commonly used tracer of dense gas in molecular clouds. Finally, N_2H^+ is more resistant to freeze-out on grains than carbon-bearing species like CO.

Figure 5 shows the HCO^+(1–0), HNC(1–0) and N_2H^+(1–0) maps, integrated from -47.6 to -44.0 km s^{-1}, -46.7 to -43.1 km s^{-1}, and -47 to -41.4 km s^{-1}, respectively. Both clumps are detected in the three molecular lines indicating mean densities of 10^5 cm^{-3}. Carbon-bearing species, like CO, tend to disappear from the gas phase in the high density centers of the cores, while nitrogen-bearing species like N_2H^+ survive almost unaffected up to much higher densities. This is evidenced in the fact that the spacial distribution of the N_2H^+ emission is similar to that of dust continuum emission (see Figure 6).

Following Purcell et al. (2009) we estimate the N_2H^+ optical depth and column density. Assuming the line widths of the individual hyperfine components are all equal, the integrated intensities of the three blended groups should be in the ratio of 1:5:3

under optically thin conditions. The optical depth can then be derived from the ratio of the integrated intensities of any group using the following equation:

$$\frac{\int T_{\rm mb,1} dv}{\int T_{\rm mb,2} dv} = \frac{1 - exp(-\tau_1)}{1 - exp(-\tau_2)} = \frac{1 - exp(-\tau_1)}{1 - exp(-a\tau_1)}, \quad (9)$$

where a is the expected ratio of τ_1/τ_2 under optically thin conditions.

To determine the optical depth we used only the intensity ratio of group 1/group 2, as Caselli et al. (1995) report anomalous excitation of the F_1,F = 1,0 → 1,1 and 1,2 → 1,2 components (in group 3). Thus we obtained $\tau_1 = 0.11$ and 0.19 for *Clump A* and *Clump B*, respectively.

Based on the expression for $T_{\rm mb}$ given by Rohlfs & Wilson (2004), the excitation temperature for N_2H^+ can be calculated with the following formula:

$$T_{\rm exc} = 4.47/\ln\left[1 + \left(\frac{T_{\rm mb}}{4.47(1 - exp(-\tau))} + 0.236\right)^{-1}\right], \quad (10)$$

and the column densities can be derived using (Chen et al. 2013):

$$N(N_2H^+) = \frac{3kW}{8\pi^3 \nu S\mu^2} \left(\frac{T_{\rm exc}}{T_{\rm exc} - T_{\rm bg}}\right) \left(\frac{\tau}{1 - exp(-\tau)}\right) \times Q(T_{\rm exc}) exp(E_u/kT_{\rm exc}) \quad (11)$$

where k is the Boltzmann constant, W is the observed line integrated intensity (obtained from a Gaussian fit), ν is the frequency of the transition, and $S\mu^2$ is the product of the total torsion-rotational line strength and the square of the electric dipole moment. $T_{\rm exc}$ and $T_{\rm bg}$ are the excitation temperature and background brightness temperature, respectively. E_u/k is the upper level energy in K, $Q(T_{\rm exc})$ is the partition function at temperature $T_{\rm exc}$ and τ is the optical depth. For group 1 the values of ν, $S\mu^2$ and E_u/k are 93176.2526 MHz, 12.42 D^2 and 4.47 K, respectively. These values were taken from the SPLATALOGUE catalogue[11].

We derive $T_{\rm exc}$ = 17.4 and 12.5 K, and $N(N_2H^+) = 8.7\times10^{13}$ and 8.1×10^{13} for *Clump A* and *Clump B*, respectively. Considering an abundance $[N_2H^+]/[H_2] = 5\times10^{-10}$ for dark molecular clouds (Ohishi et al. 1992) we obtain H_2 column densities of 1.7 and 1.6 $\times10^{23}$ for *Clump A* and *Clump B*, respectively. These column densities are higher than those obtained from CO calculations. Ambient densities are $n_{H_2} \approx 1.7\times10^5$ cm^{-3} for each clump with an effective radii in N_2H^+ of 0.53 pc. This difference may be explained by considering that the nitrogen-bearing species survive almost unaffected up to much larger densities that carbon-bearing molecules.

[11]SPLATALOGUE at `http://www.splatalogue.net/`

5. WARM AND COLD DUST DISTRIBUTION

Figure 6 shows *Herschel* and ATLASGAL maps (in original resolution) of the SDC 341.232-0.268 region. At $\lambda < 160$ μm the beam resolution allows to identify the emission associated with EGOs 1, 2, and 4. Warm dust coincident with the EGOs is also revealed by the emission in 24 μm, which can be seen in Figure 1. The presence of this emission allows us to classify the clumps as "active", according to the classification of Chambers et al. (2009). These authors proposed an evolutionary sequence in which "quiescent" clumps (containing neither IR indicator) evolve into "intermediate" (containing either a "green fuzzy" or a 24 μm point source, but not both), "active"(caracterized by the presence of a "green fuzzy" coincident with an embedded 24 μm source, such as those observed toward EGOs 1, 2, and 4), and "red" clumps (dominated by 8 μm emission, which contains PAH features). At $\lambda > 160$ μm two dust clumps are detected superimposed onto more extended submillimeter emission, indicating dust related to *Clump A* and *Clump B*.

The characterization of the dust properties of these clumps is limited by the resolution of FIR data. We study the integrated dust properties of each clump from the spectral energy distribution (SED) using the Herschel (160 up to 500 μm) and ATLASGAL maps convolved at a common beam resolution of the 500 μm map (36″). The flux densities are obtained from a circular aperture photometry integration (radius of 37.″6 and 45.″6 for *Clump A* and *Clump B*, respectively), and subtracting a background level computed from a rectangular region (width = 52.″5 and height 25.″8 in the north of the clumps). For flux uncertainty estimation, we consider the standard deviation of surface brightness in the background region and the flux calibration uncertainties. For each clumps, the final SED is depicted in Figure 7 and the fluxes and their error bars are listed in Table 4. We perform a thermal dust fit to the data considering a single-component modified blackbody (grey-boby), which depends on the optical depth, the emissivity spectral index (β_d) and the dust temperature (T_d). In the optically thin regime, the best fitting provides similar dust temperature and emissivity for both clumps, with values of

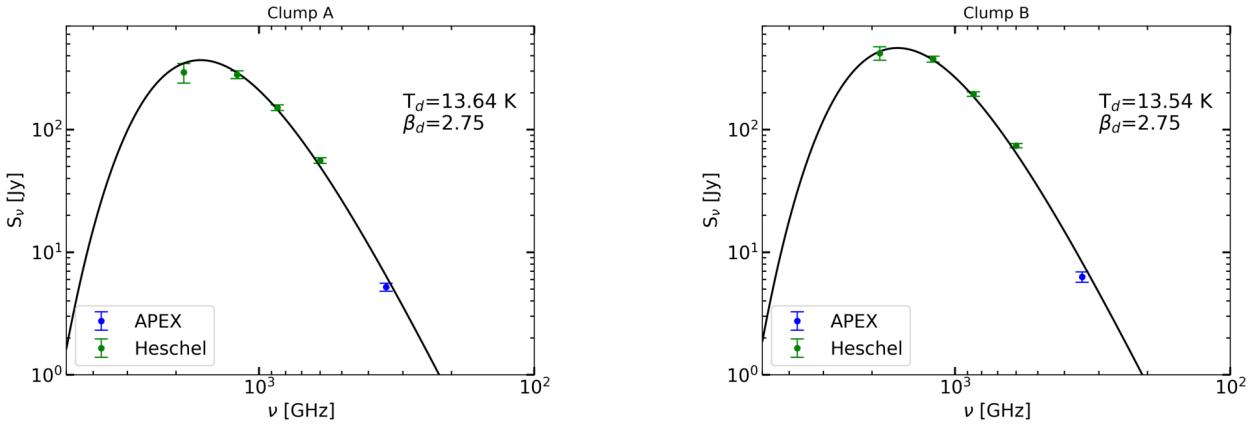

Fig. 7. Spectral energy distributions (SEDs) for *Clump A* (left) and *Clump B* (right), obtained from the fluxes at 160, 250, 350, and 500 μm from Herschel, and 870 μm from ATLASGAL. The color figure can be viewed online.

TABLE 4

MEASURED FLUXES AND DERIVED PARAMETERS OF THE FIR CLUMPS

	S_{160} [Jy]	S_{250} [Jy]	S_{350} [Jy]	S_{500} [Jy]	S_{870} [Jy]	T_d [K]	$M_{\rm dust+gas}$ [$M_\odot$]	$n_{\rm H_2}$ [10^3 cm^{-3}]
Clump A	293±53	281±21	151±8	56±3	5.2±0.4	13.6±0.47	1536±444	1.5±0.7
Clump B	421±53	376±21	195±8	74±3	6.3±0.6	13.5±0.47	2088±600	1.4±0.6

$T_d = 13.5 \pm 0.47$ K and $\beta_d = 2.7$. These dust temperatures are of the order of those found by Guzmán et al. (2015) (18.6±0.2) for proto-stellar clumps.

For *Clump A* and *Clump B*, the total mass ($M_{\rm dust+gas}$) was calculated from the optical depth of the dust obtained from the fit, using the following expression

$$M_{dust+gas} = \frac{\tau_{\nu_{fit}}}{\kappa_{870}} \left(\frac{345\,\mathrm{GHz}}{\nu_{fit}} \right)^{\beta_d} d^2 R_{\rm d}\,, \qquad (12)$$

where $\tau_{\nu_{fit}}$ is the dust optical depth ($= 10^{-26}\times$ fit amplitude), ν_{fit}=1 Hz is the frequency of the fit, $R_{\rm d} = 100$ is the typical gas-to-dust ratio, d is the distance and κ_{870}=1.00 cm^{-2} gr^{-1} is the dust opacity at 345 GHz (Ossenkopf & Henning 1994). The mass uncertainties were computed propagating the error bars for dust optical depth and distance. Additional errors may result from taking different values for the gas-to-dust ratio (in our galaxy typical values are between 100 and 150).

The results are listed in Table 4, which includes the derived masses of the clumps and their volume densities. Uncertainties in masses and ambient densities are about 35% and 60%, respectively. The total masses derived from molecular gas and dust emission are in good agrement (within errors).

6. STAR FORMATION

6.1. *Search for Additional YSOs Coincident with the IRDC*

To investigate the coincidence of the IRDC with other candidate young stellar objects (YSOs), we analyze the characteristics of the point sources in the WISE and Spitzer catalogues (Wright et al. 2010; Benjamin et al. 2003) projected in the region. In Figure 8 we mark the positions of Class I and II YSO candidates identified in the area of the molecular clumps. An inspection of the figure reveals that EGOs 1, 3, and 4 coincide with identified YSOs.

To study in some detail the nature of the EGOs we plotted their spectral energy distributions (SEDs) using the Robitaille's SED fitting tool (Robitaille et al. 2007). To perform the analysis we were able to use available data from 2MASS, IRAC-GLIMPSE, and MIPSGAL at 24 μm only. The obtained SEDs are shown in Figure 9. Clearly, EGO 1, 3 and 4 have characteristics of YSOs, and as seen in Figure 8 coincide with additional evidence of star formation. As regards EGO 2, the fit is not good; it does not coincide with other sources or with the molecular clumps. So, its status is doubtful. In Table 5 we display the main parameters obtained from the SEDs. Column 1 gives the name of the source; Columns 2

TABLE 5

PHYSICAL PARAMETERS OBTAINED FROM THE SEDS FOR THE EGOS

	Age	$M_{stellar}$	M_{env}	$\dot{M}_{acr}$	L	Stage
	10^4	$M_\odot$	$M_\odot$	$10^{-4} M_\odot$ yr^{-1}	$10^2 L_\odot$	
EGO 1	0.13	2.1	0.7	0.1	1.3	0/I
EGO 2	545	3.9	8×10^{-6}	0	1.9	0/I
EGO 3	15.7	4.1	7.1	1.4	0.8	0/I
EGO 4	4.1	8.6	0.09	12.5	14.4	0/I

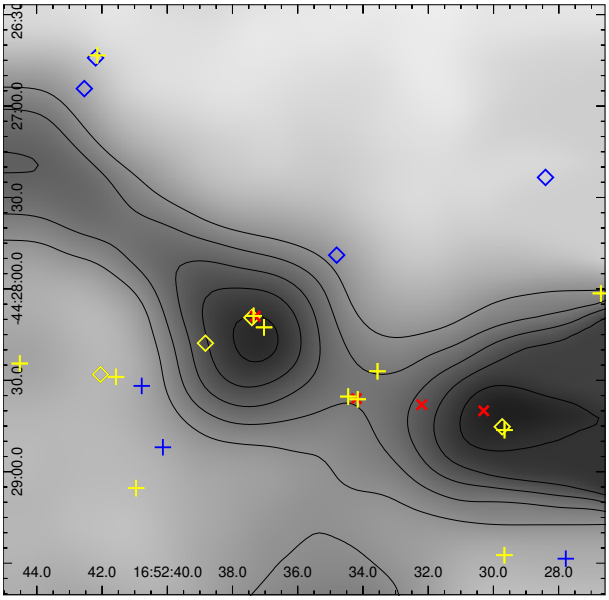

Fig. 8. Overlay of YSOs identified in the Spitzer and WISE catalogues and the molecular clumps in ^{13}CO(2-1). Contours have the same meaning as in Figure 2. Yellow and blue symbols show the position of Class I and Class II YSOs, while red crosses mark the location of EGOs. Plus signs correspond to Spitzer sources and diamonds to WISE ones. The color figure can be viewed online.

and 3, the age and mass, $M_{\rm stellar}$, of the central source; Column 4, the mass of the envelope, $M_{\rm env}$; Column 5, the infall rate, $\dot{M}_{\rm acr}$; and Column 6, the total luminosity. To perform the SEDs we adopted $d = 3.6 \pm 0.5$ kpc and a visual extinction of 3-4 mag.

Following Robitaille et al. (2007) an estimate of the evolutionary stage of the sources can be obtained based on the ratio of the infall rate and the mass of the central source. For the four candidate EGOs the ratio $\dot{M}_{\rm acr}/M_{\rm stellar} > 10^{-6}$ indicates Stage 0/I. The age of some of the sources suggests that they are still immersed in their envelopes. According to the fitting, EGO 4 would be the most massive object in the sample, and EGO 2 seems to be the most evolved one. These results should be taken with caution because of the limitations of the fitting tool that may arise from: (1) YSOs are complex 3d objects with slightly non-axisymmetric density structures, so the models are incorrect compared to actual density distributions; (2) there are often mixtures of sources and many objects appear as a single YSO, but they are often two or more objects; and (3) even in the case of an isolated YSO variability is an additional complication, since the data with which SEDs are usually constructed belong to different surveys that have been performed in different years and can produce discontinuities in the SEDs (Robitaille 2008; Deharveng et al. 2012; Offner et al. 2012).

As pointed out before, the emission at 24 μm, detected toward EGO 1, 3, and 4, suggests the existence of warm dust and embedded protostars (Jackson et al. 2008).

6.2. *Evidence for Inflow/Outflow Motions*

One way to visualize molecular outflows or infalls is to compare the optically thick ^{12}CO(2-1) emission line with the optically thin C^{18}O(2-1) molecular line toward the candidate EGOs, as shown in Figure 10 for EGO 3 and EGO 4. The ^{12}CO(2-1) line presents a double peak structure with the blue shifted peak brighter than the red-shifted one, and a minimum at the systemic velocity, while the C^{18}O(2-1) line presents a single peak centered on the absorption dip of the optically thick line. According to Chen et al. (2011) these spectra display characteristics typical of infall motions: a double-peak structure with the blue-shifted peak brighter than the red-shifted one, while an emission peak of an optically thin line appears centered on the absorption dip of the optically thick line. According to these authors, the infall motion is the only process that would consistently produce the blue profile asymmetry. The blue-shifted emission can be explained as due to high-excitation

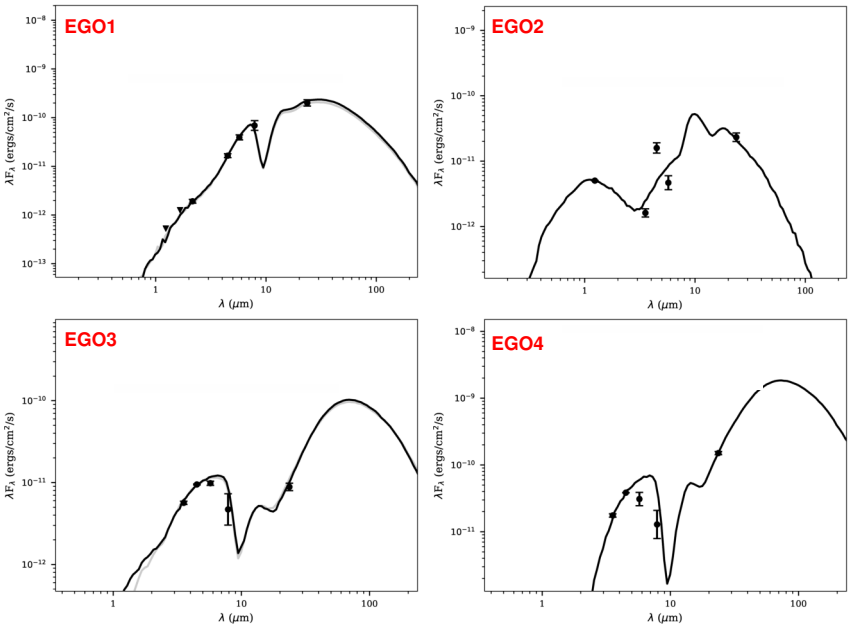

Fig. 9. Spectral energy distribution for the four candidate EGOs. The color figure can be viewed online.

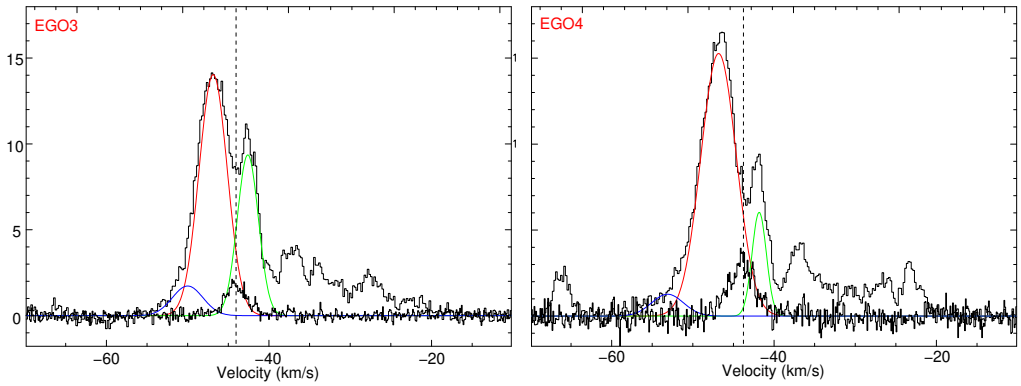

Fig. 10. ^{12}CO(2-1) and C^{18}O(2-1) profiles in the direction to EGO 3 (left) and EGO 4 (right). In both pannels red and green lines correspond with Gaussian fits from the ^{12}CO(2-1) double peak, and blue lines indicates a Gaussian component fitting the possible blue outflow wings. The color figure can be viewed online.

approaching warm gas located on the far side of the center of contraction. The emission of this gas undergoes less extinction than the emission from the red-shifted receding nearside material, given that the excitation temperature of the molecules increases toward the center of the region (Zhou 1992). Thus, the spectra of EGO 3 and EGO 4 suggest the presence of infall motions.

Following Mardones et al. (1997), we use the asymmetry parameter δv (the velocity difference between the peaks of the optically thick line and the optically thin lines, normalized by the FWHM of the thin line), to quantify the blue asymmetry. The parameter is defined as $\delta v = (v_{thick} - v_{thin}) / \Delta v_{thin}$. A statistically significant excess of blue asymmetric line profiles with $\delta v < -0.25$ indicates that the molecular gas is falling into the clump. We consider the velocity and width of the C^{18}O(2-1), from Table 2, as v_{thin} and Δv_{thin}, and calculate v_{thick} from the Gaussian fits of ^{12}CO(2-1) profiles (–46.9 and –45.3 from *Clump A* and *Clump B*, respectively). We find, for both *Clump A* and *Clump B* $\delta v \approx -0.06$, which supports the infall hypothesis.

The interpretation presented above is supported by the $M_{vir}/M(H_2)$ ratio previously derived for the objects. As the classical virial equilibrium analysis

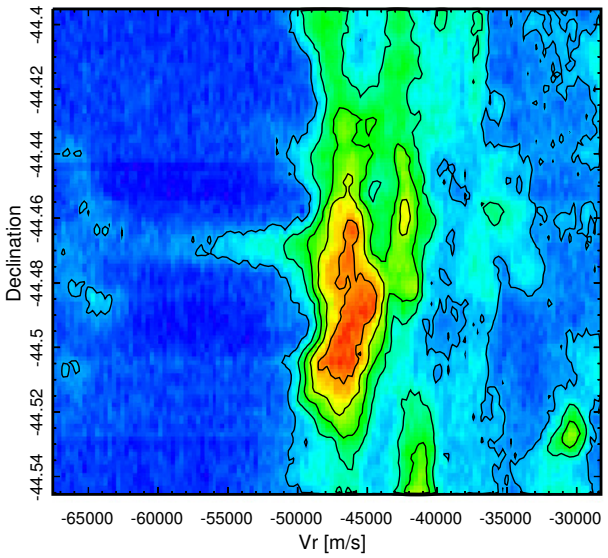

Fig. 11. Position-velocity diagram toward EGO 4 in ^{12}CO(2-1) (Dec. vs. velocity for a fixed value of R.A. = 16:52:35). The color scale indicates T_{mb} and the declination is indicated in fractions of degrees. The color figure can be viewed online.

establishes, a ratio $M_{\rm vir}/M({\rm H_2}) \lesssim 1$ indicates that a clump has too much kinetic energy and is unstable against gravitational collapse. Then, the derived ratios suggest that *Clump A* and *Clump B* are unstable and could be collapsing.

For the sake of completeness, we calculate the eventual infall rate estimated from Klaassen & Wilson (2007)

$$\dot{M}_{\rm inf} = \frac{4}{3}\pi\ n_{H2}\ \mu m_H\ r^2_{\rm clump}\ {\rm v_{inf}}\,, \qquad (13)$$

where $n_{\rm H2}$ is the H_2 volume density, $r_{\rm clump}$ is the linear radius of the infall region, and $\rm v_{inf}$ is the infall velocity of the material. One way to estimate the infall velocity is considering the two layer radiative transfer model of Myers et al. (1996). From the ^{12}CO(2-1) and C^{18}O(2-1) spectra corresponding to *Clump A* in Figure 3, we calculated $\rm v_{inf} = 0.53$ km s^{-1} using equation (9) in Myers et al. (1996). In order to get a better estimate, we also calculated the infall velocity using the Hill5 model (De Vries & Myers 2005) in the PySpecKit package (Ginsburg & Mirocha 2011)[12]. The Hill5 model employs an excitation temperature profile increasing linearly toward the center, rather than the two-slab model of Myers et al. (1996), so the Hill5 model is thought to provide a better fit to infall motions (De Vries & Myers 2005). From this model we obtained $\rm v_{inf} = 1.53 \pm 0.26$ km s^{-1}. Considering this value of $\rm v_{inf}$ = and the parameters listed in Table 3, we obtained $\dot{M}_{\rm inf} \approx 7.47{\times}10^{-4}\ M_\odot$ yr^{-1}. This result is consistent with those derived from surveys of massive YSOs such as Klaassen & Wilson (2007). *Clump B* does not show clear observational evidences of collapse.

A typical outflow appears as spatially confined wings beyond the emission from the cloud core. For EGO 3 and EGO 4, we can distinguish the presence of ^{12}CO(2-1) blue wings from ≈ –60 to –50 km s^{-1}, shown in the spectra fit in Figure 10, while the velocity range of the optically thin C^{18}O(2-1) emission is ≈ –47 to –40 km s^{-1}. The dashed line marks the systemic velocity of the clumps, which coincides with the central velocity of the C^{18}O(2-1) line. Red wings cannot be identified, although multiple components in the ^{12}CO(2-1) emission are present.

The typical signature of outflows can be seen in the position-velocity diagram. As shown in Figure 11 for EGO 4, the extension of the emission toward velocities of about –55 km s^{-1}would correspond to the blue wings shown in Figure 10. Note that the declination of this extension and the right ascension of the map coincide with the position of EGO 4.

These characteristics suggest that, although they are not spatially resolved, there may be outflows associated with EGO 3 and EGO 4.

7. SUMMARY

Based on ^{12}CO(2-1), ^{13}CO(2-1), and C^{18}O(2-1) images obtained using the APEX telescope and high density molecular tracers from the MALT90 survey such as HCO$^+$(1-0), HNC(1-0) and N_2H^+(1-0) we investigate the molecular component of the IRDC SDC 341.232-0.268. The ^{13}CO(2-1) and C^{18}O(2-1) along with MALT90 data reveal two molecular clumps (*Clump A* and *Clump B*) linked to SDC 341.232-0.268 with systemic velocities of −44.0 km s^{-1}, indicating a kinematical distance of 3.6±0.5 kpc. Four EGOs (EGO 1 at RA,Dec = 16:52:30.3, −44:28:40.0; EGO 2 at RA,Dec = 16:52:32.2, −44:28:38.0; EGO 3 at RA,Dec = 16:52:34.2, −44:28:36.0 and EGO 4 at RA,Dec = 16:52:37.3, −44:28:09.9) coincide with the molecular clumps. We calculate masses of 2400±960 and 1200±480 $M_\odot$, for *Clump A* and *Clump B*, respectively, and H_2 ambient densities >10^4 cm^{-3}. Ambient densities estimated using the N_2H^+(1-0) line are higher (≈ 10^5 cm^{-3}) and agree with the critical

[12] https://pyspeckit.readthedocs.io/en/latest/hill5infall_model.html

density of this molecule, which would be tracing the densest part of the clumps.

Both *Clump A* and *Clump B* are detected in the FIR (Herschel images) at $\lambda > 160\,\mu$m. In the NIR and MIR, at $\lambda < 160\,\mu$m (24 and 70 μm), three out of four EGOs seem to be resolved mainly at 24 μm. Molecular masses derived from the emission at 870 μm are roughly in agreement with those calculated from the molecular lines.

Spectral energy distributions (SEDs) for *Clump A* and *Clump B* built using fluxes in the FIR indicate dust temperatures of 13.5 K, typical for an IRDC.

Our search for additional signs of star formation indicates that some of the EGOs coincides with young stellar objects classified as Class I detected as point sources in the Spitzer and WISE catalogs.

Additionally, the ^{12}CO(2-1) spectra toward EGO 3 and EGO 4 present a double-peak structure with the blue-shifted peak brighter than the red-shifted one, and with the maximum in the ^{13}CO(2-1) and C^{18}O(2-1) spectra coincident with the absorption dip, which reveals the existence of infall material. This fact together with the values obtained from $M_{\rm vir}/M(H_2)$ ratio derived for the clumps reveal that they would be collapsing. Blue extended wings in the C^{18}O(2-1) spectra are also present toward these EGOs, suggesting the presence of outflows.

This project was partially financed by CONICET of Argentina under projects PIP 00356, and PIP 00107 and from UNLP, projects PPID092, PPID/G002, and 11/G139. M.R. wishes to acknowledge support from CONICYT (CHILE) through FONDECYT grant No1140839. VF acknowledges support from CONICYT Astronomy Program-2015 Research Fellow GEMINI-CONICYT (32RF0002). VF also acknowledges support from the Faculty of the European Space Astronomy Centre (ESAC), and would like to thank Ivan Valtchanov, Bruno Altieri, and Luca Conversi for their support and valuable assistance in *Herschel* data processing. We thank the referee for the careful reading of the manuscript and constructive comments which greatly improved this presentation. This work is based [in part] on observations made with the Spitzer Space Telescope, which was operated by the Jet Propulsion Laboratory, California Institute of Technology under a contract with NASA.

REFERENCES

Allen, C. W. 1973, Astrophysical quantities, (London: UK: University of London, Athlone Press)
Battersby, C., Bally, J., Jackson, J. M., et al. 2010, ApJ, 721, 222
Benjamin, R. A., Churchwell, E., Babler, B. L., et al. 2003, PASP, 115, 953
Bergin, E. A. & Tafalla, M. 2007, ARA&A, 45, 339
Beuther, H., Schilke, P., Gueth, F., et al. 2002, A&A, 387, 931
Brand, J. & Blitz, L. 1993, A&A, 275, 67
Breen, S. L., Ellingsen, S. P., Contreras, Y., et al. 2013, MNRAS, 435, 524
Bronfman, L., Nyman, L. A., & May, J. 1996, A&ASS, 115, 81
Burton, M., Walsh, A., & Balasubramanyam, R. 2002, ASPC, 267, 355
Cappa, C. E., Duronea, N., Firpo, V., et al. 2016, A&A, 585, A30
Carey, S. J., Noriega-Crespo, A., Price, S. D., et al. 2005, AAS, 207, 6333
Caselli, P., Myers, P. C., & Thaddeus, P. 1995, ApJ, 455, L77
Caswell, J. L., Fuller, G. A., Green, J. A., et al. 2010, MNRAS, 404, 1029
Chambers, E. T., Jackson, J. M., Rathborne, J. M., & Simon, R. 2009, ApJS, 181, 360
Chen, X., Ellingsen, S. P., Shen, Z.-Q., Titmarsh, A., & Gan, C.-G. 2011, ApJS, 196, 9
Chen, X., Gan, C.-G., Ellingsen, S. P., et al. 2013, ApJS, 206, 22
Chen, X., Shen, Z.-Q., Li, J.-J., Xu, Y., & He, J.-H. 2010, ApJ, 710, 150
Contreras, Y., Schuller, F., Urquhart, J. S., et al. 2013, A&A, 549, A45
Cyganowski, C. J., Whitney, B. A., Holden, E., et al. 2008, AJ, 136, 2391
De Vries, C. H. & Myers, P. C. 2005, ApJ, 620, 800
Deharveng, L., Zavagno, A., Anderson, L. D., et al. 2012, A&A, 546, A74
Dickman, R. L. 1978, ApJS, 37, 407
Ellingsen, S. P. 2006, ApJ, 638, 241
Foster, J. B., Jackson, J. M., Barnes, P. J., et al. 2011, ApJS, 197, 25
Foster, J. B., Rathborne, J. M., Sanhueza, P., et al. 2013, PASA, 30, 38
Fuller, G. A., Williams, S. J., & Sridharan, T. K. 2005, A&A, 442, 949
Ginsburg, A. & Mirocha, J. 2011, PySpecKit: Python Spectroscopic Toolkit
Griffin, M. J., Abergel, A., Abreu, A., et al. 2010, A&A, 518, L3
Guzmán, A. E., Sanhueza, P., Contreras, Y., et al. 2015, ApJ, 815, 130
Hou, L. G. & Han, J. L. 2014, A&A, 569, A125
Jackson, J. M., Chambers, E. T., Rathborne, J. M., Simon, R., & Zhang, Q. 2008, ASPC, 387, 44
Jackson, J. M., Rathborne, J. M., Foster, J. B., et al. 2013, PASA, 30, 057
Klaassen, P. D. & Wilson, C. D. 2007, ApJ, 663, 1092

Ladd, N., Purcell, C., Wong, T., & Robertson, S. 2005, PASA, 22, 62
MacLaren, I., Richardson, K. M., & Wolfendale, A. W. 1988, ApJ, 333, 821
Mardones, D., Myers, P. C., Tafalla, M., et al. 1997, ApJ, 489, 719
Molinari, S., Swinyard, B., Bally, J., et al. 2010, PASP, 122, 314
Myers, P. C., Mardones, D., Tafalla, M., Williams, J. P., & Wilner, D. J. 1996, ApJ, 465, L133
Offner, S. S. R., Robitaille, T. P., Hansen, C. E., McKee, C. F., & Klein, R. I. 2012, ApJ, 753, 98
Ohishi, M., Irvine, W. M., & Kaifu, N. 1992, IAUS, 150, 171
Ossenkopf, V. & Henning, T. 1994, A&A, 291, 943
Ott, S. 2010, ASPC, 434, 139
Peretto, N. & Fuller, G. A. 2009, A&A, 505, 405
Poglitsch, A., Waelkens, C., Geis, N., et al. 2010, A&A, 518, L2
Purcell, C. R., Longmore, S. N., Burton, M. G., et al. 2009, MNRAS, 394, 323
Purcell, C. R., Longmore, S. N., Walsh, A. J., et al. 2012, MNRAS, 426, 1972
Rathborne, J. M., Jackson, J. M., & Simon, R. 2006, ApJ, 641, 389
Rathborne, J. M., Jackson, J. M., Zhang, Q., & Simon, R. 2008, ApJ, 689, 1141
Rathborne, J. M., Simon, R., & Jackson, J. M. 2007, ApJ, 662, 1082
Rathborne, J. M., Whitaker, J. S., Jackson, J. M., et al. 2016, PASA, 33, 030
Rawlings, J. M. C., Redman, M. P., Keto, E., & Williams, D. A. 2004, MNRAS, 351, 1054
Ren, J. Z., Liu, T., Wu, Y., & Li, L. 2011, MNRAS, 415, L49
Robitaille, T. P. 2008, ASPC, 387, 290
Robitaille, T. P., Whitney, B. A., Indebetouw, R., & Wood, K. 2007, ApJS, 169, 328
Rohlfs, K. & Wilson, T. L. 2004, Tools of radio astronomy (Berlin: Springer)
Sanhueza, P., Garay, G., Bronfman, L., et al. 2010, ApJ, 715, 18
Sanhueza, P., Jackson, J. M., Foster, J. B., et al. 2012, ApJ, 756, 60
Schuller, F., Menten, K. M., Contreras, Y., et al. 2009, A&A, 504, 415
Scoville, N. Z., Sargent, A. I., Sanders, D. B., et al. 1986, ApJ, 303, 416
Sobolev, A. M., Ostrovskii, A. B., Kirsanova, M. S., et al. 2005, IAUS, 227, 174
Vassilev, V., Meledin, D., Lapkin, I., et al. 2008, A&A, 490, 1157
Wang, J., Zhang, Q., Pillai, T., Wyrowski, F., & Wu, Y. 2008, ApJ, 672, 33
Wright, E. L., Eisenhardt, P. R. M., Mainzer, A. K., et al. 2010, AJ, 140, 1868
Yang, W., Xu, Y., Chen, X., et al. 2017, ApJS, 231, 20
Zhang, Q., Sridharan, T. K., Hunter, T. R., et al. 2007, A&A, 470, 269
Zhou, S. 1992, ApJ, 394, 204

C. E. Cappa: Facultad de Ciencias Astronómicas y Geofísicas, Universidad Nacional de la Plata, Paseo del Bosque s/n, 1900, La Plata, Argentina (ccappa@fcaglp.unlp.edu.ar).
N. U. Duronea and M. M. Vazzano: Instituto Argentino de Radioastronomía, CONICET, CCT La Plata, C.C.5, 1894, Villa Elisa, Argentina (duronea@iar.unlp.edu.ar, mvazzano@iar.unlp.edu.ar).
V. Firpo: Gemini Observatory, Southern Operations Center, C/o AURA, Casilla 603, La Serena, Chile (vero.firpo@gmail.com).
V. Firpo: Departamento de Astronomía, Universidad de Chile, Casilla 36, Santiago de Chile, Chile (vero.firpo@gmail.com).
C. H. López Caraballo: Departamento de Matemáticas, Universidad de La Serena, Av. Juan Cisternas 1200, La Serena, Chile (lopezcaraballoch@gmail.com).
M. Rubio: Departamento de Astronomía, Universidad de Chile, Casilla 36, Santiago de Chile, Chile (mrubio@das.uchile.cl).

Revista Mexicana de Astronomía y Astrofísica, **55**, 305–319 (2019)

DOI: https://doi.org/10.22201/ia.01851101p.2019.55.02.16

SEARCHING FOR MID-RANGE PLANAR ORBITS TO OBSERVE DEIMOS

M. P. O. Cavalca[1], A. F. B. A. Prado[1], V. M. Gomes[2], and D. M. Sanchez[1]

Received March 7 2019; accepted July 23 2019

ABSTRACT

In this paper we search for mid-range planar orbits for a spacecraft traveling in the neighborhood of Deimos. The first task is to perform a numerical search to find and classify mid-range natural orbits around Deimos that are dominated by Mars, using the idea of "Quasi Satellite Orbits" (QSO). The influence of the eccentricity of the orbit of Deimos around Mars and the irregular shape of Mars are considered in the mathematical model, allowing an assessment of their importance. Our approach uses two different initial positions for Deimos in its orbit around Mars, at apoapsis and periapsis. The minimum, maximum, and average Deimos-spacecraft distances are also obtained.

RESUMEN

En este trabajo se localizan las órbitas planas medias para un vehículo espacial que viaja en la cercanía de Deimos. Se realiza un análisis numérico para encontrar y clasificar las órbitas medias naturales alrededor de Deimos que están dominadas por Marte, mediante el uso del concepto de las órbitas quasi-satelitales (QSO). El modelo numérico considera la influencia de la excentricidad de la órbita de Deimos en torno a Marte, así como la forma irregular de Marte, lo que nos permite evaluar su importancia. Nuestro enfoque considera dos posiciones iniciales distintas para Deimos en su órbita en torno a Marte, en apoápside y periápside. También se calculan las distancias máximas, mínimas y promedio entre Deimos y el vehículo espacial.

Key Words: planets and satellites: individual (Deimos)

1. INTRODUCTION

Mars has already been the final destination and target of observation of several missions and the interest for this planet has been growing. Among the many missions planned for the red planet, some have the exploration or observation of its moons, Phobos and Deimos, as important stages of the mission. Studying these moons remains interesting today, as there are many speculations about their origin. Among some assumptions, it is possible that they may have been formed by the agglomeration of parts of an old body that collapsed, or that they were formed by the ejection of material from Mars. They could also be captured primitive bodies, such as comets or asteroids. In this case they may contain information about the formation of the Solar System (Oberst et al. 2014). The problem in planning missions to these moons is that they have masses much smaller than Mars. This feature makes the spheres of influence (Araujo et al. 2008) of both moons to be just above or even below their surfaces (Gil & Schwartz, 2010), making it very difficult to keep a spacecraft in orbit. Alternative and appropriate forms for a spacecraft to orbit these moons were studied (Wiesel 1993) without the use of auxiliary thrusters, because this technique would lead to an increase in cost with a consequent decrease in the duration of the mission. Among the possible alternatives, there are some types of natural orbits that can be found in systems with major mass differences between the bodies. These types of orbits can be found using the circular and elliptical cases of the restricted three-body problem and using the small gravitational interaction of the moon to keep the spacecraft close to it, as if it were actually orbiting the body. In any case Mars dominates the motion of the spacecraft. They are called "Quasi-Satellite

[1]National Institute for Space Research - INPE, São José dos Campos, Brazil.
[2]São Paulo State University - UNESP/FEG, Guaratinguetá, Brazil.

Orbits" (QSO) (Benest 1976; Kogan 1989, 1990; Lidov & Vashkov'yak 1993, 1994; Mikkola et al. 2006; Gil & Schwartz 2010). Their use has been considered for future missions to the moons of Mars. Some examples of these types of missions are: Phobos and Deimos and Mars Environment (PADME) (NASA, 2018), DePhine - Deimos and Phobos Interior Explorer (Wiesel 1993) and Martian Moons Explorer (MMX) mission (Campagnola et al. 2018). There are also cases where the spacecraft can be placed at large distances from the moon and in retrograde motion, which are the so called "Distant Retrograde Orbits" (DRO) (Lam & Whiffen 2005; Villac & Aiello 2005; Whiffen 2003). Quasi-periodic orbits located further away can also be found around other bodies of the Solar System, like Mercury, as shown in Ma & Li, (2013). In the Solar System it is also possible to find different types of orbits around moons, as can be seen in Carvalho et al. (2012), Gomes & Domingos, (2016), Santos et al. (2017) and Cinelli et al. (2019). Phobos, the largest and closest moon of the Martian system, has been the main objective of many studies (Gil & Schwartz 2010). The main goal of the present paper is to show some differences and also peculiarities of orbits around Deimos, the smallest and most distant moon of Mars. The average radius of Deimos is 6.2 km (JPL/NASA, 2019a) and its distance from Mars is 23,458 km (JPL/NASA, 2019b). It is highly non-spherical and very much like Type I and II asteroids, which are composed of rocks rich in carbonaceous material. The eccentricity of the orbit of Deimos is small.

To study how to observe Deimos using QSO-type orbits, a numerical search will be performed and the orbits will be selected according to the measured values of the maximum, minimum and average distances between the spacecraft and Deimos over a certain time. In that sense, maps of those quantities will be obtained to help to find adequate orbits.

The purpose of these measurements is to offer ranges of options (not just stand-alone orbits) for a mission to Deimos. In particular, it is desired to find mid-range orbits to place a spacecraft when it arrives in the system. Those orbits are very adequate to make the first measurements of Deimos before a closer orbit is selected. An orbit that causes the spacecraft to oscillate between distances from 40 to 200 km from the center of Deimos is considered to follow this criterion. This is a study similar to the one for Phobos in Cavalca et al. (2018). The goal is to complete the study of orbits to observe both moons of Mars. It is interesting for a mission to have some variations in the distance between the spacecraft and Deimos, because in this way it is possible to observe the moon from different locations. It is also important not to go too close to the moon, to avoid a risk of collision, while going too far from the moon increases the risk that the spacecraft will escape from the vicinity of Deimos. In that sense, mid-range orbits are adequate, because they allow the spacecraft to approach Deimos at a distance as short as possible, without the risk of crashing. In particular, Deimos has a very irregular shape and these types of orbits are also interesting because they are located at a safe distance from collision, and they are not much affected by the shape of Deimos. The idea is to use these mid-range orbits to make the first scientific observations of Deimos, to measure its gravitational field with more accuracy and to better analyze its surface. After these preliminary analyses the aim is to prepare a final approach to Deimos placing the spacecraft in lower orbits, or even landing on its surface. Some related examples can be found in Zamaro & Biggs, (2016), Akim et al. (2009) and Tuchin (2008).

To describe the motion of the spacecraft around Deimos and Mars, the restricted planar elliptic three-body problem (Szebehely 1967; Domingos et al. 2008) added to the acceleration due to the non-spherical shape of Mars, represented by the term J_2 (Sanchez et al. 2009) is used. In this model, Mars is called the primary body, because it has the largest mass of the system. Deimos is called the secondary body. Finally, the spacecraft is assumed to have a negligible mass. The primary and secondary bodies, Mars and Deimos, rotate in elliptical orbits around their common center of mass. The spacecraft travels around these bodies without influencing them. In addition to the gravitational force, we will also consider the effects of the non-spherical form of Mars, by adding the J_2 term of its gravitational potential. The non-spherical shape of Deimos is not included in the model because it has only very small effects at the distances considered in the present paper. Another objective of this paper is to measure the individual contribution of each force included in the mathematical model of the final trajectories. This is done by measuring the effect of each force during the integration time. This type of study was made for the gravity field of the Earth in Sanchez, Prado & Yokoyama (2014), and adapted for the Mars-Phobos system in Cavalca et al. (2018). The present paper will study different possibilities for the mathematical model to show the relevance of certain parameters in the search for mid-range trajectories around Deimos.

The results will be shown in color maps where it is possible to identify the maximum, minimum and average distances spacecraft-Deimos as a function of the initial conditions of the spacecraft with respect to Deimos. From these results the mission designer can select the most appropriate orbits according to the goals of the mission. It is also possible to identify regions and families of orbits with certain characteristics. The influence of the position of Deimos with respect to Mars in the trajectories will also be studied. In this case, two opposing positions will be considered: periapsis and apoapsis.

The present paper has the following objectives:(i) to find and classify orbits to observe Deimos, which can keep a spacecraft in mid-range distances from Deimos over a given time; (ii) to measure the importance of the eccentricity of the orbit of Deimos, even if small, in the orbits found; (iii) to investigate the contribution of each force that acts in the dynamics of the system, and so to be able to measure which ones are the most relevant; (iv) to analyze the effects of the initial position of Deimos with respect to Mars in the trajectories of the spacecraft.

2. MATHEMATICAL MODEL

Next, the mathematical model, the parameters and other data used and calculated during the simulations are presented, as well as the forces that influence the dynamics of the system, and the criteria to select and classify the orbits. The main idea is to build general maps that can show different possibilities of orbits. Thus, these maps can serve as catalogs, to be used according to the mission requirements, contributing to the choice of the best parameters to accomplish a mission. First, the initial conditions of the spacecraft relative to Deimos are chosen, that is, the initial distance between the spacecraft and Deimos and the initial components of the velocity $v_{\rm x}$ and $v_{\rm y}$ of the spacecraft. Then, the trajectory is numerically integrated over the given time. Next, the distances spacecraft-Deimos during the whole period of the natural trajectory are calculated. Then the averages, minimum and maximum distances reached by the spacecraft from Deimos are shown. Each type of orbit can be used for a certain stage of a mission. The results show that the average distances follow the same behavior of the maximum distances, while the minimum distances present small variations.

Equations 1 and 2 are the equations of motion of the spacecraft according to the model adopted. The first two terms of the equations refer to the restricted elliptic three-body problem, where m_1, m_2 and m_3 are, respectively, the masses of Mars, Deimos and the spacecraft. Mars and Deimos, called M_1 and M_2, rotate in elliptical orbits around their center of mass. The spacecraft, called M_3, travels around these bodies and in the same plane, but without influencing the motion of M_1 and M_2. The third terms of the right side of the equations refer to the acceleration due to the non-spherical shape of Mars, represented by the term J_2 of its gravity field (Sanchez et al. 2009).

$$\ddot{x} = -Gm_1\left(\frac{x-x_1}{r_1^3}\right) - Gm_2\left(\frac{x-x_2}{r_2^3}\right) - Gm_1J_2r_{M1}^2\left(\frac{3x}{2r_1^5}\right), \quad (1)$$

$$\ddot{y} = -Gm_1\left(\frac{y-y_1}{r_1^3}\right) - Gm_2\left(\frac{y-y_2}{r_2^3}\right) - Gm_1J_2r_{M1}^2\left(\frac{3y}{2r_1^5}\right), \quad (2)$$

where the universal gravitational constant is indicated by G; r_1 is the distance from the spacecraft to M_1 (Mars); r_2 is the distance from the spacecraft to M_2 (Deimos); the radius of Mars is r_{M_1}; and the position of the spacecraft is indicated by x, y.

Then, the process to obtain the desired orbits starts by choosing the values of the initial conditions, position and velocity, and the total integration time of each orbit. During the integration the average, maximum and minimum distances spacecraft-Deimos are calculated. This is repeated for each orbit. Finally, the distances are classified and used to build maps. Equation 3 shows the calculation of the average distance spacecraft-Deimos ($r_{\rm avg}$) (Prado 2015), where r_2 is the distance between the spacecraft and Deimos and the total integration time is given by T.

$$r_{\rm avg} = \frac{1}{T}\int_0^T r_2\,(t)\,dt. \quad (3)$$

Next, the algorithm used to search for the natural orbits around Deimos is described. At first, Mars and Deimos are assumed to be fixed on the x-axis in the fixed reference system. A spacecraft is placed in this same system and aligned in the x-axis, at a given distance from Deimos. Since all orbits intersect the x-axis at some point, conducting a search restricted to this line is enough to map all the orbits around Deimos. Figure 1 shows, in the inertial system, Mars, Deimos and the spacecraft, as well as the initial conditions (position and velocity), which

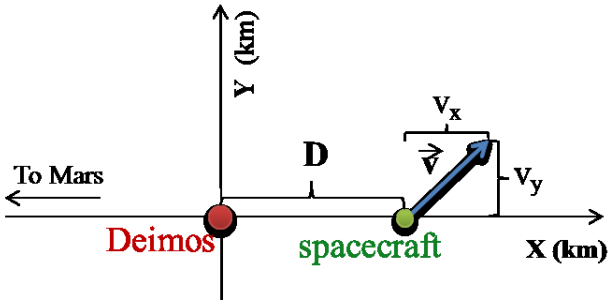

Fig. 1. Illustration of the problem showing the Mars-Deimos system and the initial conditions that define each orbit: the initial distance between Deimos and the spacecraft on the x-axis is indicated by D; and the components of the initial velocity of the spacecraft are indicated by $v_{\rm x}$ and $v_{\rm y}$. The color figure can be viewed online.

identify each orbit: D, the initial distance between the spacecraft and Deimos; and $v_{\rm x}$ and $v_{\rm y}$, the components of the initial velocity of the spacecraft.

Based on Figure 1, it is possible to calculate the complete set of initial conditions of the spacecraft and then to make the numerical integrations of the equations of motion over the given time. During the numerical integrations the possibility of collisions of the spacecraft with Deimos is tested. The averages, minimum and maximum distances between the spacecraft and Deimos are calculated for each trajectory. These results are presented in the form of maps that will assist the mission designer in selecting the most appropriate orbits for each stage of the mission. The classification of those orbits shows orbits that are close to Deimos, but that respect some given limit to avoid collisions and escapes. On the other hand, it is possible to identify orbits that stay at longer distances from Deimos, including some that leave the neighborhood of Deimos. This type of orbit can be used to naturally transfer the spacecraft from an orbit closer to Deimos to an orbit around Mars located far from Deimos. Depending on the purpose of the mission, near or distant orbits can be selected as ideal. To have a better view of the trajectories, they will be plotted in the fixed and rotating system.

The study of the contribution of each force that acts in the system, which is made by integrating each force along the time, is presented. It follows Prado (2013), who studied the perturbation suffered by a spacecraft by the gravity fields of the Sun and the Moon. (For different systems and situations see also Prado 2014; Sanchez & Prado 2017; Sanchez, Howell & Prado 2016; Short et al. 2016; Santos et al. 2015; Oliveira et al. 2014; Oliveira & Prado 2014; Carvalho et al. 2014). Four types of integrals can be used to identify different aspects of the problem. These integrals are given by:

1.
$$\frac{1}{T}\int_0^T |\mathbf{a}|\, dt. \tag{4}$$

2.
$$\frac{1}{T}\int_0^T a_v dt, \tag{5}$$
$$\text{where } a_v =< \mathbf{a}, \hat{\mathbf{v}} > \text{ and } \hat{\mathbf{v}} = \frac{\mathbf{v}}{|\mathbf{v}|}.$$

3.
$$\left(p_x^2 + p_y^2 + p_z^2\right)^{\frac{1}{2}}, \tag{6}$$
$$\text{where } p_k = \frac{1}{T}\int_0^T a_k dt, \text{with } k = x, y, z.$$

4.
$$\left(p_x^2 + p_y^2 + p_z^2\right)^{\frac{1}{2}}, \tag{7}$$
$$\text{where } p_k = \frac{1}{T}\int_0^T A_k dt, \text{with } k = x, y, z.$$

Here, $\mathbf{a}$ indicates the acceleration due to the force under study; $\mathbf{v}$ the velocity of the spacecraft; A_k the difference between the total acceleration and the Keplerian term of the acceleration, considering the same set of initial conditions and time; and T the final time of integration of the trajectory. The bold letters indicate vectors. The trajectory can be calculated for any desired time and the greater the time the greater the value of the integral. To exemplify, we can choose two trajectories close to Deimos, with only one of them colliding with Deimos. Analyzing only the value of the integral we could conclude that the trajectory that does not collide would be more disturbed than the other, because the integration time was smaller. In order to avoid this error, the value of the integral is multiplied by the normalization factor $1/T$. Using this technique it is possible to compare trajectories with different durations.

For this work, the first type of integral is used, which consists in measuring the total acceleration suffered by the spacecraft. The second type of integral measures the variation of energy of the spacecraft due to each force. If it is negative, the force removes energy from the spacecraft. Otherwise, when it is positive, energy is added to the spacecraft. The third type of integral is calculated for each component of the acceleration. It also considers compensation for negative and positive effects. The fourth type of integral measures the difference between the

TABLE 1

PHYSICAL AND ORBITAL PARAMETERS OF MARS AND DEIMOS

Celestial Body	Average radius (km)	GM (km^3/s^2)	J_2	Semi-major axis (km)	Eccentricity
Mars	3396.19	42828.0	0.00195	–	–
Deimos	6.2	9.85×10^{-5}	–	23458	0.0002

accelerations of a Keplerian orbit and a disturbed orbit having the same initial conditions. Studies that use the first and second type of integral in the construction of perturbation maps, whose objective is to identify regions of low perturbations, can be found in Sanchez, Howell & Prado, (2016).

3. RESULTS

In this section, the results of the simulations are presented, considering several sets of initial conditions. Initially, a 30-day integration time is considered for the orbit, like in Gil & Schwartz, (2010) and Cavalca et al. (2018), to keep the same values used in the literature in order to compare the results. Longer times will be tested later. Table 1 shows the orbital and physical parameters of Mars and Deimos found in the JPL HORIZONS System[3].

Combining the possible values of the initial conditions of the spacecraft relative to Deimos (D and the components of the velocity v_x and v_y), many figures can be drawn. The figures are presented in the form of color maps, showing the minimum, maximum and average spacecraft-Deimos distances. The regions indicating collisions of the spacecraft with Deimos are shown in white. Using those maps it is possible to identify the regions of interest and, if necessary, to make a more detailed search using smaller steps for the variables to find more accurate initial conditions. Some of the trajectories are also plotted to analyze their behavior.

Initially, the simulations consider the most complete model, where Mars has a non-spherical shape and Deimos is in an eccentric orbit. Afterwards, a new simulation is performed considering the same set of initial conditions, but with Mars having a spherical shape and Deimos in a circular orbit. In this way it is possible to analyze the influence of each force on the trajectory of the spacecraft and to compare the results with a more realistic model. The study of the integrals of the accelerations present in the dynamics is also made, to quantify the contribution of each force acting in the trajectory of the spacecraft.

[3]https://ssd.jpl.nasa.gov/?horizons

Figures 2 and 3 show the maximum (D_{max}), minimum (D_{min}) and average (D_{avg}) distances between the spacecraft and Deimos. The distances are presented as a function of the initial distance D (km) on the horizontal axis and the velocity v_x (km/s) on the vertical axis. The orbits begin at the moment when Deimos is at periapsis. The choices of these parameters are made after preliminary simulations varying all the parameters of the initial conditions and then selecting the most interesting ones. For the initial velocity v_y it was observed that a fixed value of -0.003 km/s generated orbits that were at short and mid-range distances from Deimos. For the initial distance, the range D from 40 to 50 km showed to be adequate, as was a range of values for v_x from -0.003 to 0.003 km/s. There were 35,760 trajectories that survive for up to 30 days and 24,340 trajectories not surviving that long, making a total of 60,100 trajectories. Each orbit is identified by a point on the graph that gives a specific value of D (horizontal axis) and v_x (vertical axes). Using this technique, it is possible to show the distances spacecraft-Deimos to select the orbits of interest. The values of D_{max}, shown in Figure 2(a), range from 80.24 to 22,330.45 km. The values of D_{min}, Figure 2(b), go from 16.00 to 45.43 km. The values of D_{avg}, Figure 2(c), go from 61.66 to 10,553.13 km. From the figures it is possible to identify that the trajectories that remain closer to the moon are located in the central part of the plot, where the lowest values of D_{max} (Figure 2a), below 200 km, are located. This corresponds to 22.55% of the total number of solutions (the solutions that end in collisions divided by the number of solutions that survive for 30 days). The lowest values of D_{avg} (Figure 2c), below 100 km, correspond to 22.33% of the total solutions. It is also observed that there is a correspondence in the dispersion of the orbits, for both the closer and the distant ones. There is also symmetry with respect to the y axis for v_x equal to zero. However, the minimum distance values, Figure 2c, behave almost inversely when compared to the maximum and average values. The highest values of D_{min}, between 40.00 and 45.46 km, are located in the same region where D_{max} and D_{avg} have the

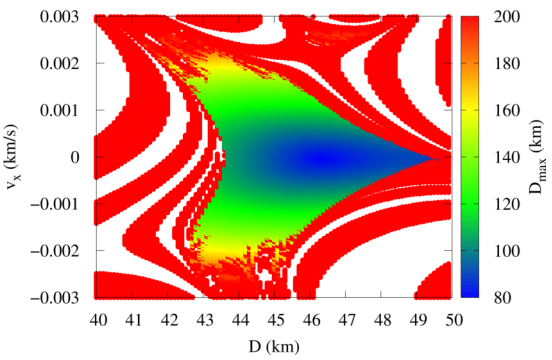

(a) Maximum distances spacecraft-Deimos.

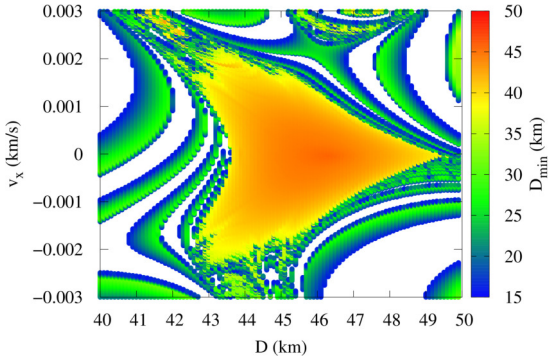

(b) Minimum distances spacecraft-Deimos.

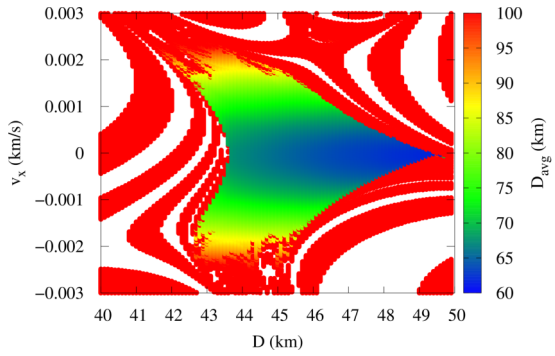

(c) Average distances spacecraft-Deimos.

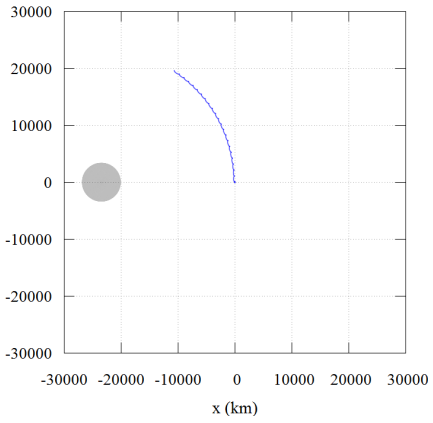

(d) Trajectory of the spacecraft for T = 30 days, $D_{\max} = 22,330.4563$ km, $D_{\min} = 16.3177$ km, $D_{\text{avg}} = 10,499.3097$ km.

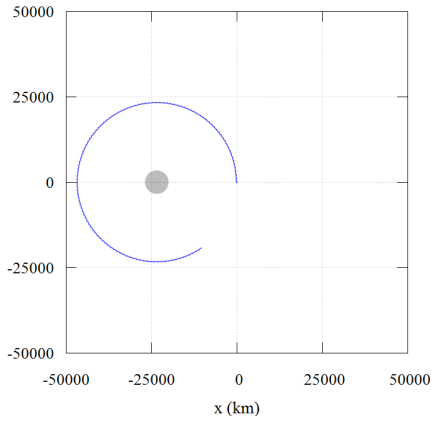

(e) Trajectory of the spacecraft for T = 150 days, $D_{\max} = 46914.6094$ km, $D_{\min} = 16.3177$ km, $D_{\text{avg}} = 32705.8703$ km.

Fig. 2. Maximum, minimum and average spacecraft-Deimos distances, in km, as a function of D (km) and v_{x} (km/s), considering v_{y} = -0.003 km/s and that Deimos is at the periapsis of its orbit around Mars. Parts (d) and (e) show the trajectory with maximum $D_{\max}$. The color figure can be viewed online.

lowest values. These trajectories are close to Deimos, but at safe distances from it, to avoid risks of collision. These trajectories are excellent options to place a spacecraft. The lowest values of $D_{\min}$, which are between 16.00 and 20.00 km, can be found, in most cases, at the limits between the areas of high values of $D_{\max}$ (over 200 km) and $D_{\min}$ (over 100 km) and areas that indicate a collision, the blank areas. This indicates that these regions are not good options for the spacecraft: they take the spacecraft far away from the moon, but can, sometimes, pass very close and even collide with Deimos. Figures 2(d) and 2(e) show the trajectory with maximum $D_{\max}$. The initial conditions are: $D = 49.9$ km, $v_{\text{x}} = 0.0012$ km/s,

TABLE 2

THE FIVE ORBITS WITH SMALLEST $D_{\max}$ (km) AROUND DEIMOS[1]

D (km)	v_x (km/s)	D_{avg} (km)	D_{min} (km)	D_{max} (km)	D^*_{avg} (km)	D^*_{min} (km)	D^*_{max} (km)	$D_{avg} - D^*_{avg}$ (km)	$D_{min} - D^*_{min}$ (km)	$D_{max} - D^*_{max}$ (km)
46.4	0	64.0228	45.3666	80.2416	61.6881	42.8124	85.1829	2.3347	2.5542	−4.9413
46.3	0	64.1237	45.4357	80.2701	61.7661	42.9782	84.6516	2.3576	2.4575	−4.3815
46.4	−0.00001	64.0212	45.3513	80.3273	61.6866	42.8118	85.1780	2.3346	2.5395	−4.8507
46.4	0.0001	64.0258	45.3519	80.3292	61.6914	42.8115	85.1919	2.3344	2.5404	−4.8627
46.3	0.00001	64.1268	45.4206	80.3681	61.7693	42.9774	84.7016	2.3575	2.4432	−4.3335

[1]Assuming v_y = -0.003 km/s, Deimos initially at periapsis, $e = 0.0002$, $J_2 = 1960.45\times10^{-6}$, $T = 30$ days. Corresponding results for the circular and spherical model are represented by an asterisk ($*$).

TABLE 3

THE FIVE ORBITS WITH SMALLEST $D_{\max}$ (km) AROUND DEIMOS*

D (km)	v_x (km/s)	D_{avg} (km)	D_{min} (km)	D_{max} (km)	$D^{\#}_{avg}$ (km)	$D^{\#}_{min}$ (km)	$D^{\#}_{max}$ (km)	$D_{avg} - D^{\#}_{avg}$ (km)	$D_{min} - D^{\#}_{min}$ (km)	$D_{max} - D^{\#}_{max}$ (km)
45.1	0	62.8565	45.0877	78.4059	65.5536	44.2349	91.7359	−2.6971	0.8528	−13.3300
45.2	0	62.7707	45.0094	78.4426	65.4260	44.3376	90.6978	−2.6553	0.6719	−12.2552
45.1	0.00001	62.8581	45.0678	78.5177	65.5567	44.2349	91.6955	−2.6986	0.8329	−13.1778
45.1	−0.00001	62.8565	45.0678	78.5178	65.5519	44.2349	91.7801	−2.6954	0.8329	−13.2623
45.2	0.00001	62.7722	44.9944	78.5269	65.4291	44.3370	90.7108	−2.6569	0.6574	−12.1838

*Assuming $v_y = -0.003$ km/s, circular orbit for Deimos and spherical shapes for the bodies and $T = 30$ days. Corresponding results for the elliptical and flat body models are represented by $D^{\#}{}_{\max}$. Deimos is assumed to be initially at periapsis.

$v_y = -0.003$ km/s and two simulation times were used: 30 and 150 days. They show clearly that the spacecraft goes away from Deimos and enters an orbit around Mars that is co-orbital with Deimos. Figures 3(a), 3(b) and 3(c) show results corresponding to Figures 2(a), 2(b) and 2(c), but now the model does not consider the effects of the flattening of Mars. The main difference is the reduction of the central blue region, which means that the maximum distances increase in this region. It happens for maximum and average distances. Therefore, the flattening of Mars helps to keep the orbits closer to Deimos in this region.

Table 2 shows the values of the maximum, minimum and average distances for the five closest orbits to Deimos, that is, those with lowest values of $D_{\max}$. Note that the trajectories keep the spacecraft in the distance range 80.24-80.36 km from Deimos over 30 days, without the need of orbital maneuvers. This means that they are good options to place the vehicle. The values corresponding to the model where Deimos is in a circular orbit and Mars has spherical shape are also presented, indicated by an asterisk ($*$). Analyzing the differences between the values of the most complete and the simplest model, one can see the importance of considering a more realistic model. Note that, when considering spherical bodies and circular orbit for the moon, the errors are of the order of 4.33 to 4.94 km for the maximum distances; 2.44 to 2.55 km for the minimum distances and 2.33 to 2.35 km for the mean distances, over a period of 30 days. Note also that, when considering the simpler model, the values of maximum distances are overestimated. This is shown by the negative values of the last column of Table 2. The values of the mean and minimum distances are underestimated, as shown by the positive values in Columns 9 and 10 of Table 2. Figure 4 shows the trajectories with both models obtained with the data given by the first line of Table 2. The trajectories for the other lines of the table are very similar and they are omitted here. The left side considers the best model (elliptical orbit for Deimos and a flat body for Mars) and the right side the simplified model (circular orbit for Deimos and a spherical body for Mars). Note that the best model gives a near periodic orbit, while the simple model gives an orbit with some oscillations in the spacecraft-Deimos distance.

Table 3 shows the comparison between the simplified and the more complete model, over 30 days.

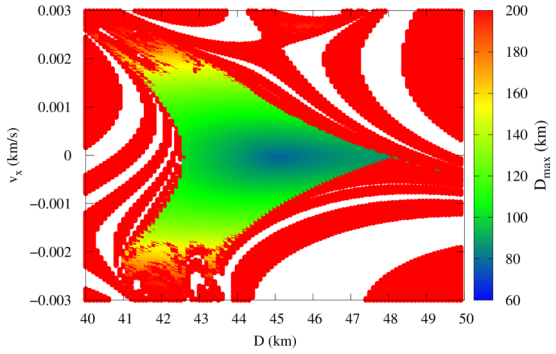

(a) Maximum distances spacecraft-Deimos neglecting the flattening of Mars.

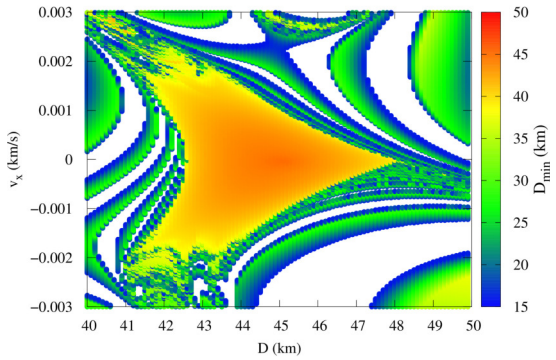

(b) Minimum distances spacecraft-Deimos neglecting the flattening of Mars.

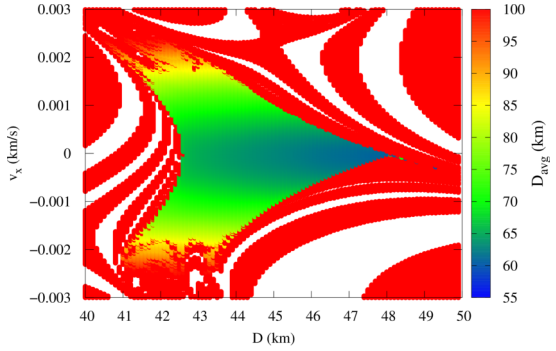

(c) Average distances spacecraft-Deimos neglecting the flattening of Mars.

Fig. 3. Maximum, minimum and average spacecraft-Deimos distances, in km, as a function of D (km) and v_x (km/s), considering v_y = -0.003 km/s. The model considers e = 0, $J_2 = 1960.45 \times 10^{-6}$, and T = 30 days. The color figure can be viewed online.

In this case, the simplified model is used as a reference. Note that the trajectories with the lowest values of maximum distances have initial conditions different from those of Table 2, where the reference case used the most complete model. The lowest maximum distance for the complete model shown in Table 2 occurs for D = 46.40 km and v_x = 0 km/s, and the value is D_{max} = 80.24 km. The lowest maximum distance obtained when considering the model simulated in Table 3 occurs for D = 45.10 km and v_x = 0.00 km/s, and it is D_{max} = 78.40 km. Considering this last set of initial conditions for the most complete model, we have a maximum distance of 91.73 km. In Table 3, the five closest trajectories are presented considering v_y = −0.003 km/s, a circular orbit for Deimos and a spherical shape for the bodies. The simulation time is equal to 30 days. The corresponding results considering the most complete model are indicated by $D^{\#}{}_{max}$. The values of $D_{max} - D^{\#}{}_{max}$ vary from −12.18 to −13.33 km, that is, they are all negative, which shows that the values of D_{max} are underestimated for the orbits near Deimos. This important fact should be noted.

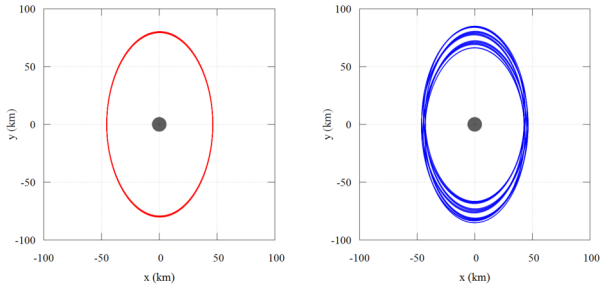

(a) Model considering an elliptical orbit for Deimos and a flat body for Mars.

(b) Model considering a circular orbit for Deimos and a spherical body for Mars.

Fig. 4. Trajectories associated with the first line of Table 2 in the rotating frame. The color figure can be viewed online.

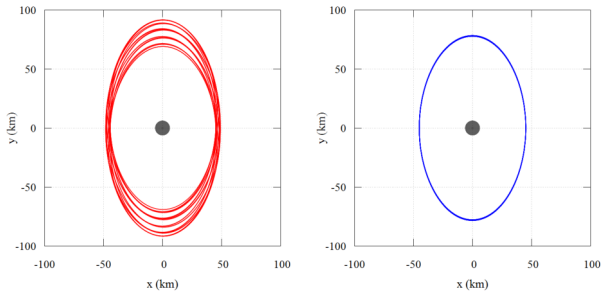

(a) Model considering an elliptical orbit for Deimos and a flat body for Mars.

(b) Model considering a circular orbit for Deimos and a spherical body for Mars.

Fig. 5. Trajectories associated with the first line of Table 3 in the rotating frame. The color figure can be viewed online.

Next, Figure 5 shows the trajectories with both models, obtained with the data of the first line of Table 3. The trajectories for the other lines of the

TABLE 4

TEMPORAL EVOLUTION OF A SINGLE ORBIT WHIT DEIMOS AT PERIAPSIS*

T (days)	5	15	30	60	90
$D_{\max}$ (km)	80.2362	80.2416	80.2416	80.2416	80.2416
$D_{\min}$ (km)	45.3702	45.3703	45.3667	45.3639	45.3639
D_{avg} (km)	64.1184	64.1287	64.0227	64.0606	64.0811
PertDeimos 10^{-8} (km/s^2)	2.41	2.41	2.41	2.41	2.41
PertMars 10^{-5} (km/s^2)	7.01	7.00	7.00	7.00	7.00
PertJ2Mars 10^{-9} (km/s^2)	4.32	4.32	4.32	4.32	4.32

*$D = 46.4$ km, $v_x = 0$, $v_y = -0.003$ km/s, considering $e = 0.0002$ and $J_2 = 1960.45 \times 10^{-6}$ for the simulation times: 5, 15, 30, 60, and 90 days.

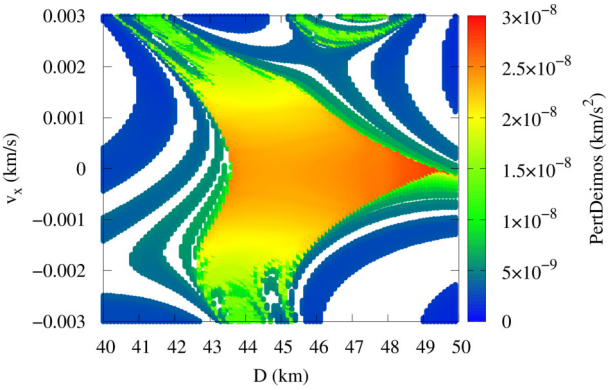

Fig. 6. Perturbation due to Deimos in km/s^2 as a function of D (km) and v_x (km/s). The color figure can be viewed online.

table are very similar and they are omitted here. The left side considers the best model (elliptical orbit for Deimos and a flat body for Mars) and the right side the simplified model (circular orbit for Deimos and a spherical body for Mars). Note that the simple model gives a near periodic orbit, while the best model gives an orbit with some oscillations in the spacecraft-Deimos distance.

To show the influence of each force on the dynamics of the system, the integral tests will be carried out (Prado 2013). These tests are performed integrating the individual acceleration of each force for the total time of the trajectory, and then dividing it by the total integration time. In Sanchez, Prado & Yokoyama, (2014) a similar study was made for another system. Dividing the total result by the integration time, we obtain the average effect of each force acting during the whole trajectory. Using this information it is possible to identify the importance of each force.

Figure 6 shows the contribution due to Deimos, in km/s^2, using the same initial conditions of Figure 2. The effect due to the gravity of Deimos (PertDeimos) varies from 1.38×10^{-9} to 2.88×10^{-8} km/s^2. The highest values are located near $v_x = 0$, including the same area where the trajectories closer to Deimos are located (with the smallest values of $D_{\max}$ and D_{avg}), which is the best region to select orbits. With a similar analysis for the other forces, it is possible to find the contribution of the gravitational field of Mars, which is approximately 7.07×10^{-5} km/s^2, at least three orders of magnitude stronger than the effect of Deimos. This measurement confirms that these types of orbits are dominated by the gravitational field of Mars, while Deimos is only a perturbation. This is an interesting result, because it quantifies the effect expected by the QSOs, where the larger mass dominates the dynamics of the system. The contribution of the term J_2 due to the gravitational potential of Mars is of the order of 4.30×10^{-9}, which is four times smaller than its equivalent in the Keplerian term of the gravity field of Mars. It is also one order of magnitude smaller then the effect of Deimos, which means that its effect needs to be included in the dynamical model. Finally, through this study, it is possible to quantify and estimate the forces that influence the motion of the spacecraft.

The next step is to verify the behavior of those orbits over longer times. Table 4 shows the distance (km) and the disturbance level (km/s^2) for simulation times of 5, 15, 30, 60, and 90 days. It is clear that some QSOs can "survive" for longer periods of time. The model considered has an elliptical orbit for Deimos and a flat Mars, so $e = 0.0002$

TABLE 5

THE FIVE ORBITS WITH SMALLEST $D_{\max}$ (km) AROUND DEIMOS[1]

D (km)	v_x (km/s)	D_{avg} (km)	D_{min} (km)	D_{max} (km)	D^*_{avg} (km)	D^*_{min} (km)	D^*_{max} (km)	$D_{avg}-D^*_{avg}$ (km)	$D_{min}-D^*_{min}$ (km)	$D_{max}-D^*_{max}$ (km)
43.8	0	61.1860	43.7992	75.9347	63.8417	43.8000	89.1615	−2.6557	−0.0008	−13.2269
43.8	−0.00001	61.1852	43.7469	76.2244	63.8406	43.7997	89.1683	−2.6554	−0.0527	−12.9439
43.8	0.00001	61.1883	43.7472	76.2267	63.8440	43.8001	89.1563	−2.6558	−0.0529	−12.9297
43.8	−0.00002	61.1860	43.6957	76.5163	63.8408	43.7996	89.1749	−2.6548	−0.1039	−12.6587
43.8	0.00002	61.1920	43.6923	76.5198	63.8477	43.7996	89.1558	−2.6556	−0.1073	−12.63606

[1]Assuming $v_y = -0.003$ km/s, Deimos initially at its apoapsis, $e = 0.0002$, $J_2 = 1960.45 \times 10^{-6}$, $T = 30$ days. Corresponding results for the circular and spherical model are represented by an asterisk (∗).

and $J_2 = 1960.45 \times 10^{-6}$, and Deimos at periapsis when the motion starts. The initial conditions of the trajectory are: $D = 46.4$ km, $v_x = 0$ and $v_y = -0.003$ km/s. The values of distances and perturbations remained stable during the time simulated. Remember that each individual result of the integrals of the accelerations is divided by the total integration time, to obtain a normalized number.

The trajectory indicated in Table 4 is shown in Figures 7 and 8, over 5, 15, 30, 60, and 90 days. The trajectory is shown in the fixed and rotating system. Deimos is plotted to scale and fixed in the origin of both coordinate systems. The trajectory illustrates very well the stability of the numbers related to it, as shown in Table 4. Note that when integrating for longer times the spacecraft completes more revolutions, but all of them have the same pattern.

Now, we study this problem considering the initial position of Deimos at apoapsis. The results are shown in Figure 9 and Table 5. In Figure 9 the same set of initial conditions used to make Figures 2 and 3 is considered: the initial vertical component of the velocity v_y is fixed in −0.003 km/s, the initial distance D ranges from 40 to 50 km and the horizontal component of the initial velocity ranges from −0.003 to 0.003 km/s. The maximum, minimum and average spacecraft-Deimos distances have a behavior similar to the one observed when Deimos is at periapsis. The lower values of D_{avg} (Figure 9c), below 100 km, follow the smaller values of D_{max} (Figure 9a), below 200 km, while the values of D_{min} behave in an opposite way. However, the results with the lowest D_{max} (Figure 9a) and D_{avg} (Figure 9c) are shifted to the left with respect to Figures 2(a) and 2(c). This means that the initial position of Deimos influences the trajectories. For Figure 9, the lowest values of D_{max} correspond to 31.03% of the total solutions, and the lowest values of D_{avg} correspond to 17.52% of the total solutions. Comparing

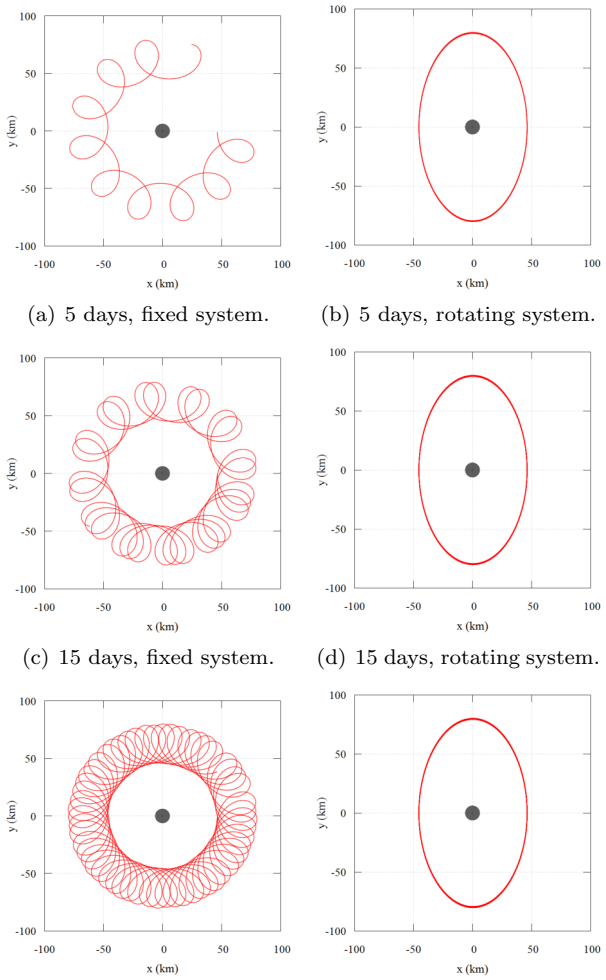

(a) 5 days, fixed system. (b) 5 days, rotating system.

(c) 15 days, fixed system. (d) 15 days, rotating system.

(e) 30 days, fixed system. (f) 30 days, rotating system.

Fig. 7. Time evolution of trajectories obtained using Deimos at periapsis, $D = 46.4$ km, $v_x = 0$, $v_y = -0.003$ km/s, considering $e = 0.0002$, $J_2 = 1960.45 \times 10^{-6}$ for the simulation times 5, 15 and 30. The color figure can be viewed online.

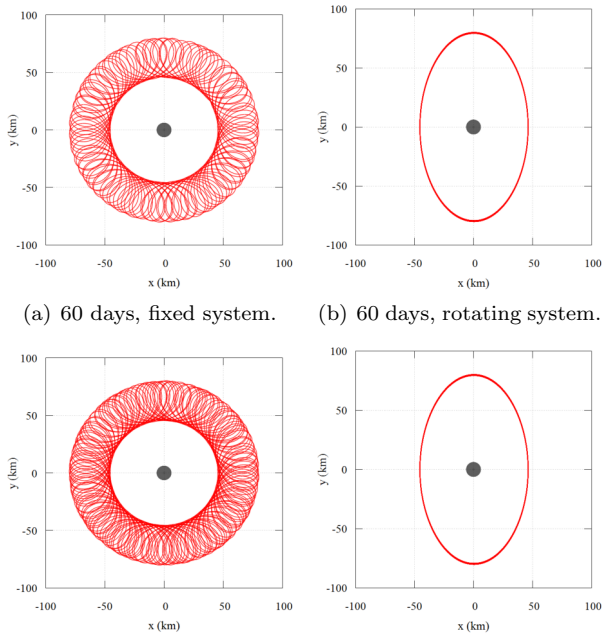

(a) 60 days, fixed system. (b) 60 days, rotating system.

(c) 90 days, fixed system. (d) 90 days, rotating system.

Fig. 8. Time evolution of trajectories obtained using Deimos at periapsis $D = 46.4$ km, $v_x = 0$, $v_y = -0.003$ km/s, considering $e = 0.0002$, $J_2 = 1960.45 \times 10^{-6}$ for the simulation times 60 and 90 days. The color figure can be viewed online.

the lowest values of D_{max} and D_{avg} with those found when Deimos is at periapsis, 22.55% and 22.33%, respectively, there is an increase of 8.48% for D_{max} and a decrease of 4.81% for D_{avg} when Deimos is initially at apoapsis. The D_{max} values, Figure 9(a), range from 75.93 to 23,534.69 km, that is, a range of values larger than the one found when Deimos is at periapsis, 80.24 to 22,330.45 km. The trajectory for the $D_{max} = 22{,}330.45$ km is similar to the one shown in Figure 2, and the spacecraft goes away from Deimos to enter an orbit around Mars that is co-orbital with Deimos. The values of D_{min}, Figure 9(b), range from 16.00 to 43.79, that is, a range of values larger than the one found when Deimos at periapsis, 16.00 to 45.43 km. The D_{avg} values, Figure 9(c), range from 57.63 to 11,173.67 km, that is, a range of values larger than when Deimos is at periapsis, from 61.66 to 10,553.13 km. The values of D_{max} and D_{avg} are the most influenced by the position of Deimos, presenting smaller minimum values and larger maximum values when Deimos is at apoapsis. Figures 9(d), 9(e) and 9(f) show the results corresponding to Figures 9(a), 9(b) and 9(c), but now the model does not consider the effects of the flattening of Mars. The main difference is a slight reduction of the central blue region, which means that the maximum distances increase in this region. This happens for the maximum and average distances.

Table 5 shows the five trajectories with the smallest values of D_{max}, obtained with Deimos at apoapsis. The initial conditions have the values $D = 43.8$ km, $v_x = 0, \pm 0.001$ or 0.002 km/s and values of the maximum distances in the interval 75.90 to 76.50 km. In Table 2, Deimos is initially at periapsis, and the initial conditions were $D = 46.30$ or 46.40 km, $v_x = 0.000$ or ± 0.001 km/s and values of maximum distances in the interval from 80.20 to 80.30 km. Comparing the values shown in Tables 5 and 2, it is clear that the values of the initial distance D and the maximum distances are smaller when the moon is at apoapsis than when it is at periapsis.

Table 5 also shows that, when considering the simplest model (with circular orbits and a spherical shape for Mars) the differences for the minimum distance are between zero and 0.1 km; for the average distance they are around 2.65 km and for the maximum distance between 12.6 and 13.2 km, for an integration time of 30 days. The negative values of the last column of Table 5 imply that, when considering the simplest model, we overestimate D_{max}. Comparing these results with those of Table 2, (for the periapsis case) it is observed that the values of the last column are of the order of 4 to 5 km, also negative, therefore smaller in magnitude than those presented in Table 5. This means that, when considering the simpler model in the apoapsis case, the values of the maximum distances are overestimated, as occurred in the periapsis case, but the errors are now about three times larger.

Figure 10 shows the trajectories with both models obtained with the data given by the first line of Table 5. The trajectories for the other lines of the table are very similar and they are omitted here. The left side considers the best model (elliptical orbit for Deimos and a flat body for Mars) and the right side the simplified model (circular orbit for Deimos and a spherical body for Mars). Note that the best model gives a near periodic orbit (but not periodic or quasi-periodic in terms of the known definitions), while the simple model gives an orbit with some oscillations in the spacecraft-Deimos distance.

To conclude this study, the trajectory with the lowest D_{max} from Table 5 is presented for $T = 30$ days in Figure 11. Deimos is plotted to scale and located at the origin. The values of distances (km) and disturbances (km/s^2) for the time evolution of the trajectory at times 5, 10, 15, 30, 60, and 90 days are shown in Table 6. Figures 12 and 13 show the trajectory at the times shown in Table 6. Again, it

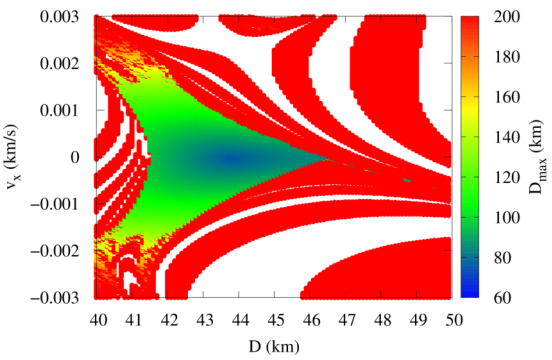

(a) Maximum distances spacecraft-Deimos.

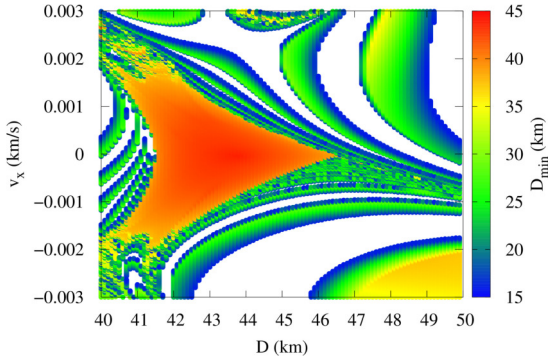

(b) Minimum distances spacecraft-Deimos.

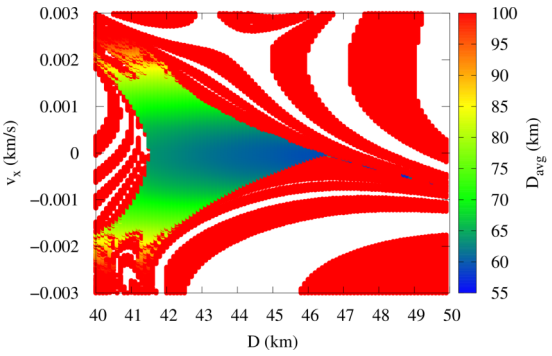

(c) Average distances spacecraft-Deimos.

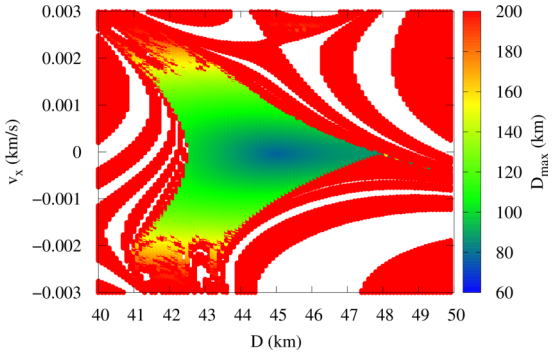

(d) Maximum distances spacecraft-Deimos neglecting the flattening of Mars.

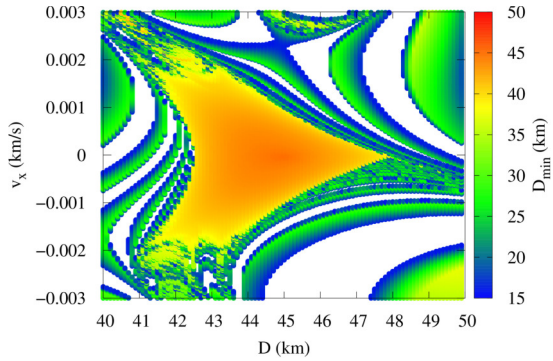

(e) Minimum distances spacecraft-Deimos neglecting the flattening of Mars.

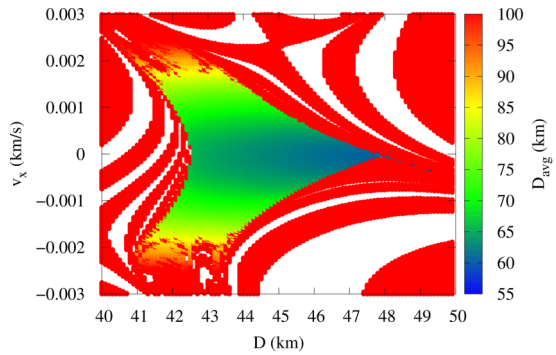

(f) Average distances spacecraft-Deimos neglecting the flattening of Mars.

Fig. 9. Maximum, minimum and average spacecraft-Deimos distances, in km, as a function of D (km) and v_x (km/s), considering $v_y = -0.003$ km/s, for orbits with Deimos initially at apoapsis. The model considers $e = 0.0002$, $J_2 = 1960.45 \times 10^{-6}$, $T = 30$ days. The color figure can be viewed online.

is seen that the trajectory is quite stable in time, as in the periapsis case. In Figures 11(a) and 11(b) the full model is used, while in Figures 11(c) and 11(d) the simplest model is considered, assuming a circular orbit for Deimos and spherical shape for Mars. It is seen that the trajectory of the most complete model shows smaller oscillations than the trajectory of the simplest model. The minimum distances are very similar, but the maximum distances are much smaller for the more complete model (75.9347 against 89.1615 km). Many more regular orbits are generated by the best model.

4. CONCLUSION

In this study a recently developed method for mapping orbits around small bodies was applied to Deimos, considering the maximum, minimum and average distances between Deimos and the space-

TABLE 6

DEIMOS AT APOAPSIS, $D = 43.8$ km, $v_x = 0$ km/s, $v_y = -0.003$ km/s*

T (days)	5	15	30	60	90
D_{max} (km)	75.9325	75.9346	75.9347	75.9347	75.9347
D_{min} (km)	43.8001	43.7999	43.7991	43.7992	43.7991
D_{avg} (km)	61.4833	61.1644	61.1860	61.2332	61.2429
PertDeimos 10^{-8} (km/s^2)	2.62	2.64	2.64	2.63	2.63
PertMars 10^{-5} (km/s^2)	7.00	7.00	7.00	7.00	7.00
PertJ2Mars 10^{-9} (km/s^2)	4.32	4.32	4.32	4.32	4.32

*An elliptical orbit for Deimos and the flattening of Mars are considered. Simulation times: 5, 15, 30, 60, and 90 days.

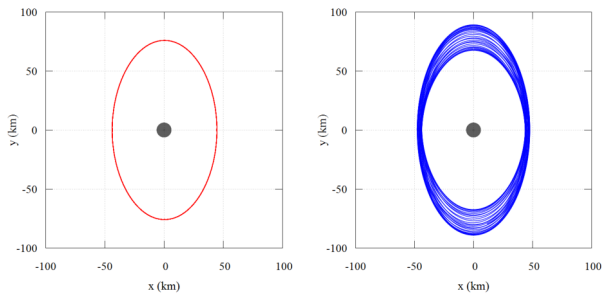

(a) Model considering an elliptical orbit for Deimos and a flat body for Mars.

(b) Model considering a circular orbit for Deimos and a spherical body for Mars.

Fig. 10. Trajectories associated with the first line of Table 5 in the rotating frame. The color figure can be viewed online.

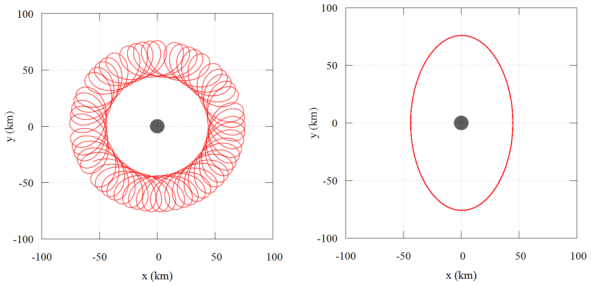

(a) 30 days, fixed system $D_{avg} = 61.1860$ km $D_{min} = 43.7991$ km $D_{max} = 75.9347$ km

(b) 30 days, rotating system PertDeimos= 2.64×10^{-8} km/s^2, PertMars= 7.00×10^{-5} km/s^2, PertJ2Mars= 4.32×10^{-9} km/s^2

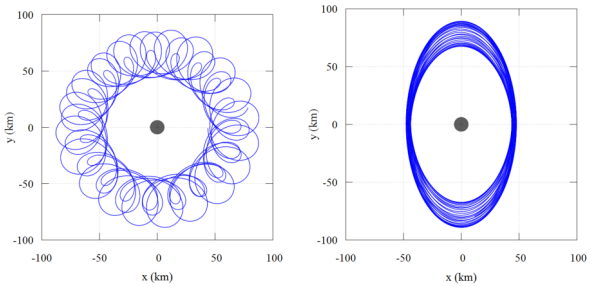

(c) 30 days, fixed system $D_{avg} = 63.8417$ km $D_{min} = 43.8000$ km $D_{max} = 89.1615$ km

(d) 30 days, rotating system PertDeimos= 2.47×10^{-8} km/s^2, PertMars= 7.00×10^{-5} km/s^2

Fig. 11. Trajectories considering an elliptical orbit for Deimos and a flat body for Mars (red), and considering a circular orbit for Deimos and a spherical shape for Mars (blue). Deimos is initially at apoapsis, $D = 43.8$ km, $v_x = 0$, $v_y = -0.003$ km/s, $T = 30$ days. The color figure can be viewed online.

craft during a given time as the main criterion to select the orbits. The trajectories were mapped and plotted according to their initial conditions (position and velocity), to identify the conditions that keep the spacecraft at mid-range distances to Deimos, and to find orbits free from risks of collision but not too far away from Deimos. The method generated several results showing its efficiency in obtaining mid-range orbits around Deimos that are affected enough by the moon to keep the spacecraft near to it, although the orbit is really dominated by Mars.

The orbits found can be used to place a spacecraft as soon as it arrives in the vicinity of Deimos, to carry out the first detailed studies of the moon without having a large risk of collision. In this way, it is not necessary to know details about the shape of Deimos in advance. After more detailed studies made from these mid-range distances, the spacecraft can be placed in orbits closer to Deimos.

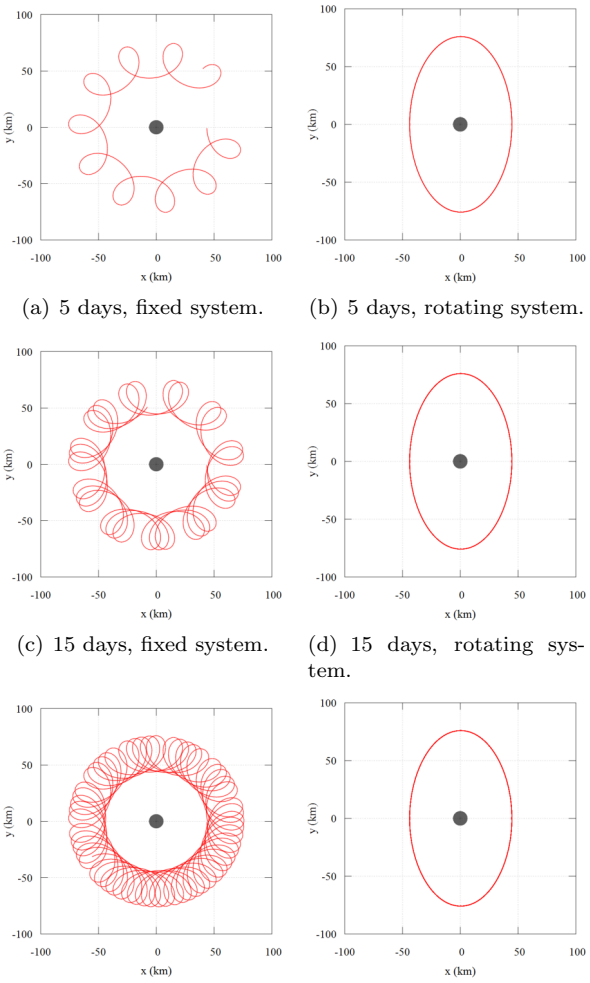

(a) 5 days, fixed system. (b) 5 days, rotating system.

(c) 15 days, fixed system. (d) 15 days, rotating system.

(e) 30 days, fixed system. (f) 30 days, rotating system.

Fig. 12. Trajectories at times 5, 10, 15, and 30 days shown in Table 6. The color figure can be viewed online.

Among the many trajectories found, those that were considered good options are the ones that have Deimos-spacecraft distances in the range of 40 to 200 km over the 30 days of simulation. Using these trajectories, it is possible to make the first detailed observations of Deimos without the risk of collision with it. It was also shown that many of these trajectories are able to survive for up to 90 days and that the orbits are very regular, keeping about the same values of distances and perturbations levels over time.

The initial position of Deimos in its orbit around Mars showed effects on the behavior of the orbit. Depending on its initial condition there are differences in the values of maximum, minimum and average spacecraft-Deimos distances when considering the moon at periapsis or apoapsis. These two positions gave good options for trajectories, but the

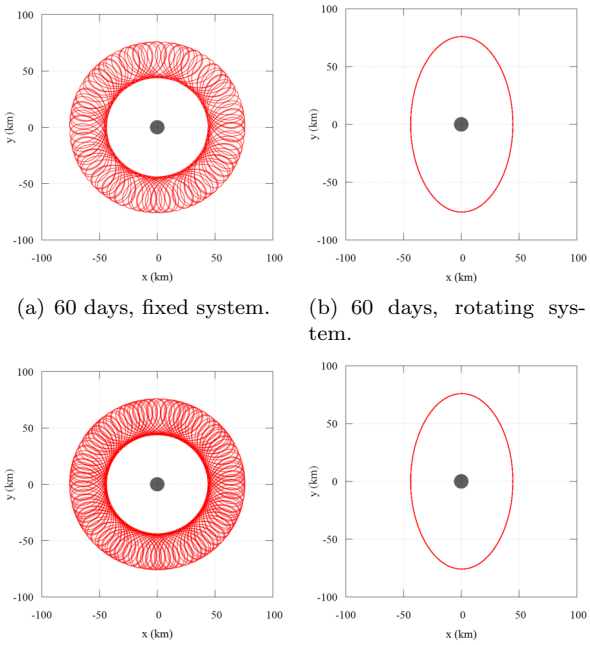

(a) 60 days, fixed system. (b) 60 days, rotating system.

(c) 90 days, fixed system. (d) 90 days, rotating system.

Fig. 13. Trajectories at times 60 and 90 days showed in Table 6. The color figure can be viewed online.

results found when Deimos is at apoapsis are better than the corresponding ones with Deimos at periapsis, because the maximum distances were smaller when at apoapsis than at periapsis.

The importance of the mathematical model adopted was also shown by comparing it with a more complete model, which considers Deimos in an elliptic orbit around Mars and the J_2 term of the gravitational potential of Mars. The simplest model considered Deimos in a circular orbit and Mars as a spherical body. It was shown that, for the two positions of Deimos, periapsis and apoapsis, if the simplest model was adopted, the values of the maximum distances were overestimated with respect to the most complete model. With Deimos at periapsis these errors are of the order of 4-5 km, while they increase to around 12-13 km for Deimos at apoapsis.

The integrals of the accelerations of each force that acts in the spacecraft over time were also studied. Using this technique, it was possible to quantitatively measure the influence of each force acting in the dynamics of the system. It was shown that the results of the contribution of the gravitational interaction of Mars are about 3 orders of magnitude larger than the effects of the gravitational field of Deimos. This proves and quantifies that Mars is the body that dominates the motion of the spacecraft, while Deimos only disturbs this motion.

The authors wish to express their appreciation for the support provided by Grants #406841/2016-0, 301338/2016-7 from the National Council for Scientific and Technological Development (CNPq); Grants #2016/24561-0 and 2014/22295-5, from São Paulo Research Foundation (FAPESP), and the financial support from the Coordination for the Improvement of Higher Education Personnel (CAPES).

REFERENCES

Akim, E. L., et al. 2009, CosRe, 47, 299, DOI: 10.1134/S0010952509040054
Araujo, R. A. N., et al. 2008, MNRAS, 391, 675, DOI: 10.1111/j.1365-2966.2008.13833.x
Benest, D. 1976, CeMec, 13, 203, DOI: 10.1007/BF01232724
Campagnola, S., et al. 2018, AcA, 146, 409, DOI: 10.1016/j.actaastro.2018.03.024
Carvalho, J. P. S., et al. 2012, AdSpR, 49, 994, DOI: 10.1016/j.asr.2011.11.036
Carvalho, J. P. S., et al. 2014, Mathem. Probl. Eng., 1(1), DOI: 10.5540/03.2013.001.01.0009
Cavalca, M. P. O., et al. 2018, RMxAA, 54, 429
Cinelli, M., et al. 2019, JGCD, 42, 123, DOI: 10.2514/1.G003652
Domingos, R. C., et al. 2008, Mathem. Problems in Eng., v. 2008, 1, DOI: 10.1155/2008/763654
Gil, P. J. S. & Schwartz, J. 2010, JGCD, 33, 901, DOI: 10.2514/1.44434
Gomes, V. M. & Domingos, R. C. 2016, Comp. Appl. Math. 35, 653, DOI: 10.1007/s40314-015-0258-8
JPL/NASA[1] 2019, "Planetary Satellite Physical Parameters", available at `https://ssd.jpl.nasa.gov/?sat_phys_par`
JPL/NASA[2] 2019, "Planets and Pluto: Physical Characteristics", available at `https://ssd.jpl.nasa.gov/?planet_phys_par\#D`
Kogan, A. I. 1989, CosRe, 26, 705
Kogan, A. I. 1990, 41st Congress of the IAF Paper, 90
Lam, T. & Whiffen, G. J. 2005, Paper AAS 05-110, 15 th AAS/AIAA Space Flight Mech. Conf. Jan., 23
Lidov, M. L. & Vashkov'yak, M. A. 1993, CosRe, 31, 75
Lidov, M. L. & Vashkov'yak, M. A. 1994, AstL, 20, 676
Ma, X. & Li, J. 2013, Ap&SS, 343, 8393, DOI: 10.1007/s10509-012-1242-z
Mikkola, S., et al. 2006, MNRAS, 369, 15, DOI: 10.1111/j.1365-2966.2006.10306.x
NASA 2018, "PADME (Phobos And Deimos and Mars Environment): A Proposed NASA Discovery Mission to Investigate the Two Moons of Mars", available at `https://ntrs.nasa.gov/search.jsp?R=20150001913`
Oberst, J., et al. 2014, P&SS, 102, 1, DOI: `https://doi.org/10.1016/j.pss.2014.05.010`
Oliveira, T. C. & Prado, A. F. B. A. 2014, AcAaU, 104, 350, DOI: 10.1016/j.actaastro.2014.06.035.
Oliveira, T. C., et al. 2014, Adv. in the Astronau. Sci., 152, 3081
Prado, A. F. B. A. 2013, Math. Problems in Eng., 2013, 1, DOI: 10.1155/2013/415015
Prado, A. F. B. A. 2014, AdSpR, 53, 877, DOI: 10.1016/j.asr.2013.12.034
Prado, A. F. B. A. 2015, ISTS, Kobe, Japan
Sanchez, D. M., et al. 2009, Mathem. Problems in Eng., 2009, 1
Sanchez, D. M., Prado, A. F. B. A., & Yokoyama, T. 2014, AdSpR, 54, 1008, DOI: 10.1016/j.asr.2014.06.003
Sanchez, D. M., Howell, K. C., & Prado, A. F. B. A. 2016, AAS/AIAA Spaceflight Mech. Meeting, NAPA, CA, February 14-18, 2016
Sanchez, D. M. & Prado, A. F. B. A. 2017, Adv. Astr. Science, 162, 1507, Proceedings of the AAS/AIAA Astro. Spec. Conf., Stevenson, WA
Santos, J. C., et al. 2015, Physics Conf. Series, 641, 012011, Oct. DOI:10.1088/1742-6596/641/1/012011
Santos, J. C., et al. 2017, Ap&SS, 362, 227, DOI: 10.1007/s10509-017-3200-2
Short, C., et al. 2016, J. Astronau. Sci., 64, DOI: 10.1007/s40295-016-0098-9
Spiridonova, S., et al. 2017, Conference: Proc. 26th Inter. Sym. Space Flight Dyn., Jun
Szebehely, V. 1967, Theory of Orbits: The Restricted Problem of Three Bodies, (New York, NY: Academic Press)
Tuchin, A. G. 2008, CosRe, 46, 506, DOI: 10.1134/S0010952508060051
Villac, B. F. & Aiello, J. J. 2005, AAS, Paper 05-188, Jan
Whiffen, G. 2003, AAS, Paper 03-354, Aug
Wiesel, G. 1993, JGCD, 16, 434, DOI: 10.2514/3.21028
Zamaro, M. & Biggs, J. D. 2016, AcAau, 119, 160, DOI: 10.1007/978-3-319-23986-6_21

M. P. O. Cavalca, A. F. B. A. Prado, and D. M. Sanchez: Instituto Nacional de Pesquisas Espaciais, Avenida dos Astronautas, 1758, Jardim da Granja, 12227-010, São José dos Campos, SP - Brasil (antonio.prado@inpe.br).
Vivian M. Gomes: Universidade Estadual Paulista Júlio de Mesquita Filho, Faculdade de Engenharia de Guaratinguetá - FEG, Av. Ariberto Pereira da Cunha, 333, Pedregulho, 12516-410, Guaratinguetá, SP - Brasil (vivianmartinsgomes@gmail.com).

Revista Mexicana de Astronomía y Astrofísica, **55**, 321–335 (2019)

DOI: https://doi.org/10.22201/ia.01851101p.2019.55.02.17

CHAOS IN GROWING BAR MODELS

Lucas Antonio Caritá[1,2,3], Irapuan Rodrigues[2], Ivânio Puerari[3], and Luiz Eduardo Camargo Aranha Schiavo[2,4]

Received December 30 2018; accepted August 3 2019

ABSTRACT

This paper aims to verify the influence of the bar, its pattern speed (Ω_b) and its rate of growth on the stability of the orbits in gravitational potentials. We studied the nature of the orbits in potentials representing galaxies with growing bars, where a linear growth was assumed. In order to study the stability of the orbits we applied SALI. We studied six models in which the bar dimensions were fixed, but we varied their pattern speed and time of bar growth. We found that when the bar growth is faster, more chaos is generated and we also noted that the higher the Ω_b, the greater its influence on the system dynamics. The initial positions of the orbits that became chaotic were located in a well-defined ring-like region, confined between the ILR and CR resonances. There was also an indication that the retrograde orbits, although much scarcer, are more conductive to chaos when they do exist.

RESUMEN

Este trabajo verifica la influencia de la barra, de su velocidad angular (Ω_b) y de su tasa de crecimiento en la estabilidad de las órbitas en potenciales gravitacionales. Estudiamos órbitas en potenciales representando galaxias con barras en crecimiento, asumiendo un crecimiento lineal. Para estudiar la estabilidad de las órbitas aplicamos SALI. Estudiamos seis modelos con dimensiones fijas de la barra, pero variamos la velocidad y el tiempo de crecimiento de la misma. Evidenciamos que cuando el crecimiento de la barra es más rápido, se genera más caos y también observamos que cuanto mayor es Ω_b, mayor será su influencia en la dinámica del sistema. Las posiciones iniciales de las órbitas que se han vuelto caóticas quedan ubicadas en una región anular bien definida, confinada entre ILR y CR. Las órbitas retrógradas, aunque mucho más escasas, parecen ser más propicias al el caos.

Key Words: chaos — galaxies: general — galaxies: kinematics and dynamics — galaxies: spiral

1. INTRODUCTION

Approximately 65% of disk galaxies show bar-like structures (Eskridge et al. 2000; Sheth et al. 2003). The characteristic of their bars varies considerably, from faint weak bars to prominent, strong and massive bars. By computational integration of stellar orbits in gravitational potential models, it is possible to study the dynamics and stability of this type of galaxy. Indeed, stellar orbits supported by a galactic potential are the basic constituents of any galactic structure. Understanding the behavior of stellar orbits is essential for understanding the formation and evolution of these structures.

In recent works, integrations of orbits in fixed-parameter bar potentials have been performed; it was concluded that for sufficiently large bar axial ratios, stable orbits having propeller shapes have a great influence on bar structure (Kaufmann & Patsis 2005). Several types of resonant orbits can shape the bar structure, besides the x_1 orbital family. Although the x_1 family is considered to be the backbone of 2D bars, in the case of 3D this family is aided by a tree of its 3D bifurcating families (Skokos

[1]Instituto Federal de Educação, Ciência e Tecnologia de São Paulo (IFSP), São José dos Campos, Brasil.
[2]Universidade do Vale do Paraíba (UNIVAP), São José dos Campos, Brasil.
[3]Instituto Nacional de Astrofísica, Óptica y Electrónica (INAOE), Puebla, México.
[4]Universidade Estadual de Campinas (UNICAMP), Campinas, Brasil.

et al. 2002b). All other bar-supporting orbits are candidates for supporting the inner parts of the bar (Gajda et al. 2016; Patsis & Katsanikas 2014). In recent studies it was verified that more massive bars have a greater tendency for chaotic orbits to occur, whereas weaker bars are less affected by chaos (Manos & Athanassoula 2011; Caritá et al. 2017).

However, it is agreed that the formation of a bar is a long and complex secular process, which may have several histories. It is also agreed that no galaxy is born barred: the bar can form, change (increase, decrease, rotate etc.) and extinguish itself with time, in processes that depend on the parameters of the galaxies that host them (Bournaud & Combes 2002). Regarding this trend, Manos & Machado (2014), Machado & Manos (2016) and Chaves-Velasquez et al. (2017) presented studies on the regular or chaotic character of orbits in time-dependent barred galaxy potentials based on an N-body simulation. They extracted parameters of bar evolution from the simulation for certain times, treating each snapshot as a time-independent model.

In Caritá et al. (2017), the SALI (Smaller Alignment Index) method was applied (Skokos 2001), to study the stability of stellar orbits in the gravitational potential of barred galaxies with fixed parameters, in which the theoretical models based on Manos & Athanassoula (2011) were used. In that work, we were exclusively interested in evaluating the influence of the bar parameters on the occurrence of chaos in the stellar orbits.

In the present paper we propose a new approach by adding some new ingredients. First of all, we study six models based on observational properties of the grand design barred galaxy NGC 936, from which we borrow the main parameters, as presented in detail in Appendix A. We also introduce analytically the growth of the bar, i.e., we set time-dependent evolving bar potentials. Moreover, we verify the influence of the pattern speed and the rate of growth of the bar on the stability of the orbits.

To perform the orbital integrations and SALI calculation, we used a slight adaptation of the LP-VIcode program (Carpintero et al. 2014), which is a fully operational code, implemented in Fortran 77, that efficiently calculates 10 different chaos indicators for dynamic systems, regardless of the number of dimensions, SALI being one of them.

2. METHODOLOGY

2.1. *The Smaller Alignment Index (SALI)*

In order to define SALI, let us consider a Hamiltonian flow of N degrees of freedom, an orbit in the $2N$dimensional phase space with initial condition $x(0) = (x_1(0), \cdots, x_{2N}(0))$ and two normalized deviation vectors $\widehat{\mathbf{w}_1}(0)$, $\widehat{\mathbf{w}_2}(0)$ from the initial condition $x(0)$.

We define

$$SALI(t) := min\{||\widehat{\mathbf{w}}_1(t) - \widehat{\mathbf{w}}_2(t)||, ||\widehat{\mathbf{w}}_1(t) + \widehat{\mathbf{w}}_2(t)||\}, \tag{1}$$

where the quantities $||\widehat{\mathbf{w}}_1(t) - \widehat{\mathbf{w}}_2(t)||$ and $||\widehat{\mathbf{w}}_1(t) + \widehat{\mathbf{w}}_2(t)||$ are called Parallel Alignment Index and Antiparallel Alignment Index, respectively.

It is evident that $SALI(t) \in [0, \sqrt{2}]$ and when $SALI = 0$ the two normalized vectors have the same direction, being equal or opposite.

The SALI value is a very useful tool for detecting chaos in Hamiltonian systems. Chaotic or regular motions are easily distinguishable applying the SALI method. In the case of chaotic orbits, the deviation vectors $\widehat{\mathbf{w}}_1(t)$ and $\widehat{\mathbf{w}}_2(t)$ align in the direction defined by the Maximum Lyapunov Exponent (MLE) and $SALI(t)$ falls exponentially to zero:

$$SALI(t) \propto e^{-(L_1 - L_2)t}, \tag{2}$$

with L_1 and L_2 the two largest Lyapunov exponents.

Furthermore, for regular motions the orbits develop on a phase space torus and eventually the vectors $\widehat{\mathbf{w}}_1(t)$ and $\widehat{\mathbf{w}}_2(t)$ fall in the torus tangent space, following a t^{-1} time dependence. In this case, SALI oscillates at nonzero values:

$$SALI(t) \approx \text{constant} > 0. \tag{3}$$

We have a clear distinction between ordered and chaotic behaviors using the SALI method in Hamiltonian systems. For mathematical SALI details, we recommend reading the papers Skokos (2001); Skokos et al. (2002a, 2003, 2004).

2.2. *Mathematical Modeling of the Gravitational Potential*

In this investigation, we used the gravitational potential divided into three basic components: bulge, disk and bar, according to the following equation:

$$\Phi_{Total} = \Phi_{Bulge} + \Phi_{Disk} + \Phi_{Bar}. \tag{4}$$

Each component of equation (4) was mathematically modeled according to a classical potential: the Plummer potential was used for the bulge (Plummer 1911), Miyamoto-Nagai's for the disk (Miyamoto & Nagai 1975) and Ferrers' for the bar (Ferrers 1877). This way of representing the total gravitational potential has been extensively used in many articles,

such as Patsis (2002); Manos & Athanassoula (2011); Skokos et al. (2002c,d); Patsis et al. (2002, 2003) and Caritá et al. (2017).

The Plummer potential is written as:

$$\Phi_{Bulge} = -\frac{GM_S}{\sqrt{x^2+y^2+z^2+\epsilon^2}}, \quad (5)$$

where ϵ is the scale-length of the bulge, M_S is its total mass, and G is the gravitational constant.

The Miyamoto-Nagai's potential is written as:

$$\Phi_{Disk} = -\frac{GM_D}{\sqrt{x^2+y^2+(A+\sqrt{z^2+B^2})^2}}, \quad (6)$$

where M_D is the total disk mass, A and B are its horizontal and vertical scale-lengths, and G is the gravitational constant.

The Ferrers' potential is written as:

$$\Phi_{Bar} = -\pi Gabc\frac{\rho_c}{3}\int_\lambda^\infty \frac{du}{\Delta(u)}(1-m^2(u))^3, \quad (7)$$

where $m^2(u) = \frac{x^2}{a^2+u} + \frac{y^2}{b^2+u} + \frac{z^2}{c^2+u}$, $\Delta^2(u) = (a^2+u)(b^2+u)(c^2+u)$, λ is the positive solution of $m^2(\lambda) = 1$ for the region outside the bar ($m \geq 1$) and $\lambda = 0$ for the region inside the bar ($m < 1$).

In this last potential, the density is given by

$$\rho_B(x,y,z) = \begin{cases} \rho_c(1-m^2)^2 & , \quad m < 1, \\ 0 & , \quad m \geq 1, \end{cases} \quad (8)$$

where the central density is $\rho_c = \frac{105}{32\pi}\frac{GM_B}{abc}$, M_B is the bar mass and $m^2 = \frac{x^2}{a^2}+\frac{y^2}{b^2}+\frac{z^2}{c^2}$, where $a > b > c > 0$ are the semi-axes of the ellipsoid which represents the bar.

In order to implement this bar model computationally, we used the analytical version given by Dr. Pfenniger, who kindly provided us with his Fortran 77 routine of the Ferrers potential. In this routine, the polynomial form of the Ferrers potential (Pfenniger 1984; Caritá et al. 2017) was used.

In the course of this work, the SALI method was applied to study stellar orbits in a gravitational potential of barred galaxies, since the motion of a test particle in a rotating 3-dimensional model of a barred galaxy is given by the Hamiltonian:

$$H(x,y,z,p_x,p_y,p_z) = \frac{1}{2}(p_x^2+p_y^2+p_z^2) + \Phi_{Total}(x,y,z) - \Omega_b(xp_y - yp_x), \quad (9)$$

where the bar rotates around the z-axis; x and y respectively are the major and minor galactic bar axes, Φ_{Total} is the total gravitational potential given by equation (4) and Ω_b is the bar pattern speed.

We emphasize that in order to follow the evolution of the orbits and that of their deviation vectors (for SALI computation), it is necessary to know the equations of motion and the variational equations linked to the Hamiltonian (9). The corresponding motion and variational equations can be checked in Manos & Machado (2014).

To study orbit stability in models with 2 degrees of freedom, in our calculations, $z = 0$ and $p_z = 0$ were adopted in the Hamiltonian shown in equation (9).

2.3. *Implementation and Computation Using the LP-VIcode*

To perform the orbital integrations and SALI calculation, the LP-VIcode (Carpintero et al. 2014) was employed, which is freely available at `http://lp-vicode.fcaglp.unlp.edu.ar/`.

LP-VIcode is an operational code in Fortran 77 that efficiently calculates 10 chaos indicators for dynamic systems, including SALI. The program reads the initial conditions for one or more orbits, integrates them (using a Bulirsch-Stoer integrator), and calculates the equations of the chosen chaos indicators. More details about the structure and operation of the LP-VIcode can be found in Carpintero et al. (2013) and Carpintero et al. (2014).

In order to integrate orbits using the program and to study their stability, the user must provide the potential expressions and the motion and variational equations. That is, there is an external routine where these equations must be written in Fortran 77 by the user.

Two actions performed in the LP-VIcode implementation and adaptation stage should be highlighted in this section: the first is the adjustments that were made in order to implement a rotating coordinate system in the code (since the general equations (of motion and variational) present in the original main program consider only a static reference frame; it is known that in order to model a rotating galactic bar it is necessary to consider a coordinate system that rotates along with the bar. To do this we inserted the pattern speed Ω_b in the motion and variational equations in the LP-VIcode main program transforming the original equations into the form which Manos & Athanassoula (2011) displayed in their text. The second important action was bar growth. As previously explained, in this work we modeled the emergence of a galactic bar. The idea was to create a system that started as a barless

galaxy and that would become a barred galaxy later on, where the bar grew over time. In order to model this evolution of the bar potential, a linear function of time was assumed for the mass of the bar in the Ferrers potential (this was done in an external routine of the LP-VIcode, the same routine where the user provides the potential and the motion and variational equations).

With these two actions we were able to use the LP- VIcode to study the dynamics of a barred galaxy, with the mass of the bar growing over time, and remaining constantly rotating around the z-axis.

3. DEVELOPMENT AND DISCUSSION

3.1. *Models and Parameters*

We studied three models X, Y and Z whose parameters are shown in Table 1. Although it is not necessary to understand the origin of these parameters for our study, the reader can find a brief description of the procedures adopted in Appendix A, where we explain that the inspiration for these parameters came from the galaxy NGC 936, and where we describe how we computed the parameters based on the works of Kent & Glaudell (1989) and Merrifield & Kuijken (1995). Each of the models was divided into two more specific models, where the rate of bar growth was varied (in one of them, the bar totally evolves with 5 turns around itself and in the other with 10 turns) generating in total six models: $X_5, X_{10}, Y_5, Y_{10}, Z_5$ and Z_{10}.

In Table 1, and all along this paper, the model system of units was defined considering the gravitational constant $G = 1$. We adopted 1 kpc for length, 10^3 km s^{-1} for velocity, 10^3 km s^{-1} kpc^{-1} for pattern speed, 1 M yr for time, and 2×10^{11} $M_\odot$ for mass. The total mass $G(M_S + M_D + M_B)$ was always equal to 1. For the energy, the unit is 10^6 km^{2}s^{-2}. The integration time was 10 000 M yr.

For all models (X, Y and Z) the masses of the bulge, disk and bar components, as well as their other parameters do not change. Therefore, the difference between these three models is basically the galactic bar pattern speed; Model X has a slower Ω_b, model Y is intermediate and model Z has a faster Ω_b.

The formation of a bar is a secular process that can have several histories. Bars can form, change (increase, decrease, rotate etc.) and extinguish themselves with time, in processes that depend on the parameters of the galaxies that host such bars Bournaud & Combes (2002). No analytical studies on gravitational bar potentials that evolve over time are known. In some recent works, such as like Manos & Machado (2014), Machado & Manos (2016) and Chaves-Velasquez et al. (2017), the authors wrote about the barred galaxy stability using time-dependent potentials. However, these studies were based on N-body simulations of barred galaxies by extracting parameters of the simulation for certain times in the system evolution, and treating each snapshot as a time-independent model.

Therefore, our intention is to carry out a study where the gravitational potential that represents the bar evolves over time in an analytical way. The idea is that our system starts as a barless galaxy and becomes a barred galaxy, whose bar grows over time.

We began the integrations with totally axisymmetric potentials, without bar, and over time we transformed these potentials into non-axisymmetric ones, with a bar.

Let us recall that the effective potential is given by $\Phi_{eff}(\mathbf{x}) = \Phi(\mathbf{x}) - \frac{1}{2}|\Omega \times \mathbf{x}|^2$ and the Lagrange points are five points where $\bigtriangledown\Phi_{eff} = 0$. Writing the potential like this, we have a rotating system representation. The quantity $E_J = \frac{1}{2}|\mathbf{v}|^2 + \Phi_{eff}$ is called the Jacobi energy and is conserved in the rotating system (for more details see Binney & Tremaine 2008). Figure 1 shows the initial effective potentials and the final effective potentials for Models X, Y, and Z, where the emergence of the bar can be clearly seen.

In order to perform this bar evolution (shown in Figure 1), it was decided to implement a linear time-dependent function of the mass of the bar in the Ferrers potential. In this process, two specific cases were created for each model: the evolution is completed in a time corresponding to 5 or 10 complete turns of the bar around itself. With this approach, we created the $X_5, X_{10}, Y_5, Y_{10}, Z_5$ and Z_{10} notations. The bar evolution time for each model obviously depends on the pattern speed of the bar Ω_b and on the length of the bar. These times were calculated to serve as parameters of the growth function of the bar and are displayed in Table 2.

The Jacobi energy $E_J = \frac{1}{2}|\mathbf{v}|^2 + \Phi_{eff}(\mathbf{x})$ is conserved in a rotating potential system representative of a fixed bar. However, this energy is not conserved during the evolution. While the mass of the bar is growing linearly, the E_J value of any particle also decreases linearly, and it is conserved again as soon as the bar growth finishes and the system bears a fixed bar (after evolution). To exemplify this statement, a random orbit was used, with an initially circular motion, integrated in Model X_5. The integration

TABLE 1

PARAMETER SETS

	M_S	ϵ_S	M_D	A	B	M_B	a	b	c	Ω_b
Model X	0.1273	0.45	0.7406	4.7	0.4	0.1321	4.0	1.1	0.4	0.05
Model Y	0.1273	0.45	0.7406	4.7	0.4	0.1321	4.0	1.1	0.4	0.06
Model Z	0.1273	0.45	0.7406	4.7	0.4	0.1321	4.0	1.1	0.4	0.07

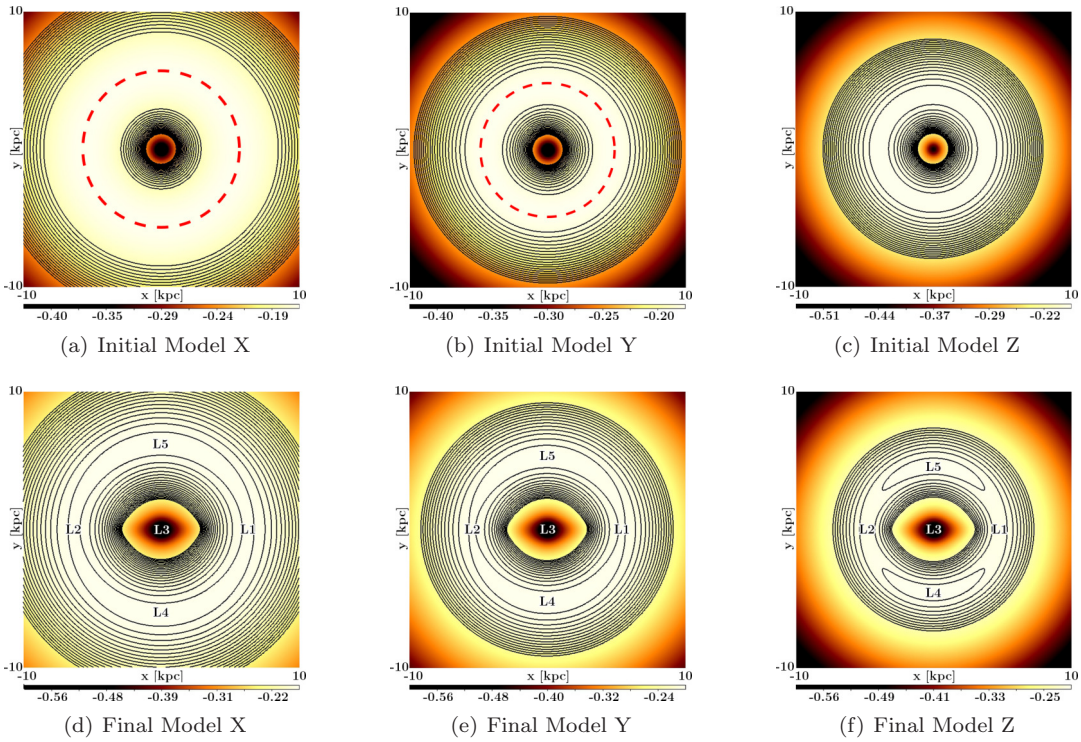

(a) Initial Model X (b) Initial Model Y (c) Initial Model Z

(d) Final Model X (e) Final Model Y (f) Final Model Z

Fig. 1. Effective potential contours of Models X, Y and Z. The top three images illustrate the initial effective potential contours, when the models did not yet have a bar, so the potential is axisymmetric. The three bottom images illustrate the final effective potential, when the bar is fully grown. Although there is no bar formed yet in the models of the first row, the effective potential, in a coordinate system that rotates with the pattern speed of the forthcoming bar, defines a radius of corrotation which is displayed in red. All images in the bottom row display the $L1 - L5$ Lagrange points. Twenty contours between energies -0.25 and -0.18 are displayed for each model. The color figure can be viewed online.

TABLE 2

TIME FOR BAR EVOLUTION IN EACH MODEL

Model	Time (Myr)
X_5	614.35
X_{10}	1228.70
Y_5	511.96
Y_{10}	1023.92
Z_5	438.82
Z_{10}	877.65

begins without the bar, the bar structure starts to emerge and its mass increases linearly until the time 614.35 Myr (as shown in Table 2). After this evolution, the system has a fixed bar until the end of the integration at 10,000 Myr. This whole process is displayed in Figure 2.

3.2. *Initial Conditions*

Galactic bars behave like rigid bodies, that is, Ω_b is always constant. However, galactic disks do not behave this way, their pattern speed Ω is a function of the radial coordinate. Thus, it is natural to imagine that resonances will appear between the bar and disk. An example is the corrotation resonance (CR), which occurs where $\Omega = \Omega_b$.

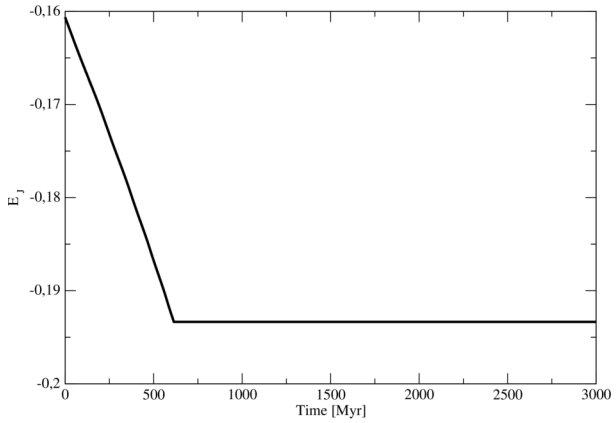

Fig. 2. This image displays the E_J behavior for a random orbit as the bar grows in Model X_5. It can be observed that E_J is not conserved during bar growth, but it is conserved after the bar has evolved. Notice that the evolution time is completely in agreement with that shown in Table 2 for Model X_5 (614.35 Myr). The integrations were made up to 10,000 Myr, and for this illustration we plot the time until 3,000 Myr. The E_J behavior for this orbit is not unique: for all integrated orbits this energy decrease occurs during the time of bar evolution.

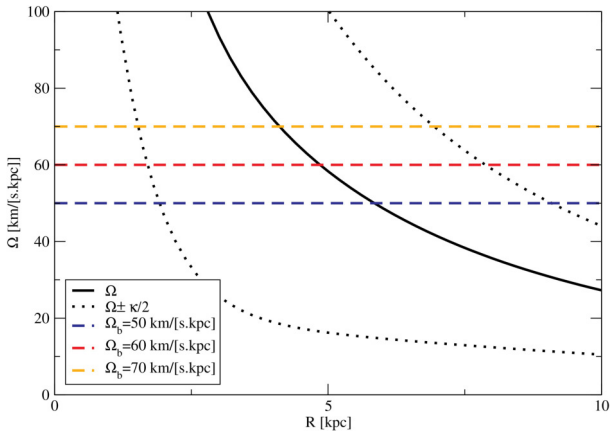

Fig. 3. Ω, $\Omega + \frac{1}{2}\kappa$ and $\Omega - \frac{1}{2}\kappa$ curves for Models X, Y e Z and the corresponding CR, ILR and OLR resonances. The color figure can be viewed online.

There will also be resonances when the following condition is satisfied:

$$\Omega = \Omega_b \pm \frac{\kappa}{m}, \tag{10}$$

where m is an integer related to the symmetry of the structure in which we are interested (m-armed spiral structures, bars etc.), and $\kappa^2 = \frac{d^2\Phi}{dR^2} + \frac{3}{R}\frac{d\Phi}{dR}$ is the epicyclic frequency. In this case, there will be two resonances, the Lindblad resonances. In Equation (10), for the negative sign, there is the Inner Lindblad Resonance (ILR); for the positive sign, the Outer Lindblad Resonance (OLR). For a galactic bar potential we have $m = 2$ because of the bisymmetric structure. Figure 3 displays the curves Ω, $\Omega + \frac{1}{2}\kappa$ and $\Omega - \frac{1}{2}\kappa$ for Models X, Y and Z.

As the galactic bar is expected to always be contained in the CR radius, its influence does not exceed the OLR radius. Therefore, we only consider orbits with initial positions inside the OLR radius. For this study, we launched particles in initially circular orbits, distributed randomly from the center up to the OLR resonance, with 10,000 prograde orbits and 10,000 retrograde orbits for each model, starting from the positions shown in Figure 4. By prograde and retrograde orbits we mean orbits launched in the direct and opposite directions, respectively, in the bar corrotating non inertial reference frame. It is important to stress that we are dealing with motions of individual particles in a gravitational potential, i.e., this is not a self-consistent N-body simulation. The same number of prograde and retrograde orbits does not mean that we are weighting them equally, since it is known that prograde orbits play a much more important role in a barred galaxy potential. It just means we are exploring possible prograde and retrograde orbits with different initial conditions.

Notice that the greater the bar pattern speed Ω_b, the smaller will be the OLR radius. According to our criterion for the choice of initial conditions, Model X has more scattered orbits than Model Y and, in turn, Model Y has more scattered orbits than Model Z. This phenomenon is clearly shown in Figure 4.

3.3. *Results and Discussion*

For efficiency, we inserted a condition in the $SALI$ calculation on the LP- VIcode program to show us the moment when $SALI < 10^{-8}$, which we consider close enough to zero to classify the orbit as chaotic. With this, we were able to create a classification for the chaos level of an orbit. The categories are as follows:

Level 1: $SALI < 10^{-8}$ for $t \in [0, 2500)$.

Level 2: $SALI < 10^{-8}$ for $t \in [2500, 5000)$.

Level 3: $SALI < 10^{-8}$ for $t \in [5000, 7500)$.

Level 4: $SALI < 10^{-8}$ for $t \in [7500, 10000]$,

where t is measured in Myr [5].

[5]All orbits were integrated to 10,000 Myr.

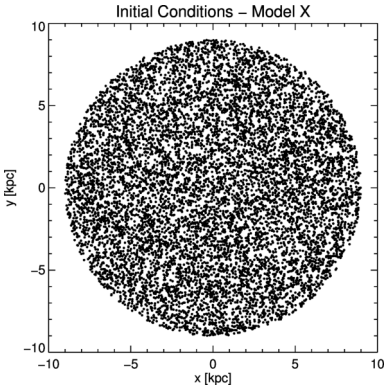

(a) Initial positions - Model X

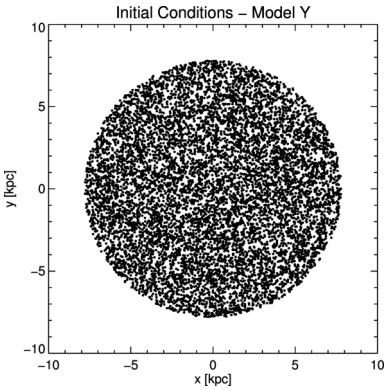

(b) Initial positions - Model Y

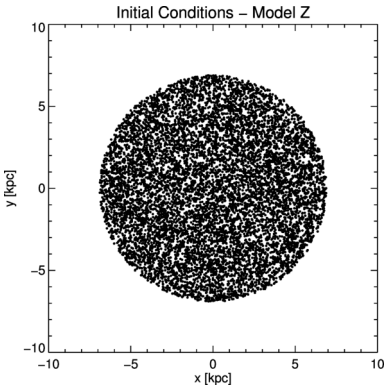

(c) Initial positions - Model Z

Fig. 4. Initial particle distributions for Models X, Y and Z. All orbits were launched with initial circular velocity and were distributed randomly inside the OLR resonance for each model. It is clear in the images that Model X has more scattered orbits than Model Y and, in turn, Model Y has more scattered orbits than Model Z; this happens because the greater the bar pattern speed Ω_b, the smaller becomes the OLR radius. This image shows dots representing 10,000 initial positions. Indeed, 10,000 prograde orbits and 10,000 retrograde orbits were computed for each model, starting from these same positions.

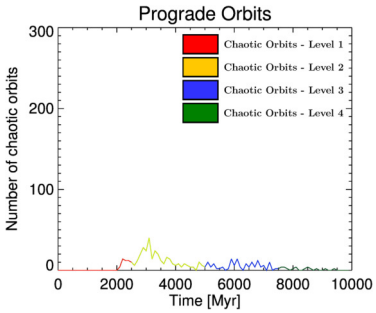

(a) Prograde - Model X_5

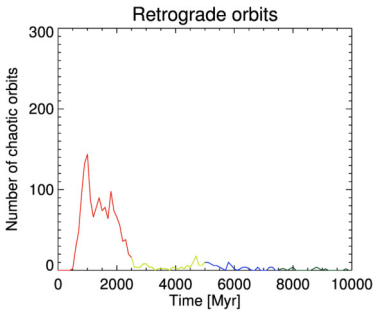

(b) Retrogrades - Model X_5

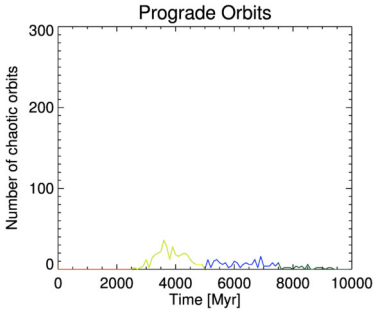

(c) Prograde - Model X_{10}

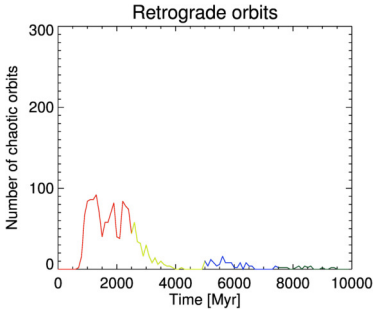

(d) Retrogrades - Model X_{10}

Fig. 5. Integration time × chaotic orbit number for Models X_5 and X_{10}. Model X_5, in which the bar grows faster, has slightly more chaos (mainly Level 1) than Model X_{10}. The colors of the line segments are defined in the legend inside the upper plot. The color figure can be viewed online.

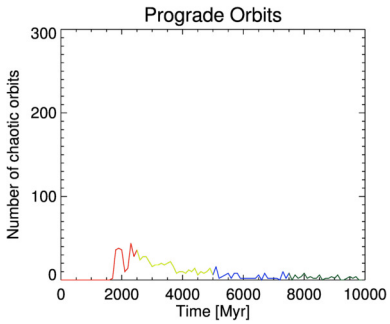

(a) Progrades - Model Y_5

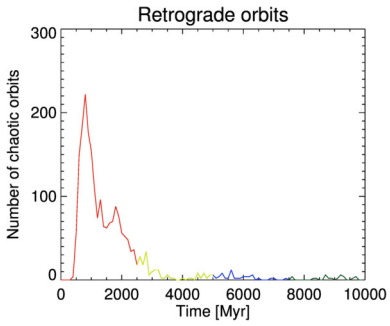

(b) Retrogrades - Model Y_5

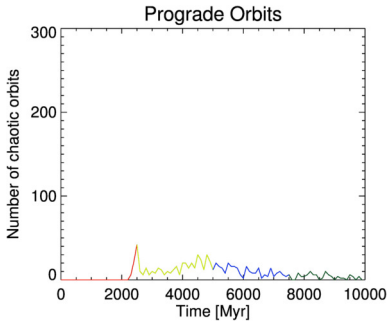

(c) Progrades - Model Y_{10}

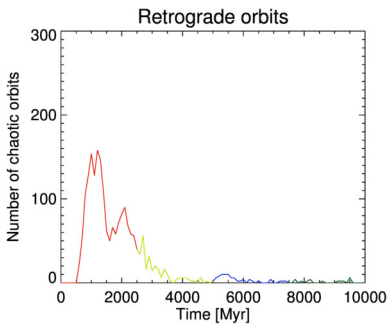

(d) Retrogrades - Model Y_{10}

Fig. 6. Integration time × chaotic orbit number for Models Y_5 and Y_{10}. Model Y_5, in which the bar grows faster, has slightly more chaos (mainly Level 1) than Model Y_{10}. The colors of the line segments are defined as in Figure 5. The color figure can be viewed online.

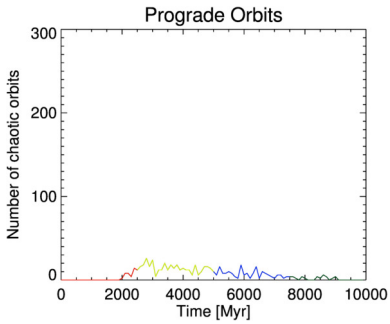

(a) Progrades - Model Z_5

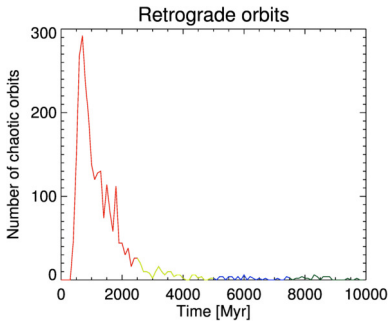

(b) Retrogrades - Model Z_5

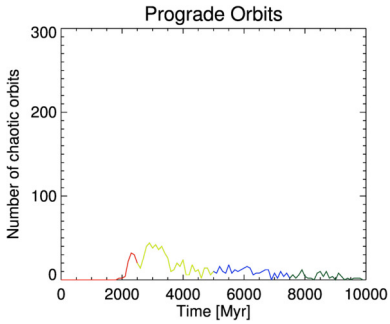

(c) Progrades - Model Z_{10}

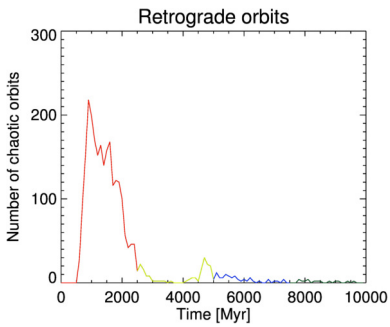

(d) Retrogrades - Model Z_{10}

Fig. 7. Integration time × chaotic orbit number for Models Z_5 and Z_{10}. Model Z_5, in which the bar grows faster, has slightly more chaos (mainly Level 1) than Model Z_{10}. The colors of the line segments are defined as in Figure 5. The color figure can be viewed online.

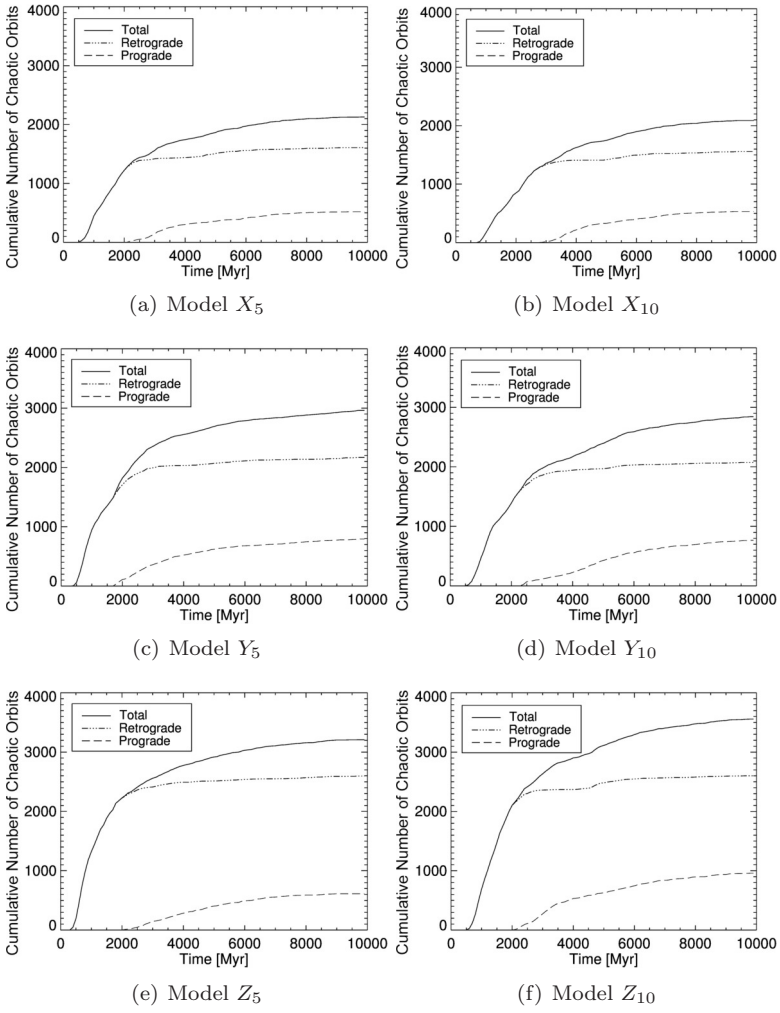

(a) Model X_5 (b) Model X_{10}

(c) Model Y_5 (d) Model Y_{10}

(e) Model Z_5 (f) Model Z_{10}

Fig. 8. Time × cumulative number of chaotic orbits for Models X_5, X_{10}, Y_5, Y_{10}, Z_5 and Z_{10}. Looking at the sequence of images, one realizes that the number of orbits that become chaotic at some point is closely related to the bar pattern speed. Clearly in Model Z, in which the bar rotates faster, there is a greater amount of chaotic motions when compared to Model X, in which the bar is slower. While Figures 5 to 7 show a slight difference indicating that models in which the bar grows faster have slightly more Level 1 chaos, here by analyzing the general context, for the cumulative number of chaotic orbits nothing can be said.

Figures 5 to 7 show the amount of chaos that arose at each integration time for each model, for both prograde and retrograde orbits. The levels of chaoticity are represented by different colors. Apparently, orbits launched as retrogrades are more conducive to chaos. This observation is consistent with Caritá et al. (2017); however it contradicts results of some classic investigations, (Athanassoula et al. 1983; and Pfenniger 1984), where there is more order in the retrograde parts of the surfaces of section of these fixed potentials. Certainly, this will lead us to further investigations in a future article.

All models studied presented strong dominant Level 1 chaos for the retrograde orbits and an apparent domain of Level 2 chaos for the prograde orbits. Some Level 1 chaos is generated in the prograde orbits, and specifically in Models X_{10} and Z_5 this type of chaos is null or practically negligible.

Figure 8 shows the cumulative number of chaotic orbits for prograde and retrograde orbits, and for the total number of orbits of the two types in all models. The distributions between order and chaos, considering the initial positions for each model, are shown in Figures 9 to 11.

In general, for the prograde orbits, the number of chaotic orbits generated was quite low, ranging from 5% to 10% of the total number of prograde orbits launched (depending on the model analyzed).

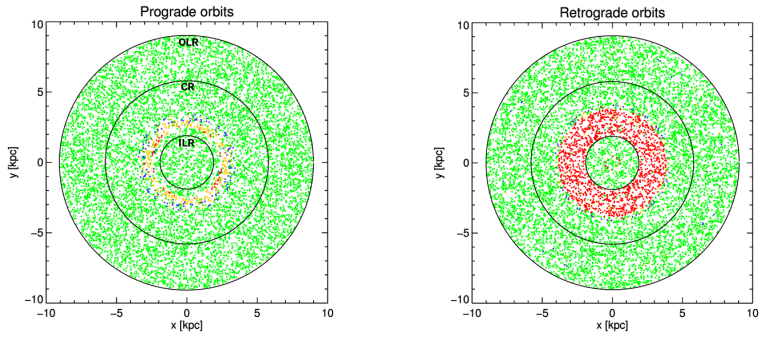

(a) Model X_5

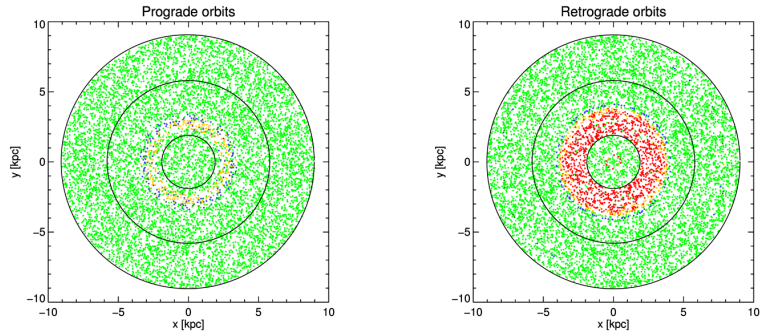

(b) Model X_{10}

Fig. 9. Each plot shows the initial positions of all Model X particles, color-coded according to their chaos level, as in the legend above. This image again reinforces the result that orbits launched as retrogrades are more conductive to chaos. The outer limit for the inicial positions is the OLR, as stated in § 3.2. The initial positions of the orbits that have become chaotic are located in a well-defined ring-like region, confined between the ILR and CR resonances. ILR, CR and OLR circles are shown in black, and identified in the upper left plot. Almost no orbit presents chaos with initial conditions outside these regions. The color figure can be viewed online.

On the other hand, for the retrograde orbits, this percentage increased considerably, to between 15% and 25% of the total number of retrograde orbits launched (depending on the model). In total numbers, considering the prograde and retrograde orbits, the percentage of chaos in the integrated orbits was always between 10% and 18% (depending on the model).

Figure 8 does not show appreciable changes with the rate of bar growth. However, in Figures 5 to 7 dissimilarities appear. The models where the bar grows over 5 turns seem to provide slightly more chaos than the models where the bar grows over 10 turns. This is an indication that an abrupt appearance of the bar causes more disturbance in the system.

Figures 9 through 11 show the stability of the orbits according to the initial positions. They all present a common feature: very well-defined ring-like regions of chaos. For the prograde orbits, there is only one ring of chaos for each model. For the retrograde orbits, there are two rings of chaos, a large and thick outer ring, surrounding a subtle inner ring, with one exception for Model Z_5. The CR resonance limits these rings; in this context, interestingly, the most prominent rings are confined between the ILR and CR resonances, with a single exception for Model Z_5. Very few orbits presented chaos with initial conditions outside these ring-like regions. In Figures 9 through 11 the difference in the amount of chaos for prograde and retrograde orbits is also clearly shown.

The greater the bar pattern speed Ω_b, the smaller the OLR radius. Figures 5 to 11 also show that the greater Ω_b, the more chaos the orbits that are within the OLR radius will present. In fact, Figures 5 through 7 make it clear that the main difference in this respect is especially in the retrograde

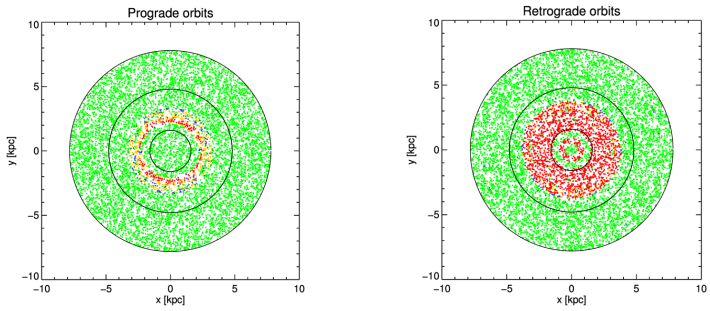

(a) Model Y_5

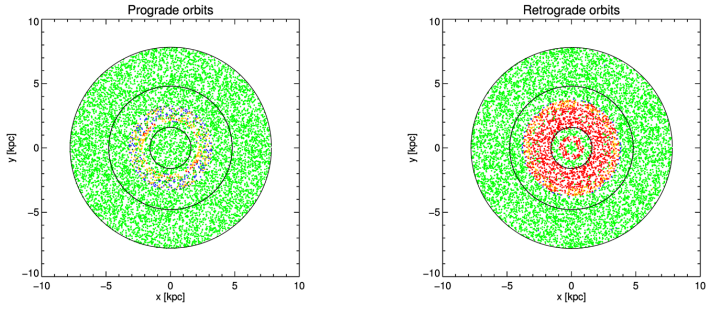

(b) Model Y_{10}

Fig. 10. Each plot shows the initial positions of all Model Y particles. All plots are organized and color-coded as in Figure 9. The color figure can be viewed online.

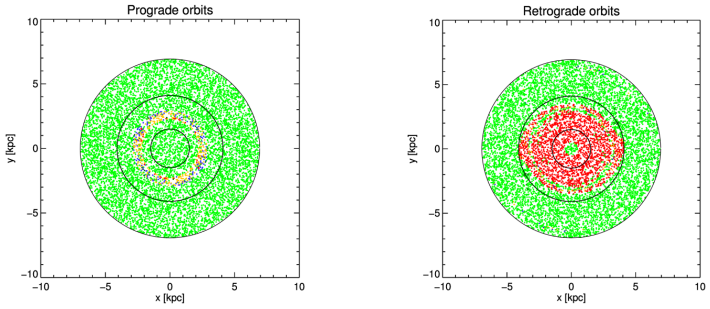

(a) Model Z_5

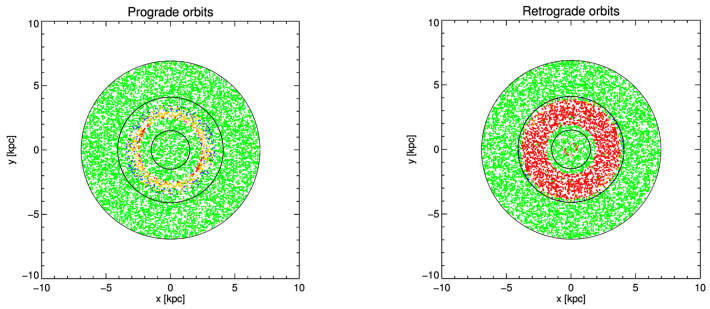

(b) Model Z_{10}

Fig. 11. Each plot shows the initial positions of all Model Z particles. All plots are organized and color-coded as in Figure 9. The color figure can be viewed online.

orbits in the Level 1 of chaos. This indicates that the bar pattern speed also influences the system sensitivity to the bar appearance, since the orbits with Level 1 of chaos presented chaos in a time close to the appearance of the bar. On the other hand, for the prograde orbits, no significant differences are displayed at this point.

As expected, the E_J of all particles is not conserved during bar evolution. As already mentioned, while the mass of the bar is growing linearly, the value E_J also decreases linearly, and it is conserved again from the moment the bar growth finishes and the system becomes fixed (after evolution). To visualize this phenomenon, Appendix B presents some images where the number of orbits for certain times during and after the growth of the bar for each model is arranged by E_J. In these images, changes in the E_J values can be seen until the times listed in Table 2 are reached. Afterwards, E_J is conserved.

4. CONCLUSIONS

The main purpose of this work was to verify the influence of the bar on the stability of orbits in the analytical gravitational potential of barred galaxies where the bar grows over time. Six models with parameters based on observational properties of the galaxy NGC 936 were studied, and their influences on the stability of the orbits were compared. The bar dimensions were maintained in all six models and the difference between these six models was the bar pattern speed and the time of growth.

We find evidence that when the bar grows faster, more chaos is generated. For the prograde orbits, the number of chaotic orbits generated was quite low, ranging from 5% to 10% of the total number of prograde orbits launched (depending on the model). For the retrograde orbits, this percentage increased considerably, to between 15% and 25% of the total number of retrograde orbits launched (depending on the model). In this context, retrograde orbits were more conducive to chaos. This last statement provides an opportunity for further investigation, which we will conduct in the future, as it apparently contradicts some classic results (Athanassoula et al. 1983; Pfenniger 1984). We found, as expected, that E_J was not conserved while the bar was evolving but it started to be conserved when the system stabilized. We also noted that the higher Ω_b, the greater its influence on the orbital dynamics.

Well-defined ring-like regions of chaos were found corresponding to different initial positions, with few orbits presenting chaos outside these regions. For the prograde orbits, there was an unique ring for each model. For the retrograde orbits, two rings of chaos appeared, almost always a large, thick outer ring, surrounding a subtle inner ring. The CR radius was the outer limit for these chaos rings, and the most prominent rings were predominantly confined between the ILR and CR resonances.

We analyzed consistent barred galaxy models for systems in rotation and studied the orbit stability using the SALI Method. The LP-VIcode program met all of our needs and only small adjustments were needed.

We acknowledge the Brazilian agencies CNPq (200906-2015-1), CAPES and FAPESP, as well as the Mexican agency CONACyT (CB-2014-240426) for supporting this work. Our sincere thanks to Dr. Pfenniger, who kindly provided us with his Fortran 77 implementation of the Ferrers bar potential. All numerical work was developed using the Hipercubo Cluster resources (FINEP 01.10.0661-00, FAPESP 2011/13250-0 and FAPESP 2013/17247-9) at IP&D–UNIVAP.

APPENDIX

A. CHOICE OF PARAMETERS - NGC 936

NGC 936 is a barred spiral galaxy, type SB0 in the Hubble scheme (Hubble 1926), which is about 19.6 Mpc away in the direction of Cetus. This galaxy has a very prominent bar and bulge, and a ring structure that surrounds the bar. It was discovered on January 6, 1785 by William Herschel and was classified at the time as a planetary nebula, because of its round shape (Herschel 1785a,b).

As the models described in the paper (Plummer, Miyamoto-Nagai and Ferrers) had already been implemented and were working well in LP-VIcode (Caritá et al. 2017), we decided to maintain the same modeling for this research with bars that grow over time. In order to adjust the necessary parameters for NGC 936, the works of Kent & Glaudell (1989) and Merrifield & Kuijken (1995) were used. We note that the Plummer, Miyamoto-Nagai and Ferrers models may not be the best for modeling galaxy NGC 936; but we emphasize that this galaxy was used only as an inspiration for our parameters. The procedures for finding the parameters are described below.

Kent & Glaudell (1989) proposed an analytical model of the NGC 936 bulge given by a truncated King model (King 1962). The model density is:

$$\rho(s) = \rho_c \left(\frac{1}{[1 + (\frac{s}{a})^2]^{\frac{3}{2}}} - \frac{1}{[1 + (\frac{s_c}{a})^2]^{\frac{3}{2}}} \right), \quad \text{(A11)}$$

where $\rho_c = 22\,L_\odot\,\mathrm{pc}^{-3}$, $a = 265$ pc, $s_c = 2.7$ kpc and the radial coordinate s is given by $s^2 = x^2 + y^2 + (z/0,63)^2$.

By varying the parameters ϵ_S and M_S in the Plummer Model, calculating the cumulative mass curve for this model and comparing it with the King model cumulative mass curve, using the smallest variance between the corresponding points in the graphs, we could estimate parameters ϵ_S and M_S for a better fit. The fit of these curves was done up to the radius 2.7 kpc and, thus, we were able to estimate the values $\epsilon_S = 0.45$ and $M_S = 5.4 \times 10^9 M_\odot$.

The work of Kent & Glaudell (1989) also allowed us to extract an approximation for the brightness profile for the disk together with the bar, as follows:

$$\Sigma = \Sigma_0 e^{-r/h} \tag{A12}$$

where $\Sigma_0 = 355\ L_\odot\,\mathrm{pc}^{-2}$ and $h = 3.5$ kpc.

By adjusting the mass growth curves and using the smallest variance (as we did with the bulge), we were able to estimate the Miyamoto-Nagai parameters A and B, as well as the mass of the disk plus the mass of the bar. The fit of the curves was done up to a radius of 10 kpc and, thus, we were able to estimate the values $A = 4.7$, $B = 0.4$ and $M_{\mathrm{disc+bar}} = 3.7 \times 10^{10} M_\odot$.

For the bar, parameters $a = 4$ kpc and $b = 1.1$ kpc of the Ferrers potential were extracted from Kent & Glaudell (1989), with dimensions 8.0×2.2 kpc. From this same work, the mass of the bar was extracted, using the luminosity information as $5.6 \times 10^9\ L_\odot$. From this fact, using the relation $\frac{M}{L} = 1$ we extracted that the mass of the bar $M_B = 5.6 \times 10^9\ M_\odot$. The parameter $c = 0.4$ kpc was taken for convenience only.

According to Merrifield & Kuijken (1995), the bar pattern speed of the galaxy NGC 936 is estimated to be $\Omega_b = 60 \pm 14\,\mathrm{km\,s^{-1}\,kpc^{-1}}$. With this, we decided to establish three models by varying the bar pattern speed. The values Ω considered by us and their respective models were chosen once the NGC 936 bar pattern speed was estimated as $\Omega_b = 60 \pm 14\,\mathrm{km\,s^{-1}\,kpc^{-1}}$ (Merrifield & Kuijken 1995); these values are shown in Table 3.

TABLE 3

MODELS X, Y AND Z VARYING THE BAR PATTERN SPEED OF NGC 936

Model X	Model Y	Model Z
$\Omega_b = 50\ \frac{\mathrm{km}}{\mathrm{s\ kpc}}$	$\Omega_b = 60\ \frac{\mathrm{km}}{\mathrm{s\ kpc}}$	$\Omega_b = 70\ \frac{\mathrm{km}}{\mathrm{s\ kpc}}$

Recall that the model units adopted were: 1 kpc for length, $10^3\,\mathrm{km\,s^{-1}}$ for velocity, $10^3\,\mathrm{km\,s^{-1}\,kpc^{-1}}$ for pattern speed, 1 Myr for time, and $2 \times 10^{11} M_\odot$ for mass. The universal gravitational constant G was always equal to 1 and the total mass $G(M_S + M_D + M_B)$ was always equal to 1. The integration time was 10 000 Myr. The following ratios were calculated: $\frac{M_S}{M_T} = \frac{0.4 \times 10^9}{42.4 \times 10^9} \approx 0.1273$, $\frac{M_D}{M_T} = \frac{31.4 \times 10^9}{42.4 \times 10^9} \approx 0.7406$ and $\frac{M_B}{M_T} = \frac{5.6 \times 10^9}{42.4 \times 10^9} \approx 0.1321$. To avoid confusion in the notations, we chose to use M_S, M_D and M_B for the ratios. In this way the models presented in Table 1 were constructed.

B. E_J BEHAVIOR

The Jacobi Energy is not conserved during bar evolution. While the bar mass is growing linearly, the value E_J per particle decreases linearly, and it is conserved again from the moment the bar growth finishes and the system becomes fixed (after evolution).

The behavior of the Jacobi energy is shown in Figure 2. In order to better visualize this phenomenon, the number of orbits per E_J for certain times during and after the growth of the bar is arranged in Figure 12 for each model. In these images it is possible to observe that the value of E_J decreases until the times shown in Table 2, after which time E_J remains constant.

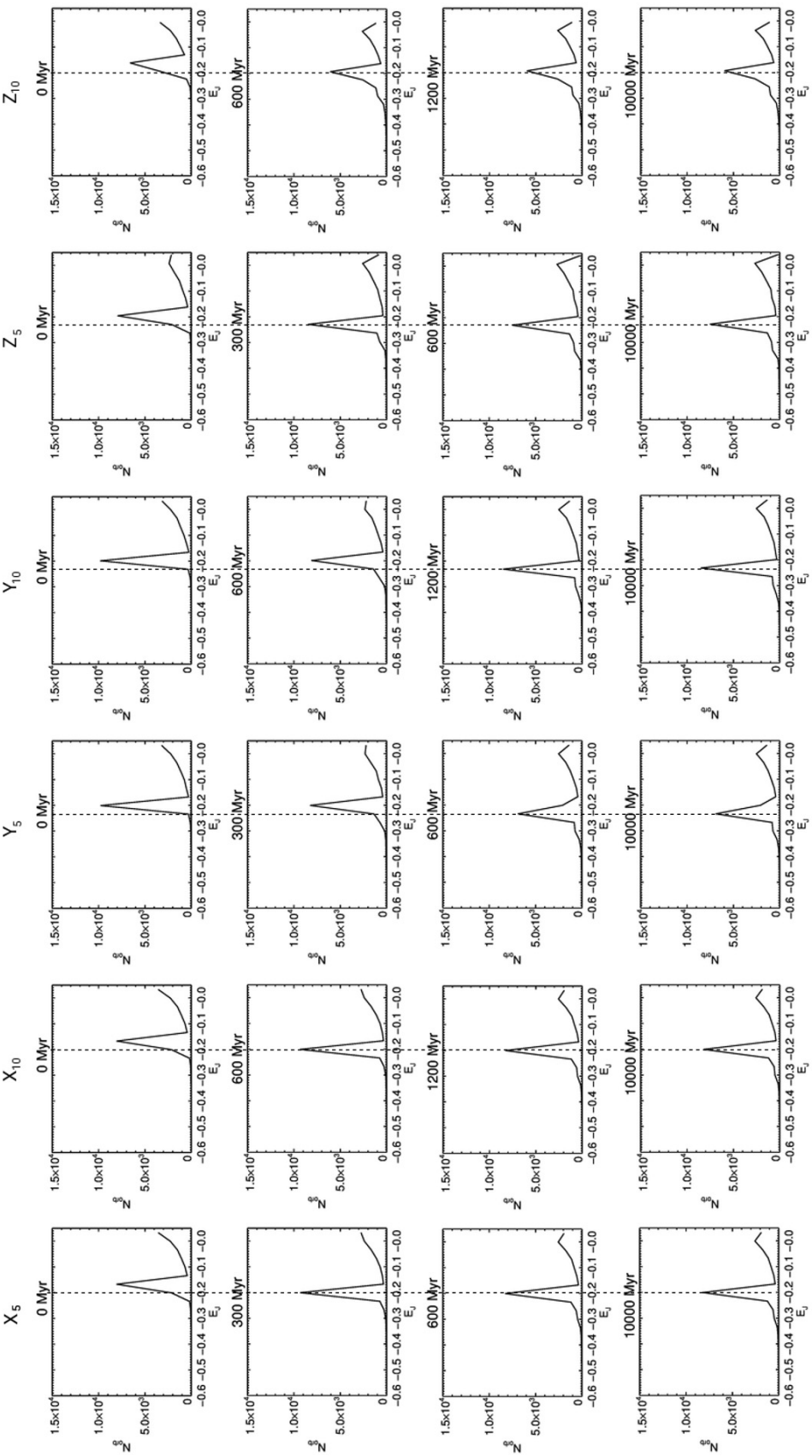

Fig. 12. Jacobi Energy × Number of Orbits for Models X_5, X_{10}, Y_5, Y_{10}, Z_5 and Z_{10}. Each column shows the time evolution of a different model. The dashed lines indicate the final E_J peak value, to show the displacements in the E_J values until the times given in Table 2 (614.35, 1228.70, 511.96, 1023.82, 438.82 and 877.65 Myr, respectively), after which E_J is conserved.

REFERENCES

Athanassoula, E., Bienayme, O., Martinet, L., & Pfenniger, D. 1983, A&A, 127, 349

Binney, J. & Tremaine, S. 2008, Galactic Dynamics, (2nd ed.; Princeton, NJ: PUP)

Bournaud, F. & Combes, F. 2002, A&A, 392, 83

Caritá, L., Rodrigues, I., & Puerari, I. 2017, Galax, 5, 101

Caritá, L. A., Rodrigues, I., Puerari, I., & Schiavo, L. E. C. A. 2018, NewA, 60, 48

Carpintero, D. D., Maffione, N., & Darriba, L. 2013, La Plata Variational Indicators code: a program to compute a suite of variational chaos indicators (User's Guide for Version 102[Kaos])

_____. 2014, A&C, 5, 19

Chaves-Velasquez, L., Patsis, P. A., Puerari, I., Skokos, C., & Manos, T. 2017, ApJ, 850, 145

Eskridge, P. B., Frogel, J. A., Pogge, R. W., et al. 2000, AJ, 119, 536

Ferrers, N. M. 1877, QJPAM, 14, 1

Gajda, G., Łokas, E. L., & Athanassoula, E. 2016, ApJ, 830, 108

Herschel, W. 1785a, RSPT, 75, 40

_____. 1785b, RSPT, 75, 213

Hubble, E. P. 1926, ApJ, 64

Kaufmann, D. E. & Patsis, P. A. 2005, ApJ, 624, 693

Kent, S. M. & Glaudell, G. 1989, AJ, 98, 1588

King, I. 1962, AJ, 67, 471

Machado, R. E. G. & Manos, T. 2016, MNRAS, 458, 3578

Manos, T. & Athanassoula, E. 2011, MNRAS, 415, 629

Manos, T. & Machado, R. E. G. 2014, MNRAS, 438, 2201

Merrifield, M. R. & Kuijken, K. 1995, MNRAS, 274, 933

Miyamoto, M. & Nagai, R. 1975, PASJ, 27, 533

Patsis, P. A. 2002, Disks of Galaxies: Kinematics, Dynamics and Peturbations, ed. E. Athanassoula, A. Bosma, & R. Mujica, ASPC, 275, 161

Patsis, P. A. & Katsanikas, M. 2014, MNRAS, 445, 3525

Patsis, P. A., Skokos, H., & Athanassoula, E. 2002, MNRAS, 337, 578

_____. 2003, MNRAS, 342, 69

Pfenniger, D. 1984, A&A, 134, 373

Plummer, H. C. 1911, MNRAS, 71, 460

Sheth, K., Regan, M. W., Scoville, N. Z., & Strubbe, L. E. 2003, ApJ, 592, L13

Skokos, H. 2001, JPhA, 34, 10029

Skokos, H., Antonopoulos, C., Bountis, T. C., & Vrahatis, M. N. 2002a, eprint arXiv:nlin/0210053

_____. 2003, PThPS, 150, 439

_____. 2004, JPhA, 37, 6269

Skokos, H., Patsis, P. A., & Athanassoula, E. 2002b, MNRAS, 333, 847

_____. 2002c, MNRAS, 333, 847

_____. 2002d, MNRAS, 333, 861

Lucas Antonio Caritá: Instituto Federal de Educação, Ciência e Tecnologia de São Paulo (IFSP), São José dos Campos, Brasil (prof.carita@ifsp.edu.br).

Lucas Antonio Caritá, Irapuan Rodrigues, and Luiz Eduardo Camargo Aranha Schiavo: Universidade do Vale do Paraíba (UNIVAP), São José dos Campos, Brasil.

Lucas Antonio Caritá and Ivânio Puerari: Instituto Nacional de Astrofísica, Óptica y Electrónica (INAOE), Puebla, México.

Luiz Eduardo Camargo Aranha Schiavo: Universidade Estadual de Campinas (UNICAMP), Campinas, Brasil.

Revista Mexicana de Astronomía y Astrofísica, **55**, 337–350 (2019)

DOI: https://doi.org/10.22201/ia.01851101p.2019.55.02.18

NGC 1261: A TIME-SERIES *VI* STUDY OF ITS VARIABLE STARS

A. Arellano Ferro[1], I. H. Bustos Fierro[2], J. H. Calderón[2,3], and J. A. Ahumada[2]

Received June 1 2019; accepted August 13 2019

ABSTRACT

Time-series *VI* CCD photometry of the globular cluster NGC 1261 is employed to study its variable star population. A membership analysis of most variables based on Gaia DR2 proper motions and colours was performed prior to the estimation of the mean cluster distance and metallicity. The light curves of the member RR Lyrae were Fourier decomposed to calculate their individual values of distance, [Fe/H], radius and mass. The *I*-band P-L for RR Lyrae stars was also employed. Our best estimates of the metallicity and distance of this Oo I cluster are $[Fe/H]_{ZW}=-1.42\pm0.05$ dex and $d=17.2\pm0.4$ kpc. No mixture of fundamental and first overtone RR Lyrae stars in the either-or or bimodal region is seen in this cluster, as it seems to be the rule for Oo I clusters with a red horizontal branch. A multi-approach search in a region of about $10'\times10'$ around the cluster revealed no new variable stars within the limitations of our CCD photometry.

RESUMEN

Empleamos una serie temporal de imágenes CCD en las bandas *VI* del cúmulo globular NGC 1261, para estudiar su población de estrellas variables. Se realizó un análisis de la membresía de las estrellas variables basado en movimientos propios y colores dados en Gaia DR2. Por medio de la descomposición de Fourier de curvas de luz de estrellas RR Lyrae, se obtuvieron sus valores individuales de distancia, [Fe/H], radio y masa. También utilizamos la relación P-L en la banda *I* para las RR Lyrae. Nuestras estimaciones de la metalicidad y la distancia medias de NGC 1261, un cúmulo de tipo Oo I, son $[Fe/H]_{ZW}=-1.48\pm0.05$ dex y $d=17.2\pm0.4$ kpc. No se observa mezcla de modos de pulsación fundamental y primer sobretono de RR Lyrae en la región bimodal, como parece ser la norma para cúmulos de tipo OoI con rama horizontal roja. Una búsqueda cuidadosa en la región de $10'\times10'$ centrada en el cúmulo no reveló nuevas variables, dentro de las limitaciones de nuestra fotometría.

Key Words: globular clusters: individual: NGC 1261 — stars: variables: RR Lyrae — stars: fundamental parameters

1. INTRODUCTION

The southern globular cluster NGC 1261 (C0310−554), also known as Caldwell 87, is located in the constellation Horologium ($\alpha=03^h12^m16.21^s$, $\delta=-55°$ 12' 58.4", J2000, Goldsbury et al. (2010)). It was discovered by James Dunlop in 1826, and remained little studied until the mid-XXth century. It is a cluster of intermediate brightness, located far from the bulge of the Galaxy ($l=270.54°$, $b=-52.12°$) and, consequently, has negligible or no reddening. The Catalog of Parameters for Milky Way Globular Clusters compiled by Harris (1996) (2010 edition), lists a metallicity [Fe/H]=−1.27, a distance to the Sun of 16.4 kpc, the level of the Horizontal Branch (HB) as $V_{HB}=16.7$ mag, and a reddening $E(B-V)=0.01$. The Catalogue of Variable Stars in Globular Clusters (CVSGC), (Clement et al. 2001) (2017 edition), lists 31 stars, although only 29 have been confirmed as variables: RR Lyrae stars (23), SX Phe (3), variable red giants or SR (2) and eclipsing binaries EC? (1). The members of the RR Lyrae population were first reported from photographic studies by Laborde & Fourcade (1966), later on by Bartolini et al. (1971), Wehlau & Demers

[1]Instituto de Astronomía, Universidad Nacional Autónoma de México, México.

[2]Universidad Nacional de Córdoba, Observatorio Astronómico, Córdoba, Argentina.

[3]Consejo Nacional de Investigaciones Científicas y Técnicas (CONICET), Buenos Aires, Argentina.

(1977), Wehlau et al. (1977) and, more recently, in the CCD studies of Salinas et al. (2007) and Salinas et al. (2016), who discovered five RR Lyrae stars, three SX Phoenicis, one long period variable and an eclipsing binary of the W UMa type.

So far, the variable star population of NGC 1261 has not been studied with the specific aim of estimating some of the physical properties of the cluster, such as the mean metallicity, distance and age, by performing a detailed analysis of the light curves. Likewise, the distribution of variables in the HB has not been discussed along with an analysis of individual membership. Studies of the distribution of RR Lyrae pulsation modes in the instability strip around the first overtone red edge (FORE), have shown that the modes are neatly split in all Oo II clusters with blue HB's; however, this happens only in some of the Oo I Type clusters with redder HB's (e. g. Arellano Ferro et al. (2018b)). It has been argued that this property is related to the distribution of stars in the zero-age horizontal branch (ZAHB) which, in turn, depends on the mass loss during the He-flashes at the asymptotic giant branch (AGB) (Arellano Ferro et al. 2018a; Caputo et al. 1978). The facts that NGC 1261 is among the few Oo I clusters with extremely red HB, has intermediate metallicity and harbours numerous RR Lyrae stars of both modes, add a particular interest to its study.

In the present work we perform such an analysis based on a new, extensive time-series of *VI* CCD images. The specific calibrations for different families of variable stars, concerning Fourier light curve decomposition, luminosity of the horizontal branch, and P-L relations are discussed. We also make use of the possibility of ensuring the membership of the variables to the cluster through the analysis of proper motions available in the Gaia DR2 catalogue. The paper is structured in the following way: In § 2, we describe our observations, the data reduction process and the transformation to the standard photometric system. In § 3, we report the periods, epochs and display the *VI* light curves of all variables detected in our photometry. We also discuss the cluster membership and some cases of clear light contamination by extremely close neighbours, as well as the corresponding corrections in amplitude and position, in the colour-magnitude diagram (CMD). Our failed efforts to find new variables are described. In § 4, we present the log P-amplitude diagram (Bailey's diagram) to confirm the Oo I type nature of NGC 1261. § 5 describes our estimation of the interstellar reddening. § 6, § 7 and § 8 contain the light curve Fourier decomposition and physical parameters estimations, and the comparison with previous determinations of [Fe/H] and distance. In § 9 we comment on the structure of the HB and the correlation with the distribution of RR Lyrae pulsation modes in the instability strip. In § 10 we summarize our work.

TABLE 1

THE TIME DISTRIBUTION OF *VI* OBSERVATIONS OF NGC 1261

Date (y/m/d)	N_V	t_V (s)	N_I	t_I (s)	Avg. seeing (")
2017/08/19	17	400	20	200	3.0
2017/08/20	19	400	25	200	2.9
2017/09/10	15	400	17	200	3.1
2017/09/15	15	400	15	200	3.0
2017/09/22	24	400	29	200	2.3
2017/10/06	15	400	19	200	3.0
2017/10/28	26	400	30	200	3.1
2017/12/07	13	400	14	200	2.4
2018/08/03	4	300	6	150-200	2.9
2018/08/04	27	300	33	150	3.4
2018/08/05	27	300	27	150	2.9
2018/08/11	–	–	23	150	3.0
2018/09/02	33	300	37	150	2.4
2018/09/14	28	300	38	150	2.3
2018/09/16	23	300	29	150	2.3
2018/11/16	18	300	21	150	2.9
2018/11/30	4	300	5	150	2.6
2018/12/16	22	300	24	150	2.5
Total:	330	–	412	–	–

Columns N_V and N_I give the number of images taken with the V and I filters respectively. Columns t_V and t_I provide the exposure time, or range of exposure times employed during each night for each filter. The average seeing is listed in the last column.

2. DATA, OBSERVATIONS AND REDUCTIONS

The data used for the present work were obtained with the 1.54−meter telescope at the Bosque Alegre Astrophysical Station of the Cordoba Observatory, (National University of Cordoba), Argentina, during seventeen nights between August 19th 2017 and November 30th 2018. A total of 330 and 412 V and I CCD images were acquired. The detector used was a CCD Alta F16M of 4096×4096 square 9-micron pixels, binned 2×2, with a scale of 0.496 arcsec/pix (after binning). The images were trimmed to 1200×1200 pixels, for a useful field of view (FoV) of approximately 10×10 arcmin^2.

Table 1 summarizes the observation dates, exposure times and average seeing conditions.

2.1. *Difference Image Analysis*

For the reduction of our data, we employed the software Difference Imaging Analysis (DIA) with its pipeline implementation DanDIA[4] (Bramich 2008;

[4]DanDIA is built from the DanIDL library of IDL routines available at `http://www.danidl.co.uk`

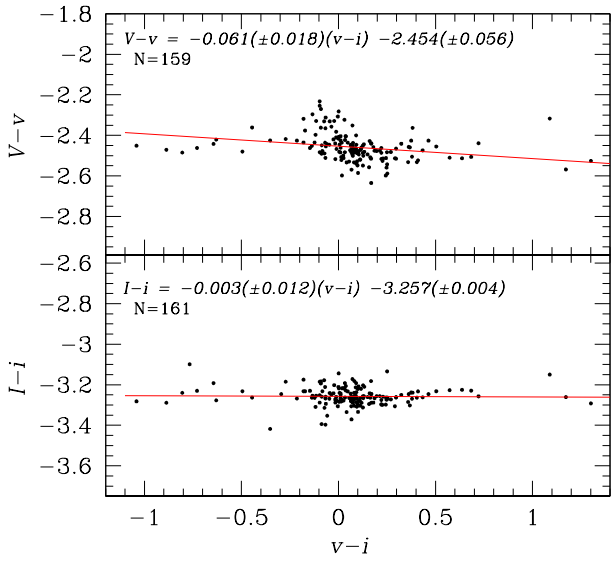

Fig. 1. Transformation relations obtained for the V and I filters between the instrumental and the standard photometric systems. We employed a set of standard stars in the field of NGC 1261 from the collection of Stetson (2000). The colour figure can be viewed online.

Bramich et al. 2013). With this, we were able to obtain high-precision photometry for all the point sources in the FoV of our CCD images. First, a reference image is created by DanDIA by stacking the best images in each filter; then, the reference image is subtracted from the rest of the images. In each reference image, we measured the fluxes (referred to as reference fluxes) and positions of all PSF-like objects (stars) by extracting a spatially variable empirical PSF. This PSF is built from about 300-400 isolated stars, and a third degree polynomial is fitted to each detected object.

Differential fluxes are converted into total fluxes. The total flux $f_{\rm tot}(t)$ in ADU/s at each epoch t can be estimated as:

$$f_{\rm tot}(t) = f_{\rm ref} + \frac{f_{\rm diff}(t)}{p(t)}, \qquad (1)$$

where $f_{\rm ref}$ is the reference flux (ADU/s), $f_{\rm diff}(t)$ is the differential flux (ADU/s) and $p(t)$ is the photometric scale factor (the integral of the kernel solution). Conversion to instrumental magnitudes was achieved using:

$$m_{\rm ins}(t) = 25.0 - 2.5 \log \left[f_{\rm tot}(t) \right], \qquad (2)$$

where $m_{\rm ins}(t)$ is the instrumental magnitude of the star at time t. The above procedure has been described in detail in Bramich et al. (2011).

2.2. *Photometric Calibrations*

2.2.1. *Relative Calibration*

To correct for possible systematic errors, we applied the methodology developed in Bramich & Freudling (2012) to solve for the magnitude offsets Z_k that should be applied to each photometric measurement from the image k. In terms of DIA, this translates into a correction for the systematic error introduced into the photometry due to a possible error in the flux-magnitude conversion factor (Bramich et al. 2015). In the present case the corrections were very small, ≈ 0.001 mag for stars brighter than $V \approx 18.0$.

2.2.2. *Absolute Calibration*

Standard stars in the field of NGC 1261 are included in the online collection of Stetson (2000)[5] and we used them to transform instrumental *vi* magnitudes into the Johnson-Kron-Cousins standard *VI* system. These stars are distributed in the cluster periphery, they are generally isolated and can be accurately measured by DanDIA. The mild colour dependence of the standard minus instrumental magnitudes is shown in Figure 1. The transformation equations are explicitly given in the figure itself.

2.2.3. *Internal Errors*

The internal errors of our CCD photometry can be evaluated via the rms diagram of Figure 2.

3. VARIABLE STARS IN NGC 1261

There are 29 variable stars listed in the Catalogue of Variable Stars in Globular Clusters (CVSGC) (Clement et al. 2001). The time-series *VI* photometry obtained in this work is reported in Table 2, of which only a small portion is included in the printed version of the paper. The full table shall be available in electronic form in the Centre de Donnés astronomiques de Strasbourg database (CDS). The variables V17, V20, V26, V27 and V31 are blended in our images and could not be resolved; therefore, they are neither included in the Table 2 nor discussed in this paper. The light curves in our data for the RRab, RRc and the SX Phe V25 are displayed in Figure 3. Our determinations of their mean magnitudes, amplitudes and periods are given in Table 3. The rms diagrams in the V and I filters and the colour-magnitude diagram (CMD) of the cluster are shown in Figures 2 and 4 respectively. The positions of the known variable stars are also shown.

[5] http://www3.cadc-ccda.hia-iha.nrc-cnrc.gc.ca/community/STETSON/standards

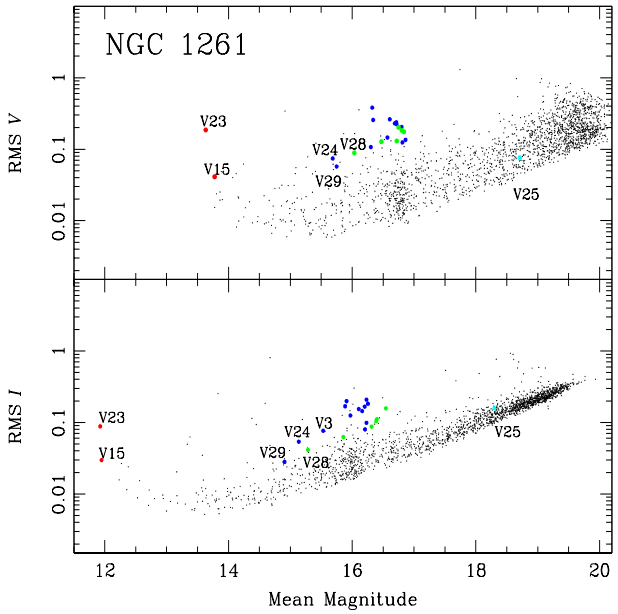

Fig. 2. rms of all light curves measured in our images as a function of the mean magnitude. Colour symbols indicate the position of the known variable stars as follows: blue and green for RRab and RRc stars respectively, red for SR stars and turquoise for the SX Phe star V25. The colour figure can be viewed online.

TABLE 2

TIME-SERIES *VI* PHOTOMETRY FOR THE VARIABLES STARS OBSERVED IN THIS WORK*

Variable Star ID	Filter	HJD (d)	$M_{\rm std}$ (mag)	$m_{\rm ins}$ (mag)	σ_m (mag)
V2	*V*	2457985.75380	16.864	19.293	0.010
V2	*V*	2457985.75851	16.830	19.259	0.010
⋮	⋮	⋮	⋮	⋮	⋮
V2	*I*	2457985.74544	16.417	19.673	0.019
V2	*I*	2457985.74783	16.367	19.622	0.018
⋮	⋮	⋮	⋮	⋮	⋮
V3	*V*	2457985.75380	16.304	18.752	0.006
V3	*V*	2457985.75851	16.294	18.741	0.006
⋮	⋮	⋮	⋮	⋮	⋮
V3	*I*	2457985.74544	15.535	18.791	0.009
V3	*I*	2457985.74783	15.537	18.794	0.009
⋮	⋮	⋮	⋮	⋮	⋮

*The standard and instrumental magnitudes are listed in Columns 4 and 5, respectively, corresponding to the variable stars in Column 1. Filter and epoch of mid-exposure are listed in Columns 2 and 3, respectively. The uncertainty in $m_{\rm ins}$ is listed in Column 6, which also corresponds to the uncertainty on $M_{\rm std}$. A full version of this table is available at the CDS database.

It is rather clear that the scatter around the horizontal branch (HB) is large and that some RR Lyrae stars appear much too bright. It is common to use the star position on the CMD as an argument against membership in the cluster, i.e., RR Lyrae stars that appear much above or below the HB. The information now available in the Gaia DR2 data base (Gaia Collaboration 2018), enables a deeper discussion on possible contamination by neighbouring unresolved stars and their proper motions. In the following section we shall refer to individual RR Lyrae stars with peculiar positions in the CMD.

Regarding the SX Phe stars, there are three of them reported in the CVSGC: V25, V26 and V30. Our light curve of V25 is shown in Figure 3. However, we have been unable to detect the faint stars V26 and V30, near the cluster core, probably because of the seeing conditions during our observations. Nevertheless, we want to point out that we see no stars, or that they are badly blended, in the positions marked in the identification chart of the discovery paper (Salinas et al. 2007).

3.1. *On the Cluster Membership and Light Contamination of Individual Variables*

With the aim of producing a colour-magnitude diagram (CMD) free of field stars, we applied the method of Bustos Fierro & Calderón (2019) to identify probable members in the field of the cluster. The method uses the high quality astrometric data available in Gaia DR2, and is based on the Balanced Iterative Reducing and Clustering using Hierarchies (BIRCH) algorithm (Zhang et al. 1996) in a four-dimensional space of physical parameters –positions and proper motions– that detects groups of stars in that 4D-space. We extracted 5258 Gaia sources that are very likely members of the cluster. The membership analysis shows that most of the stars in this field are indeed members of the cluster, but that their proper motions are quite small ($\approx$ 2 mas/yr), and that their distribution overlaps well with that of the field stars. The top two panels of Figure 4 display the full CMD diagram before and after the field star correction. Almost all known variables are matched with a member. The exceptions are stars V24, V26 and V31, that match sources of unknown membership, because their proper motions were not measured in the Gaia survey.

Plotting the positions of all Gaia DR2 sources in the field of our images we noted that, in some cases, two or even three of them can fall within the FWHM of the PSF of a detected stellar source. A direct consequence of this is an alteration of the magnitude

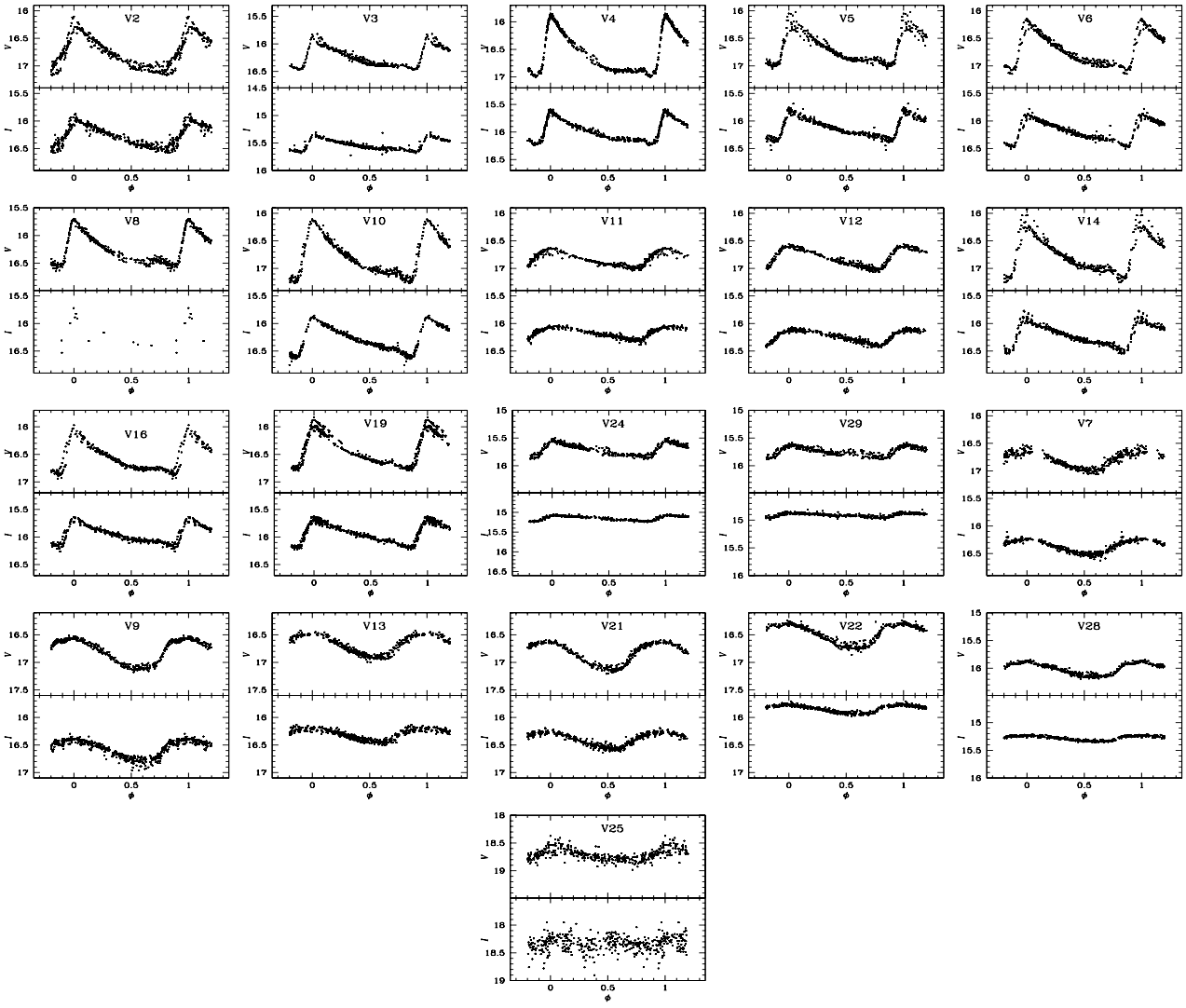

Fig. 3. *VI* light curves of known RRab, RRc stars and the SX Phe V25 in NGC 1261.

.

of the star, making it apparently brighter and, in the case of variable stars, artificially reducing the amplitude of their light curves.

In Figure 5, we show an amplification of the HB region of NGC 1261. In the left panel, known variables are plotted using the intensity weighted mean $\langle V \rangle$ and $\langle I \rangle$ listed in Table 3. RRab and RRc stars are represented by blue and green symbols respectively. It is evident that some of the RR Lyrae stars are much too bright relative to the ZAHB, namely, V3, V19, V22, V24, V28 and V29. The positions of the two RRc stars V22 and V28 are also much redder than expected. As a reference, the vertical black line that represents the empirical red edge of the first overtone instability strip (FORE) is also displayed (Arellano Ferro et al. 2016).

To help decide whether the odd positions of these stars are the result of light pollution, or simply of their being non-members, we analysed the photometric values of all Gaia sources present in a given variable star PSF. The magnitudes of the individual sources in the Gaia photometric system, G-, $G_{\rm BP}$-, and $G_{\rm RP}$-band, were transformed into V and I magnitudes using the relationships provided by J.M. Carrasco (2018: Gaia team), and available in § 5.3.7 of the Gaia DR2 documentation[6]. Then, the expected combined magnitude was calculated, and hence an

[6] `http://gea.esac.esa.int/arcfhive/documentation/GDR2/index.html`

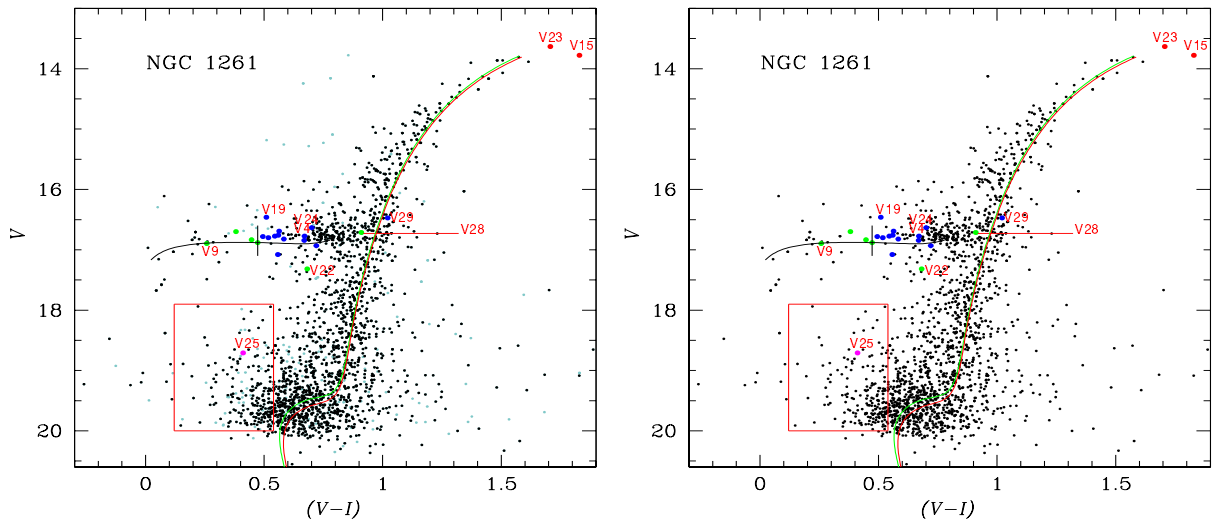

Fig. 4. Colour-magnitude diagram of NGC 1261. In the left panel, black and light blue symbols are used to distinguish between cluster members and non-members. The right panel displays only the cluster members. On the HB, blue and green symbols stand for RRab and RRc stars. Red and pink symbols represent SR and SX Phe stars. We searched for new SX Phe variables within the blue straggler region defined as the red box and found none. Isochrones and ZAHB are from the models of VandenBerg et al. (2014) for [Fe/H]=-1.4, Y=0.25 and [α/Fe]=+0.4 for 10 and 11 Gyr, and have been shifted to a distance of 17.2 kpc, and a reddening $E(B-V)$=0.01. The colour figure can be viewed online.

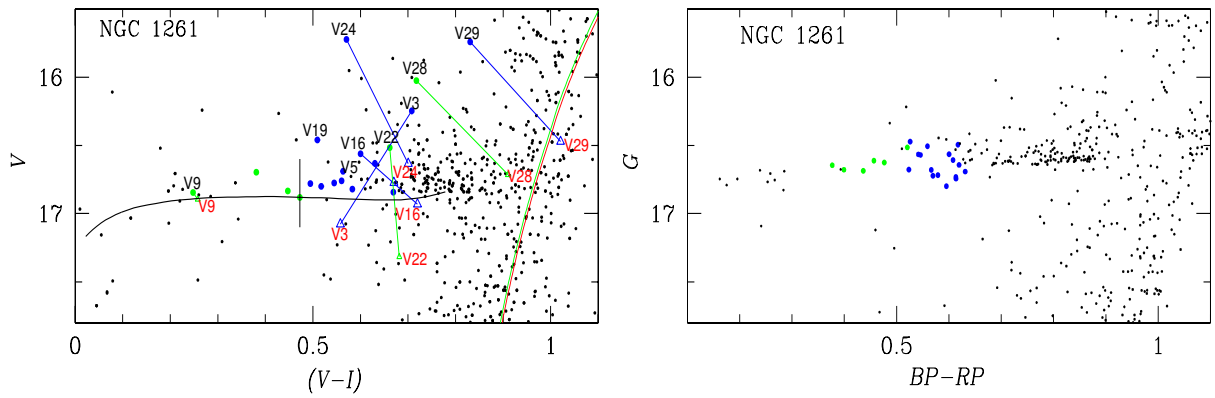

Fig. 5. Expansion of the HB branch of NGC 1261. The left panel shows the HB region built from the *VI* indices of this work. Labelled stars are those with more than one Gaia DR2 source within their PSF. Their corrected positions in the CMD are represented by open triangles and labelled with red numbers, see § 3.1 for details. The vertical black line is the empirical position of the red-edge first-overtone instability strip (FORE), defined by Arellano Ferro et al. (2016). (See the discussion in § 6 and § 9). The right panel shows the HB region built from the Gaia DR2 photometric indices. With the exception of the peculiar stars discussed in § 3.1 the resulting distribution of the RR Lyrae stars is comparable in both panels. The colour figure can be viewed online.

estimation was derived of the correction to be applied to our observed (combined) V and I magnitudes. This also enabled us to estimate the amplitude corrections.

In Table 4 we list the variable stars with two Gaia sources within their PSF. We used the variability flag in Gaia DR2 to identify the variable component when available; for stars without variability flag (V17, V24 and V29) we analysed their positions in the CMD with Gaia DR2 magnitudes and colours to decide which is the variable and which is the contaminant. Their Gaia magnitudes were transformed into the Johnson-Kron-Cousins photometric system (V_{Gaia} , I_{Gaia} and $V_{Gaia} - I_{Gaia}$), and the combined magnitudes of the pair, V_{mix} and I_{mix}, were calculated. The differences between the magnitude of

TABLE 3

DATA OF VARIABLE STARS IN NGC 1261 IN THE FoV OF OUR IMAGES

Star ID	Type	$< V >$ (mag)	$< I >$ (mag)	A_V (mag)	A_I (mag)	P (days)	$\mathrm{HJD}_{\mathrm{max}}$ + 2450000	α (J2000.0)	δ (J2000.0)	Gaia DR2 ID
V2 *Bl*	RRab	16.780	12.285	1.16	0.76	0.585730	8095.6967	03:12:11.28	−55:12:22.0	4733794790512123904
V3	RRab	16.248	15.540	0.65	0.30	0.537003	8439.8438	03:12:21.78	−55:13:50.7	4733793764014756224
V4	RRab	16.633	16.002	1.10	0.61	0.492876	8376.7150	03:12:18.56	−55:13:28.4	4733794519928245888
V5	RRab	16.690	16.127	0.96	0.64	0.513313	8012.7930	03:12:11.93	−55:13:01.9	4733794588651585664
V6 *Bl*	RRab	16.759	16.199	0.94	0.62	0.564100	8335.8557	03:12:25.05	−55:13:08.6	4733793867093968896
V7	RRc	16.835	16.388	0.47	0.32	0.333546	8095.5598	03:11:58.44	−55:10:37.3	4733797852825688704
V8	RRab	16.283	–	0.86	–	0.538204	8012.8146	03:12:00.44	−55:15:16.4	4733700580405300480
V9	RRc	16.846	16.598	0.58	0.41	0.297221	8019.6966	03:12:20.40	−55:13:35.3	4733794519928956800
V10	RRab	16.800	16.283	1.06	0.77	0.583374	8364.7012	03:12:21.99	−55:11:45.9	4733794726089585664
V11	RRab	16.843	16.174	0.39	0.26	0.662171	8335.9157	03:12:05.50	−55:11:27.7	4733794859231637376
V12	RRab	16.821	16.238	0.49	0.32	0.610285	8095.6920	03:12:26.15	−55:12:45.8	4733794657370122880
V13	RRc	16.698	16.317	0.45	0.24	0.337568	8019.7891	03:12:07.01	−55:14:33.1	4733700713548568832
V14 *Bl*	RRab	16.775	16.228	1.23	0.73	0.573977	8378.7791	03:12:09.75	−55:14:07.6	4733700717844254080
V15	SR	13.778	11.948	–	–	–	8007.7702	03:12:02.50	−55:10:48.1	4733797814168962304
V16 *Bl*	RRab	16.561	15.961	0.67	0.56	0.526160	8469.6225	03:12:13.90	−55:13:12.9	4733794588651555584
V17[1]	RRab	–	–	–	–	0.511631	7986.8406	03:12:15.50	−55:12:36.2	4733794588651549824
V19 *Bl*	RRab	16.461	15.951	0.84	0.58	0.653738	8376.7652	03:12:18.19	−55:12:44.7	4733794691727354624
V20[1]	RRab	–	–	–	–	–	–	03:12:19.31	−55:13:00.4	4733794623011123200
V21	RRc	16.881	16.408	0.54	0.34	0.336180	8439.8209	03:12:14.47	−55:12:31.3	4733794588651163648
V22	RRc	16.516	15.855	0.45	0.18	0.302567	8033.8565	03:12:16.49	−55:13:38.1	4733794519931924224
V23	SR	13.632	11.926	–	–	–	8055.6833	03:12:15.69	−55:12:40.7	4733794588651583616
V24	RRab	15.724	15.153	0.32	0.18	0.624395	8376.6983	03:12:14.43	−55:13:34.8	4733794554291694592
V25	SX Phe	18.710	18.300	0.25	0.18	0.056503	8033.7103	03:12:17.17	−55:11:22.7	4733794932246020480
V26[1]	SX Phe	–	–	–	–	–	–	03:12:17.05	−55:12:43.9	4733794588651476224
V27[1]	SR	–	–	–	–	–	–	03:12:14.63	−55:13:06.2	4733794588651284992
V28	RRc	16.025	15.285	0.25	0.11	0.287349	7986.7667	03:12:13.53	−55:13:00.8	4733794588651177344
V29 *Bl*	RRab	15.742	14.911	0.29	0.10	0.598775	7986.8960	03:12:13.05	−55:13:20.5	4733794554291844352
V30[1]	SX Phe	–	–	–	–	–	–	03:12:16.58	−55:12:54.0	4733794588648149248
V31	EC	–	–	–	0.30	0.052493	8439.8246	03:12:18.70	−55:14:16.0	4733794519931172608

Bl: RR Lyrae with Blazhko effect.
[1]Star not resolved in our images.

the variable component and the combined magnitude of the pair, ΔV and ΔI, were computed; the corrected positions are represented by triangles in the left panel of Figure 5 and labelled with red numbers. The corrected amplitudes due to the presence of the neighbour star (Amp V and Amp I) were also calculated, and are represented by colour symbols and vertical displacements in the Bailey diagram, discussed below in § 6. It can be seen in that diagram that, after the corrections of the amplitudes, most stars have moved much closer to the expected locus for this OoI type cluster.

The persistent peculiar positions of some variables in the CMD make suspicious their membership status in the cluster, or perhaps a serious light pollution by neighbouring stars is corrupting our photometry for these specific objects. In the right panel of Figure 5, we reproduced the HB of the cluster using the Gaia DR2 photometric indices. It is rewarding to see that all RR Lyrae stars fall properly on the HB, which also indicates that the selection of the true variable, performed in Table 4 for those stars contaminated by a secondary Gaia source, was correct. This figure also shows that the distribution of modes on the HB is neatly segregated, a property that will be discussed later in the paper.

We can conclude that all known variables are most likely cluster members, and that our photometry for these stars, namely V3, V16, V19, V24, V28 and V29 is seriously contaminated by an unseen, close, well within the PSF, neighbour.

We note that the two SR V15 and V23, are members; regarding the three SX Phe, V25 lies in the blue straggler region and seems a likely member, V26 has no values for proper motion and V30 is definitely not a member. The latter two were not detected in our photometry. Hence, our calculations of the physical parameters will be restricted to the non-peculiar stars and will be described below.

3.2. *Searching for New Variables*

Since prolonged time-series have proven successful to identify new variables, we have performed a systematic search for them with the few strategies discussed below.

TABLE 4

VARIABLE STARS WITH TWO GAIA DR2 SOURCES WITHIN THEIR PSF*

VAR	Gaia DR2 ID	G (mag)	$G_{BP}-G_{RP}$ (mag)	V_{Gaia} (mag)	I_{Gaia} (mag)	$V_{Gaia}-I_{Gaia}$ (mag)	V_{mix} (mag)	ΔV (mag)	I_{mix} (mag)	ΔI (mag)	Amp V (mag)	Amp I (mag)
V3	4733793764014756224	16.6773	0.5234	16.746	16.295	0.451	15.91	0.83	15.32	0.98	1.39	0.74
V3	4733793764014757248	16.4500	0.8248	16.591	15.883	0.708	–	–	–	–	–	–
V4	4733794519928245888	16.5663	0.5417	16.638	16.172	0.467	16.50	0.14	16.07	0.10	1.26	0.67
V4	4733794519931768192	18.7558	–	18.773	18.735	0.038	–	–	–	–	–	–
V9	4733794519928956800	16.6788	0.3993	16.727	16.377	0.350	16.67	0.05	16.34	0.04	0.61	0.43
V9	4733794519928957056	19.9313	–	19.949	19.910	0.038	–	–	–	–	–	–
V16	4733794588651555584	16.5656	0.6003	16.650	16.134	0.516	16.28	0.37	15.88	0.25	–	–
V16	4733794588651555840	17.6072	–	17.625	17.586	0.038	–	–	–	–	–	–
V17	4733794588651549824	16.6079	0.6079	16.694	16.172	0.522	15.76	0.93	15.14	1.03	–	–
V17	4733794588651550080	16.2219	0.7993	16.356	15.670	0.686	–	–	–	–	–	–
V22	4733794519931924224	16.6257	0.4764	16.686	16.273	0.413	15.89	0.80	15.49	0.78	0.91	0.37
V22	4733794519931924352	16.5920	0.6806	16.592	16.217	0.375	–	–	–	–	–	–
V24	4733794554291694592	16.4950	0.6173	16.583	16.053	0.530	15.67	0.91	15.27	0.78	0.73	0.36
V24	4733794554291623424	16.2512	0.3297	16.290	15.996	0.294	–	–	–	–	–	–
V27	4733794588651284992	16.5018	0.5269	16.571	16.117	0.454	16.33	0.24	15.94	0.17	–	–
V27	4733794588651285376	18.0489	–	18.067	18.028	0.038	–	–	–	–	–	–
V28	4733794588651177344	16.5151	0.5204	16.583	16.134	0.449	15.89	0.69	15.62	0.52	0.48	0.18
V28	4733794588651552256	16.6861	–	16.704	16.665	0.038	–	–	–	–	–	–
V29	4733794554291844352	16.5704	0.5458	16.588	16.550	0.038	15.92	0.73	15.64	0.54	–	–
V29	4733794554291843840	16.6775	–	16.695	16.657	0.038	–	–	–	–	–	–

*For every pair, the Gaia DR2 source in the first line is the variable and the one in the second line is the contaminant. See § 3.1 for details.

On the CMD of NGC 1261, we isolated all stars contained in regions where it is common to find variable stars, e.g. near the instability strip (IS) in the horizontal branch (HB), the blue straggler region (BS) and near the tip of the red giant branch (TRGB). We analysed the light curves of the stars in those regions and looked for variability by determining their period (if any), using the program PERIOD04 (Lenz & Breger 2005) or the string-length method (Burke et al. 1970; Dworetsky 1983); then, we plotted their apparent magnitudes with respect to their phase. For long-term variables, the magnitude is plotted as a function of heliocentric Julian day in search for hints of variability. This procedure recovered all known variables, but we found no new ones in our data.

Another method consists in the detection of variations of PSF-like peaks in stacked residual images, from which we can see the variable stars blink. Again, all previous known variables were detected, but no new variables emerged.

3.3. *About the RR Lyrae Stars from Gaia DR2 in the Field of NGC 1261*

In their catalogue of RR Lyrae stars identified via the Specific Object Study pipeline in Gaia DR2 all over the sky, Clementini et al. (2019) report 21 RR Lyrae stars within a radius of 20 arcmin around NGC 1261. Eighteen of these are known RR Lyrae stars listed in the CVSGC. Two stars, well in the outskirts of that field, (Gaia DR2 sources 4734551739843543808 and 4733801701116515200), are not members according to the method of Bustos Fierro & Calderón (2019) and are not in the field of our observations. A third star near the cluster core (Gaia DR2 source 4733794519931744000), categorised by Clementini et al. (2019) as an RRc star, is present in our light curve collection. We identified it as C1 in the chart of Figure 7, but we found no variations. The star, with mean magnitudes V=16.35 and I=15.63, lies somewhat above the red clump. Thus, we do not confirm it as an RRc star.

For clarification, we offer in Figure 7 an identification chart of all variables reported in the CVSGC. The SX Phe stars V26 and V30, although identified according to the coordinates in the CVSGC, were not resolved in the photometry of the present study.

4. BAILEY DIAGRAM AND OOSTERHOFF TYPE

The period-amplitude or Bailey diagram for RR Lyrae stars is shown in Figure 6 for the *VI* bandpasses. The periods and amplitudes are listed in Table 3. In most cases, we took the amplitudes cor-

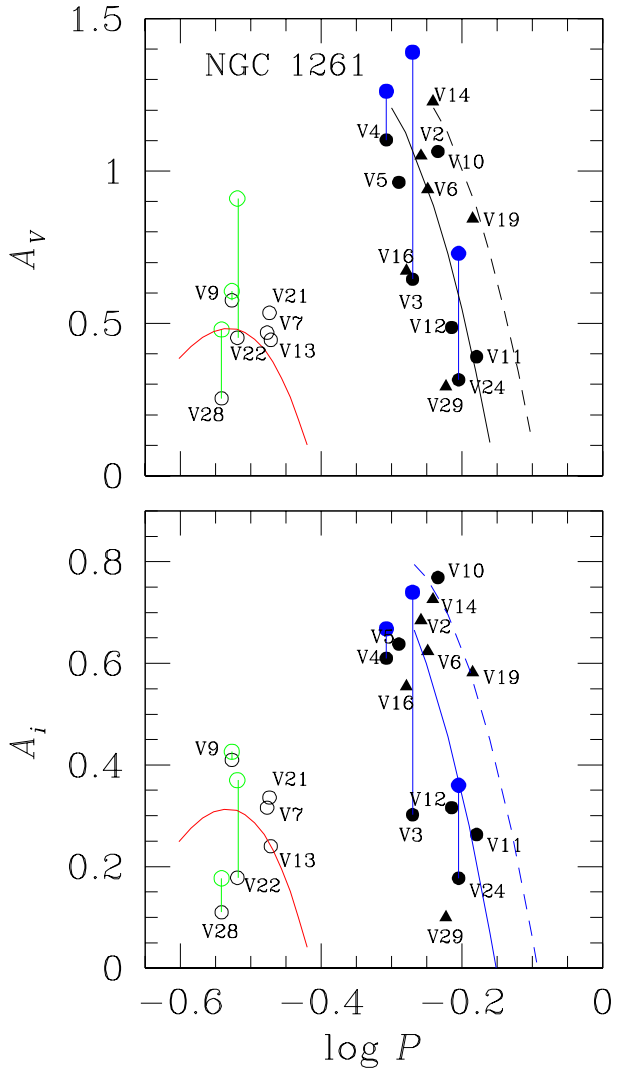

Fig. 6. Period-Amplitude diagram for NGC 1261. The amplitudes of a few variables have been corrected for the presence of an unresolved neighbour. These are plotted with green and blue symbols for RRc and RRab stars, respectively. Triangles are used for Blazhko variables. The distribution of stars is characteristic of Oo I type clusters. See § 3.1 and § 4 for details. The colour figure can be viewed online.

responding to the best fit provided by the Fourier decomposition of the light curves. In cases where the light curve showed Blazhko effect, the maximum amplitude was measured and the star was plotted with a triangular marker. The continuous and dashed black lines in the top panel of Figure 6 are the loci for unevolved and evolved stars according to Cacciari et al. (2005). The red parabolas were calculated by Arellano Ferro et al. (2015) from a sample of RRc stars in five OoI clusters, avoiding Blazhko variables. In the bottom panel, the blue solid and segmented loci for unevolved and evolved stars, respectively, are taken from Kunder et al. (2013).

As noted in § 3.1, a few variables are clearly unresolved from very close neighbours. In these cases, the amplitudes were corrected using the individual magnitudes of the components listed in Table 4. The corrected amplitudes are indicated in Figure 6 by green and blue symbols for RRc and RRab stars, respectively. It is rather clear that the amplitude corrections help sustain the fact that the distribution of stars concentrates around the unevolved sequences, as expected for Oo I type clusters.

5. COMMENT ON THE CLUSTER REDDENING

While this cluster is far away from the Galactic disk, and a very low reddening has been assigned to it, it is always a good exercise to calculate the reddening by an independent method. Individual reddenings for RRab stars can be estimated using the colour curve near minimum. Proposed originally by Sturch (1966), the method has now been calibrated in the *VI* passbands by Guldenschuh et al. (2005), who concluded that the intrinsic colour $(V-I)_0$ of RRab stars curves at phases 0.5-0.8, is 0.58 ± 0.02. We calculated the observed $(V-I)$ at this phase range in our light curves and estimated individual values of $E(V-I)$, the average of which, converted to $E(B-V) = E(V-I)/1.259$ is 0.055 ± 0.051, i.e., nearly zero, and in agreement with the interstellar reddening of $E(B-V) = 0.01$ given by the calibrations of Schlafly & Finkbeiner (2011) and Schlegel et al. (1998). In what follows we shall adopt $E(B-V) = 0.01$.

6. RR LYRAE STARS: [Fe/H] AND M_V FROM LIGHT CURVE FOURIER DECOMPOSITION

Fourier decomposition of the light curves and the use of empirical calibrations enable us to estimate some key physical stellar parameters. The Fourier series to mathematically describe the light curve is of the form:

$$m(t) = A_0 + \sum_{k=1}^{N} A_k \cos(\frac{2\pi}{P} k(t-E_0) + \phi_k)\,, \quad (3)$$

where $m(t)$ is the magnitude at time t, P is the period of pulsation, and E_0 is the epoch. When calculating the Fourier parameters, we used a least-squares approach to estimate the best fit for the amplitudes A_k and phases ϕ_k of the light curve components. The phases and amplitudes of the harmonics

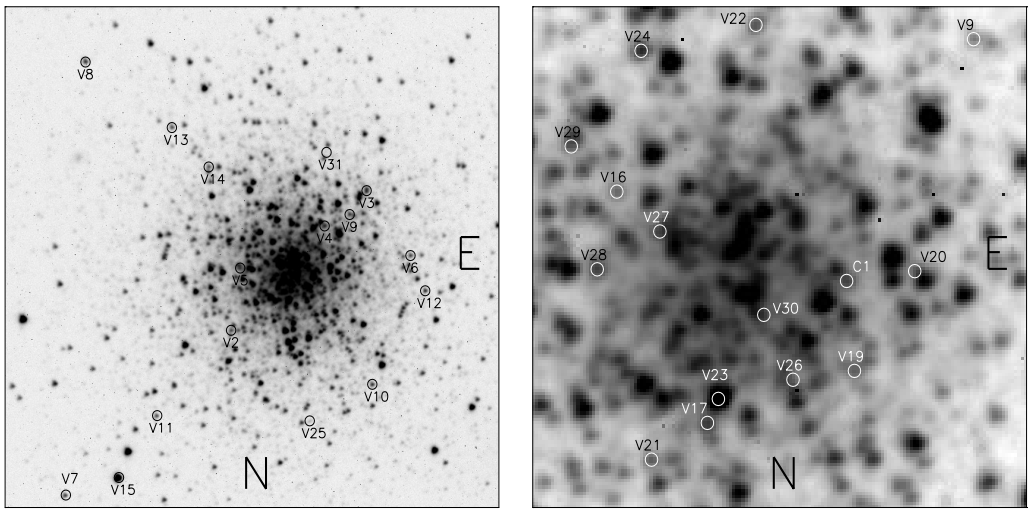

Fig. 7. Identification charts of all known variables in NGC 1261. The field of the left chart is $5.4' \times 5.4'$, and the cluster core on the right chart is $1.3' \times 1.3'$. The star labelled C1 is the one listed as an RR Lyrae by Clementini et al. (2019), but in this work it is found to be non-variable (cf. § 3.3).

TABLE 5

FOURIER COEFFICIENTS A_K FOR $K = 0, 1, 2, 3, 4$, AND PHASES ϕ_{21}, ϕ_{31} AND ϕ_{41}, FOR RRab AND RRc STARS*

Variable ID	A_0 (V mag)	A_1 (V mag)	A_2 (V mag)	A_3 (V mag)	A_4 (V mag)	ϕ_{21}	ϕ_{31}	ϕ_{41}
				RRab stars				
V2	16.788(4)	0.331(6)	0.126(6)	0.072(6)	0.029(6)	4.036(59)	8.198(99)	6.147(219)
V6	16.752(2)	0.305(4)	0.146(4)	0.098(3)	0.070(4)	3.910(33)	8.215(51)	6.205(68)
V10	16.810(3)	0.377(4)	0.189(3)	0.128(4)	0.077(4)	3.936(27)	8.255 (39)	6.191(59)
V11	16.837(3)	0.147(4)	0.060(3)	0.028(4)	0.011(4)	4.050(78)	8.587 (139)	7.709(344)
V12	16.816(2)	0.177(3)	0.070(3)	0.034(3)	0.018(3)	4.406(48)	9.254(90)	7.522(150)
V14	16.775(3)	0.368(5)	0.182(4)	0.154(5)	0.088(5)	4.079(39)	8.369 (51)	6.378(75)
				RRc stars				
V7	16.810(3)	0.181(4)	0.011(4)	0.019(4)	0.008(4)	4.665(31)	4.415(201)	2.409(509)
V9	16.846(1)	0.285(2)	0.052(2)	0.028(2)	0.028(2)	4.749(37)	2.734(64)	1.485(67)
V13	16.698(2)	0.222(3)	0.026(3)	0.013(3)	0.008(2)	4.792(114)	3.815(206)	2.681(318)
V21	16.881(1)	0.262(2)	0.022(2)	0.023(2)	0.006(2)	4.795(88)	4.115(88)	2.729(347)

*The numbers in parentheses indicate the uncertainty of the last decimal places.

in equation 3, i.e. the Fourier parameters, are defined as $\phi_{ij} = j\phi_i - i\phi_j$, and $R_{ij} = A_i/A_j$.

This approach has been regularly used for RR Lyrae stars in a large number of clusters (e.g., Arellano Ferro et al. (2018a); Deras et al. (2019) and references therein). To avoid a lengthy repetition, we refer the reader to § 4 of Deras et al. (2019) for the specific calibrations. Particularly, their equations 4 and 5 describe the calibrations for RRab stars of Jurcsik & Kovács (1996) and Kovács & Walker (2001), which render values of [Fe/H] and M_V, with standard deviations of 0.14 dex and 0.04 mag respectively, and to equations 6 and 7, that give the calibrations for RRc stars of Morgan et al. (2007) and Kovács & Kanbur (1998) with standard deviations of 0.14 dex and 0.042 mag respectively. We have not included in the calculation of physical parameters those stars that are apparently contaminated by a neighbouring source (cf. § 3.1); since the presence of a neighbour also perturbs the light curve shapes and the Fourier parameters, so that the derived physical parameters become spurious. In Table 5 we list the Fourier parameters, and in Table 6 the corresponding individual physical parameters for the

TABLE 6

PHYSICAL PARAMETERS FROM THE FOURIER FIT FOR RRab AND RRc STARS*

RRab stars							
Star	$[Fe/H]_{ZW}$	$[Fe/H]_{UVES}$	M_V	log T_{eff}	$\log(L/L_\odot)$	$M/M_\odot$	$R/R_\odot$
V2	−1.46(9)	−1.37(10)	0.570(9)	3.811(25)	1.672(3)	0.70(21)	5.49(2)
V6	−1.49(5)	−1.40(5)	0.604(5)	3.809(10)	1.658(3)	0.67(8)	5.46(1)
V10	−1.53(4)	−1.44(4)	0.517(6)	3.810(10)	1.693(2)	0.70(8)	5.66(2)
V11	−1.51(13)	−1.43(14)	0.600(6)	3.790(39)	1.660(2)	0.67(31)	5.98(2)
V12	−0.69(9)**	−0.67(4)**	0.635(4)	3.813(18)	1.646(2)	0.55(12)	5.29(1)
V14	−1.39(5)	−1.28(5)	0.562(7)	3.812(11)	1.675(3)	0.66(9)	5.49(2)
Weighted Mean	−1.48	−1.38	0.590	3.810	1.664	0.66	5.51
$\sigma_{\bar{x}}$	± 0.05	± 0.05	± 0.042	± 0.008	± 0.006	± 0.05	± 0.09
RRc stars							
Star	$[Fe/H]_{ZW}$	$[Fe/H]_{UVES}$	M_V	log T_{eff}	$\log(L/L_\odot)$	$M/M_\odot$	$R/R_\odot$
V7	−1.06(42)	−0.95(32)	0.571(18)	3.869(1)	1.672(7)	0.49(1)	4.21(4)
V9	−1.63(11)	−1.57(13)	0.512(9)	3.866(1)	1.695(4)	0.63(1)	4.37(2)
V13	−1.50(41)	−1.41(44)	0.588(10)	3.864(1)	1.677(4)	0.51(1)	4.47(2)
V21	−1.31(18)	−1.19(17)	0.571(10)	3.866(1)	1.672(4)	0.49(1)	4.25(2)
Weighted Mean	−1.51	−1.38	0.547	3.866	1.681	0.54	4.31
$\sigma_{\bar{x}}$	± 0.29	± 0.29	± 0.014	± 0.001	± 0.005	± 0.03	± 0.05

*The numbers in parentheses indicate the uncertainty on the last decimal places. See § 6 for a detailed discussion.
**Not included in the average of [Fe/H].

stars included in the calculation and the average values. For comparison, we have transformed $[Fe/H]_{ZW}$ on the Zinn & West (1984) metallicity scale into the UVES scale using the equation $[Fe/H]_{UVES} = -0.413 + 0.130\,[Fe/H]_{ZW} - 0.356\,[Fe/H]^2_{ZW}$ (Carretta et al. 2009). It should be noted that the uncertainties we have quoted in Table 6 only represent the internal errors associated to the Fourier fitting procedure, and do not include any systematic errors that may be inherent to the use of the calibrations quoted above to estimate the physical parameters. The standard deviation of the mean $\sigma_{\bar{x}}$, given below the weighted mean physical parameters, is comparable to the standard deviation of the calibrations, and represents a more reliable estimate of the systematic errors in our procedure.

7. PREVIOUS METALLICITY ESTIMATES OF NGC 1261

To our knowledge, no spectroscopic determination of the metallicity of NGC 1261 or of any of its stars has ever been published. Estimations of [Fe/H] based on photometric indices and their calibrations do exist; they use the height above the HB, the slope of the HB, and the intrinsic colour $(B-V)_0$ of the reg-giant branch (RGB) at the HB level. Ferraro et al. (1993) employed these methods and found –1.54±0.4, –1.85±0.2 and –1.26±0.04 respectively, adopting a weighted average −1.4±0.2. The value of [Fe/H] listed in the catalogue of Harris (1996) (2010 edition) is −1.27, which corresponds to the compiled average of Carretta et al. (2009) in their UVES scale, which is equivalent to -1.4 ± 0.2 in the Zinn-West scale.

Our results, based on the Fourier decomposition and calibrations discussed in § 6 and listed in Table 6 are, for the RRab stars: $[Fe/H]_{zw} = -1.48 \pm 0.05$ or $[Fe/H]_{UVES} = -1.38 \pm 0.05$, and for the RRc stars: $[Fe/H]_{zw} = -1.51 \pm 0.29$ or $[Fe/H]_{UVES} = -1.38 \pm 0.29$. Since different empirical relations have been used to estimate the metallicities of the RRab and RRc stars, there may be some systematic offset between the metallicity estimates for the two types of variable. We should note the peculiarly large value of [Fe/H] found for star V12. The reason for this is the anomalously large value of the Fourier parameter ϕ_{31} of 9.254±0.09. Star V12 is among the smallest amplitude and largest period RRab in NGC 1261, and reminds us of the case of star V12 in NGC 6171, whose light curve structure is different from that of other RRab stars (Clement & Shelton 1997), and thus is not suitable for the calculation of [Fe/H] from the Fourier analysis. Although the associated uncertainties of our average values of [Fe/H] are smaller than those of previous determinations, the values are slightly more metal-weak than those published; still, they are rather in agreement, within the given uncertainties.

8. ON THE DISTANCE TO NGC 1261

The solar distance to NGC 1261 recorded in the catalogue of Harris (1996) (2010 edition) is 16.3 kpc, calculated from the estimated mean $V = 16.70 \pm 0.05$ level HB of Ferraro et al. (1993), adopting a [Fe/H]-M_V relation with [Fe/H] and $E(B-V) = 0.01$. Our Fourier estimates of M_V and $\langle V \rangle$ for RRab and RRc stars lead to mean distances of 17.2 ± 0.4 and 17.6 ± 0.7 kpc respectively. Considering that the scatter of the 6 RRc stars in the CMD is large, and that we only used the RRab closer to the ZAHB, we should probably ignore the distance obtained from the RRc stars, in which case our best estimate of the distance to the cluster from this method is 17.2 ± 0.4 kpc. In Figure 4 we have shifted the ZAHB and isochrones to this distance, although, admittedly an eye fit of the HB suggests a brighter ZAHB for a distance of about 16.8 kpc

Another independent method to estimate the distance to the cluster is via the P-L relations of SX Phe stars and of RR Lyrae stars. In the former case, we have calculated M_V of the star V25, the only SX Phe detected in our study, using three versions of the P-L relations from Cohen & Sarajedini (2012), Poretti et al. (2008) and Arellano Ferro et al. (2011), and found 16.1, 15.5 and 15.0 kpc respectively, i.e., all values well below the estimates based on the HB luminosity.

Alternatively, the P-L in the I-band for RR Lyrae stars derived by Catelan et al. (2004); $M_I = 0.471 - 1.132 \log P + 0.205 \log Z$, with $\log Z = [M/H] - 1.765$; $[M/H] = [\mathrm{Fe/H}] - \log(0.638\, \mathrm{f} + 0.362)$ and $\log \mathrm{f} = [\alpha/\mathrm{Fe}]$ (Salaris et al. 1993), was applied to the RRab and RRc stars residing close to the ZAHB in the CMD of Figure 4. From 6 RRab and 4 RRc stars we found an average distance of 16.65 ± 0.27 kpc, which agrees very well with the results obtained from the Fourier light curve decomposition approach. In summary, the best results for the cluster distance are obtained from the Fourier light curve decomposition of the RRab stars that show little scatter near the ZAHB, and the P-L (I) relationship; these methods give an average of 16.7 kpc and an uncertainty between 0.7 and 0.3 kpc, respectively.

9. STRUCTURE OF THE HB AND AGE

NGC 1261 has a very red HB. The HB structure can be characterised by the parameter $\mathcal{L} \equiv (B-R)/(B+V+R) = -0.67$. In the HB region shown in the left panel of Figure 5, built from our VI indices, the RRab and RRc stars appear clearly well segregated by the FORE. This is confirmed in the right panel, built with the Gaia DR2 indices. Figure 8 is an updated version of Figure 9 of Arellano Ferro et al. (2018b) which includes NGC 1261 and a few other clusters. Clearly NGC 1261, like other Oo I clusters with very red HBs like NGC 6171 (M107) and NGC 6362, shows a neat segregation of pulsation modes among the RR Lyrae stars. Other Oo I clusters with a similarly red HB where the RRc-RRab distribution is yet to be explored are: NGC 362, Rup 106 and NGC 6712. In Rup 106, however, no RRc stars are known, and NGC 6712 is an interesting borderline case, since either a few RRab are sitting in the either-or region, or the FORE is shifted to the red by only about 0.04 mag (Deras 2019; private communication), which is the uncertainty in the location of the FORE. We have found that in all Oo II clusters the modes are always segregated. Only a few Oo I clusters with $\mathcal{L}$ between 0.0 and 0.7 have been found to have the inter-mode region populated by RRab and RRc stars: NGC 3201, NGC 5904 (M5), NGC 6402 (M14) and NGC 6934.

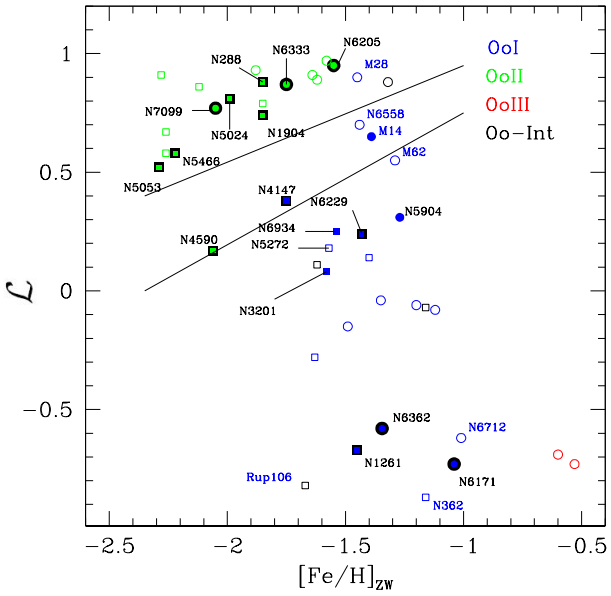

Fig. 8. The HB structure parameter $\mathcal{L}$ as function of [Fe/H]. Circles and squares are used for inner and outer halo clusters, respectively. The black-rimmed symbols represent globular clusters where the fundamental and first overtone modes are well segregated around the FORE, as opposed to filled non-rimmed symbols. The upper and lower solid lines are the limits of the Oosterhoff gap according to Bono et al. (1994). Empty symbols are clusters not yet studied by our group. The colour figure can be viewed online.

Based on Hubble Space Telescope Advanced Camera for Surveys photometry, and using the isochrone fitting between the base of the turnoff and the lower RGB, VandenBerg et al. (2013) concluded that the age of NGC 1261 is 10.75 ± 0.25 Gyr. Since the precision of our photometry, and the dispersion in the CMD near the TO are inadecuate for a subtle discussion of the age of the system, we overplotted on our observed CMD two isochrones for 10.0 and 11.0 Gyr from the *Victoria−Regina* stellar models of VandenBerg et al. (2014), for [Fe/H]=−1.4, Y=0.25 and [α/Fe]= 0.4. The isochrones and the ZAHB, shifted to a distance of 17.2 kpc and $E(B-V) = 0.01$. We can see (Figure 4) that the current data set is consistent with the age of the cluster determined by VandenBerg et al. (2013).

10. SUMMARY AND DISCUSSION

Almost all photometric studies of NGC 1261, both in the photographic plate and CCD eras, dedicated their efforts to the overall study of the cluster, its CMD structure and the estimation of its age. Only a few studies, since the pioneering works of Fourcade & Laborde (1966) and Laborde & Fourcade (1966) when the first variables in this cluster were discovered, have been devoted to the study of the cluster variable stars population. Specifically, in the CCD era and to the best of our knowledge, only the works of Salinas et al. (2007) and Salinas et al. (2016) have focused on the study of the variable stars in crowded environments, via the differential image approach (DIA). Yet these authors point out the extreme difficulty of transforming the relative fluxes rendered by DIA, into the astrophysically more useful magnitudes of a given calibrated system. We must add that time-series do not always fully cover the light curves in the phase diagrams. The present study is the first one, as far as we know, that reports complete light curves in the *VI* filters, and use them to derive physical quantities from the variable star families of NGC 1261. This approach also allows our best estimate of the cluster distance to be 17.2 ± 0.4 kpc. Individual radii and masses for the RR Lyrae stars are also reported.

A thorough multi-approach search in a region of about $10' \times 10'$ around the cluster revealed no new variable stars within the limitations of our CCD photometry. The Fourier decomposition technique was employed to derive the mean values $[\mathrm{Fe/H}]_{\mathrm{UVES}} = -1.38 \pm 0.05$ and $[\mathrm{Fe/H}]_{\mathrm{UVES}} = -1.38 \pm 0.29$ for the RRab and RRc stars, respectively. These values are given in the high dispersion spectroscopic scale established by Carretta et al. (2009). These two estimations should be considered independent, as they come from totally unrelated calibrations. The above results show a cluster slightly more metal poor and distant than generally accepted (e.g., Harris 1996).

The distribution of cluster member RR Lyrae stars on the HB shows a rather clear split of modes about the FORE, as seems to be the case for another two or perhaps three globulars with very red HB, namely, NGC 6171, NGC 6362 and probably NGC 6712. Two more clusters with a very red HB are NGC 362 and Rup 106, but no detailed study of the distribution of modes exists for NGC 362, and no RRc stars are known in Rup 106.

We are grateful to Cecilia Quiñones for her proficient help during the acquisition of the observations in Bosque Alegre. This project was partially supported by DGAPA-UNAM (Mexico) via grant IN104917-19. We have made extensive use of the SIMBAD, ADS services.

REFERENCES

Arellano Ferro, A., Ahumada, J. A., Bustos Fierro, I. H., Calderón, J. H., & Morrell, N. I. 2018a, AN, 339, 183
Arellano Ferro, A., Figuera Jaimes, R., Giridhar, S., et al. 2011, MNRAS, 416, 2265
Arellano Ferro, A., Luna, A., Bramich, D. M., 2016, Ap&SS, 361, 175
Arellano Ferro, A., Mancera Piña, P. E., Bramich, D. M., et al. 2015, MNRAS, 452, 727
Arellano Ferro, A., Rojas Galindo, F. C., Muneer, S., & Giridhar, S. 2018b, RMxAA, 54, 325
Bartolini, C., Grilli, F., & Robertson, J. W. 1971, IBVS, 594, 1
Bono, G., Caputo, F., & Stellingwerf, R. F. 1994, ApJ, 423, 294
Bramich, D. M. 2008, MNRAS, 386, L77
Bramich, D. M., Bachelet, E., Alsubai, K. A., Mislis, D., & Parley, N. 2015, A&A, 577, A108
Bramich, D. M., Figuera Jaimes, R., Giridhar, S., & Arellano Ferro, A. 2011, MNRAS, 413, 1275
Bramich, D. M. & Freudling, W. 2012, MNRAS, 424, 1584
Bramich, D. M., Horne, K., Albrow, M. D., et al. 2013, MNRAS, 428, 2275
Burke, Edward W., J., Rolland, W. W., & Boy, W. R. 1970, JRASC, 64, 353
Bustos Fierro, I. H. & Calderón, J. H. 2019, MNRAS, 488, 3024
Cacciari, C., Corwin, T. M., & Carney, B. W. 2005, AJ, 129, 267
Caputo, F., Castellani, V., & Tornambe, A. 1978, A&A, 67, 107
Carretta, E., Bragaglia, A., Gratton, R., D'Orazi, V., & Lucatello, S. 2009, A&A, 508, 695

Catelan, M., Pritzl, B. J., & Smith, H. A. 2004, ApJS, 154, 633
Clement, C. M., Muzzin, A., Dufton, Q., et al. 2001, AJ, 122, 2587
Clement, C. M. & Shelton, I. 1997, AJ, 113, 1711
Clementini, G., Ripepi, V., Molinaro, R., et al. 2019, A&A, 622, A60
Cohen, R. E. & Sarajedini, A. 2012, MNRAS, 419, 342
Deras, D., Arellano Ferro, A., Lázaro, C., et al. 2019, MNRAS, 486, 2791
Dworetsky, M. M. 1983, MNRAS, 203, 917
Ferraro, F. R., Clementini, G., Fusi-Pecci, F., Vitiello, E., & Buonanno, R. 1993, MNRAS, 264, 273
Fourcade, C. R. & Laborde, J. R. 1966, Atlas y Catálogo de Estrellas Variables en Cúmulos globulares al sur de -29°, Cordoba, Argentina
Gaia Collaboration, Brown, A. G. A., Vallenari, A., et al. 2018, A&A, 616, A1
Goldsbury, R., Richer, H. B., Anderson, J., et al. 2010, AJ, 140, 1830
Guldenschuh, K. A., Layden, A. C., Wan, Y., et al. 2005, PASP, 117, 721
Harris, W. E. 1996, AJ, 112, 1487
Jurcsik, J. & Kovács, G. 1996, A&A, 312, 111
Kovács, G. & Kanbur, S. M. 1998, MNRAS, 295, 834
Kovács, G. & Walker, A. R. 2001, A&A, 374, 264
Kunder, A., Stetson, P. B., Cassisi, S., et al. 2013, AJ, 146, 119
Laborde, J. R. & Fourcade, C. R. 1966, MmSAI, 37, 251
Lenz, P. & Breger, M. 2005, CoAst, 146, 53
Morgan, S. M., Wahl, J. N., & Wieckhorst, R. M. 2007, MNRAS, 374, 1421
Poretti, E., Clementini, G., Held, E. V., et al. 2008, ApJ, 685, 947
Salaris, M., Chieffi, A., & Straniero, O. 1993, ApJ, 414, 580
Salinas, R., Catelan, M., Smith, H. A., & Pritzl, B. J. 2007, IBVS, 5744
Salinas, R., Contreras Ramos, R., Strader, J., et al. 2016, AJ, 152, 55
Schlafly, E. F. & Finkbeiner, D. P. 2011, ApJ, 737, 103
Schlegel, D. J., Finkbeiner, D. P., & Davis, M. 1998, ApJ, 500, 525
Stetson, P. B. 2000, PASP, 112, 925
Sturch, C. 1966, ApJ, 143, 774
VandenBerg, D. A., Bergbusch, P. A., Ferguson, J. W., & Edvardsson, B. 2014, ApJ, 794, 72
VandenBerg, D. A., Brogaard, K., Leaman, R., & Casagrande, L. 2013, ApJ, 775, 134
Wehlau, A. & Demers, S. 1977, A&A, 57, 251
Wehlau, A., Flemming, T., Demers, S., & Bartolini, C. 1977, IBVS, 1361
Zhang, T., Ramakrishnan, R., & Livny, M. 1996, BIRCH: An Efficient Data Clustering Method for Very Large Databases, ed. J. Widom, in Proceedings of the 1996 ACM SIGMOD International Conference on Management of Data, 103
Zinn, R. & West, M. J. 1984, ApJS, 55, 45

J. A. Ahumada, I. H. Bustos Fierro, and J. H. Calderón: Universidad Nacional de Córdoba, Observatorio Astronómico, Córdoba, Argentina (ivanbf, calderon@oac.unc.edu.ar), (javier.ahumada@unc.edu.ar).
A. Arellano Ferro: Instituto de Astronomía, Universidad Nacional Autónoma de México, Apartado Postal 70-264, México, CDMX, C.P. 04510 (armando@astro.unam.mx).
J. H. Calderón: Consejo Nacional de Investigaciones Científicas y Técnicas (CONICET), Buenos Aires, Argentina (calderon@oac.unc.edu.ar).

Revista Mexicana de Astronomía y Astrofísica, **55**, 351–361 (2019)

DOI: https://doi.org/10.22201/ia.01851101p.2019.55.02.19

A NEW METHOD FOR ACTIVELY TUNING FBG'S TO PARTICULAR INFRARED WAVELENGTHS FOR OH EMISSION LINES SUPPRESSION

R. Benítez-Álvarez[1], F. Martínez-Piñón[1], and V. G. Orlov[2]

Received February 15 2019; accepted August 14 2019

ABSTRACT

This paper presents the conceptual design for a new method for the suppression of OH emission lines at near-infrared (NIR) wavelengths by actively adjusting the aperiodic fiber optic Bragg gratings tension. First, we prepared an experimental study in which we simulated an OH emission line using a semiconductor laser at 1548.43 nm and a commercial FBG, with a Bragg wavelength of 1547.76 nm. We demonstrated that the grating Bragg wavelength can be adjusted by controlling the linear deformation of the fiber with a force in the range of 0 to 53.88 gf (0.528 N) that provides a sensitivity of 0.014 nm g^{-1}. Second, we proposed the design of a system connected to the telescope instrumentation, with the different stages that would allow monitoring the suppression of emission lines.

RESUMEN

Este trabajo presenta el diseño conceptual de un nuevo método para la supresión de líneas de emisión de OH en longitudes de onda del infrarrojo cercano (NIR) mediante el ajuste activo de la tensión de rejillas Bragg de fibra óptica aperiódicas. En primer lugar, realizamos un estudio experimental en el que simulamos una línea de emisión de OH utilizando un láser semiconductor a 1548.43 nm y una FBG de uso comercial, con una longitud de onda de Bragg de 1547.76 nm. Demostramos que la longitud de onda de Bragg de la rejilla puede ajustarse controlando la deformación lineal de la fibra con una fuerza en el intervalo de 0 a 53.88 gf (0.528 N) que proporciona una sensibilidad de 0.014 nm g^{-1}. En segundo lugar, proponemos el diseño de un sistema conectado a la instrumentación del telescopio con las distintas etapas que permitirían monitorear la supresión de las líneas de emisión.

Key Words: atmospheric effects — infrared: general — instrumentation: photometers — methods: numerical

1. INTRODUCTION

Future advances in astronomy depend on the ability to perform deep observations at near infrared (NIR) wavelengths. To observe the early universe, for example, the observations must be performed at increasingly longer wavelengths, as the diagnostic optical spectroscopic features become more redshifted (Ellis & Bland-Hawthorn 2008). However, there are also some problems with NIR astronomy, the main concern being the background level. Of particular interest is the 1-2.5 μm region. The dominant NIR infrared background arises from very bright hydroxyl emission (Meinel 1950), resulting from the vibrational decay of an excited OH-radical. Furthermore, the intensity of the OH emission is highly variable, making accurate subtraction very difficult (Davies 2007). Astronomers have searched for a technology to suppress this background signal from OH emission lines. Two of the solutions that have been proposed are: (1) the use of space infrared telescopes such as the James Webb Telescope (Mather 2010) still under construction and with extremely high costs (Witze 2018); and (2) the use of new optical fiber devices that constitute a new discipline known as astrophotonics, which seeks to use photonic technologies within

[1]Centro de Investigación e Innovación Tecnológica CIITEC IPN, México.

[2]Instituto de Astronomía, Universidad Nacional Autónoma de México, México.

fibers (or other waveguides) to perform more complicated functions, not feasible with traditional optics (Bland-Hawthorn & Kern 2009). The use of optical fibers in astronomy dates back to 1980 (Hill et al. 1980), with significant developments through the 80′s and 90′s, such as multi object spectroscopy, integral-field spectroscopy, interferometry and photometry (Parry 1998). The primary use of optical fibers has been mainly to transport light from the telescope to an instrument. Now the application of specialty fibers used in astrophotonics includes multiple notch filters, multi-mode to single-mode converters and frequency combs (Ellis & Bland-Hawthorn 2015).

The astrophotonics solution for OH suppression at NIR wavelengths consists of the use of two innovations: aperiodic fiber Bragg gratings (AFBGs) and photonic lanterns (Ellis & Bland-Hawthorn 2008; Bland-Hawthorn et al. 2004; Ellis et al. 2012; Trinh et al. 2013; Trinh 2013; León-Saval et al. 2005; Birks et al. 2015). AFBGs have the capability to behave as complex multi-notch filters that can suppress hundreds of OH emission lines in the 1,000 to 1,800 nm band at high attenuation ($\approx 30dB$ in transmission) over a large bandpass (200 nm), with low attenuation between the lines ($< 0.2dB$) and a narrow wavelength interval [$\delta\lambda = 0.16nm$] (Bland-Hawthorn et al. 2011). The photonic lantern is a low-loss optical device that connects one multimode core to several cores (e.g. single-mode) (León-Saval et al. 2005; Birks et al. 2015) and provides a mean to capture light from the telescope as a multimode optical fiber, convert n optical modes into the output of n single-mode optical fibers, where the AFBGs are printed, and convert them back again into a multimode optical fiber end to be coupled to the spectrograph. This solution has proved to be very successful to reduce 103 OH emission lines doublets in the $1.47 - 1.7\mu m$ band by a factor of ≈1,000 using seven 50 μm core fibers connected to 19 single mode fibers with two sets of AFBGs each (GNOSIS instrument). However, the results were not as successful as expected in the reduction of the background between the OH lines (Ellis et al. 2012; Trinh et al. 2013). Despite the success of the above technique of OH emission lines reduction, we believe that it can be further improved. We propose in this work an active tension system that reduces in real time the variability of the OH emission lines. We demonstrate the effect experimentally by simulating one OH emission line with a semiconductor laser at 1548.43 nm and its suppression by tension tuning from 0 gf to 54 gf with a commercially available FBG centered at 1547.76 nm. A conceptual design of this real time active tension system is then proposed by means of software, electronics and tension actuators.

2. ATMOSPHERIC OH EMISSION

The complex chemical composition of the upper layers of the atmosphere, rich in molecules of O_2, N_2, NO, CO, CN, CO_2, H_2O, OH and the ionizing effect caused by solar ultraviolet radiation, present a marked dominant emission in the near-infrared (NIR) regions of the electromagnetic spectrum (Schlatter 2009; Rousselot et al. 2000), compared to the infrared emissions of galactic astronomical objects, which in most cases can be on the order of hundreds of times the average brightness of the night sky background (Davies 2007). Particularly relevant are the emissions caused by the vibrational decay of OH located in a thin layer 6-10 km thick in the atmosphere, at a height above sea level of 87 km (Rousselot et al. 2000). These narrow lines show a very compact concentration and are created by the reaction between atomic hydrogen and ozone, providing enough energy to keep the OH populating the vibrational level $X^2\Pi_i$ and quantum number $\nu = 9$ (Anlauf et al. 1968).

The observations made in the year 1999 using the Paranal Hill telescopes and the models proposed for the characterization of these emissions in the region 100-2,264 nm (Moorwood et al. 1999) have allowed us to identify with a good approximation the most representative components of the region comprised between 1,000 - 1,600 nm of the near infrared. However, there is still much to understand about how the emissions of the rest of the molecules in the Earth's atmosphere, combined with the residual brightness of the night sky, contribute to the integrated total brightness that hinders the astronomical observations in the NIR band. The contributions by thermal radiation both of the atmosphere and of the instruments on the Earth's surface, are an additional factor to be extracted in its entirety through appropriate radiatives models (Ellis & Bland-Hawthorn 2008) and which are integrated at the moment of the reduction of the observational data.

In this scenario, it is a challenge to understand the emission in the J and H band of the electromagnetic spectrum between 1,100 nm-1,800 nm, a very bright area attributed in part to the vibrational decay of the OH radical as well as to the emission and dispersion of zodiacal and galactic plane light, the thermal emission of the atmosphere, the thermal emission of the instruments, the thermal emission of the interstellar dust and the microwave emission of

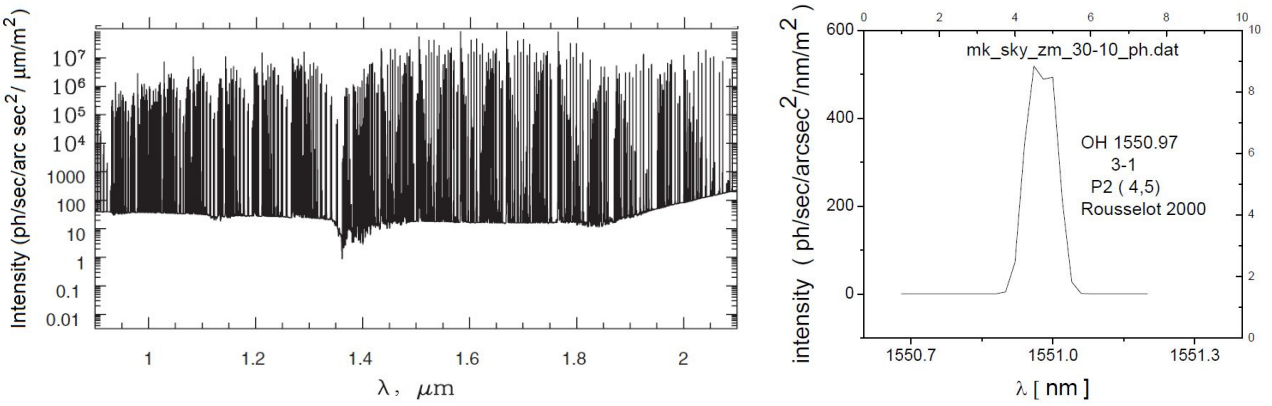

Fig. 1. OH spectrum with the added components of the scattered zodiacal light and thermal emission (Left) (Ellis & Bland-Hawthorn 2008). A typical emission line of the atmospheric OH (Right) (Rousselot et al. 2000; Near-Infrared Gemini Observatory 2015).

the cosmic background. Although there are spectroscopic techniques to subtract them, the difficulty to maintain a low level of brightness in the interlinear regions persists and is significantly compromised when masking techniques are used, dispersing additional brightness in these areas (Maihara et al. 2004).

The line width is caused by a combination of processes inside the atmosphere that contribute to a greater or lesser extent, and of which stand out: the Doppler effect due to the thermal movement of the molecules, which imprints a dominant profile in the line width, typically Gaussian; the collisional and natural effects contribute with a Lorentzian component, giving rise to a convoluted symmetry that is distinguished by the formation of weak lateral wings. To model these effects together under certain thermodynamic considerations typical of the atmospheric layer the Voigt profile model proposed by Ellis and Bland Hawthorn (Ellis & Bland-Hawthorn 2008) is considered to be one of the best approximations to the extremely narrow profile of the OH emission lines. These have been compared with the spectra obtained and cataloged by Rousselot in 2000 (Rousselot et al. 2000). This is the starting point for the understanding of the problem of the spectral reduction of the atmospheric infrared barrier.

The spectrum of Figure 1 (left) shows the "forest" of OH emission lines in the range of 1 - 2 μm plus the components of zodiacal scattered light and thermal emission which are noticeable starting from 1.8 μm (Ellis & Bland-Hawthorn 2008). Figure 1 (right) shows in detail the 1,150.97 nm emission line from the database obtained with the ISAAC instrument of the European Southern Observatory (Near-Infrared Gemini Observatory 2015).

Equation 1 shows the model relationship between the integrated flux V as a function of the collisional cross section σ of the particle, the increased FWHM linewidth γ produced by the molecules collision pressure effect, the central wavelength λ' and the variable wavelength λ.

$$V(\sigma,\gamma,\lambda) = \int_{-\infty}^{\infty} \frac{e^{(-\lambda^2/2\sigma^2)}\gamma}{\sigma\sqrt{2\pi}\pi[(\lambda-\lambda')^2+\gamma^2]} d\lambda' \,. \quad (1)$$

It is very important to model these profiles if the purpose is to design an adequate fiber optic Bragg grating system which can filter with a high performance in the infrared zone, maintaining similar narrow transmission profiles with low power losses, which could contribute to the emission in the interlinea continuum.

3. PROPERTIES OF BRAGG GRATINGS

A fiber Bragg grating (FBG) is a periodic perturbation of the refractive index along the length of a single-mode fiber, which is formed by exposure of the core to an intense optical interference pattern. The perturbation is possible because of the sensitivity to ultraviolet light of the optical fibers doped with germanium (Hill et al. 1978; Hill & Meltz 1997).

The disturbance of the refractive index in the core acquires the shape of a volume structure as shown in Figure 2 which acts as a filter and which allows it to reflect a particular wavelength band according to the design of the period of the grid; this wavelength, called Bragg wavelength, depends directly on the period Λ as well as on the effective refractive index n_{eff} of the core.

$$\lambda_B = 2n_{eff}\Lambda \,. \quad (2)$$

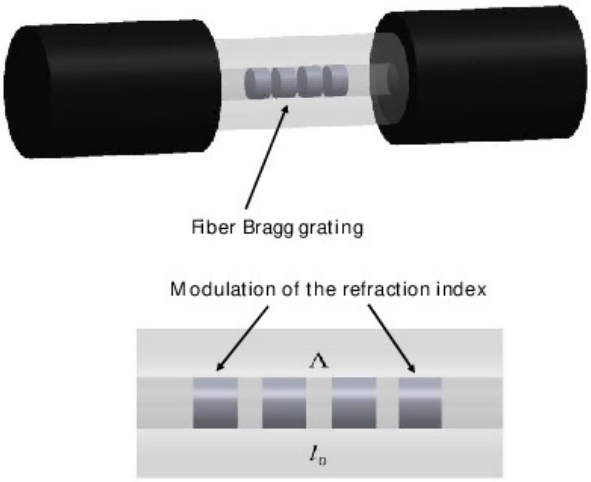

Fig. 2. Effect of the disturbance of the refractive index due to the incidence of ultraviolet radiation on the core of a single-mode optical fiber; the interference of the beam of light causes a regular modulation of the index of refraction.

For a practical grating, we must specify the grating L and the modulation amplitude Δn. The strongest response in the narrowest possible notches occurs in the weak grating limit for which (Bland-Hawthorn et al. 2011)

$$\delta\lambda = \frac{\lambda}{2}\sqrt{\left(\frac{\Delta n}{2n_{eff}}\right)^2 + \left(\frac{\Lambda}{L}\right)^2}, \tag{3}$$

where $\delta\lambda$is the approximate full width half maximum (FWHM) bandwidth of the grating, L/λ is the number of the grating planes. From this equation, the required modulation can be determined ($\Delta n \approx 10^{-4}$) and a minimum grating length could be $L = 50$ mm. The peak reflectivity of the grating rmax is given by:

$$r_{max} = \tanh^2(\zeta L), \tag{4}$$

This peak reflectivity is determined by the grating amplitude ζ (in units of inverse length) and the grating length L. The grating amplitude is related to the induced refractive index modulation Δn along the fiber axis z by:

$$\zeta(z) = \frac{\pi\Delta n(z)}{2\Lambda(n_0 + \langle\Delta n\rangle)}, \tag{5}$$

where z is the distance along the FBG. The variable ζ is the coupling efficiency of the propagating and counter-propagating electric fields and defines the grating strength. The quantity $\langle\Delta n\rangle$ is the average refractive index change within the grating modulation. For a periodic FBG the notch is far from rectangular and has a finite width; the wings of the notch are too strong and they exhibit ringing. The wings can be greatly suppressed, and the notch can be squared off by shaping (apodizing) the upper envelope of the refractive index profile (Bland-Hawthorn et al. 2011).

Figure 3 shows the characterization of a commercially available FBG (Micron Optics os1100) (Micron Optics 2017) done at our laboratory. We used a superluminiscent broad-spectrum diode (SLD1550-A1) from Thorlabs as the source. The reflected Bragg wavelength is observed as a notch in the transmission signal detected by a Yokogawa AQ6370D optical spectrum analyzer. The reflected spectrum shown was calculated.

4. APERIODIC FBGS

A practical OH emission lines suppressing filter is a highly complex grating structure. All parts of the grating contribute with important information to all of the notches. In addition to the refractive index modulation, along the grating length the flexibility in the FBG designs is achieved by incorporating phase variation (Bland-Hawthorn et al. 2011):

$$n(z) = n_0 + \frac{\Delta n(z)}{2}\left[1+\sin\left(\frac{2\pi}{\Lambda}z+\Delta\phi\right)\right], 0 \le z \le L, \tag{6}$$

where z is the physical length along the fiber axis, the term $(2\pi/\Lambda)z$ describes the phase delay at each reflecting plane in the FBG, and the parameter $\Delta\phi$ describes the phase variations (dephasing) with respect to the linear term. The simple grating uses a constant Δn, whereas the apodized grating adopts a "raised cosine" envelope in Δn to suppress the reflections at the extremes of the grating.

A complete discussion of the aperiodic gratings design is highly technical and is discussed in detail elsewhere (Feced et al. 1999; Glaesemann 2017). In summary, the coupled mode equations describing light propagation in an FBG (Feced et al. 1999) must be solved:

$$\begin{aligned} \tfrac{\partial E_b}{\partial z} + i\delta E_b - q(z)E_f = 0, \\ \tfrac{\partial E_b}{\partial z} + i\delta E_b - q(z)E_f = 0, \end{aligned} \tag{7}$$

where E_f and E_b are the amplitudes of the forward and backward propagating fields. Equation (7) constitutes a pair of non-linear partial differential equations that can be solved using a direct/inverse scattering transform. The grating function $q(z)$ is now expressed in its complex forms, such that

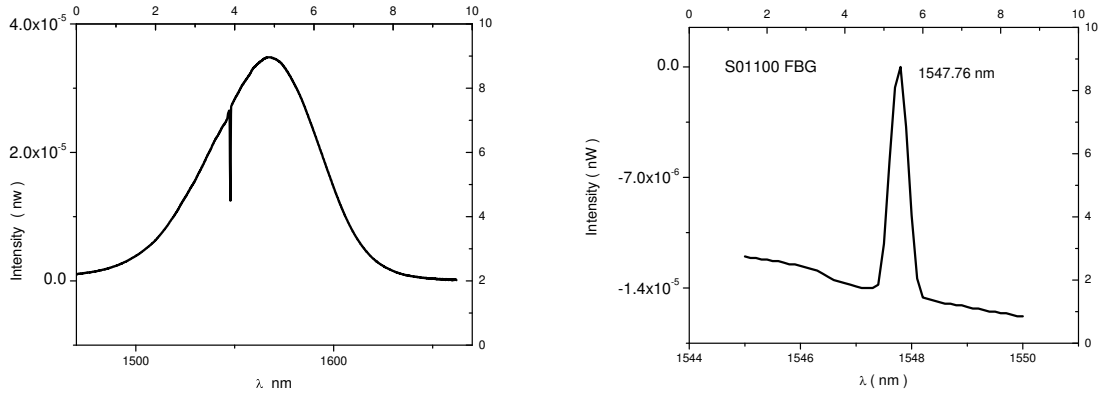

Fig. 3. Transmission spectrum of a SLD 1550 (left). Thorlabs broadband superluminiscent diode coupled to a OS100 Micron Optics FBG with a Bragg wavelength of 1547.8 nm. Calculated reflection profile (right).

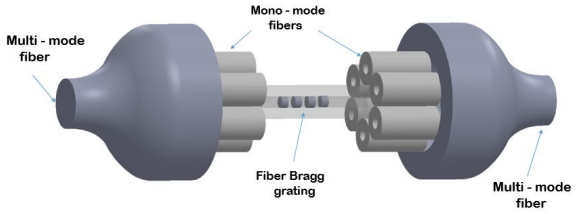

Fig. 4. Bidirectional photonic lantern assembly with the integration of several single-mode fibers with one or several Bragg gratings.

$q(z) = \zeta(z)exp[i\phi(z)]$, where the amplitude function $\zeta = |q|$ and the phase function $\phi = \mathrm{Arg}(q)$. The coupled equations must satisfy all wavelengths in a broad spectral band $\Delta\lambda$ centered at λ_0. The wavelength dependence enters through the variable δ defined as the wavelength (detuning) offset normalized to λ_0. The transmission and reflection profiles, $T(\lambda)$ and $R(\lambda)$ are computed through a matrix transformation (Feced et al. 1999).

5. PHOTONIC LANTERNS

The use of optical devices as shown in Figure 4 allows to cover several of the requirements that the study of astronomical sources demands; it is necessary that the input end be in the multimode regime so it can accept the reduced optical power available; also, the device should cover the required bandwidth of the order of hundreds of nanometers. The assembly of a set of mono and multi-mode fibers by thinning would allow coupling the light coming from extended cosmic sources that emit at several wavelengths (which are captured by the telescopes), to conveniently separate them into different waveguides in whose interior Bragg grating have been drawn, which perform the function of selective filtering for certain wave profiles. The device can be bidirectional because the remnant of the radiation processed in the single-mode fiber cluster would have to pass directly to the spectroscopic analysis system by means of another multi-mode fiber end, thus recovering part of the power of the radiation front captured by astronomical instruments. Also, each single mode fiber could include several Bragg gratings simultaneously (León-Saval et al. 2005; Birks et al. 2015).

6. OPTICAL FIBER BRAGG WAVELENGTH TUNING

The physical characteristics of the optical fiber have shown an excellent behavior to the elastic deformations when they are subjected to mechanical stresses of tension and compression. In the case of the optical fibers the modulus of elasticity is in the range of 70-73 GPa, and its performance level is below 100 kpsi (0.69 GPa); that is to say it could support loads of the order of 8.4675 N (863 grams) before its rupture (Glaesemann 2017).

To confirm the possibilities of modifying the period of the Bragg grating by deformation induced by mechanical stress, some parameters of the silicon dioxide fiber with 8.2 microns of diameter core and 125 microns of external diameter were used, simulating a modulus of elasticity of 73 Gpa. The response is practically elastic as shown in Figure 5, which opens the possibility that when tension is applied within a previously selected range, a tuning of the Bragg wavelength can be achieved by modifying the period of the grating.

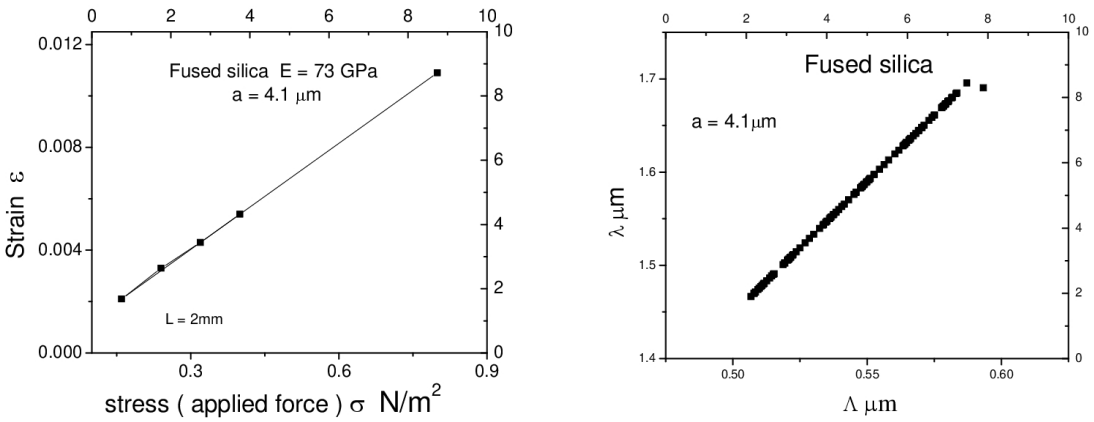

Fig. 5. Simulation of the longitudinal deformation by a force applied to a segment of a silica fiber, with an elasticity modulus of 73 GPa (left). Calculated Bragg wavelength as a function of the Λ period change under an applied force (right).

TABLE 1

SIMULATION OF A FUSED SILICA FIBER SEGMENT UNDER MECHANICAL TENSION

Modulus of Elasticity E=73GPa			
Length mm	Force N	Effort σ Gpa	Strain ε
2	0.981	0.79951	0.0109
2	1.962	0.159902	0.0021
2	2.943	0.239853	0.0033
2	3.924	0.319804	0.0043
2	4.905	0.399755	0.0054

For linearly elastic materials, it is possible to determine by the modulus of elasticity E the proportion of the deformations $\varepsilon = \Delta l/l$ when subjected to mechanical stresses $= F/s$, where s is the cross section of the optical fiber.

However, the optical fibers made of silica (silicon dioxide), can be considered as isotropic materials and the effects of longitudinal tension efforts would show a practically linear trend, as has been confirmed in the simulations.

Table 1 shows the result of the simulation of a fused silica fiber segment subjected to mechanical tension. A linear deformation can be observed, as the tension is increased. The results allow to see clearly the possibility of tuning the wavelength of the Bragg grating within a tolerance margin of less than 10 nm. By stressing an optical fiber with a Bragg grating drawn on its core, it is possible to modify the period Λ and to relate it to the modulus of elasticity and the deformation of the fiber; the development can be seen in detail in Appendix A. The Bragg wavelength is in direct proportion to the physical parameters of the fiber and to the tension force to which it is subjected (equation 9). In the case of the SMF-28 fiber, the effective refractive index is 1.4682 at 1550 nm.

For a fiber of 125 microns diameter, $g = 9.8066\,\mathrm{m/s^2}$ and $E = 70 \times 10^9\mathrm{Pa}$ (Fang et al. 2004). we obtain a constant $k = 0.009339[\mathrm{kg}^{-1}]$. In the case of the Bragg grating, the period was taken from the manufacturer's data, as well as the design wavelength at 1547.76 nm and the effective refractive index of 1.4682, with an approximate grating period of the 527 nm. Equation 8, where μ represents the mass of the suspended weight, is shown in Figure 6.

$$\lambda'_B = \lambda_B(1 + k\mu), \tag{8}$$

$$\lambda'_B = 1547.76 \times 10^2(1 + 0.009339\mu). \tag{9}$$

This is the model proposed for the tuning of the wavelength of the profile reflected by the grating when subjected to stresses, according to equation 9.

7. EXPERIMENTAL DEVELOPMENT

To carry out the simulation of a tension tuned FBG to reflect one of the emission profiles of the atmospheric OH radical, an experiment was designed and performed as shown in Figure 7. A single-mode fiber pigtailed laser diode LP1550-SDA2 from Thorlabs with a maximum optical power of 2.5 mW at a nominal current of 22.6 mA was used to simulate an OH NIR emission line at 1548.85 nm. Mechanical tension was applied by means of scale calibrated

TABLE 2

RESULTS OF THE TESTS*

Bragg OS 1100 1547.76 nm Effective index : 1.4682 Source LP 1550 SAD2 1548.8 nm						
m	Effort	Power	λ'_B	λ_{med}	Attenuation	Period Λ'
g	GPa	μW	nm	nm	db	nm
0.000	0.000	355.000	1547.760	1548.400	0.000	527.090
22.000	17.580	329.300	1548.078	1548.420	0.330	527.203
29.440	23.534	292.300	1548.185	1548.400	0.844	527.239
34.000	27.179	231.250	1548.251	1548.450	1.861	527.262
43.880	35.077	120.250	1548.394	1548.460	4.710	527.730
48.880	39.074	88.800	1548.466	1548.460	6.018	527.334
53.880	43.071	74.000	1548.538	1548.470	6.809	527.359

*Carried out on the measured transmitted optical power of the semiconductor laser and the FBG subjected to mechanical tension by different calibration weights.

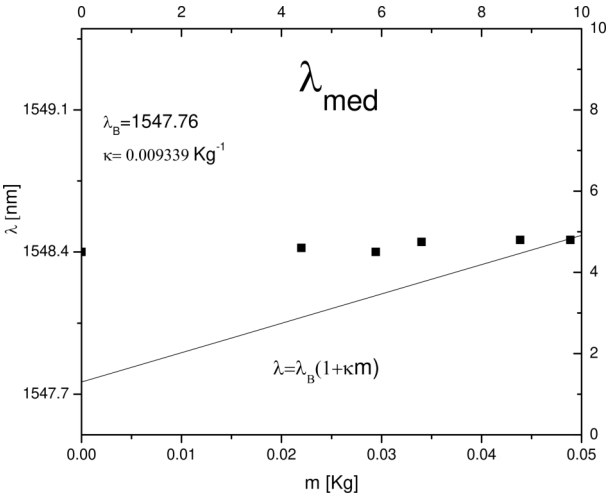

Fig. 6. The convolution of the two profiles preserves a mean wavelength that remains almost constant and very close to the wavelength of the 1548.8 nm source. Simultaneously, the average wavelength λ_{med} of the profile reflected by the grid is shown for each of the tests.

weights from 0 g to 55.83 g suspended to a commercially available Bragg grating OS1100 of Micron Optics. The FBG is printed in 10 mm of core of a compatible SMF-28 type optical fiber, coated with polyamide, a diameter of 125 microns, maximum reflectivity of 70%, FWHM = 0.25nm ± 0.05nm and a Bragg wavelength design of 1548.85 nm. The transmission spectrum was observed and recorded with an optical spectrum analyzer (OSA) Yokogawa AQ6315.

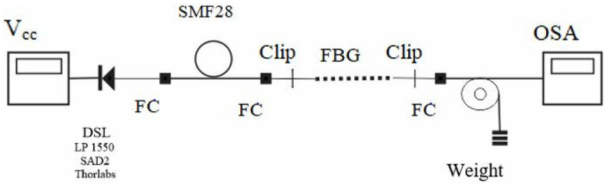

Fig. 7. Experimental assembly required for the simulation of a NIR wavelength using a semiconductor laser at 1548.85 nm and a FBG at 1547.76 nm at 0 g tension. The tension was changed from 0 to 55.83 grams with the use of calibration weights.

The experimental assembly required for the implementation of a support, which would allow the fiber segment where the grating Bragg was drawn to be maintained in position. To avoid damage of the fiber optic cladding, the ends of the FBG were covered with two adhesive tape clamps, on which neodymium magnets were placed acting as clips, leaving the assembly firmly on a metal support. The charges were fixed directly on the optical fiber, also with adhesive tape. Due of the highly sensitive response of the fiber to the deformation, the mass of the tape was taken into account as part of the mass of the total load.

8. ANALYSIS OF RESULTS

Figure 8 shows the spectral response of the FBG and how the Bragg wavelength shifts to longer wavelengths as the weight of the pulling mass is increased. As we discussed, the change of the period of the Bragg grating Λ caused by mechanical tension, proportionally displaced the peak of the wavelength in the reflected profile.

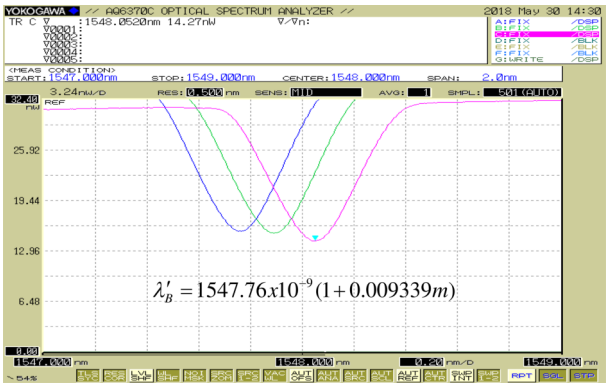

Fig. 8. Bragg Wavelength shift as the original period of the grating is modified due to the deformations to which it was subjected by test calibration weights. The color figure can be viewed online.

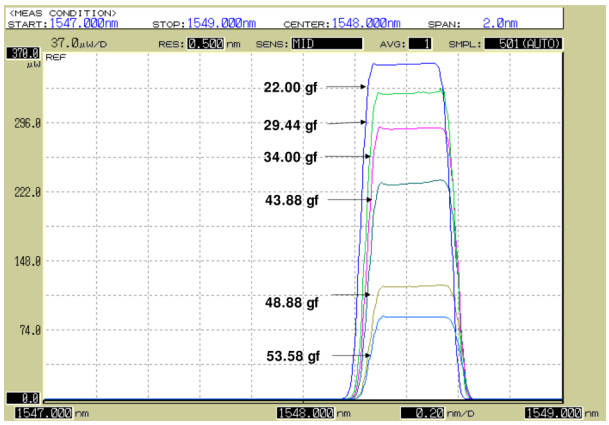

Fig. 9. Attenuation of the laser transmission profile simulating an OH emission line at 1548.43 nm as a function of the tension applied to the FBG with the calibrated weights from 22 to 53.88 g. The color figure can be viewed online.

The gradual approach followed by pulling the FBG with different calibration weights shifted the transmitted spectral response of the optical fiber Bragg grating with respect to the maximum of the laser emission line. This resulted in the convolution of the two profiles in the wavelength domain. As a consequence, the amplitude of the laser emission line at 1548.85 nm transmitted and measured by the OSA was reduced, reaching a maximum attenuation of 6.8 dB (75%) as shown in Figure 9. The results were observed and recorded in the OSA in frame accumulation mode to compare the progressive effect of the attenuation in the profile transmitted by the FBG according to equation (9). Table 2 shows the numerical results obtained in the experiment. These values show that the strain sensitivity of the FBG is 0.0014 nm g^{-1}.

The result obtained in the reduction of the simulated OH transmission profile was of a factor of 4 (6.8 dB), which is much smaller than the factor of 1000 (30 dB) obtained by the GNOSIS instrument which suppresses 103 OH doublets between 1.47 and 1.7 μm (Ellis et al. 2012). However, it is important to emphasize that in this experiment a commercial Bragg grating was used, and the spectral response obtained for the transmission profile was enough to highlight the viability of this technique. We believe that it is important to have the ability to fine tune the response of the FBGs in the field, so we could apply this technique of tension tuning also to the aperiodic FBGs. The sensitivity obtained is very close to that reported by Bland-Hawthorn (Bland-Hawthorn et al. 2004). They reported a sensitivity of 0.010 nm g^{-1} versus 0.014 nm g^{-1} from our experiment. In fact, they indicated that an offset to the printed wavelengths of 0.2 nm to shorter wavelength at 0 g axial strain was applied to allow for fine tuning.

9. CONCEPTUAL DESIGN OF AN ACTIVE TENSION TUNING SYSTEM OF APERIODIC FBGS

With the previous results, we identify a field of opportunity to improve the technique presently used with aperiodic FBGs: we propose the design of a new system, as shown in Figure 10, in which data of the optical intensity vs wavelength from the spectrograph are transferred to a computer system and the average of the target intensity peaks is calculated. This average value signal will drive a current source coupled to an actuator, the aperiodic FBG will be finely stretched to shift the Bragg wavelengths, thus reducing the average intensity of the emission lines during the observation of the NIR field. The actuator can be, for example, a small DC motor. It is expected that each aperiodic FBG can suppress approximately 50 OH emission lines; m is the number of Bragg modules required to suppress the total of emission lines in the band considered, n will be the number of single-mode optical fiber corresponding to the n number of modes at the multimode end of the optical fiber. The number of actuators will be therefore $m \times n$. For example, in the system reported by Ellis and Bland-Hawthorn (Ellis et al. 2012) two aperiodic Bragg gratings and 19 single-mode fibers are used. In our proposed system this will give a

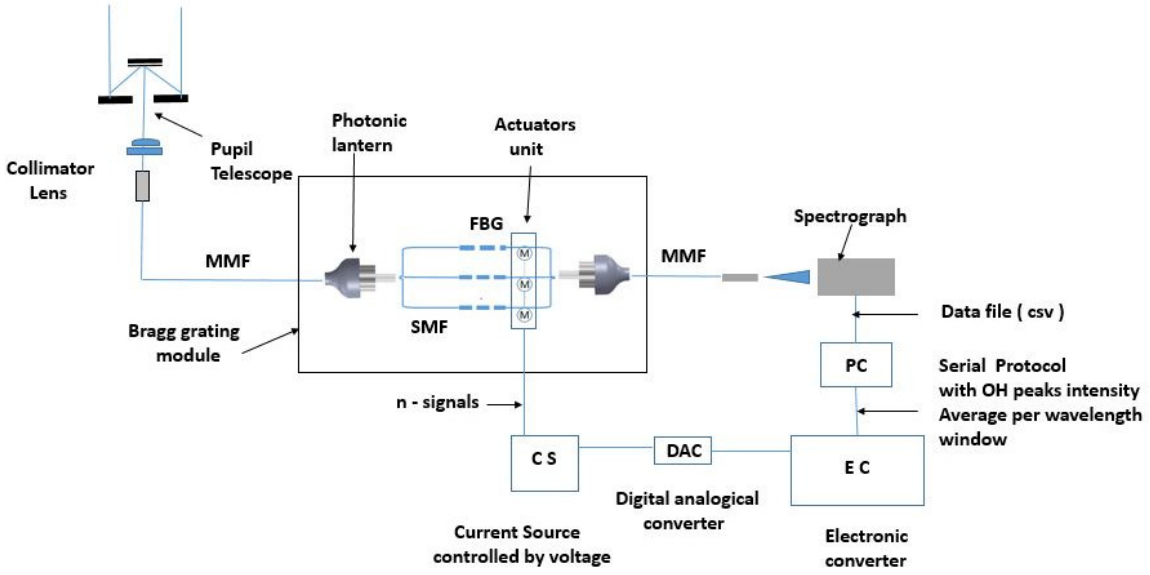

Fig. 10. Conceptual design of an active tension tuning of aperiodic FBGs. MMF: Multimode fiber. SMF: Single-mode fiber. CS: Current source controlled by voltage. DAC: Digital to analogue converter. EC: Electronic converter. PC: Personal computer, csv: comma separated values.

total of $2 \times 19 = 38$ actuators. An electronics converter will be necessary to demultiplex output data form the OSA into 38 digital ports. 38 digital to analog (DACs) will provide 38 voltage signals applied to 38 voltage-to-current converters, and then to the 38 small dc motors to change their torque, that is, the force applied to the Bragg Module. This will work as an automatic control system in real time to actively tune the suppression system.

Temperature dependence of the aperiodic FBGs was not considered in this work. However, the reported sensitivity of FBGs is approximately 0.013 nm K^{-1} (Bland-Hawthorn et al. 2004). This dependence can be compensated precisely by the active tension tuning proposed here, although a thermal chamber with an automatic temperature control system can also be used.

10. CONCLUSIONS

We have demonstrated the possibility of mechanically fine tuning the rejection Bragg wavelength of an FBG in order to better suppress the OH infrared emission lines from the upper layer of the atmosphere for ground telescopes. The tunable optical fiber grating would be used in the conjunction with photonics lanterns. In our experiment we employed a commercial optical fiber Bragg grating with a Bragg wavelength of 1547.7 nm, without tension applied. When tension is applied with a controlled force, in our simulation given by calibrated weights, the corresponding mechanical stress produced a lineal deformation that changed the Bragg period. We experimentally showed that a pulling tension of 53.88 grams force produced a reduction of 75% of the initial amplitude of the simulated emission line from a semiconductor laser of 1548.2 nm at a $25°C$. This was a relatively low value for the suppression of actual OH emission lines if it is compared with special purpose aperiodic FBGs, but it suffices to demonstrate the effect of tension tuning. The transmitted optical reduction was achieved by red shifting the optical spectrum response of a commercial Bragg filter, with a Bragg wavelength set to 1.17 nm less than the target wavelength of the peak emission line. This essentially performed an optical convolution. The conceptual design of an active tension tuning of aperiodic FBGs was proposed, in which data of the optical intensity vs wavelength from the output of the spectrograph will be transferred to a computer system, and the average of the target intensity peaks will be calculated. This average value signal will drive a current source coupled to an actuator to stretch the aperiodic FBGs to shift their Bragg wavelengths, thus reducing the average intensity of the emission lines during the observation of a NIR astronomical field. We expect that a system like this can be used to improve the instrumentation under trial in ground telescopes, and to extend their use for NIR astronomical observation.

R. Benítez-Álvarez would like to thank CONACYT for a Ph.D. studentship and SIP IPN for the BEIFI grant awarded. F. Martínez-Piñón would like to thank SIP IPN for their support of this research project.

A. APPENDIX

A Model for Bragg wavelength tuning as a function of linear deformation parameters due to mechanical tension is given as follows:

$E = 70 \times 10^9$ Pa. Silicon dioxide elasticity module;

Λ_0 = Design period of the Bragg grating;

Λ' = Period of the Bragg grating after a stress effort;

s = Cross section of the optical fiber (core and cladding);

n_{eff} = Effective refractive index of the optical fiber;

λ_B = Bragg wavelength design;

λ'_B =Bragg wavelength after mechanical stress;

μ = Mass of a test calibration weight, used to exert mechanical stress;

$$E = \frac{\sigma}{\varepsilon}, \tag{A1}$$

$$\Delta l = \frac{Fl}{sE}, \tag{A2}$$

$$\Lambda' = \Lambda_0 + \Delta l, \tag{A3}$$

$$\Lambda_0 = l_0, \tag{A4}$$

$$\lambda_B = 2n_{eff}\Lambda_0, \tag{A5}$$

$$\lambda'_B = 2n_{eff}\Lambda', \tag{A6}$$

$$\lambda'_B = 2n_{eff}(\Lambda_0 + \Delta l), \tag{A7}$$

$$\lambda'_B = 2n_{eff}(\Lambda_0 + \frac{Fl_0}{Es}), \tag{A8}$$

$$\Delta l = \frac{\mu g}{Es}\Lambda_0, \tag{A9}$$

$$k = \frac{g}{Es}, \tag{A10}$$

$$\Delta l = k\mu\Lambda_0, \tag{A11}$$

$$\lambda'_B = 2n_{eff}\left[\frac{\lambda_B}{2n_{eff}} + k\mu\Lambda_0\right], \tag{A12}$$

$$\lambda'_B = \lambda_B + 2\mu k n_{eff}\Lambda_0, \tag{A13}$$

$$\lambda'_B = \lambda_B(1 + k\mu). \tag{A14}$$

REFERENCES

Anlauf, K. G., MacDonald, R. C., & Polanyi, J. C. 1968, CPL, 1, 619
Birks, T. A., Gris-Sánchez, I., Yerolatsitis, S., León-Saval, S. G., & Thomson, R. R. 2015, AdOP, 106
Bland-Hawthorn, J., Ellis, S. C., Leon-Saval, S. G. et al. 2011, NatCo, 2, 581
Bland-Hawthorn, J., Englund, M., & Edvell, G. 2004, OExpr, 12, 5902
Bland-Hawthorn, J. & Kern, P. 2009, OExpr, 17, 1880
Davies, R. I. 2007, MNRAS, 375, 1099
Ellis, S. C. & Bland-Hawthorn, J. 2008, MNRAS, 386, 47
_____. 2015, SPIE, 9507, 95070C
Ellis, S. C., Bland-Hawthorn, J., Lawrence, J. et al. 2012, MNRAS, 425, 1682
Fang, W., et al. 2004, JPCA, 108, 5386
Feced, R., Zervas, M. N., & Muriel, M. A. 1999, IEEE Journal of Quantum Electronics, 35, 1105
Glaesemann, G. S. 2017, White paper, wp8002, July 2017
Hill, J. M., Angel, J. R. P., Scott, J. S., Lindley, D., & Hintzen, P. 1980, ApJ, 242, L69
Hill, K. O., Fujii, Y., Johnson, D. C., & Kawasaki, B. S. 1978, ApPhL, 32, 647
Hill, K. O. & Meltz, G. 1997, JLwT, 15, 1263
León-Saval, S. G., Birks, T. A., Bland-Hawthorn, J., & Englund, M. 2005, OptL, 30, 2545
Maihara, T., Iwamuro, F., Hall, D. N. B., et al. 2004, Infrared Detect. Instrum., 1946, 581
Mather, J. C. 2010, AIPC, 1294, 1
Meinel, A. B. 1950, ApJ, 111, 555
Micron Optics, 2017, Fiber Bragg Grating os1100 data sheet, http://www.micronoptics.com/wp-content/uploads/2017/07/os1100-1.pdf
Moorwood, A., Cuby, J. -G., Ballester, P. et al. 1999, Msngr, 95, 1
Othonos, A., Lee, X., & Measures, R. M. 1994, ElL, 30, 1972
Parry, I. 1998, ASPC 152, Fiber Optics in Astronomy III, ed. S. Arribas, E. Mediavilla, and F. Watson (Canary Islands, Spain: ASPC), 3
Rousselot, P., Lidman, C., Cuby, J.-G., Moreels, G., & Monnet, G. 2000, A&A, 354, 1134
Schlatter, T. W. 2009, Natl. Ocean. Atmos. Adm., 6, 1
The Mauna Kea sky background, Near-Infrared Gemini observatory, 2015, [online], Available: http://www.gemini.edu/sciops/telescopes-and-sites/observing-condition-constraints/ir-background-spectra
Trinh, C. Q., Ellis, S. C., Bland-Hawthorn, J. et al. 2013, AJ, 145, 51
Trinh, C. Q. 2013, MNRAS, 432, 3262
Witze, A. 2018, Natur, 559, 16

R. Benítez-Álvarez and F. Martínez-Piñón: Centro de Investigación e Innovación Tecnológica CIITEC IPN Cerrada Cecati S/N, Col. Santa Catarina Azcapotzalco, C.P. 02250, Ciudad de México, México.
V. G. Orlov: Instituto de Astronomía, Universidad Nacional Autónoma de México, Apdo. Postal 70-264, Cd. Universitaria, C. P. 04510, Ciudad de México, México (orlov@astro.unam.mx).

Revista Mexicana de Astronomía y Astrofísica, **55**, 363–376 (2019)

DOI: https://doi.org/10.22201/ia.01851101p.2019.55.02.20

OPTICAM: A TRIPLE-CAMERA OPTICAL SYSTEM DESIGNED TO EXPLORE THE FASTEST TIMESCALES IN ASTRONOMY

A. Castro[1,2,6], D. Altamirano[1], R. Michel[2], P. Gandhi[1], J. V. Hernández Santisteban[1,4,5], J. Echevarría[3], C. Tejada[2], C. Knigge[1], G. Sierra[2], E. Colorado[2], J. Hernández-Landa[2], D. Whiter[1], M. Middleton[1], B. García[2], G. Guisa[2], and N. Castro Segura[1]

Received February 18 2019; accepted August 14 2019

ABSTRACT

We report the development of a high-time resolution, 3-colour, simultaneous optical imaging system for the 2.1 m telescope in the San Pedro Mártir Observatory, México. OPTICAM will be equipped with three 2,048×2,048 pixel Andor Zyla 4.2-Plus sCMOS cameras and a set of SDSS filters allowing optical coverage in the 320–1,100 nm range. OPTICAM will nominally allow sub-second exposures. Given its instrumental design, a wide range of fast-variability astrophysical sources can be targeted with OPTICAM including X-ray binaries, pulsating white dwarfs, accreting compact objects, eclipsing binaries and exoplanets. OPTICAM observations will be proprietary for only six months and will then be made publicly available to the astronomical community.

RESUMEN

Informamos sobre el desarrollo de un sistema de imagen óptica simultáneo en 3 colores y alta resolución temporal para el telescopio de 2.1 m del Observatorio Astronómico Nacional en San Pedro Mártir, México. OPTICAM estará equipado con tres cámaras sCMOS Andor Zyla 4.2-Plus y un conjunto de filtros SDSS que permitirán cobertura óptica en el rango de 320–1,100 nm. OPTICAM permitirá nominalmente exposiciones en el orden de sub-segundos. Dado su diseño instrumental, un amplio rango de fuentes astrofísicas de rápida variabilidad pueden ser observadas con OPTICAM incluyendo estrellas binarias de rayos X, enanas blancas pulsantes, objetos compactos en acrecentamiento, estrellas binarias eclipsantes y exoplanetas. Las observaciones realizadas con OPTICAM serán de propiedad exclusiva durante seis meses y luego se pondrán a disposición pública para la comunidad astronómica.

Key Words: accretion, accretion discs — instrumentation: photometers — stars: imaging — telescopes

1. GENERAL

Many physical processes occurring on short time scales (of the order of milliseconds to seconds) have only recently been observed thanks to the advent of new technologies, allowing multi-wavelength high-cadence photometric measurements. As a consequence of these advances, along with the development of new observational techniques, time-domain astronomy has become a strong emerging area in modern astrophysics.

High time-resolution observations have revolutionised our view of the physical processes that take place on short timescales, providing a unique insight into physical phenomena that otherwise would be inaccessible to conventional photometry. For example, the vast majority of all known extra-solar planets have been discovered by searching for transits in the optical light curves of their host stars (e.g. Mayor, & Queloz 1995; Pepe et al. 2014); neutron star (NS)

[1]Physics and Astronomy, University of Southampton, Southampton, UK.
[2]Instituto de Astronomía, UNAM, Ensenada, México.
[3]Instituto de Astronomía, UNAM, Ciudad de México, México.
[4]Anton Pannekoek Institute, University of Amsterdam, Amsterdam, the Netherlands.
[5]SUPA School of Physics & Astronomy, University of St. Andrews, St. Andrews, UK.
[6]Royal Society Newton International Fellow.

spin periods ranging from milli-seconds to hours have been discovered by observing their X-ray and optical light curves (e.g. van der Klis 2000; Homan et al. 2001); accreting astrophysical systems from young stars and white dwarfs (WDs), to stellar black holes (BHs) in binary systems (e.g. van der Klis 2000, 2006; Patruno & Watts 2012; Ambrosino et al. 2017) and supermassive black holes (SMBHs) in quasars have been found to display the same stochastic 'flickering' variability (McHardy et al. 2006; Scaringi et al. 2015); and evidence for strong-field general relativistic precession has been found in accreting stellar-mass BHs via the detection of fast, quasi-periodic oscillations (QPOs; Motta et al. 2014).

Accretion-induced variability appears through changes in the brightness of an astrophysical object on different time-scales and across a range of wavelengths. Recent research by Scaringi et al. (2015) suggests that the characteristic time-scale of these variations depends mainly on the physical properties of the accretor and the rate at which it accretes, regardless of the nature of the accretor. Accreting WDs, NSs and BHs in binary systems provide us with the best available laboratories for studying the process of disc accretion. Particularly in the innermost disc regions, the variability time-scales can range from seconds in WDs to milli-seconds in NSs and stellar-mass BHs (Dhillon et al. 2007). Multi-wavelength high-speed observations are essential to increase our understanding of the underlying physics of the accretion process (see Middleton et al. 2017, for review). Unfortunately, in-depth and systematic studies in the optical wavelength range have not been possible due to the lack of instruments with the necessary temporal resolution and sensitivity.

Over the past decade, fast-photometric studies have provided a glimpse of their potential when used in simultaneous multi-wavelength campaigns (e.g. Gandhi et al. 2010; Scaringi et al. 2013; Shahbaz et al. 2013; Mallonn et al. 2015; Gandhi et al. 2016, 2017; Hynes et al. 2019; Malzac et al. 2018; Mouchet et al. 2017; Green et al. 2018; Paice et al. 2019; Pala et al. 2019). For example, in accreting compact objects in X-ray binaries (XRBs) the relationship between the rapid (millisecond to minutes) variability at different wavelengths has allowed the inner structure close to the event horizon of a BH or the surface of a NS to be determined through measurements of the absolute sizes of its main components, and through inferences about the plasma physics underlying the observed phenomena (e.g. Gandhi et al. 2008, 2016).

The relationship between optical and X-ray variability is known to change as a function of time and/or spectral state in both BH and NS XRBs, suggesting changes in the physical scale and geometry of the emitting regions (Kanbach et al. 2001; Durant et al. 2008; Gandhi et al. 2008, 2010, 2017, and references therein). As a consequence of the lack of current facilities providing fast-photometric, multi-band capabilities, there are only a few simultaneous observations of such systems, and even fewer observations made with high temporal resolution. In this context, fundamental contributions have been recently made through the use of the ULTRACAM (Dhillon et al. 2007) instrument in several key areas, ranging from accretion physics to exoplanets. Major contributions are also expected from its successor, HiPERCAM (Dhillon et al. 2016, 2018; Bezawada et al. 2018), a state-of-the-art quintuple-beam imager for high time-resolution observations. Other short-term events such as the transit of exoplanets, have been targeted by MuSCAT2 (Narita et al. 2019) using simultaneous 4-colour imaging at the 1.52 m Carlos Sánchez telescope. The TAOS project (e.g. Bianco et al. 2010; Geary et al. 2012; Lehner et al. 2012; Ricci et al. 2014) has focused on the comprehensive study of Kuiper Belt Objects (KBOs) through measurements in the sub-second range. KBOs have also been successfully targeted by CHIMERA (Harding et al. 2016), a wide-field, simultaneous, two-color, high-speed photometer on the Hale telescope.

As part of this new generation of time-domain instruments, we present OPtical TIming CAMera (OPTICAM[7]), a new high-speed, triple-beam, optical imaging system developed through a collaboration between research teams at the Universidad Nacional Autónoma de México (UNAM) and the Astronomy Group at the University of Southampton (AG-UoS) in the United Kingdom. OPTICAM will open new areas of opportunity for both research communities, which will benefit by accessing an instrument equipped with three high-sensitivity, high-resolution, state-of-the-art scientific complementary metal-oxide-semiconductor (sCMOS) cameras. OPTICAM will be equipped with a set of Sloan Digital Sky Survey (SDSS) filters and three $2\,048 \times 2\,048$ sCMOS detectors. The fastest timescale variations likely to be observed with OPTICAM range from milliseconds to seconds, depending on the apparent magnitude of the source. Simultaneous triple-band observations will allow problems due to stochastic variations to be

[7] https://www.southampton.ac.uk/opticam

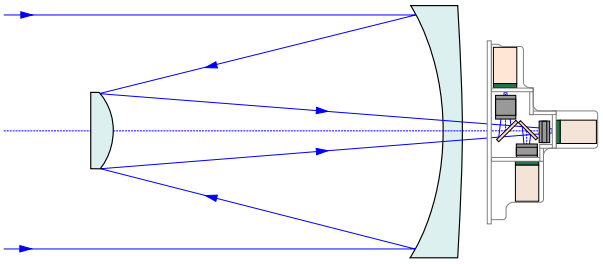

Fig. 1. Layout of the optomechanical system of the OAN-SPM 2.1 m telescope and OPTICAM. Incident light is separated into three channels by two dichroic beam splitters. See also Figure 2 and Figure 4 for a more detailed description). The diagram is not to scale but only for illustrative purposes. The color figure can beviewed online.

avoided, while providing a broad wavelength coverage across the optical spectrum. The instrument will be available as a common-user instrument for the 2.1 m telescope in the Mexican National Astronomical Observatory at San Pedro Mártir, México (OAN-SPM[8]), which is one of the best astronomical sites in the Northern Hemisphere (more details in § 2). OPTICAM will be available to the Mexican and AG-UoS astronomical communities through traditional telescope time request methods.

In this paper, we report the design and performance of OPTICAM, a triple-band high-speed optical system designed to explore sub-second variability scales. In § 2 we describe some of the characteristics of the OAN-SPM and the 2.1 m telescope. In § 3 a brief description of the opto-mechanical design is presented. Details about the utilised filter set and sCMOS camera are shown in § 4 and § 5, respectively. The flow-control and frame-acquisition system is described in § 6. An estimate of the limiting magnitude for the SDSS optical bands is provided in Section 7. In § 8, we explore some of the possible scientific cases that can be addressed using the OPTICAM instrument. Finally, in § 9, we present our conclusions and report on the current status and future time-line of OPTICAM.

2. THE OAN-SPM AND THE 2.1 M TELESCOPE

The OAN-SPM is located on the Sierra San Pedro Mártir in Ensenada, Baja California, México (2800 m; 115°27′49″ W, 31°02′39″ N). The average annual temperature in SPM is 3 °C, with extremes between -10 °C and 20 °C and an average pressure of 0.74 atm. The OAN-SPM is one of the best observing sites in the Northern Hemisphere with 82% clear sky nights (Carrasco et al. 2012). Based on results from a 3-year study, Echevarria et al. (1998) reported a median seeing of 0.61 arcsec and a first quartile of 0.50 arcsec. Later, Michel et al. (2003) also reported a median seeing of 0.6 arcsec using the Differential Image Motion Monitor (DIMM) technique. Additionally, Tapia (2003) reported that 63% of the nights between 1984 and 2003 were considered "photometric" whereas 73% of nights were suitable for high-quality spectroscopic studies.

An average seeing of 0.7 arcsec is estimated based on several long- and mid-term monitoring studies involving a variety of measurement techniques that took place at the OAN-SPM in recent years (see Table 1). These results also show a very stable, long-term sky quality at the site. In this sense, important efforts[9] are being made with the intention of issuing regional legislation for the protection and conservation of the dark skies of northwestern México. All of the aforementioned features make the OAN-SPM one of the best locations for optical Astronomy, comparable to other sites such as Roque de los Muchachos (e.g. Munoz-Tunon et al. 1997), Las Campanas (Prieto et al. 2010), Armazones and Mauna Kea (e.g. Schöck et al. 2009).

The OAN-SPM 2.1 m telescope[10] is the largest optical telescope in México and started operations in 1979. The main mirror is fixed in an equatorial Ritchey-Chrétien focus. The telescope has hyperbolic primary and secondary mirrors. Recently, a fully automated instrument rotator has been permanently mounted on the telescope focus. OPTICAM will be installed on the Cassegrain focus of the 2.1 m telescope (see Figure 1) as a common-user instrument under the normal rules of operation and management currently in use at the OAN-SPM.

3. OPTO-MECHANICAL DESIGN

OPTICAM is designed to operate at an effective $f/7.9$ on the Cassegrain focus of the OAN-SPM 2.1 m telescope. The layout of the optical system of the 2.1 m telescope and OPTICAM is shown in Figure 1. OPTICAM will have three arms. The geometric layout of the optical design of OPTICAM is shown in Figure 2. The beam enters from the OAN-SPM 2.1 m telescope (from the left as shown in the Figure 2 optical layout), passes through the first dichroic in Arm 1 where the initial beam is split. The reflected beam passes to the the first optical camera (C1). This camera is optimised for the use of u' and

[8] http://www.astrossp.unam.mx/oanspm/

[9] http://leydelcielo.astrosen.unam.mx/

[10] http://www.astrossp.unam.mx/~sectec/web/telescopios/2mt.html

TABLE 1

OAN-SPM SEEING MONITORING STUDIES

Method[a]	Reference	First Quartile [arcsec]	Median [arcsec]	Third Quartile [arcsec]
STT+CM	Echevarria et al. (1998)	0.50	0.61	···
DIMM	Conan et al. (2002)	0.61	0.77	0.99
DIMM	Michel et al. (2003)	0.48	0.60	0.81
MASS-DIMM	Skidmore et al. (2009)	0.61	0.79	1.12
g-SciDAR	Avila et al. (2011)	0.50	0.68	0.97
DIMM	Sánchez et al. (2012)	0.60	0.78	1.11
MASS	Sánchez et al. (2012)	0.25	0.37	0.56
GL	Sánchez et al. (2012)	0.45	0.59	0.84

[a]Methods: Site Testing Telescope + Carnegie Monitor (STT+CM); Differential Image Motion Monitor (DIMM); Multi-Aperture Scintillation Sensor (MASS); Generalised-Scintillation Detection and Ranging (g-SciDAR); Ground Layer (GL).

TABLE 2

FIELD-OF-VIEW OF OPTICAM ON THE 2.1 M TELESCOPE

Arm	Filter	FoV (arcmin^2)	Plate Scale ($''$/pix)
1	(u',g')	4.77×4.77	0.1397
2	(r')	4.80×4.80	0.1406
3	(i',z')	5.67×5.67	0.1661

r' filters (from 320 to 550 nm). In the same way, the transmitted beam is then split again towards the optical cameras C2 and C3, which are optimised for r' (from 560 to 690 nm), and i' and z' filters (from 690 to 1,100 nm) in Arms 2 and 3, respectively.

Custom filter exchangers (see Figure 7 and § 4) are placed in front of the sCMOS cameras (see Figure 9). The filter exchanger mechanism allows the desired filter to be placed in the optical path of the respective arm. Each filter exchanger has three available slots. The filters will be manually positioned during the first stage of operation, allowing the user to define the filters to be placed in each arm during an observation run according to Table 4. For example, the filter exchanger in Arm 1 (FE1) has a mechanical scroll bar that can be moved to place either the filter u', g' or an "empty" slot in the optical path of Arm 1. The so-called empty positions are not void spaces, but will house anti-reflectivetransparent quartz glasses to maintain the system's parafocalization. The same mechanism has been implemented in the other two arms of OPTICAM. The aforementioned empty slots can also be used in the future to house new filters for specific studies. As shown in Figure 2, the three optical paths of OPTICAM are optimised for their respective filter configurations.

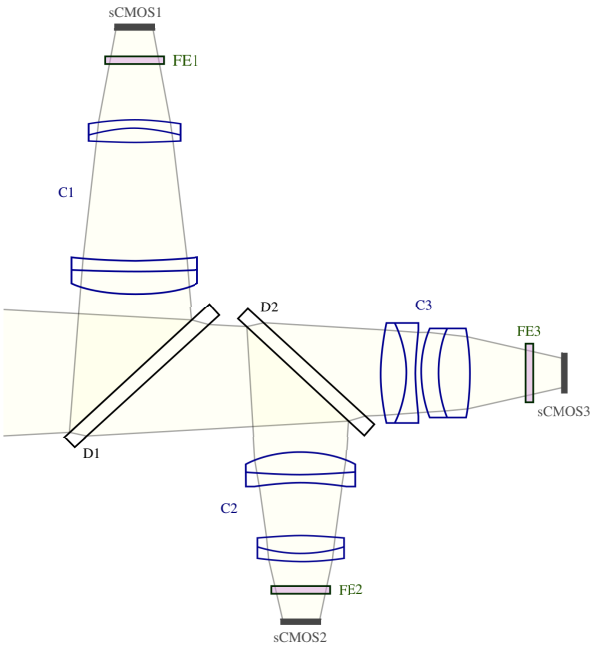

Fig. 2. Design of the OPTICAM optical layout showing the major optical components: the dichroics (D1 and D2), optical cameras (C1, C2 and C3), filter exchangers (FE1 and FE2) and sCMOS cameras (sCMOS1, sCMOS2 and sCMOS3). This diagram is not to scale. The color figure can be viewed online.

The current optical configuration will allow us to simultaneously observe the same FoV (see Table 2) with the 3 different sCMOS cameras, one in each arm. The ZEMAX® OPTICSTUDIO[11] optical design software was used to simulate and accurately model the entire optical system of OPTICAM. An isometric projection of the system is shown in Figure 3,

[11]https://www.zemax.com/products/opticstudio

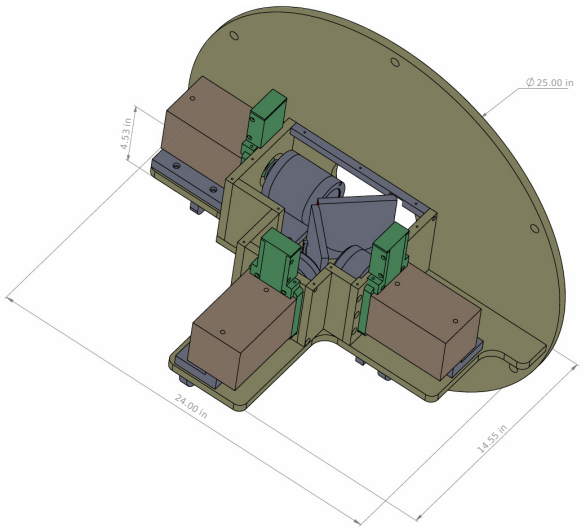

Fig. 3. 3D CAD SolidWorks render of the OPTICAM instrumental setup. In this perspective, the top cover has been removed to show an internal view of the optical design. The dichroic beam splitter and optical lens barrels can be observed. Dimensions are given in inches. The color figure can be viewed online.

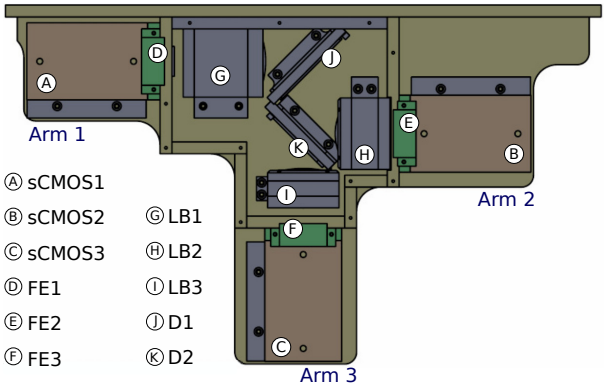

Fig. 4. The mechanical structure of the OPTICAM instrument was designed according to the specific technical requirements of the OPTICAM project. Its three arms are optimised for u'/g', r' and i'/z' filters respectively. The above figure shows the presence of three Andor Zyla 4.2-Plus USB 3.0 sCMOS cameras (sCMOS1, sCMOS2 and sCMOS3, respectively; see Figure 9), the filter exchanger mechanism (FE1, FE2 and FE3), as well as the lenses within their respective barrels (LB1, LB2 and LB3) and dichroics (D1 and D2). The color figure can be viewed online.

while a front-view is shown in Figure 4. In both figures the three sCMOS cameras are shown as brown boxes, the filter exchange mechanism in green and the lenses and dichroics in grey. A thermal analysis was made every 5 °C from -10 °C to 20 °C. We found no significant variations in any of the optical cameras. As a consequence, the system is dominated by the thermal behaviour of the telescope. This thermal analysis revealed a good performance of the instrument, concluding that no thermal compensation is required within the OPTICAM operating limits.

The mechanical structure was designed using SolidWorks® [12] V2016. The design temperature and pressure was 20°C and 1 atm, as the lenses would be manufactured and tested under these conditions. Static stress tests were carried out using the Autodesk® Simulation Mechanical[13] software. The main structure is being built in MIC-6 aluminium. The frame is made of 6061-T6 extruded aluminium alloy. DuPont® Delrin[14] acetal homopolymer resin – a highly-crystalline engineering thermoplastic – has been used in the interfaces with the doublets of the lenses. Grade 316 stainless steel was used in some other minor components in order to guarantee a higher corrosion resistant structure.

[12] https://www.solidworks.com/
[13] https://www.autodesk.com/
[14] http://www.dupont.com

TABLE 3

ASTRODON GEN2 SDSS FILTER PASSBANDS

Filter	Wavelength Range [nm]	$\Delta\lambda$ [nm]
u'	320–385	65
g'	401–550	149
r'	562–695	133
i'	695–844	149
z'	>820	···

4. FILTERS AND DICHROICS

OPTICAM will have a set of SDSS filters (Fukugita et al. 1996), which is the most common filter-set in modern astronomy. These filters provide high-transmission, allowing for the detection of faint objects, and, at the same time, cover the entire optical wavelength range. We have acquired an Astrodon[15] Gen2 set of SDSS filters ($u'g'r'i'z'$) in order to fully cover the 320–1,100 nm range. The transmission curves of the five broad-band filters and the quantum efficiency (QE) of the sCMOS camera are shown in Figure 5. This filter-set provides a peak transmission > 95% (>90% for u'). The filters u', g', r', i' and z' passbands are shown in Table 3. A plot

[15] https://astrodon.com/

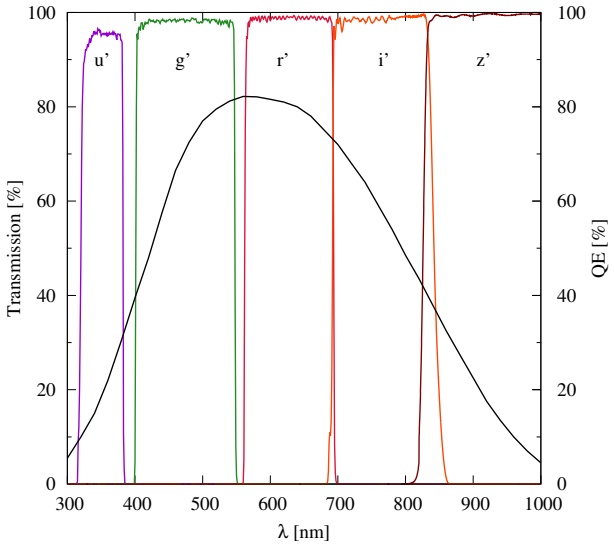

Fig. 5. Transmission profiles of the OPTICAM SDSS filter-set (colour lines) and the QE curve (black solid line) of the Andor Zyla 4.2-Plus USB 3.0 sCMOS camera. OPTICAM will allow simultaneous imaging with 3 of the 5 SDSS filters (see Table 4). The color figure can be viewed online.

comparing the transmission curves of the Astrodon Gen2 SDSS filters with other widely-used filter-sets is shown in Figure 6. The total transmission curves for each photometric band of the OPTICAM system are shown in Figure 8. Throughput estimations considered the combined action of the filters, the sCMOS detector and the dichroic beam splitters of the respective arms.

OPTICAM will simultaneously use three different Andor Zyla 4.2-Plus USB 3.0 cameras, each one associated with its respective filter exchanger. The user will select the precise combination of filters to be used at observation time among the five available photometric filters according to Table 4. The addition of a z_s filter, also from the SDSS filter-set, as well as a pair of narrow-band filters, are being considered to allow secondary science projects to be carried out. Given the current instrumental configuration of OPTICAM, the use of narrow nebular filters (bandwidth $\approx$ 3 nm), Galactic Hα and [OIII] is feasible for bright objects.

The dichroic element is a fused silica substrate with optical interference coatings on both sides of the glass and a slight angle between its faces. Two dichroic beam splitters were designed for OPTICAM. The first dichroic (D1) has a size of 109 $\times$109 $\pm$0.2 mm with a clear aperture of 96 mm in diameter, center thickness of 10 $\pm$ 0.1 mm and wedge angle 11′33″ $\pm$ 30″. The second dichroic (D2) has a size of 95 $\times$ 95 $\pm$ 0.2 mm with a clear aperture of 86 mm in diameter, center thickness of 10 $\pm$0.1 mm and wedge angle 18′38″ $\pm$ 30″. Dichroics were designed to transmit and reflect an incoming beam at a 45°angle of incidence. The dichroics have a transition zone of 20 nm and a transmission of 97% for $\lambda > 560$ nm and 98% for $\lambda > 700$ nm, respectively. Design requirements demanded a transmitted wavefront accuracy of $\lambda/4$ peak-to-valley across the whole clear apertures.

TABLE 4

FILTER OPTIONS

Filter Exchanger	Filter in each Position		
	Pos. 1	Pos. 2	Pos. 3[a]
FE1	u'	g'	...
FE2	r'	...	...
FE3	i'	z'	...

[a]Empty positions can be used as void filter selections or, if required, future filter options will be included.

5. Andor Zyla 4.2-Plus USB 3.0 CAMERAS

Andor Zyla 4.2-Plus USB 3.0 is a state-of-the-art sCMOS camera (see Figure 9) sensitive in the 300–1,100 nm range, with a maximum QE of 82% at 560 nm (see Figure 5 for more details) and a linearity better than 99.8% (>99.9% for low-flux mode). This detector has a full-frame pixel array of 2,048×2,048 pixels (6.5 μm pixels), a pixel well-depth of 30,000 e^- and exceptional data transfer efficiency. A more detailed list of specifications is shown in Table 5. The sCMOS camera is capable of delivering up to 53 frames per second (fps) in the 12-bit full-frame configuration, and up to 40 fps in the 16-bit mode. By setting a smaller area of interest (AOI), also known as region of interest (ROI), it is possible to reach even higher readout speeds (see Table 6).

The Andor Zyla 4.2-Plus USB 3.0 camera has a due detector for applications requiring high sensitivity and high temporal resolution performance. In addition, this sCMOS camera has a thermoelectrically-cooled design, thereby avoiding the requirement of an active cooling system and high-cost maintenance, and a very low read-noise compared to CCDs. Due to its FPGA processing power and the memory capacity of the Andor sCMOS cameras, it permits implementation of bias offset compensation for every pixel in the array in real-time. This feature considerably lowers noise background to negligible levels,

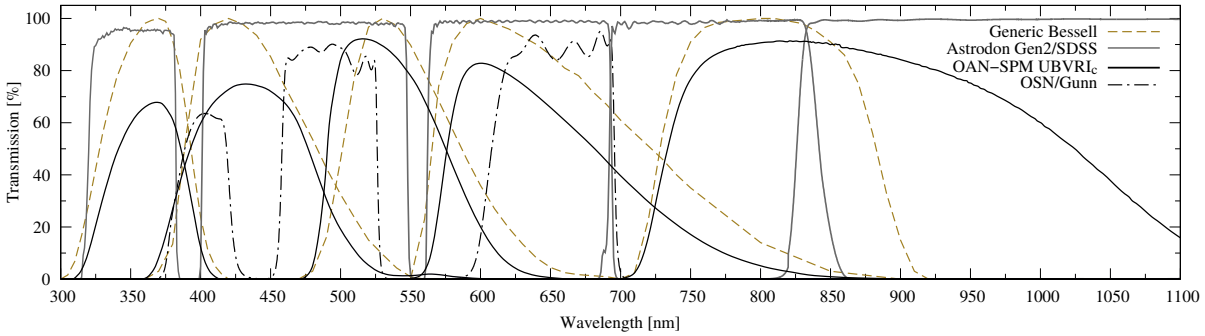

Fig. 6. Filter curves of the SDSS filters compared with the OAN-SPM/Johnson-Cousins (U, B, V, R_C and I_C; black solid), Generic Bessell (U, B, V, R, I; dashed olive) and Observatorio Sierra Nevada (OSN)/Gunn (g, r and i; black dot-dashed) filter transmission curves. The color figure can be viewed online.

TABLE 5

Andor Zyla 4.2-Plus USB 3.0 CAMERA MODEL SPECIFICATIONS[a]

General Specifications	
Sensor type	Front Illuminated Scientific CMOS
Active pixels (W × H)	$2,048 \times 2,048$ (4.2 Megapixel)
Pixel size	6.5 μm
Sensor size	13.3×13.3 mm
Pixel readout rate (MHz)	Slow Read 216 (108 MHz × 2 sensor halves)
	Fast Read 540 (270 MHz × 2 sensor halves)
Read noise (e^-) median [rms]	0.90 [1.1] @ 216 MHz
	1.10 [1.3] @ 540 MHz
Maximum QE	82 %
Sensor Operating Temperature	0 °C (up to 27 °C ambient)
Dark current, e^-/pixel/sec @ min temp	0.10 @ Air Cooled
Readout modes	Rolling-Shutter
Maximum dynamic range	33,000:1
Pixel binning	Hardware binning: 2×2, 3×3, 4×4, 8×8
Data range	12-bit & 16-bit
Interface options	USB 3.0
Hardware time-stamp accuracy	FPGA generated timestamp with 25ns accuracy
Linearity	>99.8 %

[a]More details: `https://andor.oxinst.com/products/scmos-camera-series/zyla-4-2-scmos`

thus eradicating fixed pattern noise associated with CMOS cameras.

As shown in Table 6, the maximum output frame-rate of the camera depends on both the size of the read pixel array and the bit-resolution. The pixel readout rate defines the rate at which pixels are read from the sensor. In the case of Andor Zyla 4.2-Plus USB 3.0, a rolling-shutter[16] mode is used and the digitised signals are read out sequentially at a pixel readout speed of up to 540 MHz (270 MHz × 2 halves). In rolling-shutter mode – contrary to the global-mode available in other camera models, where the whole pixel array is read out in a single scan – different rows of the pixel array are exposed at different times as the rows are sequentially read from the center towards the upper and lower ends of each of the halves of the pixel array, respectively. OPTICAM uses as a default 540 MHz rolling-shutter configuration. In its fastest configuration at full-frame, the camera will be set up with rolling-shutter, overlap enabled and 12-bit mode. The sustained frame rate for this configuration is 53 fps with 100% duty cycle, due to the rolling-shutter capability (40 fps in 16-bit mode). This rolling-shutter mode allows a new exposure to start after each row of pix-

[16]`https://andor.oxinst.com/products/scmos-camera-series/zyla-4-2-scmos`

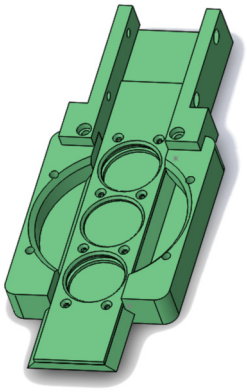

Fig. 7. A manual filter exchanger will be used for each camera during the first stage of operations of OPTICAM. The color figure can be viewed online.

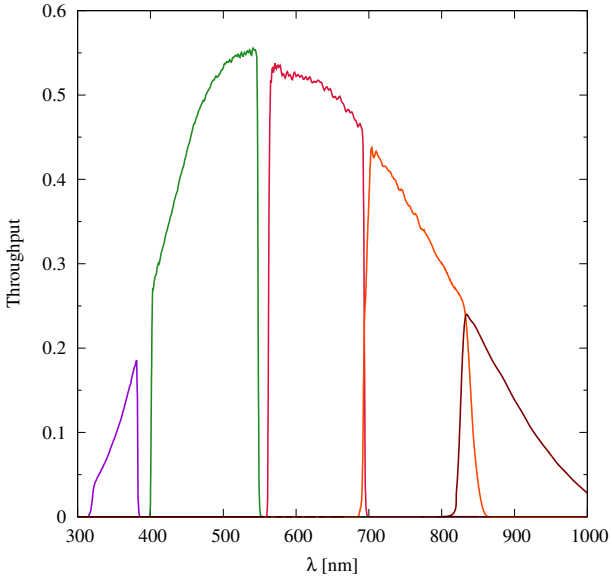

Fig. 8. Throughput estimation of OPTICAM for the u' (purple), g' (green), r' (red), i' (orange) and z' (black) bands. This calculation considers the contribution of filters, dichroics, camera lenses and the sCMOS detector. The color figure can be viewed online.

els has been read out; as a consequence, no time is lost between exposures.

Higher frame rates can be achieved by reducing the desired pixel array size. Maximum sustainable frame rates and transfer rates for various (vertically centred) ROIs, at a 540 MHz readout speed, are also shown in Table 6. The values shown in this table were obtained assuming a 1×1 binning. In the fourth column of the same table, the byte-based transfer rate through the USB 3.0 port for the respective pixel array is shown. The Andor Zyla 4.2-Plus USB 3.0 cameras nominally operate in rolling-

Fig. 9. Andor Zyla 4.2-Plus USB 3.0 sCMOS camera. Image taken from the Andor Oxford Instruments website. The color figure can be viewed online.

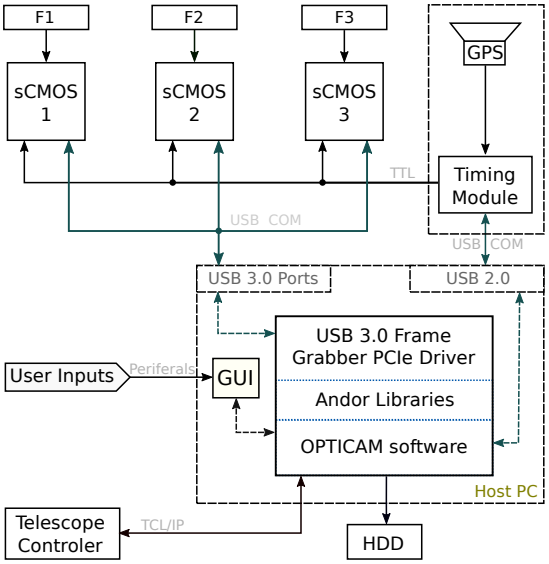

Fig. 10. Block diagram of the OPTICAM control and data-acquisition system. Details in § 6.

shutter mode. Since the actual write-speed of the host computer hard drive can limit the final sustainable frame rate, this effect has to be taken into account to avoid future data transfer malfunctions. In Table 2, detailed information is presented about the FoV and plate scales for OPTICAM, under different instrumental and AOI setups.

Image exposures can be started by a trigger event (e.g. TTL pulse or rising edge). We use a timing module described in § 6 to provide highly precise timing marks. The Andor Zyla 4.2-Plus USB 3.0 camera can be operated under room temperature conditions (up to 27 °C ambient). However, if its air-cooling system is software-enabled, the detector cools down, stabilising to a nominal operating temperature of 0 °C, regardless of the ambient temperature.

TABLE 6

MAXIMUM SUSTAINABLE FRAME RATES AND TRANSFER RATES FOR VARIOUS PIXEL ARRAYS

Array Size[a]	Frame Rate[b] [fps@12-bit]	BTR[c] [Mb/s]	Frame Rate[b] [fps@16-bit]	BTR[c] [Mb/s]
2,048×2,048	53	424	40	320
1,920×1,080	107	423.2	80	316.4
512×512	403	201.5	403	201.5
128×128	1,578	49.3	1,578	49.3

[a]The pixel array (also called the area or region of interest) will be user-defined on the GUI window.

[b]Frame rates are given in fps (frames per second).

[c]Byte-based transfer rate (BTR).

6. CONTROL AND DATA-ACQUISITION

As shown in the block diagram of Figure 10, triple-band (filters F1, F2 and F3) simultaneous imaging will be possible using a set of three Andor Zyla 4.2-Plus USB 3.0 cameras (sCMOS1, sCMOS2 and sCMOS3, respectively). Image acquisition will be controlled from a single host computer. The software for image acquisition, flow control, storage and communication between interfaces and subprograms have been developed by collaborators of the present project, mainly written in C++. Specific software elements regarding frame-reading, image memory allocation, temperature control and other image-related handlers were adopted from the Andor Software Development Kit (SDK[17]). The SDK provides us with a dynamic link library and a suite of functions able to configure the data-acquisition process from the Zyla sCMOS cameras used by OPTICAM.

Our instrumental control is closely related to the currently working OAN-SPM telescope control setups. The nominal communication standards between devices currently used at the OAN-SPM observatory have been adopted in order to deliver an instrument compatible with other systems now operating on the 2.1 m telescope. For OPTICAM, in the case of the graphical user interface (GUI), we have opted for a specific adaptation of the generic GUI (Colorado 2014) currently used at the OAN-SPM, given our simultaneous imaging and frame rate needs. This new GUI will allow the observer to control the different frame-related parameters of the observation (e.g. exposure time, filters, ROI dimensions and binning) as well as the type of exposure to be acquired (e.g. test image, object, flat). Additionally, this interface will allow the quick visualisation of some important parameters of the exposed fields (e.g. object name, coordinates, airmass, observation date and time, camera details and filter data).

High precision time stamps will be provided through a 'Silverbox 2.0' timing module specifically designed on request for our project by the KTH Royal Institute of Technology[18] staff members in Stockholm, Sweden. The module is intended for the generation of configurable and precisely synchronised timing pulses. Both the period of the pulse train and the pulse duration can be independently set to an integer factor of the base clock period. This module will be used by OPTICAM in order to acquire data from the 3 different cameras with a very accurate timing. The highly accurate clock of the Silverbox (±1 ppm precision; ppm stands for parts per million in relation to the crystal's oscillator nominal frequency) can be synchronised to either a time-pulse from the Global Positioning System (GPS), or from a custom supplied, one-pulse-per-second line, or left free-running.

Assuming a selected full-frame (4.2 Mpix), 12-bit resolution configuration (16-bit words for storage purposes; more details in § 5), each camera can provide up to 53 fps at maximum performance. Considering that each pixel is encoded with 16-bit words, this means that OPTICAM can deliver 8 Mb s^{-1} through a USB 3.0 port.

7. LIMITING-MAGNITUDE

Figure 11 shows a preliminary limiting-magnitude plot for a detection by OPTICAM (at a signal-to-noise of 5-σ) as a function of exposure time at the OAN-SPM 2.1 m telescope provided that the $f/7.5$ mount is installed. The curve was

[17]https://andor.oxinst.com/products/software-development-kit/software-development-kit

[18]https://www.kth.se/en

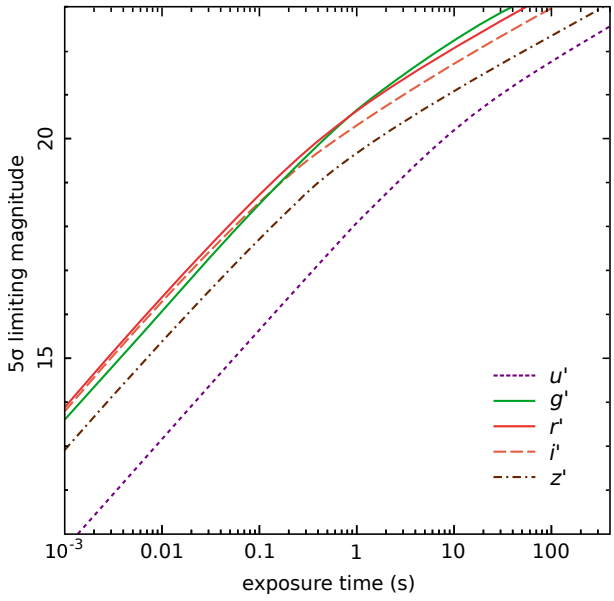

Fig. 11. Preliminary limiting-magnitude plot for a detection by OPTICAM (at a signal-to-noise of 5-σ) in the OAN-SPM 2.1 m telescope. The color figure can be viewed online.

obtained assuming dark sky conditions[19] and an average seeing value of 0.7 ″ (see § 2). Atmospheric extinction was estimated from Schuster, & Parrao (2001). Regarding the technical details of the Zyla cameras (e.g. QE and detector noise), we rely on the data provided by the Andor Zyla 4.2-Plus USB 3.0 user guide. The empirical throughput of OPTICAM at the 2.1 m telescope will be estimated during the first-light observation after some photometric standard stars are observed.

8. SCIENCE WITH OPTICAM

Due to its unique optical and timing capabilities, OPTICAM will allow us to perform strictly simultaneous, triple-band observations of a wide variety of astronomical objects with dynamical times-scales ranging from seconds in WDs to milliseconds in NSs and galactic stellar-mass BHs. The expected temporal resolution and accuracy achieved by OPTICAM will also allow the study of many other astrophysical objects including, amongst others, eclipsing binaries, exoplanets, active galactic nuclei, ultra-compact binaries, pulsars, pulsating WDs, stellar flaring events, and stellar occultations. In addition to standalone science, OPTICAM can complement simultaneous multi-wavelength campaigns of fast variability phenomena, or observations by several high-energy space observatories (e.g. AstroSat, Chandra, NICER, NuSTAR, Swift and XMM-Newton). Some of the proposed astrophysical objects and possible case-studies for use of this instrument are described below.

8.1. *X-ray Binary Systems*

The study of BH and NS XRBs has rapidly evolved over the past two decades, largely due to the availability of powerful X-ray space observatories. The X-ray phenomenology of XRBs includes week-to-year-long outbursts, where their overall luminosity can increase by several orders of magnitude. However, most of the underlying physics is still under debate. An example of this is the presence of fast periodic/quasi-periodic variability (QPOs) observed at different wavelengths, often associated with orbital motions in the inner accretion disc and/or disc precession (e.g. Ingram et al. 2016). In this context, multi-wavelength observations of such fast-time variability might allow the degeneracy between models to be broken (Hynes et al. 2003; Kalamkar et al. 2016; Veledina et al. 2017).

It is widely accepted that, given a continuous mass-transfer rate from the secondary star, outbursts of X-ray transients occur when a thermal instability occurs after the surface density at large radii reaches a critical value. From high-resolution, multi-wavelength observations of the binary BH V404 Cyg, Kimura et al. (2016) found optical oscillations on time scales of 100 seconds to 2.5 hours, well-correlated with the X-ray emission. Since these oscillations occurred at mass-accretion rates much lower than expected, it was concluded that the mass-accretion rate is not the only key factor, particularly for sources with large discs, long orbital periods and large-amplitude oscillations (Kimura et al. 2016). Muñoz-Darias et al. (2016) reported the presence of rapidly-changing P-Cygni profiles due to winds, and attributed the X-ray and optical variability patterns to insufficient mass-flow reaching the innermost regions of the accretion disc. ULTRACAM simultaneous, three-band, sub-second observations of V404 Cyg showed a steep power density spectrum dominated by slow variations on $100 - 1000$ s timescales (Gandhi et al. 2016). These observations also showed persistent sub-second flares, particularly in the r'-band. The origin of the observed lags between different wavelengths in accreting objects is also still unclear. Several promising physical processes have been put forward as explanations for

[19] http://www.astrossp.unam.mx/sitio/brillo_cielo.htm

such behaviour, e.g. reprocessing of the X-ray emission by the accretion disc, intrinsic variations of the thermal disc emission (Cameron et al. 2012) and changes in the projected direction to- and accretion flow into the compact jets (Bell et al. 2011). At the median distances of ≈ 2 kpc for BH XRBs (Gandhi et al. 2019), the typical optical luminosities of the rapid sub-second flares alone can reach peak values of $\approx 10^{36}\,\mathrm{erg\,s^{-1}}$. Such powerful and rapid flares cannot originate as thermal emission. Thus, they appear to be important probes of non-thermal processes very close to the central compact objects. To explore some of these lines of research, OPTICAM will allow us to perform high-time resolution, simultaneous observations, made jointly with other high-performance space- and ground-based observatories, in order to provide a unique time-dependant, panchromatic view of XRBs.

8.2. *Accreting White Dwarfs*

Interacting binary systems harbouring a WD are one of the most common accreting objects in the Galaxy. Due to their large number and relative proximity, accreting WDs are ideal laboratories to characterise the properties of accretion discs across a wide range of mass transfer rates. X-rays in cataclysmic variables (CVs) are thought to originate from the boundary layer (see Kuulkers et al. 2006, for review) or from the X-ray corona at low accretion rates (e.g King & Shaviv 1984). Roughly half of the gravitational potential energy is radiated from the aforementioned layer while the other half is radiated from the accretion disc through viscous processes (Dobrotka et al. 2014).

Many CVs have short orbital periods of less than 4 h (e.g. Patterson et al. 2002). HS 0728+6738 is a CV with an orbital period (P) of 3.21 h showing optical variations on a time scale of $\approx$ 7 min. Additionally, the fast variability seen in HS 0728+6738 (Rodríguez-Gil et al. 2004) outside eclipse also shows QPOs on time scales of 10–30 minutes. High cadence observations of sources in eclipse with simultaneous time-resolved multi-band coverage, will allow us to dissect the different light components of these systems. Light curves obtained with OPTICAM will allow us to retrieve the geometry and orbital parameters of this type of system. Such techniques have already succeeded in detecting the long-sought population of WDs accreting from brown dwarfs (Littlefair et al. 2006; Savoury et al. 2011; McAllister et al. 2017) which were later confirmed through spectroscopy (e.g. Hernández-Santisteban et al. 2016).

8.3. *Active Galactic Nuclei*

For AGN harbouring a SMBHs in the range $10^6 - 10^8\ M_\odot$, the lags between various bands range from seconds to a few days (Breedt et al. 2010; Cameron et al. 2012). In particular, the study of low-mass AGNs, as in the case of Narrow-Line Seyfert 1s, requires a time-resolution on the order of a dozen seconds (e.g. McHardy et al. 2016). An example is NGC 4051, a highly-variable AGN showing large variations in flux over relatively short timescales ($\approx$ hours) (e.g. McHardy et al. 2004; Silva et al. 2016). A major goal of such studies is the determination of inter-band lags, i.e. time-delays between different bands, which are thought to be due to the light-travel times between different parts of the system. The wavelength dependence of these lags can be used to infer the emissivity and temperature distributions across the accretion disc, as well as to estimate the size of the disc and its accretion rate. Thus, simultaneous coverage across multiple bands provided by OPTICAM will allow us to carry out this type of study.

8.4. *Eclipsing Binaries*

Eclipsing binaries are arguably the most important empirical calibrators in stellar astrophysics. In the case of short-period systems, their fundamental stellar and binary parameters (masses, radii, temperatures, luminosities and periods) can often be measured with both accuracy and precision. As an extreme example, high-precision photometric measurements of eclipse timings have even been used to establish the presence of an extra-solar planet orbiting the close binary NN Ser (Beuermann et al. 2010; Marsh et al. 2014; Parsons et al. 2014). This makes short-period oscillation eclipsing binaries valuable subjects for both spectroscopic and multi-band photometric studies (e.g. Lu et al. 2018). The use of an instrument such as OPTICAM – as part of simultaneous multi-wavelength coverage – will make it possible to constrain with high-precision the physical parameters of a large number of eclipsing binaries.

8.5. *Exoplanets*

Although exoplanets were first studied using the radial-velocity technique, time-resolved colour photometry provides valuable astrophysical information that has led to detection and characterisation via transits of numerous exoplanets. Such measurements usually require extremely precise relative multi-band photometry and until recently they were only possible through the use of space telescopes or large ground-based facilities (Sedaghati et al. 2015).

However, precise *BVRIz'JH* observations by Ricci et al. (2017) have recently confirmed the potential adequacy of small ground-based telescopes (in the range 36–152 cm) for exoplanetary transit research. A good example of this is the successful operation of MuSCAT-2 on the 1.52 Carlos Sánchez telescope and the current implementation of the TAOS-II[20] project at the OAN-SPM. Multi-colour, high-precision, fast-photometry obtained with OPTICAM will certainly help to increase the number of exoplanet observations at the OAN-SPM.

9. CONCLUSIONS AND DISCUSSION

OPTICAM is a high-speed optical system designed to perform triple-channel fast-photometry. OPTICAM will have a set of $u'g'r'i'z'$ SDSS filters which will provide coverage in the $320 < \lambda[\mathrm{nm}] < 1,100$ wavelength range. OPTICAM will be mounted in the Cassegrain focus of the OAN-SPM 2.1 m telescope. Incident light will be split into three different beams using a pair of dichroic beam splitters. One beam is dedicated to either the u' or g' filter, whereas the second beam is dedicated to r' and the third beam to either the i' or the z' filter. These filter combinations, and additional empty positions, will be selected through the use of a manual filter exchanger available on each arm of the optical system. The filters will be placed according to the particular science case (within the limitations established in § 4). The image acquisition will be carried out by three modern 2,048×2,048 Andor Zyla sCMOS cameras, observing the same patch of sky of approximately $5' \times 5'$ FoV (see Table 2).

The OPTICAM system will be capable of strictly simultaneous imaging, meaning that images will be acquired at exactly the same time through the use of a synchronisation card and dedicated software. OPTICAM will nominally allow sub-second imaging capabilities. Nevertheless, higher readout speeds can be reached as a function of the ROI size. The three cameras will be synchronised with the aid of a precise timing module. Each image header will be time-stamped using this dedicated timing module equipped with a precise GPS system.

A theoretical limiting magnitude curve has been provided for the purposes of this paper. As far as we know, sky brightness and extinction values have not been measured before with the SDSS filter set at the OAN-SPM site. Transformations have been made from known $UBVRI_{\mathrm{c}}$ values, and extinction values were interpolated using the Schuster, & Parrao (2001) extinction curve as a first approximation. In order to estimate the empirical throughput of OPTICAM on the 2.1 m telescope and accurately characterise the response of the instrument, as well as to measure the average values of the sky brightness and extinction, a set of spectro-photometric standard stars needs to be carefully observed at different air-masses. First on-site tests of the instrumental setup are expected to be carried out in October 2019. During this period, other, relatively well-known, bright objects will also be targeted, allowing us to make comparisons with published data of the same objects in order to establish performance comparisons with OPTICAM.

OPTICAM is a low-budget project compared to other, similar systems currently in operation (e.g. ULTRACAM and HiPERCAM). The sCMOS cameras had previously been acquired within budgetary limitations. This pre-existing condition coupled with the scientific requirements established for OPTICAM, imposed very strict design requirements in order to provide a large FoV, simultaneous triple-band imaging and an appropriate plate scale for an instrument operating under the specific sky conditions of the OAN-SPM observatory. The design requirements are particularly oriented to get a good sampling of the point spread function of a point-like source without significant spacial degradation.

The most important limitation of OPTICAM is the low instrumental sensitivity in the bands u' and z'. It will be in the observer's interest to decide when these filters should be used according to the needs of their underlying science, for example, the acquisition times required (particularly for u') to achieve a good S/N will limit the time-resolution possible (yet this is often required in some fast-photometry studies). Despite these limitations, in the context of conventional photometric studies, where timing capabilities are not critical, OPTICAM aims to be a very efficient instrumental system due mainly to its triple-band imaging capability, high time resolution and its well-defined detection band-passes.

OPTICAM is a step forwards towards a new generation of instruments with high temporal resolution, which will enable studies of very fast astrophysical phenomena occurring in the range of milliseconds and seconds, a range that previously could not be achieved by conventional CCD photometric techniques. Due to its novel design, OPTICAM can be used to observe a variety of astrophysical sources, such as XRBs, pulsating WDs, accreting compact objects, eclipsing binaries and pulsars. OPTICAM

[20] https://taos2.asiaa.sinica.edu.tw/

intends to match some of the capabilities of ULTRACAM, such as short exposure times, negligible dead-time and true simultaneous imaging with multi-wavelength coverage.

In order to maximise the long-term impact of the project, and its benefits to the astronomical community, we will ensure that all observations taken with OPTICAM become publicly available. Data will only be proprietary for six months after the observations are taken. In accordance with open-data policies, all observations will then be accessible to the entire international astronomical community. In addition, OPTICAM will serve as part of a worldwide transient network of instruments dedicated to the study of transient phenomena, such as SmartNET[21] (Middleton et al. 2017).

The authors would like to thank all the OPTICAM project members and collaborators. OPTICAM has been partially funded by the University of Southampton through the STFC Impact Acceleration Account grant and the Instituto de Astronomía, UNAM. AC is supported by a UK Royal Society Newton International Fellowship. DA acknowledges support from the Royal Society. JVHS acknowledges support from a Vidi grant of the Netherlands Organization for Scientific Research (NWO) granted to N. Degenaar and a STFC grant ST/R000824/1. MM is supported by an Ernest Rutherford STFC fellowship. The SDSS set of filters was supplied by Astrodon. All lens polishing and barrels were provided by Tucson Optical. We thank the participation of N. Ivchenko and the KTH staff for the design of the timing module. We also thank V. S. Dhillon, M. Richer and the Andor Support Team for their continuous technical support during the development of this project. We are thankful to the anonymous referee for constructive suggestions and comments.

REFERENCES

Ambrosino, F., Papitto, A., Stella, L., et al. 2017, NatAs, 1, 854
Avila, R., Sánchez, L., Cruz-González, I., et al. 2011, RMxAA, 47, 75
Bell, M. E., Tzioumis, T., Uttley, P., et al. 2011, MNRAS, 411, 402
Belloni, T., Psaltis, D., & van der Klis, M. 2002, ApJ, 572, 392
Beuermann, K., Hessman, F. V., Dreizler, S., et al. 2010, A&A, 521, L60
Bezawada, N., Gao, X., Henry, D., et al. 2018, SPIE, 1070924
Bianco, F. B., Zhang, Z.-W., Lehner, M. J., et al. 2010, AJ, 139, 1499
Breedt, E., McHardy, I. M., Arévalo, P., et al. 2010, MNRAS, 403, 605
Carrasco, E., Carramiñana, A., Sánchez, L. J., et al. 2012, MNRAS, 420, 1273
Cameron, D. T., McHardy, I., Dwelly, T., et al. 2012, MNRAS, 422, 902
Colorado, E. 2014, "CCDs OAN v4: Programa para el uso de las camaras cientificas del OAN", Techinical Report, Instituto de Astronomía, UNAM, México
Conan, R., Avila, R., Sánchez, L. J., et al. 2002, A&A, 396, 723
Dhillon, V., Dixon, S., Gamble, T., et al. 2018, Proc. SPIE, 107020L
Dhillon, V. S., Marsh, T. R., Bezawada, N., et al. 2016, Proc. SPIE, 99080Y
Dhillon, V. S., Marsh, T. R., Stevenson, M. J., et al. 2007, MNRAS, 378, 825
Dobrotka, A., Mineshige, S., & Ness, J.-U. 2014, MNRAS, 438, 1714
Durant., M., Gandhi, P., Shahbaz, T., et al. 2008, ApJ, 682, 45
Echevarría, J., Tapia, M., Costero, R., et al. 1998, RMxAA, 34, 47
Fukugita, M., Ichikawa, T., Gunn, J. E., Doi, M., Shimasaku, K., & Schneider, D. P. 1996, AJ, 111, 1748
Gandhi, P., Bachetti, M., Dhillon, V. S., et al. 2017, NatAs, 1, 859
Gandhi, P., Dhillon, V. S., Durant, M., et al. 2010, MNRAS, 407, 2166
Gandhi, P., Littlefair, S. P., Hardy, L. K., et al. 2016, MNRAS, 459, 554
Gandhi, P., Makishima, K., Durant, M., et al. 2008, MNRAS, 390, L29
Gandhi, P., Rao, A., Johnson, M. A. C., et al. 2019, MNRAS, 485, 2642
Geary, J. C., Wang, S.-Y., Lehner, M. J., et al. 2012, Proc. SPIE, 84466C
Green, M. J., Marsh, T. R., Steeghs, D. T. H, et al. 2018, MNRAS, 476, 1663
Harding, L. K., Hallinan, G., Milburb, J., Gardner, P., et al. 2016, MNRAS, 457, 3036
Hernández Santisteban, J. V., Knigge, C., Littlefair, S. P., et al. 2016, Nature, 533, 366
Homan, J., Wijnands, R., van der Klis, M., et al. 2001, ApJS, 132, 377
Hynes, R. I., Haswell, C. A., Cui, W., et al. 2003, MNRAS, 345, 292
Hynes, R. I., Robinson, E. L., Terndrup, D. M., et al. 2019, MNRAS, 487, 60
Ingram, A., van der Klis, M., Middleton, M., et al. 2016, MNRAS, 461, 1967
Kalamkar, M., Casella, P., Uttley, P., et al. 2016, MNRAS, 460, 3284
Kanbach, G., Straubmeier, C., Spruit, H. C., et al. 2001, Natur, 414, 180

[21] http://www.isdc.unige.ch/SmartNet/

Kimura, M., Isogai, K., Kato, T., et al. 2016, Natur, 529, 54
King, A. R & Shaviv, G. 1984, Natur, 308, 519
Kuulkers, E., Norton, A., Schwope, A., & Warner, B. in Compact Stellar X-ray Sources, ed. W. Lewin & M. van der Klis (Cambridge, UK. CUP)
Lehner, M. J., Wang, S., Alcock, C. A., et al. 2012, AAS/Division for Planetary Sciences Meeting Abstracts #44, 310.20
Littlefair, S. P., Dhillon, V. S., Marsh, T. R., et al. 2006, Sci, 314, 1578
Lu, H.-peng, Michel, R., Zhang, Li-yun, & Castro, A. 2018, AJ, 156, 88
Mallonn, M., Nascimbeni, V., Weingrill, J., et al. 2015, A&A, 583, A138
Malzac, J., Kalamkar, M., Vincentelli, F., et al. 2018, MNRAS, 480, 2054
Marsh, T. R., Parsons, S. G., Bours, M. C. P., et al. 2014, MNRAS, 437, 475
Mayor, M. & Queloz, D. 1995, Natur, 378, 355
McAllister, M. J., Littlefair, S. P., Dhillon, V. S., et al. 2017, MNRAS, 464, 1353
McHardy, I. M., Koerding, E., Knigge, C., et al. 2006, Nature, 444, 730
McHardy, I. M., Papadakis, I. E., Uttley, P., et al. 2004, MNRAS, 348, 783
McHardy, I. M., Connolly, S. D., Peterson, B. M., et al. 2016, AN, 337, 500
Michel, R., Echevarría, J., Costero, R., et al. 2003, RMxAC, 19, 37
Middleton, M. J., Casella, P., Gandhi, P., et al. 2017, NewAR, 79, 26
Mouchet, M., Bonnet-Bidaud, J.-M., Van Box Som, L., et al. 2017, A&A, 600, A53
Motta, S. E., Munoz-Darias, T., Sanna, A., et al. 2014, MNRAS, 439, L65
Muñoz-Darias, T., Casares, J., Mata Sánchez, D., et al. 2016, Nature, 534, 75
Munoz-Tunon, C., Vernin, J., & Varela, A. M. 1997, A&AS, 125, 183
Narita, N., Fukui, A., Kusakabe, N., et al. 2019, JATIS, 5, 015001
Paice, J. A., Gandhi, P., Charles, P. A., et al. 2019, MNRAS, 488, 512
Pala, A. F., Gänsicke, B. T., Marsh, T. R., et al. 2019, MNRAS, 483, 1080
Parsons, S. G., Marsh, T. R., Bours, M. C. P., et al. 2014, MNRAS, 438, L91
Patruno, A. & Watts, A. L. 2012, arXiv e-prints, arXiv:1206.2727P
Patterson, J., Fenton, W. H., Thorstensen, J. R., et al. 2002, PASP, 114, 1364
Pepe, F., Ehrenreich, D., & Meyer, M. R. 2014, Natur, 513, 358
Plauchu-Frayn, I., Richer, M. G., Colorado, E., et al. 2017, PASP, 129, 035003
Prieto, G., Thomas-Osip, J. E., Phillips, M. M., et al. 2010, SPIE, 77334O
Ricci, D., Sada, P. V., Navarro-Meza, S., et al. 2017, PASP, 129, 064401
Ricci, D., Sprimont, P.-G., Ayala, C., et al. 2014, RMxAC, 45, 57
Rodríguez-Gil, P., Gänsicke, B. T., Barwig, H., et al. 2004, A&A, 424, 647
Sánchez, L. J., Cruz-González, I., Echevarría, J., et al. 2012, MNRAS, 426, 635
Savoury, C. D. J., Littlefair, S. P., Dhillon, V. S., et al. 2011, MNRAS, 415, 2025
Scaringi, S., Maccarone, T. J., Kording, E., et al. 2015, SciA, 1, e1500686
Scaringi, S., Körding, E., Groot, P. J., et al. 2013, MNRAS, 431, 2535
Schöck, M., Els, S., Riddle, R., et al. 2009, PASP, 121, 384
Schuster, W. J., & Parrao, L. 2001, RMxAA, 37, 187
Sedaghati, E., Boffin, H. M. J., Csizmadia, S., et al. 2015, A&A, 576, L11
Shahbaz, T., Russell, D. M., Zurita, C., et al. 2013, MNRAS, 434, 2696
Silva, C. V., Uttley, P., & Costantini, E. 2016, A&A, 596, A79
Skidmore, W., Els, S., Travouillon, T., et al. 2009, PASP, 121, 1151
Tapia, M. 2003, RMxAC, 19, 75
van der Klis, M. 2000, ARA&A, 38, 717
van der Klis, M. 2006, Compact Stellar X-ray Sources, 39
Veledina, A., Gandhi, P., Hynes, R., et al. 2017, MNRAS, 470, 48

Angel Castro, Diego Altamirano, Poshak Gandhi, Christian Knigge, Daniel Whiter, Matthew J. Middleton and Noel Castro-Segura: Physics and Astronomy, University of Southampton, SO17 1BJ, Southampton, UK (a.castro, d.altamirano, poshak.gandhi, c.knigge, d.whiter, m.j.middleton, n.castro-segura@soton.ac.uk).
Raúl Michel, Carlos Tejada, Gerardo Sierra, Enrique Colorado, Javier Hernández Landa, Gerardo Guisa and Benjamín García: Instituto de Astronomía, Universidad Nacional Autónoma de México, 22860, Ensenada, México (rmm, ctejada, gerardo, landa, guisa, benji@astro.unam.mx).
Juan Echevarría: Instituto de Astronomía, Universidad Nacional Autónoma de México, Apartado Postal 70-264, México, CDMX, C.P. 04510 (jer@astro.unam.mx).
Juan V. Hernández Santisteban: SUPA School of Physics & Astronomy, University of St. Andrews, North Haugh, St. Andrews KY16 9SS, UK (jvhs1@st-andrews.ac.uk).

Revista Mexicana de Astronomía y Astrofísica, **55**, 377–392 (2019)

DOI: https://doi.org/10.22201/ia.01851101p.2019.55.02.21

EXTENSIVE ONLINE SHOCK MODEL DATABASE

A. Alarie and C. Morisset

Instituto de Astronomía, Universidad Nacional Autónoma de México, México.

Received February 6 2019; accepted August 15 2019

ABSTRACT

We present a new database of fully radiative shock models calculated with the shock and photoionization code MAPPINGS V. The database architecture is built to contain diverse shock grids comprising of multiple shock parameters. It can be easily accessible through the MySQL protocol. Intensities of spectral lines from infrared to X-rays are stored along with other useful outputs such as the ionic fractions/temperature, integrated densities, etc. A web page was created in order to explore interactively the database as it evolves with time. Examples of its usage are given using the Python language.

RESUMEN

Presentamos una nueva base de datos para modelos de choques puramente radiativos calculados con el código Mappings V. La arquitectura de la base de datos se diseñó para incluir diversas mallas de choques con distintos parámetros para los choques. La base es de fácil acceso mediante el protocolo MySQL. Se almacenan las intensidades de líneas espectrales que abarcan desde el infrarrojo hasta los rayos X, así como otros resultados útiles, como la fracción iónica/temperatura, las densidades integradas, etc. Se creó una página en la red para poder explorar de manera interactiva la base de datos a medida que evoluciona en el tiempo. Se dan ejemplos de su uso mediante el lenguaje Python.

Key Words: astronomical data bases: miscellaneous — Galaxy: abundances — H II regions — ISM: abundances

1. INTRODUCTION

The internet revolution has changed in a powerful and effective way how research is conducted today. Far away are the days when a researcher had to spend an incalculable amount of time in libraries searching and deciphering an ever growing and complex scientific literature. In this day and age, researchers' primary reflex is to use the internet to search for and gather essential information to the advancement of their research. Astrophysics has been particularly at the forefront in adopting this technology and applying it to very diverse goals.

Services such as the ADS[1] [SAO/NASA Astrophysics Data System Abstract Service (McKiernan 2001)] now play an indispensable role in providing easy access to millions of abstracts and to the associated papers.

Other web services have been created to facilitate the search of astrophysical data. A prominent example is the conglomerate of CDS[2] (Strasbourg Astronomical Data Center) services like VizieR[3], which became available in 1996 and was later described in Ochsenbein et al. (2000). It provides access to the most complete online library of published astronomical catalogues and data tables organized in a self-documented database system.

Another service from the CDS is the ALADIN[4] interactive sky atlas (Bonnarel et al. 2000; Boch & Fernique 2014), which allows simultaneous access to digitized images of the sky, astronomical catalogs, and databases. It is mainly used to facilitate direct comparison of observational data at any wavelength with existing reference catalogs of astronomical objects.

[1] http://http://adsabs.harvard.edu/

[2] http://cds.u-strasbg.fr/

[3] http://vizier.u-strasbg.fr/

[4] https://aladin.u-strasbg.fr/aladin.gml

While such services have proven to be valuable, other areas of astrophysics can also benefit from those innovations. This is particularly the case of computational models such as photoionization and shock models computed using various spectral synthesis codes. Most of those models available in the 'market' can be found in the form of tables that are scattered around in the published literature. The most recent model grids are available as compressed files in multiple websites that use quite different data-formats. A centralized database, readily accessible and user friendly, would no doubt be beneficial to the community. To this end the Mexican Million Models database (3MdB[5]) was created (Morisset et al. 2015). It is designed to store and distribute photoionization models computed with the code CLOUDY (Ferland et al. 2017) using the MySQL database management system. This service offers to the community an easy access to millions of online models by means of the SQL language.

This paper deals with the addition of shock models calculated with the code MAPPINGS (Sutherland & Dopita 2017). This new database which includes shock models is called "3MdBs" (i.e., 3MdB-shocks). The structure of the 3MdBs database differs from the original 3MdB (photoionization models), but the logic behind its usage has remained the same. Both databases are available at the same address and both can be used simultaneously with the appropriate SQL queries. 3MdBs includes a website[6] that allows one to explore the grid available in the database interactively, using a simple web browser. The website also contains tutorials allowing potential users to obtain the necessary information required to interact with it.

This paper is structured as follows. In § 2 we briefly introduce the modeling code MAPPINGS. § 3 explains the database structure. The grids of models available at the time of publication are presented in § 4 followed by a discussion about specials grids in § 4.4.

2. THE MODELING CODE

All the models referred to in this paper have been calculated using the shock and photoionization code MAPPINGS V[7], version 5.1.13 (Sutherland & Dopita 2017; Sutherland et al. 2018). The latest improvements made in MAPPINGS V are detailed in Sutherland & Dopita (2017).

[5] https://sites.google.com/site/mexicanmillionmodels/

[6] http://3mdb.astro.unam.mx

[7] MAPPINGS V **is freely accessible from** https://mappings.anu.edu.au/code/

2.1. *Preionization*

Preionization conditions of the gas entering the shock front are an essential parameter of the shock calculations since they greatly influence the ionization structure of the shocked gas downstream and therefore all the line emissivities and their spatially integrated intensities (Dopita & Sutherland 1995; Allen et al. 2008). Manually setting preionization would be arbitrary and far from optimal, in particular in models related to specific astrophysical situations.

Allen et al. (2008), for instance, used an iterative process to determine preionization by first integrating the upstream propagating UV radiation, which is produced by the shocked gas UV emission downstream, and second, by using the resulting UV energy distribution to calculate a photoionization model for the preshock gas as it travels towards the shock front. In the case of high velocity shocks, it is a reasonable to assume that the precursor is photoionised and in near-equilibrium conditions, as determined from the ionizing radiation field generated by the shocked gas downstream.

Since there is a strong feedback between preionization conditions and the ionization of the shocked gas downstream and its UV emission, the adopted methodology consisted in repeating the shock calculations using the preionization conditions inferred from the previous shock iteration. By repeating this iterative procedure up to at least four times, one finds that both the temperature and ionization state of the precursor converge towards a stable value; hence, so will the line emission intensities of the cooling shock.

While this method is valid for shock velocities V_s in excess of ≈ 200 km s^{-1}, it fails for slower velocities since there is insufficient time for the preshock gas to achieve equilibrium before it is shocked. In such cases, it is essential to take into consideration the time dependent aspects of the problem. MAPPINGS V now addresses the preionization problem in a fully consistent manner. For the first time, the new code treats the preshock ionization and thermal structure iteratively by solving, in a fully time-dependent manner, the photoionization of the preshock gas, its recombination, photoelectric heating and line cooling as it approaches the shock front. A detailed study of preionization in radiative shocks was presented in Sutherland & Dopita (2017). Therefore, the models in the database make use of this new treatment, in which the preshock temperature and ionization state of the gas are iteratively calculated after each shock calculation.

2.2. *Precursor Gas*

For shocks with a velocity of less than 100 km s^{-1}, we did not compute the emission of the precursor since shocks below this velocity are unable to produce any appreciable ionizing emission. For shocks with velocity greater than 100 km s^{-1}, the photoionized precursors were computed separately. These were evaluated after the ionizing radiation field generated by the shock had been computed. All precursors were calculated subsequently to each iteration using the option 'P6' in MAPPINGS V (photoionization model), the ionizing radiation emanating from the shock being the only source of ionization in the current grid. We essentially used the exact same method employed by Allen et al. (2008) to compute the precursor emission spectrum.

3. THE NEW DATABASE

All models presented in this paper are stored into an SQL[8] database freely available online. This method of distribution has three main advantages. First, it allows anyone to have access instantaneously to thousands of models without the hassle of installing and managing the database on one's own workstation. Second, any new database updates or additions become instantly available to the community, a feature which can be very useful when it involves a worldwide collaboration (which is not available when using the VizieR database system). Third, the database can be accessed and handled using anyone's preferred programming language as long as it includes a SQL client library.

In order to make use of this database and fully exploit its capabilities, the user needs to be familiar with the SQL database language, a domain-specific language designed for managing data stored in a relational database management system. This work makes use of MariaDB®, a fast, scalable and robust open source database server. In the following section, we shall explain the database structure and the variables it manages. This will be followed by a book case example of how the database is best used.

3.1. *Database Structure*

As in any database design, the data in distributed across several tables with a multicolumn setup. The whole database consists of 12 tables, each having a specific purpose, which we shall discuss in details below. An overall view of the database's structure is displayed in Figure 1, which illustrates the different relations between the tables. The architecture adopts a modular design in the form of multiple tables, all with the aim of satisfying three criteria: efficiency, simplicity and expandability. By design, an SQL database can only contain a given number of name columns, depending of its configuration. Too many columns in a table can greatly degrade its performance, and even make it unstable. It is also very rare that one needs the information contained in all tables through a single database request. Most of the time, only a fraction of the table columns are needed at a given time. For this reason, the data are scattered into different tables, each having a specific purpose, while limiting data duplication and thus optimizing the database size.

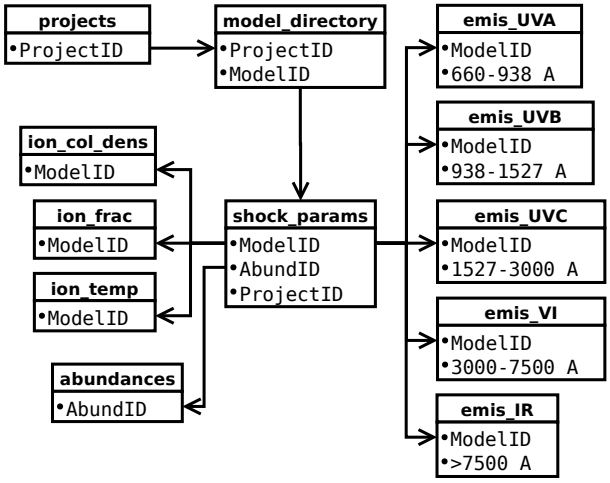

Fig. 1. Interrelation between the various database tables.

All the shock parameters are found in the table named `shock_params` (Table 4). This table includes various columns associated with the shock parameters described in § 4.1, mainly the shock velocity (`shck_vel`), the preshock density (`preshck_dens`) and the transverse magnetic field (`mag_fld`). The abundance sets used for a specific model are referenced using an abundance identification code (`AbundID`), which is linked to the table `abundances` that contains a list of all abundance sets available in the database at the time it is consulted.

A total of 4132 emission lines from ultraviolet to infrared can be extracted from the database. They are distributed among 5 tables, each covering specific wavelength intervals : 660-938 Å (`emis_UVA`), 939-1527 Å (`emis_UVB`), 1528-2999 Å (`emis_UVC`), 3000-

[8]Structured Query Language

7499 Å (`emis_VI`) and 7500Å-609μm (`emis_IR`). The complete emission lines list can be consulted via the web interface.

For each emission line of every model, the line intensities corresponding to the three different region types (namely shock, precursor and shock+precursor) are available, using the filter `WHERE emisVI.modeltype="shock"` or `"precursor"` or `"shock_plus_precursor"` respectively.

The mean temperatures, weighted by the ionic fraction of the specie involved, are given for each model in the table `temp_frac`, with the average ionic fraction listed in the column labelled `ion_frac` and the ionic column densities in the column `ion_column_frac`.

There are two more tables in the database that are usually not expected to be required. Their names are `projects` and `models_directory`. They ought to be used only when one needs to reevaluate a model, or when the latter contains information required by the web-interface.

3.2. *Website and User Credentials*

In § 4, we describe the models grids available at the time of publication. With time, other grids will be calculated and added in the database. In order to publicize these grids to the community, we created a website allowing to visualized the different grids available at the time of consultation. The website can be reached via `http://3mdb.astro.unam.mx/`.

The user credentials can be obtained via the website along with the IP adress and port needed to connect to the database.

The website is connected directly to the MariaDB[9] database. This means that it is adaptive, and any changes made to the database will automatically appears in the different sections. New grids of models can be added to the database, which then become automatically visible and accessible to the general public. Since each grid is built using a distinct range of shock parameters, and the spacing between successive values is at times non-uniform from grid to grid, the website provides a parameter explorer that allows any user to explore the database and, in an intuitive manner, to compose relatively complex SQL queries, such as the one given as example in Table 1. The website also includes interactive tutorials that aim at teaching any user how to connect and interact with the database using the Python programming language.

[9] `https://mariadb.org/`

4. THE MODEL GRIDS IN THE DATABASE

At the time of publication, 3 main grids are available in the database :

1. An exact replica of the Allen et al. (2008) grids (§ 4.1).
2. An extension of the Allen et al. (2008) grids computed for low metallicities using the abundances of Gutkin et al. (2016) (§ 4.3)
3. An extension of the Allen et al. (2008) grids computed for different shock ages (§ 4.4).

Not all the parameter grids presented in this paper are equally set in the shock parameter space (i.e., the size of the intervals and the range they cover may depend differently on the assumed abundances). The next section will describe the grids of models currently available in our database. For all models of the grid, we provide information about each of the three regions: shock, precursor and shock+precursor. The effect of dust has not been considered in the models.

4.1. *The Allen et al. (2008) Grid*

As in Allen et al. (2008), each shock model from the grid is uniquely defined through five different input parameters: the shock velocity V_s, the preshock transverse magnetic field B_0, the preshock density n_0 and one of the five abundance sets listed in Table 2. The temperatures of the ions and electrons have been set to be equal right from the shock front. The ionization state of the precursor (the gas entering the shock front) is calculated with MAPPINGS Vusing the method described in § 2.1.

The grid is divided into two sub-grids. Both of which are an exact replica of those presented by Allen et al. (2008), as they use the same shock parameters. The only exception is the use of MAPPINGS V instead of MAPPINGS III during model evaluations. Below is a summary of each sub-grid.

The first sub-grid contains 1440 models that were calculated using one of the following five abundance sets: a depleted solar set and a twice-solar set, which were both used by Dopita & Sutherland (1996), a solar abundance set labelled 'dopita2005' from Asplund et al. (2005), which was used in Dopita et al. (2005), and finally, an SMC and an LMC abundance set published by Russell & Dopita (1992). The respective abundances for each atomic element with respect to hydrogen are given in Table 2. Each model in this sub-grid was calculated using a fixed preshock

TABLE 1

EXAMPLE OF SQL COMMAND LINES USED TO GENERATE FIGURE 2

```
SELECT shock_params.shck_vel AS shck_vel,
       shock_params.mag_fld AS mag_fld,
       log10(emis_VI.NII_6583/emis_VI.HI_6563) AS NII_Hb,
       log10(emis_VI.OIII_5007/emis_VI.HI_4861) AS OIII_Hb
FROM shock_params
INNER JOIN emis_VI ON emis_VI.ModelID=shock_params.ModelID
INNER JOIN abundances ON abundances.AbundID=shock_params.AbundID
WHERE emis_VI.model_type='shock'
AND shock_params.ref='Allen08'
AND abundances.name='Allen2008_Solar'
AND shock_params.shck_vel<=200
AND shock_params.preshck_dens=1
ORDER BY shck_vel, mag_fld;
```

TABLE 2

ABUNDANCES USED IN ALLEN ET AL. 2008

Elem	Solar	2×Solar	Dopita2005	LMC	SMC
H	0.00	0.00	0.00	0.00	0.00
He	-1.01	-1.01	-1.01	-1.05	-1.09
C	-3.44	-3.14	-4.11	-3.96	-4.24
N	-3.95	-3.65	-4.42	-4.86	-5.37
O	-3.07	-2.77	-3.56	-3.65	-3.97
Ne	-3.91	-3.61	-3.91	-4.39	-4.73
Na			-6.35	-4.85	-5.92
Mg	-4.42	-4.12	-5.12	-4.53	-5.01
Al	-5.43	-5.23	-7.31	-4.28	-5.60
Si	-4.45	-4.15	-5.49	-5.29	-4.69
S	-4.79	-4.49	-5.01	-5.23*	-5.41
Cl			-6.70		-7.30
Ar	-5.44	-5.14	-5.44	-5.71	-6.29
Ca	-5.88	-5.58	-8.16	-6.03	-6.16
Fe	-4.63	-4.33	-6.55	-4.77	-5.11
Ni			-7.08	-6.04	-6.14
X	0.7073	0.6946	0.7158	0.7334	0.7535
Y	0.2745	0.2696	0.2778	0.2596	0.2432
Z	0.0183	0.0358	0.0065	0.0070	0.0033

*A typo error shows -7.23 in the Allen et al. (2008) paper although their model was obtained with the correct value of -5.23, as the one present in the grid.

density of $n_0 = 1$ cm^{-3} consisting of 36 individual shock velocities (from 100 up to 1000 km s^{-1} in steps of 25 km s^{-1}) and one of the following 8 transverse magnetic field values: $B = 10^{-4}$, 0.5, 1.0, 2.0, 3.23, 4.0, 5.0 and 10 μG.

The second sub-grid of models was calculated using only the solar abundance set of Dopita & Sutherland (1996) with 6 preshock densities (0.01, 0.1, 1.0, 10, 100 and 1000 cm^{-3}), at 36 shock velocities (100 up to 1000 km s^{-1} in steps of 25 km s^{-1}) and for 8 transverse magnetic field values ($B = 10^{-4}$, 0.5, 1.0, 2.0, 3.23, 4.0, 5.0 and 10 μG). As in the Allen et al. (2008) paper, further models were computed using additional values of B in order to cover all the magnetic parameter values $B/n^{1/2}$ from the first subgrid. This facilitates comparison of models that differ by their preshock density. We recall that models with the same ratio $B/n^{1/2}$ result in the same magnetic to gas pressure ratio. These additional values (transverse magnetic field) are $B \approx 10^{-3}$, $\approx 10^{-2}$, $\approx 10^{-1}$, 1.0, 10 and 100 μG, and were calculated for each selected preshock density.

4.2. *Comparison Between the Allen 2008 Models and Our Calculations*

The first application of the new model grid was to compare it with the previous grid from Allen et al. (2008). Figure 2 shows a classical plot of [O III]/ Hβ versus [N II]/ Hα, commonly known as a BPT diagnostic diagram (Baldwin et al. 1981). Except for the fact that our grid was computed using the code MAPPINGS V, it is otherwise equivalent to the one presented by Allen et al. (2008). We assumed the same shock parameters: a solar abundance set with shock velocities varying from 200 to 1,000 km s^{-1}. The transverse magnetic field covers the range 0.0001 to 2 μG and the preshock density is always 1 cm^{-3}. The left panel displays the line ratios from the shocked gas only, while the right panel dis-

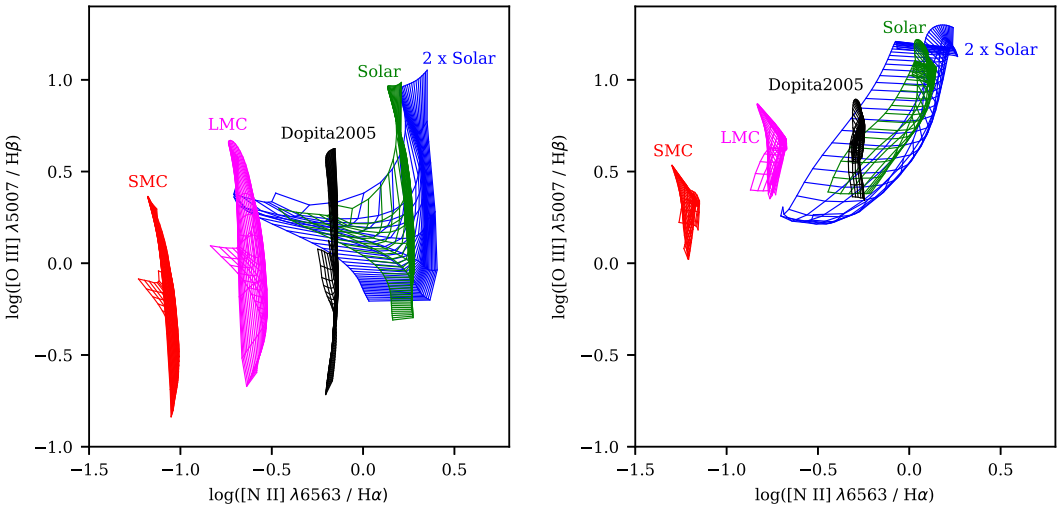

Fig. 2. The BPT [O III] λ5007/Hβ versus [N II] λ6583/ Hα diagnostic diagram (Baldwin et al. 1981) displaying shock models that use the same abundance sets as Allen et al. (2008) and which cover shock velocities ranging from 200 to 1000 km s^{-1}, all with the same preshock density of $n_0 = 1$ cm^{-3}. The left panel displays the line ratios from the shocked gas only while the right panel shows the same ratios after summing up shock and precursor line intensities. This figure is identical to Figure 20 shown in Allen et al. (2008), except that the models shown here were calculated with MAPPINGS V instead of MAPPINGS III. The color figure can be viewed online.

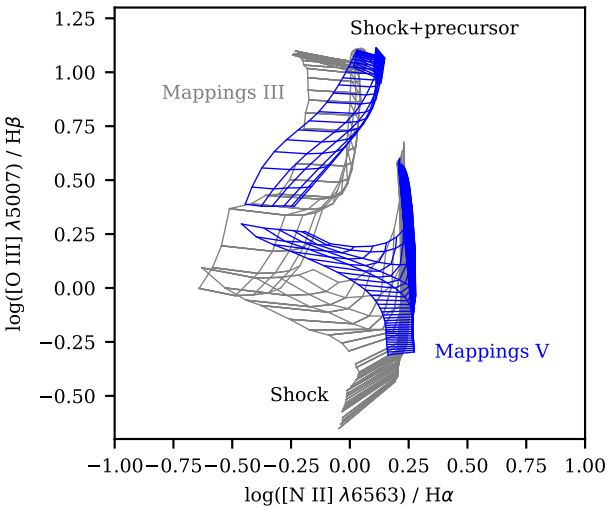

Fig. 3. Comparison of MAPPINGS III and MAPPINGS V in the BPT diagram of [O III] λ5007/ Hβ vs. [N II] λ6583/ Hα when using the same model parameters as Allen et al. (2008): a solar abundance set, a preshock density of $n_0 = 1$ cm^{-3}, shock velocities ranging from 200 to 1 000 km s^{-1} with an interval of 25 km s^{-1}, and a transverse magnetic field of 10^{-4}, 1, 2 and 4 μG cm$^{3/2}$. The models calculated by Allen et al. (2008) are shown in gray and our models using MAPPINGS V are shown in blue. This figure is similar to Figure 21 of Allen et al. (2008), which was used by the authors to compare their MAPPINGS III grid to an earlier grid from Dopita & Sutherland (1996). The color figure can be viewed online.

plays the same ratios after summing up both shock and precursor line intensities. Our figure can be directly compared to Figure 20 of Allen et al. (2008).

Figure 3 shows a direct comparison between our grid (blue lines) and the Allen et al. (2008) version using MAPPINGS III(gray lines). Although similarities do appear between the different line ratio curves, a higher value by up to ≈ 0.3 dex of our [O III]/ Hβ ratio shows up in some parts of the diagram.

Figure 4 displays the behavior as a function of shock velocity V_s of 16 different emission lines. These further illustrate the similarities and differences between both grids of models. All lines are normalized to the Hβ intensity. Colors represent whether the emission comes from the shocked gas only (red), from the preshock gas (green) or from the sum of both (blue). The models using MAPPINGS V are shown using dotted lines while the continuous lines represent the Allen et al. (2008) models. For both grids, a preshock density of 1 cm^{-3} and a magnetic field of 3.23 μG were assumed. The color shaded bands represent the range in flux variations within the MAPPINGS V grid when the magnetic field is varied between 10^{-4} and 10 μG.

We note from Figure 4 that the behavior of the emission line intensities is quite similar in the MAPPINGS V and MAPPINGS III grids, although significant differences appear for the lines [C IV] 1550Å, C III] 1909Å, [O III] 4363Å, [O III] 5007Å, and [Ne V] 14.3μm, which are predicted stronger in our new

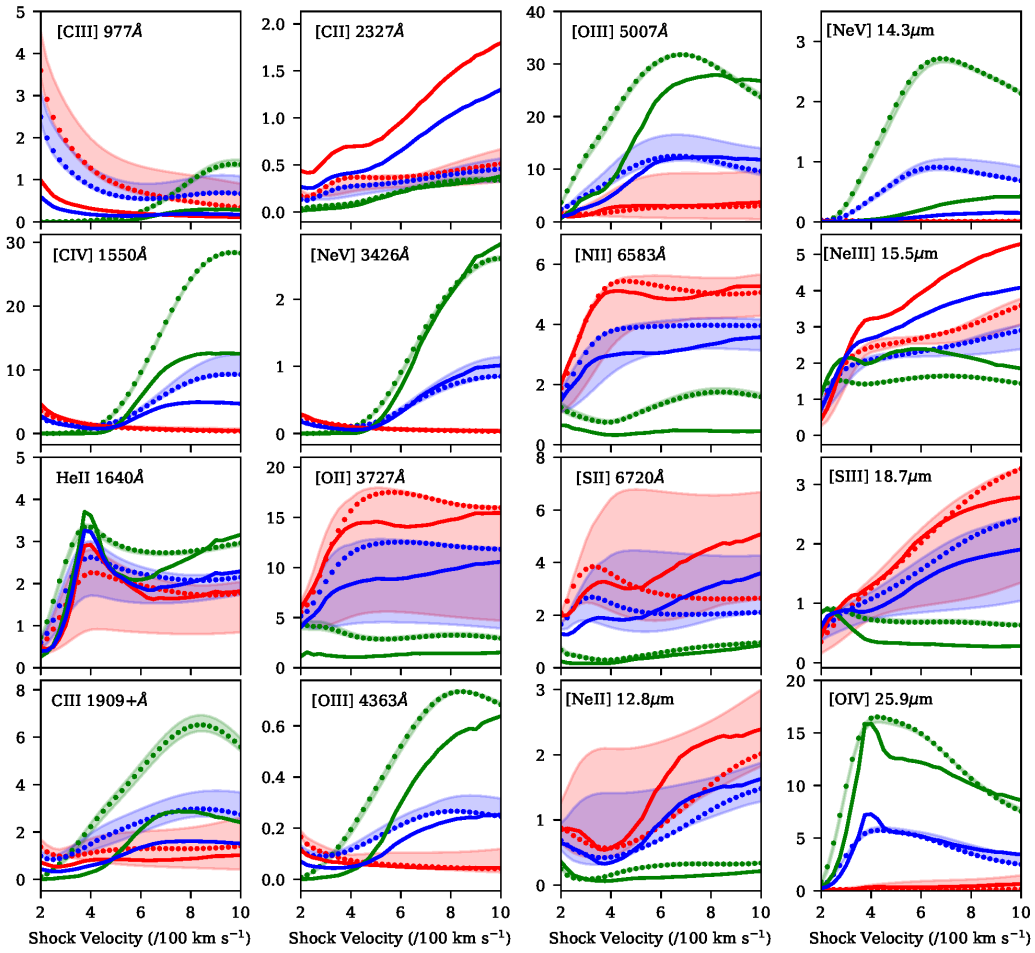

Fig. 4. Line fluxes as a function of shock velocity for 16 emission lines, normalized to Hβ. Colors represent whether the emission is from the shocked gas only (red), or from the preshock gas (green) or from the sum of both (blue). The models using MAPPINGS V are shown using dotted lines while the continuous lines represent the Allen et al. (2008) models. The color-shaded bands represent the domain of line intensity variations of the MAPPINGS V grid when gradually varying the magnetic field from 10^{-4} to 10 μG (with the same color coding as for the dotted lines). The color figure can be viewed online.

grid, while the lines [C II] 2327Å and [Ne III] 15.5μm are predicted weaker. Other lines appear stronger or weaker depending on the shock velocity considered.

Figure 5 is another illustration of the differences between the Allen et al. (2008) models and the current grid. The six panel pairs represent useful line ratio diagnostics when studying LINERs. All the sequences shown are from our grid only and they all have the same transversal magnetic field of 1 μG. The emission lines in the left panels represent shocked gas only, while those in the right panel represent the sum of shock with precursor emission lines. The model sequences shown correspond to sequences in which either the precursor density (red lines) or the shock velocity (blue lines) were varied. The line thickness (of the red and blue lines) increases as the iso-parameter takes on larger values. These models are equivalent to those presented by Molina et al. (2018) in their Figures 24 to 29. The main difference found in our grid is the [O III] 5007Å line, which can be up to 0.3 dex stronger than in Molina et al. (2018).

The line ratio differences discussed above between code versions arise either from changes implemented in the newer MAPPINGS code or from the use of a more recent atomic database. It is beyond the scope of this paper (and of the authors' expertise) to determine which of these is at play in any specific line intensity difference.

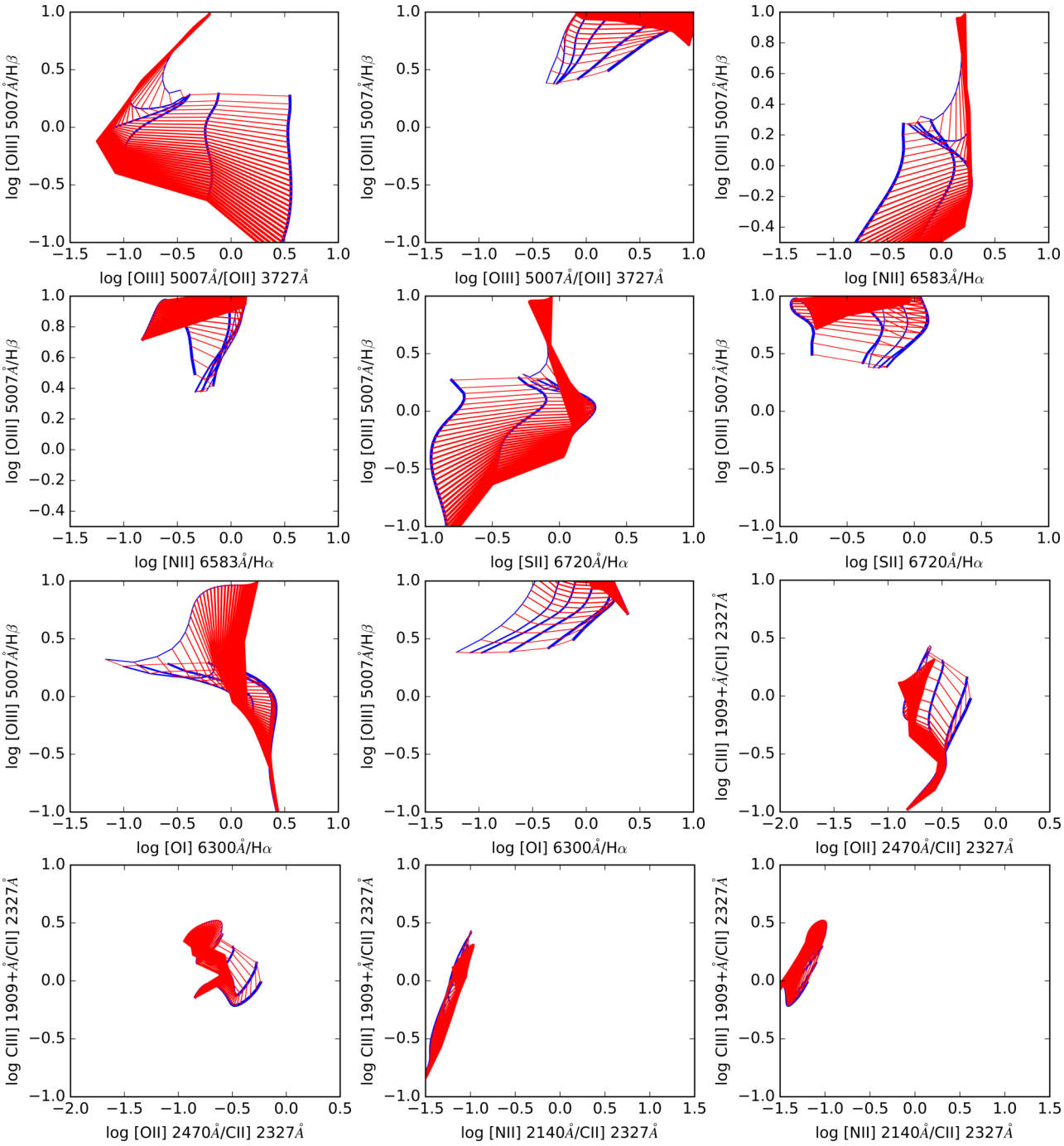

Fig. 5. Diagnostic diagrams to be compared to Molina et al. (2018), who used the Allen et al. (2008) models. All models shown have the same transverse magnetic field of 1 μG. Red lines represent shock model sequences of different n_0 values but of equal velocity, while blue lines represent shock model sequences of different V_s but of equal precursor density. The line thickness (of the red and blue lines) increases from one sequence to the next: the blue lines become thicker as the density increases and the red lines become thicker as the velocity increases. The color figure can be viewed online.

4.3. *The Low Metallicity Grid*

We have extended the grid of Allen et al. (2008) to include low metallicity abundances in order to study shocks in galaxies at different cosmic epochs. The abundance sets chosen for this grid in particular are the same as the ones derived in Gutkin et al. (2016), which were evaluated for different mass fraction of Z. We follow the same methodology as these

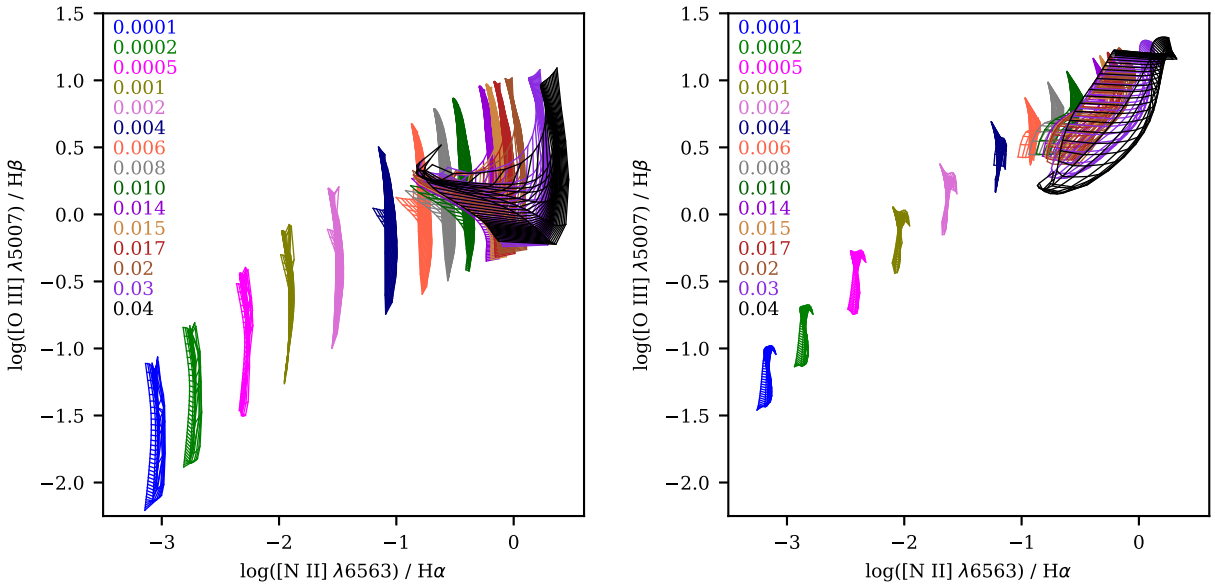

Fig. 6. Same diagrams as in Figure 2 except that the abundance sets are now from Gutkin et al. (2016). Shock velocities range from 100 to 1 000 km/s, and magnetic fields range from 0.0001 to 10 μG. The left panel corresponds to the line emission ratios from the shocked gas, while the right panel represents the line emission of both the shocked and precursor gas. The column in the upper left corner of each panel lists the mass fractions of each sequence of the corresponding color. The color figure can be viewed online.

authors, in order to retrieve the abundance of each individual element, from hydrogen to zinc.

Our database currently contains models calculated using the parameters given in Table 3. Figure 6 allows us to visualize the effect on the BPT diagram [O III]/ Hβ vs. [N II]/ Hα of adopting lower values of Z, starting with a value of (C/O)/(C/O)$_\odot$ = 1 and successively going down to 10^{-4} (shifting from left to right in the figure). Interestingly, when the metallicity decreases, the horizontal spread of [N II]/ Hα in each sequence tends to become narrower. Both changes of the shock velocity (from 100 to 1 000 km/s) and the magnetic field (from 10^{-4}) to 10 μG) lead to an increase in [O III] 5007Å/Hβ, while [N II] 6583Å/Hα remains essentially constant. It is also apparent from these figures that very low metallicity shocks lead to very low values of any collisionally excited line when normalized with respect to a recombination line of H. It is important to keep in mind that at the very low metallicity end, the lines from metals become negligible, but the hydrogen and helium recombination or collisionally excited lines are still emitted. If such shocked gas emission were superposed on the observation of a photoionized region, it might lead to an underestimation of metallic abundances, which would unavoidably result from simply assuming classical methods to determine e.g. O/H.

TABLE 3

GRID SAMPLE OF THE LOW METALLICITY GRID DESCRIBED IN § 3.2

Parameter	Sampled values
(C/O)/(C/O)$_\odot$	0.26, 1.00
Z$_{ism}$	0.0001, 0.0002 0.0005, 0.001, 0.002, 0.004 0.006, 0.008, 0.010, 0.014, 0.01524, 0.017 0.02, 0.03, 0.04
V_s (km s^{-1})	100, 125, ..., 1000
n$_0$ (cm^{-3})	1, 10, 10^2, 10^3, 10^4
B$_0$ (μG)	10^{-4}, 0.5, 1.0, 2.0, 3.23, 4.0, 5.0, 10

4.4. *Grids of Truncated/Young Shock Models*

The Allen et al. (2008) fast shock grid (§ 4.1) and the low metallicity shock grid (§ 4.3) contain models for which both the age of the shock was fixed prior to the calculations, by assuming arbitrary predetermined values. In certain cases, these parameters, when treated as free quantities, turn out to influence the line intensities in ways interesting to explore. In this section, we will indicate how the database can be used to explore the effect of the shock age on line ratios.

The great majority of shock models found in the database are complete models, that is, they have been fully integrated until the shocked gas has

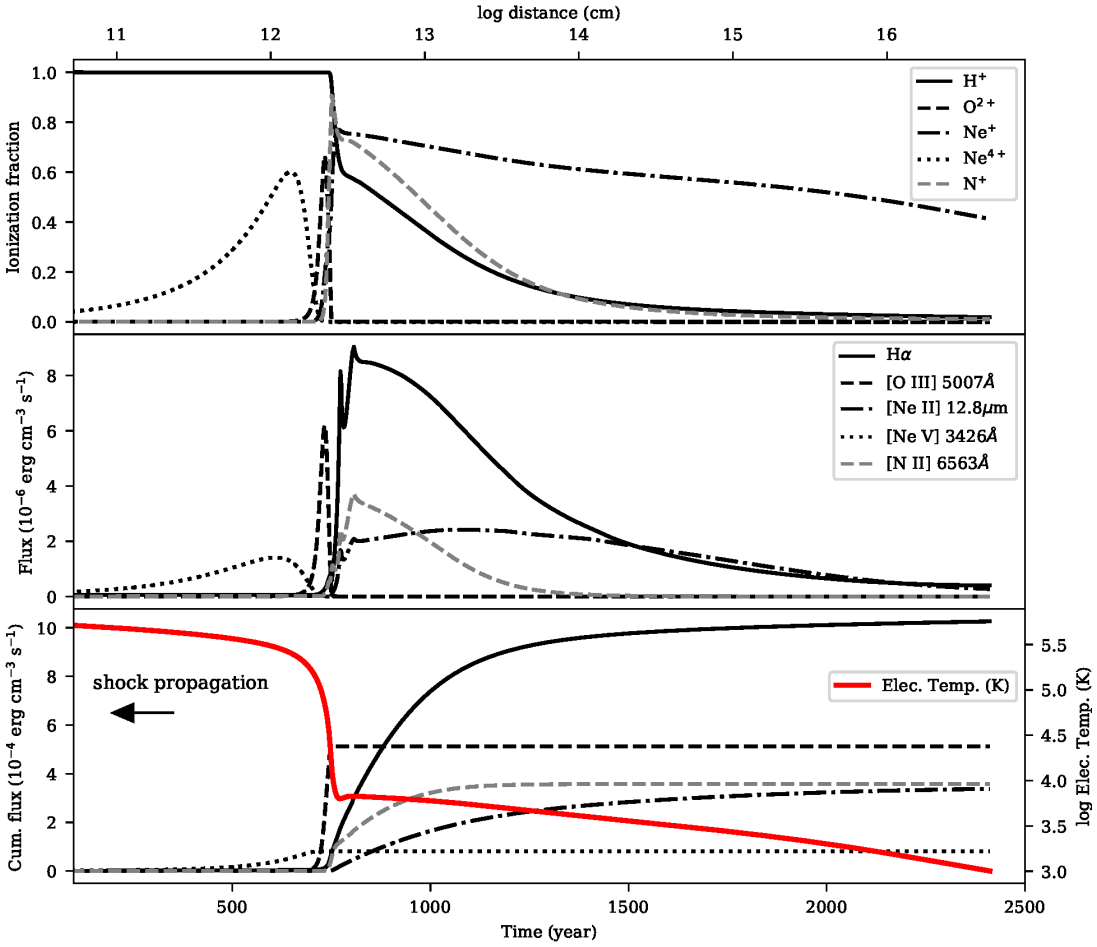

Fig. 7. Example of an ionization and emissivity structure for different elements at different ionization stages behind a 200 km s^{-1} shock propagating into a preshock density of 10 cm^{-3} and a transverse magnetic field of 1 μG with solar abundances. Top panel: Ionization fraction of H II, O III, Ne II and Ne V. Middle panel: emissivity of Hα, [O III] 5007Å, [Ne II] 12.8μm, and [Ne V] 3426Å. Bottom panel: cumulative emissivity for the same ions as plotted in the middle panel. The shock front is propagating towards the left. The color figure can be viewed online.

cooled and fully recombined. They correspond to steady-state conditions; such shocks, with time, will slow down as they progressively convert their supersonic kinetic energy into radiative cooling. Although steady-state models can reproduce the conditions encountered in a wide variety of astrophysical objects, they are not always the optimal perspective. This is the case for instance for objects in which the shocks are relatively recent and therefore possess an incomplete cooling structure. For this particular case, a grid of incomplete cooling shock models, also known as truncated models or young shocks, is needed. Only a few calculations of young shocks can be found in the literature. They were computed to match individual object such as the Cygnus Loop filaments (Raymond et al. 1980; Contini & Shaviv 1982; Raymond et al. 1988), or low-excitation Herbig-Haro objects (Binette et al. 1985). The lack of grids including young/truncated shocks compelled us to add those to our database and to provide a way of exploring them.

Figure 8 illustrates the impact on the line ratios of using incomplete shocks. It can be compared to the similar Figure 6 of Kehrig et al. (2018). A very common assumption is that when one observes high values of [S II] or [N II] or [O II] lines when normalized to an H line, this implies the presence of shocks or, on the contrary, when these ratios turn out to be small, one often concludes that shocks cannot be involved in the gas excitation. Such generalized views must be applied with greater care. For instance, at low metallicities, we find that young shock models can easily fall under the classical Kewley curve (see Kewley et al. 2001).

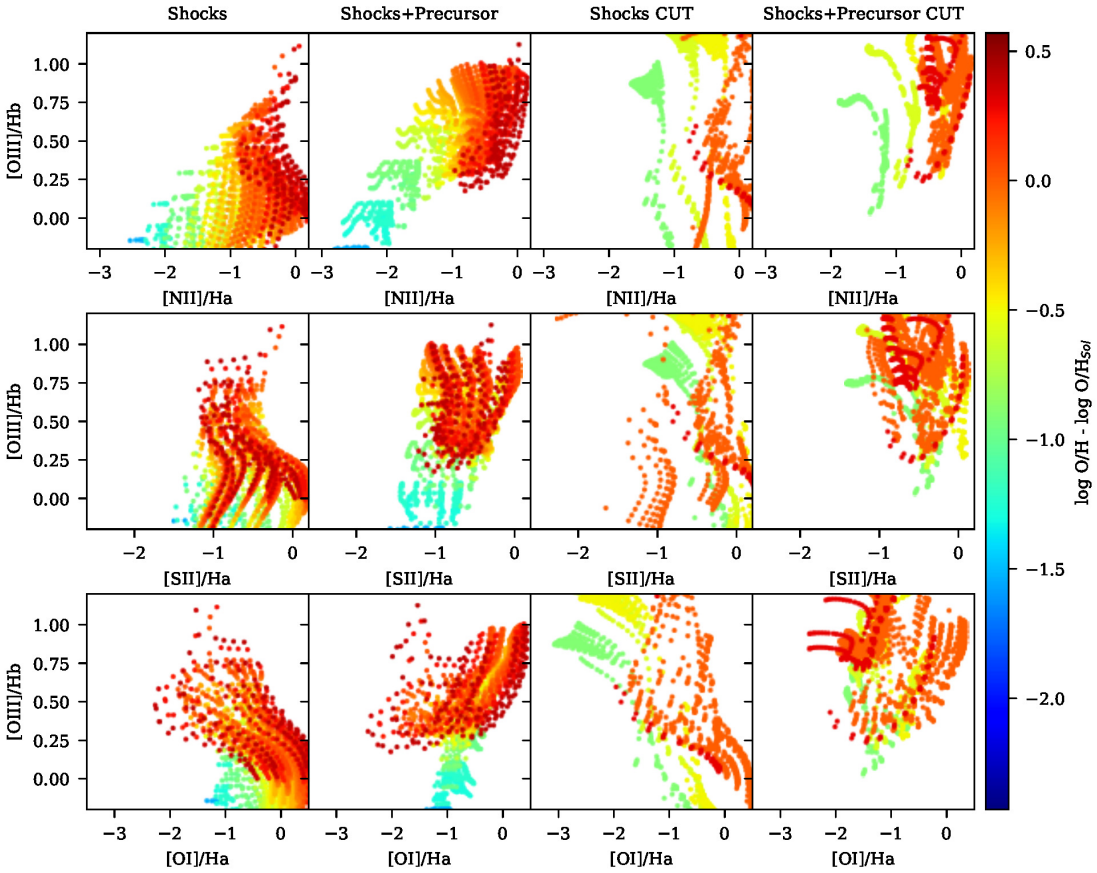

Fig. 8. Three classical BPT-type diagrams that compare complete with incomplete shock models (labeled "CUT"). All models were evaluated using a transversal magnetic field of 1 μG. The panels depict line ratios from either the shocked gas only or from both the shocked gas with the precursor emission. The color figure can be viewed online.

Truncated (or age-limited, or incomplete) shock models can be identified in the database using the `cut` keyword as a suffix at the end of the grid reference (ex: Allen08-cut, the only ones available for the moment). Before using any such model, it is important to be fully aware of what an incomplete or age-limited shock represents, which implies becoming familiar with the behavior of the ionization, temperature and line emissivities downstream from the shock front. To give an idea, Figure 7 shows how the evolution of these quantities is structured for a 200 km s^{-1} shock propagating into a gas with solar abundances and a preshock density of 10 cm^{-3}. As this figure shows, the recombination occurs in stages, with the higher ionization species recombining towards lower values as time proceeds. The gas temperature shown in the bottom panel declines markedly with time. Both of these factors and the fact that the density increases as the temperature drops[10] mean that the emissivity of any given line strongly varies with time along the cooling history of the postshock gas. The lower panel in Figure 7 shows how the cumulative (time-integrated) flux emission progresses, up to the desired final shock age. These time-integrated emission fluxes are actually stored in the database as a function of time. As revealed by the bottom panel, the line intensities are very sensitive to the time elapsed since the passage of the shock front. It is highly recommended to explore how such variations of the line intensities come about, and from there select the appropriate parameters to vary.

There are alternative parameters that can be used to specify the degree of shock completeness. The first is obviously the time elapsed (age) since the shock front initiated. The age parameter is located in the `shock_params` table in column named `time`,

[10]The transverse magnetic field will provide pressure to the gas as the temperature drops and if intense enough will suspend the usual isobaric prescription.

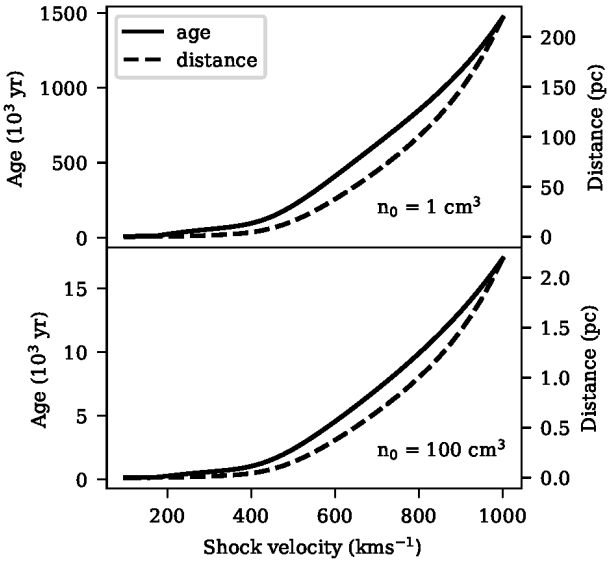

Fig. 9. Age and thickness of two shocks of different velocities that propagate in a gas cloud of density of either 1 cm^{-3} (top panel) or 100 cm^{-3} gas (bottom panel), assuming in both cases solar abundances and $B_0 = 1$ μG.

which is expressed in seconds. There is also the distance between the shock front and the final thickness of the shocked gas (at the specified shock age). This parameter is similarly located in the `shock_params` table in the column named `distance`, which is expressed in cm. Finally, there is the integrated column density of each ionic specie of the gas swept by the shock front until the gas has cooled and recombined (column named `coldens`), which is expressed in cm^{-2}. The total H column density can be found with the following summation : $N_H = N_{HI} + N_{HII}$. Complementary evaluations of how a specific line emissivity varies with age or depth requires knowing the integrated column density of the ion involved, which can be found in the `ion_col_dens` table.

Both the distance travelled by the shock wave or, alternatively, its cumulative age can vary greatly depending on the initial shock conditions, as shown in Figure 9. An easy mistake a user can make is to define diagnostic diagrams such as those presented in Figures reffig:BPTAllen and 6 and superpose them to observations characterized by ages and/or sizes that are inconsistent with those of the models. This can be avoided by varying the preshock density until its thickness fits the desired scale. In the case of a complete shock model (without an external photoionization source), the final thickness and the time spent in cooling both scale as n_0^{-1} (as seen in Figure 9).

Another potential mistake would be to use too high a preshock density, resulting in models where the density infered from its [S II] (λ6716Å/λ6731Å) doublet ratio (or its [O II] (λ3726Å/λ3729Å) doublet ratio) would be much higher than the density values derived from the observations. Consider, for instance, that a postshock temperature of $10^{5.3}$ K without magnetic field will result in a [S II] doublet ratio corresponding to a density as high as $\approx 100 n_0$. The reason is that the density increases isobarically as the shock cools and, for the $B = 0$ case, the local density across the whole shock structure grows as the ratio T_{post}/T_e where T_{post} and T_e are the postshock and the local electronic temperature, respectively.

5. FUTURE EVOLUTION OF THE DATABASE

New models will be added depending on the research necessities of the authors of this paper or upon request by anybody interested in models that have not yet been included. As the web page is dynamic and will instantly reflect the current status of the database and of its model grids, any new references or model inclusions will be easily noticed. The authors of this paper will also do their best to update the 3MdBs grid of models as soon as possible after a new version of MAPPINGSis available.

6. CONCLUDING REMARKS

In this paper, we presented an extension to the Mexican Million models database (3MdB) (Morisset et al. 2015), which comprises of the addition of shock models to the database. Important information was presented in this paper and the following is a list that summarizes the main points:

1. All shock models in the database were computed using the shock modelling code MAPPINGS V.
2. The database structure was explained in detail and information about how to connect and interact with the database was given. A website was created in order to follow the evolution of the database as new grids are added in the future.
3. At the time of publication, 3 grids are available. (1) The grid of Allen et al. (2008) was recomputed using MAPPINGS V. (2) We extended the grids of Allen et al. (2008) to low metallicity using the abundances derived by Gutkin et al. (2016). (3) Grids of truncated/young shock models were computed.

The current work is dedicated to the memory of Mike Dopita, the creator of MAPPINGS. The authors

wish to thank Luc Binette for his very useful collaboration during this study and in the writing of this paper. The current work was presented at the conference *A Star Was Born* celebrating the scientific achievements of Mike Dopita in April 2018. The 3MdBs access tools have been developed by A. Alarie while he was funded by a postdoctoral grant from CONACyT. This work is supported by grants DGAPA/PAPIIT-107215 and CONACyT-CB2015-254132.

APPENDIX

TABLE 4

FIELD LIST OF TABLE "SHOCK_PARAMS"

Field name	Description
ModelID	Unique model identification number*
ProjectID	Unique project identification number*
AbundID	Abundance identification number (same as in abundances table)
FHI	Ionization fraction of H^0
FHII	Ionization fraction of H^+
FHeI	Ionization fraction of He^0
FHeII	Ionization fraction of He^+
FHeIII	Ionization fraction of He^{++}
shck_vel	Shock velocity (km s^{-1})
preshck_dens	Preshock density (cm^{-3})
preshck_temp	Preshock electronic temperature (K)
mag_fld	Transverse magnetic field (μG)
cut_off_temp	Final electronic temperature in the last zone evaluated (K)
ref	Name of the grid in which the model is belonging
script	Main script used to evaluate a model*

*Field used internally in the web application.

TABLE 5

FIELD LIST OF TABLE "MODEL_DIRECTORY"

Field name	Description
Created	Date the model was added to the database
ModelID	Unique model identification number
Parameters	Model parameters associated with the grid (shock or photoionization*)
ProjectID	Unique project identification number
code_version	MAPPINGS version used

*To be implemented in the future.

TABLE 6

FIELD LIST OF TABLE "PROJECTS"

Field name	Description
Created	Date the grid was added to the database
ProjectID	Unique project identification number
code_version	MAPPINGS version used
model_count	number of models for this project in the database
ref	Name of the grid

TABLE 7

FIELD LIST OF TABLE "ABUNDANCES"

Field name	Description
name	Abundances file name used during the evaluation
AbundID	Abundance identification number
X	Hydrogen mass fraction
Y	Helium mass fraction
Z	Metallicity mass fraction of all element heavier than helium
HELIUM	Abundance of helium in log(He/H)
LITHIUM	Abundance of lithium in log(Li/H)
BERYLLIUM	Abundance of beryllium in log(Be/H)
BORON	Abundance of boron in log(B/H)
CARBON	Abundance of carbon in log(C/H)
NITROGEN	Abundance of nitrogen in log(N/H)
ZINC	Abundance of helium in log(Zn/H)

TABLE 8

FIELD LIST OF TABLE "ION_FRAC", "ION_TEMP" AND "ION_COL_DENS"

Field name	Ionization range*
HYDROGEN	(0 to 1)
HELIUM	(0 to 2)
BERYLLIUM	(0 to 4)
BORON	(0 to 5)
CARBON	(0 to 6)
NITROGEN	(0 to 7)
OXYGEN	(0 to 8)
FLUORINE	(0 to 8)
NEON	(0 to 8)
SODIUM	(0 to 9)
MAGNESIUM	(0 to 9)
ALUMINIUM	(0 to 9)
SILICON	(0 to 9)
PHOSPHORUS	(0 to 9)
SULPHUR	(0 to 9)
CHLORINE	(0 to 9)
ARGON	(0 to 9)
POTASSIUM	(0 to 10)
CALCIUM	(0 to 10)
SCANDIUM	(0 to 12)
TITANIUM	(0 to 12)
VANADIUM	(0 to 13)
CHROMIUM	(0 to 13)
MANGANESE	(0 to 13)
IRON	(0 to 13)
COBALT	(0 to 13)
NICKEL	(0 to 13)
COPPER	(0 to 13)
ZINC	(0 to 13)

*0=X^0, 1=X^+, 2=X^{++},...

REFERENCES

Allen, M. G., Groves, B. A., Dopita, M. A., Sutherland, R. S., & Kewley, L. J. 2008, ApJS, 178, 20

Asplund, M., Grevesse, N., & Sauval, A. J. 2005, ASPC 336, Cosmic Abundances as Records of Stellar Evolution and Nucleosynthesis, ed. T. G. Barnes III and F. N. Bash (San Francisco, CA: ASPC), 25

Baldwin, J. A., Phillips, M. M., & Terlevich, R. 1981, PASP, 93, 5

Binette, L., Dopita, M. A., & Tuohy, I. R. 1985, ApJ, 297, 476

Boch, T. & Fernique, P. 2014, ASPC 485, Astronomical Data Analysis Software and Systems XXIII, ed. N. Manset and P. Forshay (Hawaii, USA, ASPC), 277

Bonnarel, F., Fernique, P., Bienaymé, O., et al. 2000, A&AS, 143, 33

Contini, M. & Shaviv, G. 1982, Ap&SS, 85, 203

Dopita, M. A., Groves, B. A., Fischera, J., et al. 2005, ApJ, 619, 755

Dopita, M. A. & Sutherland, R. S. 1995, ApJ, 455, 468

_____. 1996, ApJS, 102, 161

Ferland, G. J., Chatzikos, M., Guzmán, F., et al. 2017, RMxAA, 53, 385

Gutkin, J., Charlot, S., & Bruzual, G. 2016, MNRAS, 462, 1757

Kehrig, C., Vílchez, J. M., Guerrero, M. A., et al. 2018, MNRAS, 480, 1081

Kewley, L. J., Dopita, M. A., Sutherland, R. S., Heisler, C. A., & Trevena, J. 2001, ApJ, 556, 121

McKiernan, G. 2001, Library Hi Tech News, 18, null

Molina, M., Eracleous, M., Barth, A. J., et al. 2018, ApJ, 864, 90

Morisset, C., Delgado-Inglada, G., & Flores-Fajardo, N. 2015, RMxAA, 51, 103

Ochsenbein, F., Bauer, P., & Marcout, J. 2000, A&AS, 143, 23

Raymond, J. C., Hartmann, L., Black, J. H., Dupree, A. K., & Wolff, R. S. 1980, ApJ, 238, 881

Raymond, J. C., Hester, J. J., Cox, D., et al. 1988, ApJ, 324, 869

Russell, S. C. & Dopita, M. A. 1992, ApJ, 384, 508

Sutherland, R., Dopita, M., Binette, L., & Groves, B. 2018, MAPPINGS V: Astrophysical Plasma Modeling Code, ascl soft

Sutherland, R. S. & Dopita, M. A. 2017, ApJS, 229, 34

A. Alarie: Instituto de Astronomía, Universidad Nacional Autónoma de México, Apdo. Postal 70264, C.P. 04510, México, CDMX, México (alexandre.alarie@gmail.com).

C. Morisset: Instituto de Astronomía, Universidad Nacional Autónoma de México, Apartado postal 106, C.P. 22800 Ensenada, Baja California, México (chris.morisset@gmail.com).

AUTHOR INDEX

Acerbi, F. Multicolor Study of V1009 Per, a Close Binary System at the Beginning of the Overcontact Phase, and of CRTS J031642.2+332639, a New Binary System in the Same Field. *R. Michel, F. Acerbi, C. Barani, & M. Martignoni*, 65

Ahumada, J. A. NGC 1261: A time-series *VI* study of its variable stars. *A. Arellano Ferro, I. H. Bustos Fierro, J. H. Calderón, & J. A. Ahumada*, 337

Alarie, A. Extensive Online Shock Model Database. *A. Alarie & C. Morisset*, 377

Alhassan, A. J. Relativistic Beaming Effects and Structural Asymmetries in Highly Asymmetric Double Radio Sources. *A. J. Alhassan, A. A. Ubachukwu, F. C. Odo, & C. C. Onuchukwu*, 151

Altamirano, D. OPTICAM: A Triple-Camera Optical System Designed to Explore the Fastest Timescales in Astronomy. *A. Castro, D. Altamirano, R. Michel, P. Gandhi, J. V. Hernández Santisteban, J. Echevarría, C. Tejada, C. Knigge, G. Sierra, E. Colorado, J. Hernández-Landa, D. Whiter, M. Middleton, B. García, G. Guisa, & N. Castro Segura*, 363

Arellano Ferro, A. NGC 1261: A time-series *VI* study of its variable stars. *A. Arellano Ferro, I. H. Bustos Fierro, J. H. Calderón, & J. A. Ahumada*, 337

Arias-Estrada, M. O. A Solar Mid-Infrared Telescope. *J. E. Mendoza-Torres, J. S. Palacios-Fonseca, M. Velázquez-de-la-Rosa, P. Rodríguez-Montero, A. De-Roa-Campoy, E. Valadez-Campos, M. O. Arias-Estrada, J. Peña-Saint-Martín, B. Rodríguez-Pedroza, I. Gómez-Arista, M. Juárez-Gama, K. Gottschalk, & I. C. Medina-Carrillo* , 11

Barani, C. Multicolor Study of V1009 Per, a Close Binary System at the Beginning of the Overcontact Phase, and of CRTS J031642.2+332639, a New Binary System in the Same Field. *R. Michel, F. Acerbi, C. Barani, & M. Martignoni*, 65

Benítez-Álvarez, R. A new method for actively tuning FBG's to particular infrared wavelengths for OH emission lines suppression . *R. Benítez-Álvarez, F. Martínez-Piñón, & V. G. Orlov*, 351

Bernal, T. Dynamics of clusters of galaxies with extended $f(\chi)$ gravity. *T. Bernal, O. López-Corona, & S. Mendoza*, 237

Bolt, G. Extensive Photometry of V1838 Aql During the 2013 Superoutburst. *J. Echevarría, E. de Miguel, J. V. Hernández Santisteban, R. Costero, R. Michel, L. J. Sánchez, J. Olivares, A. Ruelas-Mayorga, D. González-Buitrago, J. L. Jones, A. Oskanen, W. Goff, J. Ulowetz, G. Bolt, R. Sabo, F.-J. Hambsch, D. Slauson, & W. Stein* , 21

Bustos Fierro, I. H. NGC 1261: A time-series *VI* study of its variable stars. *A. Arellano Ferro, I. H. Bustos Fierro, J. H. Calderón, & J. A. Ahumada*, 337

Calcáneo-Roldán, C. Gravitational Wave Enhancement as a Tool to Distinguish Dark Matter Halo Profiles. *S. Grijalva Castillo & C. Calcáneo-Roldán*, 231

Calderón, J. Study of the Open Cluster NGC 1528 Through $uvby - \beta$ Photoelectric Photometry. *J. H. Peña, J. Calderón, & D. S. Piña*, 203

Calderón, J. H. NGC 1261: A time-series *VI* study of its variable stars. *A. Arellano Ferro, I. H. Bustos Fierro, J. H. Calderón, & J. A. Ahumada*, 337

Cappa, C. E. Millimeter and Far-IR Study of the IRDC SDC 341.232-0.268. *M. M. Vazzano, C. E. Cappa, M. Rubio, V. Firpo, C. H. López-Caraballo, & N. U. Duronea*, 289

Caritá, L. A. Chaos in Growing Bar Models. *L. A. Caritá, I. Rodrigues, I. Puerari, & L. E. C. A. Schiavo*, 321

Castro, A. OPTICAM: A Triple-Camera Optical System Designed to Explore the Fastest Timescales in Astronomy. *A. Castro, D. Altamirano, R. Michel, P. Gandhi, J. V. Hernández Santisteban, J. Echevarría, C. Tejada, C. Knigge, G. Sierra, E. Colorado, J. Hernández-Landa, D. Whiter, M. Middleton, B. García, G. Guisa, & N. Castro Segura*, 363

Castro-Segura, N. OPTICAM: A Triple-Camera Optical System Designed to Explore the Fastest Timescales in Astronomy. *A. Castro, D. Altamirano, R. Michel, P. Gandhi, J. V. Hernández Santisteban, J. Echevarría, C. Tejada, C. Knigge, G. Sierra, E. Colorado, J. Hernández-Landa, D. Whiter, M. Middleton, B. García, G. Guisa, & N. Castro Segura*, 363

Cavalca, M. P. O. Searching for Mid-Range Planar Orbits to Observe Deimos. *M. P. O. Cavalca, A. F. B. A. Prado, V. M. Gomes, & D. M. Sanchez*, 305

Chukwude, A. E. Entrainment Factor of Individual Glitch Fractional Moment of Inertia. *I. O. Eya, J. O. Urama, & A. E. Chukwude*, 3

Colorado, E. OPTICAM: A Triple-Camera Optical System Designed to Explore the Fastest Timescales in Astronomy. *A. Castro, D. Altamirano, R. Michel, P. Gandhi, J. V. Hernández Santisteban, J. Echevarría, C. Tejada, C. Knigge, G. Sierra, E. Colorado, J. Hernández-Landa, D. Whiter, M. Middleton, B. García, G. Guisa, & N. Castro Segura*, 363

Costero, R. Extensive Photometry of V1838 Aql During the 2013 Superoutburst. *J. Echevarría, E. de Miguel, J. V. Hernández Santisteban, R. Costero, R. Michel, L. J. Sánchez, J. Olivares, A. Ruelas-Mayorga, D. González-Buitrago, J. L. Jones, A. Oskanen, W. Goff, J. Ulowetz, G. Bolt, R. Sabo, F.-J. Hambsch, D. Slauson, & W. Stein* , 21

Cruz-González, I. An Alternative Approach to the Finger of God in Large Scale Structures. *L. Salas & I. Cruz-González*, 93

Dal, H. A. On the Chromospheric Activity Nature of a Low-Mass Close Binary: KIC 12004834. *E. Yoldaş & H. A. Dal*, 73

de Miguel, E. Extensive Photometry of V1838 Aql During the 2013 Superoutburst. *J. Echevarría, E. de Miguel, J. V. Hernández Santisteban, R. Costero, R. Michel, L. J. Sánchez, J. Olivares, A. Ruelas-Mayorga, D. González-Buitrago, J. L. Jones, A. Oskanen, W. Goff, J. Ulowetz, G. Bolt, R. Sabo, F.-J. Hambsch, D. Slauson, & W. Stein* , 21

De Roa Campoy, A. A Solar Mid-Infrared Telescope. *J. E. Mendoza-Torres, J. S. Palacios-Fonseca, M. Velázquez-de-la-Rosa, P. Rodríguez-Montero, A. De-Roa-Campoy, E. Valadez-Campos, M. O. Arias-Estrada, J. Peña-Saint-Martín, B. Rodríguez-Pedroza, I. Gómez-Arista, M. Juárez-Gama, K. Gottschalk, & I. C. Medina-Carrillo* , 11

Deng, X. F. The Environmental Dependence of Galaxy Age and Stellar Mass in the Redshift Region $0.6 \leq z \leq 0.75$. *Xin-Fa Deng*, 185

Duronea, N. U. Millimeter and Far-IR Study of the IRDC SDC 341.232-0.268. *M. M. Vazzano, C. E. Cappa, M. Rubio, V. Firpo, C. H. López-Caraballo, & N. U. Duronea*, 289

Echevarría, J. Extensive Photometry of V1838 Aql During the 2013 Superoutburst. *J. Echevarría, E. de Miguel, J. V. Hernández Santisteban, R. Costero, R. Michel, L. J. Sánchez, J. Olivares, A. Ruelas-Mayorga, D. González-Buitrago, J. L. Jones, A. Oskanen, W. Goff, J. Ulowetz, G. Bolt, R. Sabo, F.-J. Hambsch, D. Slauson, & W. Stein* , 21

Echevarría, J. OPTICAM: A Triple-Camera Optical System Designed to Explore the Fastest Timescales in Astronomy. *A. Castro, D. Altamirano, R. Michel, P. Gandhi, J. V. Hernández Santisteban, J. Echevarría, C. Tejada, C. Knigge, G. Sierra, E. Colorado, J. Hernández-Landa, D. Whiter, M. Middleton, B. García, G. Guisa, & N. Castro Segura*, 363

Echeverry, L. M. Minimizing Fuel consumption in Orbit Transfers using Universal Variable and Particle Swarm Optimization. *L. M. Echeverry & Y. Villanueva*, 177

Eya, I. O. Entrainment Factor of Individual Glitch Fractional Moment of Inertia. *I. O. Eya, J. O. Urama, & A. E. Chukwude*, 3

Firpo, V. Millimeter and Far-IR Study of the IRDC SDC 341.232-0.268. *M. M. Vazzano, C. E. Cappa, M. Rubio, V. Firpo, C. H. López-Caraballo, & N. U. Duronea*, 289

Flores-Durán, S. N. Metallicity Gradients in M31, M 33, NGC 300 and the Milky Way Using Abundances of Different Elements. *M. Peña & S. N. Flores-Durán*, 255

Gandhi, P. OPTICAM: A Triple-Camera Optical System Designed to Explore the Fastest Timescales in Astronomy. *A. Castro, D. Altamirano, R. Michel, P. Gandhi, J. V. Hernández Santisteban, J. Echevarría, C. Tejada, C. Knigge, G. Sierra, E. Colorado, J. Hernández-Landa, D. Whiter, M. Middleton, B. García, G. Guisa, & N. Castro Segura*, 363

García, B. OPTICAM: A Triple-Camera Optical System Designed to Explore the Fastest Timescales in Astronomy. *A. Castro, D. Altamirano, R. Michel, P. Gandhi, J. V. Hernández Santisteban, J. Echevarría, C. Tejada, C. Knigge, G. Sierra, E. Colorado, J. Hernández-Landa, D. Whiter, M. Middleton, B. García, G. Guisa, & N. Castro Segura*, 363

García-Segura, G. Enhanced Mass Loss Rates in Red Supergiants and Their Impact on the Circumstellar Medium. *L. Hernández-Cervantes, B. Pérez-Rendón, A. Santillán, G. García-Segura, & C. Rodríguez-Ibarra*, 161

Goff, W. Extensive Photometry of V1838 Aql During the 2013 Superoutburst. *J. Echevarría, E. de Miguel, J. V. Hernández Santisteban, R. Costero, R. Michel, L. J. Sánchez, J. Olivares, A. Ruelas-Mayorga, D. González-Buitrago, J. L. Jones, A. Oskanen, W. Goff, J. Ulowetz, G. Bolt, R. Sabo, F.-J. Hambsch, D. Slauson, & W. Stein* , 21

Gomes, V. M. Searching for Mid-Range Planar Orbits to Observe Deimos. *M. P. O. Cavalca, A. F. B. A. Prado, V. M. Gomes, & D. M. Sanchez*, 305

Gómez-Arista, I. A Solar Mid-Infrared Telescope. *J. E. Mendoza-Torres, J. S. Palacios-Fonseca, M. Velázquez-de-la-Rosa, P. Rodríguez-Montero, A. De-Roa-Campoy, E. Valadez-Campos, M. O. Arias-Estrada, J. Peña-Saint-Martín, B. Rodríguez-Pedroza, I. Gómez-Arista, M. Juárez-Gama, K. Gottschalk, & I. C. Medina-Carrillo* , 11

González-Buitrago, D. Extensive Photometry of V1838 Aql During the 2013 Superoutburst. *J. Echevarría, E. de Miguel, J. V. Hernández Santisteban, R. Costero, R. Michel, L. J. Sánchez, J. Olivares, A. Ruelas-Mayorga, D. González-Buitrago, J. L. Jones, A. Oskanen, W. Goff, J. Ulowetz, G. Bolt, R. Sabo, F.-J. Hambsch, D. Slauson, & W. Stein* , 21

Gottschalk, K. A Solar Mid-Infrared Telescope. *J. E. Mendoza-Torres, J. S. Palacios-Fonseca, M. Velázquez-de-la-Rosa, P. Rodríguez-Montero, A. De-Roa-Campoy, E.*

Valadez-Campos, M. O. Arias-Estrada, J. Peña-Saint-Martín, B. Rodríguez-Pedroza, I. Gómez-Arista, M. Juárez-Gama, K. Gottschalk, & I. C. Medina-Carrillo , 11

Grijalva Castillo, S. Gravitational Wave Enhancement as a Tool to Distinguish Dark Matter Halo Profiles. *S. Grijalva Castillo & C. Calcáneo-Roldán*, 231

Guisa, G. OPTICAM: A Triple-Camera Optical System Designed to Explore the Fastest Timescales in Astronomy. *A. Castro, D. Altamirano, R. Michel, P. Gandhi, J. V. Hernández Santisteban, J. Echevarría, C. Tejada, C. Knigge, G. Sierra, E. Colorado, J. Hernández-Landa, D. Whiter, M. Middleton, B. García, G. Guisa, & N. Castro Segura*, 363

Hambsch, F.-J. Extensive Photometry of V1838 Aql During the 2013 Superoutburst. *J. Echevarría, E. de Miguel, J. V. Hernández Santisteban, R. Costero, R. Michel, L. J. Sánchez, J. Olivares, A. Ruelas-Mayorga, D. González-Buitrago, J. L. Jones, A. Oskanen, W. Goff, J. Ulowetz, G. Bolt, R. Sabo, F.-J. Hambsch, D. Slauson, & W. Stein* , 21

Hernández-Cervantes, L. Enhanced Mass Loss Rates in Red Supergiants and Their Impact on the Circumstellar Medium. *L. Hernández-Cervantes, B. Pérez-Rendón, A. Santillán, G. García-Segura, & C. Rodríguez-Ibarra*, 161

Hernández-Landa, J. OPTICAM: A Triple-Camera Optical System Designed to Explore the Fastest Timescales in Astronomy. *A. Castro, D. Altamirano, R. Michel, P. Gandhi, J. V. Hernández Santisteban, J. Echevarría, C. Tejada, C. Knigge, G. Sierra, E. Colorado, J. Hernández-Landa, D. Whiter, M. Middleton, B. García, G. Guisa, & N. Castro Segura*, 363

Hernández Santisteban, J. V. Extensive Photometry of V1838 Aql During the 2013 Superoutburst. *J. Echevarría, E. de Miguel, J. V. Hernández Santisteban, R. Costero, R. Michel, L. J. Sánchez, J. Olivares, A. Ruelas-Mayorga, D. González-Buitrago, J. L. Jones, A. Oskanen, W. Goff, J. Ulowetz, G. Bolt, R. Sabo, F.-J. Hambsch, D. Slauson, & W. Stein* , 21

Hernández Santisteban, J. V. Multiwavelength Observations of MASTER OT 075353.88+174907.6: A Likely Superoutburst of a Long Period Dwarf Nova System. *A. S. Parikh, J. V. Hernández Santisteban, R. Wijnands, & D. Page*, 55

Hernández Santisteban, J. V. OPTICAM: A Triple-Camera Optical System Designed to Explore the Fastest Timescales in Astronomy. *A. Castro, D. Altamirano, R. Michel, P. Gandhi, J. V. Hernández Santisteban, J. Echevarría, C. Tejada, C. Knigge, G. Sierra, E. Colorado, J. Hernández-Landa, D. Whiter, M. Middleton, B. García, G. Guisa, & N. Castro Segura*, 363

Huepa, H. Some Remarks on the Open Cluster Upgren 1 Using $uvby - \beta$ Photoelectric Photometry. *J. H. Peña, A. Rentería, H. Huepa, & A. Pani*, 221

Ignace, R. Asymmetric Shapes of Radio Recombination Lines from Ionized Stellar Winds. *R. Ignace*, 31

Jack, D. Interstellar Absorption Towards the Novae V339 Del and V5668 Sgr. *D. Jack & K.-P. Schröder*, 139

Jesus, J. F. Exact Solution for Flat Scale-Invariant Cosmology. *J. F. Jesus*, 17

Jones, J. L. Extensive Photometry of V1838 Aql During the 2013 Superoutburst. *J. Echevarría, E. de Miguel, J. V. Hernández Santisteban, R. Costero, R. Michel, L. J. Sánchez, J. Olivares, A. Ruelas-Mayorga, D. González-Buitrago, J. L. Jones, A. Oskanen, W. Goff, J. Ulowetz, G. Bolt, R. Sabo, F.-J. Hambsch, D. Slauson, & W. Stein* , 21

Juárez-Gama, M. A Solar Mid-Infrared Telescope. *J. E. Mendoza-Torres, J. S. Palacios-Fonseca, M. Velázquez-de-la-Rosa, P. Rodríguez-Montero, A. De-Roa-Campoy, E. Valadez-Campos, M. O. Arias-Estrada, J. Peña-Saint-Martín, B. Rodríguez-Pedroza, I. Gómez-Arista, M. Juárez-Gama, K. Gottschalk, & I. C. Medina-Carrillo* , 11

Knigge, C. OPTICAM: A Triple-Camera Optical System Designed to Explore the Fastest Timescales in Astronomy. *A. Castro, D. Altamirano, R. Michel, P. Gandhi, J. V. Hernández Santisteban, J. Echevarría, C. Tejada, C. Knigge, G. Sierra, E. Colorado, J. Hernández-Landa, D. Whiter, M. Middleton, B. García, G. Guisa, & N. Castro Segura*, 363

Libeskind, N. Substructure Formation in Tidal Streams of Galactic Minor Mergers. *D. A. Noreña, J. C. Muñoz-Cuartas, L. F. Quiroga, & N. Libeskind*, 273

López-Caraballo, C. H. Millimeter and Far-IR Study of the IRDC SDC 341.232-0.268. *M. M. Vazzano, C. E. Cappa, M. Rubio, V. Firpo, C. H. López-Caraballo, & N. U. Duronea*, 289

López-Corona, O. Dynamics of clusters of galaxies with extended $f(\chi)$ gravity. *T. Bernal, O. López-Corona, & S. Mendoza*, 237

Matías Schneiter, E. 3D Hydrodynamic Numerical Models for Nebulae Around Runaway Wolf-Rayet Stars. *J. Reyes-Iturbide, Pablo F. Velázquez, M. Rosado, E. Matías Schneiter, & I. Ramírez-Ballinas*, 211

Martignoni, M. Multicolor Study of V1009 Per, a Close Binary System at the Beginning of the Overcontact Phase, and of CRTS J031642.2+332639, a New Binary System in the Same Field. *R. Michel, F. Acerbi, C. Barani, & M. Martignoni*, 65

Martínez-Piñón, F. A new method for actively tuning FBG's to particular infrared wavelengths for OH emission lines suppression . *R. Benítez-Álvarez, F. Martínez-Piñón, & V. G. Orlov*, 351

Medina-Carrillo, I. C. A Solar Mid-Infrared Telescope. *J. E. Mendoza-Torres, J. S. Palacios-Fonseca, M. Velázquez-de-la-Rosa, P. Rodríguez-Montero, A. De-Roa-Campoy, E. Valadez-Campos, M. O. Arias-Estrada, J. Peña-Saint-Martín, B. Rodríguez-Pedroza, I. Gómez-Arista, M. Juárez-Gama, K. Gottschalk, & I. C. Medina-Carrillo* , 11

Mendoza, S. Dynamics of clusters of galaxies with extended $f(\chi)$ gravity. *T. Bernal, O. López-Corona, & S. Mendoza*, 237

Mendoza-Torres, J. E. A Solar Mid-Infrared Telescope. *J. E. Mendoza-Torres, J. S. Palacios-Fonseca, M. Velázquez-de-la-Rosa, P. Rodríguez-Montero, A. De-Roa-Campoy, E. Valadez-Campos, M. O. Arias-Estrada, J. Peña-Saint-Martín, B. Rodríguez-Pedroza, I. Gómez-Arista, M. Juárez-Gama, K. Gottschalk, & I. C. Medina-Carrillo* , 11

Michel, R. Extensive Photometry of V1838 Aql During the 2013 Superoutburst. *J. Echevarría, E. de Miguel, J. V. Hernández Santisteban, R. Costero, R. Michel, L. J. Sánchez, J. Olivares, A. Ruelas-Mayorga, D. González-Buitrago, J. L. Jones, A. Oskanen, W. Goff, J. Ulowetz, G. Bolt, R. Sabo, F.-J. Hambsch, D. Slauson, & W. Stein* , 21

Michel, R. Multicolor Study of V1009 Per, a Close Binary System at the Beginning of the Overcontact Phase, and of CRTS J031642.2+332639, a New Binary System in the Same Field. *R. Michel, F. Acerbi, C. Barani, & M. Martignoni*, 65

Michel, R. OPTICAM: A Triple-Camera Optical System Designed to Explore the Fastest Timescales in Astronomy. *A. Castro, D. Altamirano, R. Michel, P. Gandhi, J. V. Hernández Santisteban, J. Echevarría, C. Tejada, C. Knigge, G. Sierra, E. Colorado, J. Hernández-Landa, D. Whiter, M. Middleton, B. García, G. Guisa, & N. Castro Segura*, 363

Middleton, M. OPTICAM: A Triple-Camera Optical System Designed to Explore the Fastest Timescales in Astronomy. *A. Castro, D. Altamirano, R. Michel, P. Gandhi, J. V. Hernández Santisteban, J. Echevarría, C. Tejada, C. Knigge, G. Sierra, E. Colorado, J. Hernández-Landa, D. Whiter, M. Middleton, B. García, G. Guisa, & N. Castro Segura*, 363

Morisset, C. Extensive Online Shock Model Database. *A. Alarie & C. Morisset*, 377

Muñoz-Cuartas, J. C. Substructure Formation in Tidal Streams of Galactic Minor Mergers. *D. A. Noreña, J. C. Muñoz-Cuartas, L. F. Quiroga, & N. Libeskind*, 273

Noreña, D. A. Substructure Formation in Tidal Streams of Galactic Minor Mergers. *D. A. Noreña, J. C. Muñoz-Cuartas, L. F. Quiroga, & N. Libeskind*, 273

Noriega-Crespo, A. The HH34 Jet/Counterjet System at 1.5 and 4.5μm. *A. C. Raga, B. Reipurth, & A. Noriega-Crespo*, 117

Odo, F. C. Relativistic Beaming Effects and Structural Asymmetries in Highly Asymmetric Double Radio Sources. *A. J. Alhassan, A. A. Ubachukwu, F. C. Odo, & C. C. Onuchukwu*, 151

Olivares, J. Extensive Photometry of V1838 Aql During the 2013 Superoutburst. *J. Echevarría, E. de Miguel, J. V. Hernández Santisteban, R. Costero, R. Michel, L. J. Sánchez, J. Olivares, A. Ruelas-Mayorga, D. González-Buitrago, J. L. Jones, A. Oskanen, W. Goff, J. Ulowetz, G. Bolt, R. Sabo, F.-J. Hambsch, D. Slauson, & W. Stein* , 21

Onuchukwu, C. C. Relativistic Beaming Effects and Structural Asymmetries in Highly Asymmetric Double Radio Sources. *A. J. Alhassan, A. A. Ubachukwu, F. C. Odo, & C. C. Onuchukwu*, 151

Onuchukwu, C. C. Selection Effects and Structural Symmetries in the Orientation Based Unified Scheme. *C. C. Onuchukwu & A. A. Ubachukwu*, 105

Orlov, V. G. A new method for actively tuning FBG's to particular infrared wavelengths for OH emission lines suppression . *R. Benítez-Álvarez, F. Martínez-Piñón, & V. G. Orlov*, 351

Oskanen, A. Extensive Photometry of V1838 Aql During the 2013 Superoutburst. *J. Echevarría, E. de Miguel, J. V. Hernández Santisteban, R. Costero, R. Michel, L. J. Sánchez, J. Olivares, A. Ruelas-Mayorga, D. González-Buitrago, J. L. Jones, A. Oskanen, W. Goff, J. Ulowetz, G. Bolt, R. Sabo, F.-J. Hambsch, D. Slauson, & W. Stein* , 21

Page, D. Multiwavelength Observations of MASTER OT 075353.88+174907.6: A Likely Superoutburst of a Long Period Dwarf Nova System. *A. S. Parikh, J. V. Hernández Santisteban, R. Wijnands, & D. Page*, 55

Palacios-Fonseca, J. S. A Solar Mid-Infrared Telescope. *J. E. Mendoza-Torres, J. S. Palacios-Fonseca, M. Velázquez-de-la-Rosa, P. Rodríguez-Montero, A. De-Roa-Campoy, E. Valadez-Campos, M. O. Arias-Estrada, J. Peña-Saint-Martín, B. Rodríguez-Pedroza, I. Gómez-Arista, M. Juárez-Gama, K. Gottschalk, & I. C. Medina-Carrillo* , 11

Pani, A. Some Remarks on the Open Cluster Upgren 1 Using $uvby - \beta$ Photoelectric Photometry. *J. H. Peña, A. Rentería, H. Huepa, & A. Pani*, 221

Parikh, A. S. Multiwavelength Observations of MASTER OT 075353.88+174907.6: A Likely Superoutburst of a Long Period Dwarf Nova System. *A. S. Parikh, J. V. Hernández Santisteban, R. Wijnands, & D. Page*, 55

Peña, J. H. On the Nature of the HADS Star V2455 Cyg. *J. H. Peña, A. Rentería, C. Villarreal, & D. S. Piña*, 193

Peña, J. H. Some Remarks on the Open Cluster Upgren 1 Using $uvby-\beta$ Photoelectric Photometry. *J. H. Peña, A. Rentería, H. Huepa, & A. Pani*, 221

Peña, J. H. Study of the Open Cluster NGC 1528 Through $uvby-\beta$ Photoelectric Photometry. *J. H. Peña, J. Calderón, & D. S. Piña*, 203

Peña, M. Metallicity Gradients in M31, M 33, NGC 300 and the Milky Way Using Abundances of Different Elements. *M. Peña & S. N. Flores-Durán*, 255

Peña-Saint-Martín, J. A Solar Mid-Infrared Telescope. *J. E. Mendoza-Torres, J. S. Palacios-Fonseca, M. Velázquez-de-la-Rosa, P. Rodríguez-Montero, A. De-Roa-Campoy, E. Valadez-Campos, M. O. Arias-Estrada, J. Peña-Saint-Martín, B. Rodríguez-Pedroza, I. Gómez-Arista, M. Juárez-Gama, K. Gottschalk, & I. C. Medina-Carrillo* , 11

Pérez-Rendón, B. Enhanced Mass Loss Rates in Red Supergiants and Their Impact on the Circumstellar Medium. *L. Hernández-Cervantes, B. Pérez-Rendón, A. Santillán, G. García-Segura, & C. Rodríguez-Ibarra*, 161

Piña, D. S. On the Nature of the HADS Star V2455 Cyg. *J. H. Peña, A. Rentería, C. Villarreal, & D. S. Piña*, 193

Piña, D. S. Study of the Open Cluster NGC 1528 Through $uvby-\beta$ Photoelectric Photometry. *J. H. Peña, J. Calderón, & D. S. Piña*, 203

Prado, A. F. B. A. Optimal Trajectories to Kuiper Belt Objects. *D. M. Sanchez, A. A. Sukhanov, & A. F. B. A. Prado*, 39

Prado, A. F. B. A. Searching for Mid-Range Planar Orbits to Observe Deimos. *M. P. O. Cavalca, A. F. B. A. Prado, V. M. Gomes, & D. M. Sanchez*, 305

Puerari, I. Chaos in Growing Bar Models. *L. A. Caritá, I. Rodrigues, I. Puerari, & L. E. C. A. Schiavo*, 321

Quiroga, L. F. Substructure Formation in Tidal Streams of Galactic Minor Mergers. *D. A. Noreña, J. C. Muñoz-Cuartas, L. F. Quiroga, & N. Libeskind*, 273

Raga, A. C. The HH34 Jet/Counterjet System at 1.5 and 4.5μm. *A. C. Raga, B. Reipurth, & A. Noriega-Crespo*, 117

Ramírez-Ballinas, I. 3D Hydrodynamic Numerical Models for Nebulae Around Runaway Wolf-Rayet Stars. *J. Reyes-Iturbide, Pablo F. Velázquez, M. Rosado, E. Matías Schneiter, & I. Ramírez-Ballinas*, 211

Reipurth, B. The HH34 Jet/Counterjet System at 1.5 and 4.5μm. *A. C. Raga, B. Reipurth, & A. Noriega-Crespo*, 117

Rentería, A. On the Nature of the HADS Star V2455 Cyg. *J. H. Peña, A. Rentería, C. Villarreal, & D. S. Piña*, 193

Rentería, A. Some Remarks on the Open Cluster Upgren 1 Using $uvby-\beta$ Photoelectric Photometry. *J. H. Peña, A. Rentería, H. Huepa, & A. Pani*, 221

Reyes-Iturbide, J. 3D Hydrodynamic Numerical Models for Nebulae Around Runaway Wolf-Rayet Stars. *J. Reyes-Iturbide, Pablo F. Velázquez, M. Rosado, E. Matías Schneiter, & I. Ramírez-Ballinas*, 211

Rodrigues, I. Chaos in Growing Bar Models. *L. A. Caritá, I. Rodrigues, I. Puerari, & L. E. C. A. Schiavo*, 321

Rodríguez-Ibarra, C. Enhanced Mass Loss Rates in Red Supergiants and Their Impact on the Circumstellar Medium. *L. Hernández-Cervantes, B. Pérez-Rendón, A. Santillán, G. García-Segura, & C. Rodríguez-Ibarra*, 161

Rodríguez-Montero, P. A Solar Mid-Infrared Telescope. *J. E. Mendoza-Torres, J. S. Palacios-Fonseca, M. Velázquez-de-la-Rosa, P. Rodríguez-Montero, A. De-Roa-Campoy, E. Valadez-Campos, M. O. Arias-Estrada, J. Peña-Saint-Martín, B. Rodríguez-Pedroza, I. Gómez-Arista, M. Juárez-Gama, K. Gottschalk, & I. C. Medina-Carrillo* , 11

Rodríguez-Pedroza, B. A Solar Mid-Infrared Telescope. *J. E. Mendoza-Torres, J. S. Palacios-Fonseca, M. Velázquez-de-la-Rosa, P. Rodríguez-Montero, A. De-Roa-Campoy, E. Valadez-Campos, M. O. Arias-Estrada, J. Peña-Saint-Martín, B. Rodríguez-Pedroza, I. Gómez-Arista, M. Juárez-Gama, K. Gottschalk, & I. C. Medina-Carrillo* , 11

Rosado, M. 3D Hydrodynamic Numerical Models for Nebulae Around Runaway Wolf-Rayet Stars. *J. Reyes-Iturbide, Pablo F. Velázquez, M. Rosado, E. Matías Schneiter, & I. Ramírez-Ballinas*, 211

Rubio, M. Millimeter and Far-IR Study of the IRDC SDC 341.232-0.268. *M. M. Vazzano, C. E. Cappa, M. Rubio, V. Firpo, C. H. López-Caraballo, & N. U. Duronea*, 289

Ruelas-Mayorga, A. Extensive Photometry of V1838 Aql During the 2013 Superoutburst. *J. Echevarría, E. de Miguel, J. V. Hernández Santisteban, R. Costero, R. Michel, L. J. Sánchez, J. Olivares, A. Ruelas-Mayorga, D. González-Buitrago, J. L. Jones, A. Oskanen, W. Goff, J. Ulowetz, G. Bolt, R. Sabo, F.-J. Hambsch, D. Slauson, & W. Stein* , 21

Sabo, R. Extensive Photometry of V1838 Aql During the 2013 Superoutburst. *J. Echevarría, E. de Miguel, J. V. Hernández Santisteban, R. Costero, R. Michel, L. J. Sánchez, J. Olivares, A. Ruelas-Mayorga, D.*

González-Buitrago, J. L. Jones, A. Oskanen, W. Goff, J. Ulowetz, G. Bolt, R. Sabo, F.-J. Hambsch, D. Slauson, & W. Stein , 21

Salas, L. An Alternative Approach to the Finger of God in Large Scale Structures. *L. Salas & I. Cruz-González*, 93

Sanchez, D. M. Optimal Trajectories to Kuiper Belt Objects. *D. M. Sanchez, A. A. Sukhanov, & A. F. B. A. Prado*, 39

Sanchez, D. M. Searching for Mid-Range Planar Orbits to Observe Deimos. *M. P. O. Cavalca, A. F. B. A. Prado, V. M. Gomes, & D. M. Sanchez*, 305

Sánchez, L. J. Extensive Photometry of V1838 Aql During the 2013 Superoutburst. *J. Echevarría, E. de Miguel, J. V. Hernández Santisteban, R. Costero, R. Michel, L. J. Sánchez, J. Olivares, A. Ruelas-Mayorga, D. González-Buitrago, J. L. Jones, A. Oskanen, W. Goff, J. Ulowetz, G. Bolt, R. Sabo, F.-J. Hambsch, D. Slauson, & W. Stein* , 21

Santillán, A. Enhanced Mass Loss Rates in Red Supergiants and Their Impact on the Circumstellar Medium. *L. Hernández-Cervantes, B. Pérez-Rendón, A. Santillán, G. García-Segura, & C. Rodríguez-Ibarra*, 161

Scarfe, C. D. Three Spectroscopic Binaries in the Bright Star Catalog Supplement. *C. D. Scarfe*, 131

Schiavo, L. E. C. A. Chaos in Growing Bar Models. *L. A. Caritá, I. Rodrigues, I. Puerari, & L. E. C. A. Schiavo*, 321

Schröder, K.-P. Interstellar Absorption Towards the Novae V339 Del and V5668 Sgr. *D. Jack & K.-P. Schröder*, 141

Sierra, G. OPTICAM: A Triple-Camera Optical System Designed to Explore the Fastest Timescales in Astronomy. *A. Castro, D. Altamirano, R. Michel, P. Gandhi, J. V. Hernández Santisteban, J. Echevarría, C. Tejada, C. Knigge, G. Sierra, E. Colorado, J. Hernández-Landa, D. Whiter, M. Middleton, B. García, G. Guisa, & N. Castro Segura*, 363

Slauson, D. Extensive Photometry of V1838 Aql During the 2013 Superoutburst. *J. Echevarría, E. de Miguel, J. V. Hernández Santisteban, R. Costero, R. Michel, L. J. Sánchez, J. Olivares, A. Ruelas-Mayorga, D. González-Buitrago, J. L. Jones, A. Oskanen, W. Goff, J. Ulowetz, G. Bolt, R. Sabo, F.-J. Hambsch, D. Slauson, & W. Stein* , 21

Stein, W. Extensive Photometry of V1838 Aql During the 2013 Superoutburst. *J. Echevarría, E. de Miguel, J. V. Hernández Santisteban, R. Costero, R. Michel, L. J. Sánchez, J. Olivares, A. Ruelas-Mayorga, D. González-Buitrago, J. L. Jones, A. Oskanen, W. Goff, J. Ulowetz, G. Bolt, R. Sabo, F.-J. Hambsch, D. Slauson, & W. Stein* , 21

Sukhanov, A. A. Optimal Trajectories to Kuiper Belt Objects. *D. M. Sanchez, A. A. Sukhanov, & A. F. B. A. Prado*, 39

Tejada, C. OPTICAM: A Triple-Camera Optical System Designed to Explore the Fastest Timescales in Astronomy. *A. Castro, D. Altamirano, R. Michel, P. Gandhi, J. V. Hernández Santisteban, J. Echevarría, C. Tejada, C. Knigge, G. Sierra, E. Colorado, J. Hernández-Landa, D. Whiter, M. Middleton, B. García, G. Guisa, & N. Castro Segura*, 363

Ubachukwu, A. A. Relativistic Beaming Effects and Structural Asymmetries in Highly Asymmetric Double Radio Sources. *A. J. Alhassan, A. A. Ubachukwu, F. C. Odo, & C. C. Onuchukwu*, 151

Ubachukwu, A. A. Selection Effects and Structural Symmetries in the Orientation Based Unified Scheme. *C. C. Onuchukwu & A. A. Ubachukwu*, 105

Ulowetz, J. Extensive Photometry of V1838 Aql During the 2013 Superoutburst. *J. Echevarría, E. de Miguel, J. V. Hernández Santisteban, R. Costero, R. Michel, L. J. Sánchez, J. Olivares, A. Ruelas-Mayorga, D. González-Buitrago, J. L. Jones, A. Oskanen, W. Goff, J. Ulowetz, G. Bolt, R. Sabo, F.-J. Hambsch, D. Slauson, & W. Stein* , 21

Urama, J. O. Entrainment Factor of Individual Glitch Fractional Moment of Inertia. *I. O. Eya, J. O. Urama, & A. E. Chukwude*, 3

Valadez-Campos, E. A Solar Mid-Infrared Telescope. *J. E. Mendoza-Torres, J. S. Palacios-Fonseca, M. Velázquez-de-la-Rosa, P. Rodríguez-Montero, A. De-Roa-Campoy, E. Valadez-Campos, M. O. Arias-Estrada, J. Peña-Saint-Martín, B. Rodríguez-Pedroza, I. Gómez-Arista, M. Juárez-Gama, K. Gottschalk, & I. C. Medina-Carrillo* , 11

Valenzuela, Octavio Obituary – Bárbara Pichardo. *O. Valenzuela*, 125

Vazzano, M. M. Millimeter and Far-IR Study of the IRDC SDC 341.232-0.268. *M. M. Vazzano, C. E. Cappa, M. Rubio, V. Firpo, C. H. López-Caraballo, & N. U. Duronea*, 289

Velázquez, Pablo F. 3D Hydrodynamic Numerical Models for Nebulae Around Runaway Wolf-Rayet Stars. *J. Reyes-Iturbide, Pablo F. Velázquez, M. Rosado, E. Matías Schneiter, & I. Ramírez-Ballinas*, 211

Velázquez-de-la-Rosa, M. A Solar Mid-Infrared Telescope. *J. E. Mendoza-Torres, J. S. Palacios-Fonseca, M. Velázquez-de-la-Rosa, P. Rodríguez-Montero, A. De-Roa-Campoy, E. Valadez-Campos, M. O. Arias-Estrada, J. Peña-Saint-Martín, B. Rodríguez-Pedroza, I. Gómez-Arista, M. Juárez-Gama, K. Gottschalk, & I. C. Medina-Carrillo* , 11

Villanueva, Y. Minimizing Fuel consumption in Orbit Transfers using Universal Variable and Particle Swarm Optimization. *L. M. Echeverry & Y. Villanueva*, 177

Villarreal, C. On the Nature of the HADS Star V2455 Cyg. *J. H. Peña, A. Rentería, C. Villarreal, & D. S. Piña*, 193

Whiter, D. OPTICAM: A Triple-Camera Optical System Designed to Explore the Fastest Timescales in Astronomy. *A. Castro, D. Altamirano, R. Michel, P. Gandhi, J. V. Hernández Santisteban, J. Echevarría, C. Tejada, C. Knigge, G. Sierra, E. Colorado, J. Hernández-Landa, D. Whiter, M. Middleton, B. García, G. Guisa, & N. Castro Segura*, 363

Wijnands, R. Multiwavelength Observations of MASTER OT 075353.88+174907.6: A Likely Superoutburst of a Long Period Dwarf Nova System. *A. S. Parikh, J. V. Hernández Santisteban, R. Wijnands, & D. Page*, 55

Yoldaş, E. On the Chromospheric Activity Nature of a Low-Mass Close Binary: KIC 12004834. *E. Yoldaş & H. A. Dal*, 73

La *Revista Mexicana de Astronomía y Astrofísica*, fundada en 1974, publica trabajos originales de investigación en todas las ramas de la astronomía, astrofísica y temas vinculados a éstas. Se editan dos números por año y su distribución es gratuita a todas las instituciones relacionadas con los campos cubiertos por esta revista.

La política editorial de la *RMxAA* consiste en enviar a arbitrar los artículos recibidos a especialistas en el campo. Los interesados en publicar en nuestra revista deberán enviar por correo electrónico, a la dirección rmaa@astro.unam.mx, la versión completa de su artículo en formato PostScript o PDF y el archivo LaTeX. Estos archivos deberán ir acompañados de una carta de presentación. Todos los trabajos deben ser preparados en inglés usando la versión más reciente del macro en LaTeX de la *RMxAA* "rmaa.cls" (disponible en https://www.irya.unam.mx/rmaa/). Se requiere un "Abstract" no mayor que 12 líneas, y un "Resumen" en español (este último podrá ser provisto por los editores de ser necesario); también se incluirán de 1 a 6 palabras clave ("Keywords") de la lista de las revistas astronómicas internacionales. Se requiere que cada tabla incluida en el texto esté numerada y con título; las figuras deberán estar en formato PostScript (.ps) o PostScript encapsulado (.eps), estar numeradas y con leyenda explicativa. Se requiere que cada tabla y figura estén mencionadas en el texto. El estilo de las referencias sigue las normas astronómicas internacionales recientes. Para mayor información sobre el estilo de la *RMxAA* se puede consultar el archivo de ejemplo que viene incluido en los macros. La publicación es gratuita para los autores.

En 1995 se inició la Serie de Conferencias de la *Revista Mexicana de Astronomía y Astrofísica*, dedicada a la publicación de las memorias de reuniones astrónomicas efectuadas en México y en otros países del continente. Hasta 1994 las memorias de reuniones astronómicas de la región se publicaron como volúmenes especiales de la *RMxAA*.

Las condiciones de publicación de cada volumen de las memorias de conferencias serán el resultado de un convenio establecido entre la *RMxAC* y los organizadores de cada evento. Los detalles de la publicación, que incluyen fechas y extensión de los textos, serán anunciados por los editores de cada conferencia. Las contribuciones extensas estarán en inglés con un resumen en español (o portugués en caso de las Reuniones regionales). Los resúmenes de las reuniones que no son temáticas tendrán una extensión máxima de 300 palabras incluyendo título, autores y afiliación; serán exclusivamente en inglés. Los macros LaTeX para las memorias se encuentran en http://www.astroscu.unam.mx/~rmaa. Todas las contribuciones y resúmenes deberán estar en estos formatos.

Se concede permiso a los autores de artículos y libros científi-cos para citar trabajos publicados en la *RMxAA* y en la *RMxAC* siempre y cuando se dé la referencia completa. También se permite la reproducción de figuras y tablas bajo las mismas condiciones.

La *RMxAA* aparece indexada en Current Contents, Science Citation Index, Astronomy and Astrophysics Abstracts, Physics Briefs, Publicaciones Científicas en América Latina, Astronomy and Astrophysics Monthly Index, PERIODICA, RedALyC, Latindex y SciELO.

The *Revista Mexicana de Astronomía y Astrofísica*, founded in 1974, publishes original research papers in all branches of astronomy, astrophysics and closely related fields. Two numbers per year are issued and are distributed free of charge to all institutions engaged in the fields covered by the *RMxAA*.

All papers received by the *RMxAA* are sent to a specialist in the field for refereeing. Authors interested in publishing in the *RMxAA* should send their papers to the e-mail address rmaa@astro.unam.mx, in PostScript or PDF format, along with the LaTeX file. A submission letter should also be sent. Papers should be prepared in English, using the most recent version of the *RMxAA* LaTeX document class "rmaa.cls" (available from https://www.irya.unam.mx/rmaa/). An "Abstract" of at most 12 lines is required, as well as a "Resumen" in Spanish. The latter can be provided by the Editors, if necessary. A total of six or fewer "Keywords", taken from the lists of international astronomical journals should be included. Tables should be numbered and include a title. Figures should be submitted in PostScript (.ps) or Encapsulated PostScript (.eps) format, should be numbered, and should include a caption. Both tables and figures should be mentioned in the text. The style of the references follows recent international astronomical usage. For more information about the style norms of *RMxAA* please consult the example included in the LaTeX package. Publication in *RMxAA* is free of charge to authors.

The Conference Series of *Revista Mexicana de Astronomía y Astrofísica* was founded in 1995 to publish the proceedings of astronomical meetings held in Mexico and other countries throughout the continent. Until 1994 such proceedings had been published as special issues of *Revista Mexicana de Astronomía y Astrofísica*.

Conditions of publication of proceedings of each conference will be the result of a mutual agreement between the *RMxAC* and the organizing committee. Details of publication, including length of papers, will be announced by the editors of each event. The extensive contributions should be in English, and should include an abstract in Spanish (or Portuguese for regional meetings). The abstracts of non-thematic meetings should not exceed 300 words including title, authors, and affiliation; they should be exclusively in English. The LaTeX templates specially prepared for proceedings can be obtained at http://www.astroscu.unam.mx/~rmaa; all papers should be submitted in this format.

Authors of scientific papers and books may quote articles published both in *RMxAA* and *RMxAC* provided that a complete reference to the source is given. Reproduction of figures and tables is also permitted on the same basis.

The *RMxAA* is indexed in Current Contents, Science Citation Index, Astronomy and Astrophysics Abstracts, Physics Briefs, Publicaciones Científicas en América Latina, Astronomy and Astrophysics Monthly Index, PERIODICA, RedALyC, Latindex, and SciELO.